

Novel Systems and Methods for Quantum Communication, Quantum Computation, and Quantum Simulation

A dissertation presented

by

Alexey Vyacheslavovich Gorshkov

to

The Department of Physics

in partial fulfillment of the requirements

for the degree of

Doctor of Philosophy

in the subject of

Physics

Harvard University

Cambridge, Massachusetts

November 2009

©2009 - Alexey Vyacheslavovich Gorshkov

All rights reserved.

Thesis advisor
Mikhail D. Lukin

Author
Alexey Vyacheslavovich Gorshkov

Novel Systems and Methods for Quantum Communication, Quantum Computation, and Quantum Simulation

Abstract

Precise control over quantum systems can enable the realization of fascinating applications such as powerful computers, secure communication devices, and simulators that can elucidate the physics of complex condensed matter systems. However, the fragility of quantum effects makes it very difficult to harness the power of quantum mechanics. In this thesis, we present novel systems and tools for gaining fundamental insights into the complex quantum world and for bringing practical applications of quantum mechanics closer to reality.

We first optimize and show equivalence between a wide range of techniques for storage of photons in atomic ensembles. We describe experiments demonstrating the potential of our optimization algorithms for quantum communication and computation applications. Next, we combine the technique of photon storage with strong atom-atom interactions to propose a robust protocol for implementing the two-qubit photonic phase gate, which is an important ingredient in many quantum computation and communication tasks.

In contrast to photon storage, many quantum computation and simulation applications require individual addressing of closely-spaced atoms, ions, quantum dots, or solid state defects. To meet this requirement, we propose a method for coherent optical far-field manipulation of quantum systems with a resolution that is not limited by the wavelength of radiation.

While *alkali* atoms are currently the system of choice for photon storage and many other applications, we develop new methods for quantum information processing and quantum simulation with ultracold *alkaline-earth* atoms in optical lattices. We show how multiple qubits can be encoded in individual alkaline-earth atoms and harnessed for quantum computing and precision measurements applications. We also demonstrate that alkaline-earth atoms can be used to simulate highly symmetric systems exhibiting spin-orbital interactions and capable of providing valuable insights into strongly correlated physics of transition metal oxides, heavy fermion materials, and spin liquid phases.

While ultracold atoms typically exhibit only short-range interactions, numerous exotic phenomena and practical applications require long-range interactions, which can be achieved with ultracold polar molecules. We demonstrate the possibility to engineer a repulsive interaction between polar molecules, which allows for the suppression of inelastic collisions, efficient evaporative cooling, and the creation of novel phases of polar molecules.

Contents

Title Page	i
Abstract	iii
Table of Contents	iv
List of Figures	x
List of Tables	xiii
Citations to Previously Published Work	xiv
Acknowledgments	xvii
Dedication	xx
1 Introduction, Motivation, and Outline	1
1.1 Quantum Systems	3
1.2 Applications of Quantum Mechanics	3
1.2.1 Quantum Communication	4
1.2.2 Quantum Computation	5
1.2.3 Quantum Simulation	6
1.2.4 Other Applications	7
1.3 Outline of the Thesis	7
1.3.1 Quantum Memory for Photons (Chapters 2 and 3)	7
1.3.2 Quantum Gate between Two Photons (Chapter 4)	8
1.3.3 Addressing Quantum Systems with Subwavelength Resolution (Chapter 5)	9
1.3.4 Alkaline-Earth Atoms (Chapters 6 and 7)	10
1.3.5 Diatomic Polar Molecules (Chapter 8)	10
2 Optimal Photon Storage in Atomic Ensembles: Theory	11
2.1 Introduction	11
2.2 Model	13
2.3 Optimal Retrieval	14
2.4 Optimal Storage	15
2.5 Adiabatic Limit	16
2.6 Fast Limit	17
2.7 Iterative Time-Reversal-Based Optimization	17
2.8 Conclusion and Outlook	18

3	Optimal Photon Storage in Atomic Ensembles: Experiment	20
3.1	Introduction	20
3.2	Experimental Setup	22
3.3	Optimization with respect to the Input Pulse	23
3.3.1	Basic Idea	24
3.3.2	Experimental Results	24
3.3.3	Comparison to Theory	26
3.3.4	Conclusion and Outlook	27
3.4	Optimization with respect to the Control Pulse	28
3.4.1	Motivation	28
3.4.2	Experimental Results	29
3.4.3	Conversion of a Single Photon into a Time-Bin Qubit	32
3.4.4	Conclusion and Outlook	33
4	Photonic Phase Gate via an Exchange of Fermionic Spin Waves in a Spin Chain	34
4.1	Introduction	34
4.2	Details of the Protocol	36
4.3	Experimental Realizations	38
4.4	Imperfections	39
4.5	Extensions	39
4.6	Conclusion	40
5	Coherent Quantum Optical Control with Subwavelength Resolution	41
5.1	Introduction and Basic Idea	41
5.2	Detailed Analysis on the Example of a Single-Qubit Phase Gate	43
5.2.1	Gate Protocol	43
5.2.2	Errors due to Spontaneous Emission and Non-Adiabaticity	44
5.2.3	Error due to Dipole-Dipole Interactions	44
5.2.4	Errors due to Imperfect Control-Field Nodes and Finite Atom Localization	45
5.2.5	Error Budget	46
5.2.6	Approaches to Node Creation	46
5.2.7	Error Estimates for Ions in Paul Traps, Solid-State Qubits, and Neutral Atoms in Optical Lattices	47
5.3	Advantages of Our Addressability Technique	48
5.4	Conclusions and Outlook	48
6	Alkaline-Earth-Metal Atoms as Few-Qubit Quantum Registers	49
6.1	Introduction	49
6.2	The Register	50
6.3	Interregister Gate	51

6.4	Electronic-Qubit Detection	53
6.5	Conclusion	56
7	Two-Orbital SU(N) Magnetism with Ultracold Alkaline-Earth Atoms	57
7.1	Introduction	57
7.2	Many-Body Dynamics of Alkaline-Earth Atoms in an Optical Lattice	58
7.3	Symmetries of the Hamiltonian	60
7.4	Spin Hamiltonians	61
7.5	The Kondo Lattice Model (KLM)	65
7.6	Experimental Accessibility	67
7.7	Outlook	68
8	Suppression of Inelastic Collisions between Polar Molecules with a Repulsive Shield	70
8.1	Introduction and Basic Idea	70
8.2	Detailed Analysis within the Born-Oppenheimer Approximation . . .	71
8.3	Processes Beyond the Born-Oppenheimer Approximation	75
8.4	Effects of Three-Body Collisions	76
8.5	Conclusions and Outlook	77
	Bibliography	78
A	Optimal Photon Storage in Atomic Ensembles: Cavity Model	109
A.1	Introduction	109
A.2	Figure of merit	116
A.3	Model	117
A.4	Optimal Strategy for Storage and Retrieval	119
A.5	Adiabatic Retrieval and Storage	121
A.5.1	Adiabatic Retrieval	121
A.5.2	Adiabatic Storage	124
A.5.3	Adiabaticity Conditions	125
A.6	Fast Retrieval and Storage	128
A.7	Summary	130
A.8	Omitted Details	131
A.8.1	Details of the Model and the Derivation of the Equations of Motion	131
A.8.2	Shaping the Control Field for the Optimal Adiabatic Storage	135
B	Optimal Photon Storage in Atomic Ensembles: Free-Space Model	137
B.1	Introduction	137
B.2	Model	139
B.3	Optimal Retrieval	143

B.4	Optimal Storage From Time Reversal: General Proof	146
B.5	Time Reversal as a Tool for Optimizing Quantum State Mappings . .	148
B.6	Adiabatic Retrieval and Storage	152
B.6.1	Adiabatic Retrieval	152
B.6.2	Adiabatic Storage	158
B.6.3	Storage Followed by Retrieval	162
B.6.4	Adiabaticity Conditions	164
B.6.5	Effects of Nonzero Spin-Wave Decay	166
B.7	Fast Retrieval and Storage	168
B.8	Effects of Metastable State Nondegeneracy	170
B.9	Summary	173
B.10	Omitted Details	174
B.10.1	Details of the Model and Derivation of the Equations of Motion	174
B.10.2	Position Dependence of Loss	178
B.10.3	Implementation of the Inverse Propagator using Time Reversal	179
B.10.4	Proof of Convergence of Optimization Iterations to the Opti- mum	181
B.10.5	Shaping the Control Field for the Optimal Adiabatic Storage	182
C	Optimal Photon Storage in Atomic Ensembles: Effects of Inhomogeneous Broadening	186
C.1	Introduction	186
C.2	Inhomogeneous Broadening with Redistribution between Frequency Classes during the Storage Time	187
C.2.1	Model	187
C.2.2	Retrieval and Storage with Doppler Broadening	191
C.3	Inhomogeneous Broadening without Redistribution between Frequency Classes during the Storage Time	197
C.3.1	Setup and Solution	198
C.3.2	Storage Followed by Backward Retrieval	201
C.3.3	Storage Followed by Backward Retrieval with the Reversal of the Inhomogeneous Profile	203
C.4	Summary	210
C.5	Omitted Details	210
C.5.1	Independence of Free-Space Retrieval Efficiency from Control and Detuning	211
D	Optimal Photon Storage in Atomic Ensembles: Optimal Control Using Gradient Ascent	212
D.1	Introduction	212
D.2	Optimization with respect to the Storage Control Field	214
D.2.1	Cavity Model	215

D.2.2	Free-Space Model	222
D.3	Optimization with respect to the Input Field	226
D.4	Optimization with respect to the Inhomogeneous Profile	228
D.4.1	Cavity Model	228
D.4.2	Free-Space Model	230
D.5	Summary	232
D.6	Omitted Details	233
D.6.1	Derivation of the Adjoint Equations of Motion in the Cavity Model	233
D.6.2	Control Field Optimization in the Cavity Model: Generalization	234
D.6.3	Control Field Optimization in the Free-Space Model: Generalization to Storage Followed by Retrieval	236
D.6.4	Optimization with Respect to the Inhomogeneous Profile: Mathematical Details	237
E	Optimal Photon Storage in Atomic Ensembles: Experiment (Part II)	240
E.1	Introduction	240
E.2	Review of the Theory	241
E.3	Experimental Arrangements	244
E.4	Signal-Pulse Optimization	246
E.5	Control-Pulse Optimization	249
E.6	Dependence of Memory Efficiency on the Optical Depth	252
E.7	Conclusions	257
F	Appendices to Chapter 4	258
F.1	The Order t^4/U^3 Hamiltonian and the Error Estimate	258
F.2	Optimization of Pulse Width	261
F.3	Bethe Ansatz Solution	262
F.4	Implementation with Fermionic Atoms	263
G	Appendices to Chapter 7	264
G.1	Nuclear-Spin Independence of the Scattering Lengths	264
G.2	Likelihood of Lossy e - e Collisions and Possible Solutions	266
G.3	Experimental Tools Available for Alkaline-Earth Atoms	267
G.4	Enhanced Symmetries	267
G.5	Brief Review of Young Diagrams	269
G.6	The $(p, q) = (1, 1)$ Spin Hamiltonian and the Spin-1 Heisenberg Antiferromagnet	269
G.7	The Kugel-Khomskii Model and the Double-Well Phase Diagram	270
G.8	Double-Well Kugel-Khomskii and RKKY Experiments	271
G.9	Effects of Three-Body Recombination	274

G.10 The $(p, 0)$ Spin Hamiltonian with $n_A = n_B \neq N/2$	275
G.11 Physics Accessible with the Alkaline-Earth Kondo Lattice Model . . .	276

List of Figures

2.1	Λ -type medium and the storage setup	12
2.2	A Gaussian-like input mode, the corresponding optimal control field, and the optimal spin wave for several optical depths d	15
2.3	Maximum total efficiency for storage followed by backward or forward retrieval, as well as the total efficiency using a naïve square control pulse	18
3.1	Schematic of the Λ -type interaction scheme and the iterative signal-pulse optimization procedure	21
3.2	Iterative signal-pulse optimization procedure: experiment and theory	25
3.3	Convergence to the same optimal signal pulse independent of the initial pulse shape	26
3.4	Optimal signal pulses for different control field profiles and the corresponding efficiencies	27
3.5	Schematic of the three-level Λ interaction scheme and control and signal fields in pulse-shape-preserving storage	29
3.6	Optimal storage of any incoming pulse and its retrieval into any desired pulse shape	31
3.7	Optimal storage followed by retrieval into a time-bin qubit	32
4.1	Photonic two-qubit phase gate	35
5.1	3-level atomic level structure and the schematic of the setup	42
5.2	Single-qubit phase gate on atom 1	43
6.1	Relevant alkaline-earth-like level structure and the iterregister gate	50
6.2	Nuclear-spin-preserving electronic-qubit detection	54
7.1	Interaction parameters between g (green) and e (yellow) atoms loaded in the lowest vibrational state of the corresponding optical lattice	59
7.2	Young diagrams describing the irreducible representations of $SU(N)$ on individual sites	62
7.3	The ground-state phase diagram for the $SU(N=2)$ Kugel-Khomskii model restricted to two wells	63

7.4	Probing the phases of the SU(N) antiferromagnet on a 2D square lattice	65
7.5	Kondo lattice model for the case $N = 2$	66
8.1	Energy levels of $H_{\text{rot}}^{(i)}$ and a sketch for the cancelation of the dipole-dipole interaction	71
8.2	Born-Oppenheimer potentials in the limit $r \gg r_B$	73
8.3	Born-Oppenheimer potentials for $\hbar\Delta = 0.015B$ at $\theta = 0$ and the inelastic cross section σ_{in}	75
A.1	Λ -type medium	111
A.2	Breakdown of optimal adiabatic storage in a cavity at $TC\gamma \lesssim 10$	128
B.1	Storage, forward retrieval, and backward retrieval setup	142
B.2	Optimal modes $\tilde{S}_d(\tilde{z})$ to retrieve from (in the forward direction) at indicated values of d	145
B.3	Input mode $\mathcal{E}_{\text{in}}(t)$ and control fields $\Omega(t)$ that maximize for this $\mathcal{E}_{\text{in}}(t)$ the efficiency of resonant adiabatic storage	161
B.4	Maximum and typical total efficiencies	163
B.5	Optimal spin-wave mode to be used during storage followed by forward retrieval	164
B.6	Breakdown of optimal adiabatic storage in free space at $Td\gamma \lesssim 10$	165
B.7	Reduction in efficiency due to metastable state nondegeneracy	172
B.8	Optimal spin-wave modes in the presence of metastable state nondegeneracy	173
C.1	Λ -type medium coupled to a classical field and a quantum field	187
C.2	Optimal spin-wave modes to retrieve from in the presence of Doppler broadening with HWHM $\Delta_{\text{I}} = 88\gamma$	195
C.3	Error $1 - \eta$ as a function of unbroadened optical depth d	196
C.4	Optimal input modes for storage followed by backward retrieval	202
C.5	The optimal (smallest) error of fast storage followed by fast backward retrieval	204
C.6	Total efficiency of fast storage followed by fast backward retrieval as a function of $Td\gamma$ in the limit when $T\gamma \rightarrow 0$, $d \rightarrow \infty$, but $Td\gamma$ is finite	206
C.7	$\Delta_{\text{I}}T$ as a function of $Td\gamma$, where Δ_{I} is the optimal HWHM of the Gaussian (G) or Lorentzian (L) inhomogeneous profile	207
C.8	The total efficiency of storage followed by backward retrieval of the resonant Gaussian-like pulse of duration T of Eq. (C.43) with and without reversible inhomogeneous broadening	208
D.1	Λ -type medium coupled to a quantum field and a two-photon-resonant classical field	213

D.2	Adiabatic and optimal control fields for the storage of a Gaussian-like input mode	218
D.3	The total efficiency of storage followed by retrieval using adiabatic equations and gradient ascent to shape the storage control field . . .	220
D.4	Adiabatic and optimal control fields for the storage followed by backward retrieval of a Gaussian-like input mode in the free-space model .	224
D.5	The total efficiency of storage followed by backward retrieval for a Gaussian-like input mode using adiabatic equations and gradient ascent to shape the storage control field	225
D.6	Comparison of the efficiency for storage followed by retrieval in the cavity model with and without controlled reversible inhomogeneous broadening (CRIB)	229
D.7	Comparison of optimized homogeneous-line storage with storage based on CRIB	231
E.1	The three-level Λ scheme, as well as the schematic, and example control and signal fields during light storage	241
E.2	Experimental apparatus and ^{87}Rb D_1 line level structure	245
E.3	Iterative signal-pulse optimization	248
E.4	Optimal signal-pulse dependence on control field power	249
E.5	Control-pulse optimization	250
E.6	Optimal control pulses for eight different signal pulse shapes	252
E.7	Memory efficiency as a function of optical depth	253
E.8	Results of the optimization procedures for different optical depths . .	254
E.9	Resonant four-wave mixing	256
G.1	A general Young diagram	268
G.2	$(p,q) = (1,1)$ Young diagram	269
G.3	A schematic diagram describing the preparation of the double-well state $ e, \uparrow\rangle_L g, \downarrow\rangle_R$	272
G.4	Proof-of-principle experiment to probe RKKY interactions in an array of isolated double wells	273
G.5	Square-lattice valence-plaquette solid for $N = 4$	275

List of Tables

5.1 Error budget for the single-qubit phase gate. 46

Citations to Previously Published Work

Most of the Chapters and Appendices of this thesis have appeared in print elsewhere. Below is a list, by Chapter and Appendix number, of previously published work. We also list the work by the author that relates to the present thesis but is not covered in the thesis in detail for space reasons.

- Chapter 2: “Universal approach to optimal photon storage in atomic media,” A. V. Gorshkov, A. André, M. Fleischhauer, A. S. Sørensen, and M. D. Lukin, *Phys. Rev. Lett.* **98**, 123601 (2007).
- Chapter 3: “Optimal control of light pulse storage and retrieval,” I. Novikova, A. V. Gorshkov, D. F. Phillips, A. S. Sørensen, M. D. Lukin, and R. L. Walsworth, *Phys. Rev. Lett.* **98**, 243602 (2007) and “Optimal light storage with full pulse-shape control,” I. Novikova, N. B. Phillips, and A. V. Gorshkov, *Phys. Rev. A* **78**, 021802(R) (2008).
- Chapter 4: “Photonic phase gate via an exchange of fermionic spin waves in a spin chain,” A. V. Gorshkov, J. Otterbach, E. Demler, M. Fleischhauer, and M. D. Lukin, e-print arXiv:1001.0968 [quant-ph].
- Chapter 5: “Coherent quantum optical control with subwavelength resolution,” A. V. Gorshkov, L. Jiang, M. Greiner, P. Zoller, and M. D. Lukin, *Phys. Rev. Lett.* **100**, 093005 (2008).

Work related to Chapter 5 is also presented in

- “Anyonic interferometry and protected memories in atomic spin lattices”, L. Jiang, G. K. Brennen, A. V. Gorshkov, K. Hammerer, M. Hafezi, E. Demler, M. D. Lukin, and P. Zoller, *Nature Phys.* **4**, 482 (2008),
- “Far-field optical imaging and manipulation of individual spins with nanoscale resolution,” P. C. Maurer, J. R. Maze, P. L. Stanwix, L. Jiang, A. V. Gorshkov, B. Harke, J. S. Hodges, A. S. Zibrov, D. Twitchen, S. W. Hell, R. L. Walsworth, and M. D. Lukin, in preparation.
- Chapter 6: “Alkaline-earth-metal atoms as few-qubit quantum registers,” A. V. Gorshkov, A. M. Rey, A. J. Daley, M. M. Boyd, J. Ye, P. Zoller, and M. D. Lukin, *Phys. Rev. Lett.* **102**, 110503 (2009).
- Chapter 7: “Two-orbital SU(N) magnetism with ultracold alkaline-earth atoms,” A. V. Gorshkov, M. Hermele, V. Gurarie, C. Xu, P. S. Julienne, J. Ye, P. Zoller, E. Demler, M. D. Lukin, and A. M. Rey, *Nature Phys.* (in press).

Work related to Chapter 7 is also presented in “Many-body treatment of the collisional frequency shift in fermionic atoms,” A. M. Rey, A. V. Gorshkov, and C. Rubbo, *Phys. Rev. Lett.* **103**, 260402 (2009).

- Chapter 8: “Suppression of inelastic collisions between polar molecules with a repulsive shield,” A. V. Gorshkov, P. Rabl, G. Pupillo, A. Micheli, P. Zoller, M. D. Lukin and H. P. Büchler, *Phys. Rev. Lett.* **101**, 073201 (2008).
- Appendix A: “Photon storage in Λ -type optically dense atomic media. I. Cavity model,” A. V. Gorshkov, A. André, M. D. Lukin, and A. S. Sørensen, *Phys. Rev. A* **76**, 033804 (2007).

- Appendix B: “Photon storage in Λ -type optically dense atomic media. II. Free-space model.” A. V. Gorshkov, A. André, M. D. Lukin, and A. S. Sørensen, *Phys. Rev. A* **76**, 033805 (2007).

Work related to Appendix B is also reported in “Fast entanglement distribution with atomic ensembles and fluorescent detection,” J. B. Brask, L. Jiang, A. V. Gorshkov, V. Vuletić, A. S. Sørensen, and M. D. Lukin, e-print arXiv:0907.3839 [quant-ph].

- Appendix C: “Photon storage in Λ -type optically dense atomic media. III. Effects of inhomogeneous broadening,” A. V. Gorshkov, A. André, M. D. Lukin, and A. S. Sørensen, *Phys. Rev. A* **76**, 033806 (2007).
- Appendix D: “Photon storage in Λ -type optically dense atomic media. IV. Optimal control using gradient ascent,” A. V. Gorshkov, T. Calarco, M. D. Lukin, and A. S. Sørensen, *Phys. Rev. A* **77**, 043806 (2008).
- Appendix E: “Optimal light storage in atomic vapor,” N. B. Phillips, A. V. Gorshkov, and I. Novikova, *Phys. Rev. A* **78**, 023801 (2008).

Work related to Appendix E is also reported in

- “Optimization of slow and stored light in atomic vapor,” I. Novikova, A. V. Gorshkov, D. F. Phillips, Y. Xiao, M. Klein, and R. L. Walsworth, *Proc. SPIE* **6482**, 64820M (2007),
- “Multi-photon entanglement: from quantum curiosity to quantum computing and quantum repeaters,” P. Walther, M. D. Eisaman, A. Nemiroski, A. V. Gorshkov, A. S. Zibrov, A. Zeilinger, and M. D. Lukin, *Proc. SPIE* **6664**, 66640G (2007),
- “Optimizing slow and stored light for multidisciplinary applications,” M. Klein, Y. Xiao, A. V. Gorshkov, M. Hohensee, C. D. Leung, M. R. Brownning, D. F. Phillips, I. Novikova, and R. L. Walsworth, *Proc. SPIE* **6904**, 69040C (2008),

-
- “Realization of coherent optically dense media via buffer-gas cooling,” T. Hong, A. V. Gorshkov, D. Patterson, A. S. Zibrov, J. M. Doyle, M. D. Lukin, and M. G. Prentiss, *Phys. Rev. A* **79**, 013806 (2009),
 - “Slow light propagation and amplification via electromagnetically induced transparency and four-wave mixing in an optically dense atomic vapor,” N. B. Phillips, A. V. Gorshkov, and I. Novikova, *J. Mod. Opt.* **56**, 1916 (2009).

Acknowledgments

I would like to begin by thanking my advisor Prof. Mikhail Lukin for making my graduate school years such a great experience through his support, encouragement, numerous ingenious ideas, and the general positive attitude. I feel very lucky to have Misha as my advisor, mentor, collaborator, and friend.

All members of the Lukin group were instrumental in creating the perfect intellectual and social atmosphere. It was a great pleasure and honor to share the office for most of my graduate school career with Liang Jiang who provided inspiration to work hard and to go to the gym daily from 10pm to 11pm. My time in the office would certainly be much more boring and lonely if not for my other officemates Emre Togan, Yiwen Chu (with special thanks for the unforgettable pumpkin cheesecake), and Norman Yao. Special thanks go to Sasha Zibrov for believing in my ability to do experiments and patiently teaching me (a theorist!) how to align optics. It was a pleasure working with all the other past and present members of the Lukin group, including Axel André, Tommaso Calarco, Paola Cappellaro, Jonathan Hodges, Philip Walther, Peter Rabl, Michal Bajcsy, Sebastian Hofferberth, Alexei Trifonov, Mohammad Hafezi, Brendan Shields, Vlatko Balic, Thibault Peyronel, Sahand Hormoz, Lily Childress, Jake Taylor, Gurudev Dutt, Matt Eisaman, Alex Nemiroski, Alexey Aki-mov, Aryesh Mukherjee, Darrick Chang, GeneWei Li, Peter Maurer, Jeronimo Maze, Garry Goldstein, Michael Gullans, Dirk Englund, Frank Koppens, Jeff Thompson, Shimon Kolkowitz, Nick Chisholm, and Ania Jayich.

It was a pleasure to work with numerous other people at Harvard. In particular, along with Sasha Zibrov and other experimentalists in the Lukin group, many other great experimentalists at Harvard educated me on experimental matters. In this regard, I would like to thank Prof. John Doyle and all of his group, including Sophia Magkiriadou, Timothée Nicolas, David Patterson, Wesley Campbell, Charlie Doret, Matt Hammon, Colin Connolly, Timur Tscherbul, Edem Tsikata, Hsin-I Lu, Yat Shan Au, and Steve Maxwell. I would also like to thank Prof. Markus Greiner and his group, including Amy Peng, Jonathon Gillen, Simon Fölling, Waseem Bakr, Widagdo Setiawan, and Florian Huber, for being always there to answer my naive questions about experiments. I thank Prof. Ron Walsworth for always being so cool and fun to talk to on both physics and non-physics matters. I would also like to acknowledge the members of his group, including Mason Klein, Yanhong Xiao, Michael Hohensee, David Phillips, and Paul Stanwix. I thank Prof. Mara Prentiss and Tao Hong for a rewarding experimental collaboration. Finally, I thank Prof. Charlie Marcus for teaching an illuminating mesoscopic physics course, and, more importantly, for taking a break from his Copenhagen sabbatical to come to Boston for my thesis defense.

I would also like to thank Prof. Eugene Demler and all of his group members, including Adilet Imambekov, Vladimir Gritsev, Takuya Kitagawa, Susanne Pielawa, Bob Cherng, and David Pekker, for teaching me the intricacies of many-body physics. For helping create a fun atmosphere, I thank the Russian-speaking physics department crowd, including Timur Gatanov, Daniyar Nurgaliev, Kirill Korolev, Pavel Petrov, Yevgeny Kats, Vasily Dzyabura, Max Metlitski, and Slava Lysov. I also thank everyone else at Harvard whom I had a chance to collaborate with or cross paths with

in one way or another, including Cenke Xu, Navin Khaneja, Subir Sachdev, Bert Halperin, Lene Hau, Gerald Gabrielse, Jene Golovchenko, Tim Kaxiras, Mark Rudner, Maria Fyta, Ludwig Mathey, Ari Turner, Ilya Finkler, Yang Qi, Josh Goldman, Steve Kolthammer, Liam Fitzpatrick, Jonathan Heckman, Lolo Jawerth, Matt Baumgart, David Hoogerhide, Mark Winkler, Yulia Gurevich, Tina Lin, Jonathan Ruel, Jonathan Fan, Pierre Striehl, and Rudro Biswas. Special thanks go to Misha's secretaries Marilyn O'Connor and Adam Ackerman for being so helpful and to Sheila Ferguson for being always there to answer my numerous questions about the Harvard Physics Department.

Numerous collaborations with scientists outside of Harvard were often key in keeping me excited about physics. In this respect, I would like to thank Prof. Ana Maria Rey for being such a perfect collaborator. I thank Prof. Irina Novikova (College of William & Mary) and her student Nate Phillips for making me part of their exciting experiments on slow and stopped light. I thank Prof. Peter Zoller and Andrew Daley for all the exciting physics we did together and for their hospitality during my numerous visits to Innsbruck. It is also a pleasure to acknowledge the rest of Peter's group, including Guido Pupillo, Gavin Brennen, Andrea Micheli, Mikhail Baranov, Sebastian Diehl, and Klemens Hammerer. I also thank Prof. Anders Sørensen for his immense help during my first project and for hospitality during my visit to Copenhagen. It was also a pleasure working with Anders' students Jonatan Brask and Martin Sørensen. I thank Prof. Hans Peter Büchler for teaching me about polar molecules, for making me part of the "blue shield" project, and for hospitality during my visit to Stuttgart. It's a pleasure to thank Prof. Michael Fleischhauer and his group members, including Gor Nikoghosyan, Johannes Otterbach, and Jürgen Kästel, for productive collaborations and for hospitality during my visits to Kaiserslautern. I thank Prof. Ignacio Cirac and his group members, including Christine Muschik, Oriol Romero-Isart, and Matteo Rizzi, for their hospitality during my visits to Munich. I thank Paul Julienne for teaching me all I know about the physics of ultracold collisions. I thank Jun Ye and his group members Martin Boyd and Tom Loftus for collaborations and discussions. It was also a pleasure working with Prof. Vladan Vuletić and his group, including Jonathan Simon, Haruka Tanji, Andrew Grier, and Marko Cetina. I learned from other numerous brilliant scientists outside of Harvard who are far too numerous to name exhaustively. To name a few, they are Michael Hermele, Christian Flindt, Victor Gurarie, Eugene Polzik, Didi Leibfried, Immanuel Bloch, Stefan Trotzky, Manuel Endres, Lucia Hackermüller, Ulrich Schneider, Herwig Ott, Wilhelm Zwerger, Ivan Deutsch, Iris Reichenbach, Josh Nunn, Mikael Afzelius, Thierry Chanelière, Chin-wen Chou, Karl Surmacz, Julien Le Gouët, Dzmityr Matsukevich, Dieter Jaksch, Vadim F. Krotov, Gretchen Campbell, Florian Schreck, Simon Stellmer, Susanne Yelin, Tun Wang, Pavel Kolchin, Dmitry V. Kupriyanov, Alex Lvovsky, Martin Kiffner, Giovanna Morigi, Hendrik Weimer, Patrick Medley, Yevhen Miroschnyenko, Tobias Schaetz, Aurelien Dantan, Marc Cheneau, and Andi Emmert.

Many great friends in the United States and in Russia, where I went regularly in

the summers, provided essential support. While they are all too numerous to name, I would like to particularly thank my workout buddy Mehmet Akçakaya.

Finally, and most importantly, I would like to thank my parents and my sister for their limitless support. This thesis is dedicated to you.

*Dedicated to my father Vyacheslav,
my mother Irina,
and my sister Natalie.*

Chapter 1

Introduction, Motivation, and Outline

To convey the main message of the thesis to a non-expert reader, before diving into details, let us begin with a paragraph-long non-technical abstract. Very small particles, such as individual atoms or photons (particles of light), obey the laws of quantum mechanics, which are strikingly different from the laws of classical mechanics that describe the motion of large objects in everyday life. Quantum mechanics allows for very peculiar effects such as the ability of particles to be in different places at the same time. Within the past twenty years, physicists have realized that quantum systems can potentially be harnessed for a variety of practical applications, such as extraordinarily powerful computers and unbreakably secure communication devices. However, due to the fragile nature of quantum effects, the realization of these ideas is very challenging. In fact, it is currently unknown if a large-scale controllable quantum system such as a quantum computer can be built, in practice or even in principle. In this thesis, we combine ideas and techniques from different areas of the physical sciences to bridge the gap between cutting-edge experimental systems and fascinating potential applications enabled by quantum mechanics. The author hopes that this work indeed helps (and will help) bring quantum computers and quantum communication devices closer to reality and at the same time provides fundamental insights into the laws of the quantum world.

Let us now discuss all of this in more detail. Why should one consider building technologies that employ the laws of quantum mechanics? There are two main reasons. The first reason is that modern devices, such as telephones and computers, are getting smaller and smaller at such a fast pace that device elements made of several atoms will soon become inevitable. At that point, one will simply be forced to face the laws of quantum mechanics as these are the laws that govern the behavior of such small objects. The second reason is that quantum technologies can be much more powerful than their classical counterparts, as we will discuss below. To put this power in perspective, it may very well be that the impact of emerging quantum technologies

will be greater than the impressive impact the introduction of classical computing had on the world [1].

Turning these ideas into real quantum technologies is, however, extremely challenging. Indeed, we do not normally encounter quantum mechanical effects in everyday life. The reason is that quantum systems interact with the environment and, as a result, quickly lose their quantum properties (decohere). The goal of a quantum engineer is, thus, to isolate from the environment a quantum system that is sufficiently large and powerful to perform the desired tasks. However, there are two more requirements that must be satisfied at the same time: first, the different parts of the isolated quantum system must be sufficiently well-coupled to each other, and, second, the quantum engineer must be able to manipulate the system into performing the desired tasks (such as, for example, initializing a quantum computer and then reading out the answer). The requirements of having a quantum system that is strongly coupled within itself and that can be well-controlled by the quantum engineer, but that is, at the same time, well-isolated from the environment, are nearly contradictory. Indeed, there is a fundamental unanswered question: to what extent can one engineer such quantum systems, both in principle and in practice? This question currently drives much theoretical and experimental effort in physics, information theory, mathematics, chemistry, materials science, and engineering. Motivated by this challenge, in this thesis, we explore new systems and develop new tools, at the interface of atomic, molecular, optical, and condensed matter physics, to bridge the gap between available experimental technology and the theoretically proposed applications.

In the remainder of this Chapter, we will first review those quantum systems that may form the basis for quantum technologies. We will then review possible applications of these systems (i.e. possible quantum technologies). Various tools are used to control quantum systems with the goal of realizing the applications. The work in this thesis covers the development of new systems, as well as new tools applied to new and existing systems. We will therefore conclude this Chapter by giving an outline of the remainder of the thesis, showing how different systems and tools discussed connect to each other and to the outlined applications of quantum mechanics. We also mention related work by the author that is not discussed in detail in the thesis.

Before proceeding, we note that this Chapter is based on existing excellent reviews, which cover both the applications of quantum mechanics and the quantum systems that can be used to get access to these applications. Specifically, quantum communication, computation, and simulation are discussed in Refs. [1, 2, 3, 4, 5], Refs. [1, 6, 4, 5, 7], and Refs. [1, 8, 9, 10], respectively.

1.1 Quantum Systems

In this Section, we review the range of quantum systems that one can potentially use to harness the power of quantum mechanics. One reason for exploring several different systems rather than focusing on a single one is that different systems possess different advantages, and the winning architecture is likely to be a hybrid combining advantages of several constituents. Another reason is the necessity to implement the same model in several systems in the context of quantum simulation (see Sec. 1.2.3).

We are mostly interested in quantum mechanical degrees of freedom accessible at low energies, and therefore treat atomic nuclei as unbreakable. The main available quantum systems can therefore be approximately divided into matter (composed of nuclei and electrons) and light (electromagnetic fields). On the matter side, for both the electrons and the nuclei, the available degrees of freedom are the motion and the spin, which often mix, even within a single atom¹. Some of the most popular matter systems include isolated neutral atoms, ions, and molecules, as well as solid-state systems, such as quantum dots [11], nitrogen-vacancy (NV) color centers in diamond [12], and nuclear spins in silicon [13]. On the side of light, the available degrees of freedom are the spatial and polarization degrees of freedom of photons [14, 2, 15]. Systems whose degrees of freedom are most conveniently described as hybrids between matter and light are also common. Examples include dark-state polaritons (coupled excitations of light and matter associated with the propagation of quantum fields in atomic media under conditions of electromagnetically induced transparency [16, 17]), exciton polaritons (photons strongly confined in semiconductor microcavities and strongly coupled to electronic excitations [18, 19]), and surface plasmons (electromagnetic excitations coupled to charge density waves propagating along conducting surfaces [20, 21]).

1.2 Applications of Quantum Mechanics

Having reviewed the range of possible quantum systems in the previous Section, we turn in this Section to the discussion of promising applications of quantum mechanics, which constitute the main motivation for the work presented in this thesis.

Of course, the most direct application of a given quantum system is the fundamental study of the quantum system itself, which is always rewarding and challenging in itself, given the peculiarity and complexity of the quantum world. More practical applications, however, also abound. These applications rely on the unusual features of quantum mechanics that have no classical counterparts. We will introduce these features as we discuss the specific applications. In Secs. 1.2.1, 1.2.2, and 1.2.3, we will

¹Consider, for example, the total electronic angular momentum $\mathbf{J} = \mathbf{L} + \mathbf{S}$, which is a sum of the electronic orbital angular momentum \mathbf{L} and the electronic spin \mathbf{S} , or the total angular momentum $\mathbf{F} = \mathbf{J} + \mathbf{I}$, which is a sum of the total electronic angular momentum \mathbf{J} and the nuclear spin \mathbf{I} .

discuss quantum communication [1, 2, 3, 4, 5], quantum computation [1, 6, 4, 5, 7], and quantum simulation [1, 8, 9, 10], respectively, followed by a brief summary of some other applications in Sec. 1.2.4. It is worth noting that while we tried to do our best to organize the various applications of quantum mechanics, the division between different applications that we discuss is not clear-cut and the application list we give is certainly not exhaustive.

1.2.1 Quantum Communication

We begin by a discussion of quantum communication, a discussion based on excellent reviews in Refs. [1, 2, 3, 4, 5]. Quantum communication holds the promise to provide unbreakably secure communication, in which unconditional security results directly from the laws of quantum mechanics, and not from the difficulty of solving a certain mathematical problem (as is often the case in classical cryptography). The basic approach to secure communication between Alice and Bob is to establish a shared random binary key that only Alice and Bob know. Transmission by Alice of a the secret message added (in binary fashion) to the key will then be absolutely secure and easily decodable by Bob via the addition of the same key. The problem of secure communication then reduces to the secure distribution of a shared key. The quantum approach to this distribution is referred to as quantum key distribution (QKD). In most naive terms, quantum key distribution can be done in a completely secure fashion because quantum information is so fragile that one cannot eavesdrop on a quantum channel without perturbing the quantum information that is being transmitted. Thus, if Alice tries to transmit a piece of quantum information to Bob, they can always check whether there is an eavesdropper or not.

To be slightly more precise, it is convenient to introduce the concept of a quantum bit. While classical information relies on the concept of a bit, which can be in states 0 or 1, quantum bits (qubits²) can be in both states (0 and 1) at the same time, a phenomenon referred to as a quantum superposition. A measurement of a quantum bit can still give only 0 or 1 (with the probability of each outcome determined by the superposition, in which the measured qubit is prepared). Moreover, the measurement destroys the underlying superposition by projecting it on the result of the measurement (0 or 1). Thus, by measuring the transmitted state, an eavesdropper Eve destroys the underlying state and, at the same time, does not acquire enough information to fully reconstruct it, which makes her detectable.

What quantum system should be used as the carrier of quantum information during quantum communication? Given their weak interactions with the environment and fast propagation speeds, photons are, in fact, the only viable information carrier for long-distance quantum communication [1, 4, 2]. However, after propagating for

²While an alternative approach to quantum information in terms of continuous variables [22], rather than qubits, exists, we will not discuss it in the present thesis.

at most 100 kilometers in an optical fiber, the photons eventually get absorbed (i.e. lost). The way around this problem of loss is a quantum repeater.

The explanation of what a quantum repeater is requires the introduction of the concept of entanglement. The concept of superposition extended to several subsystems allows for the existence of strong correlations between the subsystems that have no classical analogue. These strong correlations are the manifestation of entanglement between the subsystems. In the context of quantum communication, if Alice and Bob can each obtain a qubit, such that their two qubits are entangled, they can use the underlying correlations to generate the shared key. The problem, thus, reduces to the establishment of an entangled state shared between Alice and Bob. Since sending one photon out of an entangled pair from Alice to Bob suffers from exponential losses if Alice and Bob are far apart, a different approach is needed. This approach, termed a quantum repeater, subdivides the distance between Alice and Bob by intermediate nodes into shorter segments, establishes entanglement over these shorter segments, and then uses entanglement swapping (i.e. teleportation) to link the shorter segments into a single entangled state connecting Alice and Bob.

Quantum repeaters thus require storing photons at intermediate nodes, which calls for the creation of efficient light-matter interfaces. The creation of efficient light-matter interfaces will be the subject of Chapters 2 and 3, as well as Appendices A-E. In Chapter 4, the capabilities of quantum memories will be extended beyond storage of photons to generating nonlinear interactions between them.

1.2.2 Quantum Computation

We now turn to quantum computation, whose discussion will be based on excellent reviews in Refs. [1, 6, 4, 5, 7]. While an N -bit classical register can be in one of 2^N states, the corresponding N -qubit quantum register can be in a superposition of all 2^N states at the same time. The massive parallelism, which characterizes the processing of such a superposition, is the main feature that allows quantum computers to solve certain problems qualitatively faster than would be possible on a classical computer. Examples of such problems are factoring of large integers into prime factors, which can be done on a quantum computer using Shor's algorithm [23], and searching an unsorted database, which can be done on a quantum computer using Grover's algorithm [24]. Quantum computers may also be used as nodes in a quantum communication network, as quantum simulators (Sec. 1.2.3), and as systems that can be prepared in highly entangled many-body states such as squeezed states for precision measurements (Sec. 1.2.4). Examples of systems used for quantum computing are ions [25, 26, 27], neutral atoms in individual dipole traps [28] or in optical lattices [25, 29, 30, 31] (possibly enclosed in cavities [32]), superconducting circuits [33, 34], quantum dots [11], photons [15], and impurity spins in solids (e.g. NV centers [12] or nuclear spins in silicon [13]).

The design of a quantum computer will be the main subject of Chapter 6. How-

ever, Chapters 4, 5, and 8 will also discuss novel tools and systems that can be used for quantum computing.

1.2.3 Quantum Simulation

To understand how a given complex quantum system works means to come up with a model (e.g. a Hamiltonian) that reproduces all experimental observations and, preferably, to show that this model is the only reasonably possible one. However, for large strongly-interacting quantum systems, even if one manages to come up with the correct model, it is often close to impossible to make calculations on it (using a classical computer) that would connect the model to experimental observations. The main reason for the difficulty of doing these calculations is the mere size of the Hilbert space describing a many-particle system. This Hilbert space grows exponentially with the number of particles, making it impossible to even write down the state of the system. For example, the description of a state of 500 qubits requires 2^{500} complex amplitudes, a number that is larger than the estimated total number of atoms in the observable universe. As a result of the complexity of this problem, often the only way to learn something about a given complex quantum model is to tune another quantum system into exhibiting the same model and make measurements on that system. This process of using one quantum system to simulate the behavior of another system or of a given model is known as quantum simulation [35, 36, 37, 1, 8, 9, 10].

We have just argued that many quantum systems cannot be efficiently simulated on a *classical* computer. Can a *quantum* computer efficiently simulate any quantum system? This is indeed the case, as conjectured by Feynman [35] and as proved later by Lloyd [36]. However, even if a given quantum system is not sufficiently well-controlled, powerful, or large to be a universal quantum computer, it can still be useful as a quantum simulator. In fact, the use of quantum systems for quantum simulation is often regarded as an intermediate step towards building a true quantum computer. Examples of systems currently explored in the context of quantum simulation include matter systems such as ions [8, 37] and neutral atoms [9, 37], light systems such as photons in coupled cavity arrays [10], as well as hybrid matter-light systems such as surface plasmons [20, 21, 38, 39], dark-state polaritons [40, 41, 42], and exciton polaritons in semiconductor microcavities [19, 43, 44]. The availability for quantum simulation of such a large number of different quantum systems is quite fortunate. Indeed, the only sure way to verify that a given quantum simulator exhibits the desired model sufficiently precisely is to compare its behavior to several other quantum simulators exhibiting the same model, so the more quantum simulators are available the better.

Quantum simulation will be the main subject of Chapter 7. However, Chapters 5, 6, and 8 will also discuss novel systems and tools that can be used for quantum simulation.

1.2.4 Other Applications

While the present thesis primarily focuses on quantum communication, computation, and simulation, accurate control over quantum systems allows for many other fascinating applications. One group of such applications involves precision measurements, with examples including timekeeping [45, 46], rotation sensing [47, 48], magnetometry [49, 50, 51, 52], and electrometry [53]. Quantum mechanics also enables enhanced imaging such as optical imaging with nanoscale resolution [54] and high-sensitivity imaging with entangled light [55]. Other applications of controlled quantum systems include cold controlled chemistry [56], tests of the fundamental symmetries of nature [57], and fundamental tests of quantum mechanics [58].

While none of the Chapters in this thesis have these applications as the primary focus, the tools and systems proposed will often be useful for some of these applications. Applications of Chapter 8 to controlled chemistry [56], of Chapter 5 to imaging and magnetometry [52, 50], and of Chapters 6 and 7 to precision measurements (see Ref. [59] for the application of Chapter 7 to precise timekeeping) are just some of the examples.

1.3 Outline of the Thesis

In this Section, we show how the systems and tools developed in the following Chapters relate to each other and to the quantum mechanical applications described above. We will also mention related work by the author that is not discussed in detail in the thesis for space reasons.

1.3.1 Quantum Memory for Photons (Chapters 2 and 3)

As noted in Sec. 1.2.1, long-distance quantum communication relies on quantum repeaters, which in turn rely on quantum memories for photons and the underlying light-matter interface. Quantum memories for photons also enable more efficient eavesdropping in the context of quantum cryptography [1, 2]. Another application of quantum memories is the conversion of a heralded single-photon source into a deterministic single-photon source, which is important for linear optics quantum computing [15]. More generally, in a world of quantum computers, classical internet and classical networks will have to be replaced by quantum internet and quantum networks, which will require a light-matter interface [4, 32].

Atomic ensembles constitute one of the most promising candidate systems for implementing a quantum memory [60, 61]. The performance of ensemble-based quantum memories, however, still needs to be greatly improved before they become practically useful. Thus, in Chapter 2, we optimize and show equivalence between a wide range of techniques for storage and retrieval of photon wavepackets in Λ -type atomic media. Then in Chapter 3, in collaboration with Irina Novikova, Nathaniel Phillips, Ronald

Walsworth, and coworkers, we verify experimentally the proposed methods for optimizing photon storage. The demonstrated improvement in the efficiency of photonic quantum memories and the demonstrated control over pulse shapes will likely play an important role in realizing quantum technologies, such as quantum repeaters, that rely on photonic quantum memories. Moreover, the demonstrated optimization procedures should be applicable to a wide range of ensemble systems in both classical and quantum regimes. For the sake of clarity, it is worth noting that while the author of this dissertation was involved in suggesting, planning, analyzing, and writing up the experiments, the actual experimental work was done by the author's collaborators, most notably Irina Novikova and Nathaniel Phillips.

To avoid overwhelming the reader with details and to achieve fair coverage of other topics of the thesis, Chapters 2 and 3 provide only a very concise description of the underlying theoretical and experimental work on quantum memories by the author. The reader is referred to Appendices and references for additional information. In particular, details and extensions of the theory of Chapter 2 are presented in Appendices A-D, which cover the cavity model (Appendix A), the free-space model (Appendix B), the effects of inhomogeneous broadening (Appendix C), and the use of optimal control theory to extend photon storage to previously inaccessible regimes (Appendix D). Then, in Appendix E, we present a detailed experimental analysis of optimal photon storage that goes beyond the analysis of Chapter 3. We have also reported on the experimental demonstration of the optimal photon storage techniques of Chapter 2 in Refs. [62, 63]. In addition, we carried out an experimental and theoretical study [64] of four-wave mixing, a process that often limits the performance of quantum memories. In collaboration with Philip Walther, Matthew Eisaman, and coworkers, we also studied experimentally the application of quantum memories to quantum repeaters at single-photon level [65].

Finally, we mention two other projects closely related to the quantum memory work of Chapters 2 and 3, in which the author was involved. The first project is the collaboration with Tao Hong, Alexander Zibrov, and coworkers to produce via buffer-gas cooling a novel coherent optically dense medium and to study its properties [66]. This medium – buffer-gas cooled atomic vapor – may enable better quantum memories than the room-temperature ensembles studied in Chapter 3 and may have other applications such as wave-mixing or precision measurements. In the second project, in collaboration with Jonatan Brask (Copenhagen), Liang Jiang, and coworkers, we proposed a novel quantum repeater protocol, which makes use of the light-matter interface theory, fluorescent detection, and an improved encoding of qubits in atomic ensembles [67].

1.3.2 Quantum Gate between Two Photons (Chapter 4)

While photons interact with each other very weakly, atom-atom interactions can be very strong. It is thus natural to consider using photonic quantum memories to

effectively induce interactions between photons. Indeed, this is what we do in Chapter 4: we combine the technique of photon storage with strong atom-atom interactions to propose a robust protocol for implementing the two-qubit photonic phase gate. The π phase is acquired via the exchange of two fermionic spin-waves that temporarily carry the photonic qubits. Such a two-photon gate has numerous applications in quantum computing and communication. For example, it allows to replace a partial Bell-state measurement on two photons with a complete Bell-state measurement and to implement photon-number-splitting eavesdropping attacks [2, 3, 68, 69, 15].

1.3.3 Addressing Quantum Systems with Subwavelength Resolution (Chapter 5)

Quantum technologies discussed in Chapters 2-4 do not require addressing individual atoms. In contrast, many quantum computing and quantum simulation applications require individual addressing of closely-spaced atoms, ions, quantum dots, or solid state defects, where the close spacing is often necessary to achieve sufficiently strong coupling. To meet this requirement of individual addressing, in Chapter 5, we propose a method for coherent optical far-field manipulation of quantum systems with a resolution that is not limited by the wavelength of radiation and can, in principle, approach a few nanometers. The selectivity is enabled by the nonlinear atomic response, under the conditions of electromagnetically induced transparency, to a control beam with intensity vanishing at a certain location.

Two projects not discussed in detail in this thesis were closely related to the work presented in Chapter 5. In the first project, in collaboration with Liang Jiang and coworkers, we used the subwavelength addressability of Chapter 5 to propose a method to read and write topologically protected quantum memories, as well as to probe abelian anyonic statistics associated with topological order [70]. While topologically protected memories are of great value for quantum communication, the extension of the work of Ref. [70] to non-abelian anyons may play an important role in enabling (highly accurate) topological quantum computation [71].

The second project was motivated by the fact that, despite impressive experimental progress in ionic systems and in ultracold gases, many researchers believe that solid state systems will eventually be the backbone of quantum computers. Thus, in collaboration with Peter Maurer, Jero Maze, and coworkers, we demonstrated experimentally that the quantum Zeno effect induced by a doughnut-shaped laser beam allows for sub-wavelength manipulation of the electronic spin in nitrogen-vacancy (NV) color centers [52]. In analogy with the method of Chapter 5, this manipulation was achieved by suppressing coherent evolution on all centers except for the one that sits at the center of the doughnut. We are currently working on using this idea to develop a realistic scheme for room-temperature quantum computation. This scheme will use magnetic dipole-dipole interactions between closely spaced NV centers and

will rely on nuclear spins for quantum information storage. This project has promising applications in nanoscale magnetometry [50] and quantum computing.

1.3.4 Alkaline-Earth Atoms (Chapters 6 and 7)

As exemplified by Chapters 2-5, most experimental work on quantum computation, communication, and simulation with neutral atoms makes use of alkali atoms (atoms in the first column of Mendeleev's periodic table). The main reason is their relatively simple electronic structure (due to the presence of only one valence electron) and electronic transition wavelengths that are readily accessible with commercially available lasers. Alkaline-earth atoms – atoms in the second column of Mendeleev's periodic table and, hence, atoms with two outer electrons – have wavelengths that are less convenient. However, certain features of their more complex electronic structure make it worthwhile to consider them for quantum information processing and quantum simulation applications, which is what we argue in Chapters 6 and 7. On the quantum information processing side (Chapter 6), we show that multiple qubits can be encoded in electronic and nuclear degrees of freedom associated with individual ultracold alkaline-earth atoms trapped in an optical lattice and describe specific applications of this system to quantum computing and precision measurements. On the quantum simulation side (Chapter 7), we show that ultracold alkaline-earth atoms in optical lattices can be used to realize models that exhibit spin-orbital physics and that are characterized by an unprecedented degree of symmetry. The realization of these models in ultracold atoms may provide valuable insights into strongly correlated physics of transition metal oxides, heavy fermion materials, and spin liquid phases.

As an application of the many-body Hamiltonian studied in Chapter 7, in collaboration with Ana Maria Rey and Chester Rubbo, we carried out a many-body analysis of the collisional frequency shift in fermionic atoms [59]. This analysis, which may play a key role in improving the precision of atomic clocks based on fermionic atoms, is not presented in this thesis for space reasons.

1.3.5 Diatomic Polar Molecules (Chapter 8)

While ultracold atoms typically exhibit only short-range interactions, numerous exotic phenomena and practical applications require long-range interactions, which can be achieved with ultracold polar molecules [72, 73]. However, gases of polar molecules suffer from inelastic collisions, which reduce the lifetime of the molecules and inhibit efficient evaporative cooling [72]. Thus, in Chapter 8, we show how the application of DC electric and continuous-wave microwave fields can give rise to a three dimensional repulsive interaction between polar molecules, which allows for the suppression of inelastic collisions, while simultaneously enhancing elastic collisions. This technique may open up a way towards efficient evaporative cooling and the creation of novel long-lived quantum degenerate phases of polar molecules.

Chapter 2

Optimal Photon Storage in Atomic Ensembles: Theory

2.1 Introduction

In quantum networks, states are easily transmitted by photons, but the photonic states need to be stored locally to process the information. Motivated by this and other ideas from quantum information science, techniques to facilitate controlled interactions between single photons and atoms are now being actively explored [74, 75, 16, 17, 76, 77, 78, 79, 80, 81, 82, 83, 84, 85, 86, 87]. A promising approach to a matter-light quantum interface uses classical laser fields to manipulate pulses of light in optically dense media such as atomic gases [16, 17, 76, 77, 78, 80, 81, 79, 84, 85, 86] or impurities embedded in a solid state material [82, 83, 87]. The challenge is to map an incoming signal pulse into a long-lived atomic coherence (referred to as a spin wave), so that it can be later retrieved “on demand” with the highest possible efficiency. Using several different techniques, significant experimental progress towards this goal has been made recently [79, 80, 81]. A central question that emerges from these advances is which approach represents the best possible strategy and how the maximum efficiency can be achieved. In this Chapter, we present a physical picture that unifies several different approaches to photon storage in Λ -type atomic media and yields the optimal control strategy. This picture is based on two key observations. First, we show that the retrieval efficiency of any given stored spin wave depends only on the optical depth d of the medium. Physically, this follows from the fact that the branching ratio between collectively enhanced emission into desired modes and spontaneous decay (with a rate 2γ) depends only on d . The second observation is that the optimal storage process is the time reverse of retrieval (see also [86, 87]). This universal picture implies that the maximum efficiency is the same for all approaches considered and depends only on d . It can be attained by adjusting the control or the shape of the photon wave packet. For a more detailed analysis of all the issues raised

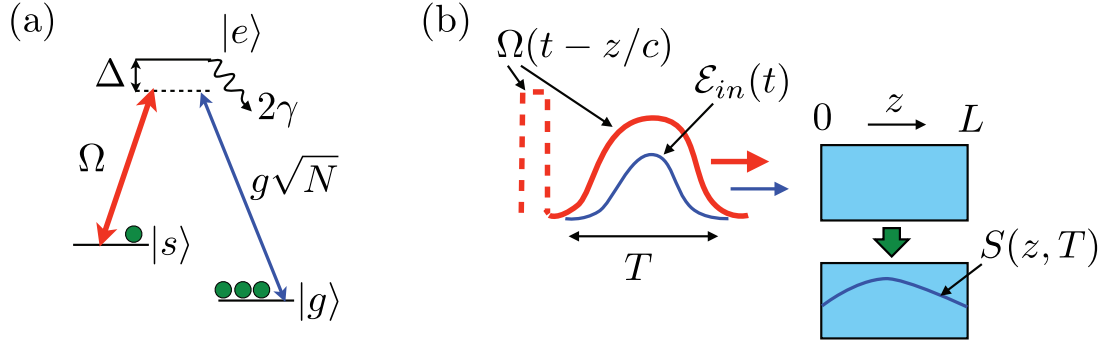


Figure 2.1: (a) Λ -type medium coupled to a classical field with Rabi frequency $\Omega(t)$ and a quantum field with an effective coupling constant $g\sqrt{N}$. (b) Storage setup. The solid Ω curve is the generic control shape for adiabatic storage; the dashed line indicates a π -pulse control field for fast storage. For retrieval, the inverse operation is performed.

in this Chapter and for various extensions, we refer the reader to Appendix B.

A generic model for a quantum memory uses the Λ -type level configuration shown in Fig. 2.1(a), in which a weak (quantum) signal field with frequency ν is detuned by Δ from the $|g\rangle - |e\rangle$ transition. A copropagating (classical) control beam with the same detuning Δ from the $|s\rangle - |e\rangle$ transition is used to coherently manipulate the signal propagation and to facilitate the light–atom state mapping. In this system several different approaches to photon storage can be taken. In electromagnetically induced transparency (EIT) [16, 17, 76, 77, 78, 80, 81, 82, 83], resonant fields ($\Delta = 0$) are used to open a spectral transparency window, where the quantum field travels at a reduced group velocity, which is then adiabatically reduced to zero. In the Raman configuration [84, 85], the fields have a large detuning ($|\Delta| \gg \gamma d$) and the photons are absorbed into the stable ground state $|s\rangle$ by stimulated Raman transitions. Finally, in the photon-echo approach [86, 87], photon storage is achieved by applying a fast resonant π pulse, which maps excitations from the unstable excited state $|e\rangle$ into the stable ground state $|s\rangle$.

A common problem in all of these techniques is that the pulse should be completely localized inside the medium at the time of the storage. For example, in the EIT configuration, a reduction in group velocity, which compresses the pulse to fit inside the medium, is accompanied by narrowing of the transparency window, which increases spontaneous emission. Similarly, in the photon-echo technique, if a photon pulse is very short, its spectral width will be too large to be absorbed by the atoms. To achieve the maximum storage efficiency one thus has to make a compromise between the different sources of errors. Ideal performance is only achieved in the limit of infinite d [16, 17].

2.2 Model

In our model, illustrated in Fig. 2.1(a) and discussed in much more detail in Appendix B, the incoming signal interacts with N atoms in the uniform medium of length L ($z = 0$ to $z = L$) and cross-section area A . The control field is characterized by the slowly varying Rabi frequency $\Omega(t - z/c)$. $P(z, t) = \sqrt{N} \sum_i |g\rangle_i \langle e| / N_z$, where the sum is over all N_z atoms in a small region positioned at z , describes the slowly varying collective $|g\rangle - |e\rangle$ coherence. All atoms are initially pumped into level $|g\rangle$. As indicated in Fig. 2.1(b), we first map a quantum field mode with slowly varying envelope $\mathcal{E}_{\text{in}}(t)$ (nonzero on $t \in [0, T]$ and incident in the forward direction at $z = 0$) to some slowly varying mode of the collective $|s\rangle - |g\rangle$ coherence $S(z, t) = \sqrt{N} \sum_i |g\rangle_i \langle s| / N_z$. Then starting at a time $T_r > T$, we perform the inverse operation to retrieve S back onto a field mode. As we explain below, the optimal efficiency is achieved by sending the retrieval control pulse in the backward direction; storage followed by forward retrieval is, however, also considered. The goal is to solve the optimal control problem (see Appendix D and Refs. [88, 89, 90] for discussions of optimal control theory) of finding the control fields that will maximize the efficiency of storage followed by retrieval for given optical depth $d = g^2 NL / (\gamma c)$ and input mode $\mathcal{E}_{\text{in}}(t)$. Here c is the speed of light, the atom-photon coupling $g = \wp(\nu / (2\hbar\epsilon_0 AL))^{1/2}$ is assumed real for simplicity, and \wp is the dipole matrix element. The efficiency is defined as the ratio of the number of retrieved photons to the number of incident photons. It is worth pointing out that, in order to avoid carrying around extra factors of 2, d is defined as half of the usual definition of optical depth: with our definition of d , in the absence of a control field, a resonant probe would suffer $\exp(-2d)$ intensity attenuation after passing through the medium.

Since the quantum memory operates in the linear regime, an analysis of the interaction process where all variables are treated as complex numbers is sufficient (as we formally prove in Appendix B). In this limit, the equations of motion read (see Appendix B)

$$(\partial_t + c\partial_z)\mathcal{E}(z, t) = ig\sqrt{N}P(z, t), \quad (2.1)$$

$$\partial_t P(z, t) = -(\gamma + i\Delta)P(z, t) + ig\sqrt{N}\mathcal{E}(z, t) + i\Omega(t - z/c)S(z, t), \quad (2.2)$$

$$\partial_t S(z, t) = i\Omega^*(t - z/c)P(z, t). \quad (2.3)$$

Here we have neglected the slow decay of S (see Sec. B.6.5 for the discussion of the effects of the decay of S). Notice that, in order to avoid carrying around extra factors of 2, Ω is defined as half of the usual definition of Rabi frequency: with our definition of Ω , a π pulse would take time $\pi / (2\Omega)$. For storage, the initial conditions are $\mathcal{E}(0, t) = \mathcal{E}_{\text{in}}(t)$, $\mathcal{E}(z, 0) = 0$, $P(z, 0) = 0$, and $S(z, 0) = 0$. Being the shape of a mode, $\mathcal{E}_{\text{in}}(t)$ is normalized according to $(c/L) \int_0^T |\mathcal{E}_{\text{in}}(t)|^2 dt = 1$, so the storage efficiency is given by $\eta_s = (1/L) \int_0^L |S(z, T)|^2 dz$. For the reverse process, i.e. retrieval, the initial conditions are $\mathcal{E}(0, t) = 0$, $\mathcal{E}(z, T_r) = 0$, $P(z, T_r) = 0$, and $S(z, T_r) = S(L - z, T)$ for

backward retrieval¹ or $S(z, T_r) = S(z, T)$ for forward retrieval. The total efficiency in both cases is $\eta_{\text{back/forw}} = (c/L) \int_{T_r}^{\infty} |\mathcal{E}_{\text{out}}(t)|^2 dt$, where $\mathcal{E}_{\text{out}}(t) \equiv \mathcal{E}(L, t)$.

2.3 Optimal Retrieval

It is instructive to first discuss the retrieval process (see Sec. B.3 for an extended discussion). In a co-moving frame $t' = t - z/c$, using a normalized coordinate $\zeta = z/L$ and a Laplace transformation in space $\zeta \rightarrow s$, Eq. (2.1) gives $\mathcal{E}(s, t') = i\sqrt{d\gamma L/c}P(s, t')/s$. Therefore, the retrieval efficiency is given by

$$\eta_r = \mathcal{L}^{-1} \left\{ \gamma d / (s s') \int_{T_r}^{\infty} dt' P(s, t') [P(s'^*, t')]^* \right\}, \quad (2.4)$$

where \mathcal{L}^{-1} means that two inverse Laplace transforms ($s \rightarrow \zeta$ and $s' \rightarrow \zeta'$) are taken and are both evaluated at $\zeta = \zeta' = 1$. To calculate η_r , we insert $\mathcal{E}(s, t')$ found from Eq. (2.1) into Eq. (2.2) and use Eqs. (2.2,2.3) to find

$$\begin{aligned} \partial_t \{ P(s, t') [P(s'^*, t')]^* + S(s, t') [S(s'^*, t')]^* \} \\ = -\gamma(2 + d/s + d/s') P(s, t') [P(s'^*, t')]^*. \end{aligned} \quad (2.5)$$

Eqs. (2.4,2.5) allow us to express η_r in terms of the initial and final values of the term inside the curly brackets in Eq. (2.5). Assuming $P(s, \infty) = S(s, \infty) = 0$ (i.e. no excitations are left in the atoms) and taking \mathcal{L}^{-1} , we get

$$\eta_r = \int_0^1 d\zeta \int_0^1 d\zeta' k_d(\zeta, \zeta') S(\zeta, T_r) S^*(\zeta', T_r), \quad (2.6)$$

$$k_d(\zeta, \zeta') = \frac{d}{2} e^{-d(1-(\zeta+\zeta')/2)} I_0\left(d\sqrt{(1-\zeta)(1-\zeta')}\right), \quad (2.7)$$

where I_0 is the zeroth-order modified Bessel function of the first kind. Note that η_r does not depend on Δ and $\Omega(t)$. Physically, this means that a fixed branching ratio exists between the transfer of atomic excitations into the output mode $\mathcal{E}_{\text{out}}(t)$ and the decay into all other directions. This ratio only depends on d and $S(\zeta, T_r)$ (see Secs. B.3 and B.6.1 for a detailed analysis of this dependence).

The efficiency η_r in Eq. (2.6) is an expectation value of a real symmetric operator $k_r(\zeta, \zeta')$ in the state $S(\zeta)$. It is, therefore, maximized when $S(\zeta)$ is the eigenvector (call it $\tilde{S}_d(\zeta)$) with the largest eigenvalue η_r^{max} of the real eigenvalue problem

$$\eta_r S(\zeta) = \int_0^1 d\zeta' k_d(\zeta, \zeta') S(\zeta'). \quad (2.8)$$

¹As discussed in Sec. B.8, we can ignore spin wave momentum if $\sqrt{d} \gg w_{sg}L/c$.

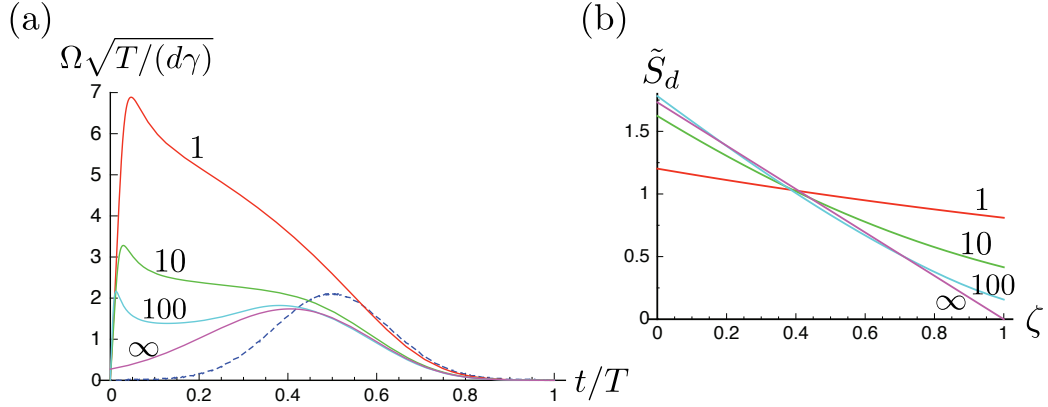


Figure 2.2: (a) Input mode $\mathcal{E}_{\text{in}}(t)$ (dashed) and control fields $\Omega(t)$ (in units of $\sqrt{d\gamma/T}$) that maximize for this $\mathcal{E}_{\text{in}}(t)$ the efficiency for resonant adiabatic storage (alone or followed by backward retrieval) at $d = 1, 10, 100$, and $d \rightarrow \infty$. (b) Optimal modes $\tilde{S}_d(1 - \zeta)$ to retrieve from backwards at $d = 1, 10, 100$, and $d \rightarrow \infty$ ($\zeta = z/L$). These are also normalized spin waves $S(\zeta, T)/\sqrt{\eta_s^{\text{max}}}$ in adiabatic and fast storage if it is optimized alone or followed by backward retrieval.

To find $\tilde{S}_d(\zeta)$, we start with a trial $S(\zeta)$ and iterate the integral in Eq. (2.8) several times. The resulting optimal spin wave $\tilde{S}_d(1 - \zeta)$ is plotted in Fig. 2.2(b) for $d = 1, 10, 100$, and $d \rightarrow \infty$. These shapes represent a compromise attaining the smoothest possible spin wave with the least amount of (backward) propagation (see Sec. B.6.1 for the details of this line of reasoning).

2.4 Optimal Storage

We now discuss storage. We claim that if, for a given d , Δ , and $\mathcal{E}_{\text{in}}(t)$, we can find a control $\Omega(t)$ that retrieves backwards from $\tilde{S}_d(1 - \zeta)$ into $\mathcal{E}_{\text{in}}^*(T - t)$, then the time reverse of this control, $\Omega^*(T - t)$, will give the optimal storage of $\mathcal{E}_{\text{in}}(t)$. To prove this, we represent our retrieval transformation as a unitary map $U[\Omega(t)]$ in the Hilbert space \mathcal{H} spanned by subspace A of spin-wave modes, subspace B of output field modes, as well as a subspace containing (empty) input and reservoir field modes (note that it is essential to include the reservoir modes, since the dynamics is unitary only in the full Hilbert space of the problem). For a given unit vector $|a\rangle$ in A (a given spin wave), the retrieval efficiency is $\eta_r = |\langle b|U[\Omega(t)]|a\rangle|^2 = |\langle a|U^{-1}[\Omega(t)]|b\rangle|^2$, where we have used the unitarity of $U[\Omega(t)]$, and where $|b\rangle$ is a normalized projection of $U[\Omega(t)]|a\rangle$ on B , i.e. the mode onto which the spin wave is retrieved. Introducing the time reversal operator \mathcal{T} (see Secs. B.4 and B.10.3), we find $\eta_r = |\langle a|\mathcal{T}\mathcal{T}U^{-1}[\Omega(t)]\mathcal{T}|b\rangle|^2$. One can show (see Secs. B.4 and B.10.3) that the time reverse of the inverse propagator

$\mathcal{T}U^{-1}[\Omega(t)]\mathcal{T}$ is simply $U[\Omega^*(T-t)]$ so that we have $\eta_r = |\langle a|\mathcal{T}U[\Omega^*(T-t)]\mathcal{T}|b\rangle|^2$. This immediately tells us that the time-reversed control $\Omega^*(T-t)$ will map the time reverse of the retrieved pulse into the complex conjugate of the original spin-wave mode with the same efficiency. The optimal spin waves are, however, real so that complex conjugation plays no role. Furthermore, the storage efficiency cannot exceed η_r^{\max} since the time reverse of such storage would then by the same argument give a retrieval efficiency higher than η_r^{\max} , which is a contradiction. Optimal storage is thus the time reverse of optimal backward retrieval and has the same efficiency $\eta_s^{\max} = \eta_r^{\max}$ (and involves the same optimal spin wave).

2.5 Adiabatic Limit

To identify the input modes, for which the optimal storage can be achieved, we use Eqs. (2.1-2.3) to analytically solve the retrieval problem in two important limits: “adiabatic” and “fast”. The “adiabatic” limit, whose two special cases are the Raman and the EIT regimes discussed above, corresponds to a smooth control field, such that P can be adiabatically eliminated in Eq. (2.2). Using the Laplace transform technique to eliminate \mathcal{E} from Eqs. (2.1,2.2), we reduce Eqs. (2.2,2.3) to a simple differential equation on S . We solve it, compute \mathcal{E} , and take the inverse Laplace transform to obtain

$$\begin{aligned} \mathcal{E}_{\text{out}}(T_r + \frac{L}{c} + t) &= -\sqrt{\frac{d\gamma L}{c}} \int_0^1 d\zeta \frac{\Omega(t)}{\gamma + i\Delta} e^{-\frac{\gamma d\zeta + h(t)}{\gamma + i\Delta}} \\ &\times I_0 \left(2\sqrt{\gamma d\zeta h(t)} / (\gamma + i\Delta) \right) S(1 - \zeta, T_r), \end{aligned} \quad (2.9)$$

where $h(t) = \int_0^t dt' |\Omega(t')|^2$. We will now show that for a given d , Δ , and spin wave $S(\zeta)$, one can always find a control $\Omega(t)$ that maps $S(\zeta)$ to any desired normalized output mode $\mathcal{E}_2(t)$ of duration T_{out} , so that $\mathcal{E}_{\text{out}}(T_r + \frac{L}{c} + t) = \sqrt{\eta_r} \mathcal{E}_2(t)$ [provided we are in the “adiabatic” limit $T_{\text{out}} d\gamma \gg 1$ (see Sec. B.6.4)]. To do this, we replace $\mathcal{E}_{\text{out}}(T_r + \frac{L}{c} + t)$ in Eq. (2.9) with $\sqrt{\eta_r} \mathcal{E}_2(t)$, integrate the norm squared of both sides from 0 to t , change variables $t \rightarrow h(t)$, and get

$$\begin{aligned} \eta_r \int_0^t dt' |\mathcal{E}_2(t')|^2 &= \frac{d\gamma L}{c} \int_0^{h(t)} dh' \left| \int_0^1 d\zeta \frac{1}{\gamma + i\Delta} e^{-\frac{\gamma d\zeta + h'}{\gamma + i\Delta}} \right. \\ &\times I_0 \left(2\sqrt{\gamma d\zeta h'} / (\gamma + i\Delta) \right) S(1 - \zeta, T_r) \Big|^2, \end{aligned} \quad (2.10)$$

which allows us to solve numerically for the unique $h(t)$. Then $|\Omega(t)| = \left(\frac{d}{dt} h(t)\right)^{1/2}$, while the phase is found by inserting $h(t)$ into Eq. (2.9). In Sec. 3.4, we verify experimentally that, in the adiabatic limit, one can indeed shape the retrieval control field to retrieve into any desired output mode.

Optimal storage controls then follow from the time reversal argument above. Fig. 2.2(a) shows a particular Gaussian-like input mode $\mathcal{E}_{\text{in}}(t)$ and the corresponding optimal² storage control shapes Ω for the case $\Delta = 0$ and $d = 1, 10, 100$, as well as the limiting shape of the optimal Ω as $d \rightarrow \infty$. As we have argued, the normalized atomic mode $S(\zeta, T)/\sqrt{\eta_s^{\text{max}}}$, into which $\mathcal{E}_{\text{in}}(t)$ is stored using these optimal control fields, is precisely $\tilde{S}_d(1 - \zeta)$, the optimal mode to retrieve backwards shown in Fig. 2.2(b). In Secs. 3.4 and E.5, we verify experimentally that, in the adiabatic limit, one can indeed shape the storage control field to store any given input mode optimally (i.e. into the optimal spin-wave mode).

2.6 Fast Limit

The “fast” limit corresponds to a short and powerful resonant retrieval control satisfying $\Omega \gg d\gamma$ that implements a perfect π pulse between the optical and spin polarizations, P and S . This retrieval and the corresponding storage technique are similar to the photon-echo method of Refs. [86, 87]. Again using the Laplace transform technique, we find for a perfect π pulse that enters the medium at time T_r

$$\mathcal{E}_{\text{out}}(T_r + \frac{L}{c} + t) = -\sqrt{\frac{\gamma d L}{c}} \int_0^1 d\zeta e^{-\gamma t} J_0(2\sqrt{\gamma d \zeta t}) S(1 - \zeta, T_r), \quad (2.11)$$

where $J_0(x) = I_0(ix)$. Since the fast retrieval control cannot be shaped, at each d , there is, thus, only one mode (of duration $T \sim 1/(\gamma d)$) that can be stored optimally. This mode is the time reverse of the output mode in Eq. (2.11) retrieved from the optimal spin wave \tilde{S}_d .

2.7 Iterative Time-Reversal-Based Optimization

We will now show that time reversal can not only be used to deduce optimal storage from optimal retrieval, but can also be used to find \tilde{S}_d in the first place. In the discussion above, the normalized projection of $U^{-1}|b\rangle$ on A (call it $|a'\rangle$) might have a component orthogonal to $|a\rangle$. In this case, the efficiency of U^{-1} as a map from B to A will be $\eta'_r = |\langle a'|U^{-1}|b\rangle| > \eta_r$. Now if the normalized projection of $U|a'\rangle$ on B is not equal to $|b\rangle$, the map U acting on $|a'\rangle$ will similarly have efficiency $\eta''_r > \eta'_r > \eta_r$. Therefore, such iterative application of U and U^{-1} converges to the optimal input in A and the corresponding optimal output in B . Indeed, a detailed calculation (Sec. B.5) shows that the search for the optimal spin wave by iterating Eq. (2.8) precisely corresponds to retrieving $S(\zeta)$ with a given control, time-reversing the output, and storing it with the time-reversed control profile.

²Although $\Omega(t=0) \rightarrow \infty$ for optimal Ω , we show in Secs. B.6.1 and B.6.4 that truncating it does not affect η_s , provided the control pulse energy is large enough to satisfy $\gamma d \int dt \Omega^2 \gg |\gamma d + i\Delta|^2$.

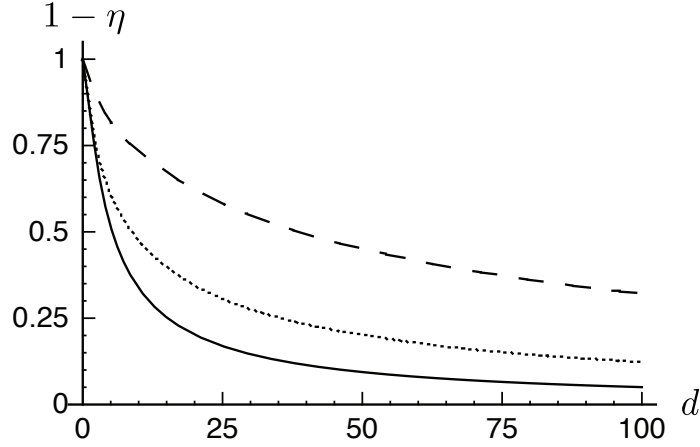


Figure 2.3: $\eta_{\text{back}}^{\text{max}}$ (solid) and $\eta_{\text{forw}}^{\text{max}}$ (dotted) are maximum total efficiency for storage followed by backward or forward retrieval, respectively. η_{square} (dashed) is the total efficiency for resonant storage of $\mathcal{E}_{\text{in}}(t)$ from Fig. 2.2(a) followed by backward retrieval, where the storage control field is a naïve square pulse.

This time-reversal optimization procedure for finding the optimal $|a\rangle \in A$ can be used to optimize not only retrieval, but also any map including storage followed by retrieval. For storage followed by backward retrieval, this procedure yields $\tilde{S}_d(1 - \zeta)$ and maximum efficiency $\eta_{\text{back}}^{\text{max}} = (\eta_{\text{r}}^{\text{max}})^2$, since $\tilde{S}_d(1 - \zeta)$ optimizes both storage and backward retrieval. Fig. 2.3 demonstrates that for resonant adiabatic storage of the field mode in Fig. 2.2(a) followed by backward retrieval, optimal controls result in a much higher efficiency $\eta_{\text{back}}^{\text{max}}$ than naïve square control pulses on $[0, T]$ with power set by $v_g T = L$ (η_{square} curve), where $v_g = c\Omega^2/(g^2 N)$ is the EIT group velocity [76].

For the case of storage followed by forward retrieval, iterations yield the maximum efficiency $\eta_{\text{forw}}^{\text{max}}$ plotted in Fig. 2.3. It is less than $\eta_{\text{back}}^{\text{max}}$ since with backward retrieval, storage and retrieval are each separately optimal, while for forward retrieval a compromise has to be made. From a different perspective, forward retrieval makes it more difficult to minimize propagation since the excitation has to propagate through the entire medium. Experimental demonstration of the iterative optimization of storage followed by forward retrieval is the subject of Secs. 3.3 and E.4.

2.8 Conclusion and Outlook

In conclusion, we have shown that the performance of EIT, Raman, and photon-echo approaches to a quantum light-matter interface can be understood and optimized within a universal physical picture based on time reversal and a fixed branching ratio between loss and the desired quantum state transfer. For a given optical depth d ,

the optimal strategy yields a universal maximum efficiency and a universal optimal spin wave, thus, demonstrating a certain degree of equivalence between these three seemingly different approaches. We showed that the optimal storage can be achieved for any smooth input mode with $Td\gamma \gg 1$ and any Δ and for a class of resonant input modes satisfying $Td\gamma \sim 1$. The presented optimization of the storage and retrieval processes leads to a substantial increase in the memory efficiency.

The results described here are of direct relevance to ongoing experimental efforts, where optical depth d is limited by experimental constraints such as density of cold atoms, imperfect optical pumping, or competing nonlinear effects. For example, in two recent experiments [80, 81], $d \sim 5$ was used. $\eta_{\text{back}}^{\text{max}}$ and η_{square} curves in Fig. 2.3 indicate that at this d , by properly shaping the control pulses, the efficiency can be increased by more than a factor of 2. In Chapter 3 and Appendix E, we demonstrate the proposed optimization procedures experimentally using classical light and find excellent agreement between the experiment and the theory presented in the present Chapter. Direct comparison to many other experiments, however, will require the inclusion of decoherence processes and other imperfections. In Appendices A-D, we discuss some of these imperfections, as well as the details of the present analysis and its extensions to atomic ensembles enclosed in a cavity (Appendix A) and to inhomogeneously broadened media (Appendix C).

Finally, we note that the time-reversal based iterative optimization we suggest is not only a convenient mathematical tool but is also a readily accessible experimental technique for finding the optimal spin wave and optimal input-control pairs: one just has to measure the output mode and generate its time reverse. Indeed, we experimentally demonstrate this optimization procedure, as well as optimal control field shaping, experimentally in Chapter 3 and Appendix E. We also expect this procedure to be applicable to the optimization of other linear quantum maps both within the field of light storage (e.g. light storage using tunable photonic crystals [91]) and outside of it.

Chapter 3

Optimal Photon Storage in Atomic Ensembles: Experiment

3.1 Introduction

In Chapter 2 and in the Introduction (Chapter 1), we argued that quantum memory for light is essential for the implementation of long-distance quantum communication [61] and of linear optical quantum computation [15]. We also argued that one of the leading candidates for implementing a quantum memory relies on auxiliary control fields to form an interface between light and collective atomic excitations in Λ -type atomic ensembles. However, we also noted that practical applications will require significant improvements in the memory efficiency beyond values achieved to date. Therefore, in Chapter 2, we proposed several protocols for obtaining the maximum memory efficiency possible at any given optical depth. In this Chapter, we demonstrate these protocols experimentally. In particular, in Sec. 3.3, we experimentally demonstrate time-reversal based iterative optimization of photon storage with respect to the input pulse, while in Sec. 3.4, we experimentally demonstrate optimization with respect to the auxiliary control field (which allows for optimal storage of input pulses of arbitrary shape). The experiment of Sec. 3.4 also demonstrates precise retrieval into any predetermined temporal profile. Both experiments agree with theoretical predictions and attain efficiencies approaching the fundamental limit. While our results are obtained in warm Rb vapor using electromagnetically induced transparency (EIT) [76, 80], the presented procedures are universal (see Chapter 2) and applicable to a wide range of systems, including ensembles of cold atoms [92, 81, 93] and solid-state impurities [94, 95], as well as to other light storage protocols (*e.g.*, the far-off-resonant Raman scheme [84]). Although our experiments use weak classical pulses, the linearity of the corresponding equations of motion allows us to expect that our results will be applicable to quantum states confined to the mode defined by the classical pulse (see Secs. B.2 and B.10.1).

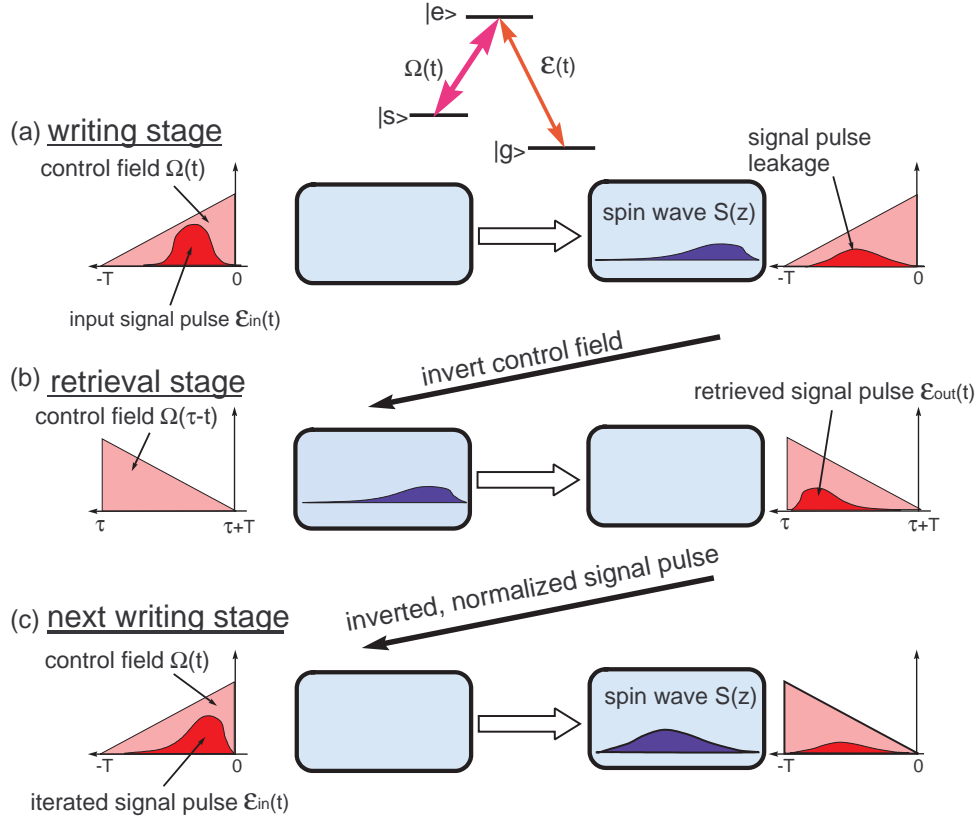


Figure 3.1: Schematic of the Λ -type interaction scheme (top) and the iterative signal-pulse optimization procedure. (a) An input signal pulse $\mathcal{E}_{in}(t)$ is mapped into a spin-wave $S(z)$ using a control field envelope $\Omega(t)$. (b) After a storage period τ , the spin-wave is mapped into an output signal pulse \mathcal{E}_{out} using the time-reversed control field envelope $\Omega(\tau-t)$. (c) The time-reversed and normalized version of the measured \mathcal{E}_{out} is used as the input \mathcal{E}_{in} in the next iteration.

We consider the propagation of a weak signal pulse (with slowly varying envelope $\mathcal{E}(t)$) in the presence of a strong classical control field (with Rabi frequency $\Omega(t)$) in a resonant Λ -type ensemble under EIT conditions, as shown at the top of Fig. 3.1. An incoming signal pulse propagates with slow group velocity v_g , which is uniform throughout the medium and is proportional to the intensity of the control field $v_g \approx 2|\Omega|^2/(\alpha\gamma) \ll c$ [16, 17]. Here, γ is the decay rate of the optical polarization, and α is the absorption coefficient, so that αL is the optical depth of the atomic medium of length L . We note a change in notation relative to the theoretical work in Chapter 2: while in Chapter 2 we used the parameter d , which, to avoid carrying around factors of 2, was equal to half of the optical depth, here we use the actual optical depth $\alpha L = 2d$, which is a more appropriate parameter for the experimental discussion of

the present Chapter. In particular, the probe intensity is attenuated by $e^{-\alpha L}$ after passing through the medium in the absence of the control field.

For quantum memory applications, a signal pulse can be “stored” (*i.e.* reversibly mapped) onto a collective spin excitation of an ensemble (spin wave) by reducing the control intensity to zero [16, 17]. For ideal writing, storage, and retrieval, the signal pulse’s frequency components must fit well within the EIT spectral window ($\Delta\omega_{\text{EIT}}$) to avoid incoherent absorptive loss: *i.e.*, $1/T \ll \Delta\omega_{\text{EIT}} \simeq \sqrt{\alpha L}v_g/L$ [16, 17], where T is the temporal length of the signal pulse. In addition, v_g must be small enough for the entire signal pulse to be spatially compressed into the ensemble before storage — *i.e.*, $v_g T \ll L$ — so as to avoid “leakage” of the front edge of the pulse outside the medium before the back edge has entered. Simultaneous satisfaction of both these conditions is possible only at very large optical depth αL . Indeed, in the limit of infinitely large optical depth and negligible ground state decoherence, any input pulse can be converted into a spin wave and back with 100% efficiency. Under the same conditions, any desired output pulse shape can be easily obtained by adjusting the control field power (and hence the group velocity) as the pulse exists the medium. However, most current experimental realizations of ensemble-based quantum memories operate at limited optical depth $\alpha L \lesssim 10$ due to various constraints (see Sec. E.6 and Refs. [81, 92, 93, 80, 94, 95]). At finite αL , losses limit the maximum achievable memory efficiency to a value below 100%, making efficiency optimization and output-pulse shaping important and nontrivial (see Chapter 2). Thus, in Secs. 3.3 and 3.4, we experimentally demonstrate how to achieve the maximum memory efficiency for any given αL by adjusting the input pulse shape and the control field, respectively. In Sec. 3.4, we also experimentally demonstrate the retrieval into any desired output mode. For the sake of clarity, it is worth noting that while the author of this dissertation was involved in suggesting, planning, analyzing, and writing up the experiments, the actual experimental work was done by the author’s collaborators, most notably Irina Novikova and Nathaniel Phillips.

3.2 Experimental Setup

The experiments were performed using a standard Rb vapor EIT setup. While the experiments of Secs. 3.3 and 3.4 were performed in different laboratories (that of Prof. Ronald Walsworth at Harvard and that of Prof. Irina Novikova at the College of William & Mary, respectively), the experimental setup was almost identical. Therefore, we describe both experimental setups in this Section at the same time. Any experimental parameter that differed between Secs. 3.3 and 3.4 is listed twice, with the value for Sec. 3.4 listed in square brackets. The experimental setup of Sec. 3.4 is also described in detail in Sec. E.3.

A cylindrical 7.5 cm-long glass cell containing isotopically enriched ^{87}Rb and 40[30] Torr Ne buffer gas was mounted inside a three-layer magnetic shield to reduce

stray magnetic fields. The Rb vapor cell was typically operated at a temperature $\simeq 60[60.5]^\circ\text{C}$, corresponding to a Rb vapor density $\simeq 2.5[2.6] \times 10^{11} \text{ cm}^{-3}$ and an optical depth $\alpha L \simeq 18[24]$. The main reason for the difference in optical depths between the two experiments is the different buffer gas pressure: optical depth is inversely proportional to the collisional halfwidth γ (see Chapter 2), which is in turn proportional to buffer gas pressure [96]. Optical fields near the 795 nm Rb D_1 transition were used for EIT and light storage. These fields were created by phase-modulating the output of an external-cavity diode laser using an electro-optical modulator (EOM) operating at the ground state hyperfine frequency of ^{87}Rb (6.8 GHz). The laser carrier frequency was tuned to the $5^2\text{S}_{1/2}F = 2 \rightarrow 5^2\text{P}_{1/2}F' = 2$ transition and served as the control field during light storage; while the high-frequency modulation sideband, resonant with the $5^2\text{S}_{1/2}F = 1 \rightarrow 5^2\text{P}_{1/2}F' = 2$ transition, served as the signal field. The amplitudes of the control and signal fields could be changed independently by simultaneously adjusting the EOM amplitude and the total intensity in the laser beam using an acousto-optical modulator (AOM). Typical peak control field and signal pulse powers were $\sim 5[18] \text{ mW}$ and $100[50] \mu\text{W}$, respectively. In the experimental setup of Sec. 3.4, the low-frequency modulation sideband was suppressed to 10% of its original intensity using a temperature-tunable Fabry-Perot etalon. While this suppression was not done in the setup of Sec. 3.3, we later checked that at the optical depth used in Sec. 3.3, the presence of the low-frequency modulation sideband played no detectable role, which is not the case at higher optical depths (see Sec. E.6 and Refs. [64, 66]). The laser beam was collimated to a Gaussian cylindrical beam of relatively large diameter ($\simeq 7[5] \text{ mm}$) and then circularly polarized using a quarter-wave plate before entering the vapor cell. The Rb atom diffusion time out of the laser beam was long enough to have negligible effects [97, 98]. We found the typical spin wave decay time to be $1/(2\gamma_s) \simeq 2[0.5] \text{ ms}$, most likely arising from small, uncompensated remnant magnetic fields. The duration of pulses used in the experiment was short enough for the spin decoherence to have a negligible effect during writing and retrieval stages and to cause a modest reduction of the efficiency $\propto \exp(-2\gamma_s\tau) = 0.82$ during the storage time $\tau = 400[100] \mu\text{s}$. For the theoretical calculations, we model the ^{87}Rb D_1 line as a homogeneously broadened Λ -system with no free parameters, as we describe in detail in Sec. E.3. We could ignore Doppler broadening since the homogeneous pressure broadened width $2\gamma \approx 2\pi \times 400[300] \text{ MHz}$ [96] of the optical transition was comparable to the width of Doppler broadening.

3.3 Optimization with respect to the Input Pulse

In this Section, we experimentally demonstrate memory optimization with respect to the input pulse shape.

3.3.1 Basic Idea

In Chapter 2 (with a more detailed discussion in Sec. B.5), a procedure to determine the optimal input signal pulse-shape for a given optical depth and control field was proposed. This optimization procedure is based on successive time-reversal iterations and shown schematically in Fig. 3.1. The atoms are initially prepared in state $|g\rangle$. Then, for a given input control field with Rabi frequency envelope $\Omega(t)$, a trial input signal pulse with envelope $\mathcal{E}_{\text{in}}(t)$ is mapped into a spin-wave $S(z)$ inside the atomic ensemble (writing stage). ($\mathcal{E}_{\text{in}}(t)$ and the input control field are taken to be non-zero over the time-interval $[-T, 0]$.) In general there will be some absorptive and leakage losses during this writing process. After a storage period τ , an output control field $\Omega(\tau - t)$ — i.e., the time-reversed version of the input control field — is used to map $S(z)$ back into an output signal pulse $\mathcal{E}_{\text{out}}(t)$, which leaves the medium and is measured (retrieval stage). The input signal pulse for the next iteration is then generated with a pulse-shape corresponding to a time-reversed version of the previous output signal pulse and an amplitude normalized to make the energy of the pulse equal to a fixed target value. These steps are then repeated iteratively, using the same input and output control fields, until the shape of the output signal pulse on a given iteration is identical to the time-reversed profile of its corresponding input signal pulse. As shown in Chapter 2 and discussed in more detail in Appendix B, the resulting signal pulse-shape provides the highest memory efficiency possible for a given optical depth and control field profile and is applicable to both quantum and weak classical signal pulses.

In the experiment reported here, we tested this optimization procedure and confirmed its three primary predictions:

1. The memory efficiency (the ratio of energies carried by the retrieved and input signal pulses) grows with each iteration until the input signal field converges to an optimal pulse-shape. See Fig. 3.2.
2. For a given control field profile and optical depth αL , the optimization procedure converges to the same input signal pulse-shape and the same maximum efficiency, independent of the initial (trial) signal pulse-shape. See Fig. 3.3.
3. For a given optical depth, different control field profiles result in different optimal signal pulse-shapes but yield the same maximum efficiency, provided spin-coherence decay during the writing and retrieval stages is small. See Fig. 3.4.

3.3.2 Experimental Results

Fig. 3.2 shows an example implementation of the iterative optimization procedure, using a step-like control field and a trial input signal pulse with a Gaussian profile. Some portions of the first input pulse were incoherently absorbed or escaped the cell before the control field was turned off; but a fraction was successfully mapped into an atomic spin-wave, stored for 400 μs , and then retrieved and detected. This

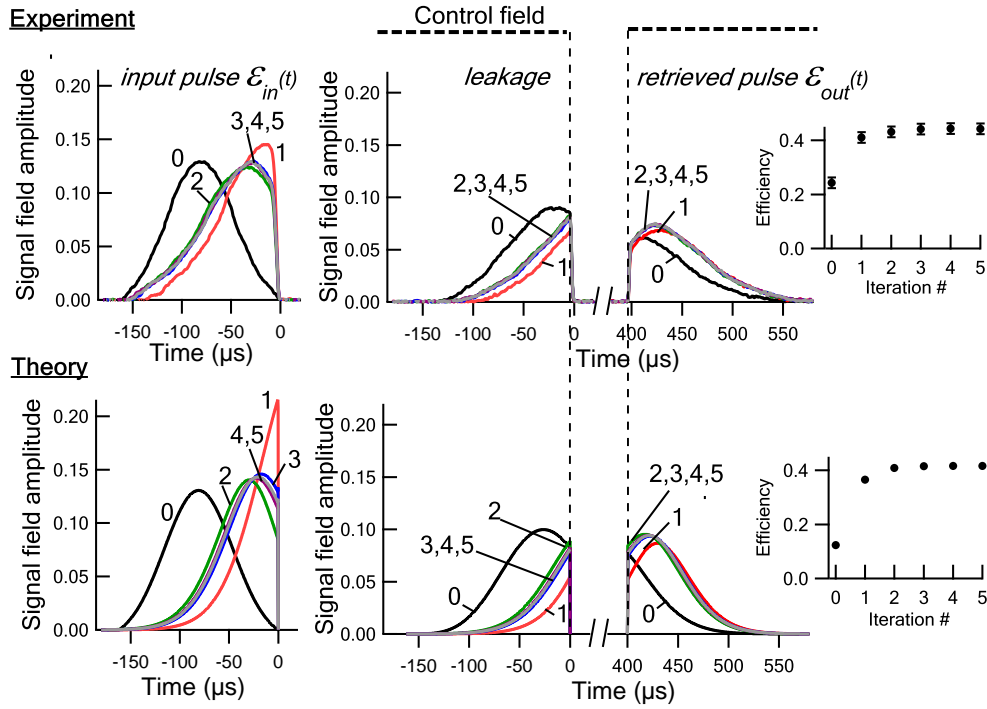


Figure 3.2: Top: Example data for the signal pulse optimization procedure, using a constant control field during writing and retrieval (timing indicated by dashed lines) and a $400 \mu\text{s}$ storage interval. *Left*: input signal pulses \mathcal{E}_{in} , labeled by the iteration number and beginning with a trial Gaussian input pulse (iteration “0”). *Center*: signal pulse leakage for each iteration. *Right*: output signal pulse \mathcal{E}_{out} for each iteration. *Inset*: Memory efficiency determined for each iteration from the measured input and output signal pulses: $\int \mathcal{E}_{\text{out}}^2 dt / \int \mathcal{E}_{\text{in}}^2 dt$. Bottom: theoretical calculation of the signal pulse optimization procedure, using the model described in the text and the experimental conditions of the measurements in the top panel. *Inset*: Calculated memory efficiency.

retrieved signal pulse-shape was used to generate a time-reversed and normalized input signal pulse for the next iteration. After a few iterations, both the input and output signal pulses converged to fixed profiles, with the memory efficiency increasing with each iteration and reaching a maximum. In general, different trial input pulses all converged to the same optimal signal pulse-shape (e.g., see Fig. 3.3). In addition, systematic variation of the signal pulse-shape uniformly yielded lower efficiencies than the pulse-shape given by the optimization procedure.

We performed similar optimization experiments for a wide range of control field profiles. Some example results are shown in Fig. 3.4. In general we found different optimized signal pulse-shapes for different control field profiles; however, the opti-

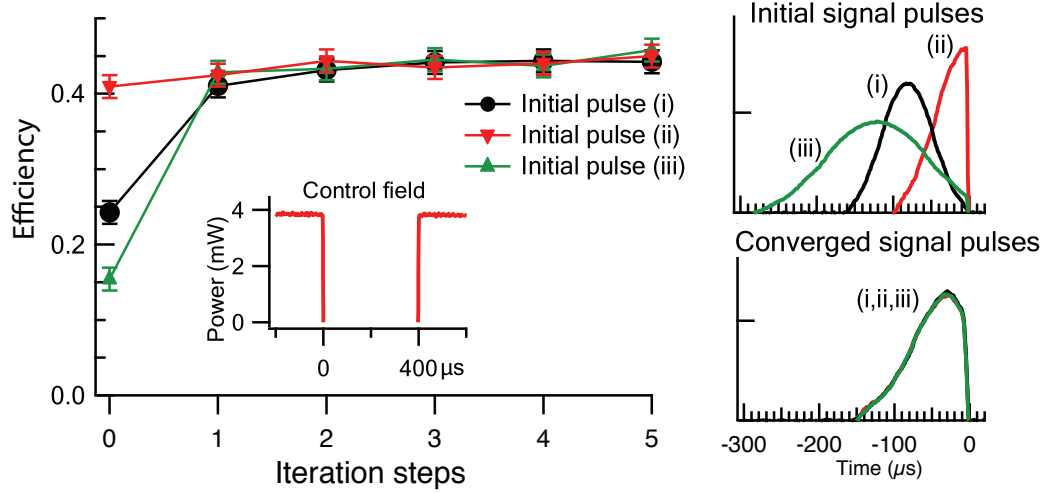


Figure 3.3: Example data illustrating that the iterative optimization procedure converges to the same signal pulse-shape and maximum efficiency independent of the initial signal pulse-shape, for a given control field profile (shown in inset) and optical depth ($\alpha L = 18$).

mized memory efficiency was independent of the control field profile. In addition, the optimized signal pulse-shape typically provides a significant improvement in efficiency compared to naïve Gaussian pulses, for a given optical depth. These observations are consistent with the theoretical prediction of Chapter 2 that optimal light-storage efficiency does not depend on the control field, but only on the optical depth, provided spin decoherence and other loss mechanisms can be neglected during the writing and retrieval stages.

3.3.3 Comparison to Theory

To compare our experimental results with theoretical calculations, we approximated the 16-level structure of the ^{87}Rb D_1 line with a single three-level Λ -system (see Sec. E.3 for details). The stored light dynamics then reduced to Eqs. (2.1-2.3), extended to allow for the decay of atomic coherence during the $400 \mu\text{s}$ storage time (see Eq. (B.3)). Using these equations and no free parameters (Sec. E.3), we calculated the results of the iterative optimization procedure: i.e., the output signal field (both signal leakage and stored/retrieved pulses), as well as the generated input signal pulse for each successive iteration. Example results of these calculations are shown in the bottom panels of Fig. 3.2. The calculated output signal pulse-shapes are qualitatively similar to the experimental results and converge to an optimal input signal pulse-shape within a few iteration steps. The calculated efficiencies for the optimization procedure, shown in Figs. 3.2 and 3.4(f), are in reasonable agreement with

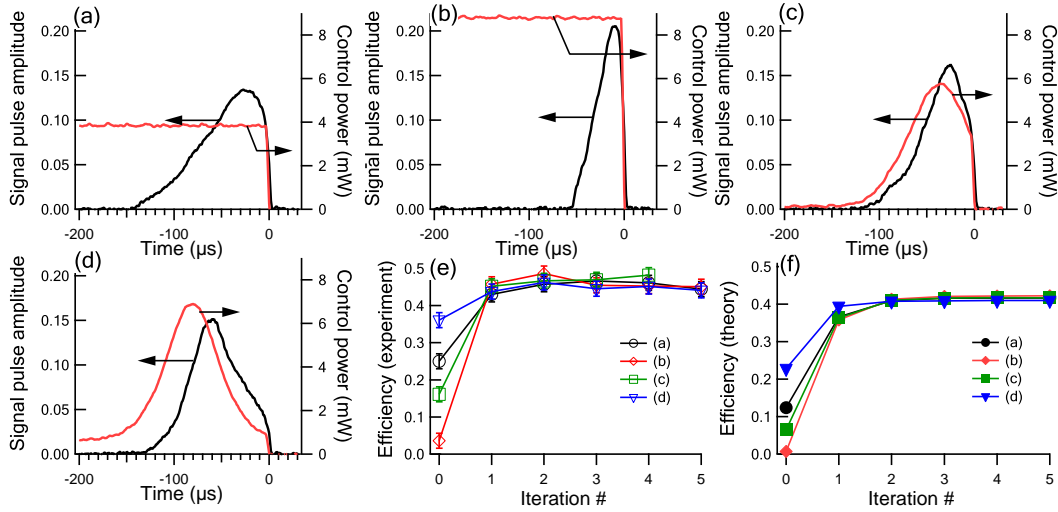


Figure 3.4: (a)-(d) Examples of optimal input signal pulses determined experimentally by application of the iterative optimization procedure, for different control field profiles. In all cases, the initial (trial) signal pulse has the same Gaussian pulse-shape and amplitude as the trial pulse used in the data shown in Fig. 3.2. (e) Experimentally measured and (f) calculated memory efficiencies as functions of the iteration number.

experiment. We also confirmed that the effects of inhomogeneous Doppler broadening were small for the buffer gas pressure used in our experiments, by repeating the calculations in a more realistic approximation that included Doppler broadening of Rb atoms as well as velocity changing collisions with buffer gas atoms (see Appendix C for the discussion of some of the underlying theory).

3.3.4 Conclusion and Outlook

In conclusion, we experimentally demonstrated an iterative optimization procedure, based on time-reversal, to find the input signal pulse-shape that maximizes the efficiency of light storage and retrieval. We confirmed the three primary predictions of the theory underlying the optimization procedure of Chapter 2: (i) efficiency grows with each iteration until the input signal field converges to its optimal pulse-shape; (ii) the result of the optimization procedure is independent of the initial (trial) signal pulse-shape; and (iii) the optimal efficiency does not depend on the control field temporal profile. We also performed theoretical calculations of the light storage process and the optimization procedure, and found good qualitative agreement with the experimental results, thus supporting the interpretation that optical depth is the key figure of merit for light storage efficiency. The optimization procedure should be ap-

plicable to both classical and quantum signal pulses and to a wide range of ensemble systems. As one example, since pulse-shape optimization with weak classical light pulses can be straightforwardly performed, such optimization could be used to determine the temporal profile of input quantum fields, for which mode-shape generation and measurement are much more difficult to carry out. Also, pulse-shape optimization of the kind demonstrated here in atomic ensembles could be applicable to other systems, *e.g.*, photonic crystals [91].

3.4 Optimization with respect to the Control Pulse

3.4.1 Motivation

The applications of photonic quantum memories to quantum communication [61] and linear optical quantum computation [15] put forth two important requirements for the quantum memory: (i) the memory efficiency is high (*i.e.*, the probability of losing a photon during storage and retrieval is low) and (ii) the retrieved photonic wavepacket has a well-controlled shape to enable interference with other photons. In Sec. 3.3, we demonstrated an iterative procedure in which the maximum memory efficiency is achieved by adjusting the shape of the incoming photon wavepacket. The advantage of this optimization procedure is the fact that the optimal wavepacket shape is produced directly by the experimental apparatus rather than by a calculation. However, one disadvantage of this procedure is that it does not work (and hence does not satisfy requirement (i)) when one does not have the freedom to choose the shape of the photonic wavepacket. The second disadvantage of this procedure is that it does not provide a way to shape the retrieved photon into any desired mode (thus, preventing the satisfaction of requirement (ii)).

To remedy these disadvantages, here we experimentally demonstrate the capability to satisfy both quantum memory requirements in an ensemble with a limited optical depth. Specifically, by adjusting the control field envelopes for several arbitrarily selected input pulse shapes, we demonstrate storage and precise retrieval into any desired output pulse shape with experimental memory efficiency very close to the fundamental limit derived in Chapter 2. This ability to achieve maximum efficiency for any input pulse shape is crucial when optimization with respect to the input pulse (Sec. 3.3) is not applicable (*e.g.*, if the photons are generated by parametric down-conversion [99]). At the same time, control over the outgoing mode, with precision far beyond the early attempts [77, 100, 101, 102], is essential for experiments based on the interference of photons stored under different experimental conditions (*e.g.*, in atomic ensembles with different optical depths), or stored a different number of times. In addition, control over output pulse duration may also allow one to reduce sensitivity to noise (*e.g.*, jitter). It is also important to note that shaping the output

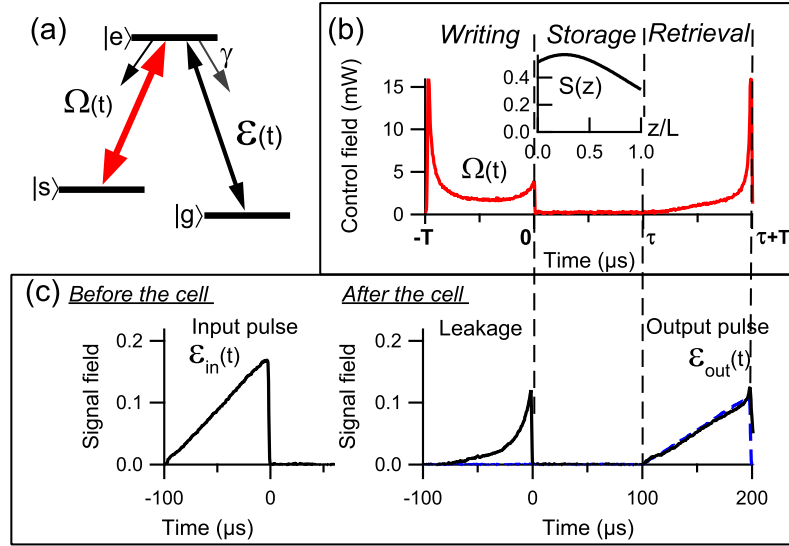


Figure 3.5: (a) Schematic of the three-level Λ interaction scheme. Control (b) and signal (c) fields in pulse-shape-preserving storage of a “positive-ramp” pulse using a calculated optimal control field envelope $\Omega(t)$. During the *writing* stage ($t < 0$), the input pulse $\mathcal{E}_{\text{in}}(t)$ is mapped onto the optimal spin-wave $S(z)$ [inset in (b)], while a fraction of the pulse escapes the cell (leakage). After a *storage* time τ , the spin-wave $S(z)$ is mapped into an output signal pulse $\mathcal{E}_{\text{out}}(t)$ during the *retrieval* stage. The dashed blue line in (c) shows the target output pulse shape.

mode via the control pulse avoids additional losses that would be present if one were to post-process the retrieved photon with an electro-optical modulator [103]. Finally, as we demonstrate in Sec. 3.4.3, full control over the output pulse shape allows one to convert single photons into time-bin qubits, which play an important role in quantum communication [104].

3.4.2 Experimental Results

An example of optimized light storage with controlled retrieval is shown in Fig. 3.5(b,c). In this measurement, we chose the input pulse¹ $\mathcal{E}_{\text{in}}(t)$ to be a “positive ramp”. According to theory presented in Chapter 2, the maximum memory efficiency is achieved only if the input pulse is mapped onto a particular optimal spin wave $S(z)$, unique for each αL . The calculated optimal spin wave for $\alpha L = 24$ is shown in the

¹Throughout this section (Sec. 3.4), all control and signal envelopes are assumed to be real. Also, in all experimental data plots, all signal pulses are shown in the same scale, and all input pulses are normalized to have the same unit area $\int_{-T}^0 |\mathcal{E}_{\text{in}}(t)|^2 dt = 1$, where t is time in μs .

inset in Fig. 3.5(b). Then, we used the method described in Secs. B.6.2 and B.10.5 to calculate the *writing* control field $\Omega(t)$ ($-T < t < 0$) that maps the incoming pulse onto the optimal spin wave $S(z)$. To calculate the *retrieval* control field $\Omega(t)$ ($\tau < t < \tau + T$) that maps $S(z)$ onto the target output pulse $\mathcal{E}_{\text{tgt}}(t)$, we employ the same writing control calculation together with the following time-reversal symmetry of the optimized light storage (see Chapter 2 and Sec. 3.3). A given input pulse, stored using its optimal writing control field, is retrieved in the time-reversed and attenuated copy of itself [$\mathcal{E}_{\text{out}}(t) \propto \mathcal{E}_{\text{in}}(\tau - t)$] when the time-reversed control is used for retrieval [$\Omega(t) = \Omega(\tau - t)$]. Thus the control field that retrieves the optimal spin wave $S(z)$ into $\mathcal{E}_{\text{tgt}}(t)$ is the time-reversed copy of the control that stores $\mathcal{E}_{\text{tgt}}(\tau - t)$ into $S(z)$. As shown in Fig. 3.5(b,c), we used this method to achieve pulse-shape-preserving storage and retrieval, *i.e.*, the target output pulse was identical to the input pulse (“positive ramp”). The measured output pulse [solid black line in Fig. 3.5(c)] matches very well the target shape [dashed blue line in the same figure]. This qualitatively demonstrates the effectiveness of the proposed control method.

To describe the memory quantitatively, we define memory efficiency η as the probability of retrieving an incoming photon after some storage time, or, equivalently, as the energy ratio between retrieved and initial signal pulses:

$$\eta = \frac{\int_{\tau}^{\tau+T} |\mathcal{E}_{\text{out}}(t)|^2 dt}{\int_{-T}^0 |\mathcal{E}_{\text{in}}(t)|^2 dt}. \quad (3.1)$$

To characterize the quality of pulse shape generation, we define an overlap integral J^2 as [14]

$$J^2 = \frac{|\int_{\tau}^{\tau+T} \mathcal{E}_{\text{out}}(t) \mathcal{E}_{\text{tgt}}(t) dt|^2}{\int_{\tau}^{\tau+T} |\mathcal{E}_{\text{out}}(t)|^2 dt \int_{\tau}^{\tau+T} |\mathcal{E}_{\text{tgt}}(t)|^2 dt}. \quad (3.2)$$

The measured memory efficiency for the experiment in Fig. 3.5 is 0.42 ± 0.02 . This value closely approaches the predicted highest achievable efficiency 0.45 for $\alpha L = 24$ (see Chapter 2), corrected to take into account the spin wave decay during the storage time. The measured value of the overlap integral between the output and the target is $J^2 = 0.987$, which indicates little distortion in the retrieved pulse shape.

The definitions of efficiency η and overlap integral J^2 are motivated by quantum information applications. Storage and retrieval of a single photon in a non-ideal passive quantum memory produces a mixed state that is described by a density matrix $\rho = (1 - \eta)|0\rangle\langle 0| + \eta|\phi\rangle\langle\phi|$ (see Sec. A.2), where $|\phi\rangle$ is a single photon state with envelope $\mathcal{E}_{\text{out}}(t)$, and $|0\rangle$ is the vacuum state. Then the fidelity between the target single-photon state $|\psi\rangle$ with envelope $\mathcal{E}_{\text{tgt}}(t)$ and the single-photon state $|\phi\rangle$ is given by the overlap integral J^2 [Eq. (3.2)], while $F = \langle\psi|\rho|\psi\rangle = \eta J^2$ is the fidelity of the output state ρ with respect to the target state $|\psi\rangle$. The overlap integral J^2 is also an essential parameter for optical quantum computation and communication protocols [61, 15], since $(1 - J^2)/2$ is the coincidence probability in the Hong-Ou-Mandel [105] interference between photons $|\psi\rangle$ and $|\phi\rangle$ [14]. One should be cautious

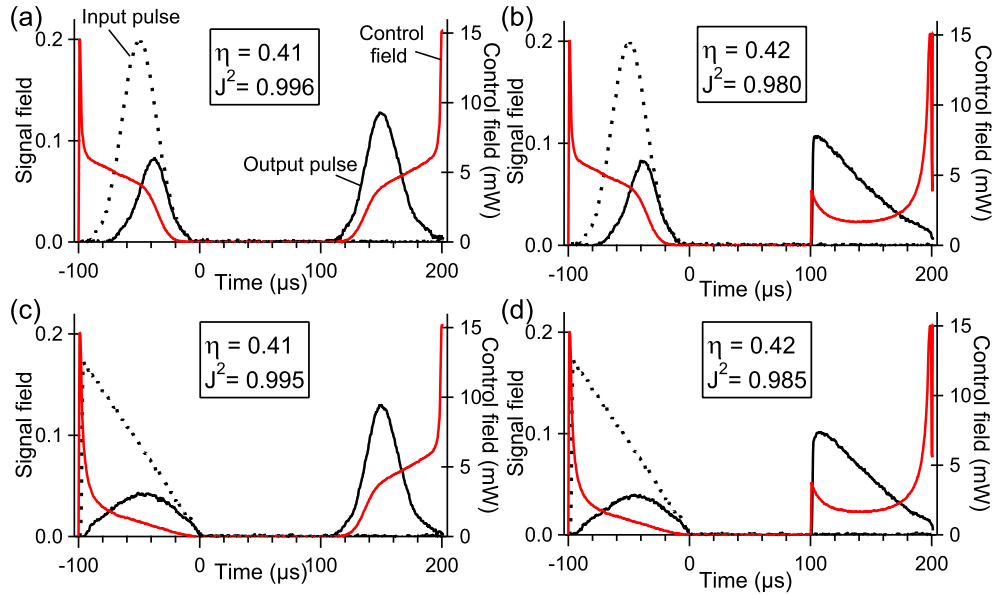


Figure 3.6: An input Gaussian pulse was optimally stored and retrieved either into its original pulse shape (a) or into a ramp pulse shape (b). Similarly, the incoming ramp pulse was optimally stored and retrieved into a Gaussian (c) or into an identical ramp (d). Input and output signal pulses are shown as dotted and solid black lines, respectively, while the optimal control fields are shown in solid red lines.

in directly using our classical measurements of η and J^2 to predict fidelity for single photon states because single photons may be sensitive to imperfections that do not significantly affect classical pulses. For example, four-wave mixing processes may reduce the fidelity of single-photon storage, although our experiments (Appendix E) found these effects to be relatively small at $\alpha L < 25$.

Fig. 3.6 shows more examples of optimal light storage with full output-pulse-shape control. For this experiment, we stored either of two randomly selected input signal pulse shapes — a Gaussian and a “negative ramp” — and then retrieved them either into their original waveforms (a,d) or into each other (b,c). Memory efficiency η and overlap integral J^2 are shown for each graph. Notice that the efficiencies for all four input-output combinations are very similar (0.42 ± 0.02) and agree well with the highest achievable efficiency (0.45) for the given optical depth $\alpha L = 24$. The overlap integrals are also very close to 1, revealing an excellent match between the target and the retrieved signal pulse shapes. Note that different input pulses stored using corresponding (different) optimized writing control fields but retrieved using identical control fields [pairs (a,c) and (b,d)] had identical output envelopes, very close to the target one. This observation, together with the fact that the measured

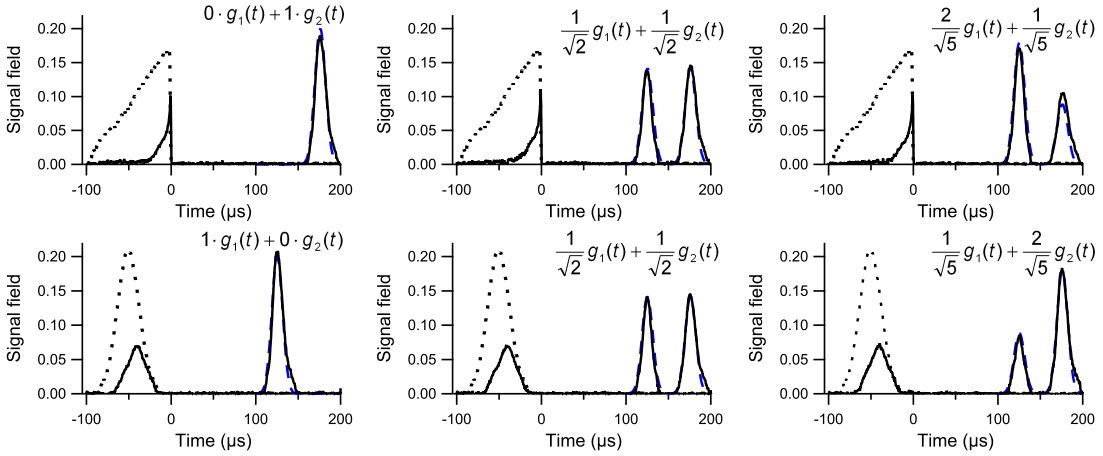


Figure 3.7: Examples of storage of signal input pulses with Gaussian and triangular envelopes, followed by retrieval in a linear combination of two time-resolved Gaussian pulse shapes $g_1(t)$ and $g_2(t)$. Input and output signal fields are shown in dotted and solid black lines, respectively. Dashed blue lines show the target envelopes.

memory efficiency is close to the fundamental limit, suggests that indeed different initial pulses were mapped onto the same optimal spin wave. This indirectly confirms our control not only over the output signal light field but also over the spin wave.

3.4.3 Conversion of a Single Photon into a Time-Bin Qubit

Our full control over the outgoing pulse shape opens up an interesting possibility to convert a single photon into a so-called “time-bin” qubit — a single photon excitation delocalized between two time-resolved wavepackets (bins). The state of the qubit is encoded in the relative amplitude and phase between the two time bins [104]. Such time-bin qubits are advantageous for quantum communication since they are insensitive to polarization fluctuations and depolarization during propagation through optical fibers [104]. We propose to efficiently convert a single photon with an arbitrary envelope into a time-bin qubit by optimally storing the photon in an atomic ensemble, and then retrieving it into a time-bin output envelope with well-controlled relative amplitude and phase using a customized retrieval control field.

To illustrate the proposed output pulse shaping, in Fig. 3.7, we demonstrate storage of two different classical input pulses (a Gaussian and a positive ramp), followed by retrieval into a time-bin-like classical output pulse, consisting of two distinct Gaussian pulses $g_{1,2}(t)$ with controllable relative amplitude and delay. We obtained the target output independently of what the input pulse shape was. We also attained the same memory efficiency as before (0.41 ± 0.02) for all linear combinations. Also, regardless

of the input, the output pulse shapes matched the target envelopes very well, as characterized by the value of the overlap integral close to unity $J^2 = 0.98 \pm 0.01$. We also verified that the envelopes of the two retrieved components of the output pulse were nearly identical by calculating the overlap integral $J^2(g_1, g_2)$ between the retrieved bins g_1 and g_2 . This parameter is important for applications requiring interference of the two qubit components [104]. The average value of $J^2(g_1, g_2) = 0.94 \pm 0.02$ was consistently high across the full range of target outputs. The relative phase of the two qubit components can be adjusted by controlling the phase of the control field during retrieval. The demonstrated control over the amplitude ratio and shape of the two output pulses is essential for achieving high-fidelity time-bin qubit generation. Our scheme is also immediately applicable to high-fidelity partial retrieval of the spin wave [77], which forms the basis for a recent promising quantum communication protocol [106].

3.4.4 Conclusion and Outlook

To conclude, we have reported the experimental demonstration of optimal storage and retrieval of arbitrarily shaped signal pulses in an atomic vapor at an optical depth $\alpha L = 24$ by using customized writing control fields. Our measured memory efficiency is close to the highest efficiency possible at that optical depth. We also demonstrate full precision control over the retrieved signal pulse shapes, achieved by shaping the retrieval control field. A high degree of overlap between the retrieved and target pulse shapes was obtained (overlap integral $J^2 = 0.98 - 0.99$) for all input and target pulse shapes tested in the experiments. We also demonstrated the potential application of the presented technique to the creation of optical time-bin qubits and to controlled partial retrieval. Finally, we observed excellent agreement between our experimental results and theoretical modeling (for deviations at higher αL , see Sec. E.6). The optimal storage and pulse-shape control presented here are applicable to a wide range of experiments, since the underlying theory applies to other experimentally relevant situations such as ensembles enclosed in a cavity discussed in Ref. [93] and Appendix A, the off-resonant regime discussed in Chapter 2 and Appendices A and B, non-adiabatic storage (*i.e.*, storage of pulses of high bandwidth) discussed in Appendix D, and ensembles with inhomogeneous broadening (including Doppler broadening [80] and line broadening in solids [87]) discussed in Appendix C. Thus, we expect this pulse-shape control to be indispensable for applications in both classical [107] and quantum optical information processing.

Chapter 4

Photonic Phase Gate via an Exchange of Fermionic Spin Waves in a Spin Chain

4.1 Introduction

While photon storage discussed in Chapters 2 and 3 does not require nonlinear interactions between photons, such interactions are essential for many potential applications in quantum communication and computation [108, 4]. However, since single-photon nonlinearities are generally very weak [109], strong photon-photon interactions require elaborate and experimentally challenging schemes [110, 111, 112, 113, 114, 115, 116, 117, 118, 119, 120, 121, 122] with a reliable, practical approach yet to emerge. In principle, a robust and conceptually simple gate between two photons can be achieved by temporarily storing their quantum information into two excitations with fermionic character and exchanging these excitations to obtain the π -phase shift. In this Chapter, we propose how to implement this scheme with the role of fermionic excitations played by spin waves in a one-dimensional spin chain.

The five steps of the protocol, labeled as (1) through (5), are schematically illustrated in Fig. 4.1(a). Two photonic wavepackets, shown in red and labeled as f and h , carry photonic qubits, in which $|0\rangle$ ($|1\rangle$) corresponds to the absence (presence) of a single photon in the mode. The goal is to implement a two-qubit phase gate, which puts a π phase on the state $|1\rangle|1\rangle$, leaving the other three basis states ($|0\rangle|0\rangle$, $|0\rangle|1\rangle$, and $|1\rangle|0\rangle$) unchanged. The two wavepackets propagate in an optical waveguide [123, 124, 125] coupled to a 1D optical lattice filled with one bosonic Λ -type atom [Fig. 4.1(b)] in state $|g\rangle$ per site and with tunneling between sites turned off [126]. In step (1), photon storage techniques (see Chapters 2 and 3, Appendices A-E, and Refs. [17, 76, 127]) are used to map the two photons [$\hat{\mathcal{E}}$ in Figs. 4.1(a,b)] via an auxiliary control field [Ω in Figs. 4.1(a,b)] onto two spin waves formed by the

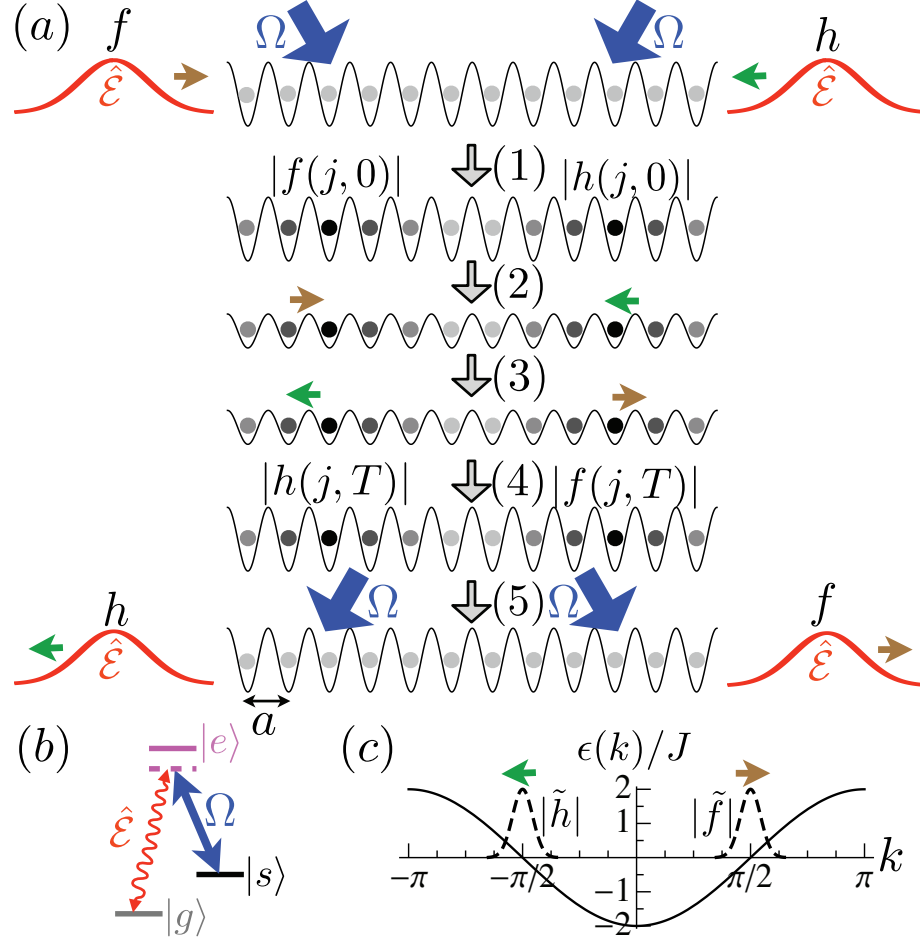


Figure 4.1: (a) Schematic diagram for the implementation of the photonic two-qubit phase gate. (b) The Λ -type atomic level diagram used for interfacing photons and spin waves. (c) The fermionic dispersion relation $\epsilon(k)$ in units of J (solid line), and, schematically, the amplitudes of the two spin waves in k -space (dashed lines).

collective atomic g - s coherence, with the amplitude of the spin wave on a given atom indicated by the darkness of the circle. (2) The lattice depth is then reduced yielding a nearest-neighbor superexchange spin Hamiltonian [126], which couples atomic states s and g and which can be adjusted in such a way that the spin waves behave as free fermions [128]. (3) The spin waves then propagate through each other, exchange places, and, being fermionic, pick up the desired π phase. (4) The superexchange is then turned off, and (5) the spin waves are retrieved back onto photonic modes.

The gate is thus achieved via an exchange of two free fermionic excitations that temporarily carry the photonic qubits. A closely related idea of endowing photons with fermionic character by means of nonlinear atom-photon interactions was first

introduced in Ref. [116]. Contrary to this, in our proposal, fermionic behavior of photons is achieved by mapping photonic qubits onto atomic states and then relying on strong atom-atom interactions. Such an approach is similar to that of Refs. [115, 127, 118], where photonic quantum information is also processed by mapping it onto atomic states and using atom-atom interactions.

Since our gate is based on the relative positions of the fermions, it is robust in that the phase is exactly π . Given that a Kerr nonlinearity yields the desired nonlinear phase for bosonic photons [111], it is not surprising that free fermions, which can be mapped in 1D onto bosons with an infinite repulsion [129], experience the phase as well. At the same time, since free fermions are not sufficient for universal quantum computation [130], the interconversion between bosonic photons and fermionic spin waves is essential to our proposal [116]. The strong collectively enhanced coupling between photons and atoms required for this interconversion (see Refs. [17, 76, 127] and Chapter 2) can be achieved in recently demonstrated waveguides that transversely confine both atoms and photons to dimensions on the order of a wavelength [123, 124, 125, 38] and that are already actively explored from both the fundamental [110, 40, 41] and the quantum-information [41, 122, 21] points of view. In addition to atom-photon interactions, our gate, similarly to Refs. [115, 118], relies on strong interatomic interactions to obtain the superexchange Hamiltonian, which contrasts with methods where atom-photon interactions alone suffice [111, 112, 113, 114, 116, 117, 122, 119, 120, 121]. At the same time, our proposals differs from Refs. [115, 118] in that it relies (in contrast to Ref. [115]) purely on tunneling for spin wave propagation and does not require (in contrast to Ref. [118]) any active manipulation of the atoms other than during photon storage and retrieval.

4.2 Details of the Protocol

We begin with a bosonic two-component single-band Hubbard model in a 1D lattice, with the transverse motion frozen. There are N sites with nearest neighbor spacing a , yielding a total length $L = Na$. The tunneling rates are t_α for species α ($\alpha = g, s$), while the s-wave interaction energies are $U_{\alpha\alpha}$ for two α -atoms and U_{sg} for an s atom with a g atom [126]. Assuming one atom per each of N sites in the weak tunneling limit $t_g, t_s \ll U_{gg}, U_{ss}, U_{sg}$, ignoring edge effects, and dropping the term $\sum_j S_j^z$ (which would contribute a simple linear phase), the superexchange XXZ Hamiltonian is ($\hbar = 1$ throughout the Chapter) [126]

$$H = \sum_{j=1}^{N-1} \left[-J(S_j^+ S_{j+1}^- + S_j^- S_{j+1}^+) + V S_j^z S_{j+1}^z \right], \quad (4.1)$$

where $V = 2 \frac{t_g^2 + t_s^2}{U_{sg}} - \frac{4t_g^2}{U_{gg}} - \frac{4t_s^2}{U_{ss}}$ and $J = \frac{2t_g t_s}{U_{sg}}$. Here $\vec{S}_j = \vec{\sigma}_j/2$, where $\vec{\sigma}_j$ are Pauli operators in the $\{s, g\}$ basis and $S_j^\pm = S_j^x \pm iS_j^y$. It is convenient to use the Jordan-

Wigner transformation [128] to map the spins onto fermions with creation operators c_j^\dagger : $S_j^+ = c_j^\dagger \exp\left(i\pi \sum_{k=1}^{j-1} n_k\right)$ and $S_j^z = n_j - \frac{1}{2}$, where $n_j = c_j^\dagger c_j$. Then, dropping the term $\sum_j n_j$, which would contribute only a linear phase,

$$H = -J \sum_j \left(c_j^\dagger c_{j+1} + c_{j+1}^\dagger c_j \right) + V \sum_j n_j n_{j+1}. \quad (4.2)$$

With $V = 0$, Eq. (4.1) is the XX Hamiltonian, while Eq. (4.2) then represents free fermions. We can obtain $V = 0$, for example, by taking $t_g = t_s = t$ and $U_{gg} = U_{ss} = 2U_{sg} = U$, so that $J = 4t^2/U$. When all three scattering lengths are similar in size, as e.g. in ground-state alkali atoms, U_{sg} can be reduced by shifting the s and g lattices relative to each other [131].

The free fermion ($V = 0$) case can be diagonalized, ignoring boundaries, by going to k -space:

$$H = \sum_k \epsilon(k) c_k^\dagger c_k, \quad (4.3)$$

where k takes N values in the first Brillouin zone from $-\pi$ to π at intervals of $2\pi/N$, $c_k^\dagger = (1/\sqrt{N}) \sum_j e^{ikj} c_j^\dagger$, and the tight-binding dispersion $\epsilon(k) = -2J \cos(k)$ is shown in Fig. 4.1(c).

With all atoms in $|g\rangle$ (denoted as $|\text{vac}\rangle$) and tunneling turned off, two counter-propagating photonic modes, labeled as f and h in Fig. 4.1(a), are incident on our 1D chain of atoms near resonance with the g - e transition [see Fig. 4.1(b)]. We then use two control fields (one for f and one for h) applied at different angles from the side of the chain [Ω in Fig. 4.1(a)] to store (see Refs. [17, 76, 127], Chapters 2 and 3, and Appendices A-E) the two photons into the s - g coherence over two spatially separated regions. As shown below, by appropriately choosing the angle of incidence of the control fields, we can arrange for the left (f) and right (h) spin waves to be centered in k -space around $k = \pi/2$ and $k = -\pi/2$, respectively, as shown in Fig. 4.1(c). This ensures that the two spin waves will move through each other with maximum speed (largest possible difference of first derivatives of $\epsilon(k)$) and with minimal distortion (vanishing second derivative of $\epsilon(k)$). Photonic bandgap effects coming from the periodicity of atomic positions [132] can be avoided if light of different wavelengths is used for the lattice and the photons, which is typically the case in experiments [133].

The XX Hamiltonian is then turned on. Since H is diagonal in the Fourier basis [Eq. (4.3)], it is convenient to define, for any function $q(j)$ on the sites j , its Fourier transform $\tilde{q}(k) = (1/\sqrt{N}) \sum_j q(j) e^{-ikj}$ together with the usual inverse relation $q(j) = (1/\sqrt{N}) \sum_k \tilde{q}(k) e^{ikj}$. Using Eq. (4.3) and $S_j^+ |\text{vac}\rangle = c_j^\dagger |\text{vac}\rangle$, it is then easy to check that the f spin wave alone evolves as $\sum_j f(j, \tau) S_+^j |\text{vac}\rangle$, where $\tilde{f}(k, \tau) = \tilde{f}(k, 0) e^{-i\tau\epsilon(k)}$. We now assume that $f(j, 0)$ is centered around $j = N/4$ and has width $\sim N$ that is nevertheless small enough for $f(j, 0)$ to be negligible near the edge ($j = 1$) and in the middle ($j = N/2$) of the chain. Furthermore, we assume that $\tilde{f}(k, 0)$ is centered around $k = \pi/2$ with Fourier-transform-limited width

$\sim 1/N$, so that, for $N \gg 1$, the dispersion is approximately linear for all relevant k : $\epsilon(k) \approx [k - (\pi/2)]v$, where the velocity (in sites per second) is $v = 2J$. Then, provided the pulse does not reach $j = N$, it moves to the right with velocity v : $f(j, \tau) \approx e^{i\tau J\pi} f(j - v\tau, 0)$. Such spin wave propagation plays an important role in quantum information transport in spin chains [134]. Similarly, the spin wave $h(j, 0)$ centered around $j = 3N/4$ with carrier momentum $-\pi/2$ approximately evolves as $h(j', \tau) \approx e^{i\tau J\pi} h(j' + v\tau, 0)$. Finally, if both f and h are stored simultaneously, they propagate as $\sum_j f(j, \tau) c_j^\dagger \sum_{j'} h(j', \tau) c_{j'}^\dagger |\text{vac}\rangle$, so that after time $\tau = T \equiv N/(2v)$ they exchange places. However, in addition, when rewriting the final state in terms of spin operators S_j^+ , an extra minus sign appears since for all relevant j and j' , $j > j'$. Thus, the state $|1\rangle|1\rangle$ picks up an extra π phase relative to the other three basis states, giving rise to the two-qubit photonic phase gate once the spin waves are retrieved.

4.3 Experimental Realizations

Two experimental systems well suited for the implementation of our phase gate are atoms confined in a hollow core photonic bandgap fiber [123, 124] and atoms trapped in the evanescent field around an ultrathin optical fiber [125]. In the former system, a running-wave red-detuned laser can be used to provide a steep transverse potential limiting atomic motion to a tube and preventing collisions with the walls of the fiber. Then either a blue-detuned [133] or another red-detuned beam can be used to create a 1D lattice in the tube. To prepare the atoms, one can load a Bose-Einstein condensate into the fiber with the lattice turned off (but the tube confinement on), and then adiabatically turn on the lattice bringing the atoms via a phase transition into the Mott state [135]. By adjusting the initial atomic density, the case of one atom per site can be achieved. The superfluid to Mott insulator transition can also be used to load the atoms in the evanescent field system.

In both experimental systems, during photon storage, the k -vector of the spin wave is determined by the projection on the atomic chain axis of the k -vector mismatch between the control and the incoming photon [17]. For example, if the wavelengths of both g - e and s - e transitions are equal to $2a$, then an angle of 60° between the control beam and the atomic chain axis gives the desired spin-wave k -vector of $\pm\pi/(2a)$. For $N = 1000$ and $2a \sim 1\mu\text{m}$, the length of the medium is $\sim 500\mu\text{m}$. Thus, one could indeed use two focused control beams to store independently two single photons from the opposite directions. One could also store photons incident from the same direction, in which case additional Raman transitions or gradients in Zeeman or Stark shifts may be used to produce the desired spin-wave carriers. Spin wave retrieval is carried out in the same manner.

4.4 Imperfections

We now consider several errors that can arise during gate execution. First, to estimate the error due to the finite t/U ratio, we perform two consecutive Shrieffer-Wolff transformations to compute the t^4/U^3 corrections to H . The error due to these corrections can be estimated as $p_1 \sim (t/U)^4$ and can be further reduced by tuning V (see Sec. F.1). Second, photon storage and retrieval with error $p_2 \sim 1/(\eta N)$ (see Appendix B) can be achieved at any detuning (see Chapter 2) and for pulse bandwidths as large as $\eta N \gamma$ (see Appendix D), where ηN is the resonant optical depth on the e - g transition whose linewidth is 2γ . Third, the error due to the decay of the s - g coherence with rate γ_0 is $p_3 \sim \gamma_0 T$. An additional error comes from the reshaping of the pulse due to the nonlinearity of the dispersion. This error falls off very quickly with N , and already for $N = 100$ is as low as 3×10^{-4} (see Secs. F.1 and F.2). Moreover, pulse shape distortion can be further corrected during retrieval (Chapters 2, 3 and Appendices B-E), making the corresponding error negligible.

With an experimentally demonstrated $\eta = 0.01$ [124, 125], we need $N \gtrsim 1000$ to achieve efficient photon storage and retrieval (small p_2). To suppress t^4/U^3 corrections to H (see Sec. F.1), we take $(t/U)^2 = 0.01$, which reduces p_1 down to $\leq 10^{-4}$ and yields velocity $v = 8.3t^2/U$ and propagation time $T = N/(2v) = N/(0.166U)$. For $U = (2\pi)4$ kHz [136] and $N = 1000$, this gives $T \sim 240$ ms, which is shorter than the experimentally observed coherence times of ~ 1 s [137, 133]. Thus, a proof-of-principle demonstration of our gate can already be carried out with current experimental technology. With improved experimental systems, a faster and higher fidelity implementation will also be possible. In particular, coherence times and η can likely be improved with better control of light and atoms. Moreover, larger U might be obtainable via magnetic [138] or optical [139] Feshbach resonances or with more intense lattice lasers.

4.5 Extensions

One possible extension of our gate is the case $V \neq 0$, which allows to obtain a phase gate with a tunable phase. For the case of no or one spin wave, the $V \neq 0$ time evolution is identical, up to unimportant linear and constant phases, to the $V = 0$ evolution. The case of two spin waves can be solved by Bethe ansatz [128] as follows. Ignoring the effects of the boundaries (since our spin waves vanish there) and considering the limit $N \rightarrow \infty$, the state corresponding to two spin waves localized in k -space near $-\pi/2$ and $\pi/2$ can be expanded in orthonormal eigenstates (see Sec. F.3)

$$|\Psi\rangle_{k,p} = \frac{1}{N} \sum_{j < j'} \left(e^{ikj} e^{ipj'} - e^{i\theta_0} e^{ipj} e^{ikj'} \right) |j, j'\rangle, \quad (4.4)$$

where p and k are quantized as before, $p < k$, $\theta_0 = -2 \tan^{-1} [V/(2J)]$, and $|j, j'\rangle = c_j^\dagger c_{j'}^\dagger |\text{vac}\rangle$. The energy of $|\Psi\rangle_{k,p}$ is given (up to an unimportant constant) by the sum of $V = 0$ energies $\epsilon(k) + \epsilon(p)$. The simultaneous propagation of f and h spin waves is then described by

$$|\Psi(\tau)\rangle = \sum_{j < j'} [f(j, \tau)h(j', \tau) - e^{i\theta_0} f(j', \tau)h(j, \tau)] |j, j'\rangle, \quad (4.5)$$

so that at $t = 0$ ($t = T$) only the first (second) term in the square brackets contributes. The phase $-e^{i\theta_0}$ picked up by the state $|1\rangle|1\rangle$ is, thus, continuously tunable from π at $V = 0$ to 0 at $|V|/J \rightarrow \infty$.

Extensions to systems other than bosonic neutral atoms can also be envisioned. First, the implementation with fermionic, rather than bosonic, neutral atoms in a chain, may offer an advantage: it may be easier to load a band insulator of fermionic g atoms than a bosonic Mott insulator (see Sec. F.4). Second, one can envision a chain of ions enclosed in a cavity [140], with the spin Hamiltonian generated by combining spin-dependent optical dipole forces with Coulomb interactions [8]. Finally, a system of dipole-dipole interacting solid state emitters (such as quantum dots or nitrogen vacancy color centers in diamond) coupled to surface plasmons in conducting nanowires [141, 38] may offer long coherence times [142, 143] and fast gate times coming from strong spin-spin interactions.

4.6 Conclusion

We have proposed a robust and conceptually simple photonic phase gate based on the exchange of two fermionic excitations that temporarily carry the photonic qubits. In addition to the possibility of tuning the acquired phase, another advantage of our protocol is that, as in Ref. [118], the spin chain can be simultaneously used not only to couple but also to store the photonic qubits, which is crucial for many quantum information processing tasks [1]. While we have described how the gate works in the occupation basis, it can easily be extended to the more convenient polarization basis [4] simply by applying the above gate to just one of the two polarizations. With currently available experimental systems already sufficient for a proof-of-principle demonstration, our protocol should be immediately useful in fields such as quantum computation and quantum communication.

Chapter 5

Coherent Quantum Optical Control with Subwavelength Resolution

5.1 Introduction and Basic Idea

In contrast to the applications presented in Chapters 2-4, which do not require the addressing of individual atoms, many quantum computing and quantum simulation applications require individual addressing of closely-spaced quantum systems such as atoms [144, 145], ions [146, 147, 27], quantum dots [148, 149, 150], or solid state defects [12]. Moreover, the achievement of a sufficiently strong coupling between individual quantum systems often requires arrays with separations smaller than the optical wavelength λ of the light that can be used to manipulate these systems. However, diffraction sets a fraction of the optical wavelength λ as the fundamental limit to the size of the focal spot of light [151]. This prohibits high-fidelity addressing of individual identical atoms if they are separated by a distance of order λ or less. In this Chapter, we propose a method for coherent optical far-field manipulation of quantum systems with resolution that is not limited by the wavelength of radiation and can, in principle, approach a few nanometers.

Our method for coherent sub-wavelength manipulation is based on the nonlinear atomic response produced by so-called dark resonances [152]. The main idea can be understood using the three-state model atom shown in Fig. 5.1(a). Consider two such atoms, atom 1 and atom 2, positioned along the x -axis at $x = 0$ and $x = d$, respectively, as shown in Fig. 5.1(b). Assume that they are prepared in the ground state $|g\rangle$ and then illuminated by the probe field with wavelength λ and Rabi frequency Ω . For $d \ll \lambda$, one cannot focus the probe on atom 1 without affecting atom 2 and other neighboring atoms. Let us suppose that Ω is uniform over the distance d . In addition, prior to turning on the probe, we turn on a two-photon-resonant

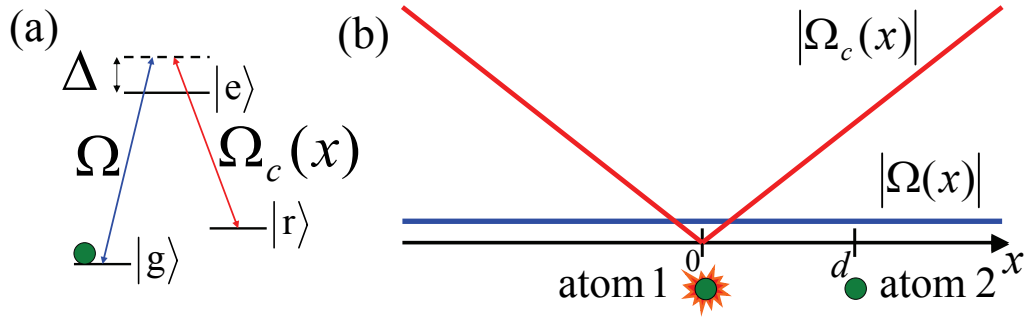


Figure 5.1: (a) 3-level atom prepared in state $|g\rangle$ and coupled at two-photon resonance to a spatially uniform probe field with Rabi frequency Ω and a spatially varying control field with Rabi frequency $\Omega_c(x)$. (b) Schematic of the setup: atom 1, at a node of the control field, responds to the probe, while atom 2, a distance d away, is subject to a large control field $\Omega_c(d) \gg \Omega$ and does not respond to the probe.

spatially varying control field (e.g. a standing wave) of wavelength $\lambda' = 2\pi/k'$ that vanishes at $x = 0$ (i.e. has a node) and has Rabi frequency $\Omega_c(x) \approx \Omega_0 k' x$ for $k'x \ll 1$. Destructive interference of excitation pathways from $|g\rangle$ and $|r\rangle$ up to $|e\rangle$ ensures that the so-called dark state $|\text{dark}(x)\rangle = (\Omega_c(x)|g\rangle - \Omega|r\rangle) / \sqrt{\Omega_c^2(x) + \Omega^2}$ is decoupled from both optical fields [152]. It is the sharp nonlinear dependence of $|\text{dark}(x)\rangle$ on $\Omega_c(x)$ that allows for sub-wavelength addressability. In particular, for atom 1 at $x = 0$, $|\text{dark}(x)\rangle = -|r\rangle$, so that atom 1 prepared in state $|g\rangle$ responds to the probe light in the usual way. On the other hand, for all x such that $\Omega_c(x) \gg \Omega$, $|\text{dark}(x)\rangle \approx |g\rangle$. The space interval around $x = 0$, in which the ground state $|g\rangle$ is not dark, therefore, has width $\sim \Omega / (\Omega_0 k')$ and can thus be made arbitrarily small by increasing the overall intensity of the control ($\propto \Omega_0^2$). In particular, atom 2 at $x = d$ prepared in $|g\rangle$ will not respond to the probe provided $\Omega_0 \gg \Omega / (k'd)$.

This selective sub-wavelength addressability can be used in a variety of ways. For example, one can accomplish selective state manipulation of proximally spaced qubits via spatially selective stimulated Raman transitions. In combination with dipole-dipole interactions, our technique can be used, for $d \ll \lambda$, to generate an efficient two-qubit gate between pairs of atoms. One can implement selective fluorescence detection [146, 147] of the internal state of an atom if $|g\rangle - |e\rangle$ corresponds to a cycling transition (this is possible either if $|r\rangle$ is above $|e\rangle$ or if spontaneous emission from $|e\rangle$ into $|r\rangle$ is much slower than into $|g\rangle$). Finally, one can perform spatially selective optical pumping of individual atoms. Addressability with $d \ll \lambda$ will be important for arrays of quantum dots [148, 149, 150] or optically active defects [12] in solid state, where $d \ll \lambda$ is often needed to achieve coupling [153, 154]. Moreover, our technique enables highly desirable high-fidelity micron-scale manipulation of atoms in optical lattices with $d = \lambda/2$ [144, 145] and ions in linear Paul traps with $d < 5 \mu\text{m}$

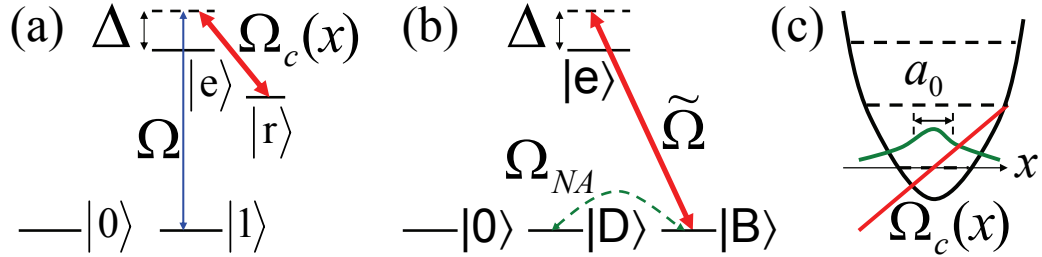


Figure 5.2: Single-qubit phase gate on atom 1. (a) Atom 1 ($\Omega_c(0) = 0$) or atom 2 ($\Omega_c(d) \neq 0$). (b) Atom 2 using basis states $\{|D\rangle, |B\rangle\}$ in place of $\{|1\rangle, |r\rangle\}$. (c) Schematic of imperfect localization of atom 1: parabolic trapping potential $mw^2x^2/2$ with three lowest energy levels indicated, ground state wavepacket of width a_0 , and control field $\Omega_c(x) \approx \Omega_0 k'x$.

[146, 147] (for ions, small d is desirable as it accompanies large vibrational frequencies [146, 147]). Below, we analyze in detail selective coherent state manipulation and then estimate manipulation errors using realistic experimental parameters.

Before proceeding, we note important prior work. Our approach is an extension of incoherent nonlinear techniques used in atom lithography [155] and biological imaging [54]. The nonlinear saturation of EIT response that forms the basis of the present work has already been used for the realization of stationary pulses of light [156] and has been suggested for achieving subwavelength localization of an atom in a standing wave ([157, 158] and references therein). Finally, alternative approaches to solving the addressability problem exist that use Bessel probe beams with nodes on all but one atom [159], place atoms into traps separated by more than λ [160, 161], and resolve closely spaced atoms spectroscopically [162] by applying spatially varying magnetic fields [163, 164] or light shifts [165, 166, 167].

5.2 Detailed Analysis on the Example of a Single-Qubit Phase Gate

5.2.1 Gate Protocol

As a specific example, we now analyze in detail a spatially selective single-qubit phase gate, $|0\rangle \rightarrow |0\rangle$, $|1\rangle \rightarrow e^{i\phi}|1\rangle$, on a qubit encoded in stable atomic states $|0\rangle$ and $|1\rangle$ of one atom in the presence of a proximal neighbor (Fig. 5.2). Consider atoms 1 and 2 that have a tripod configuration shown in Fig. 5.2(a). We assume that the optical transitions from the metastable states $|0\rangle$, $|1\rangle$, and $|r\rangle$ up to $|e\rangle$ are separately addressable via polarization or frequency selectivity. By turning on a probe field with Rabi frequency $\sim \Omega$, wavelength $\lambda = 2\pi/k$, and detuning $\Delta \gg \Omega$ for

a time $\tau \propto \Delta/\Omega^2$, we would like to apply a π -phase on state $|1\rangle$ of qubit 1 via the Stark effect. To minimize errors discussed below, we turn Ω on and off not abruptly but adiabatically (e.g. a linear ramp up from zero immediately followed by a linear ramp down to zero). To shut off the phase shift on the nearby qubit 2, we apply, at two-photon resonance with Ω , a spatially varying control field with Rabi frequency $\Omega_c(x) \approx \Omega_0 k'x$ for $k'x \ll 1$. We assume the control is turned on before and turned off after the probe pulse. For the moment we treat atoms as point particles and return to the question of finite extent of the atomic wave packets in Sec. 5.2.4.

5.2.2 Errors due to Spontaneous Emission and Non-Adiabaticity

The gate error on atom 1 due to spontaneous emission can be estimated as $\tau\gamma\rho_e \sim \tau\gamma(\Omega/\Delta)^2 \sim \gamma/\Delta$, where ρ_i is the population of state $|i\rangle$ and where we assume for simplicity that all transitions are radiatively broadened and that the decay rate of $|e\rangle$ is 2γ . To investigate the effect on atom 2, we define dark and bright states for this atom as $|D\rangle = (\Omega_c|1\rangle - \Omega|r\rangle)/\tilde{\Omega}$ and $|B\rangle = (\Omega|1\rangle + \Omega_c|r\rangle)/\tilde{\Omega}$, where $\tilde{\Omega} = \sqrt{\Omega_c^2 + \Omega^2}$ and $\Omega_c = \Omega_c(x = d)$ (see Fig. 5.2(b)). Since $|D\rangle = |1\rangle$ at the beginning and at the end of the probe pulse (i.e. when $\Omega = 0$), the phase gate will be turned off if atom 2 remains in a superposition of $|0\rangle$ and $|D\rangle$ without any phase accumulation on $|D\rangle$ or population loss into $|B\rangle$. This will be the case provided the probe field is turned on and off adiabatically as compared with $|B\rangle - |D\rangle$ energy splitting, which is equal to the Stark shift $\Delta_S = \tilde{\Omega}^2/\Delta$ of $|B\rangle$. In the limit $\Omega_c \gg \Omega$, which we will assume from now on, the non-adiabatic coupling between $|D\rangle$ and $|B\rangle$ has an effective Rabi frequency $\Omega_{NA} \sim \Omega/(\tau\Omega_c)$ [168] giving population loss from the dark state into the bright state of order $\rho_B \sim (\Omega_{NA}/\Delta_S)^2 \sim (\Omega/\Omega_c)^6$ and hence an error of the same order. The errors due to the Stark shift Ω_{NA}^2/Δ_S of $|D\rangle$ and due to spontaneous emission are smaller than $(\Omega/\Omega_c)^6$ and γ/Δ , respectively.

In the simplest case, these are the dominant sources of error, so that the total error is

$$P_e \sim (\gamma/\Delta) + (\Omega/\Omega_c)^6. \quad (5.1)$$

Plugging in $\Omega^2 \sim \Delta/\tau$ and minimizing with respect to Δ gives $\Delta \sim (\gamma\tau^3\Omega_c^6)^{1/4}$ and $P_e \sim [\gamma/(\tau\Omega_c^2)]^{3/4}$, which can be made arbitrarily small by increasing control intensity.

5.2.3 Error due to Dipole-Dipole Interactions

However, other sources of error exist. For $d \ll \lambda$, dipole-dipole interactions and cooperative decay effects may become important [169]. Cooperative decay will not qualitatively change the errors since the desired evolution is close to unitary. Assuming that we have only two atoms and that $d \ll \lambda$, taking the axis of quantization to coincide with the x -axis, the dipole-dipole Hamiltonian can be writ-

ten as $H_{dd} = (\vec{\mu}_1 \cdot \vec{\mu}_2 - 3(\vec{\mu}_1 \cdot \hat{x})(\vec{\mu}_2 \cdot \hat{x}))/d^3$, where $\vec{\mu}_i$ is the electric dipole operator of the i th atom. Since most of the population will stay in $|0\rangle$ and $|1\rangle$, the dipole-dipole interactions involving state $|r\rangle$ can be ignored. Then, provided $|0\rangle - |e\rangle$ and $|1\rangle - |e\rangle$ have different polarizations or sufficient frequency difference, $H_{dd} \approx -g_0(|0e\rangle\langle e0| + |e0\rangle\langle 0e|) - g_1(|1e\rangle\langle e1| + |e1\rangle\langle 1e|)$, where $|\alpha\beta\rangle$ denotes a two-atom state with atom 1 in $|\alpha\rangle$ and atom 2 in $|\beta\rangle$ and where g_0 and g_1 are proportional to $g = \gamma/(kd)^3$ with proportionality constants that depend on the polarizations of the transitions. Then a perturbative calculation shows that dipole-dipole interactions introduce an error¹ $\sim (\Omega g/(\Omega_c \Delta))^4$.

5.2.4 Errors due to Imperfect Control-Field Nodes and Finite Atom Localization

Additional errors are associated with imperfections in the control field node and with finite localization of atoms. If atom 1 was perfectly localized at a single point, a residual control field at the node ($\Omega_c(0) \neq 0$) would result in population $(\Omega_c(0)/\Omega)^2$ in the dark state $|D\rangle$ (now defined for atom 1). However, even if $\Omega_c(0) = 0$, atom 1 can still interact with the control field due to finite extent a_0 of its wave-function. Assuming² $\Omega_c(0) \lesssim \Omega_0 k' a_0$, the error due to finite atomic extent (discussed below) will dominate over $(\Omega_c(0)/\Omega)^2$.

To analyze the problem of localization for atoms in optical lattices and ions in linear Paul traps, we assume that atom 1 sits in the ground state of a harmonic oscillator potential with frequency ω and, therefore, has spread $a_0 = \sqrt{\hbar/(2m\omega)}$, where m is the mass of the atom, as shown schematically in Fig. 5.2(c). We assume $\Omega_c(x) = \Omega_0 k' x = \Omega_{ca}(\hat{a}^\dagger + \hat{a})$, where $\Omega_{ca} = \Omega_c(a_0)$ and \hat{a} is the oscillator annihilation operator. $\Omega_c(x)$ will then couple $|e, n\rangle$ and $|r, m\rangle$ only when $n = m \pm 1$, where $|\alpha, n\rangle$ denotes atom 1 in internal state $|\alpha\rangle$ in n th harmonic level. The dominant error can be estimated by keeping only states $|1, 0\rangle$, $|e, 0\rangle$, and $|r, 1\rangle$. A perturbative calculation shows that the two limits, in which the error is small are: (a) fast limit $\omega\tau \lesssim 1$, in which case $P_e \sim (\Omega_{ca}/\Omega)^2$; (b) adiabatic limit $\omega\tau \gg 1$, $(\Omega_{ca}/\Omega)^2$, in which case a small change in the Stark shift of $|1, 0\rangle$ can be compensated by slightly adjusting τ to yield $P_e \sim (\Omega_{ca}/\Omega)^2/(\tau\omega)^4$.

For atom 2 centered at $x = d$, we have $\Omega_c(x) = \Omega_0 k' d + \Omega_c k'(x - d)$, i.e. the desired coupling Ω_c within each harmonic level is accompanied by coupling of strength $\sim \Omega_{ca}$ between different harmonic levels. Numerical simulations show that provided $\Omega_{ca} < 0.1 \Omega_c$ (which will always hold below), this coupling has an insignificant effect.

¹If Ω_c is not sufficiently larger than Ω , $P_e \sim (\Omega g/(\Omega_c \Delta))^2$. However, $(\Omega g/(\Omega_c \Delta))^2$ and $(\Omega g/(\Omega_c \Delta))^4$ depend on d so sharply that they give almost the same resolution.

²The condition is modified in the adiabatic limit (see error #3 in Table 5.1): $\Omega_c(0) \lesssim \Omega_0 k' a_0/(\omega\tau)^2$.

	Error source	Error scaling (P_e)
1	decay error on atom 1	γ/Δ
	<i>localization error on atom 1:</i>	
2	- ions and atoms in fast limit and solid-state qubits	$(\Omega_{ca}/\Omega)^2$
3	- ions and atoms in adiabatic limit	$(\Omega_{ca}/\Omega)^2/(\tau\omega)^4$
4	unitary error on atom 2	$(\Omega/\Omega_c)^6$
5	dipole-dipole error	$(g\Omega/(\Delta\Omega_c))^4$
6	$ r\rangle$ decay on atom 2 for Rb	$(\Omega/\Omega_c)^2\gamma_r\tau$

Table 5.1: Error budget for the single-qubit phase gate.

5.2.5 Error Budget

The error budget³ for the single-qubit phase gate is summarized in Table 5.1. In general, for a given set of experimental parameters, using $\Omega^2 \sim \Delta/\tau$ to eliminate Ω in favor of Δ , one has to write the total error as the sum of the errors in Table 5.1 and minimize it with respect to Ω_0 and Δ (we assume $\Omega_0/2\pi \leq 1$ GHz). We will illustrate this procedure for three systems: ions, solid-state qubits, and neutral atoms. Since ion and neutral atom examples will have $d \sim \lambda$, we take $\Omega_c = \Omega_0$ for them, while for solid-state qubits, we take $\Omega_c = \Omega_0 k' d$. We take $\Omega_{ca} = \Omega_0 k' a_0$, except for neutral atoms, as discussed below. We note that stimulated Raman transitions [146, 147], resulting in qubit rotations, can also be treated in exactly the same way, yielding similar error probabilities. Moreover, this error analysis is readily extendable to spatially selective qubit measurements and optical pumping, as well as to dipole-dipole two-qubit gates for qubits separated by $d \ll \lambda$.

5.2.6 Approaches to Node Creation

Several approaches to control field node creation exist. One or two standing waves can be used to generate planes or lines, respectively, of zero field with field amplitudes scaling linearly near the zeros. If one has a regular array of atoms (e.g. in an optical lattice), arrays of zeros can be chosen to have spacing incommensurate or commensurate with atomic spacing, allowing to address single or multiple atoms, respectively. One can also create control field nodes using holographic techniques [170], which allow one to generate single optical vortices (such as in a Laguerre-Gaussian beam) or an arbitrary diffraction-limited two-dimensional array of them. For simplicity, we consider the case when atoms are sensitive only to one polarization

³For solid state qubits, we model imperfect localization of atom 1 by replacing $\Omega_c(0)$ with $\Omega_{ca} = \Omega_c(a_0)$ to give an error $\sim (\Omega_{ca}/\Omega)^2$, where a_0 is the electronic-wavefunction extent.

of the control field (e.g. if a magnetic field is applied to remove degeneracies). Then the quality of a standing wave node in this polarization component is determined by the interference contrast, which is limited by the mismatch between the amplitudes of this component in the two interfering waves. On the other hand, in an optical vortex, if the phase of the desired polarization component picks up a nonzero multiple of 2π around a closed loop, for topological reasons this loop must enclose a line (in three dimensions) where the amplitude of this polarization component exactly vanishes (see e.g. [171]). Furthermore, the Rabi frequency in an optical vortex rises radially from the center as $|\Omega_c(x)| \sim \Omega_0(x/w)^l$, where $w \gtrsim \lambda'$ is the beam waist and the topological charge l is a positive integer. Therefore, in some cases, the use of vortices with $l > 1$ instead of standing waves or $l = 1$ vortices can improve the resolution by decreasing the undesired coupling of the control to atom 1. We will use an $l = 2$ vortex for the neutral-atom example, in which case we take $\Omega_{ca} = \Omega_0(k'a_0)^2$ in error #2 in Table 5.1.

5.2.7 Error Estimates for Ions in Paul Traps, Solid-State Qubits, and Neutral Atoms in Optical Lattices

We first analyze ions in linear Paul traps. We consider for concreteness $^{40}\text{Ca}^+$ [172] with $|0\rangle = |4S_{1/2}, m = 1/2\rangle$, $|1\rangle = |4S_{1/2}, m = -1/2\rangle$, $|e\rangle = |4P_{1/2}, m = 1/2\rangle$, and $|r\rangle = |3D_{3/2}, m = 3/2\rangle$. Note that $\lambda = 397$ nm and $\lambda' = 866$ nm are far enough apart to ignore off-resonant cross coupling. Then, for $\tau = 1$ μs , $\omega/2\pi = 10$ MHz, and $d = 1 - 3$ μm , errors #1 and #4 from Table 5.1 form the dominant balance, so that Eq. (5.1) applies and $P_e \sim [\gamma/(\tau\Omega_c^2)]^{3/4}$, which is $\sim 10^{-4}$ for $\Omega_0/2\pi = 1$ GHz (with optimal $\Delta/(2\pi) \sim 200$ GHz and $\Omega/(2\pi) \sim 200$ MHz). This and the next two error estimates are significantly lower than the errors produced by naive probe focusing.

For solid-state qubits (e.g. Nitrogen-Vacancy color centers in diamond [143]), we take $a_0 = 0.5$ nm, $\lambda = \lambda' = 700$ nm, $\gamma/2\pi = 5$ MHz, and $\tau = 1$ μs , which, for d between 100 nm and 20 nm, makes errors #2 and #4 form the dominant balance, so that $P_e \sim (a_0/d)^{3/2}$ is between 5×10^{-4} and 5×10^{-3} . For $d < 10$ nm, $\Omega_0/2\pi = 1$ GHz is insufficient to suppress the dipole-dipole error (error #5 in Table 5.1), and the gate fidelity sharply drops.

To analyze atoms in optical lattices, we consider ^{87}Rb with $|0\rangle = |5S_{1/2}, F = 2, m_F = 2\rangle$, $|1\rangle = |5S_{1/2}, F = 1, m_F = 1\rangle$, $|e\rangle = |5P_{1/2}, F = 2, m_F = 2\rangle$, and $|r\rangle = |4D\rangle$. $|4D\rangle$ decays with rate $2\gamma_r = 1/(90$ ns); so to reduce the error $\sim \rho_r \gamma_r \tau \sim (\Omega/\Omega_c)^2 \gamma_r \tau$ on atom 2 (error #6 in Table 5.1), we choose short $\tau = 10$ ns. For $\omega/2\pi = 50$ kHz and $\Omega_0/2\pi = 1$ GHz, errors #2 and #6 form the dominant balance, so that $P_e \sim (\Omega_{ca}/\Omega_c) (\tau\gamma_r)^{1/2} \sim 0.01$. This error can be further reduced by tightening the traps for the duration of the gate either by increasing the power of or by decreasing the detuning of the lattice beams.

5.3 Advantages of Our Addressability Technique

Our selective addressability technique has several advantages that may enable it to outperform alternative all-optical addressability proposals based on the gradient method [165, 166, 167]. First, the nonlinear response provided by the dark states may potentially provide our method with superior error scaling. Second, in the gradient method, the control field typically couples states that are populated at some point during the gate. In contrast, in our method, the control field is small (ideally, vanishing) on the atom that is being manipulated, while on the neighboring atoms the population of level $|r\rangle$ (coupled by the control to level $|e\rangle$) is negligible and becomes smaller as the control power grows. As a result, in contrast to the gradient method, our method (1) avoids unwanted forces on atoms due to Stark shift gradients [and hence prevents unwanted entanglement of external and internal degrees of freedom] and (2) avoids excessive spontaneous emission, which may take place if the control field mixes populated stable states with short-lived excited states.

5.4 Conclusions and Outlook

We now outline some new avenues opened by the coherent selective addressability technique. Although we discussed in detail only the application of this technique to selective phase gates (equivalently, Raman transitions), it has obvious generalizations to geometric gates [173], fluorescence detection, and optical pumping/shelving, as well as to the generation (in combination with dipole-dipole interactions and assuming $d \ll \lambda$) of entangling gates between atoms. In addition to the applications to atoms in optical lattices, to ions in linear Paul traps, and to solid-state qubits, our technique may also allow for single-atom addressability in recently proposed sub-wavelength optical lattices [174]. Moreover, a combination of similar ideas involving dark states and the nonlinear atomic response can itself be used for creating deep sub-wavelength-separated traps and flat-bottom traps. Finally, better optimization (e.g. using optimal control theory to shape laser pulses as in Appendix D) can further reduce the errors. Therefore, we expect this technique to be of great value for fields ranging from quantum computation and quantum simulation to coherent control, all of which can benefit from high-fidelity addressability at $d \lesssim \lambda$.

Note added: after completing this work, we became aware of related proposals [175, 176, 177] to use dark state position dependence to achieve sub-wavelength resolution.

Chapter 6

Alkaline-Earth-Metal Atoms as Few-Qubit Quantum Registers

6.1 Introduction

As exemplified by experiments underlying Chapters 2-5, alkali atoms, due to their relatively simple electronic structure and convenient wavelengths, are the main workhorse for atomic experiments. In this and the following Chapter, we show that unique features of group-two (i.e. alkaline-earth) atoms make these atoms into excellent candidates for quantum computing and quantum simulation experiments despite their inconvenient wavelengths and more complex electronic structure. In the process, we use the sub-wavelength addressability proposal of Chapter 5.

Stringent requirements on the implementation of scalable quantum information systems can be significantly relaxed if the entire system can be subdivided into smaller quantum registers, in which several qubits can be stored for a long time and local quantum operations can be carried out with a very high fidelity [178, 179, 180, 181, 182, 183, 184]. In such a case, scalable quantum networks can be built even if the non-local coupling between registers has either low fidelity or is probabilistic [178, 179, 180, 181, 183, 184, 182]. Local operations can be achieved with the highest fidelity if the entire register is encoded into a single atom or molecule. While quantum registers based on individual solid-state impurities are already being explored [143, 185, 186], typical qubits encoded into hyperfine [187] or Rydberg [188] states of isolated atoms cannot be easily used as a few-qubit register. More specifically, the Hilbert space associated with such systems cannot be represented as a direct product of several sub-systems, such that e.g. one of the qubits can be measured without affecting the others.

In this Chapter, we show that individual alkaline-earth atoms can be used for the robust implementation of quantum registers, with one (electronic) qubit encoded in a long-lived optical transition and several additional qubits encoded in the nuclear spin.

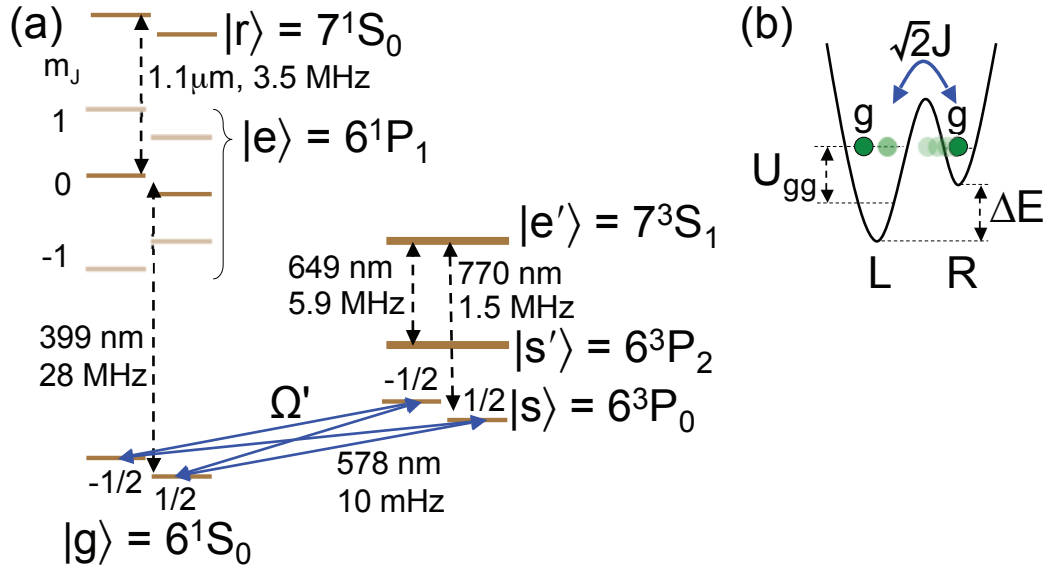


Figure 6.1: (a) On the example of ^{171}Yb ($I = 1/2$) in the Paschen-Back regime for state 1P_1 , relevant alkaline-earth-like level structure. (b) Interregister gate based on conditional resonant tunneling.

Following the proposal of Ref. [182], we use the electronic qubit as the communication qubit [183, 184, 143, 185, 186] for detecting and coupling the registers. In particular, we show that the full $(2I + 1)$ -dimensional space describing a spin- I nucleus can be preserved during electronic-qubit detection. This step uses off-resonant detection proposed in Ref. [182] and extends the proposal of Ref. [189] beyond one nuclear qubit manipulation to much larger registers (I can be as high as $9/2$, as in ^{87}Sr). We also show how to manipulate and measure individual registers in an optical lattice with subwavelength resolution. While entangling gates between alkaline-earth atoms have been studied in the context of nuclear qubits alone [190, 191] and electronic qubits alone [192], we propose a new scheme that makes use of both degrees of freedom. Our gate creates entangled states between electronic qubits using conditional resonant tunneling and an interaction blockade [193, 194].

6.2 The Register

Fig. 6.1(a) shows, as an example, the relevant alkaline-earth-like structure of ^{171}Yb ($I = 1/2$). We want to arbitrarily manipulate the $2(2I + 1)$ -dimensional Hilbert space consisting of states in the manifolds $|g\rangle = ^1S_0$ and $|s\rangle = ^3P_0$ (“g” for ground and “s” for stable). Using a differential g-factor [195], one can optically excite all $6I + 1$ individual $|g\rangle - |s\rangle$ transitions in the presence of a magnetic field B [196] [see Fig.

6.1(a)]. Thus, any unitary operation on an individual register can be achieved¹ [197].

To make single-register manipulation spatially selective, one can envision various strategies. The conceptually simplest strategy would adiabatically expand the lattice for the time of the manipulation, which can be done without changing the wavelength of the light using holographic techniques or angled beams [198]. Alternatively, we can make a temporary Raman transfer of a given pair of Zeeman levels of $|s\rangle$ up to $|s'\rangle = {}^3P_2$ via $|e'\rangle = {}^3S_1$ [Fig. 6.1(a)] [191]. One way to achieve spatial selectivity in this Raman transfer is to perform adiabatic passage, in which the beam on one of the transitions vanishes (and, thus, prohibits the transfer) at the location of one atom [175]. Subsequent manipulation of the two chosen Zeeman levels of $|s\rangle$ will then be automatically spatially selective. Any other pair of states within the register can be manipulated by swapping it in advance with the first one. Alternatively, one can use the $|s\rangle - |e'\rangle - |s'\rangle$ Lambda system to achieve spatial selectivity even without state transfer by using dark-state-based selectivity (see Chapter 5).

6.3 Interregister Gate

We now assume that atoms are prepared in a Mott insulator state [135] in an optical lattice (or a fully polarized band insulator, which may be easier to load), with one atom per site. We isolate two adjacent atoms (left and right) using a superlattice [193, 199]. We now show how to generate a two-qubit phase gate between the electronic qubits of these atoms (i.e. $|g, g\rangle \rightarrow -|g, g\rangle$) in a regime where the tunneling J is much smaller than the onsite interaction energy. As shown in Fig. 6.1(b), we bias the right well relative to the left well by a value ΔE equal to the interaction energy U_{gg} between two $|g\rangle$ -atoms. If we had bosons with $I = 0$, then after time $\tau \sim 1/J$ the state $|g, g\rangle$ would pick up a minus sign due to resonant tunneling of the right atom to the left well and back. We now demonstrate how this gate works for fermions with arbitrary I . We consider the two-well single-band

¹If the limit on gate speed imposed by the differential g -factor becomes too restrictive, nuclear spin selectivity can instead be achieved with Raman transitions from $|s\rangle$ to 3P_2 via 3S_1 [Fig. 6.1(a)] [191]. One can also use Raman transitions between Zeeman levels of $|g\rangle$ via hyperfine levels of 1P_1 . Nuclear spin can also be manipulated using radio-frequency pulses.

Hubbard Hamiltonian² derived in Sec. 7.2:

$$\begin{aligned}
\hat{H}_h &= -J \sum_{\alpha, m} (\hat{c}_{L\alpha m}^\dagger \hat{c}_{R\alpha m} + \text{h.c.}) + \Delta E \sum_{\alpha, m} \hat{n}_{R\alpha m} \\
&\quad - \sum_{i, \alpha, m} \mu_N B m g_\alpha \hat{n}_{i\alpha m} + \sum_{i, \alpha, m < m'} U_{\alpha\alpha} \hat{n}_{i\alpha m} \hat{n}_{i\alpha m'} \\
&\quad + V \sum_i \hat{n}_{ig} \hat{n}_{is} + V_{\text{ex}} \sum_{i, m, m'} \hat{c}_{igm}^\dagger \hat{c}_{ism'}^\dagger \hat{c}_{igm'} \hat{c}_{ism}. \tag{6.1}
\end{aligned}$$

Here $i = L, R$ labels sites; $\alpha = g, s$; $m, m' = -I, \dots, I$; $\hat{n}_{i\alpha} = \sum_m \hat{n}_{i\alpha m}$; $\hat{n}_{i\alpha m} = \hat{c}_{i\alpha m}^\dagger \hat{c}_{i\alpha m}$, where $\hat{c}_{i\alpha m}^\dagger$ creates an atom in state αm on site i . The tunneling rate J and the bias ΔE are assumed for notational simplicity to be state-independent. g_α is the g -factor of state α . $V = (U_{sg}^+ + U_{sg}^-)/2$ and $V_{\text{ex}} = (U_{sg}^+ - U_{sg}^-)/2$ describe the "direct" and "exchange" interactions [200]. $U_{\alpha\beta}^x = (4\pi\hbar^2 a_{\alpha\beta}^x/M) \int d^3r |\phi_\alpha(\mathbf{r})|^2 |\phi_\beta(\mathbf{r})|^2$ [201], where M is atomic mass, $a_{\alpha\beta}^x = a_{gg}, a_{ss}, a_{sg}^+, a_{sg}^-$ are the four s-wave scattering lengths, ϕ_α are the Wannier orbitals. a_{sg}^- corresponds to the antisymmetric electronic state $|gs\rangle - |sg\rangle$ (implying a symmetric nuclear state), while a_{gg}, a_{ss} , and a_{sg}^+ correspond to the three symmetric electronic states (implying antisymmetric nuclear states). Since $|g\rangle$ and $|s\rangle$ have $J = 0$ and since hyperfine mixing of $|s\rangle$ with other states is small [195], we take $a_{\alpha\beta}^x$ to be independent of nuclear spin, which is consistent with experiments [202, 196]. We note that the optical energy of $|s\rangle$ is absent in our rotating frame.

In our scheme, provided U_{gg} differs from other U 's, the interaction blockade [194] will prevent two atoms from being on the same site unless they are both in state $|g\rangle$, so we can ignore all but the U_{gg} interaction terms. In this case, the Zeeman Hamiltonian can be rotated out. The first step of the gate is to increase the bias ΔE from 0 to U_{gg} for time $\tau = \pi/(\sqrt{2}J)$, and then set it back to 0. Defining $|g, g\rangle |m_2, m_1\rangle = \hat{c}_{Lgm_2}^\dagger \hat{c}_{Rgm_1}^\dagger |0\rangle$, this gives a 2π pulse between $I(2I+1)$ states $|g, g\rangle (|m_2, m_1\rangle - |m_1, m_2\rangle)$ ($m_1 < m_2$) and $\hat{c}_{Lgm_1}^\dagger \hat{c}_{Lgm_2}^\dagger |0\rangle$, so that the former pick up a factor -1 . The $I(2I+1)$ states that pick up the factor -1 are precisely all the $|g, g\rangle$ states with an antisymmetric nuclear state since two $|g\rangle$ atoms in a symmetric nuclear state cannot sit on one site. To make *all* $(2I+1)^2$ $|g, g\rangle$ states pick up the factor -1 , we require two more steps. In the second step, we apply a phase -1 on site R on all $|g, m\rangle$ with $m > 0$, repeat the bias, and repeat the phase. In the final step, we swap $|g, m\rangle$ and $|g, -m\rangle$ on site R , repeat the first two steps, and repeat the swap. This results in $|g, g\rangle \rightarrow -|g, g\rangle$ independent of the nuclear spin, i.e. a two-qubit phase gate on the two electronic qubits. All atom pairs in the superlattice that experience only the four biases are unaffected. Thus, together with spatially selective single-atom manipulation, this gate gives universal manipulation of the full lattice of

²We estimate that we can neglect vector and tensor light shifts, as well as the effects of hyperfine mixing [195] on the g_I -factor in $|e\rangle$. In particular, our interregister gate assumes that differential vector and tensor light shifts between the two sites are $\ll J$, which is typically satisfied.

quantum registers. The gate error due to virtual tunneling is $\sim (J/U)^2$, where J/U is the smallest relevant ratio of tunneling to interaction energy or to a difference of interaction energies. This error can be reduced if $|g\rangle$ and $|s\rangle$ lattices are independent [191]. Other errors in this gate are analogous to those studied in Ref. [194].

We now point out some advantages of this gate. The gate is essentially achieved by conditioning the resonant tunneling on the internal state of the atoms rather than on the number of atoms in the wells [193, 194] or on the vibrational levels the atoms occupy [203]. Being resonant, the gate is faster ($\tau \sim 1/J$) than superexchange gates ($\tau \sim U/J^2$) [204]. At the same time, by conditioning the tunneling on the internal state, we avoid having two $|s\rangle$ -atoms in one well [192], which may be subject to collisional losses. A key property of the gate is that it couples the electronic (communication) qubits without affecting the nuclear qubits. At the same time, a remarkable feature of our gate is that it would not have worked without the use of the nuclear degree of freedom, because two $|g\rangle$ atoms would not be able to sit on the same site in that case. This is in a sense the reverse of Ref. [190], where a gate on nuclear spins relies on the underlying electronic interactions. Finally, our gate can be easily extended to bosons. In particular, a single bias interval would suffice for bosons with two internal states $|g\rangle$ and $|s\rangle$ that have different interactions U_{gg} , U_{ss} , and U_{sg} (e.g. if $|g\rangle$ and $|s\rangle$ experience different potentials).

6.4 Electronic-Qubit Detection

We now demonstrate the essential ability of our register to preserve all nuclear qubits during the fluorescence detection of the electronic qubit. The key ingredients will be off-resonant excitation [182] and/or a strong magnetic field [189]. The detection is made by cycling the $|g\rangle - (|e\rangle = {}^1P_1)$ transition ("e" for excited). To yield an error $p < 0.01$ after scattering $N \sim 100$ photons, the decay rate from $|e\rangle$ to $|g\rangle$ should exceed other decay rates from $|e\rangle$ by $> 10^4$, which is typically satisfied³ [205, 206, 207]. We can thus restrict ourselves to a $4(2I + 1)$ -dimensional space describing the $|g\rangle - |e\rangle$ transition: $|g\rangle|m_I\rangle$ ($J = 0$) and $|e, m_J\rangle|m_I\rangle$ ($J = 1$). The Hamiltonian is then⁴ ($\hbar = 1$)

$$\begin{aligned} \hat{H} = & A\hat{\mathbf{I}} \cdot \hat{\mathbf{J}} + Q \frac{3(\hat{\mathbf{I}} \cdot \hat{\mathbf{J}})^2 + 3/2\hat{\mathbf{I}} \cdot \hat{\mathbf{J}} - K}{2IJ(2I - 1)(2J - 1)} + g_J\mu_B\hat{J}_zB \\ & - g_I\mu_N\hat{I}_zB - \Omega(|g\rangle\langle e, 0| + \text{h.c.}) - \Delta \sum_m |e, m\rangle\langle e, m|. \end{aligned} \quad (6.2)$$

³If p becomes limited by the branching ratio of $|e\rangle$ decay, one should consider Be, Mg, Zn, Cd, and Hg, which have a radiatively closed $|g\rangle - |e\rangle$ transition.

⁴See footnote on p. 52.

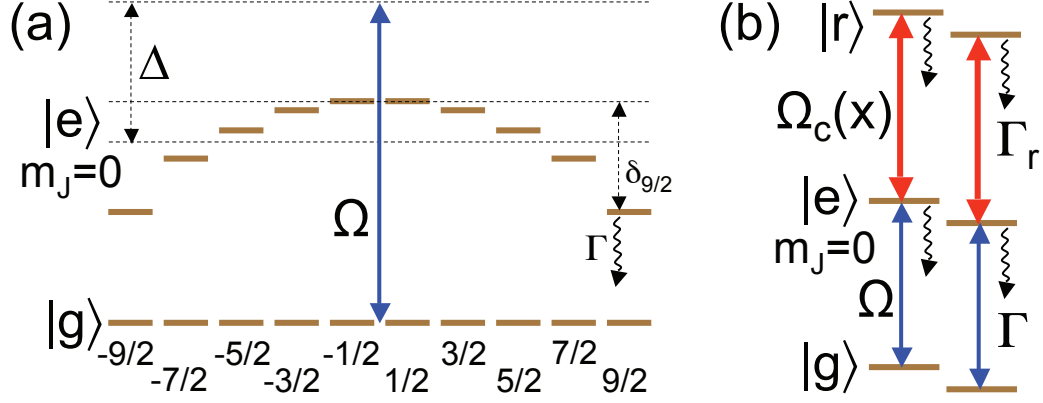


Figure 6.2: Nuclear-spin-preserving electronic-qubit detection. (a) ^{87}Sr ($I = 9/2$) in the Paschen-Back regime (the shift $-g_I\mu_N m_I B$ not shown). (b) On the example of ^{171}Yb ($I = 1/2$), dark-state-based spatial selectivity (see Chapter 5).

Here $K = I(I+1)J(J+1)$; A and Q ($Q = 0$ for $I = 1/2$) are the magnetic dipole and electric quadrupole hyperfine constants, respectively; g_J and $g_I = g_g$ are the relevant g factors; Ω and Δ are the Rabi frequency and the detuning of the π -polarized probe light. Using three Lindblad operators $\hat{L}_m = \sqrt{\Gamma}|g\rangle\langle e, m|$, the master equation is

$$\dot{\rho} = -i[\hat{H}, \rho] - \frac{1}{2} \sum_m (\hat{L}_m^\dagger \hat{L}_m \rho + \rho \hat{L}_m^\dagger \hat{L}_m - 2\hat{L}_m \rho \hat{L}_m^\dagger). \quad (6.3)$$

Two approaches to preserve nuclear coherence during fluorescence are possible. In the first one, a strong magnetic field ($g_J\mu_B B \gg A, Q$) decouples $\hat{\mathbf{I}}$ and $\hat{\mathbf{J}}$ in the Paschen-Back regime [189]. In the second one, a large detuning $\Delta \gg A, Q$ does the decoupling by means of the interference of Raman transitions via all excited states with a given $I_z + J_z$ [182]. Unless $Q \ll \Gamma$, the first approach fails because the frequencies of transitions $|g\rangle|m_I\rangle - |e, 0\rangle|m_I\rangle$ differ by $\delta_{m_I} = 3Qm_I^2$ [see Fig. 6.2(a)]. However, when $Q \ll \Gamma$, the first approach may be preferable as it allows for much faster detection than the second (off-resonant) approach. While the two approaches can work separately, their combination is sometimes advantageous and allows for the following simple estimate of the nuclear decoherence due to off-resonant excitation. We assume $\Delta \gg Q, \Omega, \Gamma$ and a magnetic field large enough to decouple $\hat{\mathbf{I}}$ and $\hat{\mathbf{J}}$ (arbitrary B can be analyzed similarly). The number of photons scattered during time τ is then $N \approx \Gamma\tau\Omega^2/\Delta^2$. Furthermore, for any two $m_I = m_1, m_2$, the four coherences $|g/e, 0\rangle|m_1\rangle - |g/e, 0\rangle|m_2\rangle$ form a closed system. Adiabatically eliminating the three coherences except for the ground one, the latter is found to decay with rate $\Gamma_{12} \approx (\delta_{m_1} - \delta_{m_2})^2\Omega^2\Gamma/(2\Delta^4)$, yielding an error $p \sim \Gamma_{12}\tau \sim N(Q/\Delta)^2$. Thus, to scatter $N = 100$ photons and obtain $p < 0.01$, we need $\Delta \gtrsim 100Q$.

To verify low p numerically, we use ^{171}Yb ($I = 1/2$) [208], ^{87}Sr ($I = 9/2$) [196], and

^{43}Ca ($I = 7/2$), for which $(\Gamma, A, Q)/(2\pi \text{ MHz}) = (28, -213, 0)$ [189], $(30.2, -3.4, 39)$ [189], and $(35, -15.5, -3.5)$ [209], respectively. Although less widely used, ^{43}Ca has the advantageous combination of small Q and large I . We prepare the atom in some state in the manifold $|g\rangle$, turn Ω on and off abruptly for a time τ , and then wait for all the population to decay down to $|g\rangle$, which transforms Eq. (6.3) into a superoperator $\hat{\mathcal{E}}$ acting on density matrices describing $|g\rangle$. Ideally, $\hat{\mathcal{E}}$ describes a unitary transformation \hat{U} that maps $|g\rangle|m\rangle \rightarrow \exp(i\phi_m)|g\rangle|m\rangle$ with $\phi_{-I} = 0$ and ϕ_m ($m > -I$) given by the phase of the diagonal elements of $\hat{\mathcal{E}}$ corresponding to the density matrix element $\rho_{m,-I}$. So $p \equiv 1 - \bar{F}$, where \bar{F} is the average gate fidelity of $\hat{\mathcal{E}}$ with respect to \hat{U} [210]:

$$\bar{F}(\hat{\mathcal{E}}, \hat{U}) \equiv \int d\psi \langle \psi | \hat{U}^\dagger \hat{\mathcal{E}}(|\psi\rangle\langle\psi|) \hat{U} | \psi \rangle. \quad (6.4)$$

We fix $N = 100$ and begin by considering the first approach (large B and $\Delta = 0$). In Yb, $B = 2\text{T}$ and $\Omega/2\pi = 30 \text{ MHz}$ ($\tau = 1.3\mu\text{s}$) give $p \approx 0.01$. Since Yb has $I = 1/2$ (hence $Q = 0$), as $B \rightarrow \infty$, $p \rightarrow 0$: for example, $B = 10 \text{ T}$ and $\Omega/2\pi = 200 \text{ MHz}$ ($\tau = 1.1\mu\text{s}$) give $p \approx 10^{-4}$. In Ca, small Q/Γ (≈ 0.1) also allows one to obtain high fidelity on resonance: $B = 1\text{T}$ and $\Omega/2\pi = 200 \text{ MHz}$ ($\tau = 0.9\mu\text{s}$) give $p \approx 0.002$. Since Q is finite here, increasing B further does not reduce p to zero. Finally, in Sr, resonant scattering gives $p \gtrsim 0.1$ due to the large Q . Turning now to the second approach ($B = 0$ and large Δ), for Yb, Ca, and Sr, $(\Delta, \Omega)/(2\pi \text{ GHz}) = (15, 0.2)$, $(6, 0.07)$, and $(3, 0.04)$, respectively, give $\tau \sim 3 \text{ ms}$ and $p \approx 0.01$. An increase of Ω (to reduce τ) leads unfortunately to larger p at least partly due to the loss of adiabaticity in the evolution of coherences. The error can be reduced by further increasing Δ (or to some extent by decreasing Ω) and thus extending τ . We note that in this (second) approach, any probe light polarization can be used. Finally, the error can sometimes be significantly reduced by combining the two approaches. For example, adding $B = 2\text{T}$ to the above example of off-resonant detection in Ca yields $p \approx 4 \times 10^{-4}$. Depending on time constraints, available magnetic fields and laser power, as well as on the desired N and p , the parameters can be further optimized and adiabatic switching of Ω can be considered.

To make detection spatially selective, we can apply the dark-state-based single-site addressability (see Chapter 5), shown in Fig. 6.2(b) on the example of Yb in the Paschen-Back regime. Let $|r\rangle$ be the second lowest 1S_0 state [Fig. 6.1(a)]. In addition to the probe laser Ω , we apply a spatially varying control field $\Omega_c(x)$ coupling $|e\rangle$ and $|r\rangle$ in two-photon resonance with Ω . If $\Omega_c(x)$ vanishes at the position of atom 1 and is strong on all the other atoms affected by Ω , only atom 1 will fluoresce, while all other atoms will be unaffected. For example, in the first Yb example above, application of $\Omega_c/2\pi = 1 \text{ GHz}$ reduces the number of scattered photons to $N \sim 0.01$ and gives only 1% decay of the $|g\rangle - |s\rangle$ coherence⁵. Alternatively, we can temporarily transfer, as

⁵ $|r\rangle$ decay rate is $\Gamma_r = (2\pi)3.5 \text{ MHz}$ [211]. The population of $|r\rangle$ is $\sim \Omega^2/\Omega_c^2$, so the dominant

described above, all Zeeman levels of $|s\rangle$ up to $|s'\rangle$ in all but one atom, apply a NOT gate on all electronic qubits, carry out the detection, and then undo the NOT gate and the Raman transfer. Finally, temporary lattice expansion and magnetic gradients [191] can also be used.

6.5 Conclusion

We have shown how to implement and couple quantum registers based on individual alkaline-earth-like atoms trapped in individual sites of an optical lattice. These quantum registers can be used as a starting point for fault-tolerant circuit-based quantum computation [183, 184]. Alternatively, they can be used for high fidelity generation (and measurement) of two-colorable graph states [212, 183, 184], which include cluster states for the use in measurement-based quantum computation [213] and GHZ states for the use in precision measurements [214]. In particular, a cluster state can be generated in a highly parallel fashion [212] by first preparing all the electrons in state $|g\rangle + |s\rangle$ and then applying the two-qubit phase gate on each edge, which our scheme allows to do in 2 steps per each dimension of the lattice. We note that assuming high fidelity detection or a restricted error model, a four-qubit register ($I \geq 7/2$) is sufficient for the fault-tolerant operation of a quantum register [183, 184]. However, even one ($I = 1/2$) or two ($I = 3/2$) extra qubits can be used to do simpler entanglement pumping and, thus, increase the fidelity of two-colorable-graph-state generation [212]. With its accessibility using current experimental techniques and with the possibility to convert the electronic qubits into flying qubits, our approach and its extensions to ions with similar internal structure should be immediately useful in fields such as precision measurements, quantum computation, and quantum communication.

error is $\sim \tau\Gamma_r\Omega^2/\Omega_c^2$.

Chapter 7

Two-Orbital SU(N) Magnetism with Ultracold Alkaline-Earth Atoms

7.1 Introduction

As exemplified by the discussion in Chapter 6, as well as in Refs. [195, 215, 216, 217, 189, 190, 191], the interest in fermionic alkaline-earth atoms stems from their two key features: (1) the presence of a metastable excited state 3P_0 coupled to the ground 1S_0 state via an ultranarrow doubly-forbidden transition [195] and (2) the almost perfect decoupling [195] of the nuclear spin I from the electronic angular momentum J in these two states, since they both have $J = 0$. This decoupling implies that s-wave scattering lengths involving states 1S_0 and 3P_0 are independent of the nuclear spin, aside from the restrictions imposed by fermionic antisymmetry. We show that the resulting SU(N) spin symmetry (where $N = 2I + 1$ can be as large as 10) together with the possibility of combining (nuclear) spin physics with (electronic) orbital physics open up a wide field of extremely rich many-body systems with alkaline-earth atoms.

In what follows, we derive the two-orbital SU(N)-symmetric Hubbard model describing alkaline-earth atoms in 1S_0 and 3P_0 states trapped in an optical lattice. We focus on specific parameter regimes characterized by full or partial atom localization due to strong atomic interactions, where simpler effective spin Hamiltonians can be derived. The interplay between orbital and spin degrees of freedom in such effective models is a central topic in quantum magnetism and has attracted tremendous interest in the condensed matter community. Alkaline earth atoms thus provide, on the one hand, a unique opportunity for the implementation of some of these models for the first time in a defect-free and fully controllable environment. On the other hand, they open a new arena to study a wide range of models, many of which have not been discussed previously, even theoretically. We demon-

strate, in particular, how to implement the Kugel-Khomskii model studied in the context of transition metal oxides [218, 219, 220, 221, 222], the Kondo lattice model [223, 224, 225, 226, 227, 228, 229, 230, 231, 232, 233, 234, 235] studied in context of manganese oxide perovskites [229] and heavy fermion materials [234], as well as various $SU(N)$ -symmetric spin Hamiltonians that are believed to have spin liquid and valence-bond-solid ground states [236, 237, 238, 239, 240, 241, 242, 243]. For example, we discuss how, by appropriately choosing the initial state, a single alkaline-earth atom species with $I = 9/2$ (such as ^{87}Sr) can be used to study experimentally such a distinctively theoretical object as the phase diagram as a function of N for all $N \leq 10$.

Before proceeding, we note that, while an orthogonal symmetry group $SO(5)$ can be realized in alkali atoms [244], proposals to obtain $SU(N>2)$ -symmetric models with alkali atoms [245, 246] and solid state systems [247, 220] are a substantial idealization due to strong hyperfine coupling and a complex solid state environment, respectively. In this context, alkaline-earth-like atoms make a truly exceptional system to study models with $SU(N>2)$ symmetry.

7.2 Many-Body Dynamics of Alkaline-Earth Atoms in an Optical Lattice

We begin with the Hamiltonian describing cold fermionic alkaline-earth atoms in an external trapping potential:

$$\begin{aligned}
 H = & \sum_{\alpha m} \int d^3\mathbf{r} \Psi_{\alpha m}^\dagger(\mathbf{r}) \left(-\frac{\hbar^2}{2M} \nabla^2 + V_\alpha(\mathbf{r}) \right) \Psi_{\alpha m}(\mathbf{r}) \\
 & + \hbar\omega_0 \int d^3\mathbf{r} (\rho_e(\mathbf{r}) - \rho_g(\mathbf{r})) \\
 & + \sum_{\alpha, m < m'} g_{\alpha\alpha} \int d^3\mathbf{r} \rho_{\alpha m}(\mathbf{r}) \rho_{\alpha m'}(\mathbf{r}) + \frac{g_{eg}^+ + g_{eg}^-}{2} \int d^3\mathbf{r} \rho_e(\mathbf{r}) \rho_g(\mathbf{r}) \\
 & + \frac{g_{eg}^+ - g_{eg}^-}{2} \sum_{mm'} \int d^3\mathbf{r} \Psi_{gm}^\dagger(\mathbf{r}) \Psi_{em'}^\dagger(\mathbf{r}) \Psi_{gm'}(\mathbf{r}) \Psi_{em}(\mathbf{r}).
 \end{aligned} \tag{7.1}$$

Here $\Psi_{\alpha m}(\mathbf{r})$ is a fermion field operator for atoms in internal state $|\alpha m\rangle$, where $\alpha = g$ (1S_0) or e (3P_0) denotes the electronic state and $m = -I, \dots, I$ denotes one of the $N = 2I + 1$ nuclear Zeeman states. The density operators are defined as $\rho_{\alpha m}(\mathbf{r}) = \Psi_{\alpha m}^\dagger(\mathbf{r}) \Psi_{\alpha m}(\mathbf{r})$ and $\rho_\alpha(\mathbf{r}) = \sum_m \rho_{\alpha m}(\mathbf{r})$. The term $V_\alpha(\mathbf{r})$ describes the external trapping potential, which we will assume to be an optical lattice independent of the nuclear spin: even for a relatively deep lattice with a 100 kHz trap frequency, tensor and vector light shifts should be well below 1 Hz [195]. $\hbar\omega_0$ is the transition energy between $|g\rangle$ and $|e\rangle$. Extra lasers can be used to drive transitions between

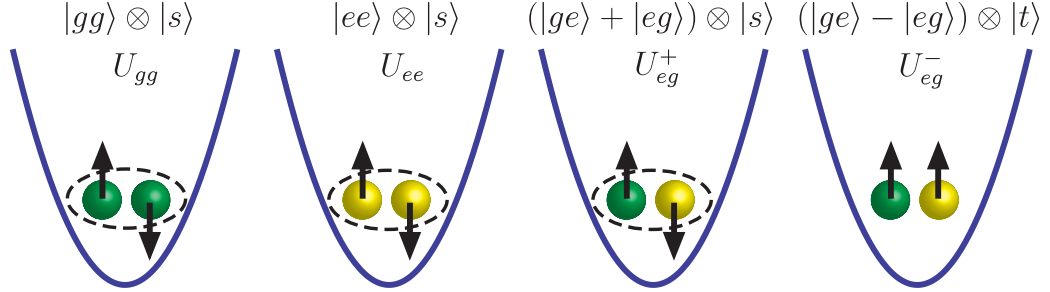


Figure 7.1: **Interaction parameters between g (green) and e (yellow) atoms loaded in the lowest vibrational state of the corresponding optical lattice.** Here we assumed $I = 1/2$, and the arrows indicate the $m_I = \pm 1/2$ spin states. $|s, t\rangle$ denote the singlet and triplet nuclear spin states of the two atoms (only one of three triplet states - $|\uparrow\uparrow\rangle$ - is shown). The dashed circle represents anti-symmetrization of the nuclear spin state (i.e. $|s\rangle$). The interaction energy U_X ($X = gg, ee, eg^+, eg^-$) is proportional to the corresponding scattering length a_X .

$|g\rangle$ and $|e\rangle$ levels [195, 215]. Since we will only need these extra lasers for system preparation, we have not included the corresponding terms in the Hamiltonian.

The interaction is characterized by four s -wave scattering lengths a_X , $X = gg, ee, eg^+, eg^-$, which define four interaction parameters $g_X = 4\pi\hbar^2 a_X/M$, where M is atomic mass. a_{gg} , a_{ee} , and a_{eg}^\pm are the scattering length for two atoms in the electronic state $|gg\rangle$, $|ee\rangle$, and $|\pm\rangle = (|ge\rangle \pm |eg\rangle)/\sqrt{2}$, respectively. As shown in Fig. 7.1, the fermionic antisymmetry then forces the nuclear state to be symmetric for the only antisymmetric electronic state $|-\rangle$ and antisymmetric otherwise. Very few a_X are known at the moment. a_{gg} is known for all isotopic combinations of Yb [248] and Sr [249]. Estimates of a_{ee} for ^{88}Sr [250] and of a_{eg}^- for ^{87}Sr [215] also exist. Finally, there is a proposal describing how to measure a_{eg}^+ via clock shifts [59].

The independence of each of the four scattering lengths from the nuclear spin state is essential to the fulfillment of the $SU(N)$ symmetry of our model (see next Section). This independence is a consequence of the decoupling between nuclear and electronic degrees of freedom exhibited during the course of a collision involving any combination of g or e states, which both have $J = 0$. While for the $|e\rangle \equiv {}^3P_0$ atom, the decoupling is slightly broken by the admixture with higher-lying P states with $J \neq 0$, this admixture is very small [195] and the resulting nuclear-spin-dependent variation of the scattering lengths is also expected to be very small, on the order of 10^{-3} (see Sec. G.1). For a_{gg} , which does not involve state $|e\rangle$, this variation should be even smaller ($\sim 10^{-9}$).

The interaction terms in Eq. (7.1) describe the most general s -wave two-body interaction consistent with elastic collisions as far as the electronic state is concerned and with the independence of the scattering length from the nuclear spin. While the

assumption of elasticity for g - g and e - g collisions is well justified, since no inelastic exit channels exist, e - e collisions are likely to be accompanied by large losses, which means that the magnitudes of the imaginary and real parts of the e - e scattering length are likely to be comparable (see Sec. G.2). Therefore, we focus below on those situations where two e atoms never occupy the same site.

We assume that only the lowest band in both e and g lattices is occupied and expand the field operators in terms of the corresponding (real) Wannier basis functions $\Psi_{\alpha m}(\mathbf{r}) = \sum_j w_\alpha(\mathbf{r} - \mathbf{r}_j) c_{j\alpha m}$, where $c_{j\alpha m}^\dagger$ creates an atom in internal state $|\alpha m\rangle$ at site j (centered at position \mathbf{r}_j). Eq. (7.1) reduces then to a two-orbital single-band Hubbard Hamiltonian

$$\begin{aligned}
 H = & - \sum_{\langle j,i \rangle, \alpha, m} J_\alpha (c_{i\alpha m}^\dagger c_{j\alpha m} + \text{h.c.}) + \sum_{j, \alpha} \frac{U_{\alpha\alpha}}{2} n_{j\alpha} (n_{j\alpha} - 1) \\
 & + V \sum_j n_{je} n_{jg} + V_{ex} \sum_{j, m, m'} c_{jgm}^\dagger c_{jem'}^\dagger c_{jgm'} c_{jem}.
 \end{aligned} \tag{7.2}$$

Here $J_\alpha = - \int d^3\mathbf{r} w_\alpha(\mathbf{r}) (-\frac{\hbar^2}{2M} \nabla^2 + V_\alpha(\mathbf{r})) w_\alpha(\mathbf{r} - \mathbf{r}_0)$ are the tunneling energies, \mathbf{r}_0 connects two nearest neighbors, h.c. stands for Hermitian conjugate, $n_{j\alpha m} = c_{j\alpha m}^\dagger c_{j\alpha m}$, and $n_{j\alpha} = \sum_m n_{j\alpha m}$. The tunneling is isotropic, which is a crucial difference between this model and its analogues in solid state systems with orbital degeneracy [218]. The sum $\langle j, i \rangle$ is over pairs of nearest neighbor sites i, j . $V = (U_{eg}^+ + U_{eg}^-)/2$ and $V_{ex} = (U_{eg}^+ - U_{eg}^-)/2$ describe the direct and exchange interaction terms. The onsite interaction energies are $U_{\alpha\alpha} = g_{\alpha\alpha} \int d^3\mathbf{r} w_\alpha^4(\mathbf{r})$ and $U_{eg}^\pm = g_{eg}^\pm \int d^3\mathbf{r} w_e^2(\mathbf{r}) w_g^2(\mathbf{r})$. Constant terms, proportional to $\sum_j n_{j\alpha}$, are omitted in Eq. (7.2). Experimental control over the parameters in Eq. (7.2) will allow us to manipulate the atoms (see Sec. G.3).

7.3 Symmetries of the Hamiltonian

To understand the properties of the Hamiltonian in Eq. (7.2), we consider its symmetries. We define $SU(2)$ pseudo-spin algebra via

$$T^\mu = \sum_j T_j^\mu = \frac{1}{2} \sum_{j\alpha\beta} c_{j\alpha m}^\dagger \sigma_{\alpha\beta}^\mu c_{j\beta m}, \tag{7.3}$$

where σ^μ ($\mu = x, y, z$) are Pauli matrices in the $\{e, g\}$ basis. We further define nuclear-spin permutation operators

$$S_n^m = \sum_j S_n^m(j) = \sum_{j, \alpha} S_n^m(j, \alpha) = \sum_{j, \alpha} c_{j\alpha n}^\dagger c_{j\alpha m}, \tag{7.4}$$

which satisfy the $SU(N)$ algebra $[S_n^m, S_q^p] = \delta_{mq} S_n^p - \delta_{pn} S_q^m$, and thus generate $SU(N)$ rotations of nuclear spins ($N = 2I + 1$).

In addition to the obvious conservation of the total number of atoms $n = \sum_j (n_{je} + n_{jg})$, H exhibits $U(1) \times SU(N)$ symmetry (see Sec. G.4 for the discussion of enhanced symmetries), where $U(1)$ is associated with the elasticity of collisions as far as the electronic state is concerned ($[T^z, H] = 0$) and $SU(N)$ is associated with the independence of scattering and of the trapping potential from the nuclear spin ($[S_n^m, H] = 0$ for all n, m). The two-orbital $SU(N)$ -symmetric Hubbard Hamiltonian in Eq. (7.2) is a generalization to $N > 2$ of its $SU(2)$ -symmetric counterpart [218] and to two orbitals of its single-orbital counterpart [237]. The $SU(N)$ symmetry and the largely independent spin and orbital degrees of freedom are two unique features present in alkaline-earths but absent in alkalis due to strong hyperfine interactions.

One important consequence of $SU(N)$ symmetry is the conservation, for any m , of S_m^m , the total number of atoms with nuclear spin m . This means that an atom with large I , e.g. ^{87}Sr ($I = 9/2$), can reproduce the dynamics of atoms with lower I if one takes an initial state with $S_m^m = 0$ for some m values. To verify $SU(N)$ symmetry of the interaction experimentally, one could, thus, put two atoms in one well in spins m and m' and confirm that collisions do not populate other spin levels. This feature of $SU(N)$ symmetry is in stark contrast to the case of weaker $SU(2)$ symmetry, where the dependence of scattering lengths on the total spin of the two colliding particles allows for scattering into spin states other than m and m' . We note that although collisions are governed by electronic interactions and obey the nuclear-spin $SU(N)$ symmetry, the nuclear spins still indirectly control the collisions via fermionic statistics and give rise to effective spin-orbital and spin-spin interactions.

One can alternatively implement the two-orbital Hubbard model with two ground-state species of alkaline-earth atoms (e.g. ^{171}Yb and ^{173}Yb , or ^{173}Yb and ^{87}Sr). If we still refer to them as $|g\rangle$ and $|e\rangle$, the nuclear distinguishability and the fact that both atoms are in the ground state will result in $a_{eg}^+ = a_{eg}^-$, corresponding to an enhanced symmetry (see Sec. G.4). While experimentally more challenging, the use of two different ground state species will solve the problem of losses associated with collisions of two excited state atoms and will reduce the (already very weak) nuclear-spin-dependence of a_{ee} and a_{eg} .

7.4 Spin Hamiltonians

One of the simplest interesting limits of Eq. (7.2) is the strongly interacting regime ($J/U \ll 1$) where the Hilbert space is restricted to a given energy manifold of the $J_g = J_e = 0$ Hamiltonian (with a fixed number of atoms on each site), and tunneling is allowed only virtually, giving rise to an effective spin (and pseudo-spin) Hamiltonian. Single-site energy manifolds can be classified according to the number of atoms $n_j = n_{jg} + n_{je}$, the pseudo-spin component T_j^z , and the spin symmetry ($SU(N)$ representation) described by a Young diagram. As shown in Fig. 7.2a, each diagram consists of n_j boxes and at most two columns of heights p and q , representing two

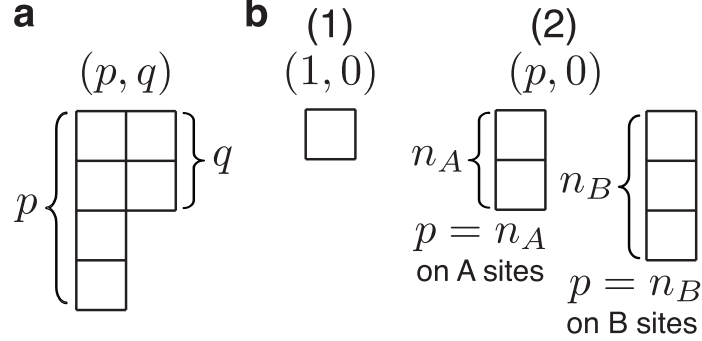


Figure 7.2: **Young diagrams describing the irreducible representations of $SU(N)$ on individual sites.** **a**, A general diagram consists of n_j boxes arranged into at most two columns (to satisfy fermionic antisymmetry with only two orbital states) whose heights we will denote by p and q , such that $N \geq p \geq q$ and $p + q = n_j$. See Sec. G.5 for a brief review of Young diagrams. **b**, The Young diagrams for the two special cases discussed in the main text: **(1)** $(p, q) = (1, 0)$ and **(2)** $(p, q) = (p, 0)$ on a bipartite lattice.

sets of antisymmetrized indices.

The $U(1) \times SU(N)$ symmetry of Eq. (7.2) restricts the order J^2 spin Hamiltonian to the form

$$\begin{aligned}
 H_{(p,q)} = & \sum_{\langle i,j \rangle, \alpha} \left[\kappa_{\alpha}^{ij} n_{i\alpha} n_{j\alpha} + \lambda_{\alpha}^{ij} S_m^{\alpha}(i, \alpha) S_n^{\alpha}(j, \alpha) \right] \\
 & + \sum_{\langle i,j \rangle} \left[\kappa_{ge}^{ij} n_{ig} n_{je} + \lambda_{ge}^{ij} S_m^g(i, g) S_n^g(j, e) \right. \\
 & \left. + \tilde{\kappa}_{ge}^{ij} S_{gm}^{em}(i) S_{en}^{gn}(j) + \tilde{\lambda}_{ge}^{ij} S_{gm}^{en}(i) S_{en}^{gm}(j) + \{i \leftrightarrow j\} \right], \quad (7.5)
 \end{aligned}$$

where the sum over n and m is implied in all but the κ terms and $S_{\beta n}^{\alpha m}(j) = c_{j\beta n}^{\dagger} c_{jam}$. $\{i \leftrightarrow j\}$ means that all 4 preceding terms are repeated with i and j exchanged. The coefficients κ , λ , $\tilde{\kappa}$, and $\tilde{\lambda}$ are of order J^2/U with the exact form determined by what single-site energy manifolds we are considering. κ terms describe nearest neighbor repulsion or attraction, while λ , $\tilde{\kappa}$, and $\tilde{\lambda}$ terms describe nearest neighbor exchange of spins, pseudo-spins, and complete atomic states, respectively. Without loss of generality, $\kappa_{\alpha}^{ij} = \kappa_{\alpha}^{ji}$ and $\lambda_{\alpha}^{ij} = \lambda_{\alpha}^{ji}$. In many cases (e.g. case (2) below), the Hilbert space, which $H_{(p,q)}$ acts on, has n_{ie} and n_{ig} constant for all i , which not only forces $\tilde{\kappa}_{ge}^{ij} = \tilde{\lambda}_{ge}^{ij} = 0$ but also allows one to ignore the constant κ_{α}^{ij} and κ_{ge}^{ij} terms. We now discuss two special cases of $H_{(p,q)}$ shown in Fig. 7.2b. A third case, $(p, q) = (1, 1)$, which reduces for $N = 2$ to the spin-1 Heisenberg antiferromagnet, is discussed in Sec. G.6.

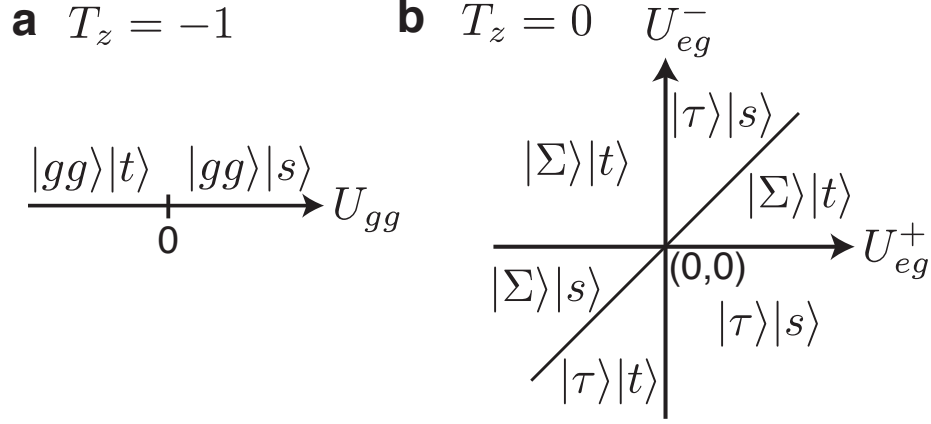


Figure 7.3: **The ground-state phase diagram for the $SU(N=2)$ Kugel-Khomskii model restricted to two wells, left (L) and right (R).** **a**, The phase diagram for $T_z = -1$ (two g atoms). $|gg\rangle = |gg\rangle_{LR}$. $|s\rangle$ and $|t\rangle$ are spin singlet and triplet states, respectively. **b**, The phase diagram for $T_z = 0$ (one g atom and one e atom). $|\Sigma\rangle = \frac{1}{\sqrt{2}}(|eg\rangle_{LR} - |ge\rangle_{LR})$ and $|\tau\rangle = \frac{1}{\sqrt{2}}(|eg\rangle_{LR} + |ge\rangle_{LR})$ are anti-symmetric and symmetric orbital states, respectively. See Sec. G.7 for a detailed discussion of both of these diagrams.

(1) In the case of one atom per site, $(p, q) = (1, 0)$. $H_{(p,q)}$ is then a generalization to arbitrary N of the $SU(N = 2)$ Kugel-Khomskii model [218, 222], and we rewrite it as (see Sec. G.7)

$$H_{(1,0)} = \sum_{\langle i,j \rangle} \left[2(\tilde{\kappa}_{ge} + \tilde{\lambda}_{ge} S_{ij}^2)(T_i^x T_j^x + T_i^y T_j^y) + \lambda_{ge} S_{ij}^2 - [A + B S_{ij}^2](T_i^z T_j^z + \frac{1}{4}) + h(1 - S_{ij}^2)(T_i^z + T_j^z) \right], \quad (7.6)$$

where $S_{ij}^2 = \sum_{mn} S_m^n(i) S_n^m(j)$ is $+1$ (-1) for a symmetric (antisymmetric) spin state, $A = 2\kappa_{ge} - \kappa_e - \kappa_g$, $B = 2\lambda_{ge} + \kappa_e + \kappa_g$, and $h = (\kappa_e - \kappa_g)/2$. The $N = 2$ Kugel-Khomskii Hamiltonian is used to model the spin-orbital interactions [219, 220, 221, 251, 252, 253, 254] (not to be confused with relativistic spin-orbit coupling) in transition metal oxides with perovskite structure [222]. Our implementation allows to realize clean spin-orbital interactions unaltered by lattice and Jahn-Teller distortions present in solids [222].

To get a sense of the competing spin and orbital orders [219, 220, 221] characterizing $H_{(1,0)}$, we consider the simplest case of only two sites (L and R) and $N = 2$ (with spin states denoted by \uparrow and \downarrow). To avoid losses in e - e collisions, we set $U_{ee} = \infty$ (see Sec. G.2). The double-well ground-state phase diagram for $T^z = 1$ (two e atoms) is then trivial, while the $T^z = -1$ (two g atoms) and $T^z = 0$ (one g atom and

one e atom) diagrams are shown in Fig. 7.3. One can see that, depending on the signs and relative magnitudes of the interactions, various combinations of ferromagnetic (triplet) and antiferromagnetic (singlet) spin and orbital orders are favored. In Sec. G.8, we propose a double-well experiment along the lines of Ref. [204] to probe the spin-orbital interactions giving rise to the $T^z = 0$ diagram in Fig. 7.3b. Multi-well extensions of this experiment may shed light on the model's many-body phase diagram, which has been studied for $N = 2$ and mostly at mean-field level or in special cases, such as in one dimension or in the presence of enhanced symmetries (see e.g. Refs. [219, 221, 220]).

(2) In order to study $SU(N)$ spin physics alone, we consider the case of g atoms only. On a bipartite lattice with sublattices A and B, we choose A sites to have $n_A < N$ atoms $[(p, q) = (n_A, 0)]$ and B sites to have $n_B < N$ atoms $[(p, q) = (n_B, 0)]$. This setup can be engineered in cold atoms by using a superlattice to adjust the depths of the two sublattices favoring a higher filling factor in deeper wells. $H_{(p,q)}$ then reduces to

$$H_{(p,0)} = \frac{2J_g^2 U_{gg}}{U_{gg}^2 - (U_{gg}(n_A - n_B) + \Delta)^2} \sum_{\langle i,j \rangle} S_{ij}^2, \quad (7.7)$$

where Δ is the energy offset between adjacent lattice sites. The coupling constant can be made either positive (antiferromagnetic) or negative (ferromagnetic) depending on the choice of parameters [204]. Three body recombination processes will likely limit the lifetime of the atoms when $n_j \geq 3$ (see Sec. G.9).

We focus on the 2D square lattice in the antiferromagnetic regime. The case $n_A + n_B = N$ shares with the $SU(2)$ Heisenberg model the crucial property that two adjacent spins can form an $SU(N)$ singlet, and has thus been studied extensively as a large- N generalization of $SU(2)$ magnetism [237, 236]. Fig. 7.4a shows the expected phase diagram for the case $n_A + n_B = N$, which features Neel (circles), valence-bond-solid (VBS) (squares) [Fig. 7.4b], and possible critical spin liquid (triangle) [239, 240] ground states. To access various ground states of the system, the initial state must be carefully prepared so that the conserved quantities S_m^m take values appropriate for these ground states. Another interesting and experimentally relevant case, $n_A = n_B \neq N/2$, which can also exhibit spin liquid and VBS-type ground states, is discussed in Sec. G.10 and in Ref. [243].

Since one can vary N just by choosing the number of initially populated Zeeman levels (e.g. via a combination of optical pumping and coherent manipulation), alkaline-earth atoms offer a unique arena to probe the phase diagram of $H_{(p,0)}$, including exotic phases such as VBS [Fig. 7.4b], as well as competing magnetically ordered states. We propose to load a band insulator of N g atoms per site, then slowly split each well into two to form an array of independent $SU(N)$ singlets in a pattern shown in Fig. 7.4b. The intersinglet tunneling rate should then be adiabatically increased up to the intrasinglet tunneling rate. As N increases, the magnetic

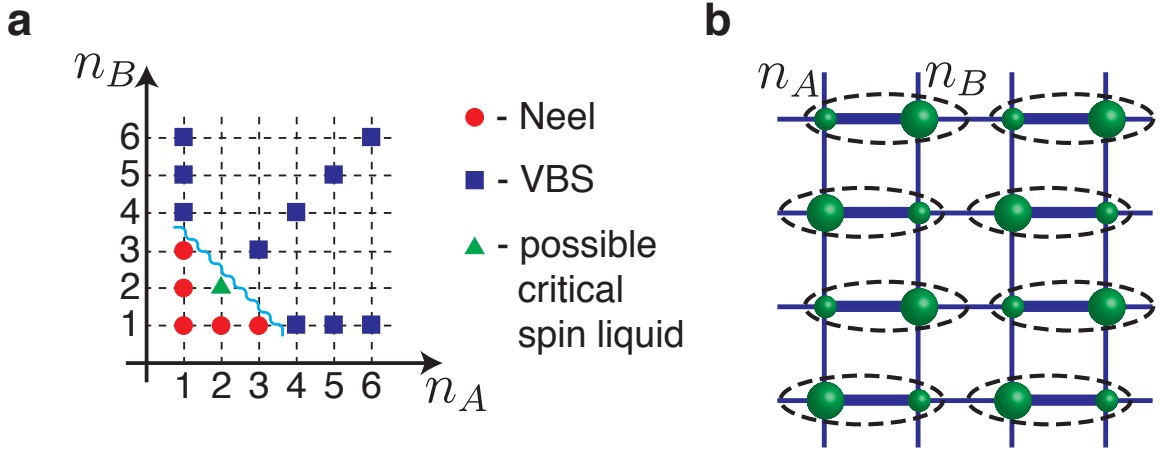


Figure 7.4: **Probing the phases of the $SU(N)$ antiferromagnet on a 2D square lattice.** **a** shows the phase diagram for the case $n_A + n_B = N$. Some points on this diagram have been explored in earlier numerical studies [238, 239, 240] and are marked according to the ground state obtained: Neel (circles), columnar-valence-bond solid (VBS) [shown schematically in **b**] (squares), and possibly critical spin liquid (triangle) [239, 240]. Since for sufficiently large N quantum fluctuations tend to destabilize long-range magnetic ordering, it is likely that VBS ordering characterizes the ground state for all $N > 4$ (i.e. above the wavy line). In **b**, thick bonds connect spins that are more strongly correlated than spins connected by thin bonds, while dashed lines encircle (approximate) $SU(N)$ singlets.

or singlet nature of the state can be probed by measuring the Neel order parameter (see the description of the Kugel-Khomskii double-well experiment in Sec. G.8) and spin-spin correlations via noise spectroscopy in the time of flight [255] (which directly measures $\sum_{j,k} \langle S_n^m(j, g) S_m^n(k, g) \rangle e^{iQ(j-k)}$).

7.5 The Kondo Lattice Model (KLM)

The $SU(N)$ Kondo lattice model (KLM) [224, 226] is another example of the rich physics, beyond the Mott regime, which could be simulated with alkaline-earth atoms. The KLM is one of the canonical models used to study strongly correlated electron systems, such as manganese oxide perovskites [229] and rare earth and actinide compounds classed as heavy fermion materials [234].

For its implementation with cold atoms (for $N = 2$, see also Refs. [232, 233]), we propose to put one e atom (localized spin) per site in a deep lattice such that $J_e \ll U_{ee}$, so that we can set $J_e = 0$ and $n_{je} = 1$ for all j in Eq. (7.2). We also suppose that we can set $U_{gg} = 0$, e.g. by taking a very shallow g -lattice (see Fig.

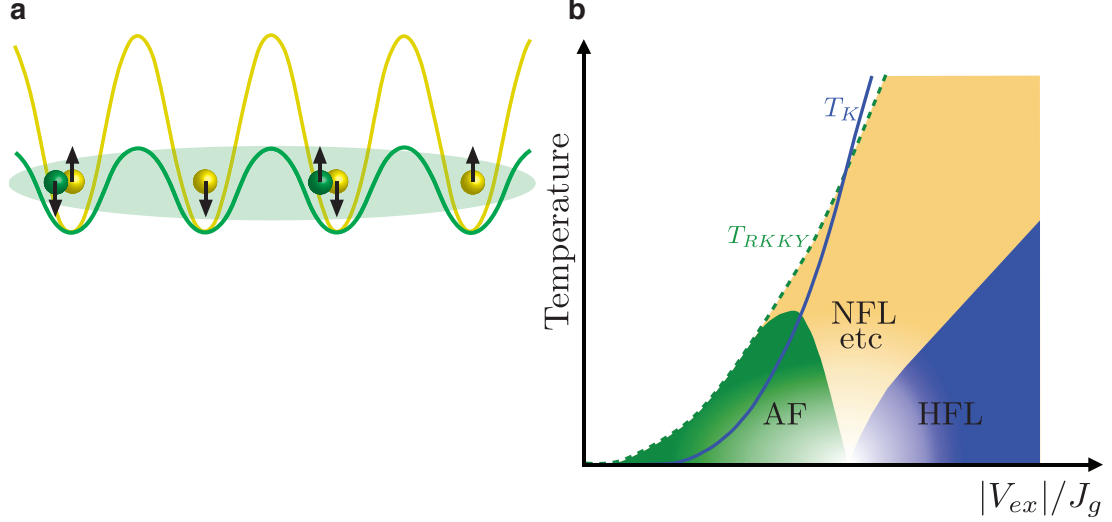


Figure 7.5: **Kondo lattice model for the case $N = 2$.** **a**, The schematic of the setup. g atoms are green; e atoms are yellow; the spin basis is $\{\uparrow, \downarrow\}$. **b**, Schematic representation of the competition between RKKY magnetism vs Kondo singlet formation in the $SU(2)$ AF KLM (see [225, 234, 235] and references therein). In this model, the localized spin-1/2 e atoms couple antiferromagnetically to the delocalized g atoms, via an on-site exchange interaction proportional to V_{ex} . This coupling favors the formation of localized Kondo singlets between e and g atoms, with characteristic energy scale $k_B T_K \sim J_g \exp(-cJ_g/|V_{ex}|)$, with c a dimensionless constant of order one [234]. On the other hand, the g atoms can mediate long-range RKKY interactions between the e atoms, giving rise to magnetic order (which can be antiferromagnetic (AF) or ferromagnetic depending on the density of g atoms), where the characteristic energy is $k_B T_{RKKY} \sim V_{ex}^2/J_g$. The competition between Kondo effect and RKKY magnetism leads to very rich physics. For small values of $|V_{ex}|/J_g$, the RKKY interaction is dominant and the system orders magnetically. At intermediate values of $|V_{ex}|/J_g$, the energy scales T_K and T_{RKKY} are of comparable strength, and a variety of novel quantum phenomena are expected to arise, including quantum criticality and non-Fermi liquid (NFL) physics [234, 235]. With further increase of the $|V_{ex}|/J_g$ coupling, magnetic order is suppressed, the localized e atoms become screened into singlet states and melt into the g -atom Fermi sea, forming the so called heavy Fermi liquid state (HFL). The large Fermi volume [230], which is set by the total number of g atoms plus e atoms, can be directly probed by measuring the momentum distribution via time of flight imaging.

7.5a). The resulting Hamiltonian is the $SU(N)$ KLM [224, 226]

$$H_{KLM} = - \sum_{\langle j,i \rangle m} J_g (c_{igm}^\dagger c_{jgm} + \text{h.c.}) + V_{ex} \sum_{j,m,m'} c_{jgm}^\dagger c_{jem'}^\dagger c_{jgm'} c_{jem}. \quad (7.8)$$

The magnitude of V_{ex} can be adjusted by shifting the e and g lattices relative to each other [191].

The properties of the $SU(N)$ KLM depend crucially on the sign of the exchange interaction. For concreteness, we focus on the antiferromagnetic (AF) case ($V_{ex} < 0$), which favors formation of spin-antisymmetric states (singlets, for $N = 2$) between mobile fermions and localized spins. This regime describes the physics of heavy fermion materials [234], and, in the case of a single localized spin, gives rise to the Kondo effect.

In the limit $|V_{ex}| \ll J_g$, g atoms mediate long-range RKKY interactions [223] between localized spins and tend to induce magnetic ordering (antiferromagnetic or ferromagnetic depending on the density of g atoms) of the latter, at least for $N = 2$. The engineering of RKKY interactions can be tested in an array of isolated double wells (see Sec. G.8). At intermediate and large $|V_{ex}|$, the formation of Kondo singlets dominates the RKKY interaction and favors a magnetically disordered heavy Fermi liquid (HFL) ground state with a significantly enhanced effective quasiparticle mass (see Fig. 7.5b). The competition between RKKY interactions and the Kondo effect in the regime where both are comparable is subtle, and the resulting phases and phase transitions [234, 235] are not well-understood. Ultracold alkaline-earth atoms provide a promising platform to study these phases and phase transitions.

In the large- N limit [224, 226], the $SU(N)$ HFL can be controllably studied, and $1/N$ expansions have successfully reproduced the experimentally observed properties of the HFL. However, very little is known about the $SU(N)$ model outside the HFL regime. Several very interesting parameter regimes in this domain can be directly probed with our system, as discussed in Sec. G.11.

7.6 Experimental Accessibility

The phenomena described in this Chapter can be probed with experimental systems under development. In this Section, we first demonstrate that temperature requirements are reasonable and then show that $SU(N)$ -breaking terms are sufficiently weak.

We begin by analyzing the temperature requirements. The key energy scale in the spin Hamiltonians [Eq. (7.5)] is the superexchange energy J^2/U , while the RKKY energy scale is $k_B T_{RKKY} \sim V_{ex}^2/J_g$. In their region of validity ($J < U$ and $|V_{ex}| < J_g$, respectively), these energy scales are limited from above by the interaction energy (U and $|V_{ex}|$, respectively), which typically corresponds to temperatures $T \lesssim 100\text{nK}$ [204]. Thanks to the additional cooling associated with certain adiabatic changes [256, 257], $T \sim 10\text{nK}$ and the Mott insulating regime have already been achieved with fermionic alkali atoms [258], and are therefore expected to be achievable with fermionic alkaline-earths, as well (a bosonic alkaline-earth Mott insulator has already been achieved [136]). Furthermore, the requirement to reach $k_B T$ smaller than J^2/U

or V_{ex}^2/J_g can often be relaxed. First, the double-well experiments, such as the ones discussed in Sec. G.8 in the contexts of the Kugel-Khomskii and the Kondo lattice models, are performed out of thermal equilibrium, and can, thus, access energy scales far below the temperature of the original cloud [204]. Second, for $SU(N)$ antiferromagnets, the energy range between J^2/U and NJ^2/U may also exhibit intriguing physics: in this regime, $SU(N)$ singlets, which require NJ^2/U energy to break, stay intact but can diffuse around. Finally, in the $V_{ex} < 0$ Kondo lattice model, exotic heavy Fermi liquid behavior is expected when $J_g \lesssim |V_{ex}|$ and the temperature is below the Kondo temperature, i.e. $k_B T \lesssim J_g \exp(-cJ_g/|V_{ex}|)$ with c is a dimensionless constant of order one [234]. Thus, with J_g chosen to be on the order of $|V_{ex}|$, $k_B T$ as high as $\sim |V_{ex}|$ may be sufficient.

We now show that the nuclear-spin dependence of interaction energies is sufficiently weak to keep the $SU(N)$ physics intact. In Sec. G.1, we estimate the nuclear-spin-dependent variation in the interaction energies to be $\Delta U_{gg}/U_{gg} \sim 10^{-9}$ and $\Delta U_{ee}/U_{ee} \sim \Delta U_{eg}^\pm/U_{eg}^\pm \sim 10^{-3}$. Since the scale of $SU(N)$ breaking is at most ΔU , a very conservative condition for the physics to be unaffected by $SU(N)$ breaking is that all important energy scales are greater than ΔU . In particular, in the spin models with more than one atom per site, the condition is $\Delta U \ll J^2/U$, which can be satisfied simultaneously with $J \ll U$ even for $\Delta U/U \sim 10^{-3}$. With one atom per site, the $SU(N)$ breaking scale is not ΔU but rather $(J/U)^2 \Delta U$, which relaxes the condition to the immediately satisfied $\Delta U/U \ll 1$. Similarly, in the Kondo lattice model, the conditions $\Delta V_{ex} \ll J, |V_{ex}|$ can be satisfied for $\Delta V_{ex}/|V_{ex}| \sim 10^{-3}$.

7.7 Outlook

The proposed experiments should be regarded as bridges aiming to connect well-understood physics to the complex and poorly understood behavior of strongly correlated systems. It is important to emphasize that, except for the one dimensional case, the phase diagram of most of the models considered is only known at mean field level or numerically in reduced system sizes. Therefore, their experimental realization in clean and controllable ultracold atomic systems can provide major advances.

Our proposal motivates other new lines of research. Ultracold bosonic or fermionic diatomic molecules [259] may give rise to similar $SU(N)$ models with large N and with the possibility of long-range interactions. Ions with alkaline-earth-like structure, such as Al^+ could also be considered in this context. It would also be interesting to explore the possibility of realizing topological phases with $SU(N)$ models for applications in topological quantum computation [243]. Beyond quantum magnetism, the fact that the formation of $SU(N)$ singlets requires N partners might give rise to novel exotic types of superfluidity and novel types of BCS-BEC crossover [246]. Practical applications of our Hubbard model, such as the calculation of the collisional frequency shift in atomic clocks [59], can also be foreseen.

Note added: After this work was submitted for publication, a theoretical study of the $SU(6)$ -symmetric ^{173}Yb system was reported [260].

Chapter 8

Suppression of Inelastic Collisions between Polar Molecules with a Repulsive Shield

8.1 Introduction and Basic Idea

In the preceding Chapters, we mostly focused on systems based on neutral atoms, which typically exhibit only short-range interactions. At the same time, numerous exotic phenomena and practical applications require long-range interactions, which can be achieved with ultracold polar molecules [72]. However, gases of polar molecules suffer from inelastic collisions, which reduce the lifetime of the molecules and interfere with evaporative cooling [72, 261]. It is therefore crucial to control inelastic collisions between polar molecules. Thus, in this Chapter, we demonstrate the possibility to engineer a three-dimensional repulsive interaction between polar molecules, which allows for the suppression of inelastic collisions, while simultaneously enhancing elastic collisions. This technique may open up a way towards efficient evaporative cooling and the creation of novel long-lived quantum degenerate phases of polar molecules.

A special property of polar molecules prepared in the lowest rotational and vibrational state is a permanent electric dipole moment d , which gives rise to tunable dipole-dipole interactions and offers a large potential for the creation of strongly correlated quantum phases [262, 263, 264, 265]. Two routes are currently explored for the experimental realization of quantum degenerate polar molecules: (i) trapping and cooling of preexisting molecules [266, 267, 268, 269, 270, 271] and (ii) synthesizing polar molecules from a cold mixture of atomic gases [272, 273, 274, 275, 276, 277, 278]. While scattering properties of polar molecules with dipole-dipole interactions are currently theoretically explored [279, 280, 281], it is expected that inelastic collisions (including three-body recombination) strongly increase for polar molecules compared to atomic systems due to the opening of additional decay channels.

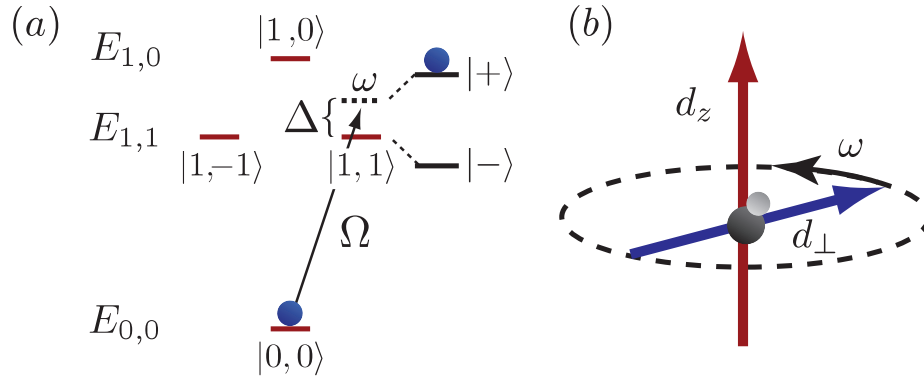


Figure 8.1: (a) Energy levels of $H_{\text{rot}}^{(i)}$: the arrow indicates the microwave field. (b) Sketch for the cancellation of the dipole-dipole interaction: d_z denotes the dipole moment induced by the static electric field, while the dipole moment d_{\perp} is rotating in an orthogonal plane due to the microwave coupling.

The main idea of our approach is to cancel the leading dipole-dipole interaction with a suitable combination of a static electric field and a continuous-wave microwave field: the former induces a dipole moment d_z , while the latter drives an additional dipole moment d_{\perp} rotating with frequency ω of the microwave field, see Fig. 8.1(b). In analogy with magic-angle techniques in NMR [282], the time-averaged interaction of the rotating dipole moment shows a negative sign allowing for a cancellation of the total dipole-dipole interaction. The remaining interaction is tunable in strength with a repulsive van der Waals behavior $V_{\text{eff}} \sim (d^4/\hbar\Delta)/r^6$, where Δ is the detuning of the microwave field and r is the intermolecular separation. The three-dimensional shield described here is thus purely repulsive. This is in contrast to the “blue shield” discussed in the context of atomic gases, which is attractive at large distances [283]. We find that the efficiency of the shield is determined by a single dimensionless parameter $\gamma = d^2m/\hbar^2r_B$ with $r_B = (d^2/B)^{1/3}$, B the rotational energy, and m the mass of the molecule. Under optimal conditions, for large values of γ , inelastic collisions can be quenched for temperatures $T \lesssim 0.01B$.

8.2 Detailed Analysis within the Born-Oppenheimer Approximation

To describe the shield quantitatively, we consider two polar molecules prepared in the vibrational ground state. At large intermolecular distances, dipole-dipole inter-

actions dominate¹, yielding the Hamiltonian

$$H = \frac{\mathbf{P}^2}{4m} + \frac{\mathbf{p}^2}{m} + \frac{\mathbf{d}_1 \mathbf{d}_2 - 3(\mathbf{d}_1 \hat{\mathbf{r}})(\mathbf{d}_2 \hat{\mathbf{r}})}{r^3} + \sum_{i=1}^2 H_{\text{rot}}^{(i)}, \quad (8.1)$$

where we have introduced the center of mass $\mathbf{R} = (\mathbf{r}_1 + \mathbf{r}_2)/2$ and the relative coordinate $\mathbf{r} = \mathbf{r}_1 - \mathbf{r}_2$, with the corresponding momenta \mathbf{P} and \mathbf{p} , respectively, while $r = |\mathbf{r}|$ and $\hat{\mathbf{r}} = \mathbf{r}/r$. Here, we are interested in polar molecules in the $^1\Sigma$ electronic ground state, and the Hamiltonian for the internal structure takes the form [284] $H_{\text{rot}}^{(i)} = B \mathbf{J}_i^2 - \mathbf{d}_i \cdot \mathbf{E}_{\text{dc}} - \mathbf{d}_i \cdot \mathbf{E}_{\text{ac}}(t)$, with the dipole operator \mathbf{d}_i and the permanent dipole moment d . The first term describes a rigid rotor accounting for rotational structure with the rotational energy B , while the last two terms describe the coupling to an external static electric field \mathbf{E}_{dc} and microwave field \mathbf{E}_{ac} . While additional interactions with the nuclear spins are in general small and can be ignored, the analysis presented here remains valid for polar molecules with an electronic spin in a strong magnetic field with the Zeeman splitting larger than the energy scales of the shield and the spin-rotation coupling; such a situation naturally appears in magnetic traps.

We choose to apply a static electric field $\mathbf{E}_{\text{dc}} = E_{\text{dc}} \mathbf{e}_z$ along the z -axis. For each molecule, a suitable basis set for the internal states is given by the eigenstates of the rotor Hamiltonian in the external static field. These states and the corresponding energies depend on the dimensionless parameter dE_{dc}/B and are denoted by $|j, m_z\rangle_i$ and E_{j, m_z} , respectively, with m_z the angular momentum along the z -axis and j denoting the different energy manifolds, see Fig. 8.1(a). In addition, we apply a circularly (σ^+) polarized microwave field $\mathbf{E}_{\text{ac}}(t)$ propagating along the z -axis and coupling dominantly the ground state $|0, 0\rangle_i$ with the first excited state $|1, 1\rangle_i$. The microwave field is characterized by the detuning $\Delta = \omega - (E_{1,1} - E_{0,0})/\hbar$ and Rabi frequency $\Omega = E_{\text{ac}} d_c/\hbar$ with the dipole coupling $d_c = |\langle 0, 0 | \mathbf{d}_i | 1, 1 \rangle|$. The leading effect of the microwave field on the internal structure of each molecule is to mix the ground state $|0, 0\rangle$ with the excited state $|1, 1\rangle$. We are interested in the regime with $\Delta, \Omega \ll B/\hbar$ and $dE_{\text{dc}} < 2B$, where the rotating wave approximation is valid. In the rotating frame, these dressed states then take the form $|+\rangle = \alpha|0, 0\rangle + \beta|1, 1\rangle$ and $|-\rangle = \beta|0, 0\rangle - \alpha|1, 1\rangle$ with the energy splitting $\Delta E = \hbar\sqrt{\Delta^2 + 4\Omega^2}$ and $\alpha = -A/\sqrt{A^2 + \Omega^2}$, $\beta = \Omega/\sqrt{A^2 + \Omega^2}$, and $A = (\Delta + \sqrt{\Delta^2 + 4\Omega^2})/2$. Throughout this Chapter, we are interested in a shield with a high barrier, which is optimized for parameters close to $dE_{\text{dc}}/B = 1$, $\hbar\Delta = 0.015B$, and $\Omega/\Delta = 0.9258$ ² (see below).

We next turn to the dipolar interaction and derive the dressed Born-Oppenheimer potentials. Each polar molecule is prepared in the internal state $|+\rangle_i$ by an adiabatic

¹ $1/r^5$ quadrupole-quadrupole and dipole-octopole interactions are expected to be small and will not affect our analysis for quadrupole and octopole moments smaller than $0.2(d^5/B)^{1/3}$ and $0.02(d^7/B^2)^{1/3}$, respectively.

²For LiCs the DC fields $\sim 2\text{kV/cm}$ and microwave intensities $\sim 10\text{W/cm}^2$ are achievable in the laboratory.

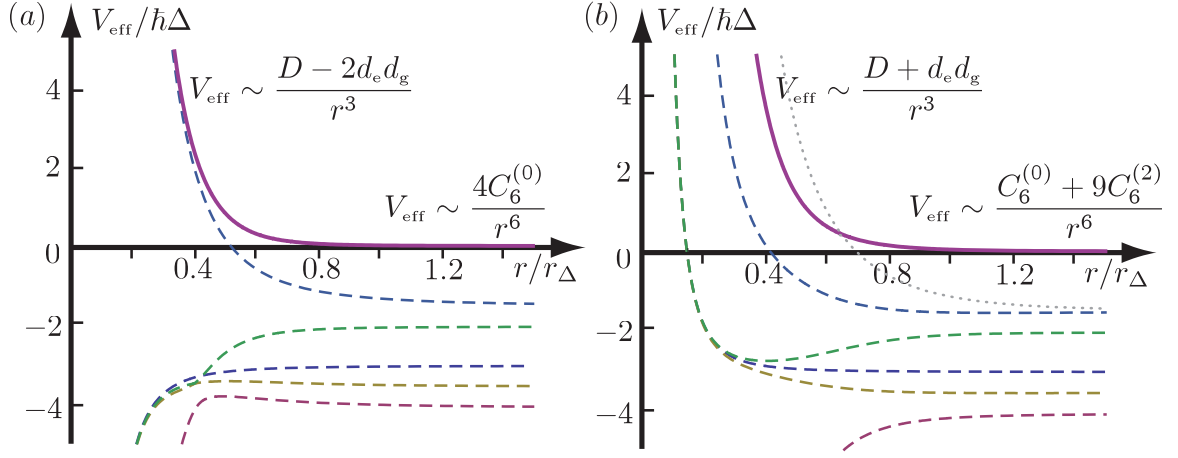


Figure 8.2: Born-Oppenheimer potentials in the limit $r \gg r_B$: (a) $\theta = 0$ and (b) $\theta = \pi/2$. The effective potential $V_{\text{eff}}(\mathbf{r})$ (solid line) is repulsive for all angles θ . The dotted line denotes the antisymmetric level relevant during a three-body collision.

switching on of the microwave field. Consequently, the effective interaction potential $V_{\text{eff}}(\mathbf{r})$ is determined by the dressed Born-Oppenheimer potential adiabatically connected to the state $|+\rangle_1|+\rangle_2$, see Fig. 8.2. The competition between the rotational splitting B and the dipole-dipole interaction provides a characteristic length scale $r_B = (d^2/B)^{1/3}$. For large interparticle distances $r \gg r_B$, the dipole-dipole interaction is weak and does not couple different rotor levels. Consequently, the only relevant coupling appears due to the microwave field between the manifolds with $j = 0$ and $j = 1$. The relevant internal states are then given by the three states $|g\rangle_i = |0, 0\rangle_i$, $|e\rangle_i = |1, 1\rangle_i$, and $|\bar{e}\rangle_i = |1, -1\rangle_i$. As the microwave field couples each polar molecule with the same phase, the Born-Oppenheimer potentials separate into 6 symmetric and 3 antisymmetric dressed potentials. The effective potential adiabatically connected to the state $|+\rangle_1|+\rangle_2$ is symmetric, and therefore, we can restrict the analysis to the symmetric potentials: a basis is given by the symmetric states $|g, g\rangle$, $|e, g\rangle$, $|e, e\rangle$, $|g, \bar{e}\rangle$, $|e, \bar{e}\rangle$, and $|\bar{e}, \bar{e}\rangle$. Within the rotating frame, the Hamiltonian projected onto this subspace reduces to

$$H = \begin{pmatrix} d_g^2 \nu & \sqrt{2} \hbar \Omega & 0 & 0 & 0 & 0 \\ \sqrt{2} \hbar \Omega & H_{eg} & \sqrt{2} \hbar \Omega & d_c^2 \mu^* / 2 & 0 & 0 \\ 0 & \sqrt{2} \hbar \Omega & H_{ee} & 0 & 0 & 0 \\ 0 & d_c^2 \mu / 2 & 0 & H_{eg} & \hbar \Omega & 0 \\ 0 & 0 & 0 & \hbar \Omega & H_{ee} & 0 \\ 0 & 0 & 0 & 0 & 0 & H_{ee} \end{pmatrix} \quad (8.2)$$

with the dipole moments $d_g = |\langle g | \mathbf{d}_i | g \rangle|$, $d_e = |\langle e | \mathbf{d}_i | e \rangle|$, and $H_{eg} = (d_e d_g - d_c^2 / 2) \nu - \hbar \Delta$ and $H_{ee} = d_e^2 \nu - 2 \hbar \Delta$. The terms $\nu = (1 - 3 \cos^2 \theta) / r^3$ and $\mu = 3 \sin^2 \theta e^{2i\phi} / r^3$ describe

the spatial dependence of the dipole-dipole interaction, with θ and ϕ being the polar and azimuthal angles of \mathbf{r} , respectively. The Born-Oppenheimer potentials then follow from a diagonalization of the Hamiltonian H and are shown in Fig. 8.2, with the level adiabatically connected to the state $|+\rangle_1|+\rangle_2$ (solid line) giving rise to the effective interaction $V_{\text{eff}}(\mathbf{r})$.

The detuning Δ introduces a new length scale in the problem $r_\Delta = (d^2/\hbar\Delta)^{1/3} \gg r_B$, e.g., for LiCs with $B/\hbar \approx 5.8\text{GHz}$, $r_B \approx 9.2\text{ nm}$ and $r_\Delta \approx 37.5\text{nm}$ at $\hbar\Delta = 0.015B$. At large interparticle distances $r > r_\Delta$, the Born-Oppenheimer potentials are well described by perturbation theory in the dipole-dipole interaction. The static electric field gives rise to a dipole moment $d_z = \alpha^2 d_g + \beta^2 d_e$ along the z -axis, while the microwave field drives an additional dipole moment $d_\perp = \sqrt{2}\alpha\beta d_c$ rotating with frequency ω in the x - y plane. The combination of the two dipole forces provides the interaction $V_{\text{eff}}(\mathbf{r}) = (d_z^2 - d_\perp^2/2)(1 - 3\cos^2\theta)/r^3$. A proper choice of the two parameters $E_{\text{dc}}d/B$ and Ω/Δ gives $d_z = d_\perp/\sqrt{2}$, providing a cancelation of the leading dipole-dipole interaction [265]. The remaining interaction then follows from second order perturbation theory and provides a van-der-Waals-type repulsion

$$V_{\text{eff}}(\mathbf{r}) = \frac{1}{r^6} \left[C_6^{(0)}(1 - 3\cos^2\theta)^2 + C_6^{(2)} 9\sin^4\theta \right] \quad (8.3)$$

with

$$\begin{aligned} \hbar C_6^{(0)} &= \frac{\alpha^2\beta^2}{\sqrt{\Delta^2 + 4\Omega^2}} \left\{ \frac{1}{2}\alpha^2\beta^2 [(d_e - d_g)^2 + d_c^2]^2 \right. \\ &\quad \left. + 2 \left[(\alpha^2 d_g + \beta^2 d_e)(d_e - d_g) + \frac{d_c^2}{2}(\beta^2 - \alpha^2) \right]^2 \right\}, \\ \hbar C_6^{(2)} &= \frac{\alpha^4\beta^2 d_c^4}{\Delta + \sqrt{\Delta^2 + 4\Omega^2}} + \frac{\alpha^2\beta^4 d_c^4}{\Delta + 3\sqrt{\Delta^2 + 4\Omega^2}}. \end{aligned} \quad (8.4)$$

For the optimal values $dE_{\text{dc}}/B = 1$ and $\Omega/\Delta = 0.9258$, the van der Waals coefficients take the form $C_6^{(0)} = 0.004\hbar\Delta r_\Delta^6$ and $C_6^{(2)} = 0.005\hbar\Delta r_\Delta^6$. At shorter distances $r_B \ll r < r_\Delta$, the effective interaction reduces to $V_{\text{eff}}(\mathbf{r}) = (d_c^2 + d_g d_e [1 - 3\cos^2\theta])/r^3$ and remains repulsive for all angles θ . Thus it is possible to create purely repulsive interaction with large and adjustable strength.

In order to determine the height of the potential barrier, a detailed analysis including all internal levels is required. Such a procedure is achieved by first deriving Born-Oppenheimer potentials accounting for the coupling of the internal states $|j, m\rangle_i$ by the dipole-dipole interaction. In the second step, the microwave field, which couples these Born-Oppenheimer potentials, is included within a rotating wave approximation. The new dressed levels in the rotating frame are shown in Fig. 8.3(a). It follows that the height of the shield (solid line) is limited by small avoided crossings. The first crossing (labeled *A*) appears with the level adiabatically connected to the symmetric state $|1, 0; 0, 0\rangle$ for a relative orientation of the molecules along the z -axis

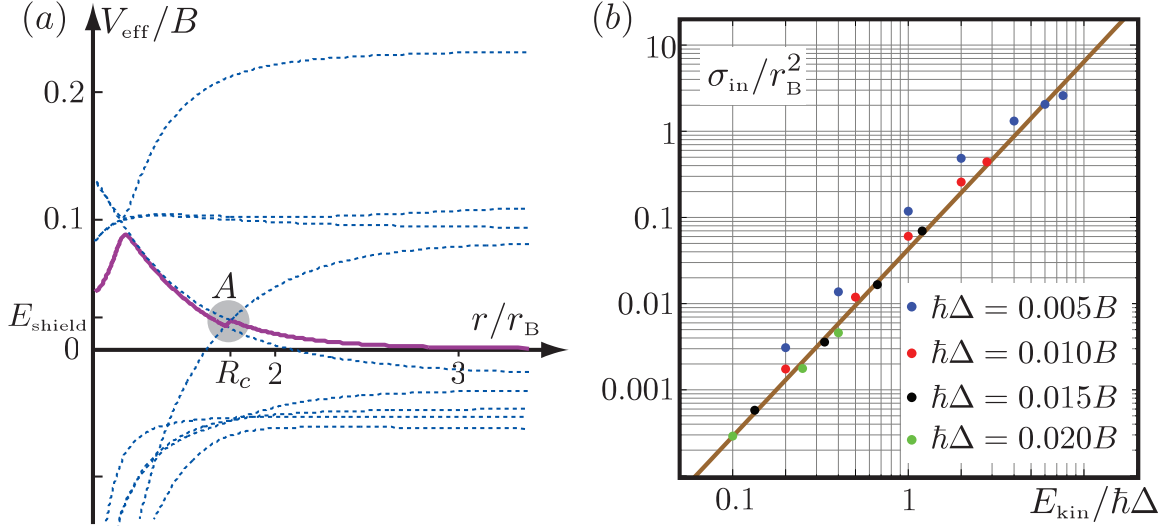


Figure 8.3: (a) Born-Oppenheimer potentials for $\hbar\Delta = 0.015B$ at $\theta = 0$. The plot shows all potentials (dashed) accessible via single-photon transitions from the state (solid) adiabatically connected to $|+\rangle_1|+\rangle_2$. The first crossing limiting the height of the shield appears in the region A for angles $\theta \approx 0$. (b) Inelastic cross section σ_{in} due to diabatic crossings for different detunings Δ as a function of incoming kinetic energy E_{kin} .

with $\theta \approx 0$, and it limits the barrier height of the shield to $E_{\text{shield}} \approx 0.02B$ for the optimal parameters. The radius R_c for the breakdown of the shield is in the range $R_c \sim r_B$, which is still large compared to the distances where additional short range interactions have to be taken into account.

8.3 Processes Beyond the Born-Oppenheimer Approximation

Next, we analyze the validity of the Born-Oppenheimer approximation and study the influence of the kinetic energy coupling different dressed potentials during a collision. The influence of the kinetic energy is determined by the dimensionless parameter $\gamma = d^2m/\hbar^2r_B$. For $\gamma \gg 1$, we can apply semiclassical theory; this condition is well satisfied for typical polar molecules like LiCs with $\gamma \approx 6900$. For a collision whose relative kinetic energy E_{kin} is below the shield barrier, the processes giving rise to inelastic loss are (i) diabatic crossing between different Born-Oppenheimer levels and (ii) quantum mechanical tunneling through the barrier. We start by studying the diabatic transitions first: the inelastic cross section within semi-classical approximation is computed by first determining the classical trajectory $r_{\text{cl}}(t)$ of a collision with

a fixed impact parameter. To determine the Landau-Zener diabatic crossings, we solve the full Schrödinger equation for the internal structure using the given relative motion $r_{\text{cl}}(t)$. The loss probability is then determined by the depletion of the adiabatic Born-Oppenheimer level at the classical turning point. Averaging over different impact parameters and angles of approach provides the inelastic cross section σ_{in} due to diabatic transitions. The main contribution comes from the Born-Oppenheimer level closely approaching the effective potential close to $\theta \approx 0$, see Figs. 8.2(a) and 8.3(a). Note that the standard Landau-Zener tunneling expression can not be applied here as the levels have no real crossing. The inelastic cross section for different Δ and E_{kin} is shown in Fig. 8.3(b). We find an algebraic behavior of the inelastic cross section with $\sigma_{\text{in}} = \rho(E_{\text{kin}}/\hbar\Delta)^\kappa r_{\text{B}}^2$ with $\kappa \approx 2.2$ and $\rho = 0.043$ at $\hbar\Delta = 0.015B$, solid line in Fig. 8.3(b). The loss rate $1/\tau_{\text{in}}$ during a two-particle collisions reduces to $1/\tau_{\text{in}} \approx 11(Bnr_{\text{B}}^3/\hbar)(T/B)^{\kappa+1/2}$, where we have replaced the collision energy with the temperature T of the gas. Consequently, for LiCs at characteristic densities $n \sim 10^{13} \text{ cm}^{-3}$, the lifetime is several seconds even for $T \sim 1\text{mK} < \hbar\Delta$.

The second scenario for an inelastic collision is quantum mechanical tunneling through the barrier. For $\gamma \gg 1$ such tunneling processes are strongly suppressed and can be studied using semiclassical techniques like WKB. The tunneling probability during a single collision is then given by the Euclidean action for the trajectory C starting at the classical turning point R_0 and ending at the inner distance R_c , where the shield starts to break down: $P_{\text{WKB}} = \exp(-2 \int_C ds \sqrt{m[V_{\text{eff}}(\mathbf{r}) - E_{\text{kin}}]}/\hbar)$. Thus, the highest tunneling probability is obtained along the collision axis with the lowest shield barrier, see discussion above. Then the characteristic scale for the tunneling amplitude at low incoming kinetic energies ($E_{\text{kin}} \ll \hbar\Delta$) is given by $P_{\text{WKB}} = \exp(-c\sqrt{\gamma})$, where the numerical constant for $\hbar\Delta/B = 0.015$ takes the form $c \approx 0.32$. Consequently, for LiCs the tunneling is strongly suppressed and can be safely ignored at low kinetic energies $E_{\text{kin}} < \hbar\Delta$.

8.4 Effects of Three-Body Collisions

It is important to note that the qualitative behavior of the shield remains robust during a three-body collision. The main modification to the shield is that the antisymmetric levels can open up an avoided crossing, as the parity symmetry present in the two-particle problem is broken for three particles. The relevant antisymmetric level is shown by a dotted line in Fig. 8.2(b). As this crossing appears at energies $\sim \hbar\Delta$, it does not modify the validity of the above discussion for incoming kinetic energies $E_{\text{kin}} < \hbar\Delta$. Thus, the shield prevents three particles from approaching each other on distances, where the formation of bound states can take place, and three-body losses are therefore effectively quenched.

8.5 Conclusions and Outlook

To summarize, we showed that properly adjusted continuous wave microwave and DC electric fields can create a repulsive shield resulting in large suppression of inelastic collisions. We now describe possible avenues opened by this work. For efficient evaporative cooling, it is important that elastic collisions allow for fast thermalization. The elastic scattering cross section at low collisional energies is determined by the s -wave scattering length a_s . For negligible tunneling across the shield (see above), a_s can be estimated from the isotropic part of the effective repulsive interaction potential $V_{\text{eff}}^{(0)}(r) = C_6/r^6$: $a_s \approx (C_6 m/\hbar^2)^{1/4} \sim r_\Delta (d^2 m/\hbar^2 r_\Delta)^{1/4}$ [285]. For LiCs at the optimal detuning $\hbar\Delta = 0.015B$, $a_s \approx 66$ nm yielding a large elastic cross section σ_{el} with suppressed losses providing an ideal system for evaporative cooling, e.g. $\sigma_{\text{el}}/\sigma_{\text{in}} \sim 10^6$ for σ_{in} at $T = 1$ mK and $\sigma_{\text{el}} = 8\pi a_s^2$.

Another application is the creation of stable three-dimensional crystalline phases. The many-body Hamiltonian for a gas of ultracold polar molecules reduces to

$$H = \sum_i \frac{\mathbf{p}_i^2}{2m} + \frac{1}{2} \sum_{i \neq j} \frac{C_6}{|\mathbf{r}_i - \mathbf{r}_j|^6}, \quad (8.5)$$

where we neglect additional terms due to the anisotropy of the effective potential and due to three-body interactions discussed in Ref. [265]. In analogy to the appearance of crystalline phases for polar molecules confined to two dimensions [286], for strong repulsive van der Waals interactions, the system will undergo a phase transition from a liquid phase to a solid phase. The dimensionless parameter controlling the transition takes the form $\lambda = C_6 m/\hbar^2 a^4$ with $n = 1/a^3$ the particle density: for weak interactions $\lambda \ll 1$ the ground state is in a liquid phase, while for strong interactions with $\lambda \gg 1$ the system is characterized by a solid phase with broken translational symmetry. Consequently, this opens up a way towards the creation of three-dimensional crystalline structures with ultracold molecular gases.

Bibliography

- [1] Zoller, P., Beth, T., Binosi, D., Blatt, R., Briegel, H., Bruss, D., Calarco, T., Cirac, J. I., Deutsch, D., Eisert, J., Ekert, A., Fabre, C., Gisin, N., Grangiere, P., Grassl, M., Haroche, S., Imamoglu, A., Karlson, A., Kempe, J., Kouwenhoven, L., Kröll, S., Leuchs, G., Lewenstein, M., Loss, D., Lütkenhaus, N., Massar, S., Mooij, J. E., Plenio, M. B., Polzik, E., Popescu, S., Rempe, G., Sergienko, A., Suter, D., Twamley, J., Wendin, G., Werner, R., Winter, A., Wrachtrup, J., and Zeilinger, A. Quantum information processing and communication - strategic report on current status, visions and goals for research in Europe. *Eur. Phys. J. D* **36**, 203 (2005).
- [2] Gisin, N., Ribordy, G., Tittel, W., and Zbinden, H. Quantum cryptography. *Rev. Mod. Phys.* **74**, 145 (2002).
- [3] Scarani, V., Bechmann-Pasquinucci, H., Cerf, N. J., Dusek, M., Lutkenhaus, N., and Peev, M. The security of practical quantum key distribution. *Rev. Mod. Phys.* **81**, 1301 (2009).
- [4] Bouwmeester, D., Ekert, A., and Zeilinger, A., editors. *The Physics of Quantum Information: Quantum Cryptography, Quantum Teleportation, Quantum Computation*. Springer, New York, (2000).
- [5] Galindo, A. and Martin-Delgado, M. A. Information and computation: Classical and quantum aspects. *Rev. Mod. Phys.* **74**(2), 347 (2002).
- [6] Nielsen, M. A. and Chuang, I. L. *Quantum Computation and Quantum Information*. Cambridge University Press, Cambridge, (2000).
- [7] Chen, G., Church, D. A., Englert, B.-G., Henkel, C., Rohwedder, B., Scully, M. O., and Zubairy, M. S. *Quantum computing devices: principles, designs, and analysis*. Chapman & Hall/CRC, New York, (2007).
- [8] Johanning, M., Varon, A. F., and Wunderlich, C. Quantum simulations with cold trapped ions. *J. Phys. B: At. Mol. Opt. Phys.* **42**, 154009 (2009).
- [9] Bloch, I., Dalibard, J., and Zwerger, W. Many-body physics with ultracold gases. *Rev. Mod. Phys.* **80**, 885 (2008).

-
- [10] Hartmann, M. J., Brandao, F. G. S. L., and Plenio, M. B. Quantum many-body phenomena in coupled cavity arrays. *Laser & Photon. Rev.* **2**, 527 (2008).
- [11] Hanson, R., Kouwenhoven, L. P., Petta, J. R., Tarucha, S., and Vandersypen, L. M. K. Spins in few-electron quantum dots. *Rev. Mod. Phys.* **79**, 1217 (2007).
- [12] Wrachtrup, J. and Jelezko, F. Processing quantum information in diamond. *J Phys.: Condens. Matter* **18**, S807 (2006).
- [13] Clark, R. G., Brenner, R., Buehler, T. M., Chan, V., Curson, N. J., Dzurak, A. S., Gauja, E., Goan, H. S., Greentree, A. D., Hallam, T., Hamilton, A. R., Hollenberg, L. C. L., Jamieson, D. N., McCallum, J. C., Milburn, G. J., Brien, J. L. O., Oberbeck, L., Pakes, C. I., Prawer, S. D., Reilly, D. J., Ruess, F. J., Schofield, S. R., Simmons, M. Y., Stanley, F. E., Starrett, R. P., Wellard, C., and Yang, C. Progress in silicon-based quantum computing. *Phil. Trans. R. Soc. Lond. A* **361**, 1451 (2003).
- [14] Loudon, R. *Quantum Theory of Light*. Oxford University Press, New York, (2000).
- [15] Kok, P., Munro, W. J., Nemoto, K., Ralph, T. C., Dowling, J. P., and Milburn, G. J. Linear optical quantum computing with photonic qubits. *Rev. Mod. Phys.* **79**, 135 (2007).
- [16] Fleischhauer, M. and Lukin, M. D. Dark-state polaritons in electromagnetically induced transparency. *Phys. Rev. Lett.* **84**, 5094 (2000).
- [17] Fleischhauer, M. and Lukin, M. D. Quantum memory for photons: Dark-state polaritons. *Phys. Rev. A* **65**, 022314 (2002).
- [18] Kavoki, A. and Malpuech, G. *Cavity Polaritons*. Elsevier, Amsterdam, (2003).
- [19] Kasprzak, J., Richard, M., Kundermann, S., Baas, A., Jeambrun, P., Keeling, J. M. J., Marchetti, F. M., Szymanska, M. H., Andre, R., Staehli, J. L., Savona, V., Littlewood, P. B., Deveaud, B., and Dang, L. S. Bose-Einstein condensation of exciton polaritons. *Nature (London)* **443**, 409 (2006).
- [20] Zayats, A. V. and Smolyaninov, I. I. Near-field photonics: surface plasmon polaritons and localized surface plasmons. *J. Opt. A: Pure Appl. Opt.* **5**, S16 (2003).
- [21] Chang, D. E., Sørensen, A. S., Demler, E. A., and Lukin, M. D. A single-photon transistor using nanoscale surface plasmons. *Nature Phys.* **3**, 807 (2007).
- [22] Braunstein, S. L. and van Loock, P. Quantum information with continuous variables. *Rev. Mod. Phys.* **77**, 513 (2005).

-
- [23] Ekert, A. and Jozsa, R. Quantum computation and Shor's factoring algorithm. *Rev. Mod. Phys.* **68**, 733 (1996).
- [24] Grover, L. K. Quantum mechanics helps in searching for a needle in a haystack. *Phys. Rev. Lett.* **79**, 325 (1997).
- [25] Cirac, J. I. and Zoller, P. New frontiers in quantum information with atoms and ions. *Phys. Today* **57**, 38 (2004).
- [26] Blatt, R. and Wineland, D. Entangled states of trapped atomic ions. *Nature (London)* **453**, 1008 (2008).
- [27] Home, J. P., Hanneke, D., Jost, J. D., Amini, J. M., Leibfried, D., and Wineland, D. J. Complete methods set for scalable ion trap quantum information processing. *Science* **325**, 1227 (2009).
- [28] Gaetan, A., Miroschnyenko, Y., Wilk, T., Chotia, A., Viteau, M., Comparat, D., Pillet, P., Browaeys, A., and Grangier, P. Observation of collective excitation of two individual atoms in the Rydberg blockade regime. *Nature Phys.* **5**, 115 (2009).
- [29] Jaksch, D. and Zoller, P. The cold atom Hubbard toolbox. *Ann. Phys.* **315**, 52 (2005).
- [30] Nelson, K. D., Li, X., and Weiss, D. S. Imaging single atoms in a three-dimensional array. *Nature Phys.* **3**, 556 (2007).
- [31] Karski, M., Forster, L., Choi, J. M., Alt, W., Widera, A., and Meschede, D. Nearest-neighbor detection of atoms in a 1D optical lattice by fluorescence imaging. *Phys. Rev. Lett.* **102**, 053001 (2009).
- [32] Kimble, H. J. The quantum internet. *Nature (London)* **453**, 1023 (2008).
- [33] Hofheinz, M., Wang, H., Ansmann, M., Bialczak, R. C., Lucero, E., Neeley, M., O'Connell, A. D., Sank, D., Wenner, J., Martinis, J. M., and Cleland, A. N. Synthesizing arbitrary quantum states in a superconducting resonator. *Nature (London)* **459**, 546 (2009).
- [34] DiCarlo, L., Chow, J. M., Gambetta, J. M., Bishop, L. S., Johnson, B. R., Schuster, D. I., Majer, J., Blais, A., Frunzio, L., Girvin, S. M., and Schoelkopf, R. J. Demonstration of two-qubit algorithms with a superconducting quantum processor. *Nature (London)* **460**, 240 (2009).
- [35] Feynman, R. Simulating physics with computers. *Int. J. Theor. Phys.* **21**, 467 (1982).

- [36] Lloyd, S. Universal quantum simulators. *Science* **273**, 1073 (1996).
- [37] Jane, E., Vidal, G., Dur, W., Zoller, P., and Cirac, J. I. Simulation of quantum dynamics with quantum optical systems. *Quant. Inf. Comp.* **3**, 15 (2003).
- [38] Akimov, A. V., Mukherjee, A., Yu, C. L., Chang, D. E., Zibrov, A. S., Hemmer, P. R., Park, H., and Lukin, M. D. Generation of single optical plasmons in metallic nanowires coupled to quantum dots. *Nature (London)* **450**, 402 (2007).
- [39] Wurtz, G. A. and Zayats, A. V. Nonlinear surface plasmon polaritonic crystals. *Laser & Photon. Rev.* **2**, 125 (2008).
- [40] Chang, D. E., Gritsev, V., Morigi, G., Vuletić, V., Lukin, M. D., and Demler, E. A. Crystallization of strongly interacting photons in a nonlinear optical fibre. *Nature Phys.* **4**, 884 (2008).
- [41] Hafezi, M., Chang, D. E., Gritsev, V., Demler, E., and Lukin, M. D. Photonic quantum transport in a nonlinear optical fiber. *arXiv:0907.5206v1 [quant-ph]* (2009).
- [42] Kiffner, M. and Hartmann, M. J. Dissipation induced Tonks-Girardeau gas of photons. *arXiv:0908.2055v2 [quant-ph]* (2009).
- [43] Deng, H., Solomon, G. S., Hey, R., Ploog, K. H., and Yamamoto, Y. Spatial coherence of a polariton condensate. *Phys. Rev. Lett.* **99**, 126403 (2007).
- [44] Amo, A., Lefrere, J., Pigeon, S., Adrados, C., Ciuti, C., Carusotto, I., Houdre, R., Giacobino, E., and Bramati, A. Superfluidity of polaritons in semiconductor microcavities. *Nature Phys.* **5**, 805 (2009).
- [45] Ye, J., Kimble, H. J., and Katori, H. Quantum state engineering and precision metrology using state-insensitive light traps. *Science* **320**, 1734 (2008).
- [46] Rosenband, T., Hume, D. B., Schmidt, P. O., Chou, C. W., Brusch, A., Lorini, L., Oskay, W. H., Drullinger, R. E., Fortier, T. M., Stalnaker, J. E., Diddams, S. A., Swann, W. C., Newbury, N. R., Itano, W. M., Wineland, D. J., and Bergquist, J. C. Frequency ratio of Al^+ and Hg^+ single-ion optical clocks; metrology at the 17th decimal place. *Science* **319**, 1808 (2008).
- [47] Durfee, D. S., Shaham, Y. K., and Kasevich, M. A. Long-term stability of an area-reversible atom-interferometer Sagnac gyroscope. *Phys. Rev. Lett.* **97**, 240801 (2006).
- [48] Kornack, T. W., Ghosh, R. K., and Romalis, M. V. Nuclear spin gyroscope based on an atomic comagnetometer. *Phys. Rev. Lett.* **95**, 230801 (2005).

- [49] Budker, D. and Romalis, M. Optical magnetometry. *Nature Phys.* **3**, 227 (2007).
- [50] Maze, J. R., Stanwix, P. L., Hodges, J. S., Hong, S., Taylor, J. M., Cappellaro, P., Jiang, L., Dutt, M. V. G., Togan, E., Zibrov, A., Yacoby, A., Walsworth, R. L., and Lukin, M. D. Nanoscale magnetic sensing with an individual electronic spin in diamond. *Nature (London)* **455**, 644 (2008).
- [51] Balasubramanian, G., Chan, I. Y., Kolesov, R., Al-Hmoud, M., Tisler, J., Shin, C., Kim, C., Wojcik, A., Hemmer, P. R., Krueger, A., Hanke, T., Leitenstorfer, A., Bratschitsch, R., Jelezko, F., and Wrachtrup, J. Nanoscale imaging magnetometry with diamond spins under ambient conditions. *Nature (London)* **455**, 648 (2008).
- [52] Maurer, P., Maze, J., Stanwix, P., Jiang, L., Gorshkov, A., Harke, B., Hodges, J., Zibrov, A., Twitchen, D., Hell, S., Walsworth, R., and Lukin, M. Far-field optical imaging and manipulation of individual spins with nanoscale resolution. (*in preparation*) (2009).
- [53] Mohapatra, A. K., Bason, M. G., Butscher, B., Weatherill, K. J., and Adams, C. S. A giant electro-optic effect using polarizable dark states. *Nature Phys.* **4**, 890 (2008).
- [54] Hell, S. W. Far-field optical nanoscopy. *Science* **316**, 1153 (2007).
- [55] Lloyd, S. Enhanced sensitivity of photodetection via quantum illumination. *Science* **321**, 1463 (2008).
- [56] Krems, R. V. Cold controlled chemistry. *Phys. Chem. Chem. Phys.* **10**, 4079 (2008).
- [57] Fortson, N., Sandars, P., and Barr, S. The search for a permanent electric dipole moment. *Phys. Today* **56**, 33 (2003).
- [58] Groblacher, S., Paterek, T., Kaltenbaek, R., Brukner, C., Zukowski, M., Aspelmeyer, M., and Zeilinger, A. An experimental test of non-local realism. *Nature (London)* **446**, 871 (2007).
- [59] Rey, A. M., Gorshkov, A. V., and Rubbo, C. Many-body treatment of the collisional frequency shift in fermionic atoms. *Phys. Rev. Lett.* **103**, 260402 (2009).
- [60] Hammerer, K., Sorensen, A. S., and Polzik, E. S. Quantum interface between light and atomic ensembles. *arXiv:0807.3358v4 [quant-ph]* (2008).

- [61] Duan, L. M., Lukin, M. D., Cirac, J. I., and Zoller, P. Long-distance quantum communication with atomic ensembles and linear optics. *Nature (London)* **414**, 413 (2001).
- [62] Novikova, I., Gorshkov, A. V., Phillips, D. F., Xiao, Y., Klein, M., and Walsworth, R. L. Optimization of slow and stored light in atomic vapor. *Proc. SPIE* **6482**, 64820M (2007).
- [63] Klein, M., Xiao, Y., Gorshkov, A. V., Hohensee, M., Leung, C. D., Browning, M. R., Phillips, D. F., Novikova, I., and Walsworth, R. L. Optimizing slow and stored light for multidisciplinary applications. *Proc. SPIE* **6904**, 69040C (2008).
- [64] Phillips, N. B., Gorshkov, A. V., and Novikova, I. Slow light propagation and amplification via electromagnetically induced transparency and four-wave mixing in an optically dense atomic vapor. *J. Mod. Opt.* **56**, 1916 (2009).
- [65] Walther, P., Eisaman, M. D., Nemiroski, A., Gorshkov, A. V., Zibrov, A. S., Zeilinger, A., and Lukin, M. D. Multi-photon entanglement: From quantum curiosity to quantum computing and quantum repeaters. *Proc. SPIE* **6664**, 66640G (2007).
- [66] Hong, T., Gorshkov, A. V., Patterson, D., Zibrov, A. S., Doyle, J. M., Lukin, M. D., and Prentiss, M. G. Realization of coherent optically dense media via buffer-gas cooling. *Phys. Rev. A* **79**, 013806 (2009).
- [67] Brask, J. B., Jiang, L., Gorshkov, A. V., Vuletic, V., Sorensen, A. S., and Lukin, M. D. Fast entanglement distribution with atomic ensembles and fluorescent detection. *arXiv:0907.3839v1 [quant-ph]* (2009).
- [68] Lütkenhaus, N. Security against individual attacks for realistic quantum key distribution. *Phys. Rev. A* **61**, 052304 (2000).
- [69] Brassard, G., Lütkenhaus, N., Mor, T., and Sanders, B. C. Limitations on practical quantum cryptography. *Phys. Rev. Lett.* **85**(6), 1330 (2000).
- [70] Jiang, L., Brennen, G. K., Gorshkov, A. V., Hammerer, K., Hafezi, M., Demler, E., Lukin, M. D., and Zoller, P. Anyonic interferometry and protected memories in atomic spin lattices. *Nature Phys.* **4**, 482 (2008).
- [71] Nayak, C., Simon, S. H., Stern, A., Freedman, M., and Sarma, S. D. Non-abelian anyons and topological quantum computation. *Rev. Mod. Phys.* **80**, 1083 (2008).
- [72] Carr, L. D., DeMille, D., Kreams, R. V., and Ye, J. Cold and ultracold molecules: science, technology and applications. *New J. Phys.* **11**, 055049 (2009).

- [73] Krems, R. V., Stwalley, W. C., and Friedrich, B. *Cold Molecules: Theory, Experiment, Applications*. CRC Press, New York, (2009).
- [74] McKeever, J., Boca, A., Boozer, A. D., Miller, R., Buck, J. R., Kuzmich, A., and Kimble, H. J. Deterministic generation of single photons from one atom trapped in a cavity. *Science* **303**, 1992 (2004).
- [75] Kuhn, A., Hennrich, M., and Rempe, G. Deterministic single-photon source for distributed quantum networking. *Phys. Rev. Lett.* **89**, 067901 (2002).
- [76] Lukin, M. D. Colloquium: Trapping and manipulating photon states in atomic ensembles. *Rev. Mod. Phys.* **75**, 457 (2003).
- [77] Liu, C., Dutton, Z., Behroozi, C. H., and Hau, L. V. Observation of coherent optical information storage in an atomic medium using halted light pulses. *Nature (London)* **409**, 490 (2001).
- [78] Phillips, D. F., Fleischhauer, A., Mair, A., Walsworth, R. L., and Lukin, M. D. Storage of light in atomic vapor. *Phys. Rev. Lett.* **86**, 783 (2001).
- [79] Julsgaard, B., Sherson, J., Cirac, J. I., Fiurášek, J., and Polzik, E. S. Experimental demonstration of quantum memory for light. *Nature (London)* **432**, 482 (2004).
- [80] Eisaman, M. D., André, A., Massou, F., Fleischhauer, M., Zibrov, A. S., and Lukin, M. D. Electromagnetically induced transparency with tunable single-photon pulses. *Nature (London)* **438**, 837 (2005).
- [81] Chanelière, T., Matsukevich, D. N., Jenkins, S. D., Lan, S. Y., Kennedy, T. A. B., and Kuzmich, A. Storage and retrieval of single photons transmitted between remote quantum memories. *Nature (London)* **438**, 833 (2005).
- [82] Hemmer, P. R., Turukhin, A. V., Shahriar, M. S., and Musser, J. A. Raman-excited spin coherences in nitrogen-vacancy color centers in diamond. *Opt. Lett.* **26**, 361 (2001).
- [83] Longdell, J. J., Fraval, E., Sellars, M. J., and Manson, N. B. Stopped light with storage times greater than one second using electromagnetically induced transparency in a solid. *Phys. Rev. Lett.* **95**, 063601 (2005).
- [84] Kozhekin, A. E., Mølmer, K., and Polzik, E. Quantum memory for light. *Phys. Rev. A* **62**, 033809 (2000).
- [85] Nunn, J., Walmsley, I. A., Raymer, M. G., Surmacz, K., Waldermann, F. C., Wang, Z., and Jaksch, D. Mapping broadband single-photon wave packets into an atomic memory. *Phys. Rev. A* **75**, 011401(R) (2007).

- [86] Moiseev, S. A. and Kröll, S. Complete reconstruction of the quantum state of a single-photon wave packet absorbed by a Doppler-broadened transition. *Phys. Rev. Lett.* **87**, 173601 (2001).
- [87] Kraus, B., Tittel, W., Gisin, N., Nilsson, M., Kröll, S., and Cirac, J. I. Quantum memory for nonstationary light fields based on controlled reversible inhomogeneous broadening. *Phys. Rev. A* **73**, 020302(R) (2006).
- [88] Pontryagin, L. S., Boltryanskii, V. G., Gamkrelidze, R. V., and Mishchenko, E. F. *The Mathematical Theory of Optimal Processes*. John Wiley & Sons, Inc., New York, (1962).
- [89] Bryson Jr., A. and Ho, Y. C. *Applied Optimal Control*. Hemisphere, Washington, DC, (1975).
- [90] Krotov, V. F. *Global Methods in Optimal Control Theory*. Marcel Dekker, New York, (1995).
- [91] Yanik, M. F., Suh, W., Wang, Z., and Fan, S. Stopping light in a waveguide with an all-optical analog of electromagnetically induced transparency. *Phys. Rev. Lett.* **93**, 233903 (2004).
- [92] Choi, K. S., Deng, H., Laurat, J., and Kimble, H. J. Mapping photonic entanglement into and out of a quantum memory. *Nature (London)* **452**, 67 (2008).
- [93] Simon, J., Tanji, H., Thompson, J. K., and Vuletić, V. Interfacing collective atomic excitations and single photons. *Phys. Rev. Lett.* **98**, 183601 (2007).
- [94] Alexander, A. L., Longdell, J. J., Sellars, M. J., and Manson, N. B. Photon echoes produced by switching electric fields. *Phys. Rev. Lett.* **96**, 043602 (2006).
- [95] Staudt, M. U., Hastings-Simon, S. R., Nilsson, M., Afzelius, M., Scarani, V., Ricken, R., Suche, H., Sohler, W., Tittel, W., and Gisin, N. Fidelity of an optical memory based on stimulated photon echoes. *Phys. Rev. Lett.* **98**, 113601 (2007).
- [96] Rotondaro, M. D. and Perram, G. P. Collisional broadening and shift of the rubidium D₁ and D₂ lines ($5^2S_{1/2} \rightarrow 5^2P_{1/2}, 5^2P_{3/2}$) by rare gases, H₂, D₂, N₂, CH₄ and CF₄. *J. Quant. Spectrosc. Radiat. Transf.* **57**, 497 (1997).
- [97] Novikova, I., Klein, M., Phillips, D. F., and Walsworth, R. L. Optimizing stored light efficiency in vapor cells. *Proc. SPIE* **5735**, 87 (2005).
- [98] Xiao, Y., Novikova, I., Phillips, D. F., and Walsworth, R. L. Diffusion-induced Ramsey narrowing. *Phys. Rev. Lett.* **96**, 043601 (2006).

-
- [99] Neergaard-Nielsen, J. S., Nielsen, B. M., Takahashi, H., Vistnes, A. I., and Polzik, E. S. High purity bright single photon source. *Opt. Express* **15**, 7940 (2007).
- [100] Eisaman, M. D., Childress, L., Andre, A., Massou, F., Zibrov, A. S., and Lukin, M. D. Shaping quantum pulses of light via coherent atomic memory. *Phys. Rev. Lett.* **93**, 233602 (2004).
- [101] Patnaik, A. K., Kien, F. L., and Hakuta, K. Manipulating the retrieval of stored light pulses. *Phys. Rev. A* **69**, 035803 (2004).
- [102] Du, S., Kolchin, P., Belthangady, C., Yin, G. Y., and Harris, S. E. Subnatural linewidth biphotons with controllable temporal length. *Phys. Rev. Lett.* **100**, 183603 (2008).
- [103] Kolchin, P., Belthangady, C., Du, S., Yin, G. Y., and Harris, S. E. Electro-optic modulation of single photons. *Phys. Rev. Lett.* **101**, 103601 (2008).
- [104] Brendel, J., Gisin, N., Tittel, W., and Zbinden, H. Pulsed energy-time entangled twin-photon source for quantum communication. *Phys. Rev. Lett.* **82**, 2594 (1999).
- [105] Hong, C. K., Ou, Z. Y., and Mandel, L. Measurement of subpicosecond time intervals between two photons by interference. *Phys. Rev. Lett.* **59**, 2044 (1987).
- [106] Sangouard, N., Simon, C., Zhao, B., Chen, Y.-A., de Riedmatten, H., Pan, J.-W., and Gisin, N. Robust and efficient quantum repeaters with atomic ensembles and linear optics. *Phys. Rev. A* **77**, 062301 (2008).
- [107] Tucker, R. S., Ku, P.-C., and Chang-Hasnain, C. J. Slow-light optical buffers: capabilities and fundamental limitations. *J. Lightwave Technol.* **23**, 4046 (2005).
- [108] Gibbs, H. M. *Optical Bistability: Controlling Light with Light*. Academic Press, Orlando, (1985).
- [109] Boyd, R. W. *Nonlinear Optics*. Academic Press, New York, (2007).
- [110] Deutsch, I. H., Chiao, R. Y., and Garrison, J. C. Diphotons in a nonlinear fabry-perot resonator: Bound states of interacting photons in an optical “quantum wire”. *Phys. Rev. Lett.* **69**, 3627 (1992).
- [111] Schmidt, H. and Imamoglu, A. Giant Kerr nonlinearities obtained by electromagnetically induced transparency. *Opt. Lett.* **21**, 1936 (1996).
- [112] Harris, S. E. and Yamamoto, Y. Photon switching by quantum interference. *Phys. Rev. Lett.* **81**, 3611 (1998).

-
- [113] Harris, S. E. and Hau, L. V. Nonlinear optics at low light levels. *Phys. Rev. Lett.* **82**, 4611 (1999).
- [114] Lukin, M. D. and Imamoglu, A. Nonlinear optics and quantum entanglement of ultraslow single photons. *Phys. Rev. Lett.* **84**, 1419 (2000).
- [115] Mašalas, M. and Fleischhauer, M. Scattering of dark-state polaritons in optical lattices and quantum phase gate for photons. *Phys. Rev. A* **69**, 061801(R) (2004).
- [116] Franson, J. D., Jacobs, B. C., and Pittman, T. B. Quantum computing using single photons and the zeno effect. *Phys. Rev. A* **70**, 062302 (2004).
- [117] André, A., Bajcsy, M., Zibrov, A. S., and Lukin, M. D. Nonlinear optics with stationary pulses of light. *Phys. Rev. Lett.* **94**, 063902 (2005).
- [118] Muschik, C. A., de Vega, I., Porras, D., and Cirac, J. I. Quantum processing photonic states in optical lattices. *Phys. Rev. Lett.* **100**, 063601 (2008).
- [119] Faraon, A., Fushman, I., Englund, D., Stoltz, N., Petroff, P., and Vučković, J. Coherent generation of non-classical light on a chip via photon-induced tunnelling and blockade. *Nature Phys.* **4**, 859 (2008).
- [120] Weber, B., Specht, H. P., Müller, T., Bochmann, J., Mücke, M., Moehring, D. L., and Rempe, G. Photon-photon entanglement with a single trapped atom. *Phys. Rev. Lett.* **102**, 030501 (2009).
- [121] Aoki, T., Parkins, A. S., Alton, D. J., Regal, C. A., Dayan, B., Ostby, E., Vahala, K. J., and Kimble, H. J. Efficient routing of single photons by one atom and a microtoroidal cavity. *Phys. Rev. Lett.* **102**, 083601 (2009).
- [122] Hafezi, M., Chang, D., Gritsev, V., Demler, E., and Lukin, M. Quantum transport of strongly interacting photons in a one-dimensional nonlinear waveguide. *arXiv:0911.4766v1 [quant-ph]* (2009).
- [123] Christensen, C. A., Will, S., Saba, M., Jo, G.-B., Shin, Y.-I., Ketterle, W., and Pritchard, D. Trapping of ultracold atoms in a hollow-core photonic crystal fiber. *Phys. Rev. A* **78**, 033429 (2008).
- [124] Bajcsy, M., Hofferberth, S., Balic, V., Peyronel, T., Hafezi, M., Zibrov, A. S., Vuletic, V., and Lukin, M. D. Efficient all-optical switching using slow light within a hollow fiber. *Phys. Rev. Lett.* **102**, 203902 (2009).
- [125] Vetsch, E., Reitz, D., Sague, G., Schmidt, R., Dawkins, S. T., and Rauschenbeutel, A. Optical interface created by laser-cooled atoms trapped in the evanescent field surrounding an optical nanofiber. *arXiv:0912.1179v1 [quant-ph]* (2009).

-
- [126] Duan, L.-M., Demler, E., and Lukin, M. D. Controlling spin exchange interactions of ultracold atoms in optical lattices. *Phys. Rev. Lett.* **91**, 090402 (2003).
- [127] Dutton, Z. and Hau, L. V. Storing and processing optical information with ultraslow light in bose-einstein condensates. *Phys. Rev. A* **70**, 053831 (2004).
- [128] Giamarchi, T. *Quantum Physics in One Dimension*. Clarendon Press, Oxford, (2003).
- [129] Girardeau, M. Relationship between systems of impenetrable bosons and fermions in one dimension. *J. Math. Phys. (N.Y.)* **1**, 516 (1960).
- [130] Terhal, B. M. and DiVincenzo, D. P. Classical simulation of noninteracting-fermion quantum circuits. *Phys. Rev. A* **65**, 032325 (2002).
- [131] Mandel, O., Greiner, M., Widera, A., Rom, T., Hänsch, T. W., and Bloch, I. Controlled collisions for multi-particle entanglement of optically trapped atoms. *Nature (London)* **425**, 937 (2003).
- [132] Petrosyan, D. Tunable photonic band gaps with coherently driven atoms in optical lattices. *Phys. Rev. A* **76**, 053823 (2007).
- [133] Schnorrberger, U., Thompson, J. D., Trotzky, S., Pugatch, R., Davidson, N., Kuhr, S., and Bloch, I. Electromagnetically induced transparency and light storage in an atomic mott insulator. *Phys. Rev. Lett.* **103**, 033003 (2009).
- [134] Osborne, T. J. and Linden, N. Propagation of quantum information through a spin system. *Phys. Rev. A* **69**, 052315 (2004).
- [135] Greiner, M., Mandel, O., Esslinger, T., Hänsch, T. W., and Bloch, I. Quantum phase transition from a superfluid to a Mott insulator in a gas of ultracold atoms. *Nature (London)* **415**, 39 (2002).
- [136] Fukuhara, T., Sugawa, S., Sugimoto, M., Taie, S., and Takahashi, Y. Mott insulator of ultracold alkaline-earth-metal-like atoms. *Phys. Rev. A* **79**, 041604(R) (2009).
- [137] Zhang, R., Garner, S. R., and Hau, L. V. Creation of long-term coherent optical memory via controlled nonlinear interactions in bose-einstein condensates. *Phys. Rev. Lett.* **103**, 233602 (2009).
- [138] Tiesinga, E., Verhaar, B. J., and Stoof, H. T. C. Threshold and resonance phenomena in ultracold ground-state collisions. *Phys. Rev. A* **47**, 4114 (1993).
- [139] Ciuryło, R., Tiesinga, E., and Julienne, P. S. Optical tuning of the scattering length of cold alkaline-earth-metal atoms. *Phys. Rev. A* **71**, 030701(R) (2005).

-
- [140] Herskind, P. F. et al. Realization of collective strong coupling with ion coulomb crystals in an optical cavity. *Nature Phys.* **5**, 494 (2009).
- [141] Chang, D. E., Sørensen, A. S., Hemmer, P. R., and Lukin, M. D. Quantum optics with surface plasmons. *Phys. Rev. Lett.* **97**, 053002 (2006).
- [142] Balasubramanian, G., Neumann, P., Twitchen, D., Markham, M., Kolesov, R., Mizuochi, N., Isoya, J., Achard, J., Beck, J., Tissler, J., Jacques, V., Hemmer, P. R., Jelezko, F., and Wrachtrup, J. Ultralong spin coherence time in isotopically engineered diamond. *Nature Mater.* **8**, 383 (2009).
- [143] Dutt, M. V. G., Childress, L., Jiang, L., Togan, E., Maze, J., Jelezko, F., Zibrov, A. S., Hemmer, P. R., and Lukin, M. D. Quantum register based on individual electronic and nuclear spin qubits in diamond. *Science* **316**, 1312 (2007).
- [144] Bloch, I. Ultracold quantum gases in optical lattices. *Nature Phys.* **1**, 23 (2005).
- [145] Jaksch, D. Optical lattices, ultracold atoms and quantum information processing. *Contemp. Phys.* **45**, 367 (2004).
- [146] Wineland, D. J., Monroe, C., Itano, W. M., Leibfried, D., King, B. E., and Meekhof, D. M. Experimental issues in coherent quantum-state manipulation of trapped atomic ions. *J. Res. Natl. Inst. Stand. Technol.* **103**, 259 (1998).
- [147] Haffner, H., Hansel, W., Roos, C. F., Benhelm, J., Chek-al kar, D., Chwalla, M., Korber, T., Rapol, U. D., Riebe, M., Schmidt, P. O., Becher, C., Guhne, O., Dur, W., and Blatt, R. Scalable multiparticle entanglement of trapped ions. *Nature (London)* **438**, 643 (2005).
- [148] Atature, M., Dreiser, J., Badolato, A., Hogege, A., Karrai, K., and Imamoglu, A. Quantum-dot spin-state preparation with near-unity fidelity. *Science* **312**, 551 (2006).
- [149] Kroutvar, M., Ducommun, Y., Heiss, D., Bichler, M., Schuh, D., Abstreiter, G., and Finley, J. J. Optically programmable electron spin memory using semiconductor quantum dots. *Nature (London)* **432**, 81 (2004).
- [150] Heidemeyer, H., Denker, U., Muller, C., and Schmidt, O. G. Morphology response to strain field interferences in stacks of highly ordered quantum dot arrays. *Phys. Rev. Lett.* **91**, 196103 (2003).
- [151] Born, M. and Wolf, E. *Principles of Optics*. Cambridge University Press, Cambridge, England, (1999).
- [152] Scully, M. O. and Zubairy, M. S. *Quantum Optics*. Cambridge University Press, Cambridge, England, (1997).

- [153] Meijer, J., Vogel, T., Burchard, B., Rangelow, I. W., Bischoff, L., Wrachtrup, J., Domhan, M., Jelezko, F., Schnitzler, W., Schulz, S. A., Singer, K., and Schmidt-Kaler, F. Concept of deterministic single ion doping with sub-nm spatial resolution. *Appl. Phys. A* **83**, 321 (2006).
- [154] Lukin, M. D. and Hemmer, P. R. Quantum entanglement via optical control of atom-atom interactions. *Phys. Rev. Lett.* **84**, 2818 (2000).
- [155] Johnson, K. S., Thywissen, J. H., Dekker, N. H., Berggren, K. K., Chu, A. P., Younkin, R., and Prentiss, M. Localization of metastable atom beams with optical standing waves: Nanolithography at the Heisenberg limit. *Science* **280**, 1583 (1998).
- [156] Bajcsy, M., Zibrov, A. S., and Lukin, M. D. Stationary pulses of light in an atomic medium. *Nature (London)* **426**, 638 (2003).
- [157] Sahrai, M., Tajalli, H., Kapale, K. T., and Zubairy, M. S. Subwavelength atom localization via amplitude and phase control of the absorption spectrum. *Phys. Rev. A* **72**, 013820 (2005).
- [158] Agarwal, G. S. and Kapale, K. T. Subwavelength atom localization via coherent population trapping. *J. Phys. B* **39**, 3437 (2006).
- [159] Saffman, M. Addressing atoms in optical lattices with Bessel beams. *Opt. Lett.* **29**, 1016 (2004).
- [160] Bergamini, S., Darquie, B., Jones, M., Jacobowicz, L., Browaeys, A., and Grangier, P. Holographic generation of microtrap arrays for single atoms by use of a programmable phase modulator. *J. Opt. Soc. Am. B* **21**, 1889 (2004).
- [161] Miroshnychenko, Y., Alt, W., Dotsenko, I., Forster, L., Khudaverdyan, M., Meschede, D., Schrader, D., and Rauschenbeutel, A. Quantum engineering: An atom-sorting machine. *Nature (London)* **442**, 151 (2006).
- [162] Thomas, J. E. Uncertainty-limited position measurement of moving atoms using optical-fields. *Opt. Lett.* **14**, 1186 (1989).
- [163] Stokes, K. D., Schnurr, C., Gardner, J. R., Marable, M., Welch, G. R., and Thomas, J. E. Precision position measurement of moving atoms using optical fields. *Phys. Rev. Lett.* **67**, 1997 (1991).
- [164] Schrader, D., Dotsenko, I., Khudaverdyan, M., Miroshnychenko, Y., Rauschenbeutel, A., and Meschede, D. Neutral atom quantum register. *Phys. Rev. Lett.* **93**, 150501 (2004).

-
- [165] Gardner, J. R., Marable, M. L., Welch, G. R., and Thomas, J. E. Suboptical wavelength position measurement of moving atoms using optical-fields. *Phys. Rev. Lett.* **70**, 3404 (1993).
- [166] Zhang, C., Rolston, S. L., and Sarma, S. D. Manipulation of single neutral atoms in optical lattices. *Phys. Rev. A* **74**, 042316 (2006).
- [167] Lee, P. J., Anderlini, M., Brown, B. L., Sebby-Strabley, J., Phillips, W. D., and Porto, J. V. Sublattice addressing and spin-dependent motion of atoms in a double-well lattice. *Phys. Rev. Lett.* **99**, 020402 (2007).
- [168] Fleischhauer, M. and Manka, A. S. Propagation of laser pulses and coherent population transfer in dissipative three-level systems: An adiabatic dressed-state picture. *Phys. Rev. A* **54**, 794 (1996).
- [169] Guo, J. and Cooper, J. Cooling and resonance fluorescence of two atoms in a one-dimensional optical molasses. *Phys. Rev. A* **51**, 3128 (1995).
- [170] Curtis, J. E., Koss, B. A., and Grier, D. G. Dynamic holographic optical tweezers. *Opt. Comm.* **207**, 169 (2002).
- [171] Nye, J. F. *Natural Focusing and Fine Structure of Light*. Institute of Physics Publishing, Bristol, (1999).
- [172] McDonnell, M. J., Stacey, D. N., and Steane, A. M. Laser linewidth effects in quantum state discrimination by electromagnetically induced transparency. *Phys. Rev. A* **70**, 053802 (2004).
- [173] Duan, L. M., Cirac, J. I., and Zoller, P. Geometric manipulation of trapped ions for quantum computation. *Science* **292**, 1695 (2001).
- [174] Yi, W., Daley, A. J., Pupillo, G., and Zoller, P. State-dependent, addressable subwavelength lattices with cold atoms. *New J. Phys.* **10**, 073015 (2008).
- [175] Cho, J. Addressing individual atoms in optical lattices with standing-wave driving fields. *Phys. Rev. Lett.* **99**, 020502 (2007).
- [176] Yavuz, D. D. and Proite, N. A. Nanoscale resolution fluorescence microscopy using electromagnetically induced transparency. *Phys. Rev. A* **76**, 041802 (2007).
- [177] Juzeliunas, G., Ruseckas, J., Ohberg, P., and Fleischhauer, M. Formation of solitons in atomic Bose-Einstein condensates by dark-state adiabatic passage. *Lithuanian J. Phys.* **47**, 351 (2007).
- [178] Dür, W. and Briegel, H. J. Entanglement purification for quantum computation. *Phys. Rev. Lett.* **90**, 067901 (2003).

- [179] Sørensen, A. S. and Mølmer, K. Measurement induced entanglement and quantum computation with atoms in optical cavities. *Phys. Rev. Lett.* **91**, 097905 (2003).
- [180] Moehring, D. L., Madsen, M. J., Younge, K. C., Kohn, Jr., R. N., Maunz, P., Duan, L. M., Monroe, C., and Blinov, B. B. Quantum networking with photons and trapped atoms (invited). *J. Opt. Soc. Am. B* **24**, 300 (2007).
- [181] Saffman, M. and Mølmer, K. Scaling the neutral-atom Rydberg gate quantum computer by collective encoding in holmium atoms. *Phys. Rev. A* **78**, 012336 (2008).
- [182] Childress, L., Taylor, J. M., Sørensen, A. S., and Lukin, M. D. Fault-tolerant quantum repeaters with minimal physical resources and implementations based on single-photon emitters. *Phys. Rev. A* **72**, 052330 (2005).
- [183] Jiang, L., Taylor, J. M., Sørensen, A. S., and Lukin, M. D. Distributed quantum computation based on small quantum registers. *Phys. Rev. A* **76**, 062323 (2007).
- [184] Jiang, L., Taylor, J. M., Sørensen, A. S., and Lukin, M. D. Scalable quantum networks based on few-qubit registers. *arXiv:quant-ph/0703029* (2007).
- [185] Neumann, P., Mizuochi, N., Rempp, F., Hemmer, P., Watanabe, H., Yamasaki, S., Jacques, V., Gaebel, T., Jelezko, F., and Wrachtrup, J. Multipartite entanglement among single spins in diamond. *Science* **320**, 1326 (2008).
- [186] Jiang, L., Dutt, M. V. G., Togan, E., Childress, L., Cappellaro, P., Taylor, J. M., and Lukin, M. D. Coherence of an optically illuminated single nuclear spin qubit. *Phys. Rev. Lett.* **100**, 073001 (2008).
- [187] Chaudhury, S., Merkel, S., Herr, T., Silberfarb, A., Deutsch, I. H., and Jessen, P. S. Quantum control of the hyperfine spin of a Cs atom ensemble. *Phys. Rev. Lett.* **99**, 163002 (2007).
- [188] Ahn, J., Weinacht, T. C., and Bucksbaum, P. H. Information storage and retrieval through quantum phase. *Science* **287**, 463 (2000).
- [189] Reichenbach, I. and Deutsch, I. H. Sideband cooling while preserving coherences in the nuclear spin state in group-II-like atoms. *Phys. Rev. Lett.* **99**, 123001 (2007).
- [190] Hayes, D., Julienne, P. S., and Deutsch, I. H. Quantum logic via the exchange blockade in ultracold collisions. *Phys. Rev. Lett.* **98**, 070501 (2007).
- [191] Daley, A. J., Boyd, M. M., Ye, J., and Zoller, P. Quantum computing with alkaline-earth-metal atoms. *Phys. Rev. Lett.* **101**, 170504 (2008).

- [192] Stock, R., Babcock, N. S., Raizen, M. G., and Sanders, B. C. Entanglement of group-II-like atoms with fast measurement for quantum information processing. *Phys. Rev. A* **78**, 022301 (2008).
- [193] Fölling, S., Trotzky, S., Cheinet, P., Feld, M., Saers, R., Widera, A., Müller, T., and Bloch, I. Direct observation of second-order atom tunnelling. *Nature (London)* **448**, 1029 (2007).
- [194] Cheinet, P., Trotzky, S., Feld, M., Schnorrberger, U., Moreno-Cardoner, M., Fölling, S., and Bloch, I. Counting atoms using interaction blockade in an optical superlattice. *Phys. Rev. Lett.* **101**, 090404 (2008).
- [195] Boyd, M. M., Zelevinsky, T., Ludlow, A. D., Blatt, S., Zanon-Willette, T., Foreman, S. M., and Ye, J. Nuclear spin effects in optical lattice clocks. *Phys. Rev. A* **76**, 022510 (2007).
- [196] Ludlow, A. D., Zelevinsky, T., Campbell, G. K., Blatt, S., Boyd, M. M., de Miranda, M. H. G., Martin, M. J., Thomsen, J. W., Foreman, S. M., Ye, J., Fortier, T. M., Stalnaker, J. E., Diddams, S. A., Le Coq, Y., Barber, Z. W., Poli, N., Lemke, N. D., Beck, K. M., and Oates, C. W. Sr lattice clock at 1×10^{-16} fractional uncertainty by remote optical evaluation with a Ca clock. *Science* **319**, 1805 (2008).
- [197] Brennen, G. K., O’Leary, D. P., and Bullock, S. S. Criteria for exact qudit universality. *Phys. Rev. A* **71**, 052318 (2005).
- [198] Peil, S., Porto, J. V., Tolra, B. L., Obrecht, J. M., King, B. E., Subbotin, M., Rolston, S. L., and Phillips, W. D. Patterned loading of a Bose-Einstein condensate into an optical lattice. *Phys. Rev. A* **67**, 051603(R) (2003).
- [199] Sebby-Strabley, J., Anderlini, M., Jessen, P. S., and Porto, J. V. Lattice of double wells for manipulating pairs of cold atoms. *Phys. Rev. A* **73**, 033605 (2006).
- [200] Roth, L. M. Simple narrow-band model of ferromagnetism due to intra-atomic exchange. *Phys. Rev.* **149**, 306 (1966).
- [201] Ho, T.-L. Spinor Bose condensates in optical traps. *Phys. Rev. Lett.* **81**, 742 (1998).
- [202] Boyd, M. M., Ludlow, A. D., Blatt, S., Foreman, S. M., Ido, T., Zelevinsky, T., and Ye, J. ^{87}Sr lattice clock with inaccuracy below 10^{-15} . *Phys. Rev. Lett.* **98**, 083002 (2007).

- [203] Strauch, F. W., Edwards, M., Tiesinga, E., Williams, C., and Clark, C. W. Tunneling phase gate for neutral atoms in a double-well lattice. *Phys. Rev. A* **77**, 050304 (2008).
- [204] Trotzky, S., Cheinet, P., Fölling, S., Feld, M., Schnorrberger, U., Rey, A. M., Polkovnikov, A., Demler, E. A., Lukin, M. D., and Bloch, I. Time-resolved observation and control of superexchange interactions with ultracold atoms in optical lattices. *Science* **319**, 295 (2008).
- [205] Lellouch, L. P. and Hunter, L. R. Measurement of the $4s4p^1P - 4s3d^1D$ spontaneous emission rate in calcium by use of a Stark-electric-quadrupole interference. *Phys. Rev. A* **36**, 3490 (1987).
- [206] Loftus, T., Bochinski, J. R., and Mossberg, T. W. Magnetic trapping of ytterbium and the alkaline-earth metals. *Phys. Rev. A* **66**, 013411 (2002).
- [207] Xu, X., Loftus, T. H., Hall, J. L., Gallagher, A., and Ye, J. Cooling and trapping of atomic strontium. *J. Opt. Soc. Am. B* **20**, 968 (2003).
- [208] Hoyt, C. W., Barber, Z. W., Oates, C. W., Fortier, T. M., Diddams, S. A., and Hollberg, L. Observation and absolute frequency measurements of the $^1S_0 - ^3P_0$ optical clock transition in neutral ytterbium. *Phys. Rev. Lett.* **95**, 083003 (2005).
- [209] Nörtershäuser, W., Trautmann, N., Wendt, K., and Bushaw, B. A. Isotope shifts and hyperfine structure in the $4s^2\ ^1S_0 \rightarrow 4s4p\ ^1P_1 \rightarrow 4s4d\ ^1D_2$ transitions of stable calcium isotopes and calcium-41. *Spectrochim. Acta, Part B* **53**, 709 (1998).
- [210] Nielsen, M. A. A simple formula for the average gate fidelity of a quantum dynamical operation. *Phys. Lett. A* **303**, 249 (2002).
- [211] Bai, Y. S. and Mossberg, T. W. Lifetime and oscillator-strength studies involving the $(6s6p)^3P_1 - (6s7s)^1S_0$ transition of atomic Yb. *Phys. Rev. A* **35**, 619 (1987).
- [212] Aschauer, H., Dür, W., and Briegel, H. J. Multiparticle entanglement purification for two-colorable graph states. *Phys. Rev. A* **71**, 012319 (2005).
- [213] Raussendorf, R. and Briegel, H. J. A one-way quantum computer. *Phys. Rev. Lett.* **86**, 5188 (2001).
- [214] Leibfried, D., Barrett, M. D., Schaetz, T., Britton, J., Chiaverini, J., Itano, W. M., Jost, J. D., Langer, C., and Wineland, D. J. Toward Heisenberg-limited spectroscopy with multiparticle entangled states. *Science* **304**, 1476 (2004).

- [215] Campbell, G. K., Boyd, M. M., Thomsen, J. W., Martin, M. J., Blatt, S., Swallows, M. D., Nicholson, T. L., Fortier, T., Oates, C. W., Diddams, S. A., Lemke, N. D., Naidon, P., Julienne, P., Ye, J., and Ludlow, A. D. Probing interactions between ultracold fermions. *Science* **324**, 360 (2009).
- [216] Lemke, N. D., Ludlow, A. D., Barber, Z. W., Fortier, T. M., Diddams, S. A., Jiang, Y., Jefferts, S. R., Heavner, T. P., Parker, T. E., and Oates, C. W. Spin-1/2 optical lattice clock. *Phys. Rev. Lett.* **103**, 063001 (2009).
- [217] Fukuhara, T., Takasu, Y., Kumakura, M., and Takahashi, Y. Degenerate fermi gases of ytterbium. *Phys. Rev. Lett.* **98**, 030401 (2007).
- [218] Kugel, K. I. and Khomskii, D. I. Crystal structure and magnetic properties of substances with orbital degeneracy. *Sov. Phys.-JETP* **37**, 725 (1973).
- [219] Arovas, D. P. and Auerbach, A. Tetrahis(dimethylamino)ethylene- C_{60} : Multi-component superexchange and Mott ferromagnetism. *Phys. Rev. B* **52**, 10114 (1995).
- [220] Li, Y. Q., Ma, M., Shi, D. N., and Zhang, F. C. SU(4) theory for spin systems with orbital degeneracy. *Phys. Rev. Lett.* **81**, 3527 (1998).
- [221] Pati, S. K., Singh, R. R. P., and Khomskii, D. I. Alternating spin and orbital dimerization and spin-gap formation in coupled spin-orbital systems. *Phys. Rev. Lett.* **81**, 5406 (1998).
- [222] Tokura, Y. and Nagaosa, N. Orbital physics in transition-metal oxides. *Science* **288**, 462 (2000).
- [223] Ruderman, M. A. and Kittel, C. Indirect exchange coupling of nuclear magnetic moments by conduction electrons. *Phys. Rev.* **96**, 99 (1954).
- [224] Coqblin, B. and Schrieffer, J. R. Exchange interaction in alloys with cerium impurities. *Phys. Rev.* **185**, 847 (1969).
- [225] Doniach, S. The Kondo lattice and weak antiferromagnetism. *Physica B+C* **91**, 231 (1977).
- [226] Coleman, P. $1/N$ expansion for the Kondo lattice. *Phys. Rev. B* **28**, 5255 (1983).
- [227] Tsunetsugu, H., Sigrist, M., and Ueda, K. The ground-state phase diagram of the one-dimensional Kondo lattice model. *Rev. Mod. Phys.* **69**, 809 (1997).
- [228] Assaad, F. F. Quantum Monte Carlo simulations of the half-filled two-dimensional Kondo lattice model. *Phys. Rev. Lett.* **83**, 769 (1999).

-
- [229] Tokura, Y., editor. *Colossal Magnetoresistive Oxides*. Gordon and Breach, New York, (2000).
- [230] Oshikawa, M. Topological approach to Luttinger's theorem and the Fermi surface of a Kondo lattice. *Phys. Rev. Lett.* **84**, 3370 (2000).
- [231] Senthil, T., Sachdev, S., and Vojta, M. Fractionalized Fermi liquids. *Phys. Rev. Lett.* **90**, 216403 (2003).
- [232] Duan, L.-M. Controlling ultracold atoms in multi-band optical lattices for simulation of Kondo physics. *Europhys. Lett.* **67**, 721 (2004).
- [233] Paredes, B., Tejedor, C., and Cirac, J. I. Fermionic atoms in optical superlattices. *Phys. Rev. A* **71**, 063608 (2005).
- [234] Coleman, P. Heavy fermions: Electrons at the edge of magnetism. In *Handbook of Magnetism and Advanced Magnetic Materials*, Kronmüller, H. and Parkin, S., editors, volume 1, 95. John Wiley and Sons (2007).
- [235] Gegenwart, P., Si, Q., and Steglich, F. Quantum criticality in heavy-fermion metals. *Nature Phys.* **4**, 186 (2008).
- [236] Read, N. and Sachdev, S. Valence-bond and spin-Peierls ground states of low-dimensional quantum antiferromagnets. *Phys. Rev. Lett.* **62**, 1694 (1989).
- [237] Marston, J. B. and Affleck, I. Large- n limit of the Hubbard-Heisenberg model. *Phys. Rev. B* **39**, 11538 (1989).
- [238] Harada, K., Kawashima, N., and Troyer, M. Néel and spin-Peierls ground states of two-dimensional SU(N) quantum antiferromagnets. *Phys. Rev. Lett.* **90**, 117203 (2003).
- [239] Assaad, F. F. Phase diagram of the half-filled two-dimensional SU(N) Hubbard-Heisenberg model: A quantum Monte Carlo study. *Phys. Rev. B* **71**, 075103 (2005).
- [240] Paramekanti, A. and Marston, J. B. SU(N) quantum spin models: a variational wavefunction study. *J. Phys.: Condens. Matter* **19**, 125215 (2007).
- [241] Greiter, M. and Rachel, S. Valence bond solids for SU(n) spin chains: Exact models, spinon confinement, and the Haldane gap. *Phys. Rev. B* **75**, 184441 (2007).
- [242] Xu, C. and Wu, C. Resonating plaquette phases in SU(4) Heisenberg antiferromagnet. *Phys. Rev. B* **77**, 134449 (2008).

- [243] Hermele, M., Gurarie, V., and Rey, A. M. Mott insulators of ultracold fermionic alkaline earth atoms: Underconstrained magnetism and chiral spin liquid. *Phys. Rev. Lett.* **103**, 135301 (2009).
- [244] Wu, C., Hu, J.-p., and Zhang, S.-c. Exact SO(5) symmetry in the spin-3/2 fermionic system. *Phys. Rev. Lett.* **91**, 186402 (2003).
- [245] Honerkamp, C. and Hofstetter, W. Ultracold fermions and the SU(N) Hubbard model. *Phys. Rev. Lett.* **92**, 170403 (2004).
- [246] Rapp, A., Hofstetter, W., and Zarand, G. Trionic phase of ultracold fermions in an optical lattice: A variational study. *Phys. Rev. B* **77**, 144520 (2008).
- [247] Affleck, I., Arovas, D. P., Marston, J. B., and Rabson, D. A. SU(2n) quantum antiferromagnets with exact C-breaking ground states. *Nuclear Physics B* **366**, 467 (1991).
- [248] Enomoto, K., Kasa, K., Kitagawa, M., and Takahashi, Y. Optical Feshbach resonance using the intercombination transition. *Phys. Rev. Lett.* **101**, 203201 (2008).
- [249] Martinez de Escobar, Y. N., Mickelson, P. G., Pellegrini, P., Nagel, S. B., Traverso, A., Yan, M., Cote, R., and Killian, T. C. Two-photon photoassociative spectroscopy of ultracold ^{88}Sr . *Phys. Rev. A* **78**, 062708 (2008).
- [250] Traverso, A., Chakraborty, R., Martinez de Escobar, Y. N., Mickelson, P. G., Nagel, S. B., Yan, M., and Killian, T. C. Inelastic and elastic collision rates for triplet states of ultracold strontium. *Phys. Rev. A* **79**, 060702(R) (2009).
- [251] Zsinas, E., Sushkov, O. P., and Oitmaa, J. Phase diagram of the spin-orbital model on the square lattice. *Phys. Rev. B* **64**, 184431 (2001).
- [252] Li, P. and Shen, S.-Q. Spin and orbital valence bond solids in a one-dimensional spin-orbital system: Schwinger boson mean-field theory. *Phys. Rev. B* **72**, 214439 (2005).
- [253] Itoi, C., Qin, S., and Affleck, I. Phase diagram of a one-dimensional spin-orbital model. *Phys. Rev. B* **61**, 6747 (2000).
- [254] Zhang, G.-M. and Shen, S.-Q. Ordered valence-bond states in symmetric two-dimensional spin-orbital systems. *Phys. Rev. Lett.* **87**, 157201 (2001).
- [255] Altman, E., Demler, E., and Lukin, M. D. Probing many-body states of ultracold atoms via noise correlations. *Phys. Rev. A* **70**, 013603 (2004).

- [256] Hofstetter, W., Cirac, J. I., Zoller, P., Demler, E., and Lukin, M. D. High-temperature superfluidity of fermionic atoms in optical lattices. *Phys. Rev. Lett.* **89**, 220407 (2002).
- [257] Werner, F., Parcollet, O., Georges, A., and Hassan, S. R. Interaction-induced adiabatic cooling and antiferromagnetism of cold fermions in optical lattices. *Phys. Rev. Lett.* **95**, 056401 (2005).
- [258] Schneider, U., Hackermüller, L., Will, S., Best, T., Bloch, I., Costi, T. A., Helmes, R. W., Rasch, D., and Rosch, A. Metallic and insulating phases of repulsively interacting fermions in a 3D optical lattice. *Science* **322**, 1520 (2008).
- [259] Ni, K. K., Ospelkaus, S., de Miranda, M. H. G., Pe'er, A., Neyenhuis, B., Zirbel, J. J., Kotochigova, S., Julienne, P. S., Jin, D. S., and Ye, J. A high phase-space-density gas of polar molecules. *Science* **322**, 231 (2008).
- [260] Cazalilla, M. A., Ho, A. F., and Ueda, M. Ultracold gases of ytterbium: Ferromagnetism and Mott states in an SU(6) Fermi system. *arXiv:0905.4948v1 [cond-mat.quant-gas]* (2009).
- [261] Bohn, J. L., Avdeenkov, A. V., and Deskevich, M. P. Rotational Feshbach resonances in ultracold molecular collisions. *Phys. Rev. Lett.* **89**, 203202 (2002).
- [262] Gøral, K., Santos, L., and Lewenstein, M. Quantum phases of dipolar bosons in optical lattices. *Phys. Rev. Lett.* **88**, 170406 (2002).
- [263] Micheli, A., Brennen, G. K., and Zoller, P. A toolbox for lattice-spin models with polar molecules. *Nature Phys.* **2**, 341 (2006).
- [264] Rezayi, E. H., Read, N., and Cooper, N. R. Incompressible liquid state of rapidly rotating bosons at filling factor $3/2$. *Phys. Rev. Lett.* **95**, 160404 (2005).
- [265] Büchler, H. P., Micheli, A., and Zoller, P. Three-body interactions with cold polar molecules. *Nat. Phys.* **3**, 726 (2007).
- [266] Weinstein, J. D., deCarvalho, R., Guillet, T., Friedrich, B., and Doyle, J. M. Magnetic trapping of calcium monohydride molecules at millikelvin temperatures. *Nature (London)* **395**, 148 (1998).
- [267] Tarbutt, M. R., Bethlem, H. L., Hudson, J. J., Ryabov, V. L., Ryzhov, V. A., Sauer, B. E., Meijer, G., and Hinds, E. A. Slowing heavy, ground-state molecules using an alternating gradient decelerator. *Phys. Rev. Lett.* **92**, 173002 (2004).
- [268] Maxwell, S. E., Brahm, N., deCarvalho, R., Glenn, D. R., Helton, J. S., Nguyen, S. V., Patterson, D., Petricka, J., DeMille, D., and Doyle, J. M. High-flux beam source for cold, slow atoms or molecules. *Phys. Rev. Lett.* **95**, 173201 (2005).

- [269] van de Meerakker, S. Y. T., Smeets, P. H. M., Vanhaecke, N., Jongma, R. T., and Meijer, G. Deceleration and electrostatic trapping of OH radicals. *Phys. Rev. Lett.* **94**, 023004 (2005).
- [270] Campbell, W. C., Tsikata, E., Lu, H.-I., van Buuren, L. D., and Doyle, J. M. Magnetic trapping and zeeman relaxation of NH ($X^3\Sigma^-$). *Phys. Rev. Lett.* **98**, 213001 (2007).
- [271] Sawyer, B. C., Lev, B. L., Hudson, E. R., Stuhl, B. K., Lara, M., Bohn, J. L., and Ye, J. Magneto-electrostatic trapping of ground state OH molecules. *Phys. Rev. Lett.* **98**, 253002 (2007).
- [272] Bahns, J. T., Gould, P. L., and Stwalley, W. C. Formation of cold ($t \leq 1$ K) molecules. *Adv. At. Mol. Opt. Phys.* **42**, 171 (2000).
- [273] Dion, C. M., Drag, C., Dulieu, O., Laburthe Tolra, B., Masnou-Seeuws, F., and Pillet, P. Resonant coupling in the formation of ultracold ground state molecules via photoassociation. *Phys. Rev. Lett.* **86**, 2253 (2001).
- [274] Jones, K. M., Tiesinga, E., Lett, P. D., and Julienne, P. S. Ultracold photoassociation spectroscopy: Long-range molecules and atomic scattering. *Rev. Mod. Phys.* **78**, 483 (2006).
- [275] Kerman, A. J., Sage, J. M., Sainis, S., Bergeman, T., and DeMille, D. Production and state-selective detection of ultracold RbCs molecules. *Phys. Rev. Lett.* **92**, 153001 (2004).
- [276] Wang, D., Qi, J., Stone, M. F., Nikolayeva, O., Wang, H., Hattaway, B., Gensemer, S. D., Gould, P. L., Eyler, E. E., and Stwalley, W. C. Photoassociative production and trapping of ultracold KRb molecules. *Phys. Rev. Lett.* **93**, 243005 (2004).
- [277] Haimberger, C., Kleinert, J., Bhattacharya, M., and Bigelow, N. P. Formation and detection of ultracold ground-state polar molecules. *Phys. Rev. A* **70**, 021402(R) (2004).
- [278] Kraft, S. D., Staunum, P., Lange, J., Vogel, L., Wester, R., and Weidemüller, M. Formation of ultracold LiCs molecules. *J. Phys. B: At. Mol. Opt. Phys.* **39**, S993 (2006).
- [279] Avdeenkov, A. V., Kajita, M., and Bohn, J. L. Suppression of inelastic collisions of polar $^1\Sigma$ state molecules in an electrostatic field. *Phys. Rev. A* **73**, 022707 (2006).

- [280] Ronen, S., Bortolotti, D. C. E., Blume, D., and Bohn, J. L. Dipolar Bose-Einstein condensates with dipole-dependent scattering length. *Phys. Rev. A* **74**, 033611 (2006).
- [281] Krems, R. V. Molecules near absolute zero and external field control of atomic and molecular dynamics. *International Reviews in Physical Chemistry* **24**, 99 (2005).
- [282] Slichter, C. P. *Principles of Magnetic Resonance*. Springer, New York, (1996).
- [283] Weiner, J., Bagnato, V. S., Zilio, S., and Julienne, P. S. Experiments and theory in cold and ultracold collisions. *Rev. Mod. Phys.* **71**, 1 (1999).
- [284] Micheli, A., Pupillo, G., Büchler, H. P., and Zoller, P. Cold polar molecules in two-dimensional traps: Tailoring interactions with external fields for novel quantum phases. *Phys. Rev. A* **76**, 043604 (2007).
- [285] Gribakin, G. F. and Flambaum, V. V. Calculation of the scattering length in atomic collisions using the semiclassical approximation. *Phys. Rev. A* **48**, 546 (1993).
- [286] Büchler, H. P., Demler, E., Lukin, M., Micheli, A., Prokof'ev, N., Pupillo, G., and Zoller, P. Strongly correlated 2D quantum phases with cold polar molecules: Controlling the shape of the interaction potential. *Phys. Rev. Lett.* **98**, 060404 (2007).
- [287] Chou, C. W., de Riedmatten, H., Felinto, D., Polyakov, S. V., van Enk, S. J., and Kimble, H. J. Measurement-induced entanglement for excitation stored in remote atomic ensembles. *Nature (London)* **438**, 828 (2005).
- [288] Thompson, J. K., Simon, J., Loh, H., and Vuletić, V. A high-brightness source of narrowband, identical-photon pairs. *Science* **313**, 74 (2006).
- [289] Turukhin, A. V., Sudarshanam, V. S., Shahriar, M. S., Musser, J. A., Ham, B. S., and Hemmer, P. R. Observation of ultraslow and stored light pulses in a solid. *Phys. Rev. Lett.* **88**, 023602 (2002).
- [290] Hastings-Simon, S. R., Staudt, M. U., Afzelius, M., Baldi, P., Jaccard, D., Tittel, W., and Gisin, N. Controlled stark shifts in Er^{3+} -doped crystalline and amorphous waveguides for quantum state storage. *Opt. Comm.* **266**, 716 (2006).
- [291] Staudt, M. U., Hastings-Simon, S. R., Afzelius, M., Jaccard, D., Tittel, W., and Gisin, N. Investigations of optical coherence properties in an erbium-doped silicate fiber for quantum state storage. *Opt. Comm.* **266**, 720 (2006).

-
- [292] Nilsson, M. and Kröll, S. Solid state quantum memory using complete absorption and re-emission of photons by tailored and externally controlled inhomogeneous absorption profiles. *Opt. Comm.* **247**, 393 (2005).
- [293] Fleischhauer, M., Yelin, S. F., and Lukin, M. D. How to trap photons? storing single-photon quantum states in collective atomic excitations. *Opt. Comm.* **179**, 395 (2000).
- [294] Moiseev, S. A. and Ham, B. S. Photon-echo quantum memory with efficient multipulse readings. *Phys. Rev. A* **70**, 063809 (2004).
- [295] Moiseev, S. A. and Noskov, M. I. The possibilities of the quantum memory realization for short pulses of light in the photon echo technique. *Laser Phys. Lett.* **1**, 303 (2004).
- [296] Moiseev, S. A. Quantum memory for intense light fields in photon echo technique. *Bull. Russ. Acad. Sci. Phys.* **68**, 1408 (2004).
- [297] Moiseev, S. A., Simon, C., and Gisin, N. Photon echo quantum memory for arbitrary non-stationary light fields. *arXiv:quant-ph/0609173v2* (2006).
- [298] Sangouard, N., Simon, C., Afzelius, M., and Gisin, N. Analysis of a quantum memory for photons based on controlled reversible inhomogeneous broadening. *Phys. Rev. A* **75**, 032327 (2007).
- [299] Roch, J. F., Vignerot, K., Grell, P., Sinatra, A., Poizat, J. P., and Grangier, P. Quantum nondemolition measurements using cold trapped atoms. *Phys. Rev. Lett.* **78**, 634 (1997).
- [300] Kuzmich, A., Bigelow, N. P., and Mandel, L. Atomic quantum non-demolition measurements and squeezing. *Europhys. Lett.* **42**, 481 (1998).
- [301] Mishina, O. S., Kupriyanov, D. V., Muller, J. H., and Polzik, E. S. Spectral theory of quantum memory and entanglement via Raman scattering of light by an atomic ensemble. *Phys. Rev. A* **75**, 042326 (2007).
- [302] Raymer, M. G. and Mostowski, J. Stimulated raman scattering: Unified treatment of spontaneous initiation and spatial propagation. *Phys. Rev. A* **24**, 1980 (1981).
- [303] Raymer, M. G., Walmsley, I. A., Mostowski, J., and Sobolewska, B. Quantum theory of spatial and temporal coherence properties of stimulated Raman scattering. *Phys. Rev. A* **32**, 332 (1985).

- [304] Scully, M. O., Fry, E. S., Ooi, C. H. R., and Wodkiewicz, K. Directed spontaneous emission from an extended ensemble of N atoms: Timing is everything. *Phys. Rev. Lett.* **96**, 010501 (2006).
- [305] Fleischhauer, M., Imamoglu, A., and Marangos, J. P. Electromagnetically induced transparency: Optics in coherent media. *Rev. Mod. Phys.* **77**, 633 (2005).
- [306] Dantan, A. and Pinard, M. Quantum-state transfer between fields and atoms in electromagnetically induced transparency. *Phys. Rev. A* **69**, 043810 (2004).
- [307] Dantan, A., Bramati, A., and Pinard, M. Atomic quantum memory: Cavity versus single-pass schemes. *Phys. Rev. A* **71**, 043801 (2005).
- [308] Dantan, A., Cviklinski, J., Pinard, M., and Grangier, P. Dynamics of a pulsed continuous-variable quantum memory. *Phys. Rev. A* **73**, 032338 (2006).
- [309] Krotov, V. F. and Feldman, I. N. An iterative method for solving optimal-control problems. *Eng. Cybern.* **21**, 123 (1983).
- [310] Konnov, A. I. and Krotov, V. F. On global methods of successive improvement of controlled processes. *Autom. Remote Control (Engl. Transl.)* **60**, 1427 (1999).
- [311] Shapiro, M. and Brumer, P. *Principles of the Quantum Control of Molecular Processes*. Hohn Wiley & Sons, Hoboken, NJ, (2003).
- [312] Kosloff, R., Rice, S. A., Gaspard, P., Tersigni, S., and Tannor, D. J. Wavepacket dancing - achieving chemical selectivity by shaping light-pulses. *J. Chem. Phys.* **139**, 201 (1989).
- [313] Khaneja, N., Reiss, T., Kehlet, C., Schulte-Herbrüggen, T., and Glaser, S. J. Optimal control of coupled spin dynamics: design of NMR pulse sequences by gradient ascent algorithms. *J. Magn. Reson.* **172**, 296 (2005).
- [314] Sklarz, S. E. and Tannor, D. J. Loading a Bose-Einstein condensate onto an optical lattice: An application of optimal control theory to the nonlinear Schrodinger equation. *Phys. Rev. A* **66**, 053619 (2002).
- [315] Calarco, T., Dorner, U., Julienne, P. S., Williams, C. J., and Zoller, P. Quantum computations with atoms in optical lattices: Marker qubits and molecular interactions. *Phys. Rev. A* **70**, 012306 (2004).
- [316] Walls, D. F. and Milburn, G. J. *Quantum Optics*. Springer, New York, (2007).
- [317] Kalachev, A. A. and Samartsev, V. V. Quantum memory and quantum computations in the optical subradiance regime. *Quantum Electron.* **35**, 679 (2005).

-
- [318] Kalachev, A. and Kröll, S. Coherent control of collective spontaneous emission in an extended atomic ensemble and quantum storage. *Phys. Rev. A* **74**, 023814 (2006).
- [319] Cohen-Tannoudji, C., Dupont-Roc, J., and Grynberg, G. *Atom-Photon Interactions: Basic Processes and Applications*. Wiley, New York, (2004).
- [320] Hald, J. and Polzik, E. S. Mapping a quantum state of light onto atoms. *J. Opt. B: Quantum Semiclassical Opt.* **3**, S83 (2001).
- [321] Sherson, J., Sørensen, A. S., Fiurášek, J., Mølmer, K., and Polzik, E. S. Light qubit storage and retrieval using macroscopic atomic ensembles. *Phys. Rev. A* **74**, 011802(R) (2006).
- [322] Fleischhauer, M. and Yelin, S. F. Radiative atom-atom interactions in optically dense media: Quantum corrections to the Lorentz-Lorenz formula. *Phys. Rev. A* **59**, 2427 (1999).
- [323] Matsko, A. B., Novikova, I., Scully, M. O., and Welch, G. R. Radiation trapping in coherent media. *Phys. Rev. Lett.* **87**, 133601 (2001).
- [324] Fleischhauer, M. Optical pumping in dense atomic media: Limitations due to reabsorption of spontaneously emitted photons. *Europhys. Lett.* **45**, 659 (1999).
- [325] André, A. *Thesis: Nonclassical states of light and atomic ensembles: Generation and New Application*. PhD thesis, Harvard University, Cambridge, (2005).
- [326] Sørensen, M. W. and Sørensen, A. S. Three-dimensional theory for light-matter interaction. *Phys. Rev. A* **77**, 013826 (2008).
- [327] Matsko, A. B., Rostovtsev, Y. V., Kocharovskaya, O., Zibrov, A. S., and Scully, M. O. Nonadiabatic approach to quantum optical information storage. *Phys. Rev. A* **64**, 043809 (2001).
- [328] Mikhlin, S. G. *Integral Equations and Their Applications to Certain Problems in Mechanics*. Pergamon Press, New York, (1957).
- [329] Fox, A. G. and Li, T. Resonant modes in a maser interferometer. *Bell Syst. Tech. J.* **40**, 453 (1961).
- [330] Gerchberg, R. W. and Saxton, W. O. Practical algorithm for determination of phase from image and diffraction plane pictures. *Optik (Stuttgart)* **35**, 237 (1972).
- [331] Gray, A. and Mathews, G. B. *A Treatise on Bessel Functions and Their Applications to Physics*. MacMillan and Co., London, (1895).

- [332] Nunn, J., Walmsley, I. A., Raymer, M. G., Surmacz, K., Waldermann, F. C., Wang, Z., and Jaksch, D. Modematching an optical quantum memory. *arXiv:quant-ph/0603268v2* (2006).
- [333] Appel, J., Marzlin, K. P., and Lvovsky, A. I. Raman adiabatic transfer of optical states in multilevel atoms. *Phys. Rev. A* **73**, 013804 (2006).
- [334] Raczyński, A., Zaremba, J., and Zielińska-Kaniasty, S. Beam splitting and Hong-Ou-Mandel interference for stored light. *Phys. Rev. A* **75**, 013810 (2007).
- [335] Sakurai, J. J. *Modern Quantum Mechanics*. Addison-Wesley, Reading, (1994).
- [336] Shuker, M., Firstenberg, O., Pugatch, R., Ben-Kish, A., Ron, A., and Davidson, N. Angular dependence of Dicke-narrowed electromagnetically induced transparency resonances. *Phys. Rev. A* **76**, 023813 (2007).
- [337] Johnsson, M. and Mølmer, K. Storing quantum information in a solid using dark-state polaritons. *Phys. Rev. A* **70**, 032320 (2004).
- [338] Javan, A., Kocharovskaya, O., Lee, H., and Scully, M. O. Narrowing of electromagnetically induced transparency resonance in a Doppler-broadened medium. *Phys. Rev. A* **66**, 013805 (2002).
- [339] Novikova, I., Matsko, A. B., and Welch, G. R. Influence of a buffer gas on nonlinear magneto-optical polarization rotation. *J. Opt. Soc. Am. B* **22**, 44 (2005).
- [340] Nilsson, M., Rippe, L., Kröll, S., Klieber, R., and Suter, D. Hole-burning techniques for isolation and study of individual hyperfine transitions in inhomogeneously broadened solids demonstrated in $\text{Pr}^{3+} : \text{Y}_2\text{SiO}_5$. *Phys. Rev. B* **70**, 214116 (2004).
- [341] Simon, C., de Riedmatten, H., Afzelius, M., Sangouard, N., Zbinden, H., and Gisin, N. Quantum repeaters with photon pair sources and multimode memories. *Phys. Rev. Lett.* **98**, 190503 (2007).
- [342] Ohtsuki, Y., Turinici, G., and Rabitz, H. Generalized monotonically convergent algorithms for solving quantum optimal control problems. *J. Chem. Phys.* **120**, 5509 (2004).
- [343] Montangero, S., Calarco, T., and Fazio, R. Robust optimal quantum gates for Josephson charge qubits. *Phys. Rev. Lett.* **99**, 170501 (2007).
- [344] Rebentrost, P., Serban, I., Schulte-Herbruggen, T., and Wilhelm, F. K. Optimal control of a qubit coupled to a non-Markovian environment. *Phys. Rev. Lett.* **102**, 090401 (2009).

- [345] Kalachev, A. Quantum storage on subradiant states in an extended atomic ensemble. *Phys. Rev. A* **76**, 043812 (2007).
- [346] Erhard, M. and Helm, H. Buffer-gas effects on dark resonances: Theory and experiment. *Phys. Rev. A* **63**, 043813 (2001).
- [347] Graf, M., Arimondo, E., Fry, E. S., Nikonov, D. E., Padmabandu, G. G., Scully, M. O., and Zhu, S.-Y. Doppler broadening and collisional relaxation effects in a lasing-without-inversion experiment. *Phys. Rev. A* **51**, 4030 (1995).
- [348] Lukin, M. D., Fleischhauer, M., Zibrov, A. S., Robinson, H. G., Velichansky, V. L., Hollberg, L., and Scully, M. O. Spectroscopy in dense coherent media: Line narrowing and interference effects. *Phys. Rev. Lett.* **79**, 2959 (1997).
- [349] Lukin, M. D., Hemmer, P. R., Löffler, M., and Scully, M. O. Resonant enhancement of parametric processes via radiative interference and induced coherence. *Phys. Rev. Lett.* **81**, 2675 (1998).
- [350] Harada, K.-i., Kanbashi, T., Mitsunaga, M., and Motomura, K. Competition between electromagnetically induced transparency and stimulated Raman scattering. *Phys. Rev. A* **73**, 013807 (2006).
- [351] Kang, H., Hernandez, G., and Zhu, Y. Resonant four-wave mixing with slow light. *Phys. Rev. A* **70**, 061804(R) (2004).
- [352] Wong, V., Bennink, R. S., Marino, A. M., Boyd, R. W., Stroud, C. R., and Narducci, F. A. Influence of coherent Raman scattering on coherent population trapping in atomic sodium vapor. *Phys. Rev. A* **70**, 053811 (2004).
- [353] Agarwal, G. S., Dey, T. N., and Gauthier, D. J. Competition between electromagnetically induced transparency and Raman processes. *Phys. Rev. A* **74**, 043805 (2006).
- [354] Happer, W. Optical pumping. *Rev. Mod. Phys.* **44**, 169 (1972).
- [355] Matsko, A. B., Novikova, I., and Welch, G. R. Radiation trapping under conditions of electromagnetically induced transparency. *J. Mod. Opt.* **49**, 367 (2002).
- [356] Novikova, I., Xiao, Y., Phillips, D. F., and Walsworth, R. L. EIT and diffusion of atomic coherence. *J. Mod. Opt.* **52**, 2381 (2005).
- [357] Rotondaro, M. D. and Perram, G. P. Collision-induced transitions between the Zeeman-split (J, m) levels of $\text{Rb}(5^2P_{1/2}, 5^2P_{3/2})$. *Phys. Rev. A* **58**, 2023 (1998).
- [358] Mikhailov, E. E., Rostovtsev, Y. V., and Welch, G. R. Group velocity study in hot ^{87}Rb vapour with buffer gas. *J. Mod. Opt.* **50**, 2645 (2003).

- [359] Boyer, V., McCormick, C. F., Arimondo, E., and Lett, P. D. Ultraslow propagation of matched pulses by four-wave mixing in an atomic vapor. *Phys. Rev. Lett.* **99**, 143601 (2007).
- [360] Wu, C. Competing orders in one-dimensional spin-3/2 fermionic systems. *Phys. Rev. Lett.* **95**, 266404 (2005).
- [361] Chen, S., Wu, C., Zhang, S.-C., and Wang, Y. Exact spontaneous plaquette ground states for high-spin ladder models. *Phys. Rev. B* **72**, 214428 (2005).
- [362] Wu, C. Hidden symmetry and quantum phases in spin-3/2 cold atomic systems. *Mod. Phys. Lett. B* **20**, 1707 (2006).
- [363] Boutassetta, N., Allouche, A. R., and Aubert-Frecon, M. Theoretical study of the electronic structure of the Sr₂ molecule. *Phys. Rev. A* **53**, 3845 (1996).
- [364] Czuchaj, E., Krosnicki, M., and Stoll, H. Valence ab initio calculation of the potential energy curves for the Sr₂ dimer. *CHem. Phys. Lett.* **371**, 401 (2003).
- [365] Wang, Y. and Dolg, M. Pseudopotential study of the ground and excited states of Yb₂. *Theor. Chem. Acc.* **100**, 124 (1998).
- [366] Machholm, M., Julienne, P. S., and Suominen, K.-A. Calculations of collisions between cold alkaline-earth-metal atoms in a weak laser field. *Phys. Rev. A* **64**, 033425 (2001).
- [367] Syassen, N., Bauer, D. M., Lettner, M., Volz, T., Dietze, D., Garcia-Ripoll, J. J., Cirac, J. I., Rempe, G., and Durr, S. Strong dissipation inhibits losses and induces correlations in cold molecular gases. *Science* **320**, 1329 (2008).
- [368] Daley, A. J., Taylor, J. M., Diehl, S., Baranov, M., and Zoller, P. Atomic three-body loss as a dynamical three-body interaction. *Phys. Rev. Lett.* **102**, 040402 (2009).
- [369] Tiesinga, E., Williams, C. J., Mies, F. H., and Julienne, P. S. Interacting atoms under strong quantum confinement. *Phys. Rev. A* **61**, 063416 (2000).
- [370] Naidon, P. and Julienne, P. S. Optical Feshbach resonances of alkaline-earth-metal atoms in a one- or two-dimensional optical lattice. *Phys. Rev. A* **74**, 062713 (2006).
- [371] Zelevinsky, T., Boyd, M. M., Ludlow, A. D., Ido, T., Ye, J., Ciuryło, R., Naidon, P., and Julienne, P. S. Narrow line photoassociation in an optical lattice. *Phys. Rev. Lett.* **96**, 203201 (2006).

-
- [372] Martinez de Escobar, Y. N., Mickelson, P. G., Yan, M., and Killian, T. C. Modification of atom scattering using an intercombination-line optical Feshbach resonance at large detuning. *arXiv:0906.1837v1 [physics.atom-ph]* (2009).
- [373] Jones, H. F. *Groups, Representations and Physics*. Institute of Physics Publishing, London, (1998).
- [374] Fulton, W. *Young Tableaux with Applications to Representation Theory and Geometry*. Cambridge University Press, Cambridge, (1997).
- [375] Girvin, S. M. and Arovas, D. P. Hidden topological order in integer quantum spin chains. *Phys. Scr.* **T27**, 156 (1989).
- [376] Brennen, G. K. and Miyake, A. Measurement-based quantum computer in the gapped ground state of a two-body Hamiltonian. *Phys. Rev. Lett.* **101**, 010502 (2008).
- [377] Verstraete, F. and Cirac, J. I. Valence-bond states for quantum computation. *Phys. Rev. A* **70**, 060302(R) (2004).
- [378] Wu, C. Orbital ordering and frustration of p-band Mott insulators. *Phys. Rev. Lett.* **100**, 200406 (2008).
- [379] Zhao, E. and Liu, W. V. Orbital order in Mott insulators of spinless p-band fermions. *Phys. Rev. Lett.* **100**, 160403 (2008).
- [380] Xu, C. and Fisher, M. P. A. Bond algebraic liquid phase in strongly correlated multiflavor cold atom systems. *Phys. Rev. B* **75**, 104428 (2007).
- [381] Wang, L., Dai, X., Chen, S., and Xie, X. C. Magnetism of cold fermionic atoms on the p band of an optical lattice. *Phys. Rev. A* **78**, 023603 (2008).
- [382] Müller, T., Fölling, S., Widera, A., and Bloch, I. State preparation and dynamics of ultracold atoms in higher lattice orbitals. *Phys. Rev. Lett.* **99**, 200405 (2007).
- [383] Anderlini, M., Lee, P. J., Brown, B. L., Sebby-Strabley, J., Phillips, W. D., and Porto, J. V. Controlled exchange interaction between pairs of neutral atoms in an optical lattice. *Nature (London)* **448**, 452 (2007).
- [384] Esry, B. D., Greene, C. H., and Burke, J. P. Recombination of three atoms in the ultracold limit. *Phys. Rev. Lett.* **83**, 1751 (1999).
- [385] Bedaque, P. F., Braaten, E., and Hammer, H. W. Three-body recombination in Bose gases with large scattering length. *Phys. Rev. Lett.* **85**, 908 (2000).

- [386] Jack, M. W. and Yamashita, M. Signatures of the quantum fluctuations of cold atoms in an optical lattice in the three-body loss rate. *Phys. Rev. A* **67**, 033605 (2003).
- [387] Kraemer, T., Mark, M., Waldburger, P., Danzl, J. G., Chin, C., Engeser, B., Lange, A. D., Pilch, K., Jaakkola, A., Nagerl, H. C., and Grimm, R. Evidence for Efimov quantum states in an ultracold gas of caesium atoms. *Nature (London)* **440**, 315 (2006).
- [388] Campbell, G. K., Mun, J., Boyd, M., Medley, P., Leanhardt, A. E., Marcassa, L. G., Pritchard, D. E., and Ketterle, W. Imaging the Mott insulator shells by using atomic clock shifts. *Science* **313**, 649 (2006).
- [389] van den Bossche, M., Zhang, F. C., and Mila, F. Plaquette ground state in the two-dimensional SU(4) spin-orbital model. *Eur. Phys. J. B* **17**, 367 (2000).
- [390] Pankov, S., Moessner, R., and Sondhi, S. L. Resonating singlet valence plaquettes. *Phys. Rev. B* **76**, 104436 (2007).
- [391] Wang, F. and Vishwanath, A. Z_2 spin-orbital liquid state in the square lattice Kugel-Khomskii model. *Phys. Rev. B* **80**, 064413 (2009).
- [392] Rachel, S., Thomale, R., Fuhringer, M., Schmitteckert, P., and Greiter, M. Spinon confinement and the Haldane gap in SU(n) spin chains. *arXiv:0904.3882v1 [cond-mat.str-el]* (2009).
- [393] Sutherland, B. Model for a multicomponent quantum system. *Phys. Rev. B* **12**, 3795 (1975).
- [394] Anderson, P. W. The resonating valence bond state in La_2CuO_4 and superconductivity. *Science* **235**, 1196 (1987).

Appendix A

Optimal Photon Storage in Atomic Ensembles: Cavity Model

A.1 Introduction

The faithful storage of a traveling light pulse in an atomic memory and the subsequent retrieval of the state are currently being pursued in a number of laboratories around the world [74, 75, 79, 77, 78, 80, 81, 287, 288, 82, 289, 83, 94, 290, 291, 95, 292]. A strong motivation for this research comes from the field of quantum communication, where quantum information is easily transmitted by photons, but the photonic states need to be stored locally to process the information. Such applications as well as other ideas from quantum-information science have led to a strong interest in techniques to facilitate a controlled interaction between atoms and single photons [4, 61]. A conceptually simple realization of a matter-light quantum interface consists of a single atom absorbing a single photon. However, due to the very weak coupling of a single atom to light, this approach is extremely challenging and requires the use of very high-finesse cavities to effectively increase the coupling [74, 75]. To circumvent the problem of weak coupling, it has recently been realized that one can use an optically thick ensemble of atoms, and several different proposals have been made for how external classical control fields can be used to controllably map photon states onto collective atomic states [293, 16, 84, 86, 79]. The goal in all of these approaches is to map an incoming signal pulse into a long-lived atomic coherence (referred to as a spin wave), so that it can be later retrieved “on demand” with the highest possible efficiency. Remarkable experimental progress has already been made toward the implementation of these protocols in atomic gases [79, 77, 78, 80, 81, 287, 288] and in impurities embedded in a solid state material [82, 289, 83, 94, 290, 291, 95]. A central question that emerges from these advances is which approach represents the best possible strategy for given experimental parameters and for desired memory characteristics, and how the control fields or possibly the shape of the input photon

wave packet can be chosen to achieve the maximum efficiency. In Chapter 2, we presented a novel physical picture that unifies a wide range of different approaches to photon storage in Λ -type atomic media and yields the optimal control strategy. This picture is based on two key observations. First, we showed that the retrieval efficiency of any given stored spin wave depends only on the optical depth of the medium and not on the properties of the control pulse. Physically, this follows from the fact that the branching ratio between collectively enhanced emission into desired modes and spontaneous decay depends only on the optical depth. The second observation is that the optimal storage process is the time reverse of retrieval (see also [86, 87, 294, 295, 296, 297, 298]). This universal picture implies that the maximum efficiency for the combined process of storage followed by retrieval is the same for all approaches considered and depends only on the optical depth¹. The optimum can be attained by adjusting the control or the shape of the photon wave packet. In the present Appendix and in Appendices B-D, we present all the details behind this universal picture and the optimal control shaping that it implies, as well as consider several extensions of this analysis beyond the results of Chapter 2. In particular, in the present Appendix, we discuss the cavity model to be compared in Appendix B to the free-space model. In Appendix B, the full analysis of the free-space model is presented, and, in addition, the effects of spin-wave decay and of nondegeneracy of the two lower levels of the Λ system are discussed. In Appendix C, we generalize our treatment to two different regimes of inhomogeneous broadening: with and without redistribution between frequency classes during the storage time. Finally, in Appendix D, we use the method of gradient ascent from optimal control theory to extend the bandwidth of the memory by an order of magnitude.

A generic model for a quantum memory uses the Λ -type level configuration shown in Fig. A.1, in which a weak (quantum) signal field (the dashed line) is detuned by a frequency Δ from the $|g\rangle - |e\rangle$ transition, whose optical coherence decays with rate $\gamma \geq \gamma_e/2$, where γ_e is the spontaneous emission rate from state $|e\rangle$. A copropagating (classical) control beam (the solid line) with the same detuning Δ from the $|s\rangle - |e\rangle$ transition and time-dependent Rabi frequency envelope Ω is used to coherently manipulate the signal propagation and map the photonic state onto the atoms, and vice versa. In the present Appendix and in Appendices B-D, we discuss several different approaches to photon storage, including far-off-resonant Raman, electromagnetically induced transparency (EIT), and photon-echo techniques. If we neglect the decay of the $|s\rangle - |g\rangle$ coherence, i.e., the decay of the spin wave, the only sources of loss in all of these approaches are the decay γ of the optical polarization on the $|g\rangle - |e\rangle$ transition during both storage and retrieval, and the leakage of the pulse through the medium during storage. To achieve the maximum storage efficiency, one has to

¹We note for the sake of clarity that the storage scheme employed in Ref. [79] cannot be regarded as a subset of the general scheme considered in the present work, and more work has to be done in order to compare the performance of the two.

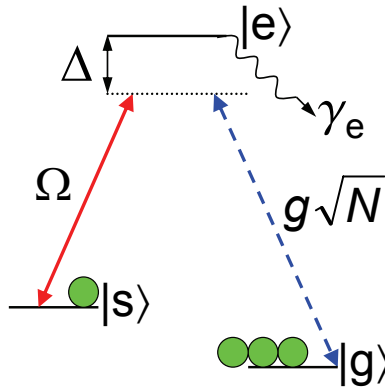


Figure A.1: Λ -type medium coupled to a classical field (solid) with Rabi frequency $\Omega(t)$ and a quantum field (dashed). Due to collective enhancement [76], the quantum field couples to the spin-wave excitations with an effective coupling constant $g\sqrt{N}$, where N is the number of atoms in the medium.

minimize these two types of loss, and, in fact, as we will show in the present Appendix and in Appendices B-D, one has to make a compromise between them.

Higher optical depth increases the coherent coupling between the quantum signal field and the atoms and, thus, allows for higher photon storage efficiencies. It has therefore been suggested to put a cavity around the atomic ensemble [61, 299, 300], which will effectively increase the free-space optical depth d by a factor equal to the number of passes a photon makes in the cavity before leaking out. We will denote this increased effective optical depth by the cooperativity parameter C . High-efficiency retrieval of a photon from an ensemble enclosed in a cavity has been recently demonstrated [288]. In addition to being a promising experimental setup in itself², the slightly simpler theoretical treatment of the cavity model offers a very useful tool for understanding the more complicated free-space model. Thus, in the present Appendix, we will treat photon storage in the cavity model, to be compared in Appendix B to the free-space model.

We will now review the three photon storage protocols (Raman, EIT, and photon echo) that are often discussed in the literature on photon storage and that we treat as special cases of our general formalism. The remainder of this Section is intended as an introduction to both the present Appendix and Appendix B and will thus make use of the figures of merit of both the cavity model (the cooperativity parameter C) and the

²For clarity, we note that, although it might, in principle, be possible to describe the experimental setup in Ref. [288] by our model, this setup is slightly different from our model in that the propagation directions of the control and the photon are orthogonal (rather than the same) and the cavity mode is a standing-wave mode (rather than a running-wave mode).

free-space model (the optical depth d). It will be implied in the following discussion that all the formulas containing C (d) refer to the cavity (free-space) model.

One possible strategy for light storage uses the Raman configuration, where the fields have a large detuning (we will show that the appropriate limit is $|\Delta| \gg \gamma d$ or $|\Delta| \gg \gamma C$ rather than $|\Delta| \gg \gamma$, as one might naively assume by analogy with the single-atom case) and the photons are absorbed into the stable ground state $|s\rangle$ by stimulated Raman transitions [84, 85, 301]. With far-off-resonant interactions, the excited state $|e\rangle$ can be adiabatically eliminated to give simplified and solvable equations [302, 303]. Based on these simplified equations, the Raman scheme for storage of quantum states of light in atomic ensembles was proposed in Ref. [84] and, simultaneously with the present work, has been analyzed in detail and optimized under the constraint of limited control power [85]. We show in the present Appendix and in Appendix B that, in the limit of large cooperativity parameter C or large optical depth d , one can ignore the decay γ of the optical $|g\rangle - |e\rangle$ coherence, as is done in Ref. [85].

An alternative storage strategy is based on electromagnetically induced transparency [293, 16, 17, 76], where resonant control fields ($|\Delta| \ll \gamma d$ or $|\Delta| \ll \gamma C$) are used to open a spectral transparency window for the quantum field. In this approach, the quantum field travels at a reduced group velocity, which is then adiabatically reduced to zero. Similarly to the Raman case, the excited state can also be eliminated on resonance, provided the control field is sufficiently weak. This again simplifies the equations to analytically solvable ones [17].

We will treat both the far-off-resonant Raman scheme and the resonant EIT scheme as special cases of a more general “adiabatic” limit, i.e., the limit in which the excited state can be adiabatically eliminated. We will show that, for the purposes of optimal photon storage, the condition of validity of the adiabatic elimination is almost independent of the single-photon detuning Δ (in particular, it is similar in the Raman and resonant cases) and is given by $Td\gamma \gg 1$ or $TC\gamma \gg 1$, where T is the duration of the incoming pulse. We will show that, provided a (smooth) incoming photon wave packet is long enough that this condition is satisfied ($T \gg 1/(d\gamma)$ or $T \gg 1/(C\gamma)$), it can be stored with the maximum possible efficiency, which depends only on the optical depth d or the cooperativity parameter C and not on the detuning Δ or the shape of the wave packet. In the case of the cavity model discussed in the present Appendix, this maximum efficiency is simply given by $C/(1 + C)$.

Finally, in the photon-echo-based approach to storage, a resonant photon is first allowed to get absorbed by the ensemble with the control field off. While the phrase “photon echo” often refers to a wide class of experiments, we shall here consider a special case where one applies then a short resonant π pulse, which maps excitations from the unstable excited state $|e\rangle$ into the stable ground state $|s\rangle$. Because this approach uses very short control pulses and because, as we will show, it is most efficient in storing short input pulses ($T \sim 1/(d\gamma)$ or $T \sim 1/(C\gamma)$), we will refer to this approach as “fast” storage. This technique was originally suggested in Ref. [86]

for the case of Doppler-broadened atoms and has since been extensively studied both theoretically (see Appendix C and Refs. [87, 292, 294, 295, 296, 297, 298]) and experimentally [94, 290, 291, 95]. In Ref. [86], it was noted that, if the photons are retrieved by using a control laser pulse traveling in the backward direction compared to storage, the Doppler broadening is reversed, and the dephasing occurring during storage is therefore also reversed, resulting in an “echo,” which may result in high efficiencies. In Refs. [87, 292], it was proposed to use controlled reversible inhomogeneous broadening (CRIB), that is, to artificially add an inhomogeneous broadening to an originally homogeneously broadened line and then to reverse this broadening to achieve an echo signal. In the present Appendix and in Appendix B, we consider a different limit of this proposal, where there is no inhomogeneous broadening of the optical transition, and storage is simply achieved by applying a fast π pulse at the right time. Retrieval, which is accomplished with a second π pulse, results [304] in a directional output (as opposed to the loss due to the decay rate γ) exactly as in the adiabatic limit. We will show that in the limit of large d or C this procedure leads to an ideal storage and retrieval of the photonic state, while at every finite value of d or C there exists an optimal input photon mode that can be stored with efficiency equal to the maximum adiabatic storage efficiency (given by $C/(1+C)$ in the case of the cavity model). For comparison, in Appendix C, we will discuss how this approach measures up to the CRIB approach and show that adding and reversing inhomogeneous broadening as proposed in Refs. [87, 292] may lead to an improvement in the storage efficiency, although the improvement is rather limited.

The optimization of storage in all of these schemes consists of finding the optimal balance between two sources of error: leakage of the input pulse through the ensemble and scattering of the input photons into 4π due to spontaneous emission. In the EIT approach, a stronger control field is desirable, since it produces more robust interference and a wider transparency window, thus minimizing spontaneous emission losses. On the other hand, higher control power means larger group velocity and hence the inability to localize the input pulse inside the medium. The optimization in this case finds the optimal power and shape for the control field, given the duration and shape of the input pulse. In contrast, in the Raman scheme, a high value of Ω is required to have a sufficient coupling of the input photon to the spin wave [85]. On the other hand, large Ω will increase the decay rate due to spontaneous emission, which is given by the optical pumping rate $\gamma\Omega^2/\Delta^2$. The optimization with respect to the shape and power of Ω for a given input mode again balances between these two sources of error. Finally, in the fast storage scheme the control fields are fixed to be perfect π pulses, but one can optimize with respect to the duration T and the shape of the input mode. The input mode should be made as short as possible in order to avoid the loss due to optical polarization decay $\exp(-\gamma T)$. However, a mode that is too short will be too wide in frequency space and will not be absorbed by the ensemble (i.e., it will leak through). The optimization with respect to the duration and shape of the input mode finds the optimal balance between these two sources of

error.

In all the photon storage techniques considered, ideal performance (i.e., unit efficiency) can be achieved in the limit of infinite optical depth d or infinite cooperativity parameter C . For example, in the EIT regime in free space, the width of the spectral transparency window is $\Delta\omega_{\text{EIT}} = v_g\sqrt{d}/L$, where L is the length of the ensemble and $v_g \propto |\Omega|^2/d$ is the EIT group velocity [305]. Thus, for a given T and a given large value of d , one can first make Ω , and hence v_g , small enough for the pulse to fit inside the medium. Then the enhancement of $\Delta\omega_{\text{EIT}}$ by an extra factor of \sqrt{d} will ensure, if d is sufficiently large, that the transparency window is still wide enough to induce negligible spontaneous emission. In the Raman regime, to avoid spontaneous emission decay via the optical pumping rate $\gamma\Omega^2/\Delta^2$, one should make Ω sufficiently small. If the optical depth or the cooperativity parameter is large enough, the coupling of the input mode to the atoms will then still be sufficient to avoid leakage even at this small value of Ω . Finally, in fast storage, the pulse that is short enough ($T\gamma \ll 1$) to avoid optical polarization decay can still be absorbed in a free-space medium provided d is large enough ($Td\gamma \gg 1$, as we will show in Appendix B). In the cavity model discussed in the present Appendix, due to the availability of only one spin-wave mode (the one that couples to the cavity mode), high-efficiency fast storage is harder to achieve than in free space: only pulses of a particular shape and duration ($T \sim 1/(C\gamma)$) give high fast storage efficiencies.

Although ideal performance can be achieved at infinite optical depth, in practice, optical depth is always limited by experimental imperfections such as a limited number of atoms in a trap (e.g., Ref. [81], where the optical depth is roughly 8), competing four-wave mixing processes (e.g., Ref. [80], where the optical depth is roughly 4), inhomogeneous broadening of impurity levels in solid state samples [292], or other types of experimental imperfections. Therefore, the optimization of storage protocols at finite optical depth is essential.

Before proceeding with our analysis, we would like to specially note the recent work of Dantan *et al.*, which also considers and illuminates some of the issues we discuss in the present Appendix [306, 307, 308] and in Appendix B [307]. In particular, in Refs. [306, 308], focusing on broadband squeezed states as the input, the authors consider adiabatic storage in a cavity, derive an efficiency expression equivalent to ours, and recognize the interesting similarity between Raman and resonant regimes, both of which feature reduced sensitivity to spontaneous emission. We show in the present Appendix how, for the case of a single incoming spatiotemporal field mode, proper control field shaping can be used to achieve the same optimal efficiency independent of detuning. This effectively makes the Raman, the resonant, and the intermediate regimes all exhibit equally reduced sensitivity to spontaneous emission. In Ref. [307], as in Appendix B, the authors compare adiabatic storage in a cavity to adiabatic storage in free space and recognize important similarities and differences. In particular, it is recognized that the error in the cavity case scales as the inverse of the atomic density (as we also find in the present Appendix), while in free space

it may scale as the inverse of the square root of the density. We show in Appendix B how proper optimization can be used to make the error in the free-space case also scale as the inverse of atomic density. We also bridge in free space the gap between the EIT and Raman cases, showing how proper control field shaping can be used to achieve the same optimal efficiency independent of detuning.

We would also like to note that the connection between optimal photon storage and time reversal that we present was first made in the context of photon-echo-based techniques. In particular, it was first shown in Ref. [86] and then discussed in detail in Refs. [87, 294, 295, 296, 297, 298] that under certain conditions, such as high optical depth and sufficiently slow optical polarization decay rate, photon-echo techniques can result in ideal storage and retrieval, and that the retrieved photon field is then the time reverse of the original input field. We generalize this result in Chapter 2, in the present Appendix, and in Appendices B-D by demonstrating that the ideas of time reversal can be used to optimize photon storage even when the dynamics of the system are not completely reversible and when the ideal unit efficiency cannot be achieved. This is the case for finite cooperativity parameter C in the cavity model and for finite optical depth d in the free-space model. We also generalize the time-reversal-based optimization of photon storage from photon-echo-based techniques to any storage technique including, but not limited to, EIT and Raman techniques in homogeneously (Chapter 2, present Appendix, and Appendices B and D) and inhomogeneously (Appendices C and D) broadened Λ -type media.

We would also like to point out that mathematically some of the optimization problems we are solving in the present work (including Chapter 2, the present Appendix, and Appendices B-D) fall into a rich and well-developed field of mathematics called optimal control theory [88, 90, 89]. In particular, we are interested in shaping the control pulse to maximize the storage efficiency (or efficiency of storage followed by retrieval) for a given input photon mode in the presence of optical polarization decay. Since in the equations of motion the control multiplies a dependent variable (optical polarization), this problem is a nonlinear optimal control problem [88]. A general solution to all nonlinear optimal control problems does not exist, so that such problems have to be treated on a case by case basis. We believe that the methods we suggest, such as the iterative time-reversal method introduced in Secs. B.4 and B.5, may be useful in solving optimal control problems in other open (as well as closed) quantum systems. Similar iterative methods are a standard tool in applied optimal control [90, 89, 309, 310] and have been used for a variety of applications, including laser control of chemical reactions [311, 312], design of NMR pulse sequences [313], loading of Bose-Einstein condensates into an optical lattice [314], and atom transport in time-dependent superlattices [315]. In fact, an optimization procedure that is based on gradient ascent [313], and that is very similar to that of Refs. [90, 89, 309, 310, 311, 312, 313, 314], is directly applicable to our problem of finding the optimal control pulse, as we will discuss in Appendix D. However, in the present Appendix and in Appendices B and C, we use time-reversal iterations for optimal control

in a way different from the methods of Refs. [90, 89, 309, 310, 311, 312, 313, 314, 315], as we will discuss in Sec. B.5. In particular, we will show that, in addition to being a convenient computational tool, our iterative optimization algorithm is, in fact, experimentally realizable (with the experimental realization presented in Secs. 3.3 and E.4).

The remainder of this Appendix is organized as follows. Section A.2 applies to both the cavity and the free-space models and discusses our figure of merit for the performance of the photon storage. The rest of the Appendix discusses storage and retrieval of photons using homogeneously broadened atomic ensembles enclosed in a cavity. In Sec. A.3, we introduce the model. In Sec. A.4, without fully solving the equations analytically, we show that both the retrieval efficiency and the optimal storage efficiency are equal to $C/(1+C)$ (where C is the cooperativity parameter), and derive the optimal storage strategy. In Secs. A.5 and A.6, we solve the equations analytically in the adiabatic and fast limits, respectively, and demonstrate that the optimal storage efficiency can be achieved for any smooth input mode at any detuning satisfying $TC\gamma \gg 1$ and a certain class of resonant input modes satisfying $TC\gamma \sim 1$, where T is the duration of the input mode. In Sec. A.7, we summarize the discussion of the cavity model. Finally, in Sec. A.8, we present some details omitted in the main text.

A.2 Figure of merit

When comparing different storage and retrieval approaches, it is essential to have a figure of merit characterizing the performance of the memory. The discussion in this Section of the appropriate figure of merit applies both to the cavity model discussed in this Appendix and in Appendices C and D and to the free-space models discussed in Appendices B-D. Throughout this work we shall assume that we initially have a single incoming photon in a known spatiotemporal mode denoted by $\mathcal{E}_{\text{in}}(t)$ (or, for the case of computing retrieval efficiency alone, a single excitation in a known atomic spin-wave mode). We define the efficiency η of all the mappings we consider (storage alone, retrieval alone, or storage followed by retrieval) as the probability to find the excitation in the output mode (photonic or atomic, as appropriate) after the interaction. Depending on the application one has in mind, this single-photon efficiency may or may not be the right quantity to consider, but provided that we are interested in a situation where we are mapping a single input mode into a single output mode, any other quantities may be derived from the single-photon efficiency η .

For all the interactions we consider, the full evolution results in a passive (beam-splitter-like) transformation

$$\hat{b}_j = \sum_k U_{jk} \hat{a}_k, \tag{A.1}$$

where \hat{a}_j and \hat{b}_k denote the annihilation operators for all the input and output modes, respectively (all photonic, spin-wave, and Langevin noise operators), with commutation relations $[\hat{a}_j, \hat{a}_k^\dagger] = \delta_{j,k}$ and $[\hat{b}_j, \hat{b}_k^\dagger] = \delta_{j,k}$. Here the matrix U has to be unitary to preserve the commutation relations. The mapping from a certain input mode \hat{a}_0 to an output mode \hat{b}_0 with efficiency η is therefore described by $\hat{b}_0 = \sqrt{\eta}\hat{a}_0 + \sqrt{1-\eta}\hat{c}$, where \hat{c} satisfies $[\hat{c}, \hat{c}^\dagger] = 1$ and represents some linear combination of all other input modes orthogonal to \hat{a}_0 . If all input modes other than \hat{a}_0 are in the vacuum state, the parameter η completely characterizes the mapping. If, for instance, the mode we are storing is in an entangled state with some other system $(|0\rangle_{\hat{a}_0}|x\rangle + |1\rangle_{\hat{a}_0}|y\rangle)/2$, where $|0\rangle_{\hat{a}_0}$ and $|1\rangle_{\hat{a}_0}$ are the zero- and one-photon Fock states of the input mode, and $|x\rangle$ and $|y\rangle$ are two orthonormal states of the other system, the fidelity of the entangled state after the mapping is easily found to be $F = (1 + \eta)/2$. Similarly, Refs. [306, 307, 308] characterize the performance in terms of squeezing preservation parameter η_{squeeze} . If the input state is a squeezed vacuum state in a given mode \hat{a}_0 , the squeezing preservation parameter can be shown to be equivalent to single-photon efficiency, i.e., $\eta_{\text{squeeze}} = \eta$. We will show below in the description of our model why in most experimental situations it is indeed reasonable to assume that the incoming noise (which is included in \hat{c}) is vacuum noise.

A.3 Model

The details of the model and the derivation of the equations of motion are provided in Sec. A.8.1. In this Section, we only give a brief introduction to the model and present the equations of motion without derivation.

We consider a medium of N Λ -type atoms with two metastable lower states, as shown in Fig. A.1, interacting with two single-mode fields. We neglect reabsorption of spontaneously emitted photons and treat the problem in a one-dimensional approximation. The $|g\rangle - |e\rangle$ transition of frequency ω_{eg} of each of the atoms is coupled to a quantized traveling-wave cavity radiation mode (e.g., a mode of a ring cavity with one of the mirrors partially transmitting) with frequency $\omega_1 = \omega_{eg} - \Delta$ described by a slowly varying annihilation operator $\mathcal{E}(t)$. The cavity decay rate is 2κ and the corresponding input-output relation is [316]

$$\hat{\mathcal{E}}_{\text{out}}(t) = \sqrt{2\kappa}\hat{\mathcal{E}}(t) - \hat{\mathcal{E}}_{\text{in}}(t). \quad (\text{A.2})$$

In addition, the transitions $|s\rangle - |e\rangle$ of frequency ω_{es} are driven by a single-mode copropagating classical plane-wave control field with frequency $\omega_2 = \omega_{es} - \Delta$ (i.e., at two-photon resonance $\omega_1 - \omega_2 = \omega_{sg}$, where $\hbar\omega_{sg}$ is the energy difference between the two metastable states) described by a slowly varying Rabi frequency envelope $\Omega(t)$.

In the dipole and rotating-wave approximations, assuming that almost all atoms are in the ground state at all times, and defining the polarization annihilation operator $\hat{P}(t) = \hat{\sigma}_{ge}(t)/\sqrt{N}$ and the spin-wave annihilation operator $\hat{S}(t) = \hat{\sigma}_{gs}(t)/\sqrt{N}$ (where

$\hat{\sigma}_{\mu\nu}$ are slowly varying collective atomic operators defined in Sec. A.8.1), to first order in $\hat{\mathcal{E}}$, the Heisenberg equations of motion are

$$\dot{\hat{\mathcal{E}}} = -\kappa\hat{\mathcal{E}} + ig\sqrt{N}\hat{P} + \sqrt{2\kappa}\hat{\mathcal{E}}_{\text{in}}, \quad (\text{A.3})$$

$$\dot{\hat{P}} = -(\gamma + i\Delta)\hat{P} + ig\sqrt{N}\hat{\mathcal{E}} + i\Omega\hat{S} + \sqrt{2\gamma}\hat{F}_P, \quad (\text{A.4})$$

$$\dot{\hat{S}} = -\gamma_s\hat{S} + i\Omega^*\hat{P} + \sqrt{2\gamma_s}\hat{F}_S, \quad (\text{A.5})$$

where we have introduced the polarization decay rate γ (equal to half of the linewidth), the spin-wave decay rate γ_s , and the corresponding Langevin noise operators \hat{F}_P and \hat{F}_S . The coupling constant g (assumed to be real for simplicity) between the atoms and the quantized field mode is collectively enhanced [76] by a factor of \sqrt{N} to $g\sqrt{N}$. Notice that in order to avoid carrying around extra factors of 2, Ω is defined as half of the traditional Rabi frequency; for example, with the present definition, a π pulse would take time $\pi/(2\Omega)$.

As described in Sec. A.8.1, under reasonable experimental conditions, the incoming noise described by \hat{F}_P and \hat{F}_S is vacuum, i.e., all normally ordered noise correlations are zero. This is precisely the reason why, as noted in Sec. A.2, efficiency is the only number we need in order to fully characterize the mapping.

We assume that all atoms are initially pumped into the ground state, i.e., no \hat{P} or \hat{S} excitations are present in the atoms. We also assume that the only input field excitations initially present are in the quantum field mode with an envelope shape $h_0(t)$ nonzero on $[0, T]$. The goal is to store the state of this mode in \hat{S} and, starting at a time $T_r > T$, retrieve it back into a field mode. Since we are interested only in computing efficiencies (defined below) and since the incoming noise is vacuum, we can ignore the noise operators in Eqs. (A.3)-(A.5) and treat these equations as complex number equations. During storage, the initial conditions are $P(0) = 0$, $S(0) = 0$, and the input mode is $\mathcal{E}_{\text{in}}(t) = h_0(t)$ (normalized according to $\int_0^T dt |\mathcal{E}_{\text{in}}(t)|^2 = 1$). We have here dropped the carets on the operators to denote their complex number representations. The storage efficiency is then

$$\eta_s = \frac{(\text{number of stored excitations})}{(\text{number of incoming photons})} = |S(T)|^2. \quad (\text{A.6})$$

Similarly, during retrieval, the initial and boundary conditions are $P(T_r) = 0$, $S(T_r) = S(T)$, and $\mathcal{E}_{\text{in}}(t) = 0$. $\mathcal{E}_{\text{out}}(t)$ then represents the shape of the quantum mode into which we retrieve, and the total efficiency of storage followed by retrieval is given by

$$\eta_{\text{tot}} = \frac{(\text{number of retrieved photons})}{(\text{number of incoming photons})} = \int_{T_r}^{\infty} dt |\mathcal{E}_{\text{out}}(t)|^2. \quad (\text{A.7})$$

If we instead take $S(T_r) = 1$, we obtain the retrieval efficiency:

$$\eta_r = \frac{(\text{number of retrieved photons})}{(\text{number of stored excitations})} = \int_{T_r}^{\infty} dt |\mathcal{E}_{\text{out}}(t)|^2. \quad (\text{A.8})$$

From now on we will neglect the slow decay of the spin wave (i.e., set $\gamma_s = 0$) but, as briefly discussed below at the ends of Secs. A.5.1 and A.5.2, spin-wave decay is not hard to include. Nonzero γ_s will simply introduce an exponential decay without making the solution or the optimal control shaping harder.

To get the closest analogy to the free-space regime, we assume we are always in the “bad cavity” limit ($\kappa \gg g\sqrt{N}$), in which \mathcal{E} in Eq. (A.3) can be adiabatically eliminated to give

$$\mathcal{E}_{\text{out}} = \mathcal{E}_{\text{in}} + i\sqrt{2\gamma C}P, \tag{A.9}$$

$$\dot{P} = -(\gamma(1+C) + i\Delta)P + i\Omega S + i\sqrt{2\gamma C}\mathcal{E}_{\text{in}}, \tag{A.10}$$

$$\dot{S} = i\Omega^*P, \tag{A.11}$$

where $C = g^2N/(\kappa\gamma)$ is the cooperativity parameter. To relate to the free space situation discussed in Appendix B, we can write the cooperativity parameter as $C = 2d[(1/(2\kappa))/(L/c)]$, where $d = g^2NL/(c\gamma)$ is the definition of optical depth used in the free-space model of Appendix B and where the factor in the square brackets (proportional to cavity finesse) is equal to the number of passes a photon would make through an empty cavity before leaking out (i.e., the photon lifetime in the cavity divided by the time a single pass takes). Thus, up to a factor of order unity, the cooperativity parameter C represents the effective optical depth of the medium in the cavity, so that the efficiency dependence on C in the cavity should be compared to the efficiency dependence on d in free space. We note that, although Eqs. (A.9)-(A.11) describe our case of quantized light coupled to the $|g\rangle - |e\rangle$ transition, they will also precisely be the equations describing the propagation of a classical probe pulse. To see this one can simply take the expectation values of Eqs. (A.3)-(A.5) and use the fact that classical probe pulses are described by coherent states.

It is convenient to reduce Eqs. (A.10) and (A.11) to a single equation

$$\left[\ddot{S} - \frac{\dot{\Omega}^*}{\Omega^*}\dot{S} \right] + (\gamma(1+C) + i\Delta)\dot{S} + |\Omega|^2S = -\Omega^*\sqrt{2\gamma C}\mathcal{E}_{\text{in}}. \tag{A.12}$$

This second-order differential equation cannot, in general, be fully solved analytically. However, in the next Section we derive a number of exact results about the optimal efficiency anyway.

A.4 Optimal Strategy for Storage and Retrieval

In this Section, we derive several important results regarding the optimal strategy for maximizing the storage efficiency, the retrieval efficiency, and the combined (storage followed by retrieval) efficiency without making any more approximations.

It is convenient to first consider retrieval. Although we cannot, in general, analytically solve for the output field $\mathcal{E}_{\text{out}}(t)$, we will now show that the retrieval efficiency is

always $C/(1+C)$ independent of the detuning Δ and the control shape $\Omega(t)$ provided that no excitations are left in the atoms at $t = \infty$, i.e., $P(\infty) = 0$ and $S(\infty) = 0$. From Eqs. (A.10) and (A.11) and using $\mathcal{E}_{\text{in}}(t) = 0$, we find

$$\frac{d}{dt} (|P|^2 + |S|^2) = -2\gamma(1+C)|P|^2. \quad (\text{A.13})$$

Using this and Eqs. (A.8) and (A.9), the retrieval efficiency becomes

$$\eta_r = \frac{C}{1+C} (|S(T_r)|^2 + |P(T_r)|^2 - |S(\infty)|^2 - |P(\infty)|^2), \quad (\text{A.14})$$

which reduces to $C/(1+C)$ for $S(T_r) = 1$, $P(T_r) = P(\infty) = S(\infty) = 0$. The value of the retrieval error ($1 - \eta_r = 1/(1+C)$) and its independence from Δ and Ω follow directly from the branching ratio between the decay rates in Eq. (A.10) (or equivalently in Eq. (A.13)). The decay rate for P into undesired modes is γ , while the decay rate for P into the desired mode \mathcal{E}_{out} is γC . The retrieval efficiency, which is the ratio between the desired decay rate and the total decay rate, is, therefore, equal to $C/(1+C)$ independent of the control field.

We have thus shown that, provided our control pulse is sufficiently long and/or powerful to leave no excitations in the atoms (we will refer to this as complete retrieval), the retrieval efficiency is independent of Δ and $\Omega(t)$ and is always equal to $C/(1+C)$. Therefore, any control field is optimal for retrieval provided it pumps all excitations out of the system. Using this knowledge of the retrieval efficiency, in the remainder of this Section we will use a time-reversal argument to deduce the optimal storage strategy and the optimal storage efficiency. Here we will only give the essence of and the intuition behind the time-reversal argument, and leave the derivation to Secs. B.4 and B.5. In the remainder of the Appendix, we will independently confirm the validity of this argument in the adiabatic and fast limits.

Applied to the present situation, the essence of the time-reversal argument is as follows. Suppose one fixes the cooperativity parameter C and the detuning Δ and considers complete retrieval from the spin wave with a given control field $\Omega(t)$ into an output mode $\mathcal{E}_{\text{out}}(t)$ of duration T_{out} . According to the time-reversal argument, the efficiency for storing the time reverse of the output field ($\mathcal{E}_{\text{in}}(t) = \mathcal{E}_{\text{out}}^*(T_{\text{out}} - t)$) with $\Omega^*(T_{\text{out}} - t)$, the time reverse of the retrieval control field, into the spin wave is equal to the retrieval efficiency³. Although this claim is not trivial to prove (see Sec. B.4),

³To be more precise, such time-reversed storage stores into the complex conjugate of the original spin-wave mode. We study in Sec. B.8 how, for the case of nonzero energy difference ω_{sg} between states $|g\rangle$ and $|s\rangle$, the position-dependent phase $\exp(2iz\omega_{sg}/c)$, by which a given spin wave and its complex conjugate differ, reduces the optimal efficiency of storage followed by backward retrieval, where backward retrieval means that the retrieval and storage controls are counter-propagating. However, in the present Appendix, we assume that, for storage followed by retrieval, the k vectors of the storage and retrieval control fields are pointing in the same direction, in which case nonzero ω_{sg} is not a problem.

it is rather intuitive: since the retrieval procedure can be regarded as a generalized beam-splitter-like transformation (Sec. A.2), the equality of the two efficiencies is simply the statement that the probability of going from a given input port of the beam splitter to a given output port is equal to the probability of going backward from that output port to the original input port.

Therefore, the time-reversal argument shows that the maximum efficiencies for storage and storage followed by retrieval are $C/(1+C)$ (i.e., the retrieval efficiency) and $C^2/(1+C)^2$ (i.e., its square), respectively. Moreover, it says that these maximum efficiencies are obtained if the input field $\mathcal{E}_{\text{in}}(t)$ and the storage control field $\Omega(t)$ are such that $\Omega^*(T-t)$, i.e., the time reverse of $\Omega(t)$, retrieves the spin-wave excitation into the output mode $\mathcal{E}_{\text{out}}(t) = \mathcal{E}_{\text{in}}^*(T-t)$, i.e., the time reverse of $\mathcal{E}_{\text{in}}(t)$. In order to say for which input fields the optimal storage control $\Omega(t)$ can be found (or, equivalently, into which output fields a spin-wave excitation can be retrieved), we need to consider the limits, in which Eq. (A.12) can be fully solved analytically. These limits, adiabatic and fast, will be discussed in the following Sections.

A.5 Adiabatic Retrieval and Storage

A.5.1 Adiabatic Retrieval

In the previous Section, we have found, based on time reversal, the maximum storage efficiency and the scenario under which it can be achieved. Since the optimal storage into a given input mode requires the ability to carry out optimal retrieval into the time reverse of this mode, we will, in the following Sections (Secs. A.5 and A.6), solve Eq. (A.12) analytically in two important limits to find out which modes we can retrieve into and store optimally. The first such limit, which we will discuss in this Section (Sec. A.5), corresponds to smooth control and input fields, such that the term in the square brackets in Eq. (A.12) can be dropped. This “adiabatic” limit corresponds to an adiabatic elimination of P in Eq. (A.10). The precise conditions for this approximation will be discussed in Sec. A.5.3. In this Section, we discuss the retrieval process.

It is instructive to recognize that in the adiabatic approximation (i.e., with \dot{P} in Eq. (A.10) replaced with 0), if one uses rescaled variables $\mathcal{E}_{\text{in}}(t)/\Omega(t)$, $\mathcal{E}_{\text{out}}(t)/\Omega(t)$, and $P(t)/\Omega(t)$ and makes a change of variables $t \rightarrow h(T_r, t)$, where

$$h(t, t') = \int_t^{t'} |\Omega(t'')|^2 dt'', \quad (\text{A.15})$$

then Eqs. (A.9)-(A.11) become independent of Ω . Eqs. (A.9)-(A.11) can then be solved in this Ω -independent form, so that for any given Ω the solution in the original variables would follow by simple rescaling. However, since the equations are sufficiently simple and in order to avoid confusion introduced by additional notation, we will solve Eqs. (A.9)-(A.11) directly without making the change of variables.

To compute the output field during adiabatic retrieval, we assume for simplicity that retrieval begins at time $t = 0$ rather than at time $t = T_r$ and adiabatically eliminate P in Eqs. (A.10) and (A.11) (i.e., replace \dot{P} in Eq. (A.10) with zero) to obtain a first-order linear ordinary differential equation for S . Then, using $S(0) = 1$ and $\mathcal{E}_{\text{in}}(t) = 0$, we solve this equation to find

$$\mathcal{E}_{\text{out}}(t) = -\sqrt{2\gamma C} \frac{\Omega(t)}{\gamma(1+C) + i\Delta} e^{-\frac{1}{\gamma(1+C) + i\Delta} h(0,t)}. \quad (\text{A.16})$$

The t -dependent phase $ih(0,t)\Delta/(\gamma^2(1+C)^2 + \Delta^2)$ in the last factor is the ac Stark shift, which results in a shift of the output field frequency away from bare two-photon resonance. Computing the retrieval efficiency using Eq. (A.16), we find

$$\eta_r = \frac{C}{1+C} \left(1 - e^{-\frac{2\gamma(1+C)}{\gamma^2(1+C)^2 + \Delta^2} h(0,\infty)} \right), \quad (\text{A.17})$$

which is equal to $C/(1+C)$ provided the control pulse is sufficiently powerful and/or long to ensure that

$$\frac{2\gamma(1+C)}{\gamma^2(1+C)^2 + \Delta^2} h(0,\infty) \gg 1, \quad (\text{A.18})$$

which is the same as the condition $P(\infty) = S(\infty) = 0$. Note that adiabatic elimination did not affect the exact value of the efficiency and kept it independent of $\Omega(t)$ and Δ by preserving the branching ratio between the desired and undesired state transfers. Also note that, unlike the general argument in the previous Section, which assumed $P(\infty) = S(\infty) = 0$, Eq. (A.17) allows for the precise calculation of the retrieval efficiency for any $h(0,\infty)$.

As noted in Sec. A.1, two important subsets of the adiabatic limit, the resonant limit and the Raman limit, are often discussed in the literature. Although, as we show in this work, the basic physics based on the branching ratio and time-reversal arguments is shared by both of these approaches to quantum memory, a more detailed discussion of the physics behind them involves significant differences. In fact, prior to this work, the fact that the two approaches are in a sense equivalent was not recognized to our knowledge: only interesting similarities were pointed out [306, 307]. As an example of an important difference, the resonant and Raman limits give different dependences on C of the duration of the output pulse in Eq. (A.16):

$$T_{\text{out}} \sim \frac{\gamma^2 C^2 + \Delta^2}{\gamma C |\Omega|^2}, \quad (\text{A.19})$$

where we assumed $C \gtrsim 1$. In the resonant limit ($\gamma C \gg |\Delta|$), $T_{\text{out}} \sim \gamma C / |\Omega|^2$, while in the Raman limit ($\gamma C \ll |\Delta|$), $T_{\text{out}} \sim \Delta^2 / (\gamma C |\Omega|^2)$. It is worth emphasizing that the Raman limit condition is $\gamma C \ll |\Delta|$ and not $\gamma \ll |\Delta|$, as one may naively think by analogy with the single-atom case.

It follows from the concept of time reversal that the modes that can be stored optimally are the time reverses of the modes onto which a spin wave can be retrieved. We will now show that, in the adiabatic limit, at any given Δ and C , we can shape $\Omega(t)$ to retrieve onto any normalized mode $e(t)$. Integrating the norm squared of Eq. (A.16) with $\mathcal{E}_{\text{out}}(t) = \sqrt{C/(1+C)}e(t)$, we get

$$\int_0^t dt' |e(t')|^2 = 1 - e^{-\frac{2\gamma(1+C)h(0,t)}{\gamma^2(1+C)^2 + \Delta^2}}. \quad (\text{A.20})$$

Solving this equation for $h(0,t)$ and then taking the square root of its derivative with respect to t , we find $|\Omega(t)|$. Knowing $h(0,t)$, the phase of $\Omega(t)$ can be determined from Eq. (A.16). Putting the magnitude and the phase together, we have

$$\Omega(t) = -\frac{\gamma(1+C) + i\Delta}{\sqrt{2\gamma(1+C)}} \frac{e(t)}{\sqrt{\int_t^\infty |e(t')|^2 dt'}} e^{-i\frac{\Delta h(0,t)}{\gamma^2(1+C)^2 + \Delta^2}}, \quad (\text{A.21})$$

where $h(0,t)$ should be determined from Eq. (A.20). For any $e(t)$, this expression gives the control $\Omega(t)$ that retrieves the spin wave into that mode. The phase of $\Omega(t)$, up to an unimportant constant phase, is given by the phase of the desired output mode plus compensation for the Stark shift (the last factor). It is also worth noting that, up to a minus sign and a factor equal to the first fraction in Eq. (A.21), $\Omega(t)$ is simply equal to $e(t)/S(t)$.

We note that, if one wants to shape the retrieval into a mode $e(t)$ that drops to zero at some time T_{out} sufficiently rapidly, $|\Omega(t)|$ in Eq. (A.21) will go to ∞ at $t = T_{\text{out}}$. The infinite part can, however, be truncated without significantly affecting the efficiency or the precision of $e(t)$ generation. One can confirm that the loss in efficiency is small by inserting into the adiabatic solution in Eq. (A.17) a value of $h(0,\infty)$ that is finite but large enough to satisfy Eq. (A.18). One can similarly confirm that the generation of $e(t)$ can be precise with truncated control fields by using Eq. (A.16). However, to be completely certain that the truncation is harmless, one has to solve Eqs. (A.9)-(A.11) numerically without making the adiabatic approximation. We will do this in Sec. A.5.3 for the case of storage, where the same truncation issue is present.

We briefly mention that the spin-wave decay rate γ_s , which we have ignored so far, simply introduces a decay described by $\exp(-\gamma_s t)$ into Eq. (A.16) and, unless we retrieve much faster than $1/\gamma_s$, makes retrieval efficiency control dependent. With nonzero γ_s , we can still shape retrieval to go into any mode: we shape the control using Eq. (A.21) as if there were no γ_s decay except that the desired output mode $e(t)$ should be replaced with the normalized version of $e(t) \exp(\gamma_s t)$, i.e.,

$$e(t) \rightarrow e(t) e^{\gamma_s t} \left[\int_0^\infty dt' |e(t')|^2 e^{2\gamma_s t'} \right]^{-\frac{1}{2}}. \quad (\text{A.22})$$

The retrieval efficiency will, however, be output-mode-dependent in this case: it will be multiplied (and hence reduced) by $[\int_0^\infty dt' |e(t')|^2 \exp(2\gamma_s t')]^{-1}$.

A.5.2 Adiabatic Storage

In principle, using the solution for retrieval from the previous Section, the time-reversal argument of Sec. A.4 immediately guarantees that, provided we are in the adiabatic limit (conditions to be discussed in Sec. A.5.3), we can always shape the control field to store any input mode $\mathcal{E}_{\text{in}}(t)$ at any detuning Δ with the maximum efficiency $C/(1+C)$. However, for completeness, and to verify that the optimal storage control field is indeed the time reverse of the control field that retrieves into $\mathcal{E}_{\text{in}}^*(T-t)$, we give in this Section the solution to adiabatic storage.

In the adiabatic approximation, we use a procedure very similar to that used in the retrieval solution, to find

$$S(T) = \sqrt{\frac{C}{1+C}} \int_0^T dt f(t) \mathcal{E}_{\text{in}}(t), \quad (\text{A.23})$$

where

$$f(t) = -\frac{\Omega^*(t) \sqrt{2\gamma(1+C)}}{\gamma(1+C) + i\Delta} e^{-\frac{h(t,T)}{\gamma(1+C) + i\Delta}}. \quad (\text{A.24})$$

The storage efficiency is then

$$\eta_s = \frac{C}{1+C} \left| \int_0^T dt f(t) \mathcal{E}_{\text{in}}(t) \right|^2. \quad (\text{A.25})$$

We are interested in computing the control that maximizes η_s for a given $\mathcal{E}_{\text{in}}(t)$. We find in Sec. A.8.2 that the maximum storage efficiency is $C/(1+C)$ and that it can be achieved (in the adiabatic limit) for any Δ and $\mathcal{E}_{\text{in}}(t)$, and that the optimal control is

$$\Omega(t) = -\frac{\gamma(1+C) - i\Delta}{\sqrt{2\gamma(1+C)}} \frac{\mathcal{E}_{\text{in}}(t)}{\sqrt{\int_0^t |\mathcal{E}_{\text{in}}(t')|^2 dt'}} e^{i\frac{\Delta h(t,T)}{\gamma^2(1+C)^2 + \Delta^2}}, \quad (\text{A.26})$$

where $h(t, T)$ can be found by inserting Eq. (A.26) into Eq. (A.15). The phase of $\Omega(t)$, up to an unimportant constant phase, is thus given by the phase of the input mode plus compensation for the Stark shift (the last factor). As for the retrieval control discussed in the previous Section, we note that, although $|\Omega(t)|$ in Eq. (A.26) goes to ∞ at $t=0$, the infinite part can be truncated without significantly affecting the efficiency. This can be confirmed analytically using Eq. (A.25) provided the adiabatic limit is satisfied. We will also confirm this numerically in the next Section without making the adiabatic approximation.

As expected from the time-reversal argument, the optimal control we derived is just the time reverse ($\Omega(t) \rightarrow \Omega^*(T-t)$) of the control that retrieves into $\mathcal{E}_{\text{in}}^*(T-t)$, the time reverse of the input mode. We verify this in Sec. A.8.2.

Although optimal storage efficiencies are the same in the Raman and adiabatic limits, as in the case of retrieval, rather different physical behavior can be seen in the

two limits. It is now the dependence on C of the optimal control intensity (which can be found from Eq. (A.26)) that can be used to separate resonant and Raman behavior. Assuming for simplicity $C \gtrsim 1$, in the resonant limit ($\gamma C \gg |\Delta|$), $|\Omega| \sim \sqrt{\gamma C/T}$, while in the Raman limit ($\gamma C \ll |\Delta|$), $|\Omega| \sim |\Delta|/\sqrt{\gamma C T}$. Since complete retrieval and optimal storage are just time reverses of each other, it is not surprising that these relations are identical to the ones we derived for the dependence of output pulse duration on C in the previous Section. This opposite dependence of $|\Omega|$ on C in the Raman and EIT limits is, in fact, the signature of a simple physical fact: while the coupling of the input photon to the spin wave increases with increasing Ω in the Raman case, it effectively decreases in the EIT regime where a very large Ω will give a very wide transparency window and a group velocity equal to the speed of light. This is why as the cooperativity parameter changes, the control has to be adjusted differently in the two regimes.

As for retrieval, we briefly mention that nonzero γ_s simply introduces $\exp(-\gamma_s(T-t))$ decay into Eq. (A.24). The optimal storage control can still be found using Eq. (A.26) as if there were no decay, except that the input mode should be replaced with the normalized version of $\mathcal{E}_{\text{in}}(t) \exp(-\gamma_s(T-t))$, i.e.,

$$\mathcal{E}_{\text{in}}(t) \rightarrow \mathcal{E}_{\text{in}}(t) e^{-\gamma_s(T-t)} \left[\int_0^T dt' |\mathcal{E}_{\text{in}}(t')|^2 e^{-2\gamma_s(T-t')} \right]^{-\frac{1}{2}}. \quad (\text{A.27})$$

However, the optimal storage efficiency will now depend on input pulse duration and shape: it will be multiplied (and hence reduced) by $\int_0^T dt' |\mathcal{E}_{\text{in}}(t')|^2 \exp(-2\gamma_s(T-t'))$. It is important to note that with nonzero spin-wave decay the optimal storage efficiency of a particular input mode is no longer identical to the retrieval efficiency into its time reverse. This is not at variance with the time-reversal argument discussed in detail in Appendix B (which still applies when $\gamma_s \neq 0$), since the corresponding optimal storage and retrieval control shapes are no longer the time reverses of each other, and, in contrast to the $\gamma_s = 0$ case, the retrieval efficiency is now control dependent. Finally, we note that, when we consider storage followed by retrieval, in order to take into account the spin-wave decay during the storage time $[T, T_r]$, one should just multiply the total efficiency by $\exp(-2\gamma_s(T_r - T))$.

A.5.3 Adiabaticity Conditions

We have found that, provided we are in the adiabatic limit, any input mode can be stored optimally. In this Section we show that, independent of Δ , the sufficient and necessary condition for optimal adiabatic storage of a pulse of duration T to be consistent with the adiabatic approximation is $TC\gamma \gg 1$.

To find the conditions for the adiabatic elimination of P in Eq. (A.10), we do the

elimination and then require its consistency by enforcing⁴

$$|\dot{P}| \ll |(\gamma C + i\Delta)P| \quad (\text{A.28})$$

(we assume for simplicity throughout this Section that $C \gtrsim 1$). During retrieval, sufficient conditions for Eq. (A.28) are

$$|\Omega| \ll |\gamma C + i\Delta|, \quad (\text{A.29})$$

$$\left| \frac{\dot{\Omega}}{\Omega} \right| \ll |\gamma C + i\Delta|, \quad (\text{A.30})$$

which limit, respectively, the power and the bandwidth of the control pulse. These are easily satisfied in practice by using sufficiently weak and smooth retrieval control pulses.

During storage, the satisfaction of Eq. (A.28) requires, in addition to conditions (A.29) and (A.30), the satisfaction of

$$\left| \frac{\dot{\mathcal{E}}_{\text{in}}}{\mathcal{E}_{\text{in}}} \right| \ll |\gamma C + i\Delta|, \quad (\text{A.31})$$

which limits the bandwidth of the input pulse. In particular, for a smooth input pulse of duration T , this condition is implied by

$$TC\gamma \gg 1. \quad (\text{A.32})$$

Let us now show that for optimal storage, the condition (A.32) also implies conditions (A.29) and (A.30) and is thus the only required adiabaticity condition (provided \mathcal{E}_{in} is smooth). Application of Eq. (A.26) reduces Eq. (A.29) to Eq. (A.32). Equation (A.30), in turn, reduces to the conditions on how fast the magnitude $|\Omega|$ and the phase ϕ (which compensates for the Stark shift) of the control can change:

$$\left| \frac{\frac{d}{dt}|\Omega|}{|\Omega|} \right|, \left| \dot{\phi} \right| \ll |\gamma C + i\Delta|, \quad (\text{A.33})$$

where $\Omega = |\Omega| \exp(i\phi)$. Application of Eq. (A.26) shows that Eq. (A.32) implies Eq. (A.33).

⁴To be precise, another condition in addition to Eq. (A.28) required for the validity of the adiabatic elimination is that $P(0)$ derived from adiabatic elimination must be much less than 1, so that it is close to the given value of $P(0) = 0$. During retrieval, this condition, however, is equivalent to condition (A.29) evaluated at $t = 0$. Similarly, during storage of a sufficiently smooth pulse (which will, thus, satisfy $\mathcal{E}_{\text{in}}(0) \lesssim 1/\sqrt{T}$), the desired condition on the adiabatic value of $P(0)$ is implied by condition (A.32). Thus, we do not state this condition on the adiabatic value of $P(0)$ separately.

We have thus shown that $TC\gamma \gg 1$ is a sufficient condition for the validity of adiabatic elimination in optimal storage. But, in fact, from the amplitude of the optimal storage control field (Eq. (A.26)), one can see that Eq. (A.29) implies that $TC\gamma \gg 1$ is also a necessary condition for the validity of adiabatic elimination in optimal storage. (To show that $TC\gamma \gg 1$ is a necessary condition, one also has to use the extra condition⁵ on the adiabatic value of $P(0)$ to rule out the special situation when $\Omega(t)$ is such that Eq. (A.28) is satisfied but Eq. (A.29) is not.)

To verify the adiabaticity condition in Eq. (A.32) and investigate the breakdown of adiabaticity for short input pulses, we consider a Gaussian-like input mode (shown in Fig. B.3)

$$\mathcal{E}_{\text{in}}(t) = A(e^{-30(t/T-0.5)^2} - e^{-7.5})/\sqrt{T}, \quad (\text{A.34})$$

where for computational convenience we have required $\mathcal{E}_{\text{in}}(0) = \mathcal{E}_{\text{in}}(T) = 0$ and where $A \approx 2.09$ is a normalization constant. We fix the cooperativity parameter C , the detuning Δ , and the pulse duration T , and use Eq. (A.26) to shape the control field. We then use Eqs. (A.10) and (A.11) *without* the adiabatic approximation to calculate numerically the actual storage efficiency that this control field gives, and multiply it by the control-independent retrieval efficiency $C/(1+C)$, to get the total efficiency of storage followed by retrieval. As we decrease T , we expect this efficiency to fall below $(C/(1+C))^2$ once $TC\gamma \gg 1$ is no longer satisfied. And indeed in Fig. A.2(a) we observe this behavior for $\Delta = 0$ and $C = 1, 10, 100, 1000$. In Fig. A.2(b), we fix $C = 10$ and show how optimal adiabatic storage breaks down at different detunings Δ from 0 to 1000γ . From Fig. A.2(b), we see that, as we move from the resonant limit ($C\gamma \gg |\Delta|$) to the Raman limit ($C\gamma \ll |\Delta|$), we can go to slightly smaller values of $TC\gamma$ before storage breaks down. However, since the curves for $\Delta = 100\gamma$ and $\Delta = 1000\gamma$ almost coincide, it is clear that $TC\gamma \gg 1$ is still the relevant condition no matter how large Δ is, which must be the case since the condition (A.29) breaks down for shorter T . The most likely reason why in the Raman limit adiabaticity is slightly easier to satisfy is because in the Raman limit it is only condition (A.29) that reduces to $TC\gamma \gg 1$, while conditions (A.30) and (A.31) reduce to $T\Delta \gg 1$, which is weaker than $TC\gamma \gg 1$ (since $\Delta \gg C\gamma$ in the Raman limit). In the resonant limit, in contrast, all three conditions (A.29)-(A.31) reduce to $TC\gamma \gg 1$.

Before turning to the discussion of fast retrieval and storage, we note that the use of Eq. (A.26) to calculate the storage control fields for Fig. A.2 resulted in a control field $\Omega(t)$ whose magnitude went to ∞ at $t = 0$, as predicted in the previous Section. To generate Fig. A.2, the optimal $|\Omega(t)|$ were therefore cut off for $t < T/100$ to take the value $|\Omega(T/100)|$. The fact that the optimal efficiency of $(C/(1+C))^2$ represented by the dashed lines in Fig. A.2 is still achieved by the dotted curves, despite the use of truncated controls, proves that truncation of the storage control does not significantly affect the storage efficiency. Since the retrieval field generation

⁵See the footnote corresponding to Eq. (A.28).

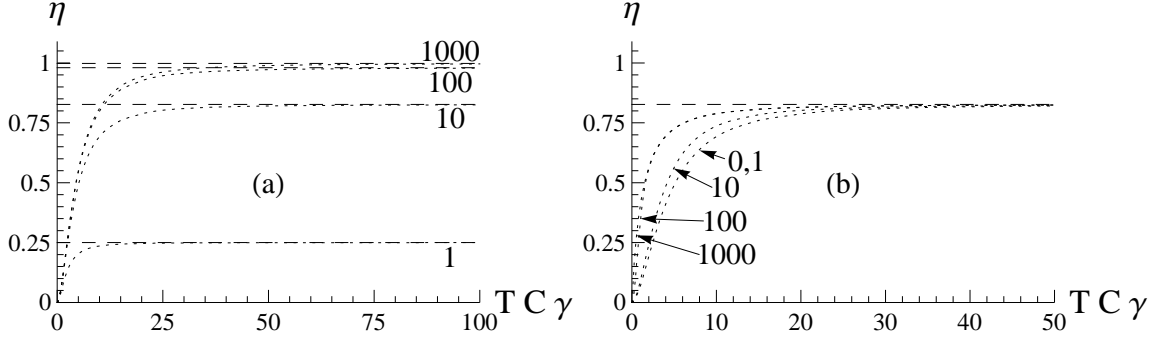


Figure A.2: Breakdown of optimal adiabatic storage in a cavity at $TC\gamma \lesssim 10$. In (a), the total efficiency of storage followed by retrieval is plotted for $\Delta = 0$ and $C = 1, 10, 100$, and 1000 . The horizontal dashed lines are the maximal values $(C/(1+C))^2$. Dotted lines are obtained for the input from Eq. (A.34) using adiabatic Eq. (A.26) to shape the storage control but then using exact Eqs. (A.10) and (A.11) to numerically compute the efficiency. In (b), the same plot is made for $C = 10$ and $\Delta/\gamma = 0, 1, 10, 100$, and 1000 .

is directly related to optimal storage by time reversal, as explained in Sec. A.4, this also means that truncating retrieval controls does not significantly affect the precision with which a given retrieval mode $e(t)$ can be generated. The losses associated with truncation are insignificant only if the conditions in Eq. (A.18) and Eq. (A.62) are still satisfied for the truncated retrieval and storage control fields, respectively. If the limit on the control pulse energy is so tight that these conditions are not satisfied, a separate optimization problem, which is beyond the scope of the present Appendix, has to be solved.

A.6 Fast Retrieval and Storage

We have shown that adiabatic storage allows us to store optimally a mode of duration T , having any smooth shape and any detuning Δ , provided that the adiabaticity condition $TC\gamma \gg 1$ is satisfied. In this Section we solve Eq. (A.12) analytically in the second important limit, the so-called “fast” limit, and show that this limit allows for optimal storage of a certain class of input modes of duration $T \sim 1/(C\gamma)$.

The fast limit corresponds to the situation when Ω is very large during a short control pulse ($|\Omega| \gg C\gamma$ and $|\Omega| \gg |\Delta|$), so that we can neglect all terms in Eq. (A.12) except $|\Omega|^2 S$ and \ddot{S} . This corresponds to keeping only terms containing Ω on the right-hand side of Eqs. (A.10) and (A.11) and results in undamped Rabi oscillations between optical and spin polarizations P and S . One can use this limit to implement a “fast” storage scheme, in which the input pulse is resonant ($\Delta = 0$) and the control pulse is

a short π pulse at $t = T$, as well as fast retrieval, in which the control is a π -pulse at $t = T_r$. Provided the π pulse is applied on resonance and at approximately constant intensity, the condition for perfect π pulse performance is $|\Omega| \gg C\gamma$ (assuming $C \gtrsim 1$). To fully describe these processes, we furthermore need to solve Eq. (A.12) while the control is off, which can also be done analytically.

During fast retrieval, assuming the π pulse takes place at time $t = 0$ instead of time $t = T_r$ and assuming the π pulse is perfect, the initial $S = 1$ results after the π pulse in $P = i$. We then solve for $P(t)$ from Eq. (A.10) and insert the solution into Eq. (A.9) to obtain

$$\mathcal{E}_{\text{out}}(t) = -\sqrt{2\gamma C}e^{-\gamma(1+C)t}. \quad (\text{A.35})$$

Consistent with the general expression in Eq. (A.14) and the branching ratio argument in Sec. A.4, the retrieval efficiency is again $C/(1+C)$.

An alternative explanation for why the fast retrieval gives the same retrieval efficiency as the adiabatic retrieval is that, thanks to the adiabatic elimination of P , the adiabatic limit effectively describes a two-level system. Therefore, Eq. (A.35) is in fact a special case of Eq. (A.16) with

$$\Omega(t) = (\gamma(1+C) + i\Delta)e^{-i\Delta t}. \quad (\text{A.36})$$

Although, at this $\Omega(t)$, Eq. (A.16) is not a good approximation to the actual output field because, for example, condition (A.29) is not satisfied, this illustrates the equivalence of the two approaches.

Since the control field in fast retrieval is not adjustable (it is always a perfect π pulse), fast retrieval gives only one possible output mode, that of Eq. (A.35). By time reversal, the time reverse of this mode of duration $T \sim 1/(\gamma C)$ is thus the only mode that can be optimally stored (with efficiency $C/(1+C)$) using fast storage at this C .

For completeness and to confirm the time-reversal argument, the optimal input mode for fast storage can also be calculated directly. For an input mode $\mathcal{E}_{\text{in}}(t)$ that comes in from $t = 0$ to $t = T$, assuming a perfect π pulse at $t = T$, we find by a method similar to the one used in fast retrieval that

$$S(T) = \sqrt{\frac{C}{1+C}} \int_0^T dt f(t) \mathcal{E}_{\text{in}}(t), \quad (\text{A.37})$$

where

$$f(t) = -e^{\gamma(1+C)(t-T)} \sqrt{2(1+C)\gamma}. \quad (\text{A.38})$$

Similarly to retrieval, Eq. (A.38) is a special case of Eq. (A.24) with $\Omega(t) = (\gamma(1+C) - i\Delta) \exp(i\Delta(T-t))$ (the time reverse of the right-hand side of Eq. (A.36)). Since $f(t)$ is real and normalized according to $\int_0^T f(t)^2 dt = 1$, this integral is a scalar product similar to Eq. (A.25) discussed in Sec. A.8.2, and the optimal fast storage efficiency of $C/(1+C)$ is achieved for a single input mode $\mathcal{E}_{\text{in}}(t) = f(t)$ (up to an arbitrary

overall unimportant phase). This optimal $\mathcal{E}_{\text{in}}(t)$ is precisely the (renormalized) time reverse of the output of fast readout in Eq. (A.35), as expected by time reversal.

Two comments are in order regarding the optimal input pulse $\mathcal{E}_{\text{in}}(t) = f(t)$. First, we would like to note that short exponentially varying pulses, as in our optimal solution $\mathcal{E}_{\text{in}}(t) = f(t)$, have been proposed before to achieve efficient photon-echo-based storage [317, 318]. Second, it is worth noting that, although $\mathcal{E}_{\text{in}}(t) = f(t)$ gives the optimal storage, generating such short exponentially rising pulses may in practice be hard for high C . Since the efficiency is given by the overlap of $\mathcal{E}_{\text{in}}(t)$ with $f(t)$ (see Eq. (A.37)), fast storage in a cavity is inferior in this respect to fast storage in free space, because in the latter case any input pulse satisfying $T\gamma \ll 1$ and $dT\gamma \gg 1$ results in storage efficiency close to unity (see Appendix B).

A.7 Summary

In conclusion, we have treated in detail the storage and retrieval of photons in homogeneously broadened Λ -type atomic media enclosed in a running-wave cavity in the bad-cavity limit. We have shown that, provided that no excitations are left in the atoms at the end of the retrieval process, the retrieval efficiency is independent of the control and the detuning and is equal to $C/(1+C)$. We have also derived the optimal strategy for storage in the adiabatic and fast limits and, therefore, demonstrated that one can store, with the optimal efficiency of $C/(1+C)$, any smooth input mode satisfying $TC\gamma \gg 1$ and having any detuning Δ and a certain class of resonant input modes satisfying $TC\gamma \sim 1$. We have also noted that the optimal storage control field for a given input mode is the time reverse of the control field that accomplishes retrieval into the time reverse of this input mode. This fact and the equality of maximum storage efficiency and the retrieval efficiency are, in fact, the consequence of a general time-reversal argument to be presented in detail in Appendix B. In Appendix B, we will also present the full discussion of photon storage in homogeneously broadened Λ -type atomic media in free space, while in Appendix C, we will consider the effects of inhomogeneous broadening on photon storage.

Finally, it is important to note that, to achieve the optimal efficiencies derived in the present Appendix, it is necessary to have rigid temporal synchronization between the input pulse and the storage control pulse, which may become difficult in practice for short input pulses. In fact, since there is only one accessible atomic mode in the case of homogeneously broadened media enclosed in a cavity (unless one varies the angle between the control and the input [288]), this temporal synchronization is necessary to obtain high efficiencies even if the cooperativity parameter is very large. This problem can, however, be alleviated whenever multiple atomic modes are accessible, which is the case for homogeneously broadened media in free space considered in Appendix B and for inhomogeneously broadened media considered in Appendix C. In those cases, infinite optical depth allows one to achieve unit efficiency

without rigid synchronization. However, despite this disadvantage of the cavity setup, we will discuss in Appendix B that the cavity setup is superior to the free-space setup in other respects, such as the enhancement of the optical depth by the cavity finesse and the avoidance of the unfavorable scaling of the error as $1/\sqrt{N}$ (vs $1/C \propto 1/N$), which sometimes occurs in the free-space model.

A.8 Omitted Details

In the preceding Sections of this Appendix, to allow for a smoother presentation, we omitted some of the details. We present them in this Section.

A.8.1 Details of the Model and the Derivation of the Equations of Motion

In Sec. A.3, we gave a brief introduction to the model and presented the equations of motion without derivation. In this Section, the details of the model and the derivation of the equations of motion (A.3)-(A.5) are provided.

The electric-field vector operator for the cavity field is given by

$$\hat{\mathbf{E}}_1(z) = \epsilon_1 \left(\frac{\hbar\omega_1}{2\epsilon_0 V} \right)^{1/2} (\hat{a}e^{i\omega_1 z/c} + \hat{a}^\dagger e^{-i\omega_1 z/c}), \quad (\text{A.39})$$

where \hat{a}^\dagger is the mode creation operator, ω_1 is the mode frequency, ϵ_1 is the polarization unit vector, ϵ_0 is the permittivity of free space, V is the quantization volume for the field, and c is the speed of light.

The copropagating single-mode classical plane-wave control field with frequency ω_2 is described by an electric-field vector

$$\mathbf{E}_2(z, t) = \epsilon_2 \mathcal{E}_2(t) \cos(\omega_2(t - z/c)), \quad (\text{A.40})$$

where ϵ_2 is the polarization unit vector, and $\mathcal{E}_2(t)$ is the amplitude. Then, using the dipole and rotating-wave approximations, the Hamiltonian is

$$\hat{H} = \hat{H}_0 + \hat{V}, \quad (\text{A.41})$$

$$\hat{H}_0 = \hbar\omega_1 \hat{a}^\dagger \hat{a} + \sum_{i=1}^N (\hbar\omega_{sg} \hat{\sigma}_{ss}^i + \hbar\omega_{eg} \hat{\sigma}_{ee}^i), \quad (\text{A.42})$$

$$\begin{aligned} \hat{V} &= - \sum_{i=1}^N \hat{\mathbf{d}}_i \cdot (\mathbf{E}_2(z_i, t) + \hat{\mathbf{E}}_1(z_i)) \\ &= -\hbar \sum_{i=1}^N (\Omega(t) \hat{\sigma}_{es}^i e^{-i\omega_2(t-z_i/c)} + \hat{a} g e^{i\omega_1 z_i/c} \hat{\sigma}_{eg}^i) + \text{h.c.} \end{aligned} \quad (\text{A.43})$$

Here h.c. stands for Hermitian conjugate, $\hat{\sigma}_{\mu\nu}^i = |\mu\rangle_i\langle\nu|$ is the internal state operator of the i th atom between states $|\mu\rangle$ and $|\nu\rangle$, z_i is the position of the i th atom, $\hat{\mathbf{d}}_i$ is the dipole moment vector operator for the i th atom, $\Omega(t) = {}_i\langle e | (\hat{\mathbf{d}}_i \cdot \boldsymbol{\epsilon}_2) | s \rangle_i \mathcal{E}_2(t) / (2\hbar)$ (assumed to be equal for all i) is the Rabi frequency of the classical field, and $g = {}_i\langle e | (\hat{\mathbf{d}}_i \cdot \boldsymbol{\epsilon}_1) | g \rangle_i \sqrt{\frac{\omega_1}{2\hbar\epsilon_0 V}}$ (assumed to be real for simplicity and equal for all i) is the coupling constant between the atoms and the quantized field mode. We note that, in order to avoid carrying extra factors of 2 around, Ω is defined as half of the traditional definition of the Rabi frequency, so that a π pulse, for example, takes time $\pi/(2\Omega)$.

In the Heisenberg picture, we introduce slowly varying collective atomic operators

$$\hat{\sigma}_{\mu\mu} = \sum_i \hat{\sigma}_{\mu\mu}^i, \quad (\text{A.44})$$

$$\hat{\sigma}_{es} = \sum_i \hat{\sigma}_{es}^i e^{-i\omega_2(t-z_i/c)}, \quad (\text{A.45})$$

$$\hat{\sigma}_{eg} = \sum_i \hat{\sigma}_{eg}^i e^{-i\omega_1(t-z_i/c)}, \quad (\text{A.46})$$

$$\hat{\sigma}_{sg} = \sum_i \hat{\sigma}_{sg}^i e^{-i(\omega_1-\omega_2)(t-z_i/c)}, \quad (\text{A.47})$$

and a slowly varying cavity mode annihilation operator

$$\hat{\mathcal{E}} = \hat{a}e^{i\omega_1 t}, \quad (\text{A.48})$$

which satisfy same-time commutation relations

$$[\hat{\sigma}_{\mu\nu}(t), \hat{\sigma}_{\alpha\beta}(t)] = \delta_{\nu\alpha} \hat{\sigma}_{\mu\beta}(t) - \delta_{\mu\beta} \hat{\sigma}_{\alpha\nu}(t), \quad (\text{A.49})$$

$$[\hat{\mathcal{E}}(t), \hat{\mathcal{E}}^\dagger(t)] = 1, \quad (\text{A.50})$$

and yield an effective rotating frame Hamiltonian

$$\hat{H} = \hbar\Delta\hat{\sigma}_{ee} - (\hbar\Omega(t)\hat{\sigma}_{es} + \hbar g\hat{\mathcal{E}}\hat{\sigma}_{eg} + h.c.). \quad (\text{A.51})$$

The equations of motion are then given by

$$\begin{aligned} \dot{\hat{\mathcal{E}}} &= -\kappa\hat{\mathcal{E}} + ig\hat{\sigma}_{ge} + \sqrt{2\kappa}\hat{\mathcal{E}}_{\text{in}}, \\ \dot{\hat{\sigma}}_{gg} &= \gamma_{\text{eg}}\hat{\sigma}_{ee} - ig\hat{\mathcal{E}}\hat{\sigma}_{eg} + ig\hat{\mathcal{E}}^\dagger\hat{\sigma}_{ge} + \hat{F}_{gg}, \\ \dot{\hat{\sigma}}_{ss} &= \gamma_{\text{es}}\hat{\sigma}_{ee} - i\Omega\hat{\sigma}_{es} + i\Omega^*\hat{\sigma}_{se} + \hat{F}_{ss}, \\ \dot{\hat{\sigma}}_{ee} &= -\gamma_e\hat{\sigma}_{ee} + i\Omega\hat{\sigma}_{es} - i\Omega^*\hat{\sigma}_{se} + ig\hat{\mathcal{E}}\hat{\sigma}_{eg} - ig\hat{\mathcal{E}}^\dagger\hat{\sigma}_{ge} + \hat{F}_{ee}, \\ \dot{\hat{\sigma}}_{ge} &= -(\gamma + i\Delta)\hat{\sigma}_{ge} + i\Omega\hat{\sigma}_{gs} + ig\hat{\mathcal{E}}(\hat{\sigma}_{gg} - \hat{\sigma}_{ee}) + \hat{F}_{ge}, \\ \dot{\hat{\sigma}}_{es} &= -(\gamma' - i\Delta)\hat{\sigma}_{es} + i\Omega^*(\hat{\sigma}_{ee} - \hat{\sigma}_{ss}) - ig\hat{\mathcal{E}}^\dagger\hat{\sigma}_{gs} + \hat{F}_{es}, \\ \dot{\hat{\sigma}}_{gs} &= -\gamma_s\hat{\sigma}_{gs} + i\Omega^*\hat{\sigma}_{ge} - ig\hat{\mathcal{E}}\hat{\sigma}_{es} + \hat{F}_{gs}, \end{aligned} \quad (\text{A.52})$$

with the input-output relation for the quantum field given by Eq. (A.2).

In Eqs. (A.52) we have introduced decay, which, in turn, necessitated the introduction of Langevin noise operators $\hat{F}_{\mu\nu}$ for the atomic operators and the input field $\hat{\mathcal{E}}_{\text{in}}$ for the quantum field. The radiative decay rate of the excited state $|e\rangle$ is $\gamma_e = \gamma_{es} + \gamma_{eg}$, the sum of decay rates into $|s\rangle$ and into $|g\rangle$. The decay rate of optical coherence $\hat{\sigma}_{ge}$ is $\gamma = \gamma_e/2 + \gamma_{\text{deph}}$ where, in addition to radiative decay, we allow for extra dephasing, such as, for example, that caused by collisions with buffer gas atoms in warm vapor cells. Similarly, the decay rate $\gamma' = \gamma_e/2 + \gamma'_{\text{deph}}$ of $\hat{\sigma}_{es}$ allows for possible extra dephasing, while the decay rate γ_s of $\hat{\sigma}_{gs}$ is due to dephasing only. In some experiments [80], γ_s comes from the transverse diffusion of atoms out of the region defined by the quantized light mode. In these cases, the decay of $\hat{\sigma}_{gs}$ will be accompanied by population redistribution between states $|g\rangle$ and $|s\rangle$. In order to ensure that the corresponding incoming noise is vacuum (which our analysis requires, as we explain below and in Sec. A.2), we will assume in such cases that the incoming atoms are fully pumped into the level $|g\rangle$, which would correspond to a $2\gamma_s$ decay rate of $\hat{\sigma}_{ss}$ into $\hat{\sigma}_{gg}$ (not included in Eqs. (A.52) since it does not affect the final equations). This is indeed the case if, as in Ref. [80], the control beam diameter is much greater than the diameter of the quantized light mode.

Assuming that almost all atoms are in the ground state at all times ($\hat{\sigma}_{gg} \approx N$ and $\hat{\sigma}_{ss} \approx \hat{\sigma}_{ee} \approx \hat{\sigma}_{es} \approx 0$), defining polarization $\hat{P} = \hat{\sigma}_{ge}/\sqrt{N}$ and spin wave $\hat{S} = \hat{\sigma}_{gs}/\sqrt{N}$, and working to first order in $\hat{\mathcal{E}}$, we obtain Eqs. (A.3)-(A.5), where $\hat{F}_P = \hat{F}_{ge}/\sqrt{2\gamma N}$ and $\hat{F}_S = \hat{F}_{gs}/\sqrt{2\gamma_s N}$.

Using the generalized Einstein relations [319, 320]

$$\langle \hat{F}_{\mu\nu}(t) \hat{F}_{\alpha\beta}(t') \rangle = \langle D(\hat{\sigma}_{\mu\nu} \hat{\sigma}_{\alpha\beta}) - D(\hat{\sigma}_{\mu\nu}) \hat{\sigma}_{\alpha\beta} - \hat{\sigma}_{\mu\nu} D(\hat{\sigma}_{\alpha\beta}) \rangle \delta(t - t'), \quad (\text{A.53})$$

where $D(\hat{\sigma}_{\mu\nu})$ denotes the deterministic part (i.e., with noise omitted) of the equation for $\hat{\sigma}_{\mu\nu}$ in Eqs. (A.52), and again using the approximation that almost all atoms are in the ground state, we find that the only nonzero noise correlations between \hat{F}_P , \hat{F}_S , \hat{F}_P^\dagger , and \hat{F}_S^\dagger are

$$\langle \hat{F}_P(t) \hat{F}_P^\dagger(t') \rangle = \langle \hat{F}_S(t) \hat{F}_S^\dagger(t') \rangle = \delta(t - t'). \quad (\text{A.54})$$

The fact that normally ordered correlations are zero means that the incoming noise is vacuum, which is precisely the reason why, as noted in Sec. A.2, efficiency is the only number we need in order to fully characterize the mapping. The property of Eqs. (A.52) that guarantees that the incoming noise is vacuum is the absence of decay out of state $|g\rangle$ into states $|e\rangle$ and $|s\rangle$. The decay into state $|e\rangle$ does not happen because the energy of an optical transition (on the order of 10^4 K) is much greater than the temperature, at which typical experiments are done. In contrast, the energy of the $|s\rangle - |g\rangle$ transition in some experiments, such as the one in Ref. [80], may be smaller than the temperature. However, the $|s\rangle - |g\rangle$ transition is typically not dipole allowed, so that the rate of $|g\rangle$ decay into $|s\rangle$ can be neglected, as well. As noted above, for the case when atoms are diffusing in and out of the quantized

light mode, to keep the decay rate of $|g\rangle$ zero, we assume that the incoming atoms are fully pumped into $|g\rangle$.

From Eq. (A.49) and with the usual $\hat{\sigma}_{gg} \approx N$ assumption, we have

$$\left[\hat{S}(t), \hat{S}^\dagger(t) \right] = 1, \quad (\text{A.55})$$

$$\left[\hat{P}(t), \hat{P}^\dagger(t) \right] = 1. \quad (\text{A.56})$$

In particular, this means that \hat{S} can be thought of as an annihilation operator for the spin-wave mode, into which we would like to store the state of the incoming photon mode.

The input and output fields, which propagate freely outside of the cavity, satisfy [316]

$$\left[\hat{\mathcal{E}}_{\text{in}}(t), \hat{\mathcal{E}}_{\text{in}}^\dagger(t') \right] = \left[\hat{\mathcal{E}}_{\text{out}}(t), \hat{\mathcal{E}}_{\text{out}}^\dagger(t') \right] = \delta(t - t') \quad (\text{A.57})$$

and can be expanded in terms of any orthonormal set of field (envelope) modes $\{h_\alpha(t)\}$ defined for $t \in [0, \infty)$, satisfying the orthonormality relation $\int_0^\infty dt h_\alpha^*(t) h_\beta(t) = \delta_{\alpha\beta}$ and completeness relation $\sum_\alpha h_\alpha^*(t) h_\alpha(t') = \delta(t - t')$, as

$$\hat{\mathcal{E}}_{\text{in}}(t) = \sum_\alpha h_\alpha(t) \hat{a}_\alpha, \quad (\text{A.58})$$

$$\hat{\mathcal{E}}_{\text{out}}(t) = \sum_\alpha h_\alpha(t) \hat{b}_\alpha, \quad (\text{A.59})$$

where annihilation operators $\{\hat{a}_\alpha\}$ and $\{\hat{b}_\alpha\}$ for the input and the output photon modes, respectively, satisfy

$$\left[\hat{a}_\alpha, \hat{a}_\beta^\dagger \right] = \left[\hat{b}_\alpha, \hat{b}_\beta^\dagger \right] = \delta_{\alpha\beta}. \quad (\text{A.60})$$

Repeating for clarity the setup from Sec. A.3, we recall that all atoms are initially pumped into the ground state, i.e., no \hat{P} or \hat{S} excitations are present in the atoms. We also assume that the only input field excitations initially present are in the quantum field mode with annihilation operator \hat{a}_0 and envelope shape $h_0(t)$ nonzero on $[0, T]$. The goal is to store the state of this mode into \hat{S} and at a time $T_r > T$ retrieve it back onto a field mode. During storage, we can, in principle, solve the operator Eqs. (A.3)-(A.5) for $\hat{S}(T)$ as some linear functional of $\hat{\mathcal{E}}_{\text{in}}(t)$, $\hat{F}_P(t)$, $\hat{F}_S(t)$, $\hat{S}(0)$, and $\hat{P}(0)$. The storage efficiency is then given by

$$\eta_s = \frac{\text{(number of stored excitations)}}{\text{(number of incoming photons)}} = \frac{\langle \hat{S}^\dagger(T) \hat{S}(T) \rangle}{\int_0^T dt \langle \hat{\mathcal{E}}_{\text{in}}^\dagger(t) \hat{\mathcal{E}}_{\text{in}}(t) \rangle}. \quad (\text{A.61})$$

Since $\hat{S}(0)$ and $\hat{P}(0)$ give zero when acting on the initial state, and since all normally ordered noise correlations are zero, only the term in $\hat{S}(T)$ containing $\hat{\mathcal{E}}_{\text{in}}(t)$ will contribute to the efficiency. Moreover, $h_0(t)\hat{a}_0$ is the only part of $\hat{\mathcal{E}}_{\text{in}}(t)$ that does not give

zero when acting on the initial state. Thus, for the purposes of finding the storage efficiency, we can ignore \hat{F}_P and \hat{F}_S in Eqs. (A.3)-(A.5) and treat these equations as complex number equations with $P(0) = 0$, $S(0) = 0$, and $\mathcal{E}_{\text{in}}(t) = h_0(t)$. We have here dropped the carets on the operators to denote their complex number representations. To get back the nonvacuum part of the original operator from its complex number counterpart, we should just multiply the complex number version by \hat{a}_0 .

Similarly, during retrieval, we can ignore $\hat{F}_P(t)$ and $\hat{F}_S(t)$ and can treat Eqs. (A.3)-(A.5) as complex number equations with the initial and boundary conditions given in Sec. A.3.

A.8.2 Shaping the Control Field for the Optimal Adiabatic Storage

In this Section, we present the derivation of Eq. (A.26), which gives the optimal storage control field during adiabatic storage. We then verify that this optimal control is just the time reverse of the control that retrieves into the time reverse of the input mode.

To solve for the control field $\Omega(t)$ that maximizes the storage efficiency η_s in Eq. (A.25), we note that $f(t)$ defined in Eq. (A.24) satisfies $\int_0^T |f(t)|^2 dt \leq 1$, with the equality achieved when

$$\frac{2\gamma(1+C)}{\gamma^2(1+C)^2 + \Delta^2} h(0, T) \gg 1, \quad (\text{A.62})$$

which is equivalent to the requirement we had in Eq. (A.18) for complete retrieval. Since we also have $\int_0^T |\mathcal{E}_{\text{in}}(t)|^2 = 1$, the integral in Eq. (A.25) can be seen as a simple scalar product between states, and the efficiency is therefore $\eta_s \leq C/(1+C)$ with the equality achieved when (up to an undefined overall unimportant phase)

$$f(t) = \mathcal{E}_{\text{in}}^*(t). \quad (\text{A.63})$$

We will now show that, for any given $\mathcal{E}_{\text{in}}(t)$, Δ , and C , there is a unique control that satisfies Eq. (A.63) and thus gives the maximum storage efficiency $C/(1+C)$. In Refs. [154, 321], this control was found through a quantum impedance matching Bernoulli equation obtained by differentiating Eq. (A.63). In order to be able in Appendix B to generalize more easily to free space, we will solve Eq. (A.63) directly. To do this, we follow a procedure very similar to that in Sec. A.5.1. We integrate the norm squared of Eq. (A.63) from 0 to t to get

$$\int_0^t |\mathcal{E}_{\text{in}}(t')|^2 dt' = e^{-\frac{2h(t,T)\gamma(1+C)}{\gamma^2(1+C)^2 + \Delta^2}} - e^{-\frac{2h(0,T)\gamma(1+C)}{\gamma^2(1+C)^2 + \Delta^2}}. \quad (\text{A.64})$$

Since $h(T, T) = 0$, the normalization of $\mathcal{E}_{\text{in}}(t)$ requires the satisfaction of Eq. (A.62). Assuming it is satisfied to the desired precision, we solve Eq. (A.64) for $h(t, T)$, and

then taking the square root of the negative of its derivative with respect to t , we find $|\Omega(t)|$. Knowing $h(t, T)$, the phase of $\Omega(t)$ can then be determined from Eq. (A.63). Putting the magnitude and the phase together, we obtain the expression for the optimal control given in Eq. (A.26).

We will now show that, as expected from the time-reversal argument, the optimal control we derived is just the time reverse ($\Omega(t) \rightarrow \Omega^*(T - t)$) of the control that retrieves into $\mathcal{E}_{\text{in}}^*(T - t)$, the time reverse of the input mode. To see this, we note that from Eq. (A.20) it follows that the magnitude of the control field $\Omega(t)$ that retrieves into $e(t) = \mathcal{E}_{\text{in}}^*(T - t)$ is determined by

$$\int_0^t dt' |\mathcal{E}_{\text{in}}(t')|^2 = e^{-\frac{2\gamma(1+C)}{\gamma^2(1+C)^2 + \Delta^2} h(0, T-t)}. \quad (\text{A.65})$$

Putting $e(t) = \mathcal{E}_{\text{in}}^*(T - t)$ into Eq. (A.21), taking the complex conjugate of the result, and evaluating at $T - t$, we get

$$\Omega^*(T - t) = -\frac{\gamma(1+C) - i\Delta}{\sqrt{2\gamma(1+C)}} \frac{\mathcal{E}_{\text{in}}(t)}{\sqrt{\int_0^t |\mathcal{E}_{\text{in}}(t')|^2 dt'}} e^{i\frac{\Delta h(0, T-t)}{\gamma^2(1+C)^2 + \Delta^2}}. \quad (\text{A.66})$$

Since $h(0, T - t)$ determined by Eq. (A.65) and $h(t, T)$ determined by Eq. (A.64) are equal, the right-hand side of Eq. (A.66) is, in fact, equal to the right-hand side of Eq. (A.26), as desired.

Appendix B

Optimal Photon Storage in Atomic Ensembles: Free-Space Model

B.1 Introduction

In Appendix A, we carried out the optimization of light storage in Λ -type optically dense atomic media enclosed in a cavity. Using the intuition gained from the cavity model discussion, we consider in the present Appendix the free-space model. In addition to a detailed presentation of the results of Chapter 2, we also discuss several extensions of the analysis of Chapter 2, such as the inclusion of the decay of coherence between the two lower levels of the Λ system and the effects of nondegeneracy of these two levels.

For a complete introduction to photon storage in Λ -type atomic media, as it applies to Appendix A and to the present Appendix, as well as for the full list of references, we refer the reader to Sec. A.1. In the present Introduction, we only list the two main results of the present Appendix. The first important result is the proof of a certain degree of equivalence between a wide range of techniques for photon storage and retrieval in Λ -type atomic media, including the approaches based on electromagnetically induced transparency (EIT), off-resonant Raman processes, and photon echo. In particular, this result means that provided there is a sufficient degree of control over the shape of the incoming photon wave packet and/or over the power and shape of the classical control pulses, all the protocols considered have the same maximum achievable efficiency that depends only on the optical depth d of the medium. The second important result is a novel time-reversal-based iterative algorithm for optimizing quantum state mappings, a procedure that we expect to be applicable beyond the field of photon storage. One of the key features of this optimization algorithm is that it can not only be used as a mathematical tool but also as an experimental technique. In fact, following this theoretical proposal, an experimental demonstration of this technique has already been carried out, as we

report in Secs. 3.3 and E.4. Both the experimental results (Secs. 3.3 and E.4.) and the theoretical results of the present Appendix indicate that the suggested optimization with respect to the shape of the incoming photon wave packet and/or the control pulse shape and power will be important for increasing the photon storage efficiencies in current experiments.

Although the slightly simpler cavity model discussed in Appendix A is similar enough to the free-space model to provide good intuition for it, the two physical systems have their own advantages and disadvantages, which we will discuss in the present Appendix. One advantage of the free-space model is the fact that it is easier to set up experimentally, which is one of the reasons we study this model in the present Appendix. Turning to the physics of the two models, the main differences come from the fact that in the cavity model the only spin wave mode accessible is the one that has the excitation distributed uniformly over all the atoms. In contrast, in the free-space model, incoming light can couple to any mode specified by a smooth excitation with position-dependent amplitude and phase. As a consequence of this, the free-space model allows for high efficiency storage of a wider range of input light modes than the cavity model. In particular, we showed in Appendix A that in the cavity model high efficiency photon-echo-based storage (which we refer to as fast storage) is possible for a single input mode of duration $\sim 1/(\gamma C)$, where γ is the optical polarization decay and C is the cavity cooperativity parameter. In contrast, we show in the present Appendix that high efficiency fast storage in a free-space atomic ensemble with optical depth d is possible for any input light mode of duration T provided $T\gamma \ll 1$ and $Td\gamma \gg 1$. However, the cavity model also has some advantages over the free-space model. In particular, the error during optimal light storage and retrieval for a given atomic ensemble scales as the inverse of the optical depth, as we have shown for the cavity model in Appendix A and for the free-space model in the present Appendix. The optimal efficiency is therefore higher when the ensemble is enclosed in a cavity, which effectively enhances the optical depth by the cavity finesse to form the cooperativity parameter C . Moreover, if one is forced to retrieve from a spatially uniform spin wave mode (e.g., if the spin wave is generated via spontaneous Raman scattering [80]), the error during retrieval will decrease faster with optical depth in the cavity model ($\sim 1/C$) than in the free-space model ($\sim 1/\sqrt{d}$).

The remainder of the present Appendix is organized as follows. In Sec. B.2, the model is introduced. In Secs. B.3, B.4, and B.5, we prove that during retrieval there exists a fixed branching ratio between the desired light emission rate and undesired polarization decay rate, and use this in combination with time reversal to derive the optimal strategy for storage and retrieval without fully solving the equations. In Secs. B.6 and B.7, the equations are solved analytically in the adiabatic and fast limits, respectively, and more specific statements about the optimal control strategy are made. In Sec. B.8, the effect of nondegeneracy of the two metastable states is discussed. In Sec. B.9, we summarize the discussion of the free-space model. In Sec. B.10, we present some details omitted in the main text.

B.2 Model

We refer the reader to Sec. B.10.1 for the details of the model and for the derivation of the equations of motion. In this Section, we only briefly summarize the model and state the equations of motion without derivation.

We consider a free-space medium of length L and cross-section area A containing $N = \int_0^L dz n(z)$ atoms, where $n(z)$ is the number of atoms per unit length. We assume that within the interaction volume the concentration of atoms is uniform in the transverse direction. The atoms have the same Λ -type level configuration as in the cavity case discussed in Appendix A and shown in Fig. A.1. They are coupled to a quantum field and a copropagating classical field. We assume that quantum electromagnetic field modes with a single transverse profile are excited. We also assume that both the quantum and the classical field are narrowband fields centered at $\omega_1 = \omega_{eg} - \Delta$ and $\omega_2 = \omega_{es} - \Delta$, respectively (where ω_{eg} and ω_{es} are atomic transition frequencies). The quantum field is described by a slowly varying operator $\hat{\mathcal{E}}(z, t)$, while the classical field is described by the Rabi frequency envelope $\Omega(z, t) = \Omega(t - z/c)$.

We neglect reabsorption of spontaneously emitted photons. This is a good approximation since we are interested in the storage of single- or few-photon pulses, in which case there will be at most a few spontaneously emitted photons. Although for an optically thick medium they can be reabsorbed and reemitted [322, 323], the probability of spontaneously emitting into the mode $\hat{\mathcal{E}}$ is given by the corresponding far-field solid angle $\sim \lambda^2/A \sim d/N$, where A is the cross section area of both the quantum field mode and the atomic medium (see Sec. B.10.1 for a discussion of why this choice is not important), $\lambda = 2\pi c/\omega_1$ is the wavelength of the quantum field, and $d \sim \lambda^2 N/A$ is the resonant optical depth of the ensemble. In most experiments, this probability is very small. Moreover, we will show that for the optimized storage process, the fraction of the incoming photons lost to spontaneous emission will decrease with increasing optical depth. In practice, however, reabsorption of spontaneously emitted photons can cause problems [324] during the optical pumping process, which is used to initialize the sample, and this may require modification of the present model.

We treat the problem in a one-dimensional approximation. This is a good approximation provided that the control beam is much wider than the single mode of the quantum field defined by the optics, as, for example, in the experiment of Ref. [80]. In this case, the transverse profile of the control field can be considered constant; and, in the paraxial approximation, the equations reduce to one-dimensional equations for a single Hermite-Gaussian quantum field mode [325, 326].

We define the polarization operator $\hat{P}(z, t) = \sqrt{N}\hat{\sigma}_{ge}(z, t)$ and the spin-wave operator $\hat{S}(z, t) = \sqrt{N}\hat{\sigma}_{gs}(z, t)$ (where $\hat{\sigma}_{\mu\nu}(z, t)$ are slowly varying position-dependent collective atomic operators defined in Sec. B.10.1). In the dipole and rotating-wave approximations, to first order in $\hat{\mathcal{E}}$, and assuming that at all times almost all atoms

are in the ground state, the Heisenberg equations of motion read

$$(\partial_t + c\partial_z)\hat{\mathcal{E}} = ig\sqrt{N}\hat{P}n(z)L/N, \quad (\text{B.1})$$

$$\partial_t\hat{P} = -(\gamma + i\Delta)\hat{P} + ig\sqrt{N}\hat{\mathcal{E}} + i\Omega\hat{S} + \sqrt{2\gamma}\hat{F}_P, \quad (\text{B.2})$$

$$\partial_t\hat{S} = -\gamma_s\hat{S} + i\Omega^*\hat{P} + \sqrt{2\gamma_s}\hat{F}_S, \quad (\text{B.3})$$

where we introduced the spin-wave decay rate γ_s , the polarization decay rate γ (equal to half of the linewidth), and the corresponding Langevin noise operators $\hat{F}_P(z, t)$ and $\hat{F}_S(z, t)$. As in the cavity case, collective enhancement [76] results in the increase of the atom-field coupling constant g (assumed to be real for simplicity) by a factor of \sqrt{N} up to $g\sqrt{N}$. Notice that in order to avoid carrying around extra factors of 2, Ω is defined as half of the traditional Rabi frequency; for example, with the present definition, a π pulse would take time $\pi/(2\Omega)$.

As we show in Sec. B.10.1 and explain in detail in Appendix A, under reasonable experimental conditions, the normally ordered noise correlations of \hat{F}_P and \hat{F}_S are zero, i.e., the incoming noise is vacuum and the transformation is passive. As we show in Sec. A.2, this implies that efficiency is the only number required to completely characterize the mapping.

As in the cavity discussion of Appendix A, we suppose that initially all atoms are in the ground state, i.e., no atomic excitations are present. We also assume that there is only one nonempty mode of the incoming quantum field and that it has an envelope shape $h_0(t)$ nonzero on $[0, T]$. The term ‘‘photon storage and retrieval’’ refers to mapping this mode onto some mode of \hat{S} and, starting at a later time $T_r > T$, retrieving it onto an outgoing field mode. Then precisely as in the cavity case in Appendix A, for the purposes of finding the storage efficiency, which is given by the ratio of the number of stored excitations to the number of incoming photons

$$\eta_s = \frac{\int_0^L dz \frac{n(z)}{N} \langle \hat{S}^\dagger(z, T) \hat{S}(z, T) \rangle}{\frac{c}{L} \int_0^T dt \langle \hat{\mathcal{E}}^\dagger(0, t) \hat{\mathcal{E}}(0, t) \rangle}, \quad (\text{B.4})$$

we can ignore \hat{F}_P and \hat{F}_S in Eqs. (B.1)-(B.3) and treat these equations as complex number equations with the interpretation that the complex number fields describe the shapes of quantum modes. In fact, although the resulting equations describe our case of quantized light coupled to the $|g\rangle - |e\rangle$ transition, they will also precisely be the equations describing the propagation of a classical probe pulse. To see this, one can simply take the expectation values of Eqs. (B.1)-(B.3) and use the fact that classical probe pulses are described by coherent states.

Going into a comoving frame $t' = t - z/c$, introducing dimensionless time $\tilde{t} = \gamma t'$ and dimensionless rescaled coordinate $\tilde{z} = \int_0^z dz' n(z')/N$, absorbing a factor of

$\sqrt{c/(L\gamma)}$ into the definition of \mathcal{E} , we reduce Eqs. (B.1)-(B.3) to

$$\partial_{\tilde{z}}\mathcal{E} = i\sqrt{d}P, \quad (\text{B.5})$$

$$\partial_{\tilde{t}}P = -(1+i\tilde{\Delta})P + i\sqrt{d}\mathcal{E} + i\tilde{\Omega}(\tilde{t})S, \quad (\text{B.6})$$

$$\partial_{\tilde{t}}S = i\tilde{\Omega}^*(\tilde{t})P, \quad (\text{B.7})$$

where we have identified the optical depth $d = g^2NL/(\gamma c)$ and where $\tilde{\Delta} = \Delta/\gamma$ and $\tilde{\Omega} = \Omega/\gamma$. We confirm in Sec. B.10.1 that from the definition it follows that d is independent of the size of the beam and, for a given transition, only depends on the density and length of the ensemble. Moreover, the definition of d that we use here can be related to the intensity attenuation of a resonant probe in our three level system with the control off, in which case the equations give an attenuation of $\exp(-2d)$ (i.e. to avoid carrying around extra factors of 2, d is defined as half of the usual optical depth). In Eqs. (B.5)-(B.7) and in the rest of this Appendix (except for Sec. B.6.5), we neglect the decay γ_s of the spin wave. However, precisely as in the cavity case, nonzero γ_s simply introduces an exponential decay without making the solution or the optimization harder, as we will discuss in Sec. B.6.5. We also note that Eqs. (B.1)-(B.3) are the same as the equations of Ref. [17] for copropagating fields, generalized to nonzero Δ and γ_s , and taken to first order in \mathcal{E} .

During storage, shown (in original variables) in Fig. B.1(a), the initial and boundary conditions are (in rescaled variables) $\mathcal{E}(\tilde{z} = 0, \tilde{t}) = \mathcal{E}_{\text{in}}(\tilde{t})$, $P(\tilde{z}, \tilde{t} = 0) = 0$, and $S(\tilde{z}, \tilde{t} = 0) = 0$, where $\mathcal{E}_{\text{in}}(\tilde{t})$ is nonzero for $\tilde{t} \in [0, \tilde{T}]$ (where $\tilde{T} = T\gamma$) and, being a shape of a mode, is normalized according to $\int_0^{\tilde{T}} d\tilde{t} |\mathcal{E}_{\text{in}}(\tilde{t})|^2 = 1$. $S(\tilde{z}, \tilde{T})$ gives the shape of the spin-wave mode, into which we store, and the storage efficiency is given by

$$\eta_s = \int_0^1 d\tilde{z} |S(\tilde{z}, \tilde{T})|^2. \quad (\text{B.8})$$

Loss during storage comes from the decay γ as well as from the “leak” $\mathcal{E}(\tilde{z} = 1, \tilde{t})$ shown in Fig. B.1(a). Then at a later time $\tilde{T}_r > \tilde{T}$ (where $\tilde{T}_r = T_r\gamma$), we want to retrieve the excitation back onto a photonic mode either in the forward direction, as shown in Fig. B.1(b), or in the backward direction [327] (i.e., with the retrieval control pulse incident from the right) as shown in Fig. B.1(c). Instead of turning our Eqs. (B.5)-(B.7) around to describe backward retrieval, we invert, for backward retrieval, the spin wave according to $S(\tilde{z}, \tilde{T}_r) = S(1-\tilde{z}, \tilde{T})$, whereas we keep $S(\tilde{z}, \tilde{T}_r) = S(\tilde{z}, \tilde{T})$ for forward retrieval. Because of the z -dependent phases in Eq. (B.60), this prescription for backward retrieval is strictly valid only for zero splitting between the two metastable states ($\omega_{sg} = 0$). In Sec. B.8, we will discuss the effect of nonzero ω_{sg} . The remaining initial and boundary conditions during retrieval are $\mathcal{E}(\tilde{z} = 0, \tilde{t}) = 0$ and $P(\tilde{z}, \tilde{T}_r) = 0$. If we renormalize the spin wave before doing the retrieval, then the retrieval efficiency will be given by

$$\eta_r = \int_{\tilde{T}_r}^{\infty} d\tilde{t} |\mathcal{E}(1, \tilde{t})|^2. \quad (\text{B.9})$$

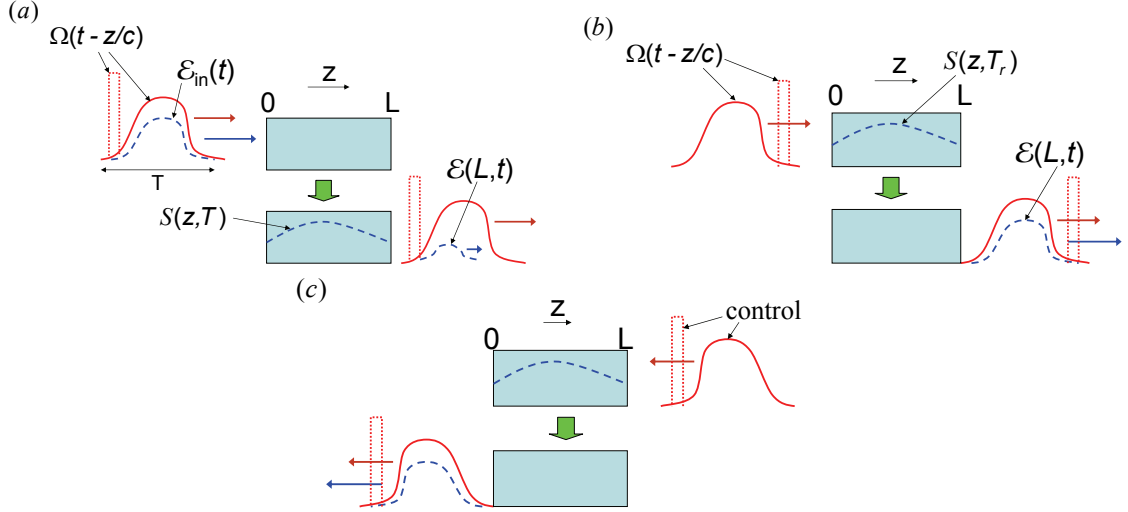


Figure B.1: (a) Storage, (b) forward retrieval, and (c) backward retrieval setup. The smooth solid curve is the generic control field shape (Ω) for adiabatic storage or retrieval; the dotted square pulse indicates a π -pulse control field for fast storage or retrieval. The dashed line indicates the quantum field \mathcal{E} and the spin-wave mode S . During storage, $\mathcal{E}(L, t)$ is the “leak,” whereas it is the retrieved field during retrieval.

If we do not renormalize the spin wave before doing the retrieval, this formula will give the total efficiency of storage followed by retrieval $\eta_{\text{tot}} = \eta_s \eta_r$.

To solve Eqs. (B.5)-(B.7), it is convenient to Laplace transform them in space according to $\tilde{z} \rightarrow u$, so that Eqs. (B.5,B.6) become

$$\mathcal{E} = i \frac{\sqrt{d}}{u} P + \frac{\mathcal{E}_{\text{in}}}{u}, \quad (\text{B.10})$$

$$\partial_{\tilde{t}} P = -\left(1 + \frac{d}{u} + i\tilde{\Delta}\right) P + i\tilde{\Omega}(t) S + i \frac{\sqrt{d}}{u} \mathcal{E}_{\text{in}}. \quad (\text{B.11})$$

As in the cavity case in Appendix A, it is also convenient to reduce Eqs. (B.5)-(B.7) to a single equation

$$\left[\ddot{S} - \frac{\dot{\tilde{\Omega}}^*}{\tilde{\Omega}^*} \dot{S} \right] + \left(1 + \frac{d}{u} + i\tilde{\Delta}\right) \dot{S} + |\tilde{\Omega}|^2 S = -\tilde{\Omega}^* \frac{\sqrt{d}}{u} \mathcal{E}_{\text{in}}, \quad (\text{B.12})$$

where the overdot stands for the \tilde{t} derivative. As in the cavity case, this second-order differential equation cannot, in general, be fully solved analytically. Similar to Appendix A, we can, however, derive several important results regarding the optimal control strategy for storage and retrieval without making any more approximations.

We discuss these results in Sec. B.3, where we optimize retrieval, and in Secs. B.4 and B.5 where we introduce the important time reversal ideas, which allow us to deduce the optimal storage from the optimal retrieval.

B.3 Optimal Retrieval

Although Eq. (B.12) cannot, in general, be fully solved analytically, we still make in this and in the following two Sections several important statements regarding the optimal strategy for maximizing the storage efficiency, the retrieval efficiency, and the combined (storage followed by retrieval) efficiency without making any more approximations. It is convenient to first consider retrieval, and we do so in this Section.

Although we cannot, in general, analytically solve for the output field $\mathcal{E}_{\text{out}}(t)$, we will show now that, as in the cavity case in Appendix A, the retrieval efficiency is independent of the control shape and the detuning provided no excitations are left in the atoms. Moreover, we will show that the retrieval efficiency is given by a simple formula that depends only on the optical depth and the spin-wave mode. From Eqs. (B.7) and (B.11), it follows that

$$\begin{aligned} \frac{d}{d\tilde{t}} (P(u, \tilde{t}) [P(u^*, \tilde{t})]^* + S(u, \tilde{t}) [S(u^*, \tilde{t})]^*) \\ = -(2 + d/u + d/u')P(u, \tilde{t}) [P(u^*, \tilde{t})]^*. \end{aligned} \quad (\text{B.13})$$

Using Eqs. (B.10) and (B.13) and assuming $P(u, \infty) = S(u, \infty) = 0$ (i.e., that no excitations are left in the atoms at $\tilde{t} = \infty$), the retrieval efficiency is

$$\begin{aligned} \eta_r &= \mathcal{L}^{-1} \left\{ \frac{d}{uu'} \int_{\tilde{T}_r}^{\infty} d\tilde{t} P(u, \tilde{t}) [P(u^*, \tilde{t})]^* \right\} \\ &= \mathcal{L}^{-1} \left\{ \frac{d}{2uu' + d(u + u')} S(u, \tilde{T}_r) [S(u^*, \tilde{T}_r)]^* \right\} \\ &= \int_0^1 d\tilde{z} \int_0^1 d\tilde{z}' S(1 - \tilde{z}, \tilde{T}_r) S^*(1 - \tilde{z}', \tilde{T}_r) k_r(\tilde{z}, \tilde{z}'), \end{aligned} \quad (\text{B.14})$$

where \mathcal{L}^{-1} means that two inverse Laplace transforms ($u \rightarrow \tilde{z}$ and $u' \rightarrow \tilde{z}'$) are taken and are both evaluated at $\tilde{z} = \tilde{z}' = 1$ and where the kernel k_r is defined as

$$k_r(\tilde{z}, \tilde{z}') = \mathcal{L}^{-1} \left\{ \frac{d}{2uu' + d(u + u')} e^{-u(1-\tilde{z}) - u'(1-\tilde{z}')} \right\} = \frac{d}{2} e^{-d\frac{\tilde{z} + \tilde{z}'}{2}} I_0(d\sqrt{\tilde{z}\tilde{z}'}), \quad (\text{B.15})$$

where I_n is the n th-order modified Bessel function of the first kind. Similarly to the cavity case in Appendix A, we see that the efficiency is independent of Δ and Ω , which reflects that in Eq. (B.11) (or, equivalently, on the right-hand side of Eq. (B.13)) there

is a fixed branching ratio between the decay rates of P . For a given u the rates are (in the original units) γ and $\gamma d/u$ into the undesired modes and the desired mode \mathcal{E}_{out} , respectively, independent of Δ and Ω . In fact, a stronger result than the independence of retrieval efficiency from Δ and Ω can be obtained: as we show in Sec. B.10.2, the distribution of spontaneous emission loss as a function of position is also independent of the control and detuning.

In contrast to the cavity case in Appendix A where there was only one spin-wave mode available, in the free-space case, the retrieval efficiency in Eq. (B.14) is different for different spin-wave modes. We can, thus, at each d , optimize retrieval by finding the optimal retrieval spin wave $\tilde{S}_d(\tilde{z})$ (we suppress here the argument \tilde{T}_r). The expression for the efficiency in the last line of Eq. (B.14) is an expectation value of a real symmetric (and hence Hermitian) operator $k_r(\tilde{z}, \tilde{z}')$ in the state $S(1 - \tilde{z})$. It is therefore maximized when $S(1 - \tilde{z})$ is the eigenvector with the largest eigenvalue of the following eigenvalue problem:

$$\eta_r S(1 - \tilde{z}) = \int_0^1 d\tilde{z}' k_r(\tilde{z}, \tilde{z}') S(1 - \tilde{z}'). \quad (\text{B.16})$$

Since eigenvectors of real symmetric matrices can be chosen real, the resulting optimal spin wave $\tilde{S}_d(\tilde{z})$ can be chosen real. To find it, we start with a trial $S(\tilde{z})$ and iterate the integral in Eq. (B.16) several times until convergence [328]. In Fig. B.2, we plot the resulting optimal spin wave $\tilde{S}_d(\tilde{z})$ for $d = 0.1, 1, 10, 100$, as well as its limiting shape ($\tilde{S}_\infty(\tilde{z}) = \sqrt{3}\tilde{z}$) as $d \rightarrow \infty$. At $d \rightarrow 0$, the optimal mode approaches a flat mode. These shapes can be understood by noting that retrieval is essentially an interference effect resembling superradiance, where the emission from all atoms contributes coherently in the forward direction. To get the maximum constructive interference, it is desirable that all atoms carry equal weight and phase in the spin wave. In particular, at low optical depth, this favors the flat spin wave. On the other hand, it is also desirable not to have a sudden change in the spin wave (except near the output end of the ensemble). The argument above essentially shows that excitations can decay through two different paths: by spontaneous emission in all directions or by collective emission into the forward direction. In Eq. (B.6), these two paths are represented by the $-P$ and $i\sqrt{d}\mathcal{E}$ terms, respectively. The latter gives rise to a decay because Eq. (B.5) can be integrated to give a term proportional to P : $\mathcal{E} = i \int d\tilde{z} \sqrt{d} P$. To obtain the largest decay in the forward direction all atoms should ideally be in phase so that the phase of $P(\tilde{z})$ is the same at all \tilde{z} . This constructive interference, however, is not homogeneous but builds up through the sample. At $\tilde{z} = 0$, we have $\mathcal{E} = 0$, and the spontaneous emission is, thus, the only decay channel, i.e., $d|P(\tilde{z} = 0)|^2/dt = -2|P(\tilde{z} = 0)|^2$. To achieve the largest retrieval efficiency, we should therefore put a limited amount of the excitation near $\tilde{z} = 0$ and only have a slow build up of the spin wave from $\tilde{z} = 0$ to $\tilde{z} = 1$. The optimal spin-wave modes in Fig. B.2 represent the optimal version of this slow build up. We will also reinterpret

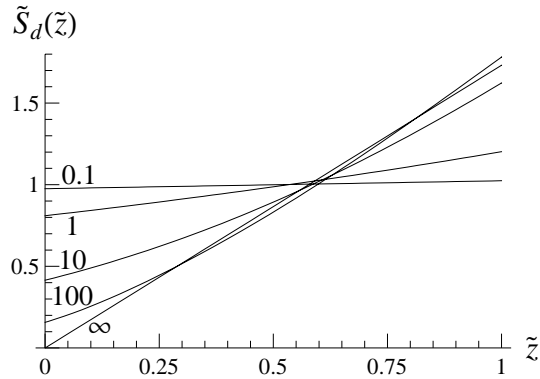


Figure B.2: Optimal modes $\tilde{S}_d(\tilde{z})$ to retrieve from (in the forward direction) at indicated values of d . The flipped versions of these modes $\tilde{S}_d(1 - \tilde{z})$ are the optimal modes for backward retrieval and are also the optimal (normalized) spin waves $S(\tilde{z}, T)/\sqrt{\eta_s^{\max}}$ for adiabatic and fast storage if it is optimized for storage alone or for storage followed by backward retrieval (η_s^{\max} is the maximum storage efficiency).

these optimal modes from a different perspective in Sec. B.6.1 using the EIT window concept.

From the qualitative argument given here, one can estimate the dependence of the optimal retrieval efficiency on the optical depth: we consider the emission into a forward mode of cross sectional area A . In the far field, this corresponds to a field occupying a solid angle of λ^2/A , where $\lambda = (2\pi c)/\omega_1$ is the wavelength of the carrier. A single atom will, thus, decay into this mode with a probability $\sim \lambda^2/A$. With N atoms contributing coherently in the forward direction, the emission rate is increased by a factor of N to $\gamma_f \sim \gamma N \lambda^2/A$. The retrieval efficiency can then be found from the rate of desired (γ_f) and undesired (γ) decays as $\eta = \gamma_f/(\gamma_f + \gamma) \sim 1 - A/(N\lambda^2)$. By noting that λ^2 is the cross section for resonant absorption of a two-level atom, we recognize $N\lambda^2/A$ as the optical depth d (up to a factor of order 1). The efficiency is then $\eta \sim 1 - 1/d$, which is in qualitative agreement with the results of the full optimization which gives $1 - \eta \approx 2.9/d$. A more detailed discussion of the dependence of retrieval efficiency on the shape of the spin wave is postponed until Sec. B.6.1, where Eq. (B.14) is rederived in the adiabatic limit and discussed in the context of the EIT window.

B.4 Optimal Storage From Time Reversal: General Proof

As already mentioned in Appendix A, the concept of time reversal allows us to deduce the optimal control strategy for storage from retrieval. In this Section, we prove this result both for the free-space case and for the cavity case (the cavity case differs only in that there is just one spin-wave mode involved). In the next Section, we generalize these ideas and show that time reversal can be generally used to optimize state mappings.

Despite the fact that our system contains nonreversible decay γ , time reversal is still an important and meaningful concept: to make time reversal applicable in this situation, we expand our system so that we not only consider the electric field and the spin wave, but also include all the reservoir modes, into which the excitations may decay. As discussed in Sec. B.2 and Sec. B.10.1, the initial state of the reservoir modes is vacuum. When considering “all the modes in the universe” [152], we have a closed system described by (possibly infinitely many) bosonic creation operators $\{\hat{O}_i^\dagger\}$ with commutation relations

$$[\hat{O}_i, \hat{O}_j^\dagger] = \delta_{ij}. \quad (\text{B.17})$$

The evolution we consider here can be seen as a generalized beam-splitter transformation, and can equivalently be specified as a Heisenberg picture map between the annihilation operators $\hat{O}_{i,\text{out}} = \sum_j U_{ij}[T, 0; \Omega(t)] \hat{O}_{j,\text{in}}$ or as a Schrödinger picture map $\hat{U}[T, 0; \Omega(t)] = \sum_{ij} U_{ij}[T, 0; \Omega(t)] |i\rangle\langle j|$ in the Hilbert space \mathcal{H} with an orthonormal basis of single excitation states $|i\rangle = \hat{O}_i^\dagger |\text{vacuum}\rangle$. To stress that the mapping depends on the classical control field $\Omega(t)$, we here include the argument $\Omega(t)$ in the evolution operator $\hat{U}[\tau_2, \tau_1; \Omega(t)]$, which takes the state from time τ_1 to τ_2 . The operator $\hat{U}[T, 0; \Omega(t)]$ must be unitary $\hat{U}^\dagger[T, 0; \Omega(t)] = \hat{U}^{-1}[T, 0; \Omega(t)] = \hat{U}[0, T; \Omega(t)]$. For simplicity of notation, we will here use the Schrödinger picture.

Let us define two subspaces of \mathcal{H} : subspace A of “initial” states and subspace B of “final states.” B^\perp , the orthogonal complement of B , can be thought of as the subspace of “decay” modes (that is, the reservoir and other states, possibly including the “initial” states, to which we do not want the initial states to be mapped). In this Section, we will use \hat{U} as the retrieval map, in which case A and B are spin-wave modes and output photon modes, respectively, while B^\perp includes A , empty input field modes, and the reservoir modes, to which the excitations can decay by spontaneous emission.

In the cavity derivation in Appendix A, we solved in the adiabatic limit for the control pulse shape $\Omega_r(t)$, which retrieves the atomic excitation into a specific mode $e(t)$. We then derived the pulse shape $\Omega_s(t)$, which optimally stores an incoming mode $\mathcal{E}_{\text{in}}(t)$, and noted that if the incoming mode is the time-reverse of the mode,

onto which we retrieved, i.e., $\mathcal{E}_{\text{in}}^*(T-t) = e(t)$, then the optimal storage control is the time-reverse of the retrieval control, i.e., $\Omega_{\text{s}}^*(T-t) = \Omega_{\text{r}}(t)$. Furthermore, in this case the storage and retrieval efficiencies were identical. As we now show, this is not a coincidence, but a very general result.

For the free-space case, we define the ‘‘overlap efficiency’’ for storing into any given mode $S(z)$ as the expectation value of the number of excitations in this mode $S(z)$. Since the actual mode (call it $S'(z)$), onto which the excitation is stored, may contain components orthogonal to $S(z)$, the overlap efficiency for storing into $S(z)$ is in general less than the (actual) storage efficiency, and is equal to it only if $S(z) = S'(z)$.

We will now prove that storing the time reverse of the output of backward retrieval from $S^*(z)$ with the time reverse of the retrieval control field gives the overlap storage efficiency into $S(z)$ equal to the retrieval efficiency. To begin the proof, we note that the probability to convert under \hat{U} an initial excitation from a state $|a\rangle$ in A into a state $|b\rangle$ in B is just

$$\eta = |\langle b|\hat{U}[T, 0; \Omega(t)]|a\rangle|^2 = |\langle a|\hat{U}^{-1}[T, 0; \Omega(t)]|b\rangle|^2, \quad (\text{B.18})$$

where, in the last expression, we have used the unitarity of $\hat{U}[T, 0; \Omega(t)]$. We now assume that $\hat{U}[T, 0; \Omega(t)]$ describes retrieval and that $|a\rangle$ stands for $S^*(z)$, while $|b\rangle$ stands for the output field mode \mathcal{E} , onto which S^* is retrieved under $\Omega(t)$. Then η is just the retrieval efficiency from S^* . The last expression then shows that if we could physically realize the operation $\hat{U}^{-1}[T, 0; \Omega(t)]$, then it would give the overlap efficiency for storage of \mathcal{E} into S^* equal to the retrieval efficiency η . The challenge is, therefore, to physically invert the evolution and realize $\hat{U}^{-1}[T, 0; \Omega(t)]$. As we now show, time reversal symmetry allows us to perform this inverse evolution in some cases. We refer the reader to Sec. B.10.3 for a careful definition of the time reversal operator $\hat{\mathcal{T}}$ and for the proof of the following equality:

$$\hat{U}^{-1}[T, 0; \Omega(t)] = \hat{\mathcal{T}}\hat{U}[T, 0; \Omega^*(T-t)]\hat{\mathcal{T}}, \quad (\text{B.19})$$

where it is implicit that the carrier wave vector of the time-reversed control pulse $\Omega^*(T-t)$ propagates in the direction opposite to the carrier of $\Omega(t)$. Physically, Eq. (B.19) means that we can realize the inverse evolution by time-reversing the initial state, evolving it using a time-reversed control pulse, and finally time-reversing the final state. Then, using Eqs. (B.18) and (B.19), the retrieval efficiency may be rewritten as

$$\eta = |\langle a|\hat{\mathcal{T}}\hat{U}[T, 0; \Omega^*(T-t)]\hat{\mathcal{T}}|b\rangle|^2. \quad (\text{B.20})$$

This means that if we can retrieve the spin wave S^* backwards onto $\mathcal{E}(t)$ using $\Omega(t)$, we can use $\Omega^*(T-t)$ to store $\mathcal{E}_{\text{in}}(t) = \mathcal{E}^*(T-t)$ onto S with the overlap storage efficiency equal to the retrieval efficiency η_{r} .

We will now prove that this time-reversed storage is also the optimal solution, i.e., that an overlap efficiency for storage into S greater than η_{r} is not possible.

To begin the proof, let us suppose, on the contrary, that we can store $\mathcal{E}_{\text{in}}(t)$ into S with an overlap efficiency $\eta_s > \eta_r$. Applying now the time reversal argument to storage, we find that backward retrieval from S^* with the time-reversed storage control will have efficiency greater than η_r . However, from Eq. (B.14), we know that the retrieval efficiency is independent of the control field and is invariant under the complex conjugation of the spin wave, so we have reached a contradiction. Therefore, the maximum overlap efficiency for storage into a given mode S is equal to the backward retrieval efficiency from S^* (and S) and can be achieved by time-reversing backward retrieval from S^* .

Finally, the strategy for storing $\mathcal{E}_{\text{in}}(t)$ with the maximum storage efficiency (rather than maximum overlap efficiency into a given mode, as in the previous paragraph) follows immediately from the arguments above: provided we can retrieve the (real) optimal backward-retrieval mode $\tilde{S}_d(L - z)$ backwards into $\mathcal{E}_{\text{in}}^*(T - t)$, the optimal storage of $\mathcal{E}_{\text{in}}(t)$ will be the time reverse of this retrieval and will have the same efficiency as the optimal retrieval efficiency at this d , i.e., the retrieval efficiency from \tilde{S}_d .

While the above argument is very general, it is important to realize its key limitation. The argument shows that it is possible to optimally store a field $\mathcal{E}_{\text{in}}(t)$ provided we can optimally retrieve onto $\mathcal{E}_{\text{in}}^*(T - t)$ (i.e., backward-retrieve $\tilde{S}_d(L - z)$ into $\mathcal{E}_{\text{in}}^*(T - t)$). It may, however, not be possible to optimally retrieve onto $\mathcal{E}_{\text{in}}^*(T - t)$ because it may, for example, be varying too fast. For this reason, we shall explore in Secs. B.6.1 and B.7, onto which fields it is possible to retrieve a given spin wave. Before we do this, however, we will show in the next Section that time reversal does not only allow one to derive the optimal storage strategy from the optimal retrieval strategy, as we did in this Section, but also allows one to find the optimal spin wave for retrieval.

B.5 Time Reversal as a Tool for Optimizing Quantum State Mappings

We will now show that time reversal can be used as a general tool for optimizing state mappings. Moreover, we will show that for the photon storage problem considered in this Appendix, in addition to being a very convenient mathematical tool, the optimization procedure based on time reversal may also be realized experimentally in a straightforward way.

In Sec. B.3 we found $\tilde{S}_d(z)$, the optimal spin wave to retrieve from, by starting with a trial spin wave $S_1(z)$ and iterating Eq. (B.16) until convergence. While we just used this as a mathematical tool for solving an equation, the iteration procedure actually has a physical interpretation. Suppose that we choose a certain classical control $\Omega(t)$ and retrieve the spin wave $S(z)$ forward onto $\mathcal{E}(t)$ and then time reverse the control to store $\mathcal{E}^*(T - t)$ backwards. By the argument in the last Section, this

will, in general, store into a different mode $S'(z)$ with a higher efficiency (since the actual storage efficiency is, in general, greater than the overlap storage efficiency into a given mode). In this way, we can iterate this procedure to compute spin waves with higher and higher forward retrieval efficiencies¹. In fact, forward retrieval followed by time-reversed backward storage can be expressed as

$$S_2(1 - \tilde{z}) = \int_0^1 d\tilde{z}' k_r(\tilde{z}, \tilde{z}') S_1^*(1 - \tilde{z}'), \quad (\text{B.21})$$

which for real S is identical to the iteration of Eq. (B.16). We note that the reason why backward storage had to be brought up here (in contrast to the rest of the Appendix, where storage is always considered in the forward direction) is because Eq. (B.16), which Eq. (B.21) is equivalent to for real S , discusses forward retrieval, whose time-reverse is backward storage.

Since the iterations used to maximize the efficiency in Eq. (B.16) are identical to Eq. (B.21), the physical interpretation of the iterations in Eq. (B.16) is that we retrieve the spin wave and store its time-reverse with the time-reversed control field (i.e., implement the inverse \hat{U}^{-1} of the retrieval map \hat{U} using Eq. (B.19)). We will explain below that this procedure of retrieval followed by time-reversed storage can be described mathematically by the operator $\hat{N}\hat{P}_A\hat{U}^{-1}\hat{P}_B\hat{U}$, where \hat{P}_A and \hat{P}_B are the projection operators on the subspaces A and B of spin wave modes and output photon modes, respectively, and where \hat{N} provides renormalization to a unit vector. It is, in fact, generally true that in order to find the unit vector $|a\rangle$ in a given subspace A of “initial” states that maximizes the efficiency $\eta = |\hat{P}_B\hat{U}|a\rangle|^2$ of a given unitary map \hat{U} (where B is a given subspace of “final” states), one can start with any unit vector $|a\rangle \in A$ and repeatedly apply $\hat{N}\hat{P}_A\hat{U}^{-1}\hat{P}_B\hat{U}$ to it. We prove in Sec. B.10.4 that this procedure converges to the desired optimal input mode $|a_{\max}\rangle$ yielding the maximum efficiency η_{\max} (provided $\langle a|a_{\max}\rangle \neq 0$) and that $\hat{N}\hat{P}_B\hat{U}|a_{\max}\rangle$ also optimizes \hat{U}^{-1} as a map from B to A .

We have just discussed the iterative optimization procedure as a purely mathematical tool for computing the optimal initial mode in the subspace A of initial states. However, in the previous Section and in Sec. B.10.3, we showed that for our system one can implement the inverse evolution U^{-1} experimentally by first time reversing the state of the system, then applying ordinary evolution but with a time-reversed control, and then time reversing the state of the system again. Thus, in addition to being a convenient mathematical tool, the time reversal based optimization technique suggested in this Appendix is an experimentally realizable procedure. In fact, we re-

¹We thank P. Meystre for pointing out that our iterative optimization schemes are reminiscent of the iterations used to find normal modes of Fabry-Perot interferometers [329]. We also thank J. Simon for pointing out that our iterative optimization schemes are reminiscent of the iterative Gerchberg-Saxton algorithm used in optics to compute the phase pattern needed to produce a desired holographic image [330].

port in Sec. 3.3 on the experimental demonstration of this procedure in the context of the optimization of the storage and retrieval of light.

As an example, let us discuss how this experimental implementation applies to the optimization of backward retrieval. The full Hilbert space is spanned by subspace A of spin-wave modes, subspace B of output field modes, as well as a subspace containing (empty) input and reservoir field modes. The goal is to optimize the retrieval time evolution map $\hat{U}[\Omega(t)]$ for some fixed detuning Δ and fixed backward-propagating Rabi frequency pulse $\Omega(t)$ (sufficiently powerful for complete retrieval) with respect to the initial spin wave $|a\rangle \in A$. From Sec. B.4, it follows that the iteration $\hat{N}\hat{P}_A\hat{U}^{-1}[\Omega(t)]\hat{P}_B\hat{U}[\Omega(t)]|a\rangle$ required for the optimization can be experimentally implemented as follows. We start with a spin-wave mode $|a\rangle$ with a real mode shape $S(z)$, carry out backward retrieval, and measure the outgoing field. We then prepare the time reverse of the measured field shape and store it back into the ensemble using the time-reversed control pulse. The projections \hat{P}_B and \hat{P}_A happen automatically since we do not reverse the reservoir modes and the leak. The renormalization can be achieved during the generation of the time-reversed field mode, while the time reversal for the spin wave will be unnecessary since a real spin wave will stay real under retrieval followed by time-reversed storage. The iteration suggested here is, thus, indeed equivalent to the iteration in Eq. (B.21) with $S(1 - \tilde{z})$ replaced with $S(\tilde{z})$ (since Eq. (B.21) optimizes forward retrieval).

For single photon states, the measurement of the outgoing field involved in the procedure above will require many runs of the experiment. To circumvent this, one can use the fact that the equations of motion (B.5)-(B.7) for the envelope of the quantum field mode are identical to the equations of motion for the classical field propagating under the same conditions. One can, thus, use the optimization procedure with classical light pulses and find optimal pairs of input pulse shapes and control fields, which will give optimal storage into the spin wave $\tilde{S}_d(1 - \tilde{z})$. However, since the equations of motion for quantum light modes are identical to the classical propagation equations, this data can then be interpreted as optimal pairs of control fields and quantized input photon modes for optimal storage of nonclassical light (such as single photons) into the optimal backward retrieval mode $\tilde{S}_d(1 - \tilde{z})$.

We will now briefly discuss the application of time reversal ideas to the optimization of the combined process of storage followed by retrieval. For real spin waves, storage and backward retrieval are time reverses of each other since real spin waves are unaltered by complex conjugation. Consequently, the time reversal iteration of storage and backward retrieval optimizes both of them, as well as the combined process of storage followed by backward retrieval. Therefore, for a given input, the storage control field that optimizes storage alone will also be optimal for storage followed by backward retrieval.

In contrast, (forward) storage and forward retrieval are not time reverses of each other, and the entire process of storage followed by forward retrieval has to be optimized as a whole. The general time reversal iteration procedure can still be used in

this case with the understanding that the spaces A and B of initial and final states are the right propagating modes to the left of the ensemble (except for later empty input modes during retrieval) and right propagating modes to the right of the ensemble (except for earlier storage leak modes), respectively, while the remaining modes are reservoir modes, spin-wave modes, leak modes, and empty incoming photon modes from the left during retrieval. Since the time-reverse of storage followed by forward retrieval is itself storage followed by forward retrieval except in the opposite direction, the optimization can be carried out physically by starting with a given input field mode, storing it and retrieving it forward with given control pulses, time reversing the output and the control pulses, and iterating the procedure. The optimal control-dependent input field, which the iteration will converge to, will then be stored into a particular optimal spin wave, which itself will be independent of the control used for the iteration. In Secs. B.6.3 and B.7 we will look at storage followed by forward retrieval in more detail.

It is important to note that the discussion in this Section assumed that the two metastable states are degenerate. If they are not degenerate, a momentum $\Delta k = \omega_{sg}/c$ will be written onto the spin wave during storage, so that its time reversal will no longer be trivial. In Sec. B.8, we will discuss in detail how the optimization is modified when the metastable states are not degenerate.

Procedures that are related to ours and that also use time-reversal iterations for optimization are a standard tool in applied optimal control [90, 89, 309, 310] and have been used for a variety of applications in chemistry [311, 312], NMR [313], and atomic physics [314, 315]. In most of these works, time reversal iterations are used as a mathematical tool for computing, for a given initial state $|a\rangle$, the optimal time-dependent control that would result in the final state with the largest projection on the desired subspace B of final states. In fact, this mathematical tool is directly applicable to our problem of shaping the control pulses, as we will discuss in Appendix D. However, our use of time reversal iterations in the present Appendix and in Appendices A and C differs in two ways from that of Refs. [90, 89, 309, 310, 311, 312, 313, 314, 315]. First, we use time reversal iterations to find the optimal $|a\rangle$ in the subspace A of initial states for a given propagator $U[\Omega(t)]$, rather than to shape the control $\Omega(t)$ itself for a given $|a\rangle$ (we shape the control by explicitly solving the equations, as explained in Secs. B.6 and B.7). Second, the time reversal iterations discussed in the references above are a purely mathematical technique, while our iterative algorithm can be implemented experimentally (as reported in Secs. 3.3 and E.4).

The main result of this Section is an iterative procedure for solving or experimentally finding the optimal retrieval spin wave, while the main result of the previous Section was that one can generate optimal pairs of inputs and control fields by time-reversing the output and the control field of such optimal retrieval. In order to say, however, for which input fields the optimal storage control $\Omega(t)$ can be found (or, equivalently, into which output fields can the optimal spin-wave excitation be

retrieved), we need to consider the limits, in which Eq. (B.12) can be fully solved analytically. These limits, adiabatic and fast, will be discussed in Secs. B.6 and B.7, respectively.

B.6 Adiabatic Retrieval and Storage

B.6.1 Adiabatic Retrieval

Solution for the output field and for the retrieval efficiency

Based on the branching ratio and the time reversal arguments, we have found the maximal storage efficiency at each d and have described the optimal storage scenario in the three preceding Sections. Since a given input mode can be optimally stored if and only if optimal retrieval can be directed into the time-reverse of this mode, in the following Sections (Secs. B.6 and B.7), we solve Eq. (B.12) analytically in two important limits to find out, which modes we can retrieve into and store optimally. The first of these two limits, which we will consider in the next five Sections (Secs. B.6.1 - B.6.5), corresponds to smooth input and control fields, such that the term in the square brackets in Eq. (B.12) can be ignored. This “adiabatic limit” corresponds to an adiabatic elimination of the optical polarization P in Eq. (B.11). The precise conditions for this adiabatic elimination will be discussed in Sec. B.6.4. In this Section (Sec. B.6.1), we consider the retrieval process.

Similar to the cavity discussion in Sec. A.5.1, it is instructive to note that in the adiabatic approximation (i.e., with $\partial_{\tilde{t}}P$ in Eq. (B.6) replaced with 0), rescaling variables \mathcal{E} and P by $\tilde{\Omega}$ and changing variables $\tilde{t} \rightarrow h(\tilde{T}_r, \tilde{t})$, where (as in Eq. A.15, except now in dimensionless form)

$$h(\tilde{t}, \tilde{t}') = \int_{\tilde{t}}^{\tilde{t}'} |\tilde{\Omega}(\tilde{t}'')|^2 d\tilde{t}'', \quad (\text{B.22})$$

makes Eqs. (B.5)-(B.7) independent of Ω . This allows one to solve these equations in an Ω -independent form and then obtain the solution for any given Ω by simple rescaling. A special case of this observation has also been made in Ref. [85], where the authors treat the Raman limit. However, since Eqs. (B.5)-(B.7) are relatively simple, we will avoid causing confusion by using new notation and will solve these equations without eliminating Ω .

To solve for the output field during adiabatic retrieval, we assume for simplicity that retrieval begins at time $\tilde{t} = 0$ rather than at time $\tilde{t} = \tilde{T}_r$ and that the initial spin wave is $S(\tilde{z}, \tilde{t} = 0) = S(\tilde{z})$. In the adiabatic approximation, Eqs. (B.7) and (B.11) reduce to a linear first order ordinary differential equation on S . Solving this equation for $S(u, \tilde{t})$ in terms of $S(u')$, expressing $\mathcal{E}(u, \tilde{t})$ in terms of $S(u, \tilde{t})$ using Eqs. (B.10)

and (B.11), and taking the inverse Laplace transform $u \rightarrow \tilde{z} = 1$, we arrive at

$$\mathcal{E}(1, \tilde{t}) = -\sqrt{d\tilde{\Omega}(\tilde{t})} \int_0^1 d\tilde{z} \frac{1}{1+i\tilde{\Delta}} e^{-\frac{h(0, \tilde{t})+d\tilde{z}}{1+i\tilde{\Delta}}} I_0 \left(2 \frac{\sqrt{h(0, \tilde{t})d\tilde{z}}}{1+i\tilde{\Delta}} \right) S(1-\tilde{z}). \quad (\text{B.23})$$

The \tilde{t} -dependent and the \tilde{z} -dependent phases in the exponent can be interpreted as the ac Stark shift and the change in the index of refraction, respectively.

By using the identity [331]

$$\int_0^\infty dr r e^{-pr^2} I_0(\lambda r) I_0(\mu r) = \frac{1}{2p} e^{\frac{\lambda^2 + \mu^2}{4p}} I_0 \left(\frac{\lambda\mu}{2p} \right) \quad (\text{B.24})$$

for appropriate μ , λ , and p , we find that for a sufficiently large $h(0, \infty)$ ($dh(0, \infty) \gg |d+i\tilde{\Delta}|^2$), the retrieval efficiency (Eq. (B.9) with \tilde{T}_r replaced with 0) is

$$\eta_r = \int_0^1 d\tilde{z} \int_0^1 d\tilde{z}' k_r(\tilde{z}, \tilde{z}') S(1-\tilde{z}) S^*(1-\tilde{z}'), \quad (\text{B.25})$$

in agreement with Eq. (B.14). So η_r is independent of detuning and control pulse shape but depends on the spin wave and the optical depth. Thus, the adiabatic approximation does not change the exact value of efficiency and keeps it independent of detuning and classical control field by preserving the branching ratio between desired and undesired state transfers. It is also worth noting that, in contrast to Eq. (B.14), Eq. (B.23) allows us to treat and optimize retrieval even when the energy in the control pulse is limited [85] (i.e., $dh(0, \infty) \lesssim |d+i\tilde{\Delta}|^2$). However, in the present Appendix, the treatment of adiabatic retrieval is focused on the case when the control pulse energy is sufficiently large ($dh(0, \infty) \gg |d+i\tilde{\Delta}|^2$) to leave no excitations in the atoms and to ensure the validity of Eq. (B.25) (or, equivalently, Eq. (B.14)).

As pointed out in Sec. A.1, two important subsets of the adiabatic limit, the resonant limit and the Raman limit, are often considered in the literature because the equations can be simplified in these limits. Although we demonstrate in this work that the basic underlying physics and hence the optimal performance are the same for these two photon storage techniques, a more detailed analysis reveals significant differences. It is precisely these differences that obstruct the underlying equivalence between the two protocols. And it is these differences that make this equivalence remarkable. As an example of such a difference, resonant and Raman limits give different dependence on d of the duration T_{out} of the output pulse. To see this, it is convenient to ignore the decay in Eq. (B.23) (due to the rescaling, this means we ignore 1 in $1+i\tilde{\Delta}$). If we do this, we obtain

$$\mathcal{E}(1, \tilde{t}) = i\sqrt{d\tilde{\Omega}(\tilde{t})} \int_0^1 dz \frac{1}{\tilde{\Delta}} e^{i\frac{h(0, \tilde{t})+dz}{\tilde{\Delta}}} J_0 \left(2 \frac{\sqrt{h(0, \tilde{t})d\tilde{z}}}{\tilde{\Delta}} \right) S(1-\tilde{z}), \quad (\text{B.26})$$

where $J_0(x) = I_0(ix)$ is the zeroth order Bessel function of the first kind. In the resonant limit ($d\gamma \gg |\Delta|$), we find the duration of the output pulse by observing that the $\tilde{\Delta} \rightarrow 0$ limit of Eq. (B.26) is

$$\mathcal{E}(1, \tilde{t}) = -\frac{\tilde{\Omega}(\tilde{t})}{\sqrt{d}} S\left(1 - \frac{h(0, \tilde{t})}{d}\right), \quad (\text{B.27})$$

with the understanding that $S(\tilde{z})$ vanishes outside of $[0, 1]$. This is just the ideal lossless and dispersionless group velocity propagation of Refs. [17, 293, 16], also known as EIT. This implies a duration $T_{\text{out}} \sim d\gamma/|\Omega|^2$ for the output pulse in the resonant limit, which is consistent with the cavity case analyzed in Appendix A if one identifies C and d . In the Raman limit ($d\gamma \ll |\Delta|$), the length of the output pulse is simply given by the fall-off of J_0 and is found from $h(0, \tilde{t})d/\tilde{\Delta}^2 \sim 1$ to be $T_{\text{out}} \sim \Delta^2/(\gamma d|\Omega|^2)$. It is worth noting that the appropriate Raman limit condition is $\gamma d \ll |\Delta|$ and not $\gamma \ll |\Delta|$ as one might naively assume by analogy with the single-atom case. It is also important to note that if one is limited by laser power (as in Ref. [85]) and desires to achieve the smallest possible T_{out} , the above formulas for T_{out} imply that EIT retrieval is preferable over Raman.

Dependence of retrieval error on optical depth d

In the cavity case analyzed in Appendix A, only one spin-wave mode is available and the retrieval error is always $1/(1+C)$ ($\approx 1/C$ for $C \gg 1$). In free space, in contrast, the retrieval error depends on the spin-wave mode $S(\tilde{z})$ and as we will explain in this Section, scales differently with d depending on the spin wave. Since the retrieval efficiency is independent of Δ , to gain some physical intuition for the error dependence on the spin wave and on d , we will focus on the $\Delta = 0$ case, for which the formalism of EIT transparency window has been developed [305]. For $\Delta = 0$ and large d , the integrand in Eq. (B.23) can be approximated with a Gaussian. Then using dimensionless momentum $\tilde{k} = kL$ and defining the Fourier transform of $S(\tilde{z})$ as $S(\tilde{k}) = (2\pi)^{-1} \int_0^1 d\tilde{z} S(\tilde{z}) \exp(-i\tilde{k}\tilde{z})$, we can write Eq. (B.23) as

$$\mathcal{E}(1, \tilde{t}) = -\frac{\tilde{\Omega}(\tilde{t})}{\sqrt{d}} \int_{-\infty}^{\infty} d\tilde{k} e^{i\tilde{k}\left(1 - \frac{h(0, \tilde{t})}{d}\right)} e^{-h(0, \tilde{t})\frac{\tilde{k}^2}{d^2}} S(\tilde{k}). \quad (\text{B.28})$$

In the limit $d \rightarrow \infty$, the Gaussian term can be replaced with 1 to yield back the group velocity propagation in Eq. (B.27). Computing the efficiency using Eq. (B.28), we find, after a change of variables $\tilde{t} \rightarrow \tau = h(0, \tilde{t})/d$,

$$\eta_{\text{r}} = \int_0^{\infty} d\tau \left| \int_{-\infty}^{\infty} d\tilde{k} e^{i\tilde{k}(1-\tau)} e^{-\frac{\tilde{k}^2}{d\tau}} S(\tilde{k}) \right|^2. \quad (\text{B.29})$$

We will now show that the Gaussian term of width $\Delta\tilde{k}_{\text{EIT}} = \sqrt{d/\tau}$ in the integrand in Eq. (B.29) can be interpreted as the effective momentum-space EIT transparency

window for the spin wave. We start by noting that the equivalent of τ in the original units (call it z_{prop}) is equal to $z_{\text{prop}} = L\tau(t) = \int_0^t v_g(t')dt'$ and, thus, represents the propagation distance ($v_g = c\Omega^2/(g^2N)$ is the EIT group velocity [305]). This interpretation of z_{prop} also follows from the fact that, if one ignores the Gaussian in Eq. (B.29), the spin wave would be evaluated at $\tilde{z} = 1 - \tau$. Thus, in terms of the propagation distance z_{prop} , the width of the momentum-space transparency window in Eq. (B.29) can be written, in original units, as $\Delta k_{\text{EIT}} = \tilde{\Delta k}_{\text{EIT}}/L = \sqrt{d/\tau}/L = \sqrt{g^2N/(\gamma cz_{\text{prop}})}$. Thus, as the propagation distance z_{prop} decreases, the width Δk_{EIT} of the transparency window gets wider and eventually becomes infinite at the $\tilde{z} = 1$ end of the ensemble, where $z_{\text{prop}} = 0$. The consistency of our expression Δk_{EIT} for the effective momentum-space EIT window with the expression for the frequency-space EIT transparency window $\Delta\omega_{\text{EIT}} = v_g\sqrt{g^2N/(\gamma cz_{\text{prop}})}$ [305] immediately follows from rescaling by v_g both $\Delta\omega_{\text{EIT}}$ and the dark state polariton [17, 293, 16] bandwidth $\Delta\omega_p = v_g\Delta k_{\text{spin}}$ (where Δk_{spin} is the width of $S(k)$ in the original units). In fact, the change of variables $t \rightarrow \tau$ that led to Eq. (B.29) precisely accomplished this rescaling of the polariton and the EIT window by the group velocity. It is worth noting that this proportionality of both the polariton bandwidth and the frequency-space EIT window width to the group velocity (and, hence, the existence of the control-independent effective momentum-space EIT window) is another physical argument for the independence of retrieval efficiency from the control power.

An important characterization of the performance of an ensemble-based memory is the scaling of error with optical depth at large optical depth. In the cavity case analyzed in Appendix A, there was only one spin-wave mode available and the retrieval error for it was $1/(1+C)$ ($\approx 1/C$ for $C \gg 1$), where the cooperativity parameter C can be thought of as the effective optical depth enhanced by the cavity. By qualitative arguments, we showed in Sec. B.3 that the retrieval efficiency in free space is $1 - \eta \sim 1/d$. A more precise value can be found numerically from the optimal spin wave (Sec. B.3), which gives a maximal retrieval efficiency that scales approximately as $\sim 2.9/d$, i.e., one over the first power of density, precisely as in the cavity case. However, this $1/d$ scaling turns out to be not the only possibility in free space. The scaling of the retrieval error with d can be either $1/d$ or $1/\sqrt{d}$ depending on the presence of steps (i.e., discontinuities in the amplitude or phase of the spin wave). Specifically, numerics show that for a spin wave that does not have steps at any $\tilde{z} < 1$, the retrieval error scales as $1/d$, while steps in the phase or amplitude of the spin wave result in a $1/\sqrt{d}$ error. In particular, a step in the amplitude of $S(\tilde{z})$ at position \tilde{z} of height l can be found numerically to contribute an error of $l^2\sqrt{2/\pi}\sqrt{1-\tilde{z}}/\sqrt{d}$ at large d . The reason for the importance of steps is that at high d , the effective EIT window is very wide and only the tails of the Fourier transform $S(\tilde{k})$ of the spin wave $S(\tilde{z})$ matter. A step, i.e., a discontinuity, in the function $S(\tilde{z})$ means that its Fourier transform falls off as $S(\tilde{k}) \sim 1/\tilde{k}$. Thus, if we assume all frequencies outside of an effective EIT window of width $\Delta\tilde{k}_{\text{EIT}} = \sqrt{d/\tau} \sim \sqrt{d/(1-\tilde{z})}$ get absorbed, the

error will be proportional to $\int_{\Delta\tilde{k}_{\text{EIT}}}^{\infty} d\tilde{k} |S(\tilde{k})|^2 \sim \sqrt{(1-\tilde{z})/d}$, precisely as found with numerics. Numerics also show that if a step in $|S(\tilde{z})|$ is not infinitely sharp, at a given d , a feature should be regarded as a step if the slope of $|S(\tilde{z})|^2$ is bigger than $\sim \sqrt{d}$ (and will then contribute a $1/\sqrt{d}$ error). The simple physical reason for this is that only if a feature in $S(\tilde{z})$ is narrower than $1/\sqrt{d}$ will it extend in \tilde{k} space outside the effective EIT window of width $\Delta\tilde{k}_{\text{EIT}} = \sqrt{d/\tau}$. While we only performed detailed analysis of steps in the amplitude of $S(\tilde{z})$, steps in the phase of $S(\tilde{z})$, as we have already noted, also contribute a $1/\sqrt{d}$ error, and we expect that similar dependence on the position and sharpness of such phase steps holds.

A useful analytical result on scaling that supports these numerical calculations is the error on retrieval from a flat spin wave $S(\tilde{z}) = 1$, which can be calculated exactly from Eq. (B.25) to be

$$1 - \eta_{\text{r}} = e^{-d}(I_0(d) + I_1(d)). \quad (\text{B.30})$$

Using the properties of modified Bessel functions of the first kind, one finds that as $d \rightarrow \infty$, the error approaches $\sqrt{2/\pi}/\sqrt{d}$, which is consistent with the general formula since a flat spin wave has one step at $\tilde{z} < 1$, i.e., a step of height 1 at $\tilde{z} = 0$. In fact, it is this analytical result that allows us to exactly identify the $\sqrt{2/\pi}$ prefactor in the error due to amplitude steps.

Based on the results of this Section and the results of Appendix A, we can identify several advantages of using a cavity setup. First, in the cavity, the optical depth is enhanced by the value of the cavity finesse from the free-space value of d to form the cooperativity parameter C . Moreover, in terms of d and C the errors during optimal storage in free space and in the cavity scale as $2.9/d$ and $1/C$, respectively. That is, even if one ignores the enhancement due to cavity finesse, the cavity offers a factor of 3 improvement. In addition to that, if one is forced to retrieve from the flat spin-wave mode $S(\tilde{z}) = 1$ (which is the case, for example, if the spin wave is generated via spontaneous Raman scattering as in Ref. [80]), the free-space error is increased from the optimal and scales as $\sqrt{2/\pi}/\sqrt{d}$, while in the cavity case the mode $S(\tilde{z}) = 1$ is, in fact, the only mode coupled to the cavity mode and is, therefore, precisely the one that gives $1/C$ scaling. Finally, because there is only one spin wave mode accessible in the cavity setup, the time reversal based iterative optimization procedure (Sec. B.5) requires only one iteration in the cavity case. On the other hand, the free-space setup described in this Appendix is much simpler to realize in practice and allows for the storage of multiple pulses in the same ensemble, e.g., time-bin encoded qubits [95].

Using the effective EIT window concept developed in this Section, we can now interpret from a different perspective the optimal retrieval spin waves computed in Sec. B.3. These spin waves represent at each d the optimal balance between maximal smoothness (to minimize the momentum space width $\Delta\tilde{k}_{\text{spin}}$ of the spin wave so that it better fits inside the effective EIT window) and least amount of propagation (to minimize τ and, thus, maximize the width $\Delta\tilde{k}_{\text{EIT}} = \sqrt{d/\tau}$ of the effective EIT window itself).

Shaping retrieval into an arbitrary mode

We have shown that optimal storage of a given input mode requires the ability to retrieve optimally into the time reverse of this input mode. Thus, by finding the modes we can retrieve into, we will also find the modes that can be optimally stored. In this Section we prove that by adjusting² the control during retrieval we can retrieve from any mode $S(\tilde{z})$ into any given normalized mode $\mathcal{E}_2(\tilde{t})$, provided the mode is sufficiently smooth to satisfy the adiabaticity condition (which in the original units means $T_{\text{out}}d\gamma \gg 1$, where T_{out} is the duration of $\mathcal{E}_2(t)$, as we discuss in Sec. B.6.4).

We know from Sec. B.3 that the retrieval efficiency η_r is independent of the detuning Δ and the control Ω , provided the retrieval is complete (for adiabatic retrieval, the condition on the control pulse energy for complete retrieval is $dh(0, \infty) \gg |d + i\tilde{\Delta}|^2$, as found in Sec. B.6.1). Thus, to find the control that retrieves $S(\tilde{z})$ into any given normalized mode $\mathcal{E}_2(\tilde{t})$ with detuning $\tilde{\Delta}$, we need to solve for $\tilde{\Omega}(\tilde{t})$ in equation (B.23) with $\mathcal{E}(1, \tilde{t}) = \sqrt{\eta_r}\mathcal{E}_2(\tilde{t})$:

$$\sqrt{\eta_r}\mathcal{E}_2(\tilde{t}) = -\sqrt{d}\tilde{\Omega}(\tilde{t}) \int_0^1 d\tilde{z} \frac{1}{1+i\tilde{\Delta}} e^{-\frac{h(0,\tilde{t})+d\tilde{z}}{1+i\tilde{\Delta}}} I_0 \left(2\frac{\sqrt{h(0,\tilde{t})d\tilde{z}}}{1+i\tilde{\Delta}} \right) S(1-\tilde{z}). \quad (\text{B.31})$$

To solve for $\tilde{\Omega}(\tilde{t})$, we integrate the norm squared of both sides from 0 to \tilde{t} and change the integration variable from \tilde{t}' to $h' = h(0, \tilde{t}')$ on the right hand side to obtain

$$\eta_r \int_0^{\tilde{t}} d\tilde{t}' |\mathcal{E}_2(\tilde{t}')|^2 = \int_0^{h(0,\tilde{t})} dh' \left| \int_0^1 d\tilde{z} \frac{\sqrt{d}}{1+i\tilde{\Delta}} e^{-\frac{h'+d\tilde{z}}{1+i\tilde{\Delta}}} I_0 \left(2\frac{\sqrt{h'd\tilde{z}}}{1+i\tilde{\Delta}} \right) S(1-\tilde{z}) \right|^2. \quad (\text{B.32})$$

In the cavity case, the corresponding equation (A.20) was solvable analytically. To solve Eq. (B.32) for $h(0, \tilde{t})$ numerically, we note that both sides of Eq. (B.32) are monotonically increasing functions of \tilde{t} and are equal at $\tilde{t} = 0$ and $\tilde{t} = \infty$ (provided $h(0, \infty)$ can be replaced with ∞ , which is the case if $dh(0, \infty) \gg |d+i\tilde{\Delta}|^2$). Therefore, Eq. (B.32) can always be solved for $h(0, \tilde{t})$. $|\tilde{\Omega}(\tilde{t})|$ is then deduced by taking the square root of the derivative of $h(0, \tilde{t})$. The phase of $\tilde{\Omega}$ is found by inserting $|\tilde{\Omega}|$ into Eq. (B.31) and is given by

$$\begin{aligned} \text{Arg} \left[\tilde{\Omega}(\tilde{t}) \right] &= \pi + \text{Arg} \left[\mathcal{E}_2(\tilde{t}) \right] - \frac{h(0, \tilde{t})}{1 + \tilde{\Delta}^2} \tilde{\Delta} \\ &\quad - \text{Arg} \left[\int_0^1 d\tilde{z} \frac{1}{1+i\tilde{\Delta}} e^{-\frac{d\tilde{z}}{1+i\tilde{\Delta}}} I_0 \left(2\frac{\sqrt{h(0,\tilde{t})d\tilde{z}}}{1+i\tilde{\Delta}} \right) S(1-\tilde{z}) \right]. \end{aligned} \quad (\text{B.33})$$

The second and third terms are the phase of the desired output and the compensation for the Stark shift, respectively. In the resonant limit ($d\gamma \gg |\Delta|$), we can set $\tilde{\Delta} = 0$.

²For some previous results regarding output field shaping [101].

Then assuming the phase of $S(\tilde{z})$ is independent of \tilde{z} , the phase of the optimal control is given (up to a constant) solely by the phase of the desired output. In the Raman limit ($d\gamma \ll |\Delta|$), the integral in the last term is approximately real but at times near the end of the output pulse ($t \approx T_{\text{out}}$) it can change sign and go through zero. At these times, the optimal $|\tilde{\Omega}(\tilde{t})|$ diverges and the phase of $\tilde{\Omega}(\tilde{t})$ changes by π . Numerical simulations show, however, that $|\tilde{\Omega}(\tilde{t})|$ can be truncated at those points without significant loss in the retrieval efficiency and in the precision of $\mathcal{E}_2(\tilde{t})$ generation. Moreover, these points happen only near the back end of the desired output pulse over a rather short time interval compared to the duration of the desired output pulse. We can therefore often even completely turn off $\tilde{\Omega}(\tilde{t})$ during this short interval without significantly affecting the result, so that the problem of generating large power and π phase shifts can be avoided altogether (see Sec. B.6.4 for another brief discussion of this issue). However, these potential difficulties in the Raman limit for generating the optimal control (which also has to be chirped according to Eq. (B.33) in order to compensate for the Stark shift) make the resonant (EIT) limit possibly more appealing than the far-off-resonant (Raman) limit.

Finally, we note that a divergence in $|\tilde{\Omega}(\tilde{t})|$ can occur at any detuning $\tilde{\Delta}$ even when the above Raman-limit divergences are not present. Specifically, similarly to the cavity discussion in Appendix A, if one wants to shape the retrieval into a mode $\mathcal{E}_2(\tilde{t})$ that drops to zero at some time T_{out} sufficiently rapidly, $|\tilde{\Omega}(\tilde{t})|$ will go to ∞ at $t = T_{\text{out}}$. However, as in the above case of the Raman-limit divergences, the infinite part can be truncated without significantly affecting the efficiency or the precision of $\mathcal{E}_2(\tilde{t})$ generation. One can confirm this by inserting into the adiabatic solution in Eq. (B.23) a control pulse that is truncated to have a value of $h(0, \infty)$ that is finite but large enough to satisfy $dh(0, \infty) \gg |d + i\tilde{\Delta}|^2$. However, to be completely certain that the truncation is harmless, one has to solve Eqs. (B.5)-(B.7) numerically without making the adiabatic approximation. We will do this in Sec. B.6.4 for the case of storage, where the same truncation issue is present.

B.6.2 Adiabatic Storage

In principle, the retrieval results of the previous Section and the time reversal argument immediately imply that in the adiabatic limit (see Sec. B.6.4 for precise conditions), any input mode $\mathcal{E}_{\text{in}}(\tilde{t})$ at any detuning $\tilde{\Delta}$ can be stored with the same d -dependent maximum efficiency if one appropriately shapes the control field. However, for completeness and to gain extra physical insight, in this Section, we present an independent solution to adiabatic storage.

Using the Laplace transform in space and a procedure similar to the one used in

Sec. B.6.1 to solve retrieval, we find that the adiabatic solution of storage is

$$S(\tilde{z}, \tilde{T}) = -\sqrt{d} \int_0^{\tilde{T}} d\tilde{t} \tilde{\Omega}^*(\tilde{t}) \frac{1}{1+i\tilde{\Delta}} e^{-\frac{h(\tilde{t}, \tilde{T})+d\tilde{z}}{1+i\tilde{\Delta}}} I_0 \left(2 \frac{\sqrt{h(\tilde{t}, \tilde{T})d\tilde{z}}}{1+i\tilde{\Delta}} \right) \mathcal{E}_{\text{in}}(\tilde{t}). \quad (\text{B.34})$$

It is important to note that the retrieval equation (B.23) and the storage equation (B.34) can be cast in terms of the same Ω -dependent function m as

$$\mathcal{E}_{\text{out}}(\tilde{t}) = \int_0^1 d\tilde{z} m[\Omega(\tilde{t}), \tilde{t}, \tilde{z}] S(1-\tilde{z}), \quad (\text{B.35})$$

$$S(\tilde{z}, \tilde{T}) = \int_0^{\tilde{T}} d\tilde{t} m[\Omega^*(\tilde{T}-\tilde{t}), \tilde{T}-\tilde{t}, \tilde{z}] \mathcal{E}_{\text{in}}(\tilde{t}). \quad (\text{B.36})$$

This is precisely the general time reversal property of our equations that we discussed abstractly in Secs. B.4 and B.5 and used to find the optimal storage strategy from optimal retrieval. However, as we said in the beginning of this Section, we will now, for completeness, optimize storage directly without using time reversal and our solution for optimal retrieval.

We would like to solve the following problem: given $\mathcal{E}_{\text{in}}(\tilde{t})$, Δ , and d , we are interested in finding $\tilde{\Omega}(\tilde{t})$ that will give the maximum storage efficiency. To proceed towards this goal, we note that if we ignore decay γ and allow the spin wave to extend beyond $\tilde{z} = 1$, we get the “decayless” storage equation

$$s(\tilde{z}) = \int_0^{\tilde{T}} d\tilde{t} q(\tilde{z}, \tilde{t}) \mathcal{E}_{\text{in}}(\tilde{t}), \quad (\text{B.37})$$

where the “decayless” mode $s(\tilde{z})$ is defined for \tilde{z} from 0 to ∞ instead of from 0 to 1 and where

$$q(\tilde{z}, \tilde{t}) = i\sqrt{d}\tilde{\Omega}^*(\tilde{t}) \frac{1}{\tilde{\Delta}} e^{i\frac{h(\tilde{t}, \tilde{T})+d\tilde{z}}{\tilde{\Delta}}} J_0 \left(2 \frac{\sqrt{h(\tilde{t}, \tilde{T})d\tilde{z}}}{\tilde{\Delta}} \right). \quad (\text{B.38})$$

Since in Eq. (B.37), both sources of storage loss (the decay γ and the leakage past $\tilde{z} = 1$) are eliminated, the transformation between input modes $\mathcal{E}_{\text{in}}(\tilde{t})$ and decayless modes $s(\tilde{z})$ becomes unitary. Indeed, we show in Sec. B.10.5 that Eq. (B.37) establishes, for a given $\tilde{\Omega}(\tilde{t})$, a 1-to-1 correspondence between input modes $\mathcal{E}_{\text{in}}(\tilde{t})$ and decayless modes $s(\tilde{z})$. Moreover, we show in Sec. B.10.5 that Eq. (B.37) also establishes for a given $s(\tilde{z})$ a 1-to-1 correspondence between input modes $\mathcal{E}_{\text{in}}(\tilde{t})$ and control fields $\tilde{\Omega}(\tilde{t})$. In particular, this means that we can compute the control field that realizes decayless storage (via Eq. (B.37)) of any given input mode $\mathcal{E}_{\text{in}}(\tilde{t})$ into any given decayless spin-wave mode $s(\tilde{z})$.

A key element in the control shaping procedure just described is the ability to reduce the problem to the unitary mapping by considering the decayless (and leakless)

solution. The reason why this shaping is useful and why it, in fact, allows us to solve the actual shaping problem in the presence of decay and leakage is that the spin wave, into which we store in the presence of decay, can be directly determined from the decayless solution: using Eqs. (B.34) and (B.37) and Eq. (B.24) (with appropriate complex values of μ , λ , and p), we find that

$$S(\tilde{z}, \tilde{T}) = \int_0^\infty d\tilde{z}' de^{-d(\tilde{z}+\tilde{z}')} I_0(2d\sqrt{\tilde{z}\tilde{z}'})s(\tilde{z}'). \quad (\text{B.39})$$

This means that, remarkably, $S(\tilde{z}, \tilde{T})$ (and hence the storage efficiency) depends on $\mathcal{E}_{\text{in}}(\tilde{t})$ and $\tilde{\Omega}(\tilde{t})$ only through the decayless mode $s(\tilde{z})$, which itself can be computed via unitary evolution in Eq. (B.37).

Computing storage efficiency from Eq. (B.39) as a functional of $s(\tilde{z})$ and maximizing it under the constraint that $s(\tilde{z})$ is normalized gives an eigenvalue problem similar to Eq. (B.16) except the upper limit of integration is ∞ and the kernel is different. After finding the optimal $s(\tilde{z})$ via the iteration scheme similar to the one used to solve Eq. (B.16), we conclude the procedure for optimal storage control shaping by using the unitary transformation in Eq. (B.37) to solve for the control in terms of $s(\tilde{z})$ and $\mathcal{E}_{\text{in}}(\tilde{t})$, as shown in Sec. B.10.5. Since efficiency is determined by $s(\tilde{z})$ alone, this gives the optimal storage with the same maximal efficiency for any input pulse shape (provided it is sufficiently smooth, as discussed in Sec. B.6.4).

Having derived the optimal storage control, we can now explicitly verify the results obtained from the time reversal reasoning. In Sec. B.10.5, we show that the mode $S(\tilde{z}, \tilde{T})$ used in optimal storage is just the optimal mode for backward retrieval; that the optimal storage efficiency and optimal retrieval efficiency are equal; and that the optimal storage control for a given input mode is the time-reverse of the control that gives optimal backward retrieval into the time-reverse of that input mode.

To give an example of optimal controls, we consider a Gaussian-like input mode (shown in Fig. B.3)

$$\mathcal{E}_{\text{in}}(\tilde{t}) = A(e^{-30(\tilde{t}/\tilde{T}-0.5)^2} - e^{-7.5})/\sqrt{\tilde{T}}, \quad (\text{B.40})$$

where for computational convenience we set $\mathcal{E}_{\text{in}}(0) = \mathcal{E}_{\text{in}}(\tilde{T}) = 0$ and where $A \approx 2.09$ is a normalization constant. Figure B.3 shows the corresponding optimal storage control shapes $\tilde{\Omega}$ for the case $\tilde{\Delta} = 0$ and $d = 1, 10, 100$, as well as the limiting shape of the optimal $\tilde{\Omega}$ as $d \rightarrow \infty$. The controls are plotted in rescaled units so that the area under the square of the curves shown is equal to $L^{-1} \int_0^{\tilde{T}} dt' v_g(t')$ (where v_g is the EIT group velocity), which is the position (in units of L), at which the front end of the pulse would get stored under ideal decayless propagation. From time reversal and the condition for complete retrieval, it follows that the control pulse energy ($\propto h(0, \tilde{T})$) and hence $L^{-1} \int_0^{\tilde{T}} dt' v_g(t')$ should diverge. Thus, at any finite d , the optimal $\tilde{\Omega}$ plotted in Fig. B.3 should actually diverge at $\tilde{t} = 0$. However, the front part of the control pulse affects a negligible piece of $\mathcal{E}_{\text{in}}(\tilde{t})$, so truncating this part (by truncating $s(\tilde{z})$ at

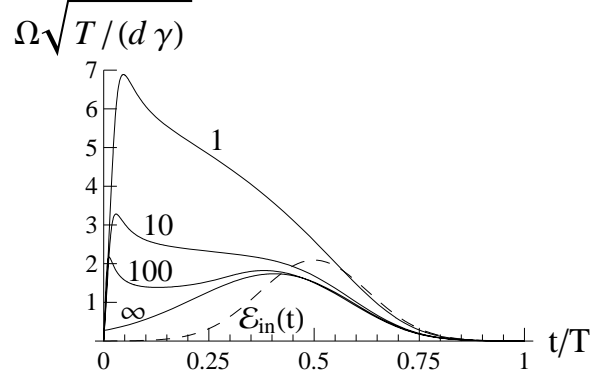


Figure B.3: Input mode $\mathcal{E}_{\text{in}}(t)$ (dashed) defined in Eq. (B.40) and control fields $\Omega(t)$ (in units of $\sqrt{d\gamma/T}$) that maximize for this $\mathcal{E}_{\text{in}}(t)$ the efficiency of resonant adiabatic storage (alone or followed by backward retrieval) at $d = 1, 10, 100$, and $d \rightarrow \infty$.

some \tilde{z} , for example) does not affect the efficiency (we will confirm this again in Sec. B.6.4). Naively, the optimal control should roughly satisfy $L^{-1} \int_0^T dt' v_g(t') = 1$: the control (and, thus, the dark state polariton group velocity) should be small enough to avoid excessive leakage; and at the same time it should be as large as possible to have the widest possible EIT transparency window to minimize spontaneous emission losses. For the truncated optimal controls, we see that $L^{-1} \int_0^T dt' v_g(t')$ (i.e., the area under the square of the curves in Fig. B.3) is, in fact, greater than 1. As d decreases, $L^{-1} \int_0^T dt' v_g(t')$ decreases as well, and allows for less and less leakage so that only as $d \rightarrow \infty$, $s(\tilde{z}) \rightarrow \sqrt{3}(1 - \tilde{z})$, $L^{-1} \int_0^T dt' v_g(t') \rightarrow 1$, and no leakage is allowed for.

Similarly to the cavity storage discussed in Appendix A, although optimal storage efficiencies are the same in the Raman and adiabatic limits, the two limits exhibit rather different physical behavior. It is now the dependence on d of the intensity of the optimal control field that can be used to distinguish between the resonant and the Raman regimes. Using an analysis very similar to pulse duration analysis of Sec. B.6.1 or alternatively relying on the fact that optimal storage is the time-reverse of optimal retrieval, we find that in the resonant limit ($d\gamma \gg |\Delta|$), $|\Omega|^2 \sim d\gamma/T$, while in the Raman limit ($d\gamma \ll |\Delta|$), $|\Omega|^2 \sim \Delta^2/(\gamma T d)$. Both of these agree with the cavity model of Appendix A (identifying C and d) while the resonant control agrees with $v_g T \sim L$. As explained in the cavity case in Sec. A.5.2, this opposite dependence of $|\Omega|$ on d in the Raman and EIT limits is the consequence of the fact that the coupling of the input photon to the spin wave has the opposite dependence on Ω in the two regimes. Finally, we note that in the Raman limit ($|\Delta| \gg d\gamma$), $|\Omega|^2 \sim \Delta^2/(\gamma T d) \gg d\gamma/T$, which means that if one is limited by control power (as in Ref. [85]), the EIT regime is preferable to the Raman regime.

B.6.3 Storage Followed by Retrieval

In the cavity case discussed in Appendix A, there was only one spin-wave mode we could write on. Moreover, this spatially uniform mode looked the same in the forward and backward directions (assuming negligible metastable state splitting ω_{sg}). Therefore, optimal storage into that mode guaranteed that the combined procedure of storage followed by retrieval was optimal as well and the total efficiency did not depend on the retrieval direction. In contrast, the free-space model allows for storage into a variety of modes, each of which has a different retrieval efficiency that is also dependent on retrieval direction. Therefore, in free space, we will first discuss the optimization of storage followed by backward retrieval and then the optimization of storage followed by forward retrieval.

Since we have shown that the optimal spin-wave mode for backward retrieval is also the optimal mode for storage, the controls found in Sec. B.6.2, which optimize storage, are also optimal for storage followed by backward retrieval. Figure B.4 shows the maximum total efficiency for storage followed by backward retrieval ($\eta_{\text{back}}^{\text{max}}$ - solid line), which in the adiabatic limit can be achieved for any input pulse. For comparison, we also show the total efficiency for storage followed by backward retrieval for a Gaussian-like input mode defined in Eq. (B.40) (assuming the adiabatic limit $Td\gamma \gg 1$) with naive square storage control pulses on $[0, T]$ with power set by $v_g T = L$, where v_g is the EIT group velocity (η_{square} - dashed line). The significant increase in the efficiency up to the input-independent optimal efficiency $\eta_{\text{back}}^{\text{max}}$ due to the use of optimal storage control pulses instead of naive ones is, of course, not unique to the input pulse of Eq. (B.40) and holds for any input pulse. In fact, since at moderate values of d the naive control pulse is far from satisfying the complete retrieval condition, it is not optimal for any input.

Since the optimal mode for storage or retrieval alone is not symmetric, a separate optimization problem has to be solved for the case of storage followed by forward retrieval. We show in Sec. B.10.5 that Eq. (B.37) sets up, for any sufficiently smooth $\mathcal{E}_{\text{in}}(\tilde{t})$, a 1-to-1 correspondence between decayless modes $s(\tilde{z})$ and control fields $\tilde{\Omega}(\tilde{t})$. Moreover, the decayless mode alone determines the total efficiency of storage followed by forward retrieval, which can be found by inserting Eq. (B.39) into Eq. (B.25). Thus, the optimization problem reduces to finding the optimal $s(\tilde{z})$ by the iterative optimization procedure except with a new kernel.

From a different perspective, since the process of storage followed by forward retrieval as a whole fits into the general setup of Sec. B.5, we can use time reversal to optimize it. In particular, we showed in Sec. B.5 how to find the optimal input mode to be used with a given pair of control pulses: we should take a trial input mode, carry out storage followed by forward retrieval, time reverse the output and the controls, and iterate until convergence. Since the reverse process is itself storage followed by forward retrieval (except in the opposite direction) and since the iterations will optimize it as well, the spin-wave mode used in optimal storage followed by forward

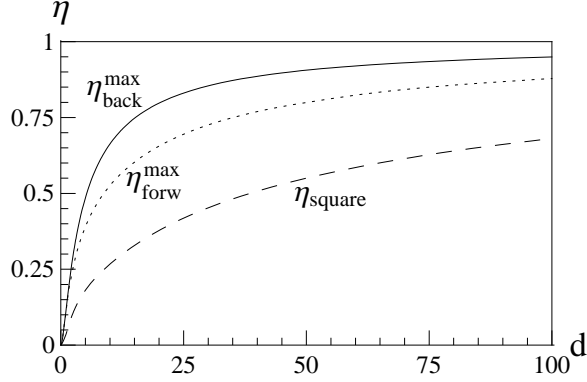


Figure B.4: $\eta_{\text{back}}^{\text{max}}$ (solid) and $\eta_{\text{forw}}^{\text{max}}$ (dotted) are maximum total efficiency for adiabatic (or fast) storage followed by backward or forward retrieval, respectively. η_{square} (dashed) is the total efficiency for resonant storage of $\mathcal{E}_{\text{in}}(t)$ from Eq. (B.40) followed by backward retrieval, where the storage control field is a naive square pulse with the power set by $v_g T = L$.

retrieval must be the one that flips under forward retrieval, followed by time reversal and (backward) storage. Moreover, it follows that the control pulse that we should use for a given $\mathcal{E}_{\text{in}}(\tilde{t})$ is the time-reverse of the control that retrieves the flipped version of the optimal spin-wave mode backwards into $\mathcal{E}_{\text{in}}^*(\tilde{T} - \tilde{t})$.

Thus, instead of computing the optimal $s(\tilde{z})$, we can solve the following eigenvalue problem that finds the optimal mode to store into

$$\lambda S(\tilde{z}) = \int_0^1 d\tilde{z}' k_r(\tilde{z}, 1 - \tilde{z}') S(\tilde{z}'). \quad (\text{B.41})$$

This eigenvalue equation is just a simple modification of the retrieval eigenvalue equation (B.16): we are now computing the mode that flips under forward retrieval followed by time reversal and storage, while Eq. (B.16) finds the mode that stays the same under backward retrieval followed by time reversal and storage. The total efficiency of storage followed by forward retrieval is then λ^2 . However, in contrast to storage followed by backward retrieval, the storage efficiency and the forward retrieval efficiency during the optimal procedure are not each equal to λ ; the storage efficiency is greater.

The optimal spin-wave modes that result from Eq. (B.41) are shown in Fig. B.5 for the indicated values of d . At small d , the optimal mode is almost flat since at small d the optimal retrieval and storage modes are almost flat and, thus, almost symmetric. As d increases, the optimal mode first bends towards the wedge $\sqrt{3}(1 - \tilde{z})$ similarly to the optimal backward retrieval mode. But then above $d \approx 3$, the optimal mode starts shaping towards the parabola $S(z) = \sqrt{15/8}(1 - 4(\tilde{z} - 1/2)^2)$, which, as

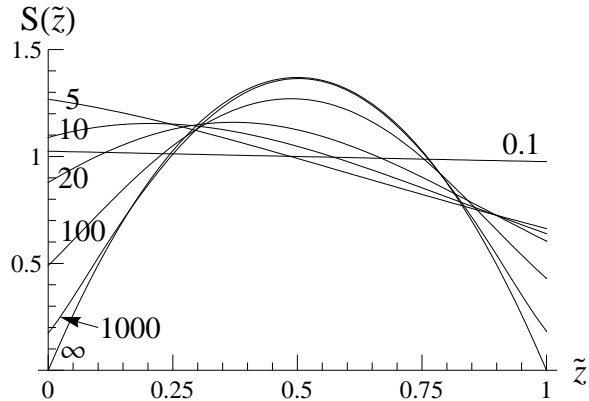


Figure B.5: For different values of d , the optimal spin-wave mode to be used during storage followed by forward retrieval.

expected, avoids the $1/\sqrt{d}$ error from discontinuities by vanishing at the edges and, simultaneously, maximizes smoothness.

The maximal total efficiency for storage followed by forward retrieval $\eta_{\text{forw}}^{\text{max}}$ is plotted as a dotted curve in Fig. B.4. $\eta_{\text{forw}}^{\text{max}}$ ($\approx 1 - 19/d$ as $d \rightarrow \infty$) is less than $\eta_{\text{back}}^{\text{max}}$ ($\approx 1 - 5.8/d$ as $d \rightarrow \infty$) since for optimal backward retrieval, storage and retrieval are each separately optimal, while for forward retrieval a compromise has to be made. From a different perspective, forward retrieval makes it more difficult to minimize propagation since the whole excitation has to propagate through the entire medium.

B.6.4 Adiabaticity Conditions

We have shown that in the adiabatic limit, any input mode can be stored with the same maximum efficiency. In this Section, we show that independent of Δ , the necessary and sufficient condition for optimal adiabatic storage of a pulse of duration T to be consistent with the adiabatic approximation is

$$Td\gamma \gg 1, \quad (\text{B.42})$$

which is identical to the corresponding condition in the cavity model in Appendix A, except with C replaced with d . In fact, we omit the derivation of this condition since the argument goes along the same lines as the corresponding argument in the cavity case in Sec. A.5.3, provided one uses the fact that in Eq. (B.11) $|u| \sim 1$ (since u is the Laplace variable corresponding to \tilde{z} , which, in turn, runs from 0 to 1).

Therefore, we immediately turn to the tasks of verifying numerically that Eq. (B.42) is indeed the correct adiabaticity condition and of investigating the breakdown of adiabaticity for short input pulses. We consider adiabatic storage of a Gaussian-like input mode defined in Eq. (B.40) and shown in Fig. B.3. We use our adiabatic

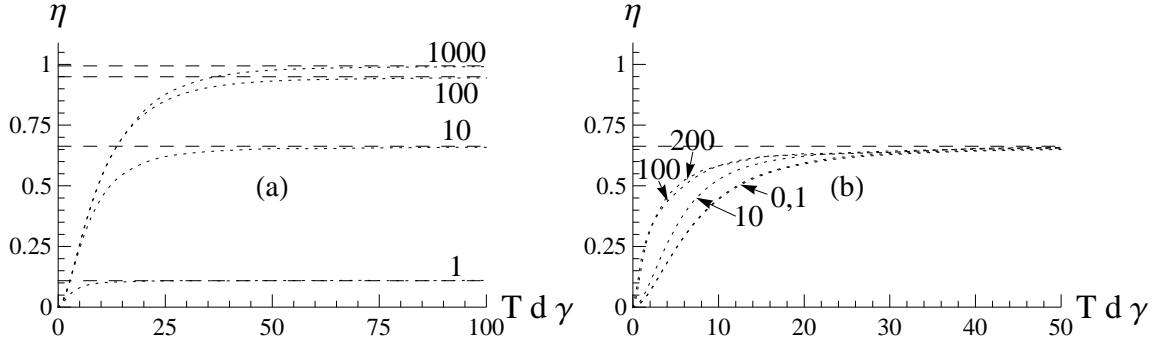


Figure B.6: Breakdown of optimal adiabatic storage in free space at $Td\gamma \lesssim 10$. In (a), the total efficiency of storage followed by backward retrieval is plotted for $\Delta = 0$ and $d = 1, 10, 100$, and 1000 . The horizontal dashed lines are the maximal values. Dotted lines are obtained for the input from Fig. B.3 using adiabatic equations to shape the storage control but then using exact equations to numerically compute the efficiency. In (b), the same plot is made for $d = 10$ and $\Delta/\gamma = 0, 1, 10, 100, 200$.

equations to shape the control pulse but then compute the total efficiency of storage followed by backward retrieval numerically from Eqs. (B.5)-(B.7) *without* making the adiabatic approximation. As $Td\gamma$ decreases to 1 and below, we expect the efficiency to be reduced from its optimal value. In Fig. B.6(a), the total efficiency of this procedure is plotted as a function of $Td\gamma$ for $\Delta = 0$ and $d = 1, 10, 100$, and 1000 . The dashed lines are the true optimal efficiencies. As expected, when $Td\gamma \lesssim 10$, the efficiency drops. In Fig. B.6(b), we fix $d = 10$ and show how optimal adiabatic storage breaks down at different detunings Δ from 0 to 200γ . As in the cavity case of Appendix A, we see from Fig. B.6(b) that as we move from the resonant limit ($d\gamma \gg |\Delta|$) to the Raman limit ($d\gamma \ll |\Delta|$), we can go to slightly smaller values of $Td\gamma$ before storage breaks down. However, since the curves for $\Delta = 100\gamma$ and $\Delta = 200\gamma$ almost coincide, $Td\gamma \gg 1$ is still the relevant condition no matter how high Δ is.

Before concluding the discussion of adiabaticity conditions, we note that, exactly as in the cavity case discussion in Sec. A.5.3, the magnitudes $|\Omega(t)|$ of the optimal control pulses, which go to ∞ at $t = 0$, had to be truncated to generate Fig. B.6. Moreover, Raman-limit divergences discussed (for the case of retrieval) in Sec. B.6.1 had to be truncated at two places near $t = 0.2T$ for $\Delta/\gamma = 100$ and 200 in Fig. B.6(b). As in Sec. A.5.3, the fact that the optimal efficiency given by the dashed lines in Fig. B.6 is achieved by the dotted curves (obtained with truncated controls) is the proof that truncation of the storage controls does not significantly affect the storage efficiency. Since time reversal discussed Sec. B.4 relates retrieval to optimal storage, this also means that truncation of the retrieval control fields does not significantly affect the precision, with which a given output mode $\mathcal{E}_2(\tilde{t})$ can be generated. The

losses associated with truncation are insignificant only if condition $dh(0, \infty) \gg |d + i\tilde{\Delta}|^2$ (see Sec. B.6.1) is satisfied for the truncated retrieval control pulse (the same condition with ∞ replaced with \tilde{T} applies to storage). If the energy in the control pulse is so tightly limited that this condition is violated, a separate optimization problem has to be solved. This problem has been considered in Ref. [85] for the special case of Raman storage in free space in the limit of negligible spontaneous emission loss. Although Eqs. (B.23) and (B.34) allow one to treat and optimize the case of limited control pulse energy, this problem is beyond the scope of the present Appendix.

B.6.5 Effects of Nonzero Spin-Wave Decay

We have so far assumed that the spin-wave decay rate in Eq. (B.3) is negligible (i.e., $\gamma_s = 0$). If this decay rate is not negligible but the corresponding incoming noise is vacuum (which is often true experimentally, as noted in Sec. B.10.1 and as explained in detail in Sec. A.8.1), the effect of nonzero spin-wave decay can be included simply by adding a term $-\tilde{\gamma}_s S$ to the right-hand side of Eq. (B.7) (where $\tilde{\gamma}_s = \gamma_s/\gamma$). In this Section, we discuss the effects such a term has on the adiabatic solution and optimal control field shaping discussed in Secs. B.6.1, B.6.2, and B.6.3. We will show, in particular, that nonzero γ_s simply introduces exponential decay into the retrieval and storage solutions without making the optimization harder. We will also show that with nonzero spin-wave decay, optimal efficiencies become dependent on the input mode (or, equivalently, on the control fields).

We first consider adiabatic retrieval discussed in Sec. B.6.1. One can easily check that nonzero spin-wave decay rate γ_s simply introduces decay described by $\exp(-\tilde{\gamma}_s \tilde{t})$ into Eq. (B.23), and, unless we retrieve much faster than $1/\gamma_s$, this makes the retrieval efficiency control dependent. Moreover, if a given fixed control field is not strong enough to accomplish retrieval in a time much faster than $1/\gamma_s$, the problem of finding the optimal retrieval mode for this particular retrieval control will give a different answer from the $\gamma_s = 0$ case. In particular, for forward retrieval, as we increase γ_s (or, alternatively, decrease the power of the retrieval control), to minimize propagation time at the cost of sacrificing smoothness, the optimal retrieval mode will be more and more concentrated towards the $z = L$ end of the ensemble. As in the $\gamma_s = 0$ case, we can find these optimal modes either by computing the (now Ω -dependent) kernel to replace k_r in Eq. (B.25) and its eigenvector with the largest eigenvalue or, equivalently, by doing the iteration of retrieval, time reversal, and storage.

The inclusion of nonzero γ_s also does not prevent us from being able to shape retrieval to go into any mode, as described for $\gamma_s = 0$ in Sec. B.6.1. We should just shape the control according to Eq. (B.31) as if there were no spin wave decay except the desired output mode $\mathcal{E}_2(t)$ on the left hand side should be replaced with

the normalized version of $\mathcal{E}_2(t) \exp(\gamma_s t)$, i.e.,

$$\mathcal{E}_2(\tilde{t}) \rightarrow \mathcal{E}_2(\tilde{t}) e^{\tilde{\gamma}_s \tilde{t}} \left[\int_0^\infty d\tilde{t}' |\mathcal{E}_2(\tilde{t}')|^2 e^{2\tilde{\gamma}_s \tilde{t}'} \right]^{-\frac{1}{2}}. \quad (\text{B.43})$$

The retrieval efficiency will, however, be output-mode-dependent in this case: it will be multiplied (and hence reduced) by a factor of $[\int_0^\infty d\tilde{t}' |\mathcal{E}_2(\tilde{t}')|^2 \exp(2\tilde{\gamma}_s \tilde{t}')]^{-1}$. Since this factor is independent of the spin wave, even with nonzero γ_s , the optimal retrieval into $\mathcal{E}_2(t)$ is achieved by retrieving from $\tilde{S}_d(z)$.

We now turn to adiabatic storage discussed in Sec. B.6.2. One can easily check that nonzero spin-wave decay γ_s simply introduces $\exp(-\tilde{\gamma}_s(\tilde{T} - \tilde{t}))$ decay into Eq. (B.38) (or, equivalently, into the integrand on the right hand side of Eq. (B.34)). Eq. (B.39) holds even with nonzero γ_s . The optimal storage control can then be found from Eq. (B.37) as if there were no decay but the input mode were replaced according to

$$\mathcal{E}_{\text{in}}(\tilde{t}) \rightarrow \mathcal{E}_{\text{in}}(\tilde{t}) e^{-\tilde{\gamma}_s(\tilde{T} - \tilde{t})} \left[\int_0^{\tilde{T}} d\tilde{t}' |\mathcal{E}_{\text{in}}(\tilde{t}')|^2 e^{-2\tilde{\gamma}_s(\tilde{T} - \tilde{t}')} \right]^{-\frac{1}{2}}. \quad (\text{B.44})$$

However, the optimal storage efficiency will now depend on input pulse duration and shape: it will be multiplied (and hence reduced) by $\int_0^{\tilde{T}} d\tilde{t}' |\mathcal{E}_{\text{in}}(\tilde{t}')|^2 \exp(-2\tilde{\gamma}_s(\tilde{T} - \tilde{t}'))$. It is also important to note that nonzero γ_s still keeps the general time reversal relationship between storage and retrieval exhibited in Eqs. (B.35) and (B.36). However, for $\mathcal{E}_2(\tilde{t}) = \mathcal{E}_{\text{in}}^*(\tilde{T} - \tilde{t})$,

$$\int_0^{\tilde{T}} d\tilde{t} |\mathcal{E}_{\text{in}}(\tilde{t})|^2 e^{-2\tilde{\gamma}_s(\tilde{T} - \tilde{t})} > \left[\int_0^{\tilde{T}} d\tilde{t} |\mathcal{E}_2(\tilde{t})|^2 e^{2\tilde{\gamma}_s \tilde{t}} \right]^{-1}, \quad (\text{B.45})$$

which means that with nonzero γ_s , the optimal storage efficiency of a given input mode is greater than the optimal retrieval efficiency into the time-reverse of that mode. Because the two controls involved are not time-reverses of each other, the inequality of the two efficiencies is consistent with the time reversal arguments. As in the cavity case in Appendix A, the main reason for this deviation from the $\gamma_s = 0$ behavior is the dependence of the retrieval efficiency on the control.

Finally, we discuss the effects of nonnegligible spin-wave decay on storage followed by retrieval considered in Sec. B.6.3. Using the fact that nonzero γ_s keeps the general time reversal relationship between storage and retrieval exhibited in Eqs. (B.35) and (B.36), it is not hard to verify that nonzero γ_s still allows one to use time reversal iterations to optimize storage followed by retrieval. In particular, suppose that one is given a storage control field and a (forward or backward) retrieval control field. Then one can find the optimal input mode to be used with these control fields by the following procedure: start with a trial input mode, store and retrieve it with the given pair of controls, time-reverse the whole procedure, and then repeat the full cycle

until convergence is reached. Now suppose, on the other hand, one is given an input mode and is asked to choose the optimal storage and retrieval controls. Because of the spin wave decay, it is desirable to read out as fast as possible. As we discuss in the next Section, fast readout may be achieved in a time $T \sim 1/\gamma d$, so that if we assume that $\gamma_s \ll d\gamma$, the spin-wave decay during the retrieval will be negligible. If we further assume that the given input mode satisfies the adiabatic limit $Td\gamma \gg 1$, then one should shape the storage control to store into the appropriate optimal spin-wave mode ($\tilde{S}_d(1 - \tilde{z})$ or a mode from Fig. B.5, depending on the direction of retrieval) as if γ_s were zero and the input were proportional to $\mathcal{E}_{\text{in}}(\tilde{t}) \exp(-\tilde{\gamma}_s(\tilde{T} - \tilde{t}))$ (see Eq. (B.44)). The total optimal efficiency will now depend on input pulse duration and shape: it will be multiplied (and hence reduced relative to the $\gamma_s = 0$ case) by $\int_0^{\tilde{T}} d\tilde{t} |\mathcal{E}_{\text{in}}(\tilde{t})|^2 \exp(-2\tilde{\gamma}_s(\tilde{T} - \tilde{t}))$. Finally, we note that when we consider storage followed by retrieval, in order to take into account the spin wave decay during the storage time $[\tilde{T}, \tilde{T}_r]$, one should just multiply the total efficiency by $\exp(-2\tilde{\gamma}_s(\tilde{T}_r - \tilde{T}))$.

B.7 Fast Retrieval and Storage

We have shown that in the adiabatic limit ($Td\gamma \gg 1$, where T is the duration of the incoming pulse), one can optimally store a mode with any smooth shape and any detuning Δ . In this Section, we solve Eq. (B.12) analytically in the second important limit, the “fast” limit, and demonstrate that this limit allows one to store optimally a certain class of input modes that have duration $T \sim 1/(d\gamma)$. We also show that efficient (but not optimal) fast storage of any smooth pulse is possible as long as $T\gamma \ll 1$ and $Td\gamma \gg 1$.

Exactly as in the cavity case in Sec. A.6, in the fast limit, one assumes that Ω is very large during a short control pulse ($|\Omega| \gg d\gamma$ and $|\Omega| \gg |\Delta|$) and keeps only terms containing $\tilde{\Omega}$ on the right-hand side of Eqs. (B.6) and (B.7) (or, equivalently, neglects all terms in Eq. (B.12) except $|\tilde{\Omega}|^2 S$ and \tilde{S}). This gives Rabi oscillations between P and S and allows one to implement a fast storage scheme, in which the input pulse is resonant ($\Delta = 0$) and the control pulse is a short π pulse at $t = T$, as well as fast retrieval, in which the control is a π pulse at $t = T_r$.

During fast retrieval, assuming that the π pulse is perfect and that it enters the medium at $\tilde{t} = 0$ (instead of $\tilde{t} = \tilde{T}_r$), the initial spin wave $S = S(\tilde{z})$ is mapped after the π pulse onto the optical polarization $P = iS(\tilde{z})$. We then solve Eq. (B.11) for $P(u, \tilde{t})$, express $\mathcal{E}(u, \tilde{t})$ in terms of $P(u, \tilde{t})$ using Eq. (B.10), and take the inverse Laplace transform $u \rightarrow \tilde{z} = 1$ to arrive at

$$\mathcal{E}_{\text{out}}(\tilde{t}) = -\sqrt{d} \int_0^1 d\tilde{z} e^{-\tilde{t}} J_0\left(2\sqrt{d\tilde{t}\tilde{z}}\right) S(1 - \tilde{z}). \quad (\text{B.46})$$

When computing the fast retrieval efficiency, one can take the time integral analytically to find that the efficiency is again given by Eq. (B.14), which is consistent with

the general proof in Sec. B.3 and the branching ratio argument. In the cavity case discussion in Appendix A, we noted that the fast solution was a special case of the adiabatic solution with a suitable control. Similarly, the expression in Eq. (B.46) is also a special case of Eq. (B.23) if we use

$$\tilde{\Omega}(\tilde{t}) = (1 + i\tilde{\Delta})e^{-i\tilde{\Delta}\tilde{t}} \quad (\text{B.47})$$

and take the limit $\tilde{\Delta} \rightarrow \infty$ (although this violates the approximations made in deriving Eq. (B.23)).

Since the π -pulse control field in fast retrieval is fixed, optimal fast retrieval yields a single possible output mode, that of Eq. (B.46) with the optimal spin wave $S(\tilde{z}) = \tilde{S}_d(\tilde{z})$. By time reversal, the time-reversed version of this input mode (of duration $T \sim 1/(\gamma d)$) is, therefore, the only mode that can be optimally stored using fast storage at this optical depth d .

In order to confirm the time reversal argument and for the sake of completeness, one can also compute the optimal input mode for fast storage directly. For an input mode $\mathcal{E}_{\text{in}}(\tilde{t})$ nonzero for $\tilde{t} \in [0, \tilde{T}]$ and assuming that a perfect π pulse arrives at $\tilde{t} = \tilde{T}$, we find that

$$S(\tilde{z}, \tilde{T}) = -\sqrt{d} \int_0^{\tilde{T}} d\tilde{t} e^{-(\tilde{T}-\tilde{t})} J_0\left(2\sqrt{d(\tilde{T}-\tilde{t})}\tilde{z}\right) \mathcal{E}_{\text{in}}(\tilde{t}). \quad (\text{B.48})$$

One can see that the fast retrieval and storage equations (B.46) and (B.48) obey, as expected, the same general time reversal relationship that we have already verified in the adiabatic limit in Eqs. (B.35) and (B.36). One can also explicitly verify that the maximization of the storage efficiency derived from Eq. (B.48) yields an optimal $\mathcal{E}_{\text{in}}(\tilde{t})$ that is the normalized time reverse of Eq. (B.46) evaluated with the optimal spin wave $S(\tilde{z}) = \tilde{S}_d(\tilde{z})$. It is worth noting that short exponentially varying pulses, reminiscent of our optimal solution, have been proposed before to achieve efficient photon-echo based storage [318].

The solutions above give an incoming mode $\mathcal{E}_{\text{in}}(\tilde{t})$ that is optimal for fast storage alone or for fast storage followed by backward retrieval. Similarly, at each d , there is a mode that gives the optimal efficiency for fast storage followed by forward retrieval. This optimal input mode is the time-reverse of the output of fast forward retrieval from the spin-wave mode optimal for storage followed by forward retrieval (as computed through Eq. (B.41) and shown in Fig. B.5).

Finally, we note an important difference between fast storage in a cavity discussed in Appendix A and fast storage in free space. In a cavity, there is only one accessible spin-wave mode, and hence only one input mode that can be stored using fast storage (i.e., any input mode orthogonal to it will have zero storage efficiency). As shown in Appendix A, this input mode is exponentially rising with a time constant $\sim 1/(\gamma C)$, where C is the cooperativity parameter. Therefore, generating this mode, and hence obtaining high efficiency, may be hard in practice at high values of C . In contrast,

in free space, any sufficiently smooth spin wave will have a high retrieval efficiency, and, by time-reversal, the time-reverses of the pulses fast retrieved from these spin waves can also be fast stored with high efficiency. One can, thus, explicitly verify using Eq. (B.48), which allows one to compute these storage efficiencies, that if, in the original units, $T\gamma \ll 1$ but at the same time $Td\gamma \gg 1$, the free-space fast-storage efficiency is close to unity.

B.8 Effects of Metastable State Nondegeneracy

In the discussion of backward retrieval we have so far assumed that the two metastable states $|g\rangle$ and $|s\rangle$ are nearly degenerate. This has meant that during backward retrieval we could simply use the same equations as for forward retrieval but with the spin wave flipped: $S(z) \rightarrow S(L - z)$. If $|g\rangle$ and $|s\rangle$ are not degenerate and are split by $\omega_{sg} = c\Delta k$, then during backward retrieval, instead of retrieving from $S(L - z)$, we will have to redefine the slowly varying operators (see Eq. (B.60)) and retrieve from $S(L - z) \exp(-2i\Delta kz)$, which significantly lowers the efficiency unless $\Delta kL \ll \sqrt{d}$. This condition on Δk can be understood based on the concept of the effective EIT window for the Fourier transform of the spin wave. As explained in Sec. B.6.1, the width of this window is of order (in the original units) $\sim \sqrt{d}/L$. The extra phase just shifts the Fourier transform off center by $2\Delta k$, so that the efficiency will not be significantly affected provided the shift is much smaller than the window width. We have confirmed numerically for $S(\tilde{z}) = 1$ and for $S(\tilde{z}) = \sqrt{3}\tilde{z}$ that the ΔkL needed to decrease retrieval efficiency by 50% from its $\Delta kL = 0$ value indeed scales as \sqrt{d} (with proportionality constants ≈ 0.46 and ≈ 0.67 , respectively).

There are two ways to understand physically why nondegeneracy of the metastable states ruins the backward retrieval efficiency. The first explanation, also noted in Ref. [332], comes from the fact that metastable state nondegeneracy breaks the momentum conservation on backward retrieval. During storage, momentum Δk is written onto the ensemble. Momentum conservation on backward retrieval, however, will require $-\Delta k$ momentum in the spin wave. The second explanation comes from the fact that if $\Delta k \neq 0$, then backward retrieval of optimal storage is no longer its time reverse. If we had not defined slowly varying operators, the spin wave that we store into our atoms would have had $\exp(i\Delta kz)$ phase written on it. Since time reversal consists of moving in the opposite direction and taking a complex conjugate, backward retrieval will be the time-reverse of storage only if $\Delta k = 0$, in which case complex conjugation is trivial. Thus, if $\Delta k \neq 0$, the optimization of storage does not simultaneously optimize backward retrieval (unless, of course, we can apply the desired position-dependent phase to the atoms during the storage time, e.g., by a magnetic field gradient, or alternatively apply a π pulse that flips the two metastable states [332]).

We would like now to optimize storage followed by backward retrieval in the

presence of nondegeneracy ($\Delta k \neq 0$). Following the general recipe of Sec. B.5, in order to carry out the optimization, one has to start with an input pulse and a control pulse, do storage, then do backward retrieval with another control pulse. Then one has to time reverse the full process of storage and retrieval, and iterate till one gets convergence to a particular input (and spin wave). Specifically, we start with a trial spin wave $S_1(z)$. To find the spin wave (in terms of operators that are slowly varying for forward propagation as defined in Eq. (B.60)) that the optimal storage plus backward retrieval should use, we first rewrite $S_1(z)$ for backward-propagation slowly varying operators (i.e., add the $2\Delta kz$ phase), and then retrieve it backwards, time reverse, and store. Using Eq. (B.21), the iteration we get is (dropping an unimportant constant phase and going to our rescaled units)

$$S_2(\tilde{z}) = \int_0^1 d\tilde{z}' k_r(\tilde{z}, \tilde{z}') e^{-i2\Delta\tilde{k}\tilde{z}'} S_1^*(\tilde{z}'), \quad (\text{B.49})$$

where $\Delta\tilde{k} = L\Delta k$. This iteration finds the eigenvector with the largest eigenvalue for the eigenvalue problem

$$\lambda S(\tilde{z}) = \int_0^1 k_r(\tilde{z}, \tilde{z}') e^{-i2\Delta\tilde{k}\tilde{z}'} S^*(\tilde{z}'). \quad (\text{B.50})$$

$|\lambda|^2$ will then give the total maximum efficiency of storage followed by backward retrieval. In contrast to the $\Delta k = 0$ case, the efficiencies of storage and retrieval in the optimal process are not generally equal. It is important to note that since the process we are optimizing followed by its time reverse corresponds to two iterations of Eq. (B.49), after a sufficient number of steps, λ settles into an oscillation between $|\lambda| \exp(i\alpha)$ and $|\lambda| \exp(-i\alpha)$ for some phase α . The eigenvector will oscillate between two values differing only by an unimportant constant phase, so that either one can be used.

While this procedure allows us to find the optimal spin waves, we should, for completeness, also determine, as in the $\Delta k = 0$ case, which input fields the optimum can be achieved for. To do this, we, as before, consider the exactly solvable adiabatic and fast limits. In the adiabatic limit, the argument that retrieval can be shaped into any mode did not require the spin wave $S(z)$ to be real, and it is therefore still applicable. By time reversal, we can, therefore, still achieve the maximum efficiency of storage followed by backward retrieval for any incoming mode of duration T such that $Td\gamma \gg 1$. Similarly, in the fast limit, using fast retrieval and time reversal we can find at each d a pulse shape with $Td\gamma \sim 1$ that gives the maximum efficiency. For completeness, we note that one can also generalize to $\Delta k \neq 0$ the method that uses the decayless mode $s(z)$ to shape the optimal storage control, as described in Sec. B.6.2. However, since the optimal control is unique, this method will, of course, yield the same control as the method based on retrieval and time reversal (as we showed explicitly in Sec. B.6.2 and Sec. B.10.5 for $\Delta k = 0$). We will, thus, omit here the extension of this method to the $\Delta k \neq 0$ case.

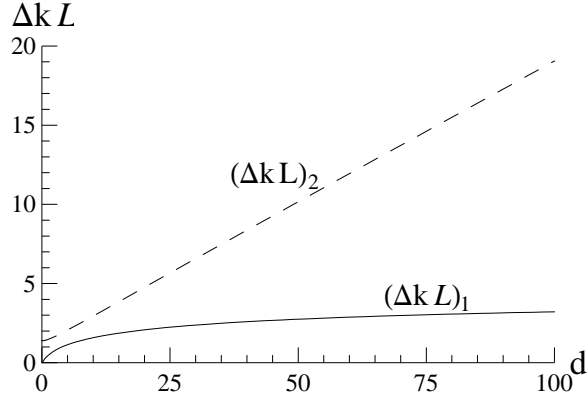


Figure B.7: If the two metastable states are not degenerate, the efficiency of storage followed by backward retrieval will be lowered relative to the degenerate case, because the energy difference $\hbar\omega_{sg}$ introduces a momentum difference $\Delta k = \omega_{sg}/c$ between the quantum and classical fields. As a function of d , the figure shows the momentum ΔkL , at which the optimal total efficiency of storage followed by backward retrieval falls to half of the $\Delta kL = 0$ value (dashed), and at which it is decreased to the optimal efficiency with forward retrieval (solid).

We have, thus, demonstrated that we can optimize storage followed by backward retrieval for any given d and Δk . We also recall that we have shown in Sec. B.6.3 that for $\Delta k = 0$ optimal storage followed by retrieval is accomplished with backward retrieval. However, as we increase ΔkL , the optimal total efficiency with backward retrieval will drop down to the optimal total efficiency with forward retrieval at some value of $(\Delta kL)_1$. Increasing ΔkL further up to another value $(\Delta kL)_2$ will decrease the optimal total efficiency with backward retrieval to half of its $\Delta kL = 0$ value (and then further down to zero). Figure B.7 shows a plot of $(\Delta kL)_1$ (solid) and $(\Delta kL)_2$ (dashed) as a function of d . As noted above, without reoptimization, $(\Delta kL)_2$ would go as \sqrt{d} , but with optimization we see that it is linear in d , i.e., optimization makes the error less severe. $(\Delta kL)_1$ grows even slower than \sqrt{d} . This is not surprising because at $\Delta kL = 0$ optimal forward and optimal backward errors both fall off as $1/d$, except with different coefficients and, thus, eventually get very close to each other, so it takes a small ΔkL to make them equal.

In Figs. B.8(a) and B.8(b), we show the magnitude $|S(\tilde{z})|$ and the phase $\text{Arg}[S(\tilde{z})]$, respectively, of the optimal mode (defined for the forward-propagating slowly varying operators as in Eq. (B.60)) at $d = 20$ for different values of ΔkL . As we increase ΔkL , the optimal mode becomes concentrated more and more near the back end, i.e., it becomes favorable to effectively decrease the optical depth (i.e., decrease effective L) in order to decrease effective ΔkL . The phase of the optimal mode is approximately linear, i.e., $S(\tilde{z}) \propto \exp(-i\tilde{k}_0\tilde{z})$ for some \tilde{k}_0 . At $\Delta kL = 0$, $\tilde{k}_0 = 0$. Interestingly,

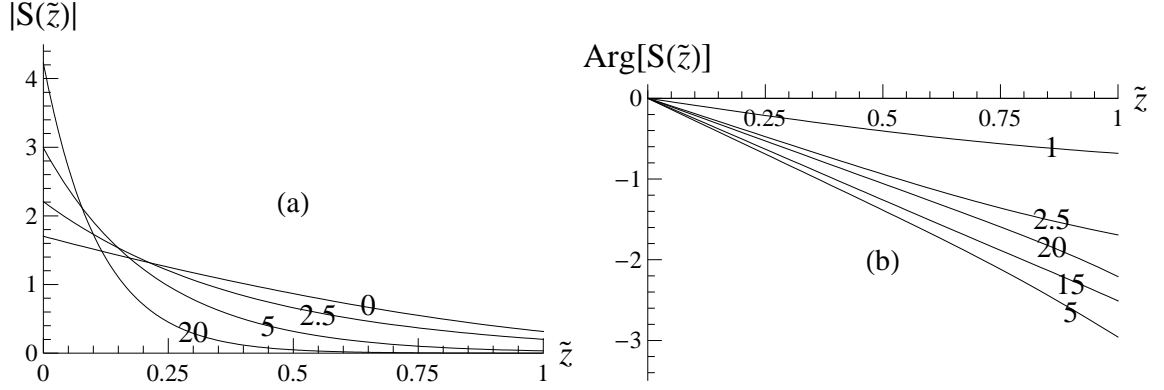


Figure B.8: (a) The magnitude and (b) the phase of the optimal mode for storage followed by backward retrieval at $d = 20$ for the indicated values of ΔkL . The phase of the optimal mode at $\Delta kL = 0$ is 0. The phase is plotted for the forward-propagation slowly varying operators as defined in Eq. (B.60).

instead of just growing from 0 linearly with ΔkL , \tilde{k}_0 first increases but then above $\Delta kL \sim 7.5$ starts decreasing again.

B.9 Summary

In conclusion, in this Appendix, we have presented a detailed analysis of the storage and retrieval of photons in homogeneously broadened Λ -type atomic media in free space and made a comparison to the cavity model described in Appendix A. From the investigation in the present Appendix emerges a new physical picture of the process of storage and retrieval in this system: first of all, the retrieval is essentially an interference effect where the emission from all the atoms interferes constructively in the forward direction. This constructive interference enhances the effective decay rate into the forward direction to $d\gamma$. The branching ratio between the desired forward radiation and the unwanted spontaneous emission is then simply given by the ratio between the various decay rates and is $\eta \sim d\gamma/(\gamma + d\gamma) \sim 1 - 1/d$, irrespective of the method being used to drive the excitation out of the atoms. Secondly, the storage process is most conveniently viewed as the time reverse of retrieval.

In the present Appendix, we have used this physical picture to derive the optimal strategy for storage and retrieval and the optimal efficiency that is independent of whether one works in the Raman, EIT, photon-echo, or any other intermediate regime. In particular, we showed how to achieve the optimal storage of any smooth input mode at any detuning of duration $T \gg 1/(d\gamma)$ (the adiabatic limit, including Raman and EIT) and of a particular class of resonant input modes of duration $T \sim 1/(d\gamma)$ (the fast or photon-echo limit). This analysis is extendable to other systems. In

particular, in Appendix C, we consider the effects of inhomogeneous broadening on photon storage in Λ -type atomic media. Extensions to other systems, such as the double- Λ system [333] or the tripod system [334], should also be possible.

We also suggested a novel time reversal based iterative procedure for optimizing quantum state mappings. Moreover, we showed that for the case of photon storage, this procedure is not only a convenient mathematical tool but is also a readily accessible experimental technique for finding optimal spin waves and optimal input-control pairs: one just has to be able to measure the output mode and to generate its time reverse. As we report in Secs. 3.3 and E.4, this procedure has already been implemented experimentally with classical light. We also expect this optimization procedure to be applicable to other systems used for light storage, such as tunable photonic crystals [91].

The presented optimization of the storage and retrieval processes leads to a substantial increase in the memory efficiency whenever reasonable synchronization between the input photon wave packet and the control pulse can be achieved. We, therefore, expect this work to be important in improving the efficiencies in current experiments, where optical depth is limited by various experimental imperfections such as a limited number of atoms in a trap [81], competing four-wave mixing processes in a warm vapor cell [80], or inhomogeneous broadening in solid state samples [292].

B.10 Omitted Details

In the preceding Sections of this Appendix, to allow for a smoother presentation, we omitted some of the details. We present them in this Section.

B.10.1 Details of the Model and Derivation of the Equations of Motion

In Sec. B.2, we presented a short introduction to the model and stated the equations of motion without derivation. In this Section, we provide the details of the model, as well as the derivation of the equations of motion (B.5)-(B.7). Since the model and the assumptions made are very similar to those presented in the cavity case in Appendix A, we will often review some of them only briefly.

The electric field vector operator for the quantum field is given by [14]

$$\hat{\mathbf{E}}_1(z) = \epsilon_1 \left(\frac{\hbar\omega_1}{4\pi c\epsilon_0 A} \right)^{1/2} \int d\omega \hat{a}_\omega e^{i\omega z/c} + h.c., \quad (\text{B.51})$$

where h.c. stands for Hermitian conjugate and where we have a continuum of annihilation operators \hat{a}_ω for the field modes of different frequencies ω that satisfy the

commutation relation

$$[\hat{a}_\omega, \hat{a}_{\omega'}^\dagger] = \delta(\omega - \omega'). \quad (\text{B.52})$$

By assumption, the field modes corresponding to \hat{a}_ω for different ω have the same transverse profile and are nonempty only around $\omega = \omega_1$. We have here assumed that the cross section A of the beam is identical to the cross section of the ensemble. In typical experiments, the beam is smaller than the size of the ensemble, and in this case the relevant number of atoms N should only be the number of atoms interacting with the beam. However, as we see from the final equations (B.5)-(B.7), the only relevant quantity is the optical depth d , which does not depend on the area A , so that when everything is expressed in terms of d , the precise definition of N and A is irrelevant (see the end of this Section).

The copropagating classical control field vector

$$\mathbf{E}_2(z, t) = \epsilon_2 \mathcal{E}_2(t - z/c) \cos(\omega_2(t - z/c)) \quad (\text{B.53})$$

is a plane wave with polarization unit vector ϵ_2 and carrier frequency ω_2 modulated by an envelope $\mathcal{E}_2(t - z/c)$, which we assume to be propagating with group velocity equal to the speed of light c since almost all the atoms are assumed to be in the ground state $|g\rangle$ and are, thus, unable to significantly alter the propagation of a strong classical field coupled to the $|s\rangle$ - $|e\rangle$ transition.

The Hamiltonian in Eqs. (A.41)-(A.43) is then modified to

$$\hat{H} = \hat{H}_0 + \hat{V}, \quad (\text{B.54})$$

$$\hat{H}_0 = \int d\omega \hbar \omega \hat{a}_\omega^\dagger \hat{a}_\omega + \sum_{i=1}^N (\hbar \omega_{se} \hat{\sigma}_{ss}^i + \hbar \omega_{ge} \hat{\sigma}_{ee}^i), \quad (\text{B.55})$$

$$\begin{aligned} \hat{V} = & -\hbar \sum_{i=1}^N \left(\Omega(t - z_i/c) \hat{\sigma}_{es}^i e^{-i\omega_2(t - z_i/c)} \right. \\ & \left. + g \sqrt{\frac{L}{2\pi c}} \int d\omega \hat{a}_\omega e^{i\omega z_i/c} \hat{\sigma}_{eg}^i + h.c. \right). \end{aligned} \quad (\text{B.56})$$

Here $\hat{\sigma}_{\mu\nu}^i = |\mu\rangle_{ii}\langle\nu|$ is the internal state operator of the i th atom between states $|\mu\rangle$ and $|\nu\rangle$, z_i is the position of the i th atom, $\hat{\mathbf{d}}$ is the dipole moment vector operator, $\Omega(t - z/c) = \langle e | (\hat{\mathbf{d}} \cdot \epsilon_2) | s \rangle \mathcal{E}_2(t - z/c) / (2\hbar)$ is the Rabi frequency of the classical field, and $g = \langle e | (\hat{\mathbf{d}} \cdot \epsilon_1) | g \rangle \sqrt{\frac{\omega_1}{2\hbar\epsilon_0 AL}}$ (assumed to be real for simplicity) is the coupling constant between the atoms and the quantized field mode, where we have chosen the length of the quantization volume to be identical to the ensemble length (this choice does not affect the results obtained below). We note that in order to avoid carrying extra factors of 2 around, Ω is defined as half of the traditional definition of the Rabi frequency, so that a π pulse, for example, takes time $\pi/(2\Omega)$.

Since the position dependence along the ensemble matters, we divide our ensemble into thin slices along the length L of the ensemble ($z = 0$ to $z = L$) and introduce slowly varying operators

$$\hat{\sigma}_{\mu\mu}(z, t) = \frac{1}{N_z} \sum_{i=1}^{N_z} \hat{\sigma}_{\mu\mu}^i(t), \quad (\text{B.57})$$

$$\hat{\sigma}_{es}(z, t) = \frac{1}{N_z} \sum_{i=1}^{N_z} \hat{\sigma}_{es}^i(t) e^{-i\omega_2(t-z_i/c)}, \quad (\text{B.58})$$

$$\hat{\sigma}_{eg}(z, t) = \frac{1}{N_z} \sum_{i=1}^{N_z} \hat{\sigma}_{eg}^i(t) e^{-i\omega_1(t-z_i/c)}, \quad (\text{B.59})$$

$$\hat{\sigma}_{sg}(z, t) = \frac{1}{N_z} \sum_{i=1}^{N_z} \hat{\sigma}_{sg}^i(t) e^{-i(\omega_1-\omega_2)(t-z_i/c)}, \quad (\text{B.60})$$

$$\hat{\mathcal{E}}(z, t) = \sqrt{\frac{L}{2\pi c}} e^{i\omega_1(t-z/c)} \int d\omega \hat{a}_\omega(t) e^{i\omega z/c}, \quad (\text{B.61})$$

where sums are over all N_z atoms in a slice of atoms positioned at z that is thick enough to contain $N_z \gg 1$ atoms but thin enough that the resulting collective fields can be considered continuous. The normalization of $\hat{\mathcal{E}}$ is chosen to ensure that it is dimensionless, which will be necessary to yield the simple dimensionless expressions in Eqs. (B.5)-(B.7). For these slowly varying operators, the effective Hamiltonian is

$$\begin{aligned} \hat{H} = & \int d\omega \hbar\omega \hat{a}_\omega^\dagger \hat{a}_\omega - \hbar\omega_1 \frac{1}{L} \int_0^L dz \mathcal{E}^\dagger(z, t) \mathcal{E}(z, t) \\ & + \int_0^L dz \hbar n(z) \left[\Delta \hat{\sigma}_{ee}(z, t) - \left(\Omega(t-z/c) \hat{\sigma}_{es}(z, t) \right. \right. \\ & \left. \left. + g \hat{\mathcal{E}}(z, t) \hat{\sigma}_{eg}(z, t) + h.c. \right) \right], \end{aligned} \quad (\text{B.62})$$

and the same-time commutation relations are

$$[\hat{\sigma}_{\mu\nu}(z, t), \hat{\sigma}_{\alpha\beta}(z', t)] = \frac{1}{n(z)} (\delta_{\nu\alpha} \hat{\sigma}_{\mu\beta}(z, t) - \delta_{\mu\beta} \hat{\sigma}_{\alpha\nu}(z, t)) \delta(z - z'), \quad (\text{B.63})$$

$$[\hat{\mathcal{E}}(z, t), \hat{\mathcal{E}}^\dagger(z', t)] = L \delta(z - z'). \quad (\text{B.64})$$

Under the same assumptions as in the cavity case in Appendix A and defining $\hat{P} = \sqrt{N} \hat{\sigma}_{ge}$ and $\hat{S} = \sqrt{N} \hat{\sigma}_{gs}$, the Heisenberg equations of motion yield Eqs. (B.1)-(B.3), where, as in the cavity case in Appendix A, γ may include extra dephasing in addition to radiative decay. We note that \hat{P} and \hat{S} are defined to be dimensionless in order to yield fully dimensionless Eqs. (B.5)-(B.7). The \sqrt{N} in the definitions of \hat{P} and \hat{S}

is required in order to have the final dimensionless equations depend on g , N , and L only through the optical depth d . Similarly to the cavity case in Appendix A, from the generalized Einstein relations, the only nonzero noise correlations are [320]

$$\langle \hat{F}_P(z, t) \hat{F}_P^\dagger(z', t') \rangle = \frac{N}{n(z)} \delta(z - z') \delta(t - t'), \quad (\text{B.65})$$

$$\langle \hat{F}_S(z, t) \hat{F}_S^\dagger(z', t') \rangle = \frac{N}{n(z)} \delta(z - z') \delta(t - t'). \quad (\text{B.66})$$

Again the fact that normally ordered correlations are zero, as in the cavity case in Appendix A, means that the incoming noise is vacuum, which is precisely the reason why, as noted in Sec. A.2, efficiency is the only number we need in order to fully characterize the mapping. The property of our system that guarantees that the incoming noise is vacuum is the absence of decay out of state $|g\rangle$ into states $|e\rangle$ and $|s\rangle$. We refer the reader to Sec. A.8.1 for a detailed discussion of why this is a reasonable assumption in most experimental realizations.

We will now show how our field and atomic operators can be expanded in terms of modes, which is necessary in order to obtain and interpret the final complex number equations (B.5)-(B.7). Under the assumption that almost all atoms are in the ground state at all times, commutation relations (B.63) imply

$$\left[\hat{S}(z, t), \hat{S}^\dagger(z', t) \right] = \frac{N}{n(z)} \delta(z - z'), \quad (\text{B.67})$$

$$\left[\hat{P}(z, t), \hat{P}^\dagger(z', t) \right] = \frac{N}{n(z)} \delta(z - z'). \quad (\text{B.68})$$

Equation (B.67) allows us to expand $\hat{S}(z, t)$ in terms of any basis set of spatial modes $\{g_\alpha(z)\}$ satisfying the orthonormality relation $\int_0^L dz g_\alpha^*(z) g_\beta(z) = \delta_{\alpha\beta}$ and the completeness relation $\sum_\alpha g_\alpha^*(z) g_\alpha(z') = \delta(z - z')$ as

$$\hat{S}(z, t) = \sqrt{\frac{N}{n(z)}} \sum_\alpha g_\alpha(z) \hat{c}_\alpha(t), \quad (\text{B.69})$$

where the annihilation operators $\{\hat{c}_\alpha\}$ for the spin-wave modes satisfy

$$\left[\hat{c}_\alpha(t), \hat{c}_\beta^\dagger(t) \right] = \delta_{\alpha\beta}. \quad (\text{B.70})$$

For the freely propagating input field $\hat{\mathcal{E}}_{\text{in}}(t) = \hat{\mathcal{E}}(0, t)$ and output field $\hat{\mathcal{E}}_{\text{out}}(t) = \hat{\mathcal{E}}(L, t)$ we have the following commutation relations:

$$\left[\hat{\mathcal{E}}_{\text{in}}(t), \hat{\mathcal{E}}_{\text{in}}^\dagger(t') \right] = \frac{L}{c} \delta(t - t'), \quad (\text{B.71})$$

$$\left[\hat{\mathcal{E}}_{\text{out}}(t), \hat{\mathcal{E}}_{\text{out}}^\dagger(t') \right] = \frac{L}{c} \delta(t - t'), \quad (\text{B.72})$$

which differ from their cavity case counterparts in Eq. (A.57) only in normalization. These commutation relations allow us to expand, as in the cavity case in Appendix A, the input and the output field in terms of any basis set of field (envelope) modes $\{h_\alpha(t)\}$ defined for $t \in [0, \infty)$, satisfying the orthonormality relation $\int_0^\infty dt h_\alpha^*(t) h_\beta(t) = \delta_{\alpha\beta}$ and the completeness relation $\sum_\alpha h_\alpha^*(t) h_\alpha(t') = \delta(t - t')$, as

$$\hat{\mathcal{E}}_{\text{in}}(t) = \sqrt{\frac{L}{c}} \sum_\alpha h_\alpha(t) \hat{a}_\alpha, \quad (\text{B.73})$$

$$\hat{\mathcal{E}}_{\text{out}}(t) = \sqrt{\frac{L}{c}} \sum_\alpha h_\alpha(t) \hat{b}_\alpha, \quad (\text{B.74})$$

where annihilation operators $\{\hat{a}_\alpha\}$ and $\{\hat{b}_\alpha\}$ for the input and the output photon modes, respectively, satisfy the usual bosonic commutation relations (see Eq. (A.60)).

All atoms are initially pumped into the ground state, i.e., no \hat{P} or \hat{S} excitations are present in the atoms. We also assume that the only input field excitations initially present are in the quantum field mode with annihilation operator \hat{a}_0 corresponding to an envelope shape $h_0(t)$ nonzero on $[0, T]$. Precisely as in the cavity case in Appendix A, the only parts of the operators that will contribute to the efficiency will be the parts proportional to \hat{a}_0 . We can therefore reduce our problem to complex number equations. These equations and the corresponding initial and boundary conditions are given in Sec. B.2. To get back the nonvacuum part of the original operator from its complex number counterpart, one can just multiply the complex number version by \hat{a}_0 .

We conclude this Section with a verification that $d = g^2 NL / (\gamma c)$ is independent of the size of the beam and, for a given transition, depends only on the density of the atoms and the length of the ensemble. This can be seen directly by inserting the definition of g into d and defining the atomic number density $\rho(z) = n(z)/A$ (which, by assumption, is uniform in the direction transverse to the propagation direction). The expression for d then becomes $d = |\langle e | (\hat{\mathbf{d}} \cdot \epsilon_1) | g \rangle|^2 \omega_1 \int \rho(z) dz / (2\hbar \epsilon_0 \gamma c)$. So it is indeed independent of the size of the beam and, for a given transition, only depends on the density and length of the ensemble.

B.10.2 Position Dependence of Loss

We have shown in Sec. B.3 that, provided the retrieval control pulse is long and/or powerful enough to leave no atomic excitations (i.e., the retrieval is complete), the retrieval efficiency η_r depends only on the optical depth d and the spin wave $S(\tilde{z})$ but not on the detuning $\tilde{\Delta}$ and the control field envelope $\tilde{\Omega}(\tilde{t})$. In this Section, we show that for complete retrieval, not only the total efficiency but also the distribution of spontaneous emission loss (or more precisely loss due to polarization decay γ) as a function of position is independent of the control and the detuning.

Equations of motion (B.5)-(B.7) imply that

$$\partial_{\tilde{z}}|\mathcal{E}(\tilde{z}, \tilde{t})|^2 + \partial_{\tilde{t}}|P(\tilde{z}, \tilde{t})|^2 + \partial_{\tilde{t}}|S(\tilde{z}, \tilde{t})|^2 = -2|P(\tilde{z}, \tilde{t})|^2. \quad (\text{B.75})$$

Integrating both sides with respect to \tilde{z} from 0 to 1 and with respect to \tilde{t} from \tilde{T}_r to ∞ , using the initial conditions $S(\tilde{z}, \tilde{T}_r) = S(\tilde{z})$ (where $\int_0^1 d\tilde{z}|S(\tilde{z})|^2 = 1$) and $P(\tilde{z}, \tilde{T}_r) = 0$, the boundary condition $\mathcal{E}(0, \tilde{t}) = 0$, and the complete retrieval condition $S(\tilde{z}, \infty) = P(\tilde{z}, \infty) = 0$, we find, using Eq. (B.9), that

$$\eta_r = 1 - \int_0^1 d\tilde{z} l(\tilde{z}), \quad (\text{B.76})$$

where the position-dependent loss per unit length is

$$l(\tilde{z}) = 2 \int_0^\infty d\tilde{t} |P(\tilde{z}, \tilde{t})|^2. \quad (\text{B.77})$$

Computing $l(\tilde{z})$, we find

$$\begin{aligned} l(\tilde{z}) &= 2\mathcal{L}^{-1} \left\{ \int_{\tilde{T}_r}^\infty d\tilde{t} P(u, \tilde{t}) [P(u', \tilde{t})]^* \right\}_{u, u' \rightarrow \tilde{z}} \\ &= \mathcal{L}^{-1} \left\{ \frac{2}{2 + \frac{d}{u} + \frac{d}{u'}} S(u) [S(u')]^* \right\}_{u, u' \rightarrow \tilde{z}}, \end{aligned} \quad (\text{B.78})$$

where \mathcal{L}^{-1} with subscript $u, u' \rightarrow \tilde{z}$ means that inverse Laplace transforms are taken with respect to u and u' and are both evaluated at \tilde{z} . In the last equality, Eq. (B.13) and the conditions at $\tilde{t} = \tilde{T}_r$ and $\tilde{t} = \infty$ were used. Therefore, we see that $l(\tilde{z})$ is independent of the detuning and the control. Moreover, the inverse Laplace transforms \mathcal{L}^{-1} can be taken analytically to give

$$\begin{aligned} l(\tilde{z}) &= |S(\tilde{z})|^2 - \text{Re} \left[S(\tilde{z}) d \int_0^{\tilde{z}} d\tilde{z}' S^*(\tilde{z} - \tilde{z}') e^{-\frac{d\tilde{z}'}{2}} \right] \\ &\quad + \int_0^{\tilde{z}} d\tilde{z}' \int_0^{\tilde{z}} d\tilde{z}'' S(\tilde{z} - \tilde{z}') S^*(\tilde{z} - \tilde{z}'') \frac{d^2}{4} e^{-\frac{d}{2}(\tilde{z}' + \tilde{z}'')} \\ &\quad \times \left[2I_0 \left(d\sqrt{\tilde{z}'\tilde{z}''} \right) - \frac{\tilde{z}' + \tilde{z}''}{\sqrt{\tilde{z}'\tilde{z}''}} I_1 \left(d\sqrt{\tilde{z}'\tilde{z}''} \right) \right]. \end{aligned} \quad (\text{B.79})$$

B.10.3 Implementation of the Inverse Propagator using Time Reversal

In Sec. B.4, we exploited the fact that time reversal could be used to realize the inverse evolution $\hat{U}^{-1}[T, 0; \Omega(t)]$. In this Section, we would like to explain carefully what we mean by the time reversal operator \hat{T} and to prove Eq. (B.19).

To define the time reversal operator $\hat{\mathcal{T}}$, we first choose a basis for our single-excitation Hilbert space consisting of $\{\hat{\sigma}_{sg}^i|\text{ground}\rangle\}$, $\{\hat{\sigma}_{eg}^i|\text{ground}\rangle\}$, and $\{\hat{a}_z^\dagger|\text{ground}\rangle\}$, where $|\text{ground}\rangle$ is the state with no photons and no atomic excitations (i.e., all atoms in the ground state), i runs over all atoms, z runs over all positions, and $\hat{a}_z^\dagger = (2\pi c)^{-1/2} \int d\omega \exp(-i\omega z/c) \hat{a}_\omega^\dagger$. We then define the time reversal operator $\hat{\mathcal{T}}$ (equivalent to the complex conjugation operator K in Ref. [335]) as follows: $\hat{\mathcal{T}}|\psi(t)\rangle$ means taking the complex conjugates of the expansion coefficients of a state $|\psi(t)\rangle$ in the above basis, while $\hat{\mathcal{T}}\hat{O}\hat{\mathcal{T}}$ means taking complex conjugates of the matrix elements of the operator \hat{O} when \hat{O} is written in the above basis (we will, thus, write $\hat{\mathcal{T}}\hat{O}\hat{\mathcal{T}} = \hat{O}^*$). For example, this definition implies that in addition to complex conjugating the envelope of the photon, time reversal flips the photon momentum: $\hat{\mathcal{T}}a_\omega\hat{\mathcal{T}} = \hat{a}_{-\omega}$ and $\hat{\mathcal{T}}\hat{a}_\omega|\text{ground}\rangle = \hat{a}_{-\omega}|\text{ground}\rangle$. Some of the properties of $\hat{\mathcal{T}}$ are $\hat{\mathcal{T}}^2 = \hat{\mathbf{1}}$ and $|\langle\psi_1|\hat{\mathcal{T}}|\psi_2\rangle| = |\langle\hat{\mathcal{T}}\psi_1|\psi_2\rangle|$.

We now turn to the proof of Eq. (B.19). We start by noting that

$$\hat{U}^{-1}[T, 0; \Omega(t)] = \hat{U}[0, T; \Omega(t)] = \hat{\mathcal{T}}\hat{\mathcal{T}}\hat{U}[0, T; \Omega(t)]\hat{\mathcal{T}}\hat{\mathcal{T}} = \hat{\mathcal{T}}\hat{U}^*[0, T; \Omega(t)]\hat{\mathcal{T}} \quad (\text{B.80})$$

and, therefore, using Eq. (B.18),

$$\eta = |\langle b|\hat{U}[T, 0; \Omega(t)]|a\rangle|^2 = |\langle a|\hat{\mathcal{T}}\hat{U}^*[0, T; \Omega(t)]\hat{\mathcal{T}}|b\rangle|^2. \quad (\text{B.81})$$

To evaluate $\hat{U}^*[0, T; \Omega(t)]$ and to find a way to implement it physically, let us first consider the simplest case, where the Hamiltonian responsible for the evolution is independent of time and respects time reversal symmetry $\hat{\mathcal{T}}\hat{H}\hat{\mathcal{T}} = \hat{H}$. This is equivalent to $\hat{H}^* = \hat{H}$. In this case, the evolution operator is given by $\hat{U}[T, 0] = \exp(-i\hat{H}T/\hbar)$, and, therefore, $\hat{U}^*[0, T] = \hat{U}[T, 0]$. So if the Hamiltonian obeys time reversal symmetry, one can physically implement $\hat{U}^*[0, T]$ simply by evolving the system for a time T . Applied to Eq. (B.81), this would mean that the probability to go from $|a\rangle$ to $|b\rangle$ due to unitary evolution \hat{U} is the same as the probability to make the transition from $\hat{\mathcal{T}}|b\rangle$ to $\hat{\mathcal{T}}|a\rangle$ due to this evolution. In other words, according to time reversal, if our Hamiltonian obeyed time reversal symmetry, we would be able to map the time reverse $\mathcal{E}^*(T-t)$ of the output mode onto the spin wave S^* with the overlap storage efficiency equal to the retrieval efficiency from the spin wave S .

In general, the interaction does not obey time reversal symmetry because of the classical control, which may depend on time and may be complex. To extend the discussion to this situation, we shall use the equation of motion for the propagator

$$i\hbar \frac{d\hat{U}[\tau_1, \tau_2; \Omega(t)]}{d\tau_1} = \hat{H}[\tau_1; \Omega(t)]\hat{U}[\tau_1, \tau_2; \Omega(t)], \quad (\text{B.82})$$

where we have highlighted the dependence of the Hamiltonian on the control field by including $\Omega(t)$ as an argument of \hat{H} . By taking the complex conjugate of Eq. (B.82), we can turn it into the equation for the time-reversed inverse propagator

$$\begin{aligned} \hat{\mathcal{T}}\hat{U}^{-1}[\tau_2, \tau_1; \Omega(t)]\hat{\mathcal{T}} &= \hat{U}^*[\tau_1, \tau_2; \Omega(t)]: \\ -i\hbar\frac{d\hat{U}^*[\tau_1, \tau_2; \Omega(t)]}{d\tau_1} &= \hat{H}^*[\tau_1; \Omega(t)]\hat{U}^*[\tau_1, \tau_2; \Omega(t)]. \end{aligned} \quad (\text{B.83})$$

Note that we have not made any assumptions about time reversal symmetry being a symmetry for the system.

In order to implement the evolution in the last expression of Eq. (B.81), we need to realize a time evolution $\hat{U}[T, 0; \Omega'(t)]$ such that $\hat{U}[T, 0; \Omega'(t)] = \hat{U}^*[0, T, \Omega(t)]$. To do this, we consider operators $\hat{U}[\tau, 0; \Omega'(t)]$ and $\hat{U}^*[T - \tau, T, \Omega(t)]$ whose equality at time $\tau = T$ will imply the desired evolution. The equation of motion for these operators are, using Eqs. (B.82) and (B.83),

$$\begin{aligned} i\hbar\frac{d\hat{U}^*[T - \tau, T; \Omega(t)]}{d\tau} &= \hat{H}^*[T - \tau; \Omega(t)]\hat{U}^*[T - \tau, T; \Omega(t)], \\ i\hbar\frac{d\hat{U}[\tau, 0; \Omega'(t)]}{d\tau} &= \hat{H}[\tau; \Omega'(t)]\hat{U}[\tau, 0; \Omega'(t)]. \end{aligned} \quad (\text{B.84})$$

Since the two operators are the same at time $\tau = 0$, $\hat{U}[0, 0, \Omega'(t)] = \hat{U}^*[T, T, \Omega(t)] = \hat{\mathbf{1}}$, the two operators will be identical (and, in particular, equal at $\tau = T$) if they obey the same differential equation, which is the case if

$$\hat{H}[t, \Omega'(t)] = \hat{H}^*[T - t; \Omega(t)]. \quad (\text{B.85})$$

We would like to evaluate the right-hand side of Eq. (B.85). By inspecting the Hamiltonian in Eqs. (B.54)-(B.56), we see that the only non-trivial parts are the classical control field (including the carrier ω_2) and the exponential in the interaction with the quantum field (the part of Eq. (B.56) containing g). According to the right hand side of Eq. (B.85), we would like to apply the complex conjugation to \hat{H} and evaluate it at time $T - t$. The interaction with the quantum field is actually invariant not only under the change of time but also under complex conjugation since applying time reversal to $\hat{a}_\omega e^{i\omega z/c}$ simply changes ω to $-\omega$, which can be changed back to ω by flipping the sign of the integration variable. The application of complex conjugation and the change of time to the interaction with the classical field is equivalent to using the time-reversed control field envelope $\Omega'(t) = \Omega^*(T - t)$ and a carrier wave vector propagating in the opposite direction. Combining this result with Eq. (B.80), we arrive at Eq. (B.19). This means that by using the time-reversed control field $\Omega^*(T - t)$, we can map $\hat{\mathcal{T}}|b\rangle$ onto $\hat{\mathcal{T}}|a\rangle$ with the probability equal to the probability that $|a\rangle$ goes to $|b\rangle$ using $\Omega(t)$.

B.10.4 Proof of Convergence of Optimization Iterations to the Optimum

In Sec. B.5, we omitted the proof that iterative application of $\hat{\mathcal{N}}\hat{P}_A\hat{U}^{-1}\hat{P}_B\hat{U}$ to a unit vector $|a\rangle \in A$ converges to $|a_{\max}\rangle$ (unless $\langle a|a_{\max}\rangle = 0$) and that $\hat{\mathcal{N}}\hat{P}_B\hat{U}|a_{\max}\rangle$

optimizes \hat{U}^{-1} as a map from B to A . In this Section, we present this proof.

For any unit vector $|a\rangle$ in the subspace A of “initial” states, the efficiency is defined as $\eta = |\hat{P}_B \hat{U}|a\rangle|^2$, where \hat{P}_B denotes the projection on the subspace B of “final” states. We are looking for $|a_{\max}\rangle \in A$ that gives the maximum efficiency $\eta_{\max} = |\hat{P}_B \hat{U}|a_{\max}\rangle|^2$. By appropriately adjusting the phases, we can write $\sqrt{\eta_{\max}} = \langle b_{\max}|\hat{U}|a_{\max}\rangle$ for some unit vector $|b_{\max}\rangle = \hat{N} \hat{P}_B \hat{U}|a_{\max}\rangle \in B$. From the unitarity of \hat{U} (see, for example, Eq. (B.18)), it follows that $|b_{\max}\rangle$ optimizes \hat{U}^{-1} as a mapping from B to A . We will prove two claims, from which the desired convergence result will follow immediately. Claim (1): if $|a_1\rangle$ is orthogonal to $|a_{\max}\rangle$, $\hat{U}|a_1\rangle$ is orthogonal to $|b_{\max}\rangle$. Proof: suppose $\langle b_{\max}|\hat{U}|a_1\rangle = \beta \neq 0$, then defining $|\tilde{a}\rangle = (\sqrt{\eta_{\max}}|a_{\max}\rangle + \beta^*|a_1\rangle)/\sqrt{\eta_{\max} + |\beta|^2}$, we have $\langle b_{\max}|\hat{U}|\tilde{a}\rangle = \sqrt{\eta_{\max} + |\beta|^2} > \sqrt{\eta_{\max}}$, which contradicts the fact that $|a_{\max}\rangle$ was optimal. A similar proof can be given for claim (2): if $|b_1\rangle$ is orthogonal to $|b_{\max}\rangle$, $\hat{U}^{-1}|b_1\rangle$ is orthogonal to $|a_{\max}\rangle$. From these two claims it immediately follows that if we start with a state orthogonal to $|a_{\max}\rangle$, we will never approach $|a_{\max}\rangle$. On the other hand, we will show now that if we start with $|a\rangle = \alpha|a_{\max}\rangle + \sqrt{1 - |\alpha|^2}|a_1\rangle$ (for some unit $|a_1\rangle$ orthogonal to $|a_{\max}\rangle$ and for some $\alpha \neq 0$), we will indeed approach $|a_{\max}\rangle$. We have $\hat{P}_B \hat{U}|a\rangle = \alpha \langle b_{\max}|\hat{U}|a_{\max}\rangle |b_{\max}\rangle + \sqrt{1 - |\alpha|^2} \langle b_1|\hat{U}|a_1\rangle |b_1\rangle$ for some unit $|b_1\rangle \in B$. By claim (1), the two parts of $\hat{P}_B \hat{U}|a\rangle$ are orthogonal and, since $|a_{\max}\rangle$ is optimal, $|\langle b_{\max}|\hat{U}|a_{\max}\rangle| > |\langle b_1|\hat{U}|a_1\rangle|$. Thus, the fraction of $|b_{\max}\rangle$ in $\hat{P}_B \hat{U}|a\rangle$ is greater than the fraction of $|a_{\max}\rangle$ in $|a\rangle$. After the application of $\hat{P}_A \hat{U}^{-1}$ and during subsequent iterations, the optimal fraction will similarly grow. This shows that we will indeed reach the optimum, unless we start with something orthogonal to it.

B.10.5 Shaping the Control Field for the Optimal Adiabatic Storage

In this Section, we use Eq. (B.37) to find the control field for the storage of any given mode $\mathcal{E}_{\text{in}}(\tilde{t})$ into any given decayless spin-wave mode $s(\tilde{z})$. We then verify that the optimal storage control found through this procedure using the optimal decayless spin-wave mode $s(\tilde{z})$ gives storage into $\tilde{S}_d(1 - \tilde{z})$, the optimal mode for backward retrieval, with efficiency equal to the optimal retrieval efficiency η_r^{\max} . We also verify that this control field is the time-reverse of the control field that retrieves the optimal spin-wave mode into $\mathcal{E}_{\text{in}}^*(\tilde{T} - \tilde{t})$, that is, the time-reverse of the input mode.

In order to solve for $\Omega(\tilde{t})$ from Eq. (B.37), we note that $q(\tilde{z}, \tilde{t})$ satisfies

$$\int_0^\infty d\tilde{z} q(\tilde{z}, \tilde{t}) q^*(\tilde{z}, \tilde{t}') = \delta(\tilde{t} - \tilde{t}'), \quad (\text{B.86})$$

$$\int_0^T d\tilde{t} q(\tilde{z}, \tilde{t}) q^*(\tilde{z}', \tilde{t}) = \delta(\tilde{z} - \tilde{z}'), \quad (\text{B.87})$$

where we have used the identity

$$\int_0^\infty dx J_0(ax) J_0(bx) x = \frac{1}{a} \delta(a - b), \quad (\text{B.88})$$

and where Eq. (B.87) requires $h(0, \tilde{T}) = \infty$ (we will discuss below that this requirement can be relaxed without significant loss in efficiency). Using Eq. (B.86), we see that $\int_0^\infty d\tilde{z} |s(\tilde{z})|^2 = 1$, as expected from unitarity (since we neglect both the leakage and the decay rate γ in Eq. (B.37), the transformation between $\mathcal{E}_{\text{in}}(\tilde{t})$ and $s(\tilde{z})$ is unitary). Using Eq. (B.86), we can also invert Eq. (B.37) to get

$$\mathcal{E}_{\text{in}}(\tilde{t}) = \int_0^\infty d\tilde{z} q^*(\tilde{z}, \tilde{t}) s(\tilde{z}). \quad (\text{B.89})$$

Clearly, Eqs. (B.37) and (B.89) establish a 1-to-1 correspondence, for a given $\tilde{\Omega}(\tilde{t})$, between input modes $\mathcal{E}_{\text{in}}(\tilde{t})$ and decayless modes $s(\tilde{z})$. This 1-to-1 correspondence is the demonstration of the unitarity of the map defined by Eq. (B.37). For the purposes of shaping the control field, it is crucial that Eqs. (B.37) and (B.89) also establish a 1-to-1 correspondence, for a given $\mathcal{E}_{\text{in}}(\tilde{t})$, between controls $\tilde{\Omega}(\tilde{t})$ (satisfying $h(0, \tilde{T}) = \infty$ and nonzero whenever $\mathcal{E}_{\text{in}}(\tilde{t})$ is nonzero) and normalized decayless propagation modes $s(\tilde{z})$. In particular, Eq. (B.37) itself allows to determine $s(\tilde{z})$ from $\tilde{\Omega}(\tilde{t})$ and $\mathcal{E}_{\text{in}}(\tilde{t})$. To solve for $\tilde{\Omega}(\tilde{t})$ given $s(\tilde{z})$ and $\mathcal{E}_{\text{in}}(\tilde{t})$, we integrate, as in Sec. B.6.1, from 0 to \tilde{t} the norm squared of both sides of Eq. (B.89) and change the integration variable from \tilde{t}' to $h' = h(\tilde{t}', \tilde{T})$ on the right-hand side to obtain

$$\int_0^{\tilde{t}} d\tilde{t}' |\mathcal{E}_{\text{in}}(\tilde{t}')|^2 = \int_{h(\tilde{t}, \tilde{T})}^{h(0, \tilde{T})} dh' \frac{d}{d\tilde{\Delta}^2} \left| \int_0^\infty d\tilde{z} e^{-i\frac{d\tilde{z}}{\tilde{\Delta}}} J_0 \left(2\sqrt{\frac{h'd\tilde{z}}{\tilde{\Delta}^2}} \right) s(\tilde{z}) \right|^2. \quad (\text{B.90})$$

Using $h(\tilde{T}, \tilde{T}) = 0$ and the normalization of $s(\tilde{z})$ and $\mathcal{E}_{\text{in}}(\tilde{t})$, the evaluation of Eq. (B.90) at $\tilde{t} = \tilde{T}$, implies that $h(0, \tilde{T}) = \infty$ (unless the expression inside the absolute value sign vanishes for all h' greater than some finite value). This divergence is, however, just a mathematical convenience: truncating $|\Omega(t)|$ does not significantly affect the efficiency, as we discuss in Secs. B.6.1, B.6.2, and B.6.4. We also give in Sec. B.6.2 approximate expressions for how big the optimal $|\Omega|$ is in the Raman and resonant limits. Replacing $h(0, \tilde{T})$ with ∞ , we use Eq. (B.90) to solve numerically for $h(\tilde{t}, \tilde{T})$, exactly as in Sec. B.6.1. $|\tilde{\Omega}(\tilde{t})|$ is then deduced by taking the square root of the negative of the derivative of $h(\tilde{t}, \tilde{T})$. The phase of $\tilde{\Omega}$ is found by inserting $|\tilde{\Omega}|$ into Eq. (B.89) is given by

$$\begin{aligned} \text{Arg} \left[\tilde{\Omega}(\tilde{t}) \right] &= \frac{\pi}{2} + \text{Arg} \left[\mathcal{E}_{\text{in}}(\tilde{t}) \right] + \frac{h(\tilde{t}, \tilde{T})}{\tilde{\Delta}} \\ &+ \text{Arg} \left[\int_0^\infty d\tilde{z} e^{i\frac{d\tilde{z}}{\tilde{\Delta}}} J_0 \left(2\sqrt{\frac{h(\tilde{t}, \tilde{T})d\tilde{z}}{\tilde{\Delta}^2}} \right) s^*(\tilde{z}) \right]. \end{aligned} \quad (\text{B.91})$$

The various terms in Eq. (B.91) can be interpreted in a way similar to the terms in the phase of the retrieval control in Eq. (B.33) in Sec. B.6.1. The only minor difference in the interpretation is that in the limit $\tilde{\Delta} \rightarrow 0$, the third term seems to diverge. However, one can check that in this limit the last term cancels (up to a constant) with the third term to ensure that the phase of the optimal control is still given solely by the phase of the desired output, as expected for the resonant limit. Finally, we note that the same remarks as at the end of Sec. B.6.1 regarding the ability to truncate the divergences of $|\tilde{\Omega}(\tilde{t})|$ without significant loss in efficiency apply.

Using Eq. (B.39), we show in Sec. B.6.2 how to find the optimal decayless mode $s(z)$, which should then be used in Eq. (B.37) to shape the optimal control (using Eqs. (B.90) and (B.91)). Having derived the optimal storage control in this way, we can now explicitly verify the results obtained from the time reversal reasoning. Two of these results are that the mode $S(\tilde{z}, \tilde{T})$ used in optimal storage is just the optimal mode for backward retrieval and that the optimal storage efficiency and the optimal retrieval efficiency are equal. One can explicitly verify these statements by checking that the application of Eq. (B.39) to the iteration used to find the optimal $s(\tilde{z})$ gives the iteration used to find the optimal backward retrieval mode, i.e.,

$$S_2(\tilde{z}) = \int_0^1 d\tilde{z}' k_r(\tilde{z}, \tilde{z}') S_1(\tilde{z}'), \quad (\text{B.92})$$

where $k_r(\tilde{z}, \tilde{z}')$ is defined in Eq. (B.15). Thus, $S(\tilde{z}, \tilde{T})$ that we compute from the optimal $s(\tilde{z})$ using Eq. (B.39) is indeed the optimal mode for backward retrieval, and the optimal storage efficiency is indeed equal to the optimal retrieval efficiency η_r^{\max} :

$$S(\tilde{z}, \tilde{T}) = \sqrt{\eta_r^{\max}} \tilde{S}_d(1 - \tilde{z}). \quad (\text{B.93})$$

Another consequence of time reversal is the fact that the optimal storage control for a given input mode is the time reverse of the control that gives optimal backward retrieval into the time reverse of that input mode. One can verify this directly by comparing the expressions of the magnitude and phase of the two controls. However, a simpler approach is to consider $\mathcal{E}_{\text{out}}(\tilde{t})$ given by Eq. (B.23) for the case of retrieval with a certain control $\tilde{\Omega}(\tilde{t})$ from the optimal mode, i.e., $S(\tilde{z}) = \tilde{S}_d(\tilde{z})$. We then use Eq. (B.34) to compute the spin wave $S_2(\tilde{z})$ that results from storing $\mathcal{E}_{\text{out}}^*(\tilde{T} - \tilde{t})$ with $\tilde{\Omega}^*(\tilde{T} - \tilde{t})$. In the limit $\tilde{T} \rightarrow \infty$ (to make sure that we fully retrieve \mathcal{E}_{out} before sending its time reverse back in), we can take the time integral explicitly to find

$$S_2(\tilde{z}) = \int_0^1 d\tilde{z}' k_r(\tilde{z}, \tilde{z}') \tilde{S}_d(1 - \tilde{z}') = \eta_r^{\max} \tilde{S}_d(1 - \tilde{z}), \quad (\text{B.94})$$

where in the last step we used the definition of $\tilde{S}_d(1 - \tilde{z})$ as the eigenvector of k_r with the largest eigenvalue η_r^{\max} equal to the optimal retrieval efficiency. Thus, the total efficiency of optimal retrieval followed by time-reversed storage is $(\eta_r^{\max})^2$. So

we have shown explicitly that the time reverse of optimal retrieval gives storage into \tilde{S}_d with the maximum efficiency η_r^{\max} , confirming what we have shown in Sec. B.4 based on general time reversal arguments. Since we have shown in this Section that the optimal control field is unique, we have therefore confirmed that the control that optimally stores a given input and the control that optimal retrieves into the time reverse of that input are time-reverses of each other.

Appendix C

Optimal Photon Storage in Atomic Ensembles: Effects of Inhomogeneous Broadening

C.1 Introduction

In Chapter 2 and Appendices A and B, we carried out the optimization of photon storage in homogeneously broadened Λ -type media. At the same time, many experimental realizations, such as the ones using warm atomic vapors [80] or the ones using impurities in solid state samples [94, 290, 291, 95], have some degree of inhomogeneous broadening, whose presence will modify the optimal control strategy and the values for the maximum efficiency. The subject of the present Appendix is the extension of the analysis of Chapter 2 and Appendices A and B to include inhomogeneous broadening.

The remainder of the present Appendix is organized as follows. In Sec. C.2, we discuss the effects of inhomogeneous broadening assuming that the atoms fully redistribute themselves between frequency classes during the storage time, which would be the case, for example, in Doppler-broadened atoms with sufficiently long storage times. In particular, we optimize the storage process and show that at high enough optical depth, all atoms contribute coherently as if the medium were homogeneously broadened. Then in Sec. C.3, we discuss the effects of inhomogeneous broadening assuming there is no redistribution between frequency classes during the storage time, which would be the case in atomic vapors for short storage times or in solid state samples. In particular, we discuss the advantages and limitations of reversing the inhomogeneous broadening during the storage time [87], as well as suggest a method for achieving high efficiencies with a nonreversible spectrally well-localized inhomogeneous profile. In Sec. C.4, we summarize our analysis of the effects of inhomogeneous broadening. Finally, in Sec. C.5, we present some details omitted in the main text.

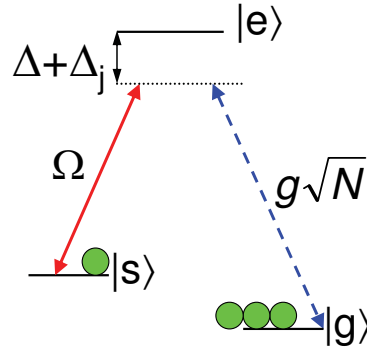


Figure C.1: Λ -type medium coupled to a classical field (solid) with Rabi frequency $\Omega(t)$ and a quantum field (dashed). Collective enhancement [76] effectively increases the atom-field coupling constant g up to $g\sqrt{N}$, where N is the number of atoms in the medium. Δ_j is a frequency shift due to inhomogeneous broadening.

C.2 Inhomogeneous Broadening with Redistribution between Frequency Classes during the Storage Time

In this Section, we consider a particular case of inhomogeneously broadened media: the case of a Doppler-broadened atomic vapor in free space. We first describe our model in Sec. C.2.1. We then use this model in Sec. C.2.2 to analyze storage and retrieval of photons in Doppler-broadened media.

C.2.1 Model

As in Appendix B, we consider a free-space medium of length L and cross-section area A containing $N = \int_0^L dz n(z)$ atoms, where $n(z)$ is the number of atoms per unit length. We assume that within the interaction volume the concentration of atoms is uniform in the transverse direction. The atoms have the Λ -type level configuration shown in Fig. C.1. They are coupled with a collectively enhanced coupling constant $g\sqrt{N}$ (g assumed to be real for simplicity) to a narrowband quantum field centered at a frequency ω_1 and described by a slowly varying operator $\hat{\mathcal{E}}(z, t)$. The atoms are also coupled to a copropagating narrowband classical control field centered at frequency ω_2 with a Rabi frequency envelope $\Omega(z, t) = \Omega(t - z/c)$. We assume that quantum electromagnetic field modes with a single transverse profile are excited. As discussed in detail in Appendix B, we neglect reabsorption of spontaneously emitted photons and treat the problem in a one-dimensional approximation.

In order to model the inhomogeneous broadening, we sort all the atoms into

separate velocity classes labeled by j , such that all atoms in a certain velocity class have approximately the same velocity v_j . We will assume that during the experiment the atoms do not change their positions significantly compared to the longitudinal variation of the fields. Therefore, the Doppler effect will be the only effect of nonzero atomic velocities that we will consider.

Furthermore, we will assume that the difference in the Doppler shifts of the two optical transitions can be neglected so that atoms in all velocity classes can simultaneously stay in two-photon resonance with the two fields. For copropagating beams, this assumption is exactly satisfied if the two metastable states are degenerate. Moreover, below we shall consider a storage technique which we refer to as fast storage (see Chapter 2 and Appendix B), where the control field consists of a simple π pulse, which will work perfectly provided its Rabi frequency is much greater than the broadened linewidth. In this case, the assumption of equal Doppler shifts of the two optical transitions is thus not needed. However, we shall also consider the so-called adiabatic storage schemes (see Chapter 2 and Appendix B), where the splitting of the two metastable levels by a nonzero frequency difference ω_{sg} , as well as Doppler broadening occurring for noncopropagating fields, will play a role [336]. In order to ensure that the difference in Doppler shifts has a negligible effect in this situation, we consider copropagating beams and assume that the total accumulated phase difference $T\bar{v}\omega_{sg}/c$ is much less than unity, where \bar{v} is the thermal speed of the atoms, c is the speed of light, and T is the duration of the incoming quantum light pulse. This condition is usually satisfied even in room-temperature experiments, such as the experiment using ^{87}Rb vapor in Ref. [80], where $\omega_{sg} = (2\pi)6.8$ GHz and $T \sim 200 \mu\text{s}$, which gives $T\bar{v}\omega_{sg}/c < 0.01$.

For simplicity, we also assume that the velocities do not change during the processes of storage and retrieval but fully rethermalize during the storage time $[T, T_r]$. The atoms thus fully redistribute themselves among different velocity classes during the storage time, and at time T_r the spin wave is the same across all velocity classes. In addition to being relevant for Doppler broadening, much of the discussion of this Section will also apply to solid state systems with inhomogeneous broadening. The fact that solid state impurities do not have the redistribution between frequency classes during the storage time (which we assume in this Section) will, however, introduce modifications. Some of these modification are discussed in Sec. C.3.

We assume that the control is detuned by Δ with respect to stationary atoms, $\omega_2 = \omega_{es} - \Delta$, while the quantum field is in two-photon resonance, i.e., $\omega_1 = \omega_{eg} - \Delta$ (where ω_{es} and ω_{eg} are atomic transition frequencies). We define the same slowly varying operators as in Eqs. (B.57)-(B.61), except now, at each z and t , we have continuous atomic operators for each velocity class. For example, we define

$$\hat{\sigma}_{\mu\mu}^j(z, t) = \sqrt{p_j} \frac{1}{N_z^j} \sum_{i=1}^{N_z^j} \hat{\sigma}_{\mu\mu}^{j(i)}(t), \quad (\text{C.1})$$

where j indicates the velocity class, i runs over the N_z^j atoms near z in the velocity class j , p_j is the fraction of atoms in the velocity class j , $\sum_j p_j = 1$, and $\sigma_{\mu\nu}^{j(i)} = |\mu\rangle_{j(i)}\langle\nu|$ indicates the internal state operator between states $|\mu\rangle$ and $|\nu\rangle$ for the i th atom in the j th velocity class.

As in Appendices A and B, we use the dipole and rotating-wave approximations, assume that almost all atoms are in the ground state at all times, and consider equations of motion only to first order in \mathcal{E} . As described in Appendices A and B, under reasonable experimental conditions, the incoming noise corresponding to the decay of atomic coherences is vacuum, and efficiency is the only number we need in order to fully characterize the mapping. Following then the same steps as in Sec. B.2, we obtain complex number equations

$$(\partial_t + c\partial_z)\mathcal{E} = ig\sqrt{N} \sum_j \sqrt{p_j} P_j n(z) L/N, \quad (\text{C.2})$$

$$\partial_t P_j = -(\gamma + i(\Delta + \Delta_j)) P_j + ig\sqrt{N} \sqrt{p_j} \mathcal{E} + i\Omega S_j, \quad (\text{C.3})$$

$$\partial_t S_j = i\Omega^* P_j, \quad (\text{C.4})$$

where γ is the polarization decay rate, $\Delta_j = \omega_{es}^j - \omega_{es} = \omega_{es} v_j/c$ is the Doppler shift due to the velocity v_j of the j th velocity class, P_j is the complex number representing the optical polarization $\sqrt{N} \hat{\sigma}_{ge}^j$, and S_j is the complex number representing the spin wave $\sqrt{N} \hat{\sigma}_{gs}^j$. We assume in Eq. (C.4) that the decay rate of the spin wave S_j is negligible. As in Eqs. (B.5)-(B.7), we now go into the comoving frame $t' = t - z/c$, introduce the dimensionless time $\tilde{t} = \gamma t'$ and a dimensionless rescaled coordinate $\tilde{z} = \int_0^z dz' n(z')/N$, absorb a factor of $\sqrt{c/(L\gamma)}$ into the definition of \mathcal{E} , and obtain

$$\partial_{\tilde{z}} \mathcal{E} = i\sqrt{d} \sum_j \sqrt{p_j} P_j, \quad (\text{C.5})$$

$$\partial_{\tilde{t}} P_j = -(1 + i(\tilde{\Delta} + \tilde{\Delta}_j)) P_j + i\sqrt{d} \sqrt{p_j} \mathcal{E} + i\tilde{\Omega} S_j, \quad (\text{C.6})$$

$$\partial_{\tilde{t}} S_j = i\tilde{\Omega}^* P_j, \quad (\text{C.7})$$

where we have identified the optical depth $d = g^2 NL/(\gamma c)$, and where $\tilde{\Omega} = \Omega/\gamma$, $\tilde{\Delta} = \Delta/\gamma$, and $\tilde{\Delta}_j = \Delta_j/\gamma$. Note that d is defined here as the optical depth that the sample would have had if there were the same number of atoms but no inhomogeneous broadening. This quantity should not be confused with the actually measured optical depth d' . With inhomogeneous broadening, the measured value will be lower: $d' < d$. Later, we shall derive explicit relations between these two quantities. It is essential to realize that both quantities d and d' play a role in the performance of the memory, as we shall see below.

We assume that all atoms are initially pumped into the ground state, i.e., no P or S excitations are present in the atoms. We also assume that the only input field excitations initially present are in the quantum field mode with a normalized envelope

shape $\mathcal{E}_{\text{in}}(\tilde{t})$ nonzero on $[0, \tilde{T}]$ (where $\tilde{T} = T\gamma$). The goal is to store the state of this mode into some spin-wave mode and at a time $\tilde{T}_r > \tilde{T}$ retrieve it onto an output field mode. The initial conditions for storage are $S_j(\tilde{z}, 0) = 0$ and $P_j(\tilde{z}, 0) = 0$ for all j and $\mathcal{E}(0, \tilde{t}) = \mathcal{E}_{\text{in}}(\tilde{t})$, and the storage efficiency is given by

$$\eta_s = \frac{\text{(number of stored excitations)}}{\text{(number of incoming photons)}} = \int_0^1 d\tilde{z} |S(\tilde{z}, \tilde{T})|^2, \quad (\text{C.8})$$

where $S(\tilde{z}, \tilde{T}) = \sum_j \sqrt{p_j} S_j(\tilde{z}, \tilde{T})$ is the spin wave, to which all S_j average after rethermalization. The initial conditions for retrieval are $\mathcal{E}(0, \tilde{t}) = 0$, and, for all j , $P_j(\tilde{z}, \tilde{T}_r) = 0$, and $S_j(\tilde{z}, \tilde{T}_r) = \sqrt{p_j} S(\tilde{z}, \tilde{T})$ or $S_j(\tilde{z}, \tilde{T}_r) = \sqrt{p_j} S(1 - \tilde{z}, \tilde{T})$ for forward or backward retrieval, respectively (as in Appendix B). The total efficiency of storage followed by retrieval is then given by

$$\eta_{\text{tot}} = \frac{\text{(number of retrieved photons)}}{\text{(number of incoming photons)}} = \int_{\tilde{T}_r}^{\infty} d\tilde{t} |\mathcal{E}_{\text{out}}(\tilde{t})|^2, \quad (\text{C.9})$$

where $\mathcal{E}_{\text{out}}(\tilde{t}) = \mathcal{E}(1, \tilde{t})$. If during retrieval we instead start with $S_j(\tilde{z}, \tilde{T}_r) = \sqrt{p_j} S(\tilde{z})$ for some normalized spin wave $S(\tilde{z})$, then the same equation will give the retrieval efficiency from this mode:

$$\eta_r = \frac{\text{(number of retrieved photons)}}{\text{(number of stored excitations)}} = \int_{\tilde{T}_r}^{\infty} d\tilde{t} |\mathcal{E}_{\text{out}}(\tilde{t})|^2. \quad (\text{C.10})$$

For completeness, we note that, for the cavity model described in Appendix A, the equations corresponding to Eqs. (C.5)-(C.7) above are (without rescaling of variables)

$$\mathcal{E}_{\text{out}} = \mathcal{E}_{\text{in}} + i\sqrt{2\gamma C} \sum_j \sqrt{p_j} P_j, \quad (\text{C.11})$$

$$\partial_t P_j = -(\gamma + i(\Delta + \Delta_j)) P_j - \gamma C \sqrt{p_j} \sum_k \sqrt{p_k} P_k + i\Omega S_j + i\sqrt{2\gamma C} \sqrt{p_j} \mathcal{E}_{\text{in}}, \quad (\text{C.12})$$

$$\partial_t S_j = i\Omega^* P_j, \quad (\text{C.13})$$

where C is the cooperativity parameter equal to the optical depth of the ensemble multiplied by the cavity finesse. The initial conditions for storage in the cavity model are $S_j(0) = 0$ and $P_j(0) = 0$ for all j and $\mathcal{E}_{\text{in}}(t) \neq 0$, while the initial conditions for retrieval are $S_j(T_r) = \sqrt{p_j} S(T)$ and $P_j(T_r) = 0$ for all j and $\mathcal{E}_{\text{in}}(t) = 0$. It is assumed that during the storage time atoms rethermalize and all S_j average to the same value $S(T) = \sum_j \sqrt{p_j} S_j(T)$.

In the homogeneously broadened case discussed in Appendices A and B, we defined the so-called adiabatic and fast regimes for storage and retrieval. Both of these limits can also be achieved in the presence of Doppler broadening. The adiabatic regime corresponds to smooth control and input fields such that the optical polarization P_j

in Eq. (C.6) (or Eq. (C.12) for the case of the cavity model) can be adiabatically eliminated. The fast regime corresponds to storage and retrieval techniques in which the control field consists of a very short and powerful resonant π pulse between states $|s\rangle$ and $|e\rangle$. The only difference in the requirements from the homogeneously broadened case is that now the control field Ω in the π pulse must also be much greater than the inhomogeneous width. We refer the reader to Appendix A for a detailed discussion of the adiabatic and fast photon storage techniques, as well as for a full list of references.

Equations (C.5)-(C.7) can be solved numerically by introducing sufficiently many discrete velocity classes. However, when the control is constant (i.e., a step) or when we are in the fast limit, these equations can be solved without discretizing the velocity distribution by using Laplace transformation in time, $\tilde{t} \rightarrow v$. In this case, the inverse Laplace transform has to be taken numerically at the end. Alternatively, in the case of retrieval alone or in the case of storage followed by retrieval, if one is interested only in the efficiency and not in the output mode, one can compute this efficiency both in the free-space model and in the cavity model without computing $\mathcal{E}_{\text{out}}(\tilde{t})$ directly from the Laplace transform $\mathcal{E}_{\text{out}}(v)$ as

$$\eta_r = \frac{1}{2\pi} \int_{-\infty}^{\infty} d\xi |\mathcal{E}_{\text{out}}(v = i\xi)|^2. \quad (\text{C.14})$$

Below we shall use both the numerical method with discrete velocity classes and the method of the Laplace transformation in time.

C.2.2 Retrieval and Storage with Doppler Broadening

An important result in the discussion of homogeneously broadened ensembles in Appendices A and B was the result that the retrieval efficiency is independent of the shape of the control and the detuning, provided that all excitations are pumped out of the system. Moreover, in both the cavity and the free-space cases we were able to deduce in Appendices A and B explicit formulas for the retrieval efficiency. Although in the inhomogeneously broadened case discussed in the present Appendix we have not been able to find an explicit formula for the retrieval efficiency, we will present now the proof that even with inhomogeneous broadening the retrieval efficiency is independent of the detuning Δ and the control shape $\Omega(t)$.

We consider first the cavity model given in Eqs. (C.11)-(C.13). Since we are interested in retrieval, we set $\mathcal{E}_{\text{in}} = 0$. We also consider a general situation, in which $S_j(t = 0)$ are not necessarily equal for different velocity classes j (we also shifted for simplicity the beginning of retrieval from $t = T_r$ to $t = 0$). Then, using Eq. (C.11), the retrieval efficiency is

$$\eta_r = \int_0^{\infty} dt |\mathcal{E}_{\text{out}}(t)|^2 = 2\gamma C \sum_{j,k} \sqrt{p_j p_k} \int_0^{\infty} dt P_j(t) P_k^*(t), \quad (\text{C.15})$$

and the following identity can be explicitly verified from Eqs. (C.12) and (C.13):

$$\begin{aligned} \frac{d}{dt}(P_j P_k^* + S_j S_k^*) &= -(2\gamma + i(\Delta_j - \Delta_k))P_j P_k^* \\ &\quad - \gamma C \sum_i \sqrt{p_i}(\sqrt{p_j} P_i P_k^* + \sqrt{p_k} P_j P_i^*). \end{aligned} \quad (\text{C.16})$$

If M is the number of velocity classes, Eq. (C.16) stands for M^2 equations in M^2 variables $P_i P_k^*$. We can write them in matrix form and, in principle, invert the $M^2 \times M^2$ matrix on the right-hand side and thus solve for $P_j P_k^*$ as a linear combination of $\frac{d}{dt}(P_a P_b^* + S_a S_b^*)$ for various a and b . Inserting this into Eq. (C.15), applying the fundamental theorem of calculus, and assuming the retrieval is complete (i.e., no excitations remain in the atoms), the retrieval efficiency can be expressed as a linear combination of $S_a(0)S_b^*(0)$, and is thus independent of control and detuning.

In Sec. C.5.1, we present an analogous derivation, which shows that the free-space retrieval efficiency in the presence of inhomogeneous broadening is also independent of detuning and control. Numerical calculations also show that adiabatic elimination of P_j , as in the homogeneously broadened case discussed in Appendices A and B, does not change the exact value of the efficiency.

Since the retrieval efficiency is thus independent of the exact method used for retrieval, we shall here mainly consider the fast retrieval from $S(\tilde{z})$. In this case Laplace transformation in time can be used to solve the problem analytically. We will focus for the rest of this Section on the free-space model. We assume that the retrieval π pulse arrives at $\tilde{t} = 0$ and that it perfectly transfers $P_j(\tilde{z}) = 0$, $S_j(\tilde{z}) = \sqrt{p_j}S(\tilde{z})$ to $P_j(\tilde{z}) = i\sqrt{p_j}S(\tilde{z})$, $S_j(\tilde{z}) = 0$. After the π pulse, we Laplace-transform Eqs. (C.5) and (C.6) in time $\tilde{t} \rightarrow v$ and obtain

$$\partial_z \mathcal{E} = i\sqrt{d} \sum_j \sqrt{p_j} P_j, \quad (\text{C.17})$$

$$v P_j - i\sqrt{p_j} S(\tilde{z}) = -(1 + i\tilde{\Delta}_j) P_j + i\sqrt{d}\sqrt{p_j} \mathcal{E}. \quad (\text{C.18})$$

Solving for P_j from the second equation and inserting it into the first equation, we find

$$\mathcal{E}(\tilde{z} = 1, v) = - \int_0^1 d\tilde{z} S(\tilde{z}) \sqrt{d} f(v) e^{-df(v)(1-\tilde{z})}, \quad (\text{C.19})$$

where

$$f(v) = \sum_j p_j \frac{1}{1 + v + i\tilde{\Delta}_j} = \int_{-\infty}^{\infty} d\tilde{\Delta} p(\tilde{\Delta}) \frac{1}{1 + v + i\tilde{\Delta}}, \quad (\text{C.20})$$

and where $p(\tilde{\Delta})$ is the Doppler profile.

In Doppler-broadened media, the resonant optical depth is reduced by a factor of $\sim \gamma/\Delta_I$, where Δ_I is the width of the (inhomogeneous) Doppler profile. The naive expectation would therefore be that we could simply treat Doppler-broadened

atoms as Doppler-free but with a reduced optical depth. As we will show below, this prescription would be correct if the broadened line shape were a Lorentzian, as considered, e.g., in Ref. [337, 338, 339]. For a Gaussian profile this prescription is, however, not applicable, and qualitatively different behavior is obtained.

To proceed, we first evaluate $f(v)$ for three different inhomogeneous profiles $p(\tilde{\Delta})$. For a homogeneously broadened ensemble, the line shape function $p(\tilde{\Delta})$ is just a δ function:

$$p(\tilde{\Delta}) = \delta(\tilde{\Delta}), \quad (\text{C.21})$$

$$f(v) = \frac{1}{1+v}. \quad (\text{C.22})$$

If we have a Lorentzian inhomogeneous profile with Δ_I half width at half maximum (HWHM), we get (with $\tilde{\Delta}_I = \Delta_I/\gamma$)

$$p(\tilde{\Delta}) = \frac{\tilde{\Delta}_I}{\pi} \frac{1}{\tilde{\Delta}^2 + \tilde{\Delta}_I^2}, \quad (\text{C.23})$$

$$f(v) = \frac{1}{1+v + \tilde{\Delta}_I}. \quad (\text{C.24})$$

For a Gaussian inhomogeneous profile with (rescaled by γ) standard deviation σ (and rescaled HWHM $\tilde{\Delta}_I = \sigma\sqrt{2\ln 2}$),

$$p(\tilde{\Delta}) = \frac{1}{\sqrt{2\pi}\sigma^2} \exp\left(-\frac{\tilde{\Delta}^2}{2\sigma^2}\right), \quad (\text{C.25})$$

$$f(v) = \sqrt{\frac{\pi}{2\sigma^2}} e^{\frac{(1+v)^2}{2\sigma^2}} \operatorname{erfc}\left[\frac{1+v}{\sqrt{2}\sigma}\right], \quad (\text{C.26})$$

where the last equality assumes $\operatorname{Re}[v] \geq 0$, and the complementary error function is defined as $\operatorname{erfc}(x) = 1 - \pi^{-1/2} 2 \int_0^x \exp(-x'^2) dx'$. Using the definition of erfc , we can analytically continue $f(v)$ into $\operatorname{Re}[v] < 0$.

If we insert the Lorentzian result for $f(v)$ from Eq. (C.24) into Eq. (C.19) and rescale v , we find that, compared to homogeneous broadening (Eq. (C.22)), the Lorentzian broadening effectively just replaces γ with $\gamma + \Delta_I$, which is equivalent to reducing d by a factor of $1/(1 + \Delta_I/\gamma)$ (which for $\Delta_I \gg \gamma$ is equal to γ/Δ_I). Therefore, since we have shown that the retrieval efficiency is independent of the retrieval method, the naive rescaling of d to $d\gamma/\Delta_I$ can indeed be used to calculate the retrieval efficiency when the broadening is Lorentzian. Similarly, the same can be shown for the cavity model.

For Doppler broadening, $p(\tilde{\Delta})$ is, however, Gaussian as in Eq. (C.25). Using Eqs. (C.14) and (C.19), we can write the retrieval efficiency in the form

$$\eta[S(\tilde{z})] = \int_0^1 d\tilde{z} \int_0^1 d\tilde{z}' k(\tilde{z}, \tilde{z}') S(\tilde{z}) S^*(\tilde{z}') \quad (\text{C.27})$$

for some complicated kernel k . Applying the iterative technique used in Sec. B.3 or by directly diagonalizing k on a grid, we can compute the optimal retrieval modes (i.e., the eigenvectors with the largest eigenvalues) for each d and σ .

Before plotting and analyzing the optimal spin waves and the maximum efficiency obtained using Eq. (C.27), let us discuss what we expect. Assuming $\Delta_I \gg \gamma$, the resonant optical depth is reduced to $d' = d(\gamma/\Delta_I)\sqrt{\pi \ln 2}$ in the presence of Gaussian broadening. In contrast to retrieval with a Lorentzian profile, however, retrieval with a Gaussian profile is not equivalent to Doppler-free retrieval with reduced optical depth (as we can see by comparing Eqs. (C.26) and (C.22)). Moreover, we will show now that, with true (Gaussian) Doppler broadening, at high enough optical depth all atoms contribute coherently as if the medium were homogeneously broadened, which is the main result of this Section. Although this result holds for any control, it is most easily explained in the case of fast retrieval: after the π pulse, the spontaneous emission (or more precisely the polarization decay at a rate γ) and the dephasing due to the inhomogeneous broadening will cause the polarization $P(t) = \sum_j \sqrt{p_j} P_j(t)$ (with an initial velocity-symmetric polarization $P_j(0) = \sqrt{p_j} P(0)$) to decay as (using the original units)

$$P \sim e^{-\gamma t} \int d\Delta e^{-i\Delta t} p(\Delta/\gamma)/\gamma = \exp[-\gamma t - \Delta_I^2 t^2/(4 \ln 2)], \quad (\text{C.28})$$

where we have used $p(\Delta/\gamma)$ from Eq. (C.25). Thus, losses induced by Gaussian broadening are non-Markovian. Since the time required for fast retrieval varies as $t \sim 1/(\gamma d)$ (see, for example, Appendix B), Doppler-induced losses become negligible compared to spontaneous emission losses for sufficiently large d ($d \gg (\Delta_I/\gamma)^2$ or, equivalently, $d' \gg \Delta_I/\gamma$), and the system will behave as if there were no inhomogeneous broadening. The essential step in this last derivation is that the second moment $\langle \Delta^2 \rangle$ with respect to $p(\Delta/\gamma)$ is finite, and the result is thus applicable to any inhomogeneous profile falling off faster than a Lorentzian. In contrast, for a Lorentzian profile, the optical polarization decay would be

$$P \sim \exp(-\gamma t - \Delta_I t), \quad (\text{C.29})$$

and we recover the effective rescaling of γ up to $\gamma + \Delta_I$, which is equivalent to a simple rescaling of d down to d' .

We now turn to the discussion of the optimal velocity-symmetric spin-wave modes $S(\tilde{z})$ obtained under Gaussian broadening using Eq. (C.27). These optimal modes are plotted (for forward retrieval) in Fig. C.2 for $d' = 0.17, 0.67, 3.69, 14.25$ and $\Delta_I = 88\gamma$, which corresponds to the Rb D1 line at room temperature (assuming 2γ is the natural linewidth). Indeed, at sufficiently high optical depth, the optimal mode approaches $S(\tilde{z}) = \sqrt{3}\tilde{z}$ (which we have derived in the homogeneously broadened case considered in Appendix B), since according to the argument above, Doppler broadening plays no role at sufficiently high d .

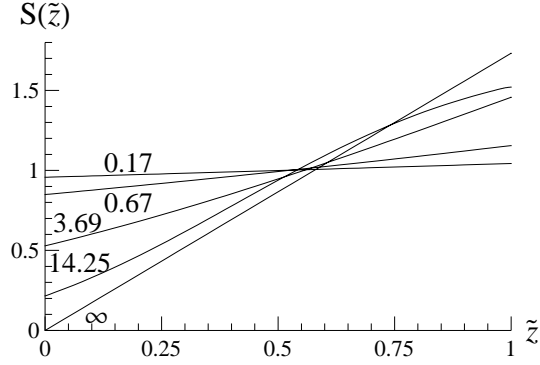


Figure C.2: Optimal spin-wave modes to retrieve from (in the forward direction) at the indicated values of d' in the presence of (Gaussian) Doppler broadening with HWHM $\Delta_I = 88\gamma$.

The above calculation (via Eq. (C.27)) of the optimal spin wave yields the optimal retrieval efficiency. Using the general time-reversal arguments presented in Appendix B, which still apply with Doppler broadening, we can, however, also use these optimal modes, to calculate the optimal efficiency for the combined process of storage followed by retrieval. The optimal symmetric modes ($S_j(\tilde{z}) = S(\tilde{z})$ for all j) for retrieval, which we have found above, are all real. Time reversal thus shows that the optimal storage into the symmetric mode, is obtained by time-reversing retrieval, and has the same efficiency as the retrieval. Note, however, that, in general, asymmetric modes may also be excited during storage. In this Section, however, we assume that the atoms rethermalize during the storage time. This washes out any amplitude on asymmetric modes and the only relevant efficiency is the efficiency of storage onto the symmetric mode. The total maximum efficiency for storage followed by retrieval will thus be the square of the maximum retrieval efficiency (obtained as the largest eigenvalue of the kernel in Eq. (C.27)). With circles in Fig. C.3, we show the maximum total efficiency for storage followed by backward retrieval for $\Delta_I = 88\gamma$. The solid line in Fig. C.3 is the Doppler-free maximum efficiency $\eta_{\text{back}}^{\text{max}}(d)$ from Fig. B.4. The dotted line is the efficiency one would naively expect from a simple rescaling of the resonant optical depth, $\eta_{\text{back}}^{\text{max}}(d')$, where $d' = d(\gamma/\Delta_I)\sqrt{\pi \ln 2}$. The dashed line is $5.8(\pi/(4d'^2) + 1/d)$, which approximates the error fall-off of the points obtained from the full numerical optimization of Eq. (C.27) (circles) reasonably well and comes from the following heuristic model: $t = 1/(\gamma d)$ is inserted into Eq. (C.28), the exponential is expanded to first order, and a prefactor of 5.8 is introduced to match the Doppler-free error at large d , which is $\sim 5.8/d$, as found in Appendix B.

Above, we found the optimal spin-wave modes for retrieval and the optimal retrieval efficiency by computing the eigenvector with the largest eigenvalue of the kernel

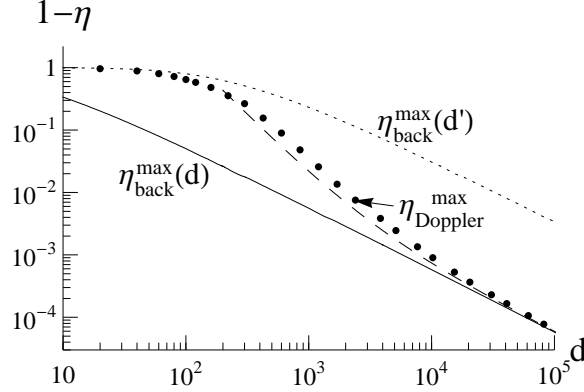


Figure C.3: Error $1 - \eta$ as a function of unbroadered optical depth d for different efficiencies η . $\eta_{\text{back}}^{\text{max}}(d)$ (solid) is the Doppler-free maximum total efficiency for any storage followed by backward retrieval. The maximum total efficiency for storage followed by backward retrieval with Doppler broadening of HWHM $\Delta_{\text{I}} = 88\gamma$ (circles) does not follow $\eta_{\text{back}}^{\text{max}}(d')$ (dotted), which is the efficiency one would expect from naive rescaling of resonant optical depth, but follows more closely the heuristic model $5.8 (\pi/(4d'^2) + 1/d')$ (dashed) described in the text.

in Eq. (C.27). As in the homogeneously broadened case discussed in Appendix B, one can, in fact, interpret the iterations used in finding the largest eigenvalue as the iterations of retrieval followed by storage of time-reversed output and control pulses. To show this, we note that the retrieval in Eq. (C.19) inverse-Laplace-transformed back to \tilde{t} and the storage equation, which is obtained using the same steps, can be written as

$$\mathcal{E}_{\text{out}}(\tilde{t}) = \int_0^1 d\tilde{z} \tilde{m}(\tilde{t}, \tilde{z}) S(1 - \tilde{z}), \quad (\text{C.30})$$

$$S(\tilde{z}, \tilde{T}) = \int_0^{\tilde{T}} d\tilde{t} \tilde{m}(\tilde{T} - \tilde{t}, \tilde{z}) \mathcal{E}_{\text{in}}(\tilde{t}), \quad (\text{C.31})$$

for some function \tilde{m} . Since these equations satisfy the general time-reversal form of Eqs. (B.35) and (B.36), the same results as in the homogeneously broadened case apply. In particular, using Eqs. (C.30) and (C.31), one can check that the maximization of retrieval efficiency through the iterative integration of the kernel in Eq. (C.27) is equivalent to retrieval followed by time reversal and storage. From Eqs. (C.30) and (C.31), it also follows that, in order to optimize fast storage followed by fast forward retrieval, one should start with any trial input mode, store it, retrieve forward, time-reverse the whole process, and then iterate till convergence is reached, exactly as in the homogeneously broadened case of Appendix B.

It is worth noting that a connection between time reversal and optimal photon

storage in the photon-echo technique was first made for the case of ideal, reversible storage in Refs. [86, 87, 294, 295, 296, 297]. In the present Appendix, in Chapter 2, and in Appendices A, B, and D, we extend this connection to a wide range of storage techniques in Λ -type media and show that optimal storage is intimately connected with time reversal, even when the dynamics of the system are not completely reversible, and when the ideal unit efficiency cannot be achieved.

We have thus shown that time-reversal iterations can be used to optimize storage followed by retrieval not only in the case of homogeneously broadened media discussed in Chapter 2 and Appendices A and B, but also in the case of Doppler-broadened media. As explained in Appendix B, such time-reversal iterations not only constitute a convenient mathematical tool; they can, in fact, be used experimentally to find the optimal input modes. In particular, as explained in Appendix B, since the envelope \mathcal{E} of the quantum light mode obeys the same equations of motion as classical light pulses, one can first use the iterative procedure to optimize the storage of classical light pulses, which can be easily measured and reversed, and then directly apply this knowledge to the storage of quantum states of light. In fact, the first experiment on time-reversal-based optimization has already been successfully carried out for classical light and confirmed the validity of the suggested procedure, as we report in Sec. 3.3.

C.3 Inhomogeneous Broadening without Redistribution between Frequency Classes during the Storage Time

In the previous Section, we treated the case when inhomogeneously broadened atoms redistribute themselves among different frequency classes during the storage time, which is the case in Doppler-broadened atomic vapors for sufficiently long storage times. This redistribution, however, does not take place in some other possible experimental realizations, e.g., in Doppler-broadened atomic vapors with short storage times or in solid state media. Therefore, in this Section, we consider what happens when the redistribution among frequency classes does not take place.

In the case of fast storage and retrieval, provided the π pulse is applied at a sufficiently high power, it does not matter whether the two optical transitions are broadened independently or not, i.e., whether the $|s\rangle - |g\rangle$ transition is broadened. However, in the case of adiabatic storage and retrieval the assumption that the control and the quantum field are always in two-photon resonance is crucial. Although the only regime of storage and retrieval in inhomogeneously broadened media we will consider in this Section is the fast regime, the analysis will also be extendable to the adiabatic limit provided the $|s\rangle - |g\rangle$ transition is homogeneously broadened. In this case, Eqs. (C.5)-(C.7) apply without modification. The proof in Sec. C.5.1 that the retrieval efficiency is independent of the detuning and the control, therefore, also

applies.

Using the solution technique based on the Laplace transformation in time introduced in Sec. C.2, one can show that when storage is followed by forward retrieval and the inhomogeneous profile is Lorentzian, it actually does not matter whether the atoms redistribute themselves among different frequency classes during the storage time or keep their frequencies unchanged: the same efficiency and output field are obtained. In this case, the results from Appendix B about homogeneous broadening are directly applicable if one replaces d by d' . This is, however, not true for backward retrieval with a Lorentzian inhomogeneous profile or for retrieval in either direction with a Gaussian inhomogeneous profile. To obtain the efficiency in this situation, it is therefore necessary to take into account the fact that the transition frequency of each individual atom is the same during both storage and retrieval. Furthermore, by controlling and reversing the inhomogeneous broadening, one can even achieve rephasing of atomic excitations and, in fact, attain an increase in total efficiency relative to an unbroadened case [292, 87]. An exhaustive study of the problem of storage followed by retrieval in media with no redistribution between frequency classes during the storage time is beyond the scope of this work. Here we restrict ourselves only to the investigation of fast storage followed by fast backward or forward retrieval in such media. We also include the possibility of reversing the inhomogeneous profile during the storage time as suggested in Refs. [292, 87]. In particular, in Sec. C.3.1, we set up the equations for the problem of fast storage followed by fast retrieval in *either* direction with and without the reversal of the inhomogeneous profile. In Secs. C.3.2 and C.3.3, we then discuss the results that these equations yield for the cases of storage followed by *backward* retrieval without and with the reversal of the inhomogeneous profile, respectively.

C.3.1 Setup and Solution

In this Section, assuming that the redistribution between frequency classes takes place neither during the processes of storage and retrieval nor during the storage time, we set up and solve the problem of fast storage followed by fast retrieval in the forward or backward direction with or without the reversal of the inhomogeneous broadening. Any storage with no redistribution between frequency classes (not only the fast limit) can be computed numerically with discrete frequency classes for any kind of inhomogeneous profile and any control. To do this, one can just use Eqs. (C.5)-(C.7) for both storage and retrieval and, depending on the direction of retrieval and on whether the inhomogeneous profile is reversed during the storage time, make the appropriate modification to the stored spin waves $S_j(\tilde{z}, \tilde{T})$ before retrieving it. However, as we now show, the case of fast storage and fast retrieval can also be solved¹ almost com-

¹Adiabatic storage and retrieval with a step (i.e., constant) control profile can also be solved using this technique. However, we will not pursue this investigation in the present work.

pletely analytically using Laplace transformation in time, $\tilde{t} \rightarrow v$. Before the storage π pulse is applied, $\tilde{\Omega} = 0$ in Eq. (C.6). Then for the fast storage of a resonant input mode $\mathcal{E}_{\text{in}}(\tilde{t})$, Eqs. (C.5) and (C.6) can be solved to give

$$P_j(\tilde{z}, v) = i\sqrt{d} \frac{\sqrt{P_j}}{1 + v + i\tilde{\Delta}_j} \mathcal{E}_{\text{in}}(v) e^{-dzf(v)}, \quad (\text{C.32})$$

where v is the Laplace variable, and $f(v)$ is defined in Eq. (C.20) and is computed for various inhomogeneous profiles in Eqs. (C.21)-(C.26).

To find the initial conditions for the subsequent retrieval, we take the inverse Laplace transform $u \rightarrow \tilde{t} = \tilde{T}$ of Eq. (C.32) and multiply P_j by -1 to account for the two π pulses (i.e., the storage and retrieval π pulses). If we are interested in backward retrieval, $P_j(\tilde{z})$ should be flipped to $P_j(1 - \tilde{z})$. If we are interested in reversing the inhomogeneous profile, the frequency classes should be reversed. Thus, for example, for backward retrieval with the reversal of inhomogeneous broadening, the initial condition for retrieval is $P_j(\tilde{z}, \tilde{T}_r) = -P_{-j}(1 - \tilde{z}, \tilde{T})$. Using Eqs. (C.5) and (C.6) with $\tilde{\Omega} = 0$, we can then implement fast retrieval. The time Laplace transform of the output field can then be found to be equal to

$$\mathcal{E}_{\text{out}}(v) = \mathcal{L}^{-1}\{A(v, v')B(v, v')\mathcal{E}_{\text{in}}(v')\}_{v' \rightarrow \tilde{T}}, \quad (\text{C.33})$$

where \mathcal{L}^{-1} indicates that we should take the inverse Laplace transform $v' \rightarrow \tilde{T}$, $A(v, v')$ depends on the direction of retrieval and is given by

$$A(v, v') = \frac{e^{-d(f(v)+f(v'))} - 1}{f(v) + f(v')}, \quad (\text{C.34})$$

$$A(v, v') = \frac{e^{-df(v)} - e^{-df(v')}}{f(v) - f(v')} \quad (\text{C.35})$$

for backward and forward retrieval, respectively, and $B(v, v')$ depends on whether the inhomogeneous profile is reversed or not and is given by

$$B(v, v') = \frac{f(v) + f(v')}{2 + v + v'}, \quad (\text{C.36})$$

$$B(v, v') = \frac{f(v) - f(v')}{v' - v} \quad (\text{C.37})$$

for reversed and not reversed cases, respectively.

For homogeneous broadening (Eqs. (C.21) and (C.22)) and for a Lorentzian inhomogeneous profile (Eqs. (C.23) and (C.24)), the inverse Laplace transforms $v' \rightarrow \tilde{T}$ and $v \rightarrow \tilde{t}$ can be taken analytically in terms of Bessel functions and convolutions. The case of homogeneous broadening has been studied in Appendix B, while the analytical answer for the Lorentzian case is too complicated to yield any significant

insight. For a Gaussian inhomogeneous profile (Eqs. (C.25) and (C.26)), the inverse Laplace transforms have to be taken numerically. In all three cases, the efficiency can be computed via Eq. (C.14) without taking the $v \rightarrow \tilde{t}$ inverse Laplace transform.

If we are interested not only in computing the total efficiency of storage followed by retrieval for some given input photon mode, but also in maximizing the efficiency with respect to the input mode shape, we can again take advantage of time reversal. We will show now that in all four cases (i.e., either of the two retrieval directions, with or without the reversal of broadening), the optimal input pulse shape can be found by starting with any trial input, carrying out storage followed by retrieval, then time-reversing the output, and iterating the procedure till convergence is reached. To begin the proof, we note that $A(v, v')$ and $B(v, v')$ are symmetric with respect to the exchange of the two arguments. Therefore, Eq. (C.33) and the convolution theorem for Laplace transforms imply that we can write

$$\mathcal{E}_{\text{out}}(\tilde{t}) = \int_0^{\tilde{T}} d\tilde{t}' \mathcal{E}_{\text{in}}(\tilde{t}') m'(\tilde{t}, \tilde{T} - \tilde{t}') \quad (\text{C.38})$$

for some function m' that is symmetric with respect to the exchange of its two arguments. One can also check that m' , and hence the optimal input mode, are real. Assuming, therefore, a real $\mathcal{E}_{\text{in}}(\tilde{t})$, the total efficiency is

$$\eta = \int_0^{\tilde{T}} d\tilde{t} \int_0^{\tilde{T}} d\tilde{t}' \mathcal{E}_{\text{in}}(\tilde{t}) \mathcal{E}_{\text{in}}(\tilde{t}') k_{\text{tot}}(\tilde{t}, \tilde{t}'), \quad (\text{C.39})$$

where the kernel $k_{\text{tot}}(\tilde{t}, \tilde{t}')$ (the subscript “tot” stands for the total efficiency, i.e., storage followed by retrieval) is given by

$$k_{\text{tot}}(\tilde{t}, \tilde{t}') = \int_0^{\tilde{T}} d\tilde{t}'' m'(\tilde{t}'', \tilde{T} - \tilde{t}) m'(\tilde{t}'', \tilde{T} - \tilde{t}'), \quad (\text{C.40})$$

where we assumed \tilde{T} is sufficiently large that the interval $[0, \tilde{T}]$ includes the whole retrieved pulse. To find the optimal $\mathcal{E}_{\text{in}}(\tilde{t})$, one can thus start with a trial input mode $\mathcal{E}_1(\tilde{t})$ and iterate the action of the kernel according to

$$\mathcal{E}_2(\tilde{t}') = \int_0^{\tilde{T}} d\tilde{t} \mathcal{E}_1(\tilde{t}) k_{\text{tot}}(\tilde{t}, \tilde{t}'). \quad (\text{C.41})$$

Using the symmetry of m' , one can immediately see that this iteration is equivalent to carrying out storage followed by retrieval, time-reversing the output, repeating the procedure, and time-reversing the output again. We will use these time-reversal iterations in the following Sections to compute the optimal input modes. It is important to note that, as we have explained at the end of Sec. C.2.2, the time-reversal iterations that we have just described not only constitute a convenient mathematical tool; they can, in fact, be used experimentally to find the optimal input modes.

In this Section, we set up and solved the problem of fast storage followed by fast backward or forward retrieval with or without the reversal of the inhomogeneous profile. In the next two Sections, we would like to analyze these solutions for the case of backward retrieval.

C.3.2 Storage Followed by Backward Retrieval

In this Section, using the results of Sec. C.3.1, we would like to study the efficiency of fast storage followed by fast backward retrieval in inhomogeneously broadened media without redistribution between velocity classes, and without the reversal of the inhomogeneous broadening during the storage time. This problem is motivated by solid state implementations such as the one described in Refs. [340, 290, 291, 95], where the line shape is created by pumping back some atoms from a broad spectral hole feature. In this situation, one can consider what happens when one expands the spectral region and pumps more and more atoms into the absorptive feature. In this case, the resonant optical depth d' is expected to be independent of the width of the spectral feature that is pumped back into the absorption profile, whereas the unbroadened optical depth d would increase with an increasing number of atoms being pumped back. From the analysis of Sec. C.2, we expect the behavior to be different depending on whether the line shape falls off as a Lorentzian or faster. In particular, we found in Sec. C.2 that for a well-localized inhomogeneous line (e.g., a Gaussian), the losses due to dephasing are non-Markovian and, therefore, scale as $1/d'^2$, in contrast to the losses due to the exponential polarization decay with the rate γ , which scale as $1/d$. As another application of this idea, we show in this Section that, for a Gaussian inhomogeneous profile, by increasing d , the error during fast storage followed by fast backward retrieval can be lowered from the $1/d'$ scaling for the homogeneously broadened line ($d = d'$) to the $1/d'^2$ scaling for sufficiently large d . Experimentally, d' can be quite large ($d' \approx 50$ should be feasible by using a sufficiently high impurity concentration and a sufficiently long sample length [292, 290, 291, 95]), so that this could potentially yield a very high efficiency.

We begin the analysis by using the time reversal iterations suggested at the end of Sec. C.3.1 to compute the optimal input pulse and the maximum possible efficiency at various values of d and d' assuming the inhomogeneous profile is Gaussian (Eq. (C.25)). To compute the standard deviation σ of the Gaussian profile from the values of d and d' , we use the following relationship:

$$d' = d \times \int_{-\infty}^{\infty} d\tilde{\Delta} p(\tilde{\Delta}) \frac{1}{1 + \tilde{\Delta}^2} = \sqrt{\frac{\pi}{2}} \frac{d}{\sigma} e^{\frac{1}{2\sigma^2}} \operatorname{erfc} \left[\frac{1}{\sqrt{2}\sigma} \right], \quad (\text{C.42})$$

where the second factor in the integrand is the homogeneous line shape of HWHM equal to 1 (recall that our frequencies are rescaled by γ).

In Fig. C.4, we show (solid lines) the optimal input modes for $d' = 20$ and $d = 20, 60,$ and 120 . We see that these optimal input modes (for this value of d') are very

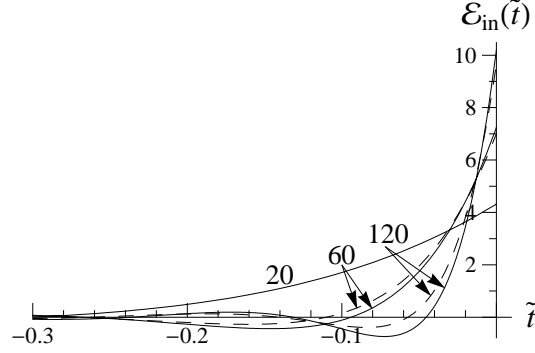


Figure C.4: The solid lines show the optimal input modes for $d' = 20$ and $d = 20, 60$, and 120 (the value of d is indicated on the plot) for storage followed by backward retrieval in a medium with a Gaussian inhomogeneous profile, without the reversal of the inhomogeneous broadening, and without averaging over frequency classes during the storage time. The dashed lines show the corresponding optimal modes for $d' = d$, i.e., for the case of no inhomogeneous broadening.

similar to the optimal input modes (dashed lines) for the same d but without the inhomogeneous broadening (i.e., $d' = d$). The optimal modes thus have a duration of approximately $1/(d\gamma)$, as discussed in Sec. B.7, and consist of a roughly triangular pulse preceded by a few “wiggles.” These wiggles can be traced back to the zeroth-order Bessel function of the first kind (i.e., J_0) in Eq. (B.48) and can be associated with Rabi oscillations between the electric field \mathcal{E} and the optical polarization P . In Fig. C.4, we assume that the storage π pulse is applied at $\tilde{t} = 0$. Although the true optimal input pulses extend to $\tilde{t} = -\infty$, they can, in practice, be truncated after about two or three wiggles without decreasing the efficiency by more than 10^{-4} .

To verify the prediction that, for sufficiently large d , the error should be limited by $1/d^2$, we computed the optimal (smallest) error by optimizing with respect to the input mode at different values of d' and d . The optimization was done numerically using the time-reversal iterations suggested at the end of the previous Section. Figure C.5(a) shows a log-log surface plot of this optimal (smallest) error $1 - \eta$ as a function of d' and d/d' . As expected, we find that, for any fixed d' , the error is very well approximated by $c_1 + c_2/d$ at large d , where the constants $c_1(d')$ and $c_2(d')$ depend on d' . $c_2(d')$ is of order unity and increases approximately linearly from about 0.2 at $d' = 2$ to 4.2 at $d' = 20$. $c_1(d')$ represents the d' -limited error, i.e., the limit $d/d' \rightarrow \infty$, when the $1/d$ error becomes negligible. This d' -limited error can be seen at the $d/d' = 10^3$ edge of the box in Fig. C.5(a) and is also plotted separately as a thin solid line in the log-log plot in Fig. C.5(b). The dotted line in Figs. C.5(a) and C.5(b) is $14.2/d'^2$ and is shown to indicate that the d' -limited error indeed scales as $1/d'^2$. To include the requirement that the efficiency drops to zero at $d' = 0$ and to

reproduce the $14.2/d'^2$ dependence that we see at larger d' , a dashed heuristic curve $1/(1 + 14.2/d'^2)$ is shown in Fig. C.5(b). We see that it matches the exact value of the d' -limited error (thin solid line) very well.

We compare this d' -limited error to the smallest possible error for the homogeneously broadened case $d = d'$, which can be seen at the $d/d' = 1$ edge of the box in Fig. C.5(a) and which is also plotted separately as a thick solid line in Fig. C.5(b). This thick solid line is the same as the solid curve in Fig. B.4 and in Fig. C.3. Since we know from the discussion in Appendix B that at high enough values of d ($= d'$), this error scales as $\sim 5.8/d$, we plot this $5.8/d$ scaling as the dash-dotted line in Figs. C.5(a) and C.5(b). We thus see that, for a fixed d' , by increasing the number of atoms in the absorption line so that we go from $d/d' = 1$ to $d/d' \rightarrow \infty$ (in such a way that the inhomogeneous line is Gaussian), one can significantly lower the optimal (smallest) error from a $1/d'$ homogeneous error to a $1/d'^2$ inhomogeneous-broadening-limited error. Although we have investigated only backward retrieval, we expect that for the case of optimal storage followed by forward retrieval, the same result will apply, and that the optimal $1/d'$ homogeneous error can also be reduced to a d' -limited $1/d'^2$ error. We also expect these error scalings to hold not only for the Gaussian inhomogeneous profile but also for any inhomogeneous profile (such as, for example, a square profile) whose tails fall off faster than Lorentzian.

To summarize, we have shown that, even without any additional experimental requirements, the storage and retrieval by two fast π pulses may be a very promising route to a quantum memory. Indeed, if the absorptive feature is sufficiently well localized (falling off faster than a Lorentzian), the error may be limited to $\sim 1/d'^2$. In a practical realization, it would, however, be necessary to include other imperfections such as imperfect π pulses, imperfect synchronization between the storage π pulse and the input pulse, and the limitations associated with the creation of an absorption line. Furthermore, the optimal scenario described in this Section applies only to a single input pulse shape at any given values of d and d' . For other pulse shapes, it may be advantageous to combine the ideas of this Section with the reversible broadening of the next Section and optimize with respect to both the width (and shape) of the original nonreversible line and the width (and shape) of the extra reversible broadening.

C.3.3 Storage Followed by Backward Retrieval with the Reversal of the Inhomogeneous Profile

In the previous Section, we assumed that the inhomogeneous broadening had a fixed distribution, e.g., due to different environments for each individual atom. In this Section, using the results of Sec. C.3.1, we investigate the possibility of improving the efficiency of fast storage followed by fast backward retrieval by adding and reversing inhomogeneous broadening in an originally homogeneously broadened medium.

The possible advantage of inhomogeneous broadening was first considered in Ref.

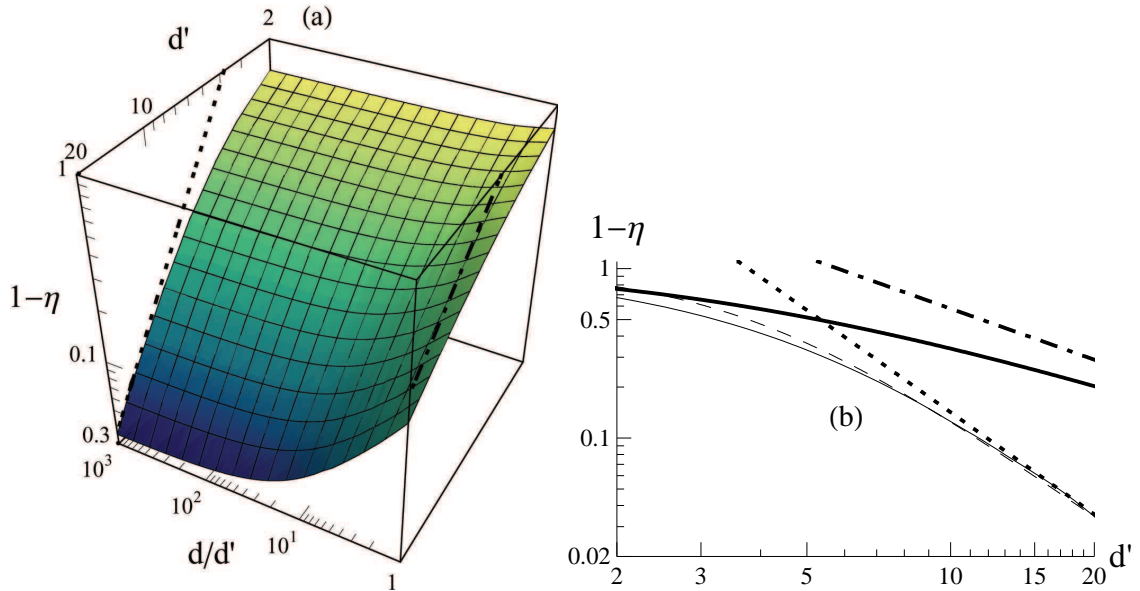


Figure C.5: (a) As a function of d' and d/d' , the optimal (smallest) error of fast storage followed by fast backward retrieval (surface). $5.8/d'$ (dash-dotted line) is the limiting behavior, found in Appendix B, of the homogeneous error ($d/d' = 1$) for large enough d ($= d'$). $14.2/d'^2$ (dotted) approximates the d' -limited error ($d/d' \rightarrow \infty$) near $d' \sim 10 - 20$ and, probably, above. (b) As a function of d' , dash-dotted and dotted lines are the same as in (a). The thick and thin solid lines are the $d/d' = 1$ and $d/d' \rightarrow \infty$ error curves, respectively, which can be read out from the surface plot in (a). $1/(1 + 14.2/d'^2)$ (dashed line) is a heuristic curve that matches the d' -limited error (thin solid line) very well.

[86], where it was noted that Doppler broadening automatically reverses during backward retrieval. This results in a reversal of the dephasing occurring during storage and gives rise to photon echo. In Refs. [292, 87] it was then suggested that similar effects could be realized in solid state systems. Under the name of controlled reversible inhomogeneous broadening (CRIB), the authors of Ref. [87] suggest implementing the equivalent of the fast storage protocol considered in Appendix B, but in addition they suggest controllably adding inhomogeneous broadening to the transition and then reverse the broadening during retrieval to obtain a rephasing². Several experimental

²For clarity, we note that, although fast storage is indeed mentioned in Ref. [87] as a way of extending storage time beyond $1/\gamma$, the authors mainly focus on using only two levels and replacing the application of two π pulses necessary for fast storage and retrieval with an application to each atom of a position-dependent phase shift $|g\rangle \rightarrow \exp(2i\omega_{eg}z/c)|g\rangle$, where z is the position of the atom. The treatment of this method is, however, mathematically identical to the treatment of fast storage with perfect π pulses and no decoherence during storage. Reference [292], in contrast, fully

groups are currently working on the realization of CRIB [292, 94, 290, 291, 95]. We will show that, although the introduction of reversible inhomogeneous broadening can improve the efficiency of fast storage of a single pulse, the improvement relative to the fast storage technique without inhomogeneous broadening is limited. We will also show that CRIB can perform slightly better than optimal adiabatic storage in a homogeneously broadened medium (discussed in Secs. B.6.2 and B.6.3), but only for short pulses, for which the adiabaticity condition $Td\gamma \gg 1$ is not satisfied.

For concreteness, we consider the storage of a resonant Gaussian-like pulse of variable time duration T defined, as in Eq. (B.40), by

$$\mathcal{E}_{\text{in}}(\tilde{t}) = A(e^{-30(\tilde{t}/\tilde{T}-0.5)^2} - e^{-7.5})/\sqrt{\tilde{T}} \quad (\text{C.43})$$

and shown in Fig. B.3. $A \approx 2.09$ is a normalization constant. We also restrict ourselves to the situation where the medium is initially homogeneously broadened. Although this is often a good approximation, the hole-burning technique in the solid state [340], for example, will always result in some residual inhomogeneous broadening of the prepared line, something that one may have to take into account in a complete assessment of the performance of CRIB.

To investigate the performance of CRIB, we use the techniques described in Sec. C.3.1. Let us initially assume $T\gamma \ll 1$, so that the decay can be ignored. As a test case, we take the resonant Gaussian-like pulse of Eq. (C.43) and implement fast storage of it (with a π pulse at $t = T$) followed by fast backward retrieval. From the discussion of CRIB [87], it is expected that adding some broadening and thereby increasing the width of the absorption line, at the expense of a decreased resonant optical depth, may increase the total efficiency. Excessive broadening will, however, make the medium transparent and decrease the efficiency. At each value of $Td\gamma$, there is thus an optimal inhomogeneous width. In Fig. C.6, the total efficiency is plotted as a function of $Td\gamma$, for the homogeneously broadened case (dash-dotted line) and for an inhomogeneously broadened medium (solid lines) with Gaussian (G) or Lorentzian (L) inhomogeneous profiles optimized with respect to the inhomogeneous width. The horizontal dashed line is 1. These curves are calculated by numerically computing, at each $Td\gamma$, the efficiency as a function of the inhomogeneous width and then finding the width that gives the maximum efficiency at the chosen value of $Td\gamma$. Note that, even though we neglect the decay ($\gamma T \ll 1$), the quantity $Td\gamma = g^2 N T L / c$ may still attain a non-negligible value for a sufficiently high optical depth $d \gg 1$. In other words, the curves in Fig. C.6 represent the limit $T\gamma \rightarrow 0$ and $d \rightarrow \infty$ with finite $Td\gamma$. Below $Td\gamma \sim 1$, adding broadening only lowers the efficiency, so that the optimal curves (solid) join the unbroadened curve (dash-dotted). We see, however, that at intermediate values of $Td\gamma \sim 10$, introducing reversible inhomogeneous broadening can increase the efficiency. The gain in efficiency is, however, limited. In an experimental

concentrates on what we call fast storage.

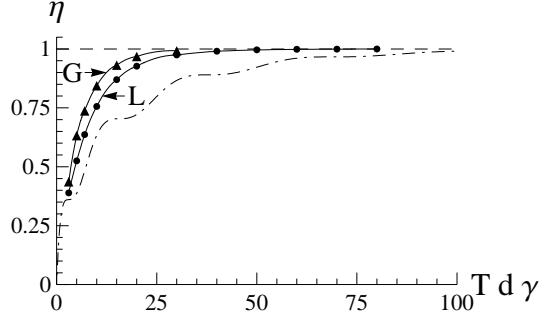


Figure C.6: Total efficiency of fast storage followed by fast backward retrieval as a function of $Td\gamma$ in the limit when $T\gamma \rightarrow 0$, $d \rightarrow \infty$, but $Td\gamma$ is finite. The curves show the efficiency without inhomogeneous broadening (dash-dotted line) and with (solid lines) Gaussian (G) or Lorentzian (L) inhomogeneous profiles optimized with respect to the inhomogeneous width. The horizontal dashed line is 1.

realization, one should therefore evaluate whether this gain justifies the additional experimental efforts needed to implement the controlled reversible inhomogeneous broadening.

In Fig. C.7, we plot $\Delta_I T$ as a function of $Td\gamma$, where Δ_I is the optimal HWHM of the Gaussian (G) or Lorentzian (L) inhomogeneous profile used to construct Fig. C.6. The points are connected with straight lines for better visibility. The dashed and dotted lines are $1.4(Td\gamma - 2)^{1/2}$ and $2.25(Td\gamma - 2)^{1/2}$, respectively, which indicates that the optimal inhomogeneous HWHM Δ_I scales approximately as $\sqrt{Td\gamma}/T$, which is different from the naive guess $\Delta_I \sim 1/T$. We also see that, at a given $Td\gamma$, the optimal Gaussian profile is wider; and, moreover, from Fig. C.6, we see that optimal Gaussian broadening gives greater efficiency than optimal Lorentzian broadening. One could imagine that these two results are the consequence of the Gaussian frequency profile of the input pulse. However, we ran an equivalent simulation with an input pulse that has a Lorentzian spectrum; and also in this case the optimal Gaussian profile is wider than the optimal Lorentzian profile and the optimal Gaussian broadening gives a greater efficiency than the optimal Lorentzian broadening. These results reflect the fact that the storage we are considering is a dynamical process and is therefore not accurately described by its continuous-wave absorption profile. We believe that the advantage of Gaussian broadening over Lorentzian comes from the fact that, as shown in Sec. C.2, due to their non-Markovian nature, the dephasing losses associated with Gaussian (and, hence, fast-falling) inhomogeneous broadening are smaller than the losses associated with Lorentzian broadening.

To investigate the performance of the storage and retrieval protocol at a finite optical depth, we now relax the assumption $\gamma T \ll 1$. With the pulse considered here (Eq. (C.43)), the effect of the spontaneous emission γ on fast storage with CRIB

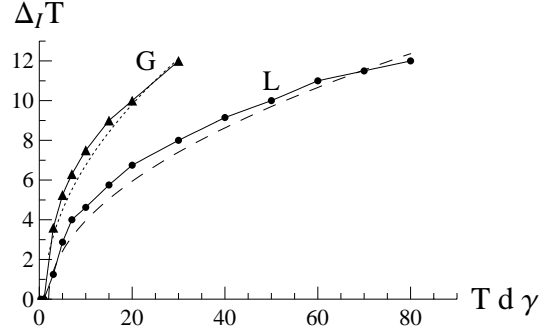


Figure C.7: $\Delta_I T$ as a function of $T d \gamma$, where Δ_I is the optimal HWHM of the Gaussian (G) or Lorentzian (L) inhomogeneous profile. The points are connected with straight lines to guide the eye. The dashed and dotted lines are $1.4(T d \gamma - 2)^{1/2}$ and $2.25(T d \gamma - 2)^{1/2}$, respectively.

can be estimated based on simple arguments: the pulse is symmetric around $T/2$ so the excitation spends on average a time $T/2$ in the sample both during storage and retrieval. In each of these processes, the efficiency is therefore decreased by $[\exp(-\gamma T/2)]^2$ so that the total efficiency is reduced by approximately $\exp(-2\gamma T)$. We have explicitly verified this simple estimate for a few cases and found it to be true both with and without broadening. The optimization of broadening without decay therefore gives the same optimal inhomogeneous width as with decay. Since we have in Sec. B.6.4 calculated adiabatic efficiencies for the same pulse shape, we can now compare the performance of fast storage with and without CRIB to adiabatic storage. In Fig. C.8(a), with $d = 100$, we compare the storage of the Gaussian-like pulse of duration T of Eq. (C.43) (shown in Fig. B.3) followed by backward retrieval using “optimal” adiabatic storage (dotted) or using fast storage without inhomogeneous broadening (dash dotted) or with reversible optimal-width Lorentzian (L) or Gaussian (G) broadening (solid). The horizontal dashed line is the optimal adiabatic efficiency, while the second dashed line is $\exp(-2\gamma T)$, by which fast efficiencies are rescaled relative to the $T\gamma \rightarrow 0$ limit of Fig. C.6. Figure C.8(b) is the same as Fig. C.8(a) but for $d = 1000$.

First of all, from Fig. C.8, it is clear that, when $T\gamma \gtrsim 1$, fast storage efficiency, with or without CRIB, deteriorates because the spontaneous emission decreases the total efficiency by $\exp(-2\gamma T)$. Optimal adiabatic storage, on the other hand, does well in this limit (provided we have a reasonable d). Moreover, in the adiabatic limit $T d \gamma \gg 1$, optimal adiabatic storage with homogeneous broadening is always more efficient than fast storage with or without CRIB. This follows from the fact that in the adiabatic limit ($T d \gamma \gg 1$) the error in fast storage ($\approx 1 - \exp(-2\gamma T) \approx 2\gamma T$) is greater than the error in adiabatic storage ($\sim 5.8/d$).

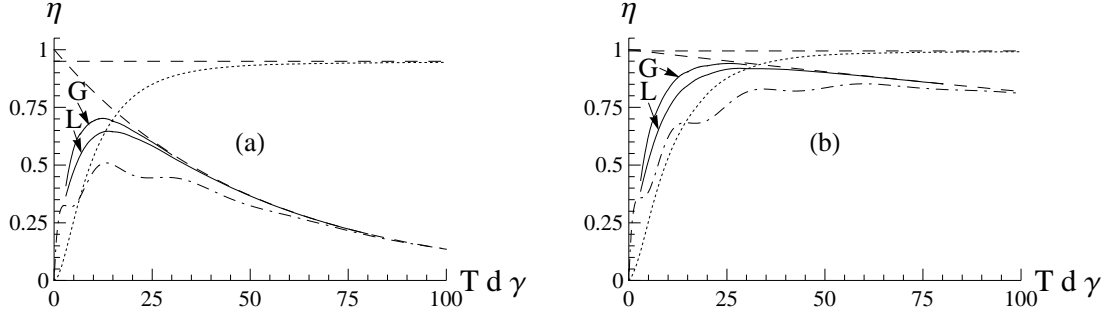


Figure C.8: Storage and backward retrieval with and without reversible inhomogeneous broadening at finite optical depth $d = 100$ (a), and (b) 1000. The curves show the total efficiency of storage followed by backward retrieval of the resonant Gaussian-like pulse of duration T of Eq. (C.43) (shown in Fig. B.3) with “optimal” resonant adiabatic storage (dotted) or with fast storage without inhomogeneous broadening (dash dotted) or with reversible optimal-width Lorentzian (L) or Gaussian (G) broadening (solid). The horizontal dashed line is the optimal adiabatic efficiency while the second dashed line is $\exp(-2\gamma T)$, by which fast efficiencies are rescaled relative to the $T\gamma \rightarrow 0$ limit of Fig. C.6.

Secondly, when $Td\gamma \lesssim 1$, neither of the methods does very well. This follows directly from the general time-reversal argument described in detail in Appendix B. According to these arguments, the optimal storage is obtained as the time reverse of optimal retrieval. One cannot therefore store faster than one can retrieve. The fastest retrieval is obtained by using the fast retrieval method where the excitation is transferred from state $|s\rangle$ into state $|e\rangle$ with a π pulse. With this procedure, all atoms radiate in phase and, by constructive interference, give a short output pulse of duration $T \sim 1/(d\gamma)$, as explained in Sec. B.7. This procedure gives the fastest possible retrieval, and its time reverse is the fastest possible storage (which works optimally only for certain input mode shapes). The storage and retrieval of any mode thus becomes inefficient for $Td\gamma < 1$. The particular Gaussian mode function that we consider here does not correspond to the optimal mode and therefore its fast storage-plus-retrieval efficiency (dash-dotted line in Fig. C.8) does not reach the optimal efficiency (horizontal dashed line in Fig. C.8).

Third, when $Td\gamma \lesssim 25$, reversible inhomogeneous broadening (CRIB) does help, and, with it, the fast method may do slightly better than the adiabatic method without inhomogeneous broadening. An interesting possibility is whether the controlled addition and reversing of inhomogeneous broadening could improve the adiabatic storage in the regime when the adiabaticity condition $Td\gamma \gg 1$ is not satisfied, but this investigation is beyond the scope of the present work.

To summarize this investigation of the possible advantages of introducing a re-

versible inhomogeneous broadening, we conclude that it does provide an improvement of the efficiency, but that this improvement is limited. The fast storage technique where one just applies a resonant π pulse without the additional broadening gives comparable results for the pulse shape that we have considered here. Moreover, even with an optimized inhomogeneous width, fast storage with CRIB performs only slightly better than optimal adiabatic storage in the original homogeneously broadened system and only when the input pulse does not satisfy the adiabaticity condition $Td\gamma \gg 1$; while, for pulses satisfying the adiabaticity condition, adiabatic storage performs better. Intuitively one might expect that a homogeneously broadened absorption line would not be able to efficiently store an input pulse with a bandwidth that is much longer than the width of this line. One could have therefore expected a large efficiency gain from the use of CRIB to shape the atomic line to match the spectral profile of the input photon wave packet. The reason why such line shaping is not necessarily much more effective than using the unmodified line is because storage is a dynamical process; therefore, the relationship between the storage capability of the medium and its continuous wave absorption spectrum is not trivial.

We should add, however, that we have here only considered a specific input shape and the picture may be different if other inputs are considered. We also emphasize that, unlike most results in this Appendix and in Appendices A and B, the efficiencies presented in this Section do not represent the true optimum for our input pulse, since one could optimize, for example, the time, at which the storage π pulse is applied. Finally, it is worth noting that if one is free to choose the shape and duration of the input pulse, then for any given d and any given inhomogeneous profile, as explained in Sec. C.3.1, one can use the time-reversal iterations to find the optimal input pulse and the maximum efficiency. We have checked for a Gaussian inhomogeneous profile that at any given d , as the inhomogeneous width increases from zero, the maximum efficiency drops. Although we have not checked this statement for other inhomogeneous profiles, we believe it to be generally true that, if one has the freedom of optimizing the shape and duration of the input pulse, then the addition and subsequent reversal of inhomogeneous broadening only lowers the maximum efficiency.

We note, however, that our result that the adiabatic storage efficiency is always comparable to or better than the efficiency of fast storage (with or without CRIB) has been found assuming that in the adiabatic storage the $|g\rangle - |s\rangle$ transition is not inhomogeneously broadened. Although this holds in Doppler-broadened atomic vapors, the broadening of the $|g\rangle - |s\rangle$ transition may be hard to suppress in many of the systems considered for photon storage with CRIB (such as the rare-earth-ion-doped crystal [292]). Therefore, although adiabatic storage in some of these systems seems possible [289], fast storage may still be a better option. Moreover, although we showed that, for fast storage of a single input mode, adding inhomogeneous broadening may provide only small gains in efficiency, these gains might be much more significant if several time-separated modes are to be stored together and the shape of the inhomogeneous profile is allowed to be optimized. Further investigations are

required to clarify these issues.

C.4 Summary

In conclusion, we have extended in this Appendix the analysis of photon storage in Appendices A and B to include the effects of inhomogeneous broadening. In particular, we showed that in Doppler-broadened atomic vapors, at high enough optical depth, all atoms contribute coherently as if the medium were homogeneously broadened. We also showed that high-efficiency photon storage (error scaling as $\sim 1/d'^2$, where d' is the observed optical depth) can be achieved in solid state systems by creating a stationary spectrally well-localized inhomogeneous profile. Finally, we demonstrated that the addition of reversible inhomogeneous broadening (CRIB) to an originally homogeneously broadened line does provide an improvement of the efficiency of fast storage followed by fast retrieval, but that this improvement is limited: in particular, in the adiabatic limit $Td\gamma \gg 1$ optimal adiabatic storage outperforms fast storage with or without CRIB. These results aim at understanding the fundamental limits for storage imposed by the optical depth of the medium. For a complete investigation of the photon storage problem in inhomogeneously broadened media, there are several other effects and experimental imperfections that should be included, such as, for example, velocity changing collisions during the processes of storage and retrieval in Doppler-broadened gases and imperfect synchronization between the input pulse and the storage control pulse. A study of the former is in progress.

The presented optimization of the storage and retrieval processes in inhomogeneously broadened media leads to a substantial increase in the memory efficiency. We therefore expect this work to be important in improving the efficiencies in current experiments, where the optical depth is limited and where inhomogeneous broadening plays an important role, such as in Doppler-broadened atoms in warm vapor cells [80] and in inhomogeneously broadened solid state samples [290, 291, 95, 292].

Note added. As we were writing up the present work, a related paper appeared [298], which discusses some of the issues considered in this Appendix.

C.5 Omitted Details

In the preceding Sections of this Appendix, to allow for a smoother presentation, we omitted some of the details. We present them in this Section.

C.5.1 Independence of Free-Space Retrieval Efficiency from Control and Detuning

We showed in Sec. C.2.2 that for the case of inhomogeneous broadening that leaves the $|s\rangle - |g\rangle$ transition homogeneously broadened, the retrieval efficiency in the cavity model is independent of the control field and the detuning (provided all excitations are pumped out of the atoms). In this Section, we show the the same result holds in the free-space model.

We consider a general situation in which $S_j(\tilde{z}, \tilde{t} = 0)$ are not necessarily equal for different velocity classes j (we assume here that retrieval begins at $\tilde{t} = 0$). Laplace transforming Eqs. (C.5)-(C.7) in space ($\tilde{z} \rightarrow u$) and using $\mathcal{E}_{\text{in}} = 0$, we obtain

$$\mathcal{E} = i \frac{\sqrt{d}}{u} P, \quad (\text{C.44})$$

$$\partial_{\tilde{t}} P_j = -(1 + i(\tilde{\Delta} + \tilde{\Delta}_j)) P_j - \frac{d}{u} \sqrt{p_j} P + i\tilde{\Omega} S_j, \quad (\text{C.45})$$

$$\partial_{\tilde{t}} S_j = i\tilde{\Omega}^* P_j, \quad (\text{C.46})$$

where $P = \sum_k \sqrt{p_k} P_k$. The retrieval efficiency is then

$$\eta_r = \sum_{j,k} \sqrt{p_j p_k} \mathcal{L}^{-1} \left\{ \frac{d}{uu'} \int_0^\infty d\tilde{t} P_j(u, \tilde{t}) [P_k(u^*, \tilde{t})]^* \right\}, \quad (\text{C.47})$$

where \mathcal{L}^{-1} stands for inverse Laplace transforms $u \rightarrow \tilde{z}$ and $u' \rightarrow \tilde{z}'$ with the evaluation of both at $\tilde{z} = \tilde{z}' = 1$. From Eqs. (C.45) and (C.46), it follows that

$$\begin{aligned} \frac{d}{dt} (P_j(u, \tilde{t}) [P_k(u^*, \tilde{t})]^* + S_j(u, \tilde{t}) [S_k(u^*, \tilde{t})]^*) = \\ -(2 + i(\Delta_j - \Delta_k)) P_j(u, \tilde{t}) [P_k(u^*, \tilde{t})]^* \\ - \frac{d}{u} \sqrt{p_j} P(u, \tilde{t}) [P_k(u^*, \tilde{t})]^* - \frac{d}{u'} \sqrt{p_k} P_j(u, \tilde{t}) [P(u^*, \tilde{t})]^*. \end{aligned} \quad (\text{C.48})$$

If M is the number of velocity classes, Eq. (C.48) stands for M^2 equations in M^2 variables $P_i P_k^*$. We can write them in a matrix form and, in principle, invert the $M^2 \times M^2$ matrix on the right-hand side and thus solve for $P_j P_k^*$ as a linear combination of $\frac{d}{dt} (P_a P_b^* + S_a S_b^*)$ for various a and b . Inserting this into Eq. (C.47), applying the fundamental theorem of calculus, and assuming the retrieval is complete (i.e., no excitations remain in the atoms), the retrieval efficiency can be expressed as \mathcal{L}^{-1} of a linear combination (with u - and u' -dependent coefficients) of $S_a(u, 0) [S_b(u^*, 0)]^*$, and is thus independent of control and detuning.

Appendix D

Optimal Photon Storage in Atomic Ensembles: Optimal Control Using Gradient Ascent

D.1 Introduction

Most of the results on photon storage presented in Chapter 2 and Appendices A-C were obtained based on physical arguments and on exact solutions available in certain limits. However, the optimization problems discussed there fall naturally into the framework of optimal control problems, for which powerful numerical optimization methods exist [90, 89]. Thus, in the present Appendix, we apply these optimal control methods to the problem of photon storage. As a result, we open up the possibility of efficient photon storage in previously inaccessible regimes by increasing the bandwidth of the memory and provide simple intuitive understanding for the optimization methods underlying photon storage.

We refer the reader to Sec. A.1 for a comprehensive introduction to photon storage in Λ -type atomic media and for the full list of references. Here we summarize only a few important points. In a typical photon storage protocol, an atomic ensemble with Λ -type level structure shown in Fig. D.1 is assumed to start with all N atoms pumped into the metastable state $|g\rangle$. The incoming quantum light mode is coupled to the $|g\rangle - |e\rangle$ transition with a collectively enhanced coupling constant $g\sqrt{N}$ and is mapped onto the collective coherence (called a spin wave) between the metastable states $|s\rangle$ and $|g\rangle$ using a classical two-photon-resonant control pulse with time-dependent Rabi frequency $\Omega(t)$. Ideal mapping of the light mode onto the spin wave and back can be achieved in an ensemble that has infinite resonant optical depth d on the $|g\rangle - |e\rangle$ transition. However, despite the existence of proposals for achieving high values of d [291], in most current experiments d (or the cooperativity parameter C for ensembles enclosed in a cavity [93]) is limited to $d \sim 10$ due to experimental

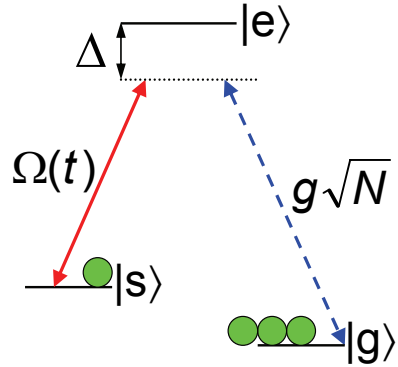


Figure D.1: Λ -type medium coupled to a quantum field (dashed) with a collectively enhanced coupling constant $g\sqrt{N}$ and a two-photon-resonant classical field (solid) with time-dependent Rabi frequency $\Omega(t)$.

imperfections such as competing four-wave mixing processes [80], spatially-varying light shifts [93], number of atoms in a trap [81, 287], or inhomogeneous broadening and short interaction lengths [83, 95]. As a result of the limited optical depth, the experimentally demonstrated efficiencies for the light-matter interface are low, which makes the optimization of photon storage protocols at finite values of d crucial. The optimization in Chapter 2 and Appendices A-C, as well as in the present Appendix, relies on the knowledge of the shape of the incoming photon mode. Note that such knowledge is not incompatible with storing unknown quantum states because the mode usually acts simply as a carrier while the information is stored in the quantum state of the harmonic oscillator corresponding to this mode [2]. A different type of problem is the storage of an unknown mode or, equivalently, the storage of multiple photonic modes within an ensemble [341]. While we believe that the optimization procedures considered here will probably also be relevant to this situation, we shall not discuss it in more detail here.

The main tool used in this Appendix is a numerical iterative optimization with respect to some set of control parameters, which are updated to yield higher photon storage efficiency at every iteration. Such iterative optimization methods are a standard tool in applied optimal control theory [90, 89]. These methods and their variations are already being used in a variety of applications including laser control of chemical reactions [312, 311, 342], design of NMR pulse sequences [313], loading of Bose-Einstein condensates into an optical lattice [314], atom transport in time-dependent superlattices [315], quantum control of the hyperfine spin of an atom [187], and design of quantum gates [343, 344]. Although advanced mechanisms for updating the control parameters from one iteration to the next exist and exhibit superior convergence characteristics [90, 309, 310, 314], we will concentrate in the present

Appendix on optimization via a simple gradient ascent method [90, 89, 313, 187], except for Sec. D.3 where advanced updating mechanisms will also be used. Gradient ascent methods are often more efficient than simple variations of the control parameters using, e.g., genetic algorithms. Moreover, we will show that gradient ascent optimization has the advantage that it can often be understood physically and can provide deeper intuition for the photon storage problem. In particular, in Appendices A-C, we used involved physical arguments and exact analytical solutions available in certain limits to derive a time-reversal-based iterative optimization with respect to the shape of the incoming photon mode. In the present Appendix, we show that these time-reversal iterations and the general and often discussed connection between optimality and time reversal in photon storage (see Chapter 2 and Refs. [86, 87, 345]) naturally follow from the gradient ascent method. The results of Appendices A-C are, however, still crucial since they show in certain cases that the solutions obtained via the local gradient ascent method represent global, rather than local, optima.

In addition to considering optimization with respect to the shape of the input mode, we consider in the present Appendix optimization with respect to the storage control field. In particular, we show that shaping the control field via the gradient ascent method allows for efficient storage of pulses that are an order of magnitude shorter than when the control field is optimized in the adiabatic approximation discussed in Chapter 2 and Appendices A and B. In other words, this new control shaping method increases the bandwidth of the memory. Finally, we discuss the performance of optimal control pulses in the context of photon storage via controlled reversible inhomogeneous broadening (CRIB) [87]. In particular, assuming one is interested in storing a single known incoming light mode and assuming one can shape control pulses with sufficient precision, we are not able to identify any advantages of CRIB-based photon storage compared to photon storage with optimal control pulses in homogeneously broadened media.

The remainder of the Appendix is organized as follows. In Secs. D.2, D.3, and D.4, we show how gradient ascent can be used to optimize with respect to the control field, the input mode, and the inhomogeneous profile, respectively. We summarize the discussion in Sec. D.5 and, finally, present some details omitted in the main text in Sec. D.6.

D.2 Optimization with respect to the Storage Control Field

In principle, both the incoming light mode and the classical control pulse may be adjusted to maximize the light storage efficiency. However, it is often easier to vary the classical control pulse. In particular, the photonic state we wish to store may be some non-classical state generated by an experimental setup, where we cannot completely control the shape of the outgoing wave packet. This is, e.g., the case

for single photons generated by parametric down conversion [341, 99] or by single nitrogen-vacancy centers in diamond [12], where the shape of the wave packet will be, respectively, set by the bandwidth of the setup and the exponential decay associated with spontaneous emission. Alternatively, the wave packet may also be distorted in an uncontrollable way by the quantum channel used for transmitting the photonic state [2]. In this Section, we therefore discuss optimization with respect to the storage control field in both the cavity model (Sec. D.2.1) and the free space model (Sec. D.2.2).

D.2.1 Cavity Model

As discussed in Appendices A and B, the cavity model, in which the atomic ensemble is enclosed in a cavity, is theoretically simpler than the free space model because only one collective atomic mode can be excited. In addition, as shown in Appendices A and B, the cavity setup can yield higher efficiencies in certain cases than the free space model due to the enhancement of the optical depth by the cavity finesse and due to (for certain spin wave modes) better scaling of the error with the optical depth d ($1/d$ in the cavity vs. $1/\sqrt{d}$ in free space). We, therefore, start with the cavity model. As in Appendix A, to get the closest analogy to the free-space regime, we will discuss in the present Appendix only the so-called “bad cavity” limit, in which the cavity mode can be adiabatically eliminated. However, the method of gradient ascent can easily be applied outside of this limit, as well.

To simplify the discussion, we first consider the simplest example, in which one stores a given resonant input mode into a homogeneously broadened ensemble enclosed in a cavity and having negligible spin-wave decay rate. It is important to note that, because only one spin-wave mode is accessible in the cavity model, the retrieval efficiency is independent of how the storage is done (see Appendix A). This makes it meaningful to optimize storage separately from retrieval [the latter does not have to be optimized since its efficiency depends only on the cooperativity parameter (see Appendix A)].

We follow the derivation of Appendix A to adiabatically eliminate the cavity mode and to reduce the equations of motion to the following complex number equations on the time interval $t \in [0, T]$:

$$\dot{P}(t) = -\gamma(1 + C)P(t) + i\Omega(t)S(t) + i\sqrt{2\gamma C}\mathcal{E}_{\text{in}}(t), \quad (\text{D.1})$$

$$\dot{S}(t) = i\Omega(t)P(t). \quad (\text{D.2})$$

Here the optical polarization $P(t)$ on the $|g\rangle - |e\rangle$ transition and the spin polarization $S(t)$ on the $|g\rangle - |s\rangle$ transition satisfy initial conditions $P(0) = 0$ and $S(0) = 0$, respectively, corresponding to the absence of atomic excitations at $t = 0$. In this example, the shape of the incoming mode $\mathcal{E}_{\text{in}}(t)$ is assumed to be specified, real, and normalized according to $\int_0^T dt \mathcal{E}_{\text{in}}^2(t) = 1$. γ is the decay rate of the optical polarization

and C is the collectively enhanced cooperativity parameter equal to the optical depth of the atomic ensemble times the cavity finesse. The goal is to find the slowly varying control field Rabi frequency envelope $\Omega(t)$ (assumed to be real) that maximizes the storage efficiency $\eta_s = |S(T)|^2$. [To avoid carrying around extra factors of 2, $\Omega(t)$ is defined as half of what is usually called the Rabi frequency: it takes time $\pi/(2\Omega)$ to do a π pulse]. For the moment, we suppose that there is no constraint on the energy of the control pulse and return to the possibility of including such a constraint below. It is worth noting that due to their linearity, the equations of motion (and all the results of the present Appendix) apply equally well both to classical input fields with pulse shapes proportional to $\mathcal{E}_{\text{in}}(t)$ and to quantum fields whose excitations are confined to the mode described by $\mathcal{E}_{\text{in}}(t)$. The efficiency η is thus the only parameter required to fully characterize the memory (see Sec. A.2).

Since the optimization of η_s is constrained by the equations of motion (D.1) and (D.2), we introduce Lagrange multipliers $\bar{P}(t)$ and $\bar{S}(t)$ to ensure that the equations of motion are fulfilled, and turn the problem into an unconstrained maximization of [90, 89]

$$\begin{aligned}
 J &= S(T)S^*(T) \\
 &+ \int_0^T dt \left[\bar{P}^* \left(-\dot{P} - \gamma(1+C)P + i\Omega S + i\sqrt{2\gamma C}\mathcal{E}_{\text{in}} \right) + c.c. \right] \\
 &+ \int_0^T dt \left[\bar{S}^* \left(-\dot{S} + i\Omega P \right) + c.c. \right], \tag{D.3}
 \end{aligned}$$

where c.c. stands for the complex conjugate¹.

The optimum requires that J is stationary with respect to any variation in P , S , and Ω . As shown in Sec. D.6.1, setting J to be stationary with respect to variations in P and S requires that the Lagrange multipliers (also referred to as the adjoint variables) \bar{P} and \bar{S} satisfy the equations of motion

$$\dot{\bar{P}} = \gamma(1+C)\bar{P} + i\Omega\bar{S}, \tag{D.4}$$

$$\dot{\bar{S}} = i\Omega\bar{P}, \tag{D.5}$$

subject to boundary conditions at time $t = T$

$$\bar{P}(T) = 0, \tag{D.6}$$

$$\bar{S}(T) = S(T). \tag{D.7}$$

¹In order to understand why complex conjugates have to be added in Eq. (D.3) and how to take variations with respect to complex variables, one could rewrite the equations in terms of real variables, that is, the real and imaginary parts of P and S . The variations with respect to the real and imaginary parts can now be seen to be equivalent to treating the variables and their complex conjugates as independent variables. Note, however, that this convention means that the gradient ascent update for any complex variable Q is $Q \rightarrow Q + (1/\lambda)\delta J/\delta Q^*$ (we will use this for the optimization with respect to complex $\mathcal{E}_{\text{in}}(t)$ and complex $\Omega(t)$).

These are the same equations as for S and P [Eqs. (D.1) and (D.2)] except that there is no input field and that the decay with rate $\gamma(1+C)$ is replaced with growth, which will function as decay for backward evolution. This backward evolution, in fact, corresponds to retrieval with the time-reversed control field and can be implemented experimentally as such (see Appendices A, B and Sec. 3.3). It is satisfying to have obtained this purely mathematical and simple derivation of the often discussed connection between optimality and time reversal in photon storage (see Chapters 2 and 3, Appendices A-C, and Refs. [86, 87, 345, 294, 295, 296, 297]). As explained in Sec. A.1 and as shown in detail in Appendix B, this connection goes beyond the perfect reversibility of unitary evolution discussed in Refs. [86, 87, 294, 295, 296, 297] by including systems with non-reversible dynamics, as exemplified, for example, by the decay rate γ in the present model.

Eqs. (D.4)-(D.7) ensure that J is stationary with respect to variations in P and S . To find the optimum it remains to set to zero the functional derivative of J with respect to Ω . This functional derivative is given by

$$\frac{\delta J}{\delta \Omega(t)} = -2 \text{Im} [\bar{S}^* P - \bar{P} S^*], \quad (\text{D.8})$$

where "Im" denotes the imaginary part.

In general, if one has a real function of several variables, one way to find a local maximum is to pick a random point, compute partial derivatives at that point, move a small step up the gradient, and then iterate. The same procedure can be applied to our optimal control problem [90, 89]. The gradient ascent procedure for finding the optimal storage control pulse $\Omega(t)$ is to take a trial $\Omega(t)$ and then iteratively update $\Omega(t)$ by moving up the gradient in Eq. (D.8) according to

$$\Omega(t) \rightarrow \Omega(t) - \frac{1}{\lambda} \text{Im} [\bar{S}^* P - \bar{P} S^*]. \quad (\text{D.9})$$

where $1/\lambda$ regulates the step size. In order to compute the right hand side of Eq. (D.9), one has to evolve the system forward in time from $t = 0$ to $t = T$ using Eqs. (D.1) and (D.2) to obtain $S(t)$ and $P(t)$. Then project the final atomic state described by $S(T)$ and $P(T)$ onto S according to Eqs. (D.6) and (D.7) to obtain $\bar{P}(T)$ and $\bar{S}(T)$. Then evolve \bar{S} and \bar{P} backwards in time from $t = T$ to $t = 0$ according to Eqs. (D.4) and (D.5).

In general, as in any gradient ascent method, the step size $1/\lambda$ in Eq. (D.9) has to be chosen not too big (one should not go up the gradient so quickly as to miss the peak) but not too small (in order to approach the peak relatively quickly). To achieve faster convergence, one could use a different step size $1/\lambda$ for each iteration; but for the problems considered in the present Appendix, convergence is usually sufficiently fast that we do not need to do this (unless the initial guess is too far from the optimum, in which case changing λ a few times helps). Moreover, in some optimization problems [315], $1/\lambda$ has to be chosen such that it depends on the argument of the function we

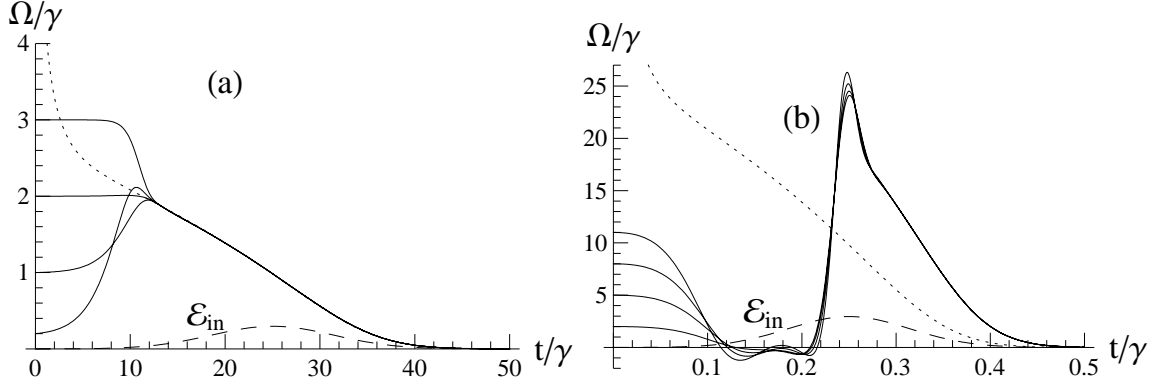


Figure D.2: Adiabatic (dotted) and optimal (solid) control fields for the storage of a Gaussian-like input mode $\mathcal{E}_{\text{in}}(t)$ (dashed) in the cavity model with $C = 10$ and $T = 50/\gamma$ (a) and $T = 0.5/\gamma$ (b). The four different optimal control pulses correspond to four different initial guesses for the gradient ascent optimization. The adiabatic control field agrees with the optimal one in the adiabatic limit ($TC\gamma \gg 1$) (a) and deviates from it otherwise (b).

are trying to optimize, i.e., in this case the time t ; this is not required for the present problems, and $1/\lambda$ is just taken to be a constant.

For example, let us take $C = 1$, $T\gamma = 10$, and a Gaussian-like input mode

$$\mathcal{E}_{\text{in}}(t) = A(e^{-30(t/T-0.5)^2} - e^{-7.5})/\sqrt{T}, \quad (\text{D.10})$$

where $A \approx 2.09$ is a normalization constant and where the mode is chosen to vanish at $t = 0$ and $t = T$ for computational convenience. Starting with an initial guess $\Omega(t) = \sqrt{\gamma/T}$ and using $\lambda = 0.5$, it takes about 45 iterations for the efficiency to converge to within 0.001 of the optimal efficiency of $C/(1+C) = 0.5$ (see Appendix A for the derivation of this formula). If, however, λ is too small (e.g. $\lambda = 0.1$), then the step size is too large, and, instead of increasing with each iteration, the efficiency wildly varies and does not converge.

We now compare the optimal control field shaping to the adiabatic control field shaping presented in Appendix A. We first take $C = 10$ and consider the input mode in Eq. (D.10) with $T = 50/\gamma$. Following Appendix A, we calculate the storage control field using the adiabatic equations [Eq. (A.26)], then numerically compute the storage efficiency with this control field, and multiply it by the complete retrieval efficiency $C/(1+C)$ to obtain the total efficiency. Since we are in the adiabatic limit ($TC\gamma = 500 \gg 1$), the resulting total efficiency is equal to the maximum possible efficiency $C^2/(1+C)^2 = 0.83$ (see Appendix A). Fig. D.2(a) shows the input mode in Eq. (D.10) (dashed line) and the adiabatic storage control field (dotted line). The optimal control field shaping using gradient ascent via Eq. (D.9) also yields the

maximum possible efficiency $C^2/(1+C)^2 = 0.83$ independent of the initial guess for $\Omega(t)$. The four solid lines in Fig. D.2(a) show $\Omega(t)$ resulting from optimal control field shaping for four different initial guesses, $\Omega(t)/\gamma = 0.2, 1, 2,$ and 3 . The four optimal control fields and the adiabatic control field agree except at small times. The reason for the disagreement is that the dependence of storage efficiency on the front Section of the control field is very weak because this Section affects only the front part of the excitation, and a large part of this anyway leaks out at the back end of the atomic ensemble. In fact, the dependence is so weak that gradient ascent leaves the front part of the initial guesses almost unperturbed.

It is worth noting that, in general, gradient ascent methods are not guaranteed to yield the global optimum, and the iterations may get trapped in a local maximum. However, for our photon storage problem, we know what the global optimum is in some cases. In particular, we have shown in Appendix A (for the cavity model) and in Appendix B (for the free space model) that, in the adiabatic limit, adiabatic control field shaping yields the global optimum. Since control shaping via gradient ascent agrees with the adiabatic shaping in this limit, we have a strong indication that gradient ascent always yields the global optimum also outside of the adiabatic limit. The global optimum is here the (unique) maximum possible efficiency, which, within the numerical error, is achievable for a variety of control fields due to the lack of sensitivity to the control field for small times (see Fig. D.2).

We now repeat the same steps except that we use $T = 0.5/\gamma$. The resulting control fields are shown in Fig. D.2(b). Again the four optimal control fields correspond to different initial guesses [$\Omega(t)/\gamma = 2, 5, 8,$ and 11]. The adiabatic control field now differs from the optimal one on the entire time interval. The reason is that the adiabatic limit ($TC\gamma \gg 1$) is not satisfied to a sufficient degree ($TC\gamma = 5$), and, as a result, the adiabatic approximation does not work well. Indeed, the efficiency yielded by the adiabatic control (0.49) is much smaller than that yielded by the optimal control (0.81). Physically, the breakdown of the adiabatic approximation means that the optical polarization $P(t)$ no longer follows the spin wave $S(t)$ adiabatically, but rather evolves dynamically according to the full differential equation (D.1). Since in this regime ($TC\gamma \sim 1$) the optimal control field is turned on abruptly following a time period when it is off [see Fig. D.2(b)], the optimal storage procedure acquires some characteristics of photon-echo type fast storage (see Chapter 2, Appendices A and B, and Ref. [86]). In fast storage, the input pulse is first absorbed on the $|e\rangle - |g\rangle$ transition in the absence of the control field, and is then mapped to the $|s\rangle - |g\rangle$ coherence via a control π pulse. This connection is not surprising since fast storage is indeed optimal for certain input modes of duration $T \sim 1/(C\gamma)$. Finally, we note that all the initial guesses for Ω that we tried yielded the same optimal control (up to the unimportant front part) and the same efficiency, which is a signature of the robustness of the optimization protocol and is another strong indication that, for this optimal control problem, gradient ascent yields the global, rather than local, optimum.

Having performed the comparison of the control fields generated by adiabatic

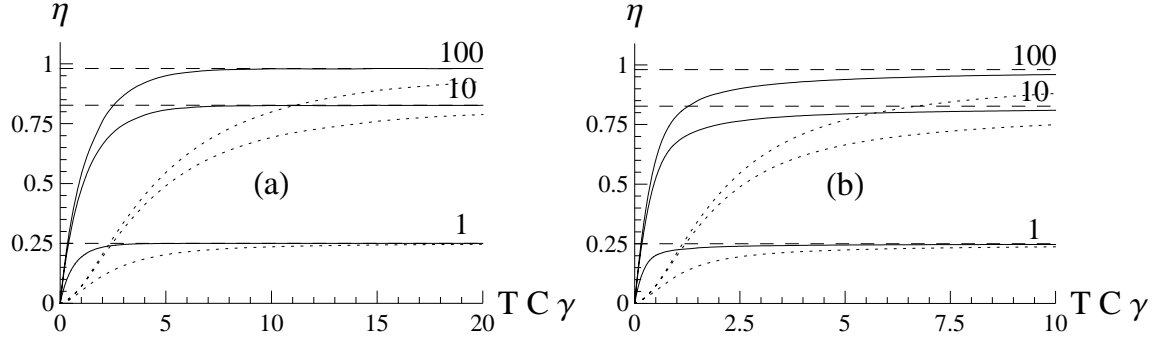


Figure D.3: (a) The total efficiency of storage followed by retrieval for the Gaussian-like input mode in Eq. (D.10) using adiabatic equations (dotted) and gradient ascent (solid) to shape the storage control field. Results are shown as a function of $TC\gamma$ for the indicated values of C ($= 1, 10, 100$). The dashed lines are $C^2/(1+C)^2$, the maximum efficiency possible at any given C . (b) Same for $\mathcal{E}_{\text{in}}(t) = 1/\sqrt{T}$.

shaping and by gradient ascent, we turn to the investigation of the dependence on C and on $TC\gamma$ of the efficiency achieved by these two methods. In Fig. D.3(a), we compare the efficiency of storage followed by retrieval of the input mode of Eq. (D.10) obtained using the adiabatic control field (dotted lines) and using the control found via gradient ascent (solid lines). The efficiencies are plotted as a function of $TC\gamma$ for three indicated values of C ($= 1, 10, 100$). Dashed lines correspond to $C^2/(1+C)^2$, the maximum efficiency possible at any given C . We note that the dotted lines have already been shown in Fig. A.2(a). According to the arguments presented in Appendices B and C, we note that it is impossible to retrieve into a mode much shorter than $1/(\gamma C)$, and hence, by time-reversal, it is impossible to efficiently store such a short mode. Fig. D.3(a) confirms that indeed, when $TC\gamma \ll 1$, even optimal controls cannot give high efficiency. Using gradient ascent instead of adiabatic shaping, one can, however, efficiently store input modes that are about an order of magnitude shorter and, thus, an order of magnitude larger in bandwidth. It is worth repeating that although the method of gradient ascent is generally not guaranteed to yield the global maximum, the fact that it does give the known global maximum in the limit $TC\gamma \gg 1$ suggests that it probably yields the global maximum at all values of $TC\gamma$.

To confirm the robustness and generality of the optimization procedure, we show in Fig. D.3(b) the results of the same optimization as in Fig. D.3(a) but for a square input mode $\mathcal{E}_{\text{in}}(t) = 1/\sqrt{T}$ instead of the Gaussian-like input mode of Eq. (D.10). As in Fig. D.3(a), we see that gradient ascent control shaping improves the threshold in the value of $TC\gamma$, where efficiency abruptly drops, by an order of magnitude. This can again be interpreted as an effective increase in the bandwidth of the memory by an order of magnitude. The optimal storage efficiency for the square input pulse falls to half of the maximum at smaller $TC\gamma$ than for the Gaussian-like input pulse because

the latter has a duration (half-width at half maximum, for example) significantly shorter than T [see Eq. (D.10) or Fig. D.2]. On the other hand, as $TC\gamma$ is increased, the maximum is approached slower for the square input mode than for the Gaussian-like mode. This is because the high frequency components contributed by the sharp edges of the square pulse are difficult to store.

Most experiments have features that go beyond the simple model we have just described. Therefore, in Sec. D.6.2, we generalize this model and the optimization procedure to include the possibility of complex control field envelopes $\Omega(t)$ and input mode envelopes $\mathcal{E}_{\text{in}}(t)$, nonzero single-photon detuning Δ and spin wave decay rate γ_s , and (possibly reversible [87]) inhomogeneous broadening. Our model of inhomogeneous broadening is applicable both to Doppler broadening in gases and to the broadening of optical transitions in solid state impurities caused by the differences in the environments of the impurities [292]. For the case of Doppler broadened gases, we also allow for the possibility of modeling velocity changing collisions with rate γ_c . Finally, in Sec. D.6.2, we also show how to take into account the possibility that the classical driving fields available in the laboratory are not sufficiently strong to realize the optimal control fields, which may be the case for short input modes and/or large single-photon detuning Δ , both of which require control pulses with large intensities.

Although a comprehensive study of optimization for $\Delta \neq 0$ is beyond the scope of the present Appendix, we will now prove that the maximum efficiency for $\Delta \neq 0$ is exactly equal to the maximum efficiency for $\Delta = 0$. Suppose we know the control field $\Omega_0(t)$ that achieves the optimum for a given resonant input $\mathcal{E}_{\text{in}}(t)$. Then, for an input at $\Delta \neq 0$ with the same envelope $\mathcal{E}_{\text{in}}(t)$, we can construct the control field $\Omega(t)$ as a sum of two parts [written in the two-photon-resonant rotating frame as in Eqs. (D.30) and (D.31)]

$$\Omega(t) = \Omega_2 e^{-i\Delta_2 t} + \Omega_0(t) e^{i\Delta t}. \quad (\text{D.11})$$

The first part is a far-detuned control ($\Delta_2 \gg \Omega_2, \gamma$) that Stark-shifts level $|e\rangle$ into resonance with the input (i.e. such that $\Omega_2^2/\Delta_2 = \Delta$), while the second part is resonant with the Stark-shifted $|e\rangle - |s\rangle$ transition and has the envelope equal to the optimal resonant control. The reason why an extra detuning Δ is needed to bring the second term in two-photon resonance is because Ω_2 Stark-shifts both $|e\rangle$ and $|s\rangle$ by Δ . The resulting efficiency must be equal to the optimal resonant efficiency up to an error on the order of the small population mixing between $|e\rangle$ and $|s\rangle$ caused by Ω_2 ; that is, $\sim (\Omega_2/\Delta_2)^2 = \Delta/\Delta_2$. To verify mathematically that the control in Eq. (D.11) works, one can write P and S as a sum of a slowly varying piece and a rapidly oscillating piece, extract separate equations for the rapidly and slowly oscillating variables, and finally adiabatically eliminate the rapidly oscillating variables. We have also numerically verified the performance of the control in Eq. (D.11) and the scaling of the error ($\sim \Delta/\Delta_2$) by integrating the equations of motion for the case of homogeneous broadening at several different values of $T\gamma$ and C for the pulse shape in Eq. (D.10). Thus, the optimal off-resonant efficiency is greater than or equal to

the optimal resonant efficiency for the same input envelope $\mathcal{E}_{\text{in}}(t)$. Carrying out the same argument backwards [i.e. using $\Omega_2(t)$ to shift $|e\rangle$ *out* of resonance], we conclude that the optimal efficiency must be the same on and off resonance. When applying this idea in practice, one should, of course, realize that, in addition to a possible technical limit on the available control power, the three-level approximation and the rotating-wave approximation may start to break down for sufficiently large values of Δ_2 and Ω_2 .

D.2.2 Free-Space Model

Although the cavity model discussed in Sec. D.2.1 is theoretically simpler and results, in certain cases, in higher efficiencies than the free space model, the latter is easier to set up experimentally. Moreover, because of the accessibility of a large number of spin wave modes, the free space model can provide higher efficiencies in some other cases (see Chapter 2 and Appendix B) and can, in principle, function, as a multi-mode memory. Therefore, we turn in the present Section to the analysis of the free space model.

To demonstrate how optimization with respect to the control field works in the free space model, we again begin with a simple example of resonant photon storage in a homogeneously broadened atomic ensemble with negligible spin-wave decay. It is important to note that, in contrast to the cavity model, the free space model gives access to many different spin-wave modes, which makes the retrieval efficiency dependent on how storage is carried out (see Appendix B). Therefore, optimization of storage alone is not a priori very practical. However, as shown in Appendix B, the optimization of storage alone is indeed useful because, in many cases, it also optimizes storage followed by backward retrieval.

In order to have slightly simpler mathematical expressions, we work in the co-moving frame (see Appendix B), although the same argument can be carried out using the original time variable, as well. The complex number equations of motion on the interval $t \in [0, T]$ are then (see Appendix B)

$$\partial_{\tilde{z}}\mathcal{E}(\tilde{z}, \tilde{t}) = i\sqrt{d}P(\tilde{z}, \tilde{t}), \tag{D.12}$$

$$\partial_{\tilde{t}}P(\tilde{z}, \tilde{t}) = -P(\tilde{z}, \tilde{t}) + i\sqrt{d}\mathcal{E}(\tilde{z}, \tilde{t}) + i\tilde{\Omega}(\tilde{t})S(\tilde{z}, \tilde{t}), \tag{D.13}$$

$$\partial_{\tilde{t}}S(\tilde{z}, \tilde{t}) = i\tilde{\Omega}(\tilde{t})P(\tilde{z}, \tilde{t}), \tag{D.14}$$

with initial and boundary conditions

$$\mathcal{E}(0, \tilde{t}) = \mathcal{E}_{\text{in}}(\tilde{t}), \tag{D.15}$$

$$P(\tilde{z}, 0) = 0, \tag{D.16}$$

$$S(\tilde{z}, 0) = 0. \tag{D.17}$$

These equations are written using dimensionless variables, in which (co-moving) time and Rabi frequency are rescaled by γ ($\tilde{t} = t\gamma$ and $\tilde{\Omega} = \Omega/\gamma$) and the position is rescaled

by the length L of the ensemble ($\tilde{z} = z/L$). $\mathcal{E}(\tilde{z}, \tilde{t})$ describes the slowly varying electric field envelope, the input mode $\mathcal{E}_{\text{in}}(\tilde{t})$ satisfies the normalization constraint $\int_0^{\tilde{T}} |\mathcal{E}_{\text{in}}(\tilde{t})|^2 d\tilde{t} = 1$, d is the resonant optical depth, and $\tilde{\Omega}(\tilde{z})$ and $\mathcal{E}_{\text{in}}(\tilde{t})$ are for now assumed to be real. [To avoid carrying around extra factors of 2, d is defined as half of what is often referred as the optical depth: the steady-state solution with $\Omega = 0$ gives probe intensity attenuation $|\mathcal{E}(\tilde{z} = 1)|^2 = e^{-2d} |\mathcal{E}(\tilde{z} = 0)|^2$.] The goal is to maximize the storage efficiency

$$\eta_s = \int_0^1 d\tilde{z} \left| S(\tilde{z}, \tilde{T}) \right|^2 \quad (\text{D.18})$$

with respect to $\tilde{\Omega}(\tilde{t})$. A procedure analogous to that used in the cavity model in Sec. D.2.1 yields equations of motion (also referred to as the adjoint equations) for the Lagrange multipliers $\bar{\mathcal{E}}(\tilde{z}, \tilde{t})$, $\bar{P}(\tilde{z}, \tilde{t})$, and $\bar{S}(\tilde{z}, \tilde{t})$:

$$\partial_{\tilde{z}} \bar{\mathcal{E}} = i\sqrt{d} \bar{P}, \quad (\text{D.19})$$

$$\partial_{\tilde{t}} \bar{P} = \bar{P} + i\sqrt{d} \bar{\mathcal{E}} + i\tilde{\Omega} \bar{S}, \quad (\text{D.20})$$

$$\partial_{\tilde{t}} \bar{S} = i\tilde{\Omega} \bar{P}, \quad (\text{D.21})$$

with initial and boundary conditions

$$\bar{\mathcal{E}}(1, \tilde{t}) = 0, \quad (\text{D.22})$$

$$\bar{P}(\tilde{z}, \tilde{T}) = 0, \quad (\text{D.23})$$

$$\bar{S}(\tilde{z}, \tilde{T}) = S(\tilde{z}, \tilde{T}). \quad (\text{D.24})$$

As in the cavity discussion in Sec. D.2.1, these equations describe backward retrieval and provide a simple mathematical connection between optimality and time-reversal. In order to move up the gradient, one should update $\Omega(\tilde{t})$ according to

$$\tilde{\Omega}(\tilde{t}) \rightarrow \tilde{\Omega}(\tilde{t}) - \frac{1}{\lambda} \int_0^1 d\tilde{z} \text{Im} \left[\bar{S}^*(\tilde{z}, \tilde{t}) P(\tilde{z}, \tilde{t}) - \bar{P}(\tilde{z}, \tilde{t}) S^*(\tilde{z}, \tilde{t}) \right]. \quad (\text{D.25})$$

We showed in Chapter 2 and Appendix B that, in the adiabatic limit ($Td\gamma \gg 1$) and for a certain class of input modes of duration $T \sim 1/(d\gamma)$, one can achieve a universally optimal (for a fixed d) storage efficiency that cannot be exceeded even if one chooses a different input mode. We showed that in that case the obtained control field will also maximize the total efficiency of storage followed by backward retrieval. However, this would not necessarily be the case for a general input mode in the non-adiabatic limit ($Td\gamma \lesssim 1$), which is precisely the limit, in which gradient ascent optimization becomes most useful. Moreover, for the case of forward retrieval, the control field that maximizes the storage efficiency does not maximize the total efficiency of storage followed by retrieval even in the adiabatic limit. Thus, in Sec. D.6.3, we describe how to use gradient ascent to maximize (still with respect to the storage control field) the total efficiency of storage followed by retrieval.

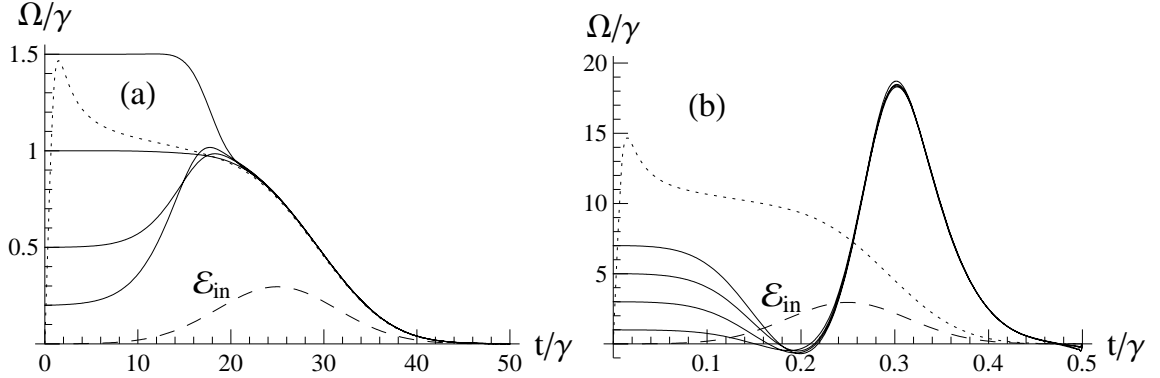


Figure D.4: Adiabatic (dotted) and optimal (solid) control fields for the storage followed by backward retrieval of a Gaussian-like input mode $\mathcal{E}_{\text{in}}(t)$ (dashed) in the free-space model with $d = 10$ and $T = 50/\gamma$ (a) and $T = 0.5/\gamma$ (b). Four optimal control pulses were obtained using four different initial guesses for the gradient ascent procedure. The adiabatic control field agrees with the optimal one in the adiabatic limit ($Td\gamma \gg 1$) (a) and deviates from it otherwise (b).

As in the cavity model in Sec. D.2.1, we now compare adiabatic shaping of the storage control field (see Chapter 2 and Appendix B) to the optimal shaping via gradient ascent. To compare with the results of Appendix B, we maximize the total efficiency of storage followed by backward retrieval rather than the storage efficiency alone. We assume that $d = 10$ and that $\mathcal{E}_{\text{in}}(t)$ is the Gaussian-like input mode in Eq. (D.10), shown as a dashed line in Figs. D.4(a) and D.4(b). We first consider the case $T = 50/\gamma$ and shape the storage control using adiabatic shaping (Sec. B.6.2). Then we numerically compute the total efficiency of storage followed by complete backward retrieval using this storage control field (the total efficiency is independent of the retrieval control field provided no excitations are left in the atoms). The adiabatic storage control is shown as a dotted line in Fig. D.4(a). Since for this input mode the adiabatic limit is satisfied ($Td\gamma = 500 \gg 1$), the adiabatic storage control yields an efficiency of 0.66, which is the maximum efficiency possible at this d (see Chapter 2). For the same reason, the adiabatic control agrees with the control field computed via gradient ascent (solid line), which also yields an efficiency of 0.66. Fig. D.4(a) shows four solid lines (optimal control fields) corresponding to four initial guesses $\Omega(t)/\gamma = 0.2, 0.5, 1, \text{ and } 1.5$. As in the cavity model discussion in Sec. D.2.1, the difference between the four optimal controls and the adiabatic control is inconsequential.

Repeating the calculation for $T = 0.5/\gamma$, we obtain Fig. D.4(b). Since the adiabatic limit ($Td\gamma \gg 1$) is no longer satisfied ($Td\gamma = 5$), the adiabatic approximation does not work and the adiabatic control differs from the optimal control and gives a lower efficiency: 0.24 vs. 0.58. As in Fig. D.4(a), the four optimal control fields plot-

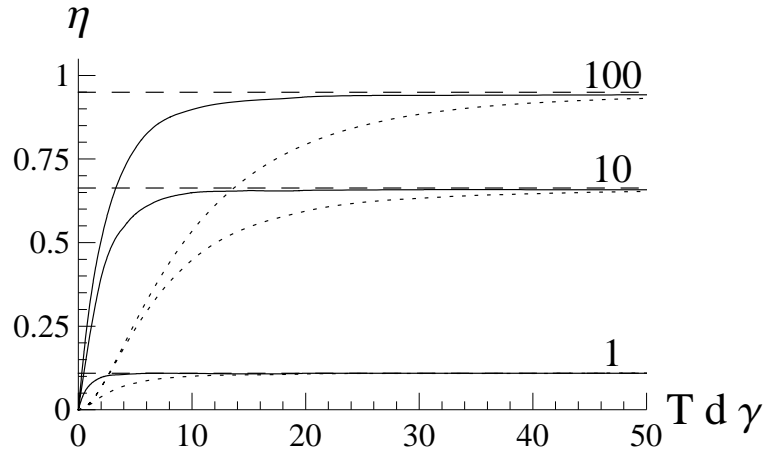


Figure D.5: The total efficiency of storage followed by backward retrieval for the Gaussian-like input mode in Eq. (D.10) using adiabatic equations (dotted) and gradient ascent (solid) to shape the storage control field. The results are shown for the indicated values of d ($= 1, 10, 100$), as a function of $Td\gamma$. The dashed lines represent the maximum efficiency possible at the given d (see Chapter 2).

ted correspond to different initial guesses $\Omega(t)/\gamma = 1, 3, 5$, and 7 . As in the cavity discussion, Fig. D.4(b) indicates that, in the regime $Td\gamma \sim 1$, where the adiabatic approximation no longer holds, the optimal control field acquires characteristics of the control field used in fast storage.

As in the analysis of the cavity model in Sec. D.2.1, we now analyze the dependence on d and $Td\gamma$ of the efficiency yielded by the adiabatic control shaping and the optimal control shaping. In Fig. D.5, we compare the efficiency of storage followed by complete backward retrieval of the input mode in Eq. (D.10) obtained using the control field shaped using the adiabatic equations (dotted lines) and using gradient ascent (solid lines). The efficiencies are plotted as a function of $Td\gamma$ for three indicated values of d ($= 1, 10, 100$). Horizontal dashed lines represent the maximum efficiency possible at the given d (see Chapter 2). The dotted lines are the same as in Fig. B.6(a). Similar to the corresponding discussion of the cavity model in Sec. D.2.1, Fig. D.5 confirms the predictions of Appendices B and C that efficient photon storage is not possible for $Td\gamma \lesssim 1$. It also illustrates that optimal control fields open up the possibility of efficient storage of input modes with a bandwidth that is an order of magnitude larger than the bandwidth allowed by the adiabatic storage. In addition, the same reasoning as in the cavity discussion leads to the conclusion that for this problem, gradient ascent most likely yields the global, rather than local, maximum at all values of $Td\gamma$.

Various generalizations of the presented procedure can be made. First, the generalization to limited control pulse energy, (possibly reversible [87]) inhomogeneous

broadening, complex Ω and \mathcal{E}_{in} , and nonzero Δ , γ_s , and γ_c can be carried out exactly as in the cavity case (Sec. D.6.2). Second, in the case of backward retrieval, if the two metastable states are nondegenerate and have a frequency difference ω_{sg} , one should incorporate an appropriate position-dependent phase shift of the spin wave of the form $\exp(-2i\Delta\tilde{k}\tilde{z})$, where $\Delta\tilde{k} = L\omega_{sg}/c$ (see Sec. B.8). Finally, another extension can be made for the cases when the total efficiency depends on the retrieval control field (e.g. if γ_s and/or γ_c are nonzero). In those cases, one can simultaneously optimize with respect to both the storage and the retrieval control fields. However, one may then need to put a limit on the energy in the retrieval control pulse since, for the case of $\gamma_s \neq 0$, for example, the faster one retrieves, the higher is the efficiency, and the optimal retrieval control field may, in principle, end up having unlimited power (e.g. an infinitely short π pulse).

D.3 Optimization with respect to the Input Field

Although it is usually easier to optimize with respect to the control field, optimization with respect to the input mode can also be carried out in certain systems. For both classical and quantum light, the mode shape can often be controlled by varying the parameters used during the generation of the mode. For example, if the photon mode is created by releasing some generated collective atomic excitation, one can, under certain assumptions, generate any desired mode shape (see Chapter 2). For the case of classical light, one can also shape the input light pulse simply using an acousto-optical modulator. An important advantage of optimizing with respect to the input mode is that the iterations can be carried out experimentally (see Sec. 3.3 and Appendix B). In this Section, we consider the maximization of light storage efficiency with respect to the shape of the input mode.

The gradient ascent method, used in Sec. D.2 to optimize with respect to the control field, can be easily applied to the optimization with respect to the input mode shape both in the cavity model and in the free space model. Since one is interested in finding the optimal input mode shape, the optimization has to be carried out subject to the normalization condition $\int_0^T dt |\mathcal{E}_{\text{in}}(t)|^2 = 1$. This condition can be included by adding an extra term with a Lagrange multiplier to the functional J to be optimized. The iterations are then done as follows: one first integrates the storage equations for a trial input mode; then integrates the adjoint equations corresponding to backward retrieval (as in Secs. D.2.1 and D.2.2); then updates the trial input mode by adding to it a small correction proportional to the output of backward retrieval [$-i\bar{P}(t)$ in the cavity model or $\bar{\mathcal{E}}(0, \tilde{t})$ in the free space model]; and finally renormalizes the new input mode to satisfy the normalization condition.

An important feature that distinguishes the optimization with respect to the input mode from the optimization with respect to the control field is the possibility of

making finite (not infinitesimal) steps. Standard gradient-ascent improvement [such as via Eqs. (D.9) and (D.25)] is, in principle, infinitesimal due to its reliance on the small parameter $1/\lambda$. Several decades ago, Krotov introduced and developed an important powerful and rapidly converging global improvement method [90, 309, 310, 314] that is not characterized by a small parameter. Largely thanks to the presence of the normalization condition on the input mode, this method can be applied to derive non-infinitesimal quickly converging updates for the problem of optimization of light storage efficiency with respect to the input mode. For the cavity model of Sec. D.2.1, this update is given by

$$\mathcal{E}_{\text{in}}(t) \rightarrow -i\bar{P}(t), \quad (\text{D.26})$$

followed by a renormalization of $\mathcal{E}_{\text{in}}(t)$, while for the free-space model of Sec. D.2.2, the update is given by

$$\mathcal{E}_{\text{in}}(\tilde{t}) \rightarrow \bar{\mathcal{E}}(0, \tilde{t}), \quad (\text{D.27})$$

followed by renormalization. These updates precisely correspond to the time-reversal-based iterations introduced in Chapter 2 and Appendices A and B. In these iterations, optimization of light storage with respect to the input field is done by carrying out storage of a trial input mode followed by backward retrieval, and then using the normalized output of backward retrieval as the input mode in the next iteration. The beauty of this update procedure is the possibility of carrying it out experimentally. In fact, the extension of this procedure to the optimization of storage followed by forward retrieval, suggested in Chapter 2 and Appendix B, has already been demonstrated experimentally, as we report in Sec. 3.3.

In the language of gradient ascent, one can still think of Eqs. (D.26) and (D.27) as steps along the gradient. These steps are, however, finite, not infinitesimal. This allows one to think of time-reversal-based optimization with respect to the input mode as simple intuitive walk up the gradient. As shown in Appendix A, the fact that only one collective atomic mode can be excited in the cavity model makes the iterations of Eq. (D.26) converge to the optimum in a single step. Using the terminology of gradient ascent, the optimization with respect to the input field in the cavity model can, surprisingly, be achieved with a single large step up the gradient.

We note that the optimization procedure discussed in this Section can be easily generalized to include inhomogeneous broadening and (for the case of Doppler broadened gases) the presence of velocity changing collisions. One can show that, even with these features, the iterative optimization procedure still works in exactly the same way by updating the input mode with the output of time-reversed retrieval.

D.4 Optimization with respect to the Inhomogeneous Profile

Having discussed optimization with respect to the control field and the input mode, we now turn to the optimization with respect to the shape of the inhomogeneous profile. This optimization is most relevant in the context of controlled reversible inhomogeneous broadening (CRIB) [87]. The main idea of CRIB is that by introducing inhomogeneous broadening into a homogeneously broadened medium (via Stark or Zeeman shifts, for example) and by optimizing the shape and width of this inhomogeneous profile, one can better match the absorption profile of the medium to the spectrum of the incoming photon mode and, thus, increase the storage efficiency [87]. At the same time, one can minimize the losses caused by dephasing of different frequency classes with respect to each other by using an echo-like process triggered by a reversal of the inhomogeneous profile between the processes of storage and retrieval [86, 87]. We refer the reader to Appendices A and C for a full list of references, and to Ref. [298] and Appendix C for examples of recent theoretical studies.

D.4.1 Cavity Model

As in Sec. D.2, we begin the discussion with the theoretically simpler cavity model. Although one can, of course, optimize with respect to the inhomogeneous profile in the problem of storage alone (i.e. not followed by retrieval), in the context of CRIB it is more relevant to consider the problem of storage followed by retrieval with the reversed inhomogeneous profile [87]. Moreover, although the approach can be extended to nonzero single-photon detuning and arbitrary control fields, we suppose for simplicity that the input mode $\mathcal{E}_{\text{in}}(t)$ is resonant and that the storage and retrieval control pulses are π pulses. Following the convention of Chapter 2 and Appendices A-C, we refer to this use of π -pulse control fields as fast storage and fast retrieval.

We leave most of the mathematical details of the problem to Sec. D.6.4. Here we only note that we describe the inhomogeneous profile by a discrete number of frequency classes. The index j labels the frequency class with detuning Δ_j from the center of the line containing a fraction p_j of atoms ($\sum_j p_j = 1$). In Sec. D.6.4, we show how to carry out optimization with respect to p_j and/or Δ_j .

We now present the results of gradient ascent optimization with respect to the inhomogeneous profile for a particular example. We suppose that the input pulse is the Gaussian-like mode in Eq. (D.10) and that $C = 50$. The total efficiency of storage followed by retrieval, as a function of $TC\gamma$, is shown in Fig. D.6(a) for various storage protocols. The dash-dotted line gives the efficiency of fast storage (i.e. storage obtained by applying a control π pulse on the $|g\rangle - |e\rangle$ transition at the end of the input mode at time T) followed by fast retrieval using a homogeneous line. As discussed in Appendices A and B, a homogeneous ensemble enclosed in a cavity has

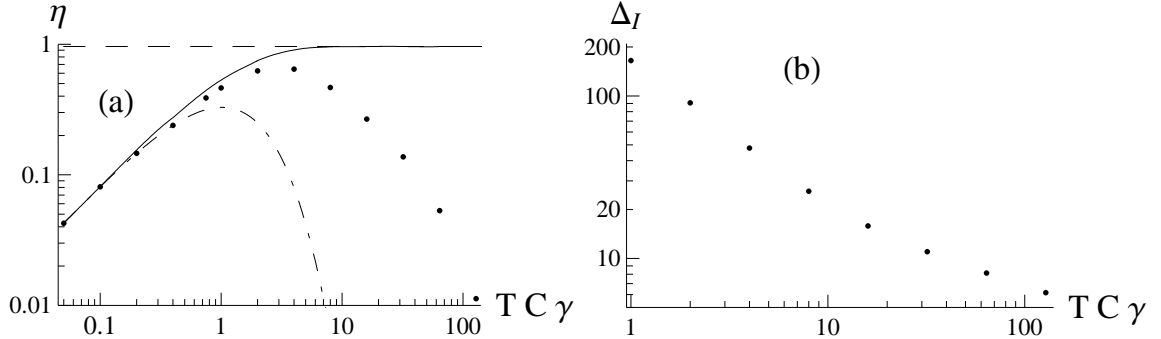


Figure D.6: Comparison of the efficiency for storage followed by retrieval in the cavity model with and without controlled reversible inhomogeneous broadening (CRIB). We consider storage of the Gaussian-like input mode of duration T [Eq. (D.10)] in a cavity with $C = 50$. (a) The figure shows the efficiency of fast storage followed by fast retrieval with a homogeneous line (dash-dotted), fast storage followed by fast retrieval with a reversible optimized inhomogeneous profile, i.e. CRIB (circles), optimal storage and retrieval with a homogeneous line as in Fig. D.3(a) (solid), and the asymptotic value $C^2/(C+1)^2$ (dashed). (b) The optimal inhomogeneous width Δ_I for CRIB.

only one accessible spin-wave mode and can, therefore, fast-store only one input mode, which has duration $T \sim 1/(C\gamma)$. As a result, the decay at $TC\gamma \gg 1$ of the efficiency represented by the dash-dotted line is dominated by leakage of the input mode into the output mode and not by polarization decay. We now consider introducing reversible inhomogeneous broadening and iteratively optimizing with respect to its shape (using Eq. (D.53) or Eq. (D.55)). As expected, the efficiency grows with each iteration independently of the choice of the number of frequency classes, the choice of Δ_j , and the initial guess for p_j . The landscape in the control space, however, depends on the number of frequency classes and on Δ_j . This landscape is also not as simple as in Secs. D.2 and D.3, i.e. there exist local maxima. We did not perform an exhaustive search, but out of all the initial configurations, number of frequency classes, and Δ_j distributions that we tried, the highest efficiencies were obtained for the cases when gradient ascent converged to only two nonempty frequency classes with opposite detunings (we have not been able to come up with a simple physical reason for this). We therefore focus on the case of only two frequency classes with detunings $\pm\Delta_I$ and optimize with respect to Δ_I [using Eq. (D.56)]. The optimized efficiency is shown with circles in Fig. D.6(a). For $TC\gamma$ less than about 0.75, it is optimal to have $\Delta_I = 0$. For larger $TC\gamma$, the optimal Δ_I is shown in Fig. D.6(b): at small $TC\gamma$, it scales approximately as $\propto (TC\gamma)^{-1}$ and then slower. The presence of two frequency classes and hence two accessible spin wave modes instead of one allows us to reduce the leakage error, so that the efficiency [circles in Fig. D.6(a)] is now limited by polarization decay.

Finally, we would like to compare the broadening-optimized efficiency to the homogeneous control-optimized efficiency. Repeating the optimization procedure of Sec. D.2.1 for $C = 50$, we obtain the solid line in Fig. D.6(a). The maximum efficiency possible at this C is $C^2/(C+1)^2$ and is shown as the dashed line. The dashed line and the solid line are the same as in Fig. D.3(a), except that now $C = 50$. The fact that the solid line in Fig. D.6(a) lies above the circles indicates that we have not been able to identify any advantage of fast storage with CRIB compared to optimal storage in the homogeneous medium. Moreover, all inhomogeneous broadening configurations we tried to introduce into the optimized homogeneous protocol converged back to the homogeneous profile. These results suggest that if one wants to store a single mode of known shape using a homogeneously broadened ensemble of Λ -type systems enclosed in a cavity and can shape and time the control field with sufficient precision, it may be better to use optimal homogeneous storage and not to use CRIB.

It is, however, worth noting that we have only carried out the simplest optimization of fast storage with CRIB. In particular, the performance of fast storage with CRIB may be further enhanced by optimizing with respect to the time, at which the storage π pulse is applied. Such optimization represents an optimal control problem with a free terminal time [90] and is beyond the scope of the present Appendix (although it can be carried out in a straightforward manner by repeating the optimization above systematically for different times of the π -pulse application).

It is also important to note that the use of CRIB in the cavity model may allow for implementing a multimode memory [341] in the cavity setup. Unlike the free space model, which allows for the storage of multiple temporal input modes using, e.g., Raman- or EIT-based protocols (Chapter 2, Appendix B, and Refs. [84, 16, 17]), the homogeneously broadened cavity model only has a single accessible spin-wave mode. Therefore, if we do not use CRIB or some other inhomogeneous broadening mechanism, it can only store a single input mode

D.4.2 Free-Space Model

Having discussed the optimization with respect to the inhomogeneous profile in the cavity model, we note that the same procedure can be carried out for the free space model in an analogous manner. The appropriate update equations are listed at the end of Sec. D.6.4.

In Appendix C, we compared storage using adiabatic control shaping in a homogeneous ensemble to fast storage with CRIB. We found that fast storage with CRIB can indeed do better than adiabatic homogeneous storage for $Td\gamma \sim 1$. We show now that this result was mainly due to imperfect control field optimization outside of the adiabatic limit and that, in the present work, we have not been able to identify any advantages of fast storage with CRIB compared to optimal homogeneous storage. We consider storage of the resonant Gaussian-like input mode in Eq. (D.10) in a free space atomic ensemble with $d = 100$ followed by backward retrieval. The total efficiency

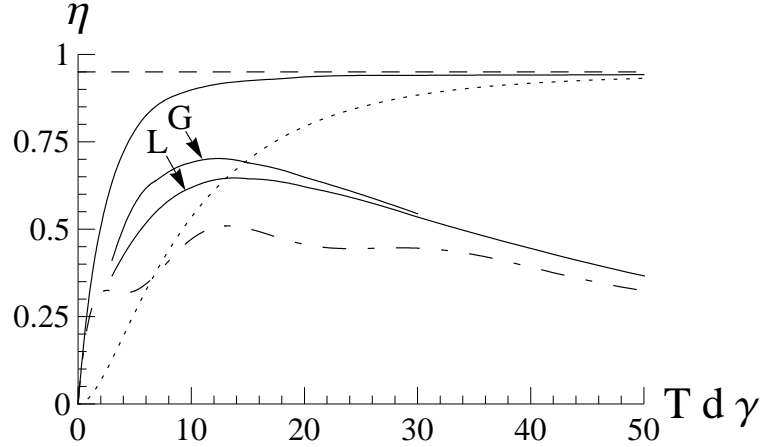


Figure D.7: Comparison of optimized homogeneous-line storage with storage based on CRIB. For $d = 100$, the plot shows the efficiency of storage followed by backward retrieval of the Gaussian-like input mode of duration T [Eq. (D.10)]. The curves show results for fast storage and retrieval with a homogeneous line (dash-dotted), fast storage and retrieval with an optimized reversible Gaussian (G) or Lorentzian (L) inhomogeneous profile, i.e. CRIB (solid lines labeled G and L), storage and retrieval with a homogeneous line using adiabatic (dotted) or optimal (unlabeled solid line) control field shaping (same as in Fig. D.5), and the asymptotic value (dashed).

for various storage protocols is shown in Fig. D.7 as a function of $Td\gamma$. The dash-dotted line and the two solid lines labeled G and L are taken from Fig. C.8(a). The dash-dotted line is the efficiency of fast storage followed by fast backward retrieval using a homogeneous line. The two solid lines labeled G and L are obtained using fast storage with optimal-width reversible inhomogeneous broadening with Gaussian profile and Lorentzian profile, respectively. Although the optimization with respect to the inhomogeneous width can be done efficiently via gradient ascent [using Eq. (D.58)], we have already performed this optimization in Appendix C by sampling a sufficiently large set of inhomogeneous widths. The remaining third solid line and the dotted line (both taken from Fig. D.5) correspond to homogeneous storage with optimal storage controls (solid) and with adiabatic controls (dotted). The dashed line (also from Fig. D.5) is the maximum possible efficiency at this d . The plot shows that while adiabatic control field shaping (dotted) makes homogeneous storage less efficient for some values of $Td\gamma$ than fast storage with CRIB (solid lines labeled G and L), optimal control field shaping (unlabeled solid line) may enable homogeneous storage to be more efficient than fast storage with CRIB at all values of $Td\gamma$.

As in Sec. D.4.1, we note, however, that we have presented only the simplest optimization of CRIB and that the full investigation of the advantages of CRIB is beyond the scope of the present Appendix. In particular, the CRIB efficiency

may be enhanced by optimizing with respect to the time, at which the storage π -pulse is applied. Moreover, CRIB might be useful in circumstances such as when a homogeneously broadened three-level system is not available, when more complicated inputs (such as time-bin qubits) are used, or when precise shaping and timing of the control pulse is harder to achieve than controlled reversible broadening. Finally, CRIB-based memories may even be implemented without any optical control fields [298].

D.5 Summary

In conclusion, we have shown that the powerful numerical optimal control method of gradient ascent allows one to obtain simple intuitive understanding and to achieve a significantly improved efficiency and a higher bandwidth in the problem of photon storage in Λ -type atomic ensembles. First, we showed how to apply gradient ascent to numerically compute optimal control fields even outside of the adiabatic limit both with and without a constraint on the energy in the control pulse. In particular, this opens up the possibility of efficient storage of input modes that are an order of magnitude shorter (and hence an order of magnitude larger in bandwidth) than the shortest modes that can be efficiently stored using adiabatic control field shaping. Second, we showed that gradient ascent provides an alternative justification for the often discussed connection between optimality and time-reversal in photon storage, as well as for the iterative time-reversal-based optimization procedure with respect to the input field introduced in Chapter 2 and Appendices A-C and demonstrated experimentally in Secs. 3.3 and E.4. In particular, we confirmed that the iterative procedure works even in the presence of inhomogeneous broadening and (for the case of Doppler broadened gases) in the presence of velocity changing collisions. Finally, we showed how to use gradient ascent to optimize with respect to inhomogeneous broadening and demonstrated how this can significantly increase the efficiency of fast storage followed by fast backward retrieval in the presence of controlled reversible inhomogeneous broadening (CRIB) [87]. Provided one is interested in storing a single input photon mode of known shape and provided the control pulses can be generated with sufficient precision, we have not, however, been able to identify any advantages of CRIB-based photon storage compared to photon storage with optimal control pulses in homogeneously broadened media.

In general, gradient ascent methods do not guarantee the attainment of the global maxima. The global maximum is, however, indeed attained for our problem in the regimes where this maximum is known. This strongly suggests that, for the optimization with respect to the input mode and with respect to the storage control, gradient ascent may indeed be yielding the global optimum. We also note that one can optimize simultaneously with respect to various combinations of the control parameters simply by simultaneously updating each of them along the corresponding

gradient. One can also include other possible control parameters that are available in a given experimental setup but have not been discussed in the present Appendix. For example, for the case of photon storage in solid-state systems, one can consider optimizing with respect to the number of atoms put back into the antihole [87, 292] or with respect to a time-dependent reversible inhomogeneous profile. Other light storage systems, such as photonic crystals [91] or cavity models where the cavity field cannot be eliminated, are also susceptible to gradient ascent optimization. Therefore, we expect the optimization procedures described in the present Appendix to allow for increased efficiencies and increased bandwidths in many current experiments on quantum memories for light, many of which are narrowband and suffer from low efficiencies. Such improvements would facilitate advances in fields such as quantum communication and quantum computation.

D.6 Omitted Details

In the preceding Sections of this Appendix, to allow for a smoother presentation, we omitted some of the details. We present them in this Section.

D.6.1 Derivation of the Adjoint Equations of Motion in the Cavity Model

In Sec. D.2.1, we omitted the derivations of the adjoint equations of motion (D.4) and (D.5) and of the corresponding boundary conditions (D.6) and (D.7). We provide these derivations in this Section.

Varying J given in Eq. (D.3) with respect to S , S^* , P , and P^* , we obtain

$$\begin{aligned}
 \delta J &= S(T)\delta S^*(T) \\
 &+ \int_0^T dt \bar{P}^* \left(-\delta \dot{P} - \gamma(1+C)\delta P + i\Omega\delta S \right) \\
 &+ \int_0^T dt \bar{S}^* \left(-\delta \dot{S} + i\Omega\delta P \right) \\
 &+ c.c., \tag{D.28}
 \end{aligned}$$

where "c.c." means complex conjugate taken of the whole expression after the equal sign. Integrating by parts the terms containing time derivatives, we obtain

$$\begin{aligned}
 \delta J &= S(T)\delta S^*(T) \\
 &- \bar{P}^*(T)\delta P(T) + \int_0^T dt \dot{\bar{P}}^* \delta P + \int_0^T dt \bar{P}^* \left(i\Omega\delta S - \gamma(1+C)\delta P \right) \\
 &- \bar{S}^*(T)\delta S(T) + \int_0^T dt \dot{\bar{S}}^* \delta S + \int_0^T dt \bar{S}^* (i\Omega\delta P) \\
 &+ c.c.. \tag{D.29}
 \end{aligned}$$

Since the initial conditions are fixed, we have here used $\delta S(0) = \delta P(0) = \delta S^*(0) = \delta P^*(0) = 0$ to simplify the expression.

The optimum requires that $\delta J = 0$ for any variations δP and δS . Hence we collect the terms multiplying, e.g., $\delta P(T)$ and set the result to zero. Carrying out this procedure for $\delta P(T)$, $\delta S(T)$, and their conjugates, we obtain the boundary conditions (D.6) and (D.7). Collecting terms proportional to δP , δS , and their conjugates, we obtain adjoint equations of motion (D.4) and (D.5).

D.6.2 Control Field Optimization in the Cavity Model: Generalization

In Sec. D.2.1, we showed how to perform control field optimization in the simplest possible version of the cavity model: a resonant input mode with a real envelope was stored using a control pulse with a real envelope and unlimited power into a homogeneously broadened ensemble with infinite spin-wave lifetime. In this Section, we show how to optimize the control field in a more general model that includes the possibility of complex control field envelopes $\Omega(t)$ and input mode envelopes $\mathcal{E}_{\text{in}}(t)$, nonzero single-photon detuning Δ and spin wave decay rate γ_s , and (possibly reversible [87]) inhomogeneous broadening such as Doppler broadening in gases or the broadening of optical transitions in solid state impurities [292]. For the case of Doppler broadened gases, we also include velocity changing collisions with rate γ_c . We also show how to take into account possible experimental restrictions on the strength of the classical control fields.

Using the notation of Appendix C, the complex number equations describing the generalized model are

$$\begin{aligned} \dot{P}_j &= -[\gamma + i(\Delta + \Delta_j)] P_j - \gamma C \sqrt{p_j} P + i\Omega S_j \\ &\quad + i\sqrt{2\gamma C} \sqrt{p_j} \mathcal{E}_{\text{in}} + \gamma_c (\sqrt{p_j} P - P_j), \end{aligned} \quad (\text{D.30})$$

$$\dot{S}_j = -\gamma_s S_j + i\Omega^* P_j + \gamma_c (\sqrt{p_j} S - S_j), \quad (\text{D.31})$$

where j labels the frequency class with detuning Δ_j from the center of the line containing a fraction p_j of atoms ($\sum_j p_j = 1$) and where the total optical and spin polarizations are $P = \sum_k \sqrt{p_k} P_k$ and $S = \sum_k \sqrt{p_k} S_k$, respectively. The terms proportional to γ_c describe completely rethermalizing collisions with rate γ_c [346]. One can, of course, also take γ_c to be different for P and S . For example, if $\gamma_c \ll \gamma$, which is often the case, one can drop the terms proportional to γ_c in Eq. (D.30) [347]. In addition to moving atoms from one frequency class to the other, collisions also result in line broadening, which can be taken into account by increasing γ [152]. We assume that the goal is to maximize the efficiency $\eta_s = |S(T)|^2$ of storage into the symmetric mode $S(T)$ with respect to the control pulse $\Omega(t)$ for a given input mode shape $\mathcal{E}_{\text{in}}(t)$ satisfying the normalization condition $\int_0^T dt |\mathcal{E}_{\text{in}}(t)|^2 = 1$. A procedure very similar to

that described in Sec. D.2.1 and in Sec. D.6.1 yields the following equations of motion for the adjoint variables:

$$\dot{\bar{P}}_j = [\gamma - i(\Delta + \Delta_j)] \bar{P}_j + \gamma C \sqrt{p_j} \bar{P} + i\Omega \bar{S}_j - \gamma_c (\sqrt{p_j} \bar{P} - \bar{P}_j), \quad (\text{D.32})$$

$$\dot{\bar{S}}_j = \gamma_s \bar{S}_j + i\Omega^* \bar{P}_j - \gamma_c (\sqrt{p_j} \bar{S} - \bar{S}_j), \quad (\text{D.33})$$

where $\bar{P} = \sum_k \sqrt{p_k} \bar{P}_k$ and $\bar{S} = \sum_k \sqrt{p_k} \bar{S}_k$. The corresponding initial conditions for backward propagation are

$$\bar{P}_j(T) = 0, \quad (\text{D.34})$$

$$\bar{S}_j(T) = \sqrt{p_j} S(T). \quad (\text{D.35})$$

Similarly to Sec. D.2.1, after taking an initial guess for $\Omega(t)$ and solving for P_j , S_j , \bar{P}_j , and \bar{S}_j , one updates $\Omega(t)$ by moving up the gradient

$$\Omega(t) \rightarrow \Omega(t) + \frac{1}{\lambda} i \sum_j (\bar{S}_j^* P_j - \bar{P}_j S_j^*). \quad (\text{D.36})$$

Short input modes and/or large single-photon detuning Δ require control pulses with large intensities that might not be available in the laboratory. There exist ways to include a bound on the control field amplitude [90]. Alternatively, one may want to consider a slightly simpler optimization problem with a limit on the control pulse energy $\int_0^T |\Omega(t)|^2 dt \leq E$ for some E [85]. In order to carry out the optimization subject to this constraint, one should first carry out the optimization without the constraint and see whether the optimal control satisfies the constraint or not. If it does not satisfy the constraint, one has to add a term $\mu'(E - \int_0^T |\Omega(t)|^2 dt)$ to J , so that the update becomes

$$\Omega(t) \rightarrow \Omega(t) + \frac{1}{\lambda} \left[i \sum_j (\bar{S}_j^* P_j - \bar{P}_j S_j^*) - \mu' \Omega(t) \right], \quad (\text{D.37})$$

where μ' is adjusted to satisfy the constraint. By redefining μ' and λ , this update can be simplified back to Eq. (D.36) followed by a renormalization to satisfy the constraint. Depending on how severe the energy constraint is, one can then sometimes (but not always) further simplify the update by completely replacing $\Omega(t)$ with the gradient [i.e. set $\lambda = \mu'$ in Eq. (D.37)] followed by a renormalization of $\Omega(t)$, as is done, for example, in Ref. [312] for the problem of laser control of chemical reactions.

We note that these optimization protocols can be trivially extended to the full process of storage followed by retrieval, which, in the presence of inhomogeneous broadening, one might not be able to optimize by optimizing storage and retrieval separately. Similarly, one may include the possibility of reversing the inhomogeneous profile between the processes of storage and retrieval [87].

D.6.3 Control Field Optimization in the Free-Space Model: Generalization to Storage Followed by Retrieval

In Sec. D.2.2, we showed how to use gradient ascent to find the control field that maximizes the storage efficiency. However, the obtained storage control field does not always maximize the total efficiency of storage followed by retrieval. Therefore, in this Section, we consider the maximization of the total efficiency of storage followed by retrieval with respect to the storage control field. While we demonstrate the procedure only for the case of forward retrieval, the treatment of backward retrieval is analogous.

We suppose that the control field $\Omega(t)$ consists of a storage control pulse on $t \in [0, T]$ and a retrieval control pulse on $t \in [T_r, T_f]$. We want to optimize with respect to the former given the latter and the input mode (note that the total efficiency is independent of the retrieval control for sufficiently strong retrieval control pulses, and it is therefore often less important to optimize with respect to the retrieval control pulse). Here $0 < T \leq T_r < T_f$, and the subscripts in T_r and T_f stand for "retrieval" and "final". The time interval $[T, T_r]$ corresponds to the waiting (i.e. storage) time between the processes of storage (which ends at $t = T$) and retrieval (which begins at $t = T_r$).

We suppose that storage is described by Eqs. (D.12)-(D.17) on $t \in [0, T]$. Then forward retrieval that follows after the storage time interval $[T, T_r]$ is described by the same equations (D.12)-(D.14) but on the time interval $t \in [T_r, T_f]$ with initial and boundary conditions

$$\mathcal{E}(0, \tilde{t}) = 0, \tag{D.38}$$

$$P(\tilde{z}, \tilde{T}_r) = 0, \tag{D.39}$$

$$S(\tilde{z}, \tilde{T}_r) = S(\tilde{z}, \tilde{T}), \tag{D.40}$$

where $\tilde{T}_r = T_r \gamma$ (similarly, $\tilde{T}_f = T_f \gamma$). Eq. (D.39) assumes that the polarization has sufficient time to decay before retrieval starts, while Eq. (D.40) assumes that spin-wave decay is negligible during the storage time. The goal is to maximize the total efficiency of storage followed by retrieval,

$$\eta_{\text{tot}} = \int_{\tilde{T}_r}^{\tilde{T}_f} d\tilde{t} |\mathcal{E}(1, \tilde{t})|^2, \tag{D.41}$$

with respect to the storage control field. Constructing J and taking appropriate variations, we obtain initial and boundary conditions for backward propagation:

$$\bar{\mathcal{E}}(1, \tilde{t}) = \mathcal{E}(1, \tilde{t}) \text{ for } \tilde{t} \in [\tilde{T}_r, \tilde{T}_f], \tag{D.42}$$

$$\bar{P}(\tilde{z}, \tilde{T}_f) = 0, \tag{D.43}$$

$$\bar{S}(\tilde{z}, \tilde{T}_f) = 0, \tag{D.44}$$

and

$$\bar{\mathcal{E}}(1, \tilde{t}) = 0 \text{ for } \tilde{t} \in [0, \tilde{T}], \quad (\text{D.45})$$

$$\bar{P}(\tilde{z}, \tilde{T}) = 0, \quad (\text{D.46})$$

$$\bar{S}(\tilde{z}, \tilde{T}) = \bar{S}(\tilde{z}, \tilde{T}_r). \quad (\text{D.47})$$

By taking the variational derivative of J with respect to $\tilde{\Omega}(\tilde{t})$ on the storage interval, we find that the update is exactly the same as for the optimization of storage alone and can be done via Eq. (D.25).

We note that if the retrieval control pulse leaves no atomic excitations, one can obtain the same optimization equations by solving the storage optimization problem in Sec. D.2.2 but changing the function to be maximized from the number of spin-wave excitations $\int_0^1 d\tilde{z} S(\tilde{z}, \tilde{T}) S^*(\tilde{z}, \tilde{T})$ to the complete retrieval efficiency from $S(\tilde{z}, \tilde{T})$ [Eq. (B.14)]. It is also worth noting that the derivation presented here can trivially be extended to apply to backward (instead of forward) retrieval and to include complex Ω and \mathcal{E}_{in} , (possibly reversible [87]) inhomogeneous broadening, and nonzero Δ , γ_s , and γ_c .

D.6.4 Optimization with Respect to the Inhomogeneous Profile: Mathematical Details

In Sec. D.4, we presented the results on the optimization of photon storage with respect to the inhomogeneous broadening without providing the mathematical details. In this Section, we present these details.

We first consider the cavity model, but turn briefly to the free-space model at the end of this Section. We suppose for simplicity that the input mode $\mathcal{E}_{\text{in}}(t)$ is resonant and that the storage and retrieval control pulses are π pulses at $t = T$ and $t = T_r$, respectively. In order to simplify notation, we define $x_j = \sqrt{p_j}$, satisfying the normalization $\sum_j x_j^2 = 1$. The storage equation (D.30) on the interval $t \in [0, T]$ then becomes

$$\dot{P}_j = -(\gamma + i\Delta_j)P_j - \gamma C x_j P + i\sqrt{2\gamma C} x_j \mathcal{E}_{\text{in}}, \quad (\text{D.48})$$

with $P = \sum_k x_k P_k$ and with the initial condition $P_j(0) = 0$. A π -pulse at $t = T$ mapping P onto S followed by another π -pulse at $t = T_r$ mapping S back onto P result in an overall 2π pulse, so that $P_j(T_r) = -P_j(T)$. Assuming the broadening is reversed at some time between T and T_r , the equations for retrieval on the interval $t \in [T_r, T_f]$ are

$$\dot{P}_j = -(\gamma - i\Delta_j)P_j - \gamma C x_j P. \quad (\text{D.49})$$

The total efficiency of storage followed by retrieval is then

$$\eta_{\text{tot}} = \int_{T_r}^{T_f} dt |\mathcal{E}_{\text{out}}(t)|^2 = \int_{T_r}^{T_f} dt \left| i\sqrt{2\gamma C} P(t) \right|^2. \quad (\text{D.50})$$

One can show that the equations of motion for the adjoint variables (i.e. the Lagrange multipliers) \bar{P}_j are

$$\dot{\bar{P}}_j = (\gamma + i\Delta_j)\bar{P}_j + \gamma C x_j \bar{P} - 2\gamma C x_j P \quad (\text{D.51})$$

for $t \in [T_r, T_f]$ with $\bar{P}_j(T_f) = 0$ and

$$\dot{\bar{P}}_j = (\gamma - i\Delta_j)\bar{P}_j + \gamma C x_j \bar{P} \quad (\text{D.52})$$

for $t \in [0, T]$ with $\bar{P}_j(T) = -\bar{P}_j(T_r)$, where we defined $\bar{P} = \sum_k x_k \bar{P}_k$. The last term in Eq. (D.51) describes an incoming field that is the time-reverse of the retrieved field. Assuming we are optimizing with respect to x_j , the update is

$$x_j \rightarrow x_j + \frac{1}{\lambda} A_j, \quad (\text{D.53})$$

followed by a rescaling of all x_j by a common factor to ensure the normalization $\sum_j x_j^2 = 1$. Here A_j is given by

$$\begin{aligned} A_j = & -\gamma C \operatorname{Re} \left[\int_0^T dt + \int_{T_r}^{T_f} dt \right] (\bar{P}_j^* P + \bar{P}^* P_j) \\ & - \sqrt{2\gamma C} \operatorname{Im} \int_0^T dt \mathcal{E}_{\text{in}} \bar{P}_j^* + 2\gamma C \operatorname{Re} \int_{T_r}^{T_f} dt P_j^* P, \end{aligned} \quad (\text{D.54})$$

where Re denotes the real part. Numerics show that the update can usually be simplified in a way that avoids the search for convenient values of λ and does not lose convergence. Specifically, taking $\lambda \rightarrow 0$ in Eq. (D.53), we obtain

$$x_j \rightarrow A_j, \quad (\text{D.55})$$

followed by renormalization. By defining a particular functional form for the dependence of x_j on Δ_j , one could also consider optimization with respect to only a few parameters, such as, for example, the width Δ_I and the degree of localization n of the inhomogeneous profile of the form $p_j = x_j^2 \propto 1/[1 + (\Delta_j/\Delta_I)^n]$.

Equivalently, instead of optimizing with respect to x_j , one can optimize with respect to Δ_j . To illustrate this procedure, we consider a simple optimization procedure with respect to a single parameter, the inhomogeneous width Δ_I . We write $\Delta_j = \Delta_I f_j$ for some fixed dimensionless parameters f_j and consider maximizing the efficiency with respect to Δ_I for fixed x_j and f_j . The equations of motion and the initial conditions for both P_j and \bar{P}_j stay the same as in the optimization with respect to x_j while the update becomes

$$\Delta_I \rightarrow \Delta_I + \frac{1}{\lambda} \operatorname{Im} \sum_j \left[\int_0^T dt - \int_{T_r}^{T_f} dt \right] \bar{P}_j^* f_j P_j. \quad (\text{D.56})$$

By adjusting f_j and x_j , one can choose a particular inhomogeneous profile shape (e.g. Lorentzian, Gaussian, or a square) and optimize with respect to its width.

Having discussed the cavity case, we now list the corresponding free-space results. In free space, the update of x_j via Eq. (D.55) would use

$$A_j = -\sqrt{d} \operatorname{Im} \int_0^1 d\tilde{z} \left[\int_0^{\tilde{T}} d\tilde{t} + \int_{\tilde{T}_r}^{\tilde{T}_f} d\tilde{t} \right] (\bar{P}_j^* \mathcal{E} + \bar{\mathcal{E}}^* P_j). \quad (\text{D.57})$$

Similarly, the update of $\tilde{\Delta}_I = \Delta_I/\gamma$ would be

$$\tilde{\Delta}_I \rightarrow \tilde{\Delta}_I + \frac{1}{\lambda} \operatorname{Im} \sum_j \int_0^1 d\tilde{z} \left[\int_0^{\tilde{T}} d\tilde{t} - \int_{\tilde{T}_r}^{\tilde{T}_f} d\tilde{t} \right] \bar{P}_j^* f_j P_j. \quad (\text{D.58})$$

Appendix E

Optimal Photon Storage in Atomic Ensembles: Experiment (Part II)

E.1 Introduction

We argued in the Introduction (Chapter 1), in Chapters 2 and 3, and in Appendices A-D that the ability to store light pulses in matter and retrieve them is an important step in the realization of quantum networks and certain quantum cryptography protocols [4, 61]. We also argued that mapping quantum states of light onto an ensemble of identical radiators (*e.g.*, atoms, ions, solid-state emitters, *etc.*) offers a promising approach to the practical realization of such a photonic quantum memory [16, 17, 76, 79, 87]. However, we also noted that memory efficiency must be significantly improved before practical applications become possible.

In this Appendix, we present a comprehensive experimental analysis of two memory optimization protocols demonstrated experimentally in Chapter 3 that are based on the theoretical proposal in Chapter 2 and Appendix B. The first protocol, demonstrated in Sec. 3.3, iteratively optimizes the input pulse shape for any given control field, while the second protocol, demonstrated in Sec. 3.4, uses optimal control fields calculated for any given input pulse shape. In this Appendix, we experimentally demonstrate their mutual consistency by showing that both protocols yield the same optimal control-signal pairs and memory efficiencies. We also show that for moderate optical depths ($\lesssim 25$), the experimental results presented here (as well as in Chapter 3) are in excellent agreement with a simple three-level theoretical model of Chapter 2 and Appendix B with no free parameters; we discuss the details of the correspondence between the actual atomic system and this simple model. Lastly, we study the dependence of memory efficiency on the optical depth. We show that for higher optical depths ($\gtrsim 25$), the experimental efficiency falls below the theoretically predicted values; we discuss possible effects, such as spin-wave decay and four-wave mixing, that may limit the experimentally observed memory efficiency.

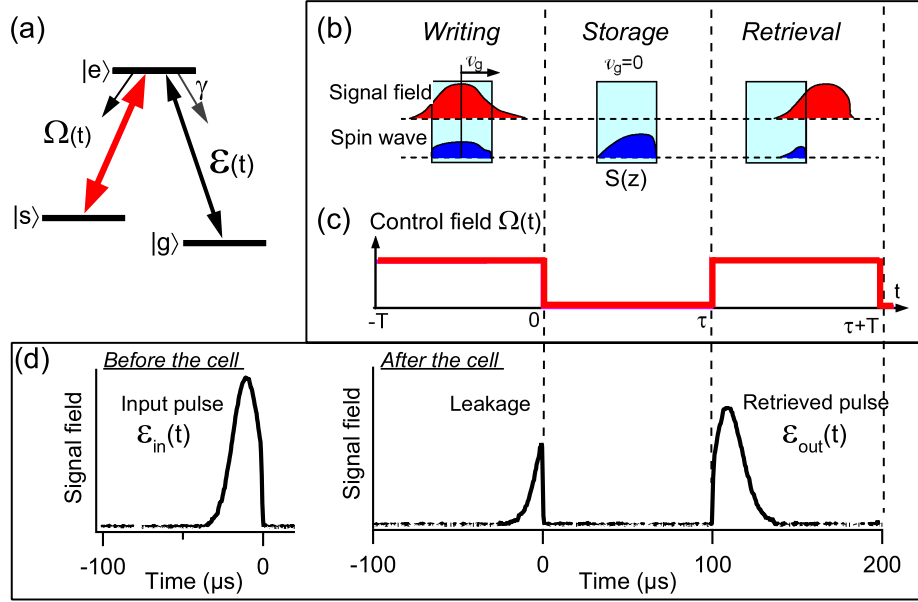


Figure E.1: (a) The three-level Λ scheme used in theoretical calculations. The schematic (b) and example control (c) and signal (d) fields during light storage. At the writing stage ($t < 0$), an input signal pulse $\mathcal{E}_{\text{in}}(t)$ propagates through the atomic medium with low group velocity v_g in the presence of a control field envelope $\Omega(t)$. While compressed inside the cell, the pulse is mapped onto a spin-wave $S(z)$ by turning the control field off at time $t = 0$. After a storage period τ , the spin-wave is mapped back into an output signal pulse $\mathcal{E}_{\text{out}}(t)$ using the retrieval control field envelope $\Omega(t)$ ($t > \tau$).

The remainder of this Appendix is organized as follows. In Sec. E.2, we briefly summarize the three-level theory governing the two procedures for optimizing photon storage. In Sec. E.3, we describe our experimental system and discuss its correspondence to the three-level model. In Secs. E.4 and E.5, we present the results of experimental studies of both optimization procedures and demonstrate their consistency. In Sec. E.6, we investigate the dependence of memory efficiency on the optical depth of the medium. Finally, in Sec. E.7, we conclude with the summary of our results.

E.2 Review of the Theory

In this Section, we briefly review the necessary concepts from the theoretical work of Chapter 2 and Appendix B, on which our experiments rely. We consider the propagation of a weak signal pulse with envelope $\mathcal{E}(t)$ and a strong (classical) control

field with a Rabi frequency¹ envelope $\Omega(t)$ in a resonant Λ -type atomic medium under the conditions of electromagnetically induced transparency (EIT), as shown in Fig. E.1(a). The control field creates a strong coupling between the signal field and a collective atomic spin excitation (spin wave) [76]. As a result, the initial pulse gets spatially compressed and slowed down inside the atomic ensemble. The group velocity of the pulse is proportional to the control field intensity [305]:

$$v_g \approx 2|\Omega|^2/(\alpha\gamma) \ll c, \quad (\text{E.1})$$

where γ is the decay rate of the optical polarization and α is the absorption coefficient (*i.e.*, unsaturated absorption per unit length), so that αL is the optical depth of an atomic medium of length L . Notice that throughout this Appendix, we use traditional definition of the optical depth of a sample as the *intensity* attenuation $\exp(-\alpha L)$ of a weak resonant signal field with no control field. This definition differs by a factor of 2 from optical depth d defined in Chapter 2 and Appendices A-D as the *amplitude* attenuation of a weak resonant signal field. There the intensity attenuation was given by $\exp(-2d)$, so that the two optical depth definitions are related by $\alpha L = 2d$.

Fig. E.1(b) illustrates schematically the three stages of the light storage process (writing, storage, and retrieval), while Figs. E.1(c) and E.1(d) show control and signal fields, respectively, during a typical experimental run. At the writing stage, a signal pulse $\mathcal{E}_{\text{in}}(t)$ is mapped onto the collective spin excitation $S(z)$ by adiabatically reducing the control field to zero. This spin wave is then preserved for some storage time τ (storage stage), during which all optical fields are turned off. Finally, at the retrieval stage, the signal field $\mathcal{E}_{\text{out}}(t)$ is retrieved by turning the control field back on [76, 16, 17]. In the ideal case, the retrieved signal pulse is identical to the input pulse, provided the same constant control power is used at the writing and the retrieval stages. However, to realize this ideal storage, two conditions must be met. On the one hand, the group velocity v_g of the signal pulse inside the medium has to be low enough to spatially compress the whole pulse into the length L of the ensemble and avoid “leaking” the front edge of the pulse past the atoms. This requires $Tv_g \ll L$, where T is the duration of the incoming signal pulse. On the other hand, all spectral components of the incoming pulse must fit inside the EIT transparency window to minimize spontaneous emission losses $1/T \ll \Delta\omega_{\text{EIT}} \simeq \sqrt{\alpha L}v_g/L$ [16, 17]. The simultaneous satisfaction of both conditions is possible only at very high optical depth $\alpha L \gg 1$, as shown in Refs. [16, 17] and Chapter 2.

Experimental realization of very high optical depth in atomic ensembles requires high atomic density and/or large sample length. At high atomic density, EIT performance can be degraded by competing processes, such as stimulated Raman scattering

¹As in Refs. [16, 17], Chapters 2 and 3, and Appendices A-D, we define the Rabi frequency Ω as $|\Omega|^2 = \wp_{es}^2 I / (2\hbar^2 \epsilon_0 c)$, where I is the control intensity. With this definition, Ω is actually half of the usual definition of the Rabi frequency: with our definition, a π pulse would take time $\pi/(2\Omega)$.

and four-wave mixing [348, 349, 350, 351, 352, 353]. Furthermore, spin-exchange collisions [354] and radiation trapping [323, 355, 63] may reduce spin wave lifetime by orders of magnitude, limiting storage time and signal pulse durations. In addition, achieving high optical depth in some experimental arrangements may be challenging, such as in magneto-optical traps (see *e.g.*, Refs. [81, 92]). Therefore, it is crucial to be able to maximize memory efficiency by balancing the absorptive and leakage losses at moderately large αL via optimal shaping of control and/or signal temporal profiles. To characterize our memory for light, we define memory efficiency η as the probability of retrieving an incoming single photon after storage, or, equivalently, as the energy ratio between initial and retrieved signal pulses:

$$\eta = \frac{\int_{\tau}^{\tau+T} |\mathcal{E}_{\text{out}}(t)|^2 dt}{\int_{-T}^0 |\mathcal{E}_{\text{in}}(t)|^2 dt}. \quad (\text{E.2})$$

The goal of any optimization procedure then is to maximize η under the restrictions and limitations of a given system.

In the theoretical treatment of the problem, the propagation of a signal pulse in an idealized three-level Λ system, shown in Fig. E.1(a), is described by three complex, dependent variables, which are functions of time t and position z , as shown in Refs. [76, 16, 17] and in Appendix B. These variables are the slowly-varying envelope \mathcal{E} of the signal field, the optical polarization P of the $|g\rangle - |e\rangle$ transition, and the spin coherence S . The equations of motion for these variables are (see Refs. [76, 16, 17], Chapter 2 and Appendix B)

$$(\partial_t + c\partial_z)\mathcal{E}(z, t) = ig\sqrt{N}P(z, t), \quad (\text{E.3})$$

$$\partial_t P(z, t) = -\gamma P(z, t) + ig\sqrt{N}\mathcal{E}(z, t) + i\Omega(t - z/c)S(z, t), \quad (\text{E.4})$$

$$\partial_t S(z, t) = -\gamma_s S(z, t) + i\Omega(t - z/c)P(z, t), \quad (\text{E.5})$$

where $g\sqrt{N} = \sqrt{\gamma\alpha c/2}$ is the coupling constant between the atomic ensemble and the signal field, and γ and γ_s are the polarization decay rates for the transitions $|g\rangle - |e\rangle$ and $|g\rangle - |s\rangle$, respectively. While, in general, Eqs. (E.3-E.5) cannot be fully solved analytically, they reveal several important properties of the optimization process, as we point out in Chapter 2 and Appendix B. These properties are most evident in the case when spin wave decay rate γ_s is negligible during the processes of writing and retrieval ($\gamma_s T \ll 1$), which will hold for most of the discussion in the present Appendix, except for parts of Sec. E.6. In this case, the highest achievable memory efficiency depends only on the optical depth αL and the mutual propagation direction of the control fields during the writing and retrieval stages². For each

²The present experiment uses co-propagating writing and retrieval control fields, which corresponds to “forward retrieval,” using the terminology of Chapter 2 and Appendices A-D. Although backward retrieval is more efficient than forward retrieval for degenerate lower levels $|s\rangle$ and $|g\rangle$ of the Λ -system (Chapter 2 and Appendix B), for the present experiment the hyperfine splitting between $|s\rangle$ and $|g\rangle$ makes forward retrieval more efficient (see Sec. B.8).

optical depth, there exists a unique spin wave, $S_{\text{opt}}(z)$, which provides the maximum memory efficiency. Thus, the focus of the optimization process becomes identifying a matching pair of *writing* control and signal pulses that maps the signal pulse onto this optimal spin wave. Note that no additional optimization is required with respect to the *retrieval* control field, because, as shown in Sec. 2.3, the memory efficiency does not depend on it, provided spin wave decay is negligible during retrieval.

In the present experiments and in Chapter 3, the optimization procedures are tested using weak classical signal pulses rather than quantum fields. Such experimental arrangements greatly improved the experimental simplicity and the accuracy of data analysis. At the same time, the linear equations of motion for classical and quantum signal pulses are identical, which makes the presented results applicable to quantized signal fields, such as, *e.g.*, single photons. It is also important to note that the theoretical work in Chapter 2 and Appendices A-D considered a wide range of interaction processes for storing and retrieving photon wave packets (*e.g.*, EIT, far-off-resonant Raman, and spin echo techniques) under a variety of conditions including ensembles enclosed in a cavity (Appendix A), inhomogeneous broadening (Appendix C), and high-bandwidth non-adiabatic storage ($1/T \sim \alpha L\gamma$) (Appendix D). Since the proposed optimization procedures are, to a large degree, common to all interaction schemes and conditions, our results are relevant to a wide range of experimental systems.

E.3 Experimental Arrangements

The schematic of the experimental apparatus is shown in Fig. E.2. We used an external cavity diode laser (ECDL) tuned near the ^{87}Rb D_1 transition ($\lambda = 795$ nm) with total available laser power ≈ 45 mW. After separating a fraction of original light for a reference beam using a polarizing beam splitter (PBS), the main laser beam passed through an electro-optical modulator (EOM), which modulated its phase at the frequency of the ground-state hyperfine splitting of ^{87}Rb ($\Delta_{\text{HF}} = 6.835$ GHz) and produced modulation sidebands separated by that frequency. We tuned the zeroth order (carrier frequency) field to the $5^2S_{1/2}F = 2 \rightarrow 5^2P_{1/2}F' = 2$ transition. This field was used as the control field during light storage. The +1 modulation sideband played the role of the signal field and was tuned to the $5^2S_{1/2}F = 1 \rightarrow 5^2P_{1/2}F' = 2$ transition.

To carry out the optimization procedure, we had to independently manipulate the amplitudes of the control and the signal fields. We used an acousto-optical modulator (AOM) to adjust the control field intensity. However, since all optical fields traversed the AOM, the intensities of all modulation comb fields were also changed. Thus, we accordingly adjusted the rf power at the EOM input (which controls the strength of the modulation sidebands) to compensate for any changes in the signal field amplitude caused by AOM modulation.

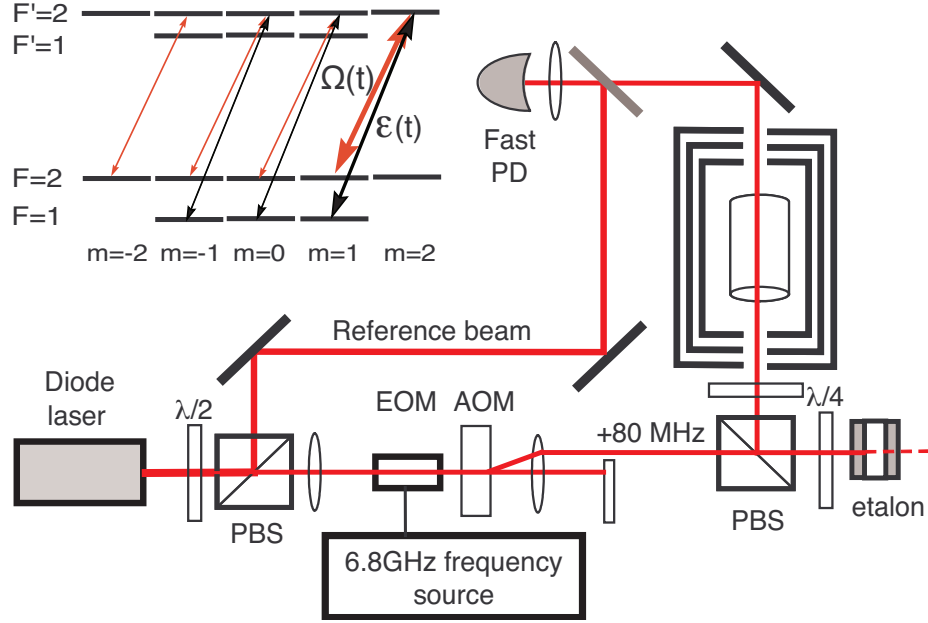


Figure E.2: Experimental apparatus (see text for abbreviations). *Inset*: Schematic of the ^{87}Rb D₁ line level structure and relevant Λ systems formed by control and signal fields.

To minimize the effects of resonant four-wave mixing, we filtered out the other (-1) first order modulation sideband (detuned by Δ_{HF} to the red from the carrier frequency field) by reflecting the modulation comb off of a temperature-tunable Fabry-Perot etalon (FSR = 20 GHz, finesse ≈ 100). The etalon was tuned in resonance with this unwanted modulated sideband, so that most of this field was transmitted. At the same time, the control and signal field frequencies were far from the etalon resonance, and were reflected back with no losses. Such filtering allowed for suppression of the -1 modulated sideband intensity by a factor of ≈ 10 .

Typical peak control field and signal field powers were 18 mW and $50 \mu\text{W}$, respectively. The beam was weakly focused to ≈ 5 mm diameter and circularly polarized with a quarter-wave plate ($\lambda/4$). A cylindrical Pyrex cell (length and diameter were 75 mm and 22 mm, respectively) contained isotopically enriched ^{87}Rb and 30 Torr Ne buffer gas, so that the pressure broadened optical transition linewidth was $2\gamma = 2\pi \times 290$ MHz [96]. The cell was mounted inside three-layer magnetic shielding to reduce stray magnetic fields. The temperature of the cell was controllably varied between 45°C and 75°C using a bifilar resistive heater wound around the innermost magnetic shielding layer.

We used relatively short pulses, so that spin decoherence had a negligible effect during writing and retrieval stages (except for parts of Sec. E.6) and only caused a

modest reduction of the efficiency during the storage time $\propto \exp(-2\gamma_s\tau)$. The Rb atom diffusion time out of the laser beam ($\simeq 2$ ms) was long enough to avoid diffusion-related effects on EIT dynamics [356, 98]. We extracted the spin wave decoherence time by measuring the reduction of the retrieved pulse energy as a function of storage time and fitting it to an exponential decay. We found the typical decay time to be $1/(2\gamma_s) \simeq 500 \mu\text{s}$, most likely arising from small, uncompensated, remnant magnetic fields.

After the cell, the output laser fields were recombined with the reference beam (at the unshifted laser frequency) at a fast photodetector, and the amplitude of each field was analyzed using a microwave spectrum analyzer. Because of the 80 MHz frequency shift introduced by the AOM, the beatnote frequencies of the +1 and -1 modulation sidebands with the reference beam differed by 160 MHz, which allowed for independent measurement of the amplitude of each of these fields, as well as of the control field.

To conclude this Section, we explain the direct correspondence between the experimental system and the theory based on three-level atoms [Fig. E.1(a)] that we reviewed in Sec. E.2. The goal is to use the structure of the D_1 line of ^{87}Rb (see inset in Fig. E.2) to identify the optical depth αL and the control field Rabi frequency Ω for the effective three level system. We first solve for the ground-state population distribution after control field optical pumping of the Rb D_1 line, taking into account Doppler broadening, pressure broadening, and collisional depolarization of the excited state sublevels [354]. We find the depolarization to be fast enough (for 30 Torr Ne, $\gamma_{\text{depol}} = 2\pi \times 190$ MHz [357]) to ensure roughly equal populations in each of $|F, m_F\rangle = |1, -1\rangle, |1, 0\rangle, |1, 1\rangle$, and $|2, 2\rangle$ ground state sublevels. Given this population distribution, we calculate the optical depth αL for the signal field as a function of Rb number density. For example, we find that at 60.5°C (Rb vapor density of $2.5 \times 10^{11} \text{ cm}^{-3}$) the optical depth is $\alpha L = 24.0$. Moreover, approximately 60% of this optical depth comes from atomic population of $|F, m_F\rangle = |1, 1\rangle$ due to the large corresponding Clebsch-Gordan coefficient. Thus, to calculate Ω , we use the dipole matrix element of the $|F = 2, m_F = 1\rangle \rightarrow |F' = 2, m_F = 2\rangle$ transition. Approximating a transverse Gaussian laser beam profile with a uniform cylindrical beam of diameter 5 mm of the same power, we find, for example, that for the control power of 16 mW, $\Omega = 2\pi \times 6.13$ MHz. Since the collisionally broadened optical transition linewidth ($2\gamma = 2\pi \times 290$ MHz) is comparable to the width of the Doppler profile, the effects of Doppler broadening are negligible, making Eqs. (E.3-E.5) directly applicable. We note that all the theoretical modeling is done with no free parameters.

E.4 Signal-Pulse Optimization

One approach to the optimization of light storage is based on important time-reversal properties of photon storage that hold even in the presence of irreversible

polarization decay (Chapter 2 and Appendix B). In particular, for co-propagating³ writing and retrieval control fields, the following is true under optimized conditions (see Fig. E.1): if a signal pulse $\mathcal{E}_{\text{in}}(t)$ is mapped onto a spin wave using a particular control field $\Omega(t)$ and retrieved after some storage time τ using the time-reversed control field $\Omega(T - t)$, the retrieved signal pulse shape $\mathcal{E}_{\text{out}}(t)$ is proportional to the time-reversed input signal pulse $\mathcal{E}_{\text{in}}(T - t)$, but attenuated due to imperfect memory efficiency. (Here and throughout this Appendix, control and signal envelopes are assumed to be real.) This symmetry also gives rise to an experimentally realizable iteration procedure, which, for any given writing control field, determines the optimal incoming signal pulse shape. This procedure has been demonstrated experimentally in Sec. 3.3. The present experiment was performed independently on a different (although similar) experimental setup. Therefore, in order to use this procedure in Sec. E.6 to study the dependence of memory efficiency on the optical depth, we verify in this Section its successful performance in the present experimental setup. In addition, the implementation of iterative signal optimization in this experimental setup will allow us, in Sec. E.5, to compare and verify the consistency of signal and control optimizations.

The sequence of experimental steps for the iterative optimization procedure is shown in Fig. E.3. The plots show the control field and the measured and simulated signal fields (solid red lines in the top panel, solid black lines, and dashed blue lines, respectively). Before each iteration, we optically pumped all atoms into the state $|g\rangle$ by applying a strong control field. We started the optimization sequence by sending an arbitrary signal pulse $\mathcal{E}_{\text{in}}^{(0)}(t)$ into the cell and storing it using a chosen control field $\Omega(t)$. In the particular case shown in Fig. E.3, the group velocity was too high, and most of the input pulse escaped the cell before the control field was reduced to zero. However, a fraction of the pulse, captured in the form of a spin wave, was stored for a time period $\tau = 100 \mu\text{s}$. We then retrieved the excitation using a time-reversed control field $\Omega(t) = \Omega(\tau - t)$ and recorded the output pulse shape $\mathcal{E}_{\text{out}}^{(0)}(t)$. For the sample sequence shown, the control fields at the writing and retrieval stages were constant and identical. This completes the initial (zeroth) iteration step. The efficiency of light storage at this step was generally low, and the shape of the output pulse was quite different from the time-reverse of the initial pulse. To create the input pulse $\mathcal{E}_{\text{in}}^{(1)}(t)$ for the next iteration step, we digitally time-reversed the output $\mathcal{E}_{\text{out}}^{(0)}(t)$ of the zeroth iteration and renormalized it to compensate for energy losses during the zeroth iteration: $\mathcal{E}_{\text{in}}^{(1)}(t) \propto \mathcal{E}_{\text{out}}^{(0)}(\tau - t)$. Then, these steps were repeated iteratively until the rescaled output signal pulse became identical to the time-reversed profile of the input pulse. As expected, the memory efficiency grew with each iteration and converged to $43 \pm 2\%$.

To verify that the obtained efficiency is indeed the maximum possible at this optical depth and to confirm the validity of our interpretation of the results, we compare

³See footnote on p. 243.

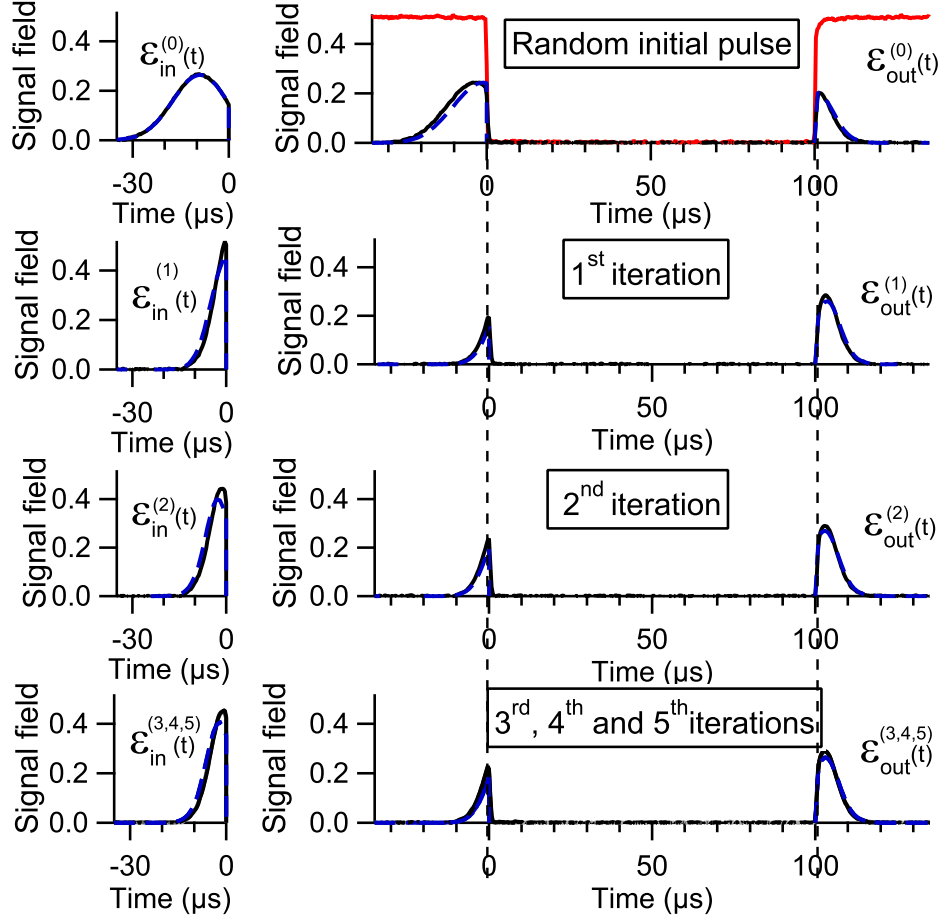


Figure E.3: Iterative signal pulse optimization. The experimental data (solid black lines) is taken at $60.5\text{ }^\circ\text{C}$ ($\alpha L = 24$) using 16 mW constant control field during writing and retrieval (solid red line in the top panel) with a $\tau = 100\text{ }\mu\text{s}$ storage interval. Numerical simulations are shown with blue dashed lines. *Left*: Input pulses for each iteration. *Right*: Signal field after the cell, showing leakage of the initial pulse for $t < 0$ and the retrieved signal field \mathcal{E}_{out} for $t > 100\text{ }\mu\text{s}$. Here and throughout this Appendix, all pulses are shown in the same scale, and all input pulses are normalized to have the same area $\int_{-T}^0 |\mathcal{E}_{\text{in}}(t)|^2 dt = 1$, where t is time in μs .

the experimental data to numerical simulations in Fig. E.3. Using the calculated optical depth and the control Rabi frequency (see Sec. E.3), we solve Eqs. (E.3-E.5) analytically in the adiabatic limit $T\alpha L\gamma \gg 1$ (see Secs. B.6 and B.6), which holds throughout this Appendix. There is a clear agreement between the calculated and measured lineshapes and amplitudes of the signal pulses. Also, theory and exper-

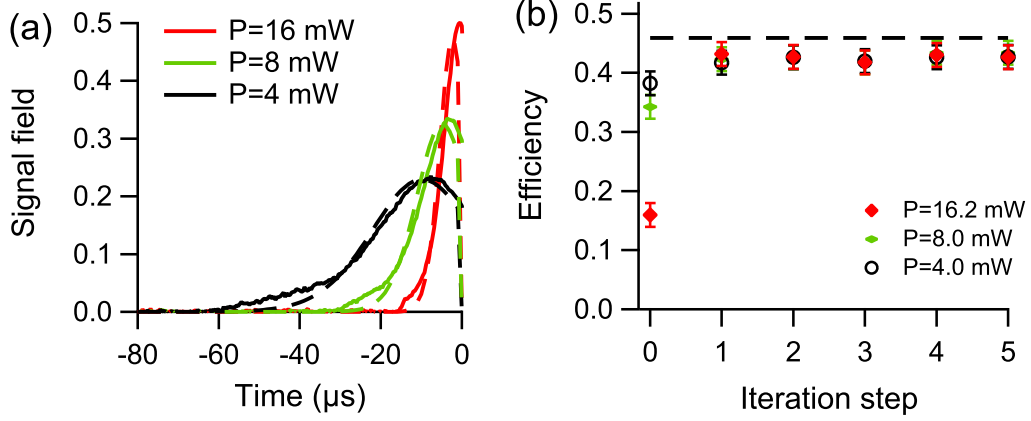


Figure E.4: (a) Experimental (solid) and theoretical (dashed) optimized signal pulses obtained after five steps of the iteration procedure for three different powers of the constant control fields during writing and retrieval stages. (b) Corresponding memory efficiencies determined for each iteration step. Theoretically predicted optimal efficiency value is shown by the dashed line. The temperature of the cell was $60.5\text{ }^\circ\text{C}$ ($\alpha L = 24$).

iment converge to the optimal signal pulse shape in a similar number of iteration steps (2-3), and the experimental efficiency ($43 \pm 2\%$) converged to a value close to the theoretical limit of 45% (see below).

As in Sec. 3.3, we confirmed that the final memory efficiency and the final signal pulse after a few iteration steps are independent of the initial signal pulse $\mathcal{E}_{\text{in}}^{(0)}(t)$. We also confirmed that the optimization procedure yields the same memory efficiency for different control fields. While constant control fields of three different powers yield different optimal signal pulses [Fig. E.4(a)], the measured efficiency [Fig. E.4(b)] converged after a few iteration steps to the same value of $43 \pm 2\%$. With no spin wave decay, the highest achievable memory efficiency for the optical depth $\alpha L = 24$ is 54% (see Chapter 2 and Appendix B). Taking into account spin wave decay during the $100\text{ }\mu\text{s}$ storage time by a factor of $\exp[-100\mu\text{s}/500\mu\text{s}] = 0.82$, the highest expected efficiency is 45% [dashed line in Fig. E.4(b)], which matches our experimental results reasonably well.

E.5 Control-Pulse Optimization

The iterative optimization procedure described in the previous Section has an obvious advantage: the optimal signal pulse shape is found directly through experimental measurements without any prior knowledge of the system parameters (*e.g.*,

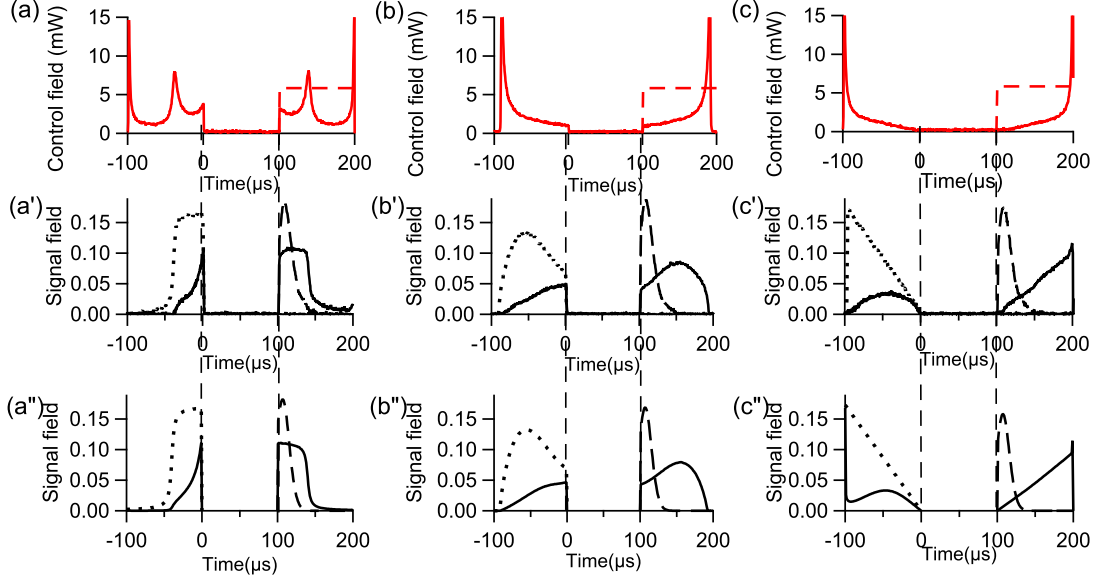


Figure E.5: Storage of three signal pulses (a' , b' , c') using calculated optimal storage ($t < 0$) control fields (a), (b), (c). Input signal pulse shapes are shown in black dotted lines. The same graphs also show the leakage of the pulses (solid black lines for $t < 0$) and retrieved signal pulses ($t > 100 \mu\text{s}$) using flat control fields at the retrieval stage (dashed red lines), or using time-reversed control fields (solid red lines). Graphs (a'' , b'' , c'') show the results of numerical calculations of (a' , b' , c'). The temperature of the cell was $60.5 \text{ }^\circ\text{C}$ ($\alpha L = 24$).

optical depth, control field Rabi frequency, various decoherence rates, *etc.*). However, in some situations, it is difficult or impossible to shape the input signal pulse (*e.g.*, if it is generated by parametric down-conversion [99]). In these cases, the *control field* temporal profile must be adjusted in order to optimally store and retrieve a given signal pulse, as we have demonstrated experimentally and analyzed in Sec. 3.4. We now repeat this analysis in greater detail and compare to the results of signal-pulse optimization from Sec. E.4.

To find the optimal writing control field for a given input pulse shape $\mathcal{E}_{\text{in}}(t)$, we maximize η [Eq. (E.2)] within the three-level model [Eqs. (E.3-E.5)]. In this model, for a given optical depth αL and a given retrieval direction (coinciding with the storage direction in the present experiment⁴), there exists an optimal spin wave $S_{\text{opt}}(z)$, which gives the maximum memory efficiency. One way to calculate the control field required to map the input pulse onto this optimal spin wave is to first calculate an artificial “decayless” spin wave mode $s(z)$, which, like $S_{\text{opt}}(z)$, depends only on the optical

⁴See footnote on p. 243.

depth and not on the shape of the incoming pulse. This “decayless” mode $s(z)$ hypothetically allows for unitary reversible storage of an arbitrary signal pulse in a semi-infinite and polarization-decay-free atomic ensemble, in which the group velocity of the pulse is still given by Eq. (E.1). The unitarity of the mapping establishes a 1-to-1 correspondence between a given input signal pulse shape $\mathcal{E}_{\text{in}}(t)$ and an optimal writing control field that maps this input pulse onto $s(z)$. The same control field maps this input pulse onto the true optimal spin wave $S_{\text{opt}}(z)$, once polarization decay and the finite length of the medium are taken into account. The details of this construction are described in Sec. B.6.2.

As an example of control field optimization, we consider the storage of three different initial pulse shapes, shown by dotted black lines in the middle row in Fig. E.5: a step with a rounded leading edge (a'), a segment of the sinc-function (b'), and a descending ramp (c'). The top row (a,b,c) shows the corresponding calculated optimal writing ($t < 0$) control pulses. Since the shape and power of the *retrieval* control pulse do not affect the memory efficiency (Sec. 2.3), we show, in the top row of Fig. E.5, two retrieval control fields for each input pulse: a flat control field (dashed) and the time-reverse of the writing control (solid). As expected, the flat control field (the same for all three inputs) results in the same output pulse [dashed in (a', b', c')] independent of the input signal pulse, because the excitation is stored in the same optimal spin wave in each case. On the other hand, using the time-reversed writing control field for retrieval yields output pulses that are time-reversed (and attenuated) copies of the corresponding input pulses. This means that the time-reversal iterations of Sec. E.4 starting with these control-signal pairs converge on the zeroth iteration, which proves the consistency of the signal optimization of Sec. E.4 with the control optimization of the present Section. The experimental data also agrees very well with numerical simulations [bottom row (a'', b'', c'') in Fig. E.5], supporting the validity of our interpretation of the data.

To further test the effectiveness of the control optimization procedure, we repeated the same measurements for eight different randomly selected pulse shapes, shown as black lines in Fig. E.6(a). Pulses #4, #6, and #8 are the same as the input pulses (a'), (b'), and (c') in Fig. E.5. For each of the eight input pulses, we calculated the optimal writing control [red lines in Fig. E.6(a)] and then measured the memory efficiency [Fig. E.6(b)], retrieving with either a constant control pulse or a time-reversed writing control pulse (open red diamonds and solid black circles, respectively). The measured efficiencies are in good agreement with each other and with the theoretically calculated maximum achievable memory efficiency of 45% (horizontal dashed line) for the given optical depth.

By performing these experiments, we found that knowledge of accurate values for the experimental parameters, such as optical depth or control field intensity, is critical for calculations of the optimal control field. Even a few percent deviation in their values caused measurable decreases in the output signal pulse amplitude. In our experiment, effective optical depth and control field Rabi frequency were computed

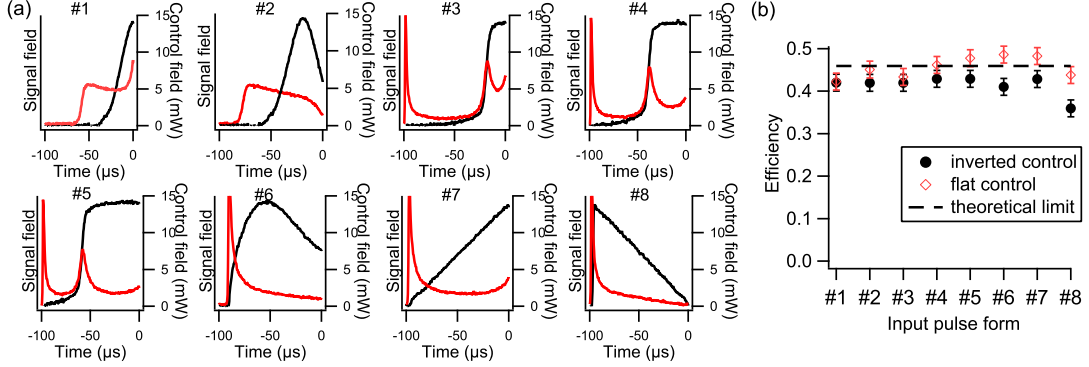


Figure E.6: (a) Eight randomly selected signal pulse shapes (black lines) and their corresponding optimal control fields (red lines). (b) Memory efficiency for the eight signal pulse shapes using calculated optimized control fields at the writing stage, and flat control fields (open red diamonds) or inverted writing control fields (solid black circles) at the retrieval stage. Theoretically predicted optimal memory efficiency is shown by a dashed line. The temperature of the cell was $60.5\text{ }^{\circ}\text{C}$ ($\alpha L = 24$).

accurately directly from measurable experimental quantities with no free parameters. The accuracy of the parameters was also verified by the excellent agreement of experimental and theoretical results of iterative optimization in Sec. E.4. We note that for some other systems, the necessary experimental parameters may be difficult to compute directly with high accuracy; in that case, they can be extracted from the iteration procedure of Sec. E.4.

E.6 Dependence of Memory Efficiency on the Optical Depth

In the previous two Sections, we verified at optical depth $\alpha L = 24$, the consistency of the signal and control optimization methods and their agreement with the three-level theory. In this Section, we study the dependence of memory efficiency on optical depth. To verify the theoretical prediction that the optimal efficiency depends only on the optical depth of the sample, we repeated the iterative signal optimization procedure (Sec. E.4) for several constant control field powers at different temperatures of the Rb cell ranging from 45°C ($\alpha L = 6$) to 77°C ($\alpha L = 88$). In Fig. E.7(a), we plot the measured efficiencies (markers) along with the maximum achievable efficiency predicated by the theory without spin decay (thin black line) and with spin decay during the storage time (thick black line). This graph allows us to make several important conclusions.

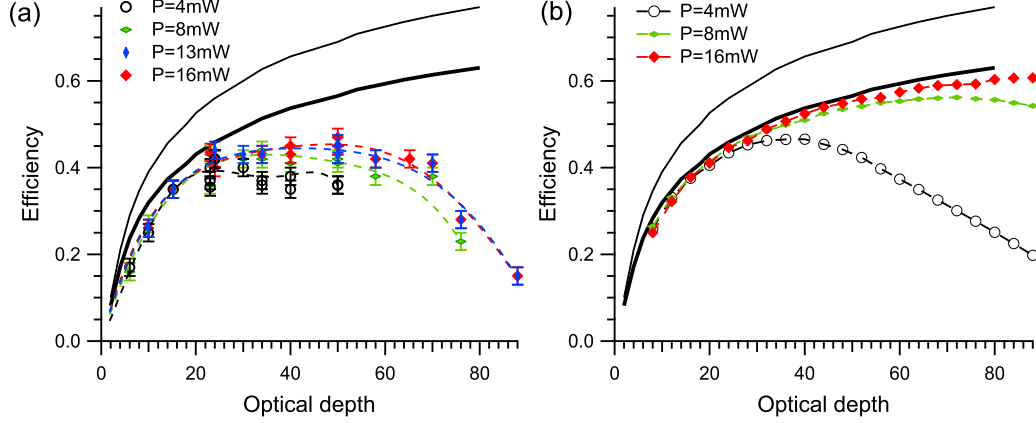


Figure E.7: Memory efficiency as a function of optical depth obtained by carrying out iterative signal optimization until convergence. (a) At each optical depth, we considered constant control fields at four different power levels (indicated on the graph) during writing and retrieval stages. Note that many experimental data points overlap since the converged efficiencies are often the same for different control fields. Dashed lines are to guide the eye. Thin and thick black solid lines show the theoretically predicted maximum efficiency assuming no spin-wave decay and assuming an efficiency reduction by a factor of 0.82 during the $100 \mu\text{s}$ storage period, respectively. (b) Thin and thick black lines are the same as in (a), while the three lines with markers are calculated efficiencies for three different control fields (indicated on the graph) assuming spin wave decay with a $500 \mu\text{s}$ time constant during all three stages of the storage process (writing, storage, retrieval).

First of all, it demonstrates that for relatively low optical depths ($\alpha L \leq 25$), the optimized memory efficiency for different control fields is the same, to within the experimental uncertainty, and approximately matches the theoretical value (thick black line). This confirms that the optimization procedure yields the maximum efficiency achievable for a given optical depth. However, for $\alpha L > 20$, the efficiency obtained with the lowest control field power (black empty circles) dropped below the efficiency obtained for higher control powers. As we will now show, the most probable reason for such deviation is spin wave decay during writing and retrieval.

As the optical depth increases, the duration of the optimal input pulse increases as well, as shown in Fig. E.8(a), following the underlying decrease of group velocity: $T \sim L/v_g \propto \alpha L$ (Sec. B.6.1). Thus, above a certain value of αL , the duration of the optimal pulse for a given control field becomes comparable with the spin wave lifetime, and the spin wave decoherence during storage and retrieval stages can no longer be ignored. Further increase of the optical depth leads to a reduction of retrieval efficiency, even though the iterative optimization procedure is still valid (Sec. B.6.5)

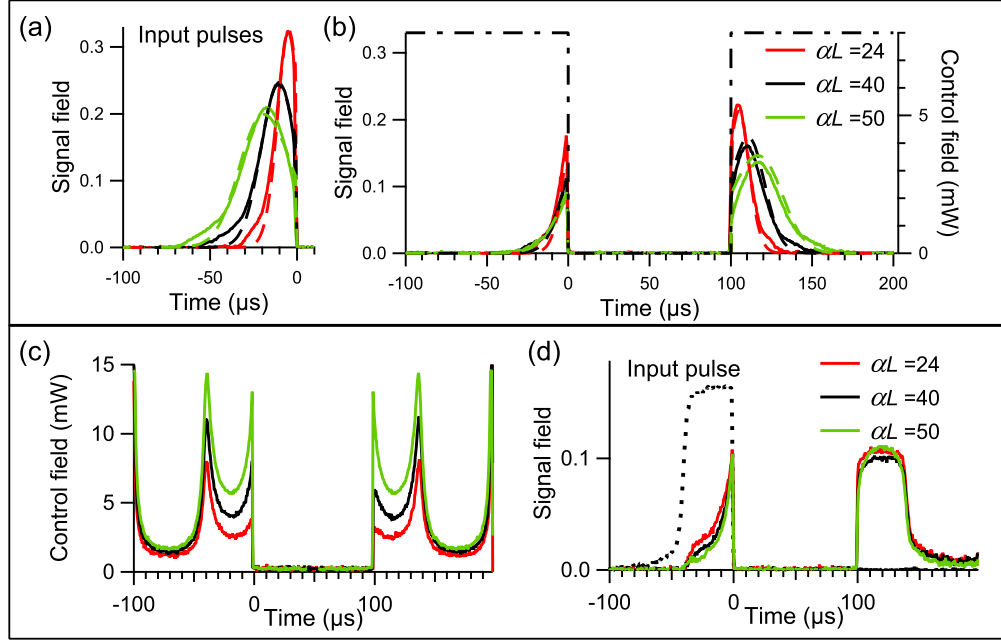


Figure E.8: Results of the optimization procedures for different optical depths: $\alpha L = 24$ (red), $\alpha L = 40$ (black), and $\alpha L = 50$ (green). The top panel [(a) and (b)] shows storage and retrieval (b) of the optimized input signal pulses (a) obtained by running iterative optimization until convergence for a constant control field of power 8mW [dash-dotted line in (b)]. Solid lines correspond to experimental results, while dashed lines show the results of numerical simulations. In the bottom panel [(c) and (d)], (c) shows the calculated optimal writing control fields ($t < 0$) for a step-like signal pulse [dotted line in (d)] and the time-reverses of these control fields used during retrieval ($t > 100 \mu\text{s}$), while (d) shows the resulting storage followed by retrieval.

and produces signal pulses that are stored and retrieved with the highest efficiency possible for a given control field and αL . Fig. E.7(b) shows the calculated maximum achievable efficiencies for different constant control powers as a function of the optical depth, taking into account spin wave decay with a $500 \mu\text{s}$ time constant during all three stages of light storage. For each control field power, the efficiency peaks at a certain optical depth, and then starts to decrease as optical depth increases further. Since lower control powers require longer optimal input pulses $T \sim L/v_g \propto 1/|\Omega|^2$ [see Fig. E.4(a)], the corresponding efficiency reaches its peak at lower optical depths. Thus, the problem of efficiency reduction posed by spin-wave decay during writing and retrieval can be alleviated by using higher control powers, and hence shorter optimal signal pulses. While this effect explains the reduction of maximum memory efficiency attained with the lowest control power for $\alpha L > 20$ [Fig. E.7(a)], other ef-

fects, discussed below, degrade the efficiency for all other control powers for $\alpha L > 25$, as indicated by the divergence of experimental data in Fig. E.7(a) from the corresponding theoretical efficiencies in Fig. E.7(b) (red and green lines). Remarkably, at these optical depths, the iterative signal optimization procedure still yields efficiencies that grow monotonically at each iteration step for the three highest control powers. This suggests that iterative signal optimization may still be yielding the optimum efficiency, although this optimum is lower than what the simple theoretical model predicts.

To further test the applicability of our optimization procedures at higher optical depths, we complemented the signal-pulse optimization [Fig. E.8(a,b)] with the corresponding control field optimization [Fig. E.8(c,d)]. We stored and retrieved input pulse #4 from Fig. E.6(a) using calculated optimal writing control fields [$t < 0$ in Fig. E.8(c)] at different optical depths $\alpha L = 24, 40, \text{ and } 50$. As expected, the overall control power was higher at higher optical depths to keep the group velocity unchanged: $L/T \sim v_g \propto \Omega^2/(\alpha L)$. For each optical depth, we used a time-reversed writing control field to retrieve the stored spin wave. This resulted in the output signal pulse shape identical to the time-reversed (and attenuated) copy of the input pulse, as shown in Fig. E.8(d). Although the memory efficiency drops below the theoretical value at these high optical depths [$\alpha L = 50$ for the green lines in Fig. E.8(c,d)], the results suggest that the calculated control field may still be optimal, since it yields the time-reverse of the input signal at the output.

To gain insight into what may limit the memory efficiency for $25 < \alpha L < 60$, we investigated the effect of resonant four-wave mixing. Thus far, we have considered only the ground-state coherence created by the control and signal fields in the one-photon resonant Λ configuration [Fig. E.1(a)]. However, the strong control field applied to the ground state $|g\rangle$ can also generate an additional Stokes field E_S , as shown in Fig. E.9(a). This process is significantly enhanced in EIT media [348, 349]. In particular, it has been shown that a weak signal pulse traversing an atomic ensemble with reduced group velocity generates a complimentary Stokes pulse that travels alongside with a comparably low group velocity [358, 359].

To determine the effect of resonant four-wave mixing on light storage, we first carried out iterative signal optimization for a constant control field pulse of 16 mW power at different optical depths, but then detected not only the signal field, but also the Stokes field, at the retrieval stage [see Fig. E.9(b)]. We see that at low optical depths, the retrieved Stokes pulse [blue empty diamonds] is negligible compared to the output signal pulse [red filled diamonds, which are the same as the red filled diamonds in Fig. E.7(a)]. However, at $\alpha L \gtrsim 25$, the energy of the output pulse in the Stokes channel becomes significant. While the energy of the retrieved signal pulse stayed roughly unchanged for $25 < \alpha L < 60$, the energy of the output Stokes pulse showed steady growth with increasing αL . Moreover, the combined energy (black empty circles) of the two pulses retrieved in the signal and Stokes channels added up to match well the theoretically predicted highest achievable efficiency (solid black

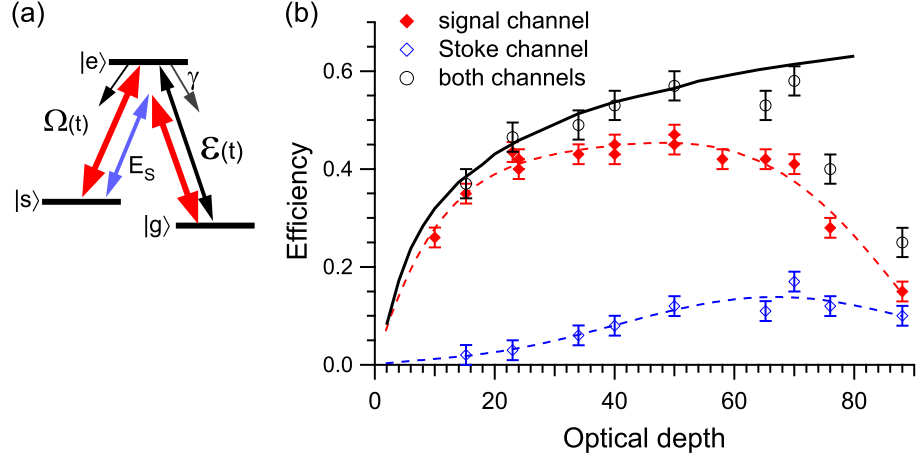


Figure E.9: (a) Level diagram illustrating Stokes field (E_S) generation due to resonant four-wave mixing. (b) Memory efficiency for retrieval in the signal channel [same as the red filled diamonds in Fig. E.7(a)], Stokes channel, and the total for both channels. The efficiencies are obtained by carrying out iterative optimization till convergence for constant writing and retrieval control fields of 16 mW power. Dashed lines are to guide the eye. The solid line (same as the thick black line in Fig. E.7) shows the theoretically predicted maximum efficiency assuming an efficiency reduction by a factor of 0.82 during the 100 μ s storage period.

line). We will study elsewhere whether this match is incidental and whether it can be harnessed for memory applications. For the purposes of the present work, we simply conclude that the effects of four-wave mixing become significant around the same value of αL (~ 25) where experiment starts deviating from theory. Therefore, four-wave mixing may be one of the factors responsible for the low experimental efficiencies at high optical depths. For a more detailed study for four-wave mixing in our system, we refer the reader to Ref. [64].

For $\alpha L > 60$, iterative signal optimization still converges, but efficiency does not grow monotonically at each iteration step, which clearly indicates the breakdown of time-reversal-based optimization. In addition, the final efficiency is significantly lower than the theoretical value (Fig. E.7). Many factors, other than four-wave mixing, may be contributing to the breakdown of time-reversal-based optimization and to the rapid decrease of memory efficiency at $\alpha L > 60$. First of all, the absorption of the control field at such high optical depths is significant (measured to be $> 50\%$). In that case, the reabsorption of spontaneous radiation contributes appreciably to spin wave decoherence [323, 355] and can make the spin wave decay rate γ_s grow with αL , reducing the light storage efficiency [63]. Spin-exchange collision rate [354], which destroys the spin-wave coherence, also becomes significant at high Rb density,

reducing spin wave lifetime even further.

E.7 Conclusions

We have studied in detail two quantum memory optimization protocols in warm Rb vapor and demonstrated their consistency for maximizing memory efficiency. We have also observed good agreement between our experimental data and theoretical predictions for relatively low optical depths (< 25), both in terms of the highest memory efficiency and in terms of the optimized pulse shapes. At higher optical depths, however, the experimental efficiency was lower than predicted. We observed that resonant four-wave mixing processes became important at these higher optical depths. We expect our studies to be of importance for enhancing the performance of ensemble-based quantum memories for light.

Appendix F

Appendices to Chapter 4

Here we present supplementary materials for Chapter 4.

F.1 The Order t^4/U^3 Hamiltonian and the Error Estimate

In this Section, we consider the t^4/U^3 corrections to the spin Hamiltonian and estimate the gate errors in the presence of these corrections.

We begin with the bosonic two-component single-band Hubbard model in a 1D lattice, with the transverse motion frozen:

$$H = - \sum_{j,\alpha} t_\alpha (a_{j\alpha}^\dagger a_{j+1\alpha} + a_{j+1\alpha}^\dagger a_{j\alpha}) + U_{sg} \sum_j m_{jg} m_{js} + \sum_{j,\alpha} \frac{U_{\alpha\alpha}}{2} m_{j\alpha} (m_{j\alpha} - 1), \quad (\text{F.1})$$

where $a_{j\alpha}^\dagger$ creates a boson on site j in internal state $\alpha = g, s$ and $m_{j\alpha} = a_{j\alpha}^\dagger a_{j\alpha}$. We assume that there is one atom per each of the N sites and that $t_g, t_s \ll U_{gg}, U_{ss}, U_{sg}$. To obtain the spin Hamiltonian to order t^3/U^4 , we perform two consecutive Schrieffer-Wolff transformations. To simplify the resulting Hamiltonian, we assume that $t_g = t_s = t$ and $U_{gg} = U_{ss} = U$, which ensures that all the terms that are odd under the exchange of $|s\rangle$ and $|g\rangle$ vanish. Defining β via $U_{sg} = U/\beta$, defining $\epsilon = (t/U)^2$, ignoring boundary effects, and dropping terms proportional to identity, the resulting Hamiltonian is

$$H = \sum_{j=1}^{N-1} \left[-J(S_j^+ S_{j+1}^- + S_j^- S_{j+1}^+) + V S_j^z S_{j+1}^z - J_2(S_j^+ S_{j+2}^- + S_j^- S_{j+2}^+) + V_2 S_j^z S_{j+2}^z \right], \quad (\text{F.2})$$

where

$$J = \left[2\beta - \frac{4\beta(2 - 3\beta + \beta^2 + 2\beta^3)}{2 + \beta} \epsilon \right] \frac{t^2}{U}, \quad (\text{F.3})$$

$$V = \left[4(\beta - 2) - \frac{8(-2 - \beta - 2\beta^2 + \beta^3 + 2\beta^4)}{2 + \beta} \epsilon \right] \frac{t^2}{U}, \quad (\text{F.4})$$

$$J_2 = - \frac{2\beta(-1 - 6\beta - \beta^2 + \beta^3)}{2 + \beta} \frac{t^2}{U} \epsilon, \quad (\text{F.5})$$

$$V_2 = \frac{4(-4 - \beta - 2\beta^2 - \beta^3 + \beta^4)}{2 + \beta} \frac{t^2}{U} \epsilon. \quad (\text{F.6})$$

So t^3/U^4 terms modified the original J and V terms, as well as generated next-nearest-neighbor hopping ($\propto J_2$) and next-nearest-neighbor interactions ($\propto V_2$). We note that β can be adjusted by shifting g and s lattices relative to each other or by using a Feshbach resonance [138, 139].

We apply the Jordan-Wigner transformation defined in Chapter 4 and rewrite H as

$$H = H_0 + H_1 + H_V, \quad (\text{F.7})$$

$$\begin{aligned} H_0 &= \sum_j \left[-J(c_j^\dagger c_{j+1} + c_{j+1}^\dagger c_j) - J_2(c_j^\dagger c_{j+2} + c_{j+2}^\dagger c_j) \right] \\ &= \sum_k \epsilon(k) c_k^\dagger c_k, \end{aligned} \quad (\text{F.8})$$

$$H_1 = \sum_j \left[-J_2(-2n_{j+1})(c_j^\dagger c_{j+2} + c_{j+2}^\dagger c_j) + V_2 n_j n_{j+2} \right], \quad (\text{F.9})$$

$$H_V = V \sum_j n_j n_{j+1}. \quad (\text{F.10})$$

In H_V and in the expression for the next-nearest-neighbor interaction ($\propto V_2$), we omitted the terms that give unimportant linear and constant phases. Here c_k are defined as in Chapter 4 and the dispersion is

$$\epsilon(k) = -2J \cos(k) - 2J_2 \cos(2k). \quad (\text{F.11})$$

In other words, t^3/U^4 terms result in a deviation of the dispersion from the $\cos(k)$ behavior. Notice that H_1 and H_V vanish in the single-spin-wave subspace.

To minimize pulse distortion, we find k_0 (near $\pi/2$ for $\epsilon \ll 1$) such that $\epsilon''(k_0) = 0$. We then define the velocity as $v = \epsilon'(k_0)$ and propagation time as $T = N/(2v)$. The propagation of the single f spin wave is then given by

$$|\psi_1(\tau)\rangle = e^{-iH\tau} |\psi_1(0)\rangle, \quad (\text{F.12})$$

where

$$|\psi_1(0)\rangle = \sum_j f(j, 0)|j\rangle, \quad (\text{F.13})$$

$$|j\rangle = c_j^\dagger |\text{vac}\rangle,$$

$$f(j, 0) = \frac{1}{\mathcal{N}} \begin{cases} \exp\left(-\frac{(N/4-j)^2}{4w^2} + ik_0j\right) & \text{if } j \leq N/2, \\ 0 & \text{if } j > N/2, \end{cases} \quad (\text{F.14})$$

and \mathcal{N} is a normalization constant ensuring that $\sum_j |f(j, 0)|^2 = 1$.

Ideal propagation is given by

$$|\psi_1^{(0)}(T)\rangle = \sum_j f^{(0)}(j, T)|j\rangle, \quad (\text{F.15})$$

where

$$f^{(0)}(j, T) = \frac{1}{\mathcal{N}} \begin{cases} 0 & \text{if } j \leq N/2, \\ \exp\left(-\frac{(3N/4-j)^2}{4w^2} + ik_0j - i\epsilon(k_0)T\right) & \text{if } j > N/2. \end{cases} \quad (\text{F.16})$$

We can then find w that minimizes the deviation of true evolution from ideal propagation

$$E_1 = \left| |\psi_1^{(0)}(T)\rangle - |\psi_1(T)\rangle \right|^2. \quad (\text{F.17})$$

We use E_1 instead of infidelity $1 - \left| \langle \psi_1^{(0)}(T) | \psi_1(T) \rangle \right|^2$ because the former is more strict: it makes sure that the phase is correct.

We then define the propagation of both spin waves as

$$|\psi_2(\tau)\rangle = e^{-iH\tau} |\psi_2(0)\rangle, \quad (\text{F.18})$$

where

$$|\psi_2(0)\rangle = \sum_{j < j'} f(j, 0)h(j', 0)|j, j'\rangle, \quad (\text{F.19})$$

and

$$h(j, 0) = \frac{1}{\mathcal{N}} \begin{cases} 0 & \text{if } j \leq N/2, \\ \exp\left(-\frac{(3N/4-j)^2}{4w^2} - ik_0j\right) & \text{if } j > N/2. \end{cases} \quad (\text{F.20})$$

Since we would like to obtain a nonlinear phase equal exactly to π , ideal propagation is given by

$$|\psi_2^{(0)}(T)\rangle = - \sum_{j < j'} h^{(0)}(j, T) f^{(0)}(j', T) |j, j'\rangle, \quad (\text{F.21})$$

where

$$h^{(0)}(j, T) = \frac{1}{\mathcal{N}} \begin{cases} \exp\left(-\frac{(N/4-j)^2}{4w^2} - ik_0j - i\epsilon(k_0)T\right) & \text{if } j \leq N/2, \\ 0 & \text{if } j > N/2. \end{cases} \quad (\text{F.22})$$

We want to minimize the deviation of true evolution from ideal propagation

$$E_2 = \left| |\psi_2^{(0)}(T)\rangle - |\psi_2(T)\rangle \right|^2. \quad (\text{F.23})$$

Numerics show that, for $\epsilon \ll 1$, out of the two terms in H_1 , the first term ($\propto J_2$) has the dominant effect on E_2 . Moreover, the main effect is simply a phase, which can be approximated by $\theta_J = 8J_2 \sin(k_0)^2/v$. On the other hand, the main effect of H_V is also a phase [see Eq. (F.26) evaluated at $k = -p = k_0$]:

$$\theta_V = 2 \tan^{-1} \left[\frac{\sin(k_0)}{\frac{V}{2J} + \cos(k_0)} \right] - 2k_0. \quad (\text{F.24})$$

Thus, in order to ensure that the overall phase picked up during the evolution of two spin waves is π , for a given $\epsilon \ll 1$, we can solve for β the equation $\theta_J + \theta_V = 0$. For example, for $\epsilon = 0.01$, we get $\beta = 2.353$. Using these values of ϵ and β , we then solve $\epsilon''(k_0) = 0$ to obtain $k_0 = 1.492$ and $v = \epsilon'(k_0) = 8.3t^2/U = 0.083U$, so that $T = N/(2v) = N/(0.166U)$. For $N = 100$, we then minimize E_1 to obtain $w = 6.6$ and $E_1 = 3 \times 10^{-4}$. Numerics then give $E_2 \approx 2E_1$. In other words, in this example, the effect of V_2 is so small and θ_V compensates so well for θ_J that the full gate error is dominated by simple errors from H_0 and not by the errors due to H_1 or H_V .

If, alternatively, we took $V = 0$ and did not compensate for θ_J , the gate error would have been $\sim E_2 \sim \theta_J^2 \sim \epsilon^2 = (t/U)^4$. The procedure described above for setting $\theta_J + \theta_V = 0$ reduces this error, so that at $\epsilon = 0.01$, this error is so small that it is overwhelmed by $2E_1$ even at $N = 100$, where $2E_1 \approx 6 \times 10^{-4}$.

We also note that one might be able to work at ϵ as large as 0.1, which might allow to shorten the gate time T . At $\epsilon = 0.1$, it is more difficult to use V for compensating the phase θ_J because the tuning of β strongly affects all the terms in the Hamiltonian at this large value of ϵ . However, if one is content with an imperfect nonlinear phase (such as $\approx 0.8\pi$ instead of π), then at $N = 100$ and $\epsilon = 0.1$, numerics give an error as low as 0.002.

F.2 Optimization of Pulse Width

In Chapter 4, we noted that the error due to the nonlinearity of the dispersion falls off very quickly with N . In the previous Section, we used numerical optimization to compute the optimal wavepacket width w . In this Section, we describe the two

errors that contribute to wavepacket distortion in the presence of H_0 and discuss how fast the optimized error falls off.

We consider the Hamiltonian H_0 in Eq. (F.8) and assume that $J_2 = 0$, so that $\epsilon(k) = -2J \cos(k)$. We study the propagation of the f spin wave, whose initial state is defined in Eqs. (F.13,F.14) with $k_0 = \pi/2$. We would like to minimize E_1 [Eq. (F.17)] with respect to the width w of the spin wave.

Two effects contribute to E_1 . The first effect is due to the nonlinearity of the dispersion. Since the spin wave is centered at the inflection point ($\epsilon''(k_0) = 0$), the leading nonlinearity in the dispersion is $\sim J(\Delta k)^3 \sim J/w^3$, where Δk is the spread of the spin wave in k space. Perturbative treatment then gives an error $p_1 \propto (TJ/w^3)^2 \propto N^2/w^6 = 1/(N^4 x^6)$, where we defined $x = w/N$. The second effect is due to the cut off of the Gaussian wavepacket at $j = 0$ and $j = N/2$. The corresponding error p_2 has a sharp dependence on x : it falls off very quickly as x decreases.

The total error E_1 can be estimated as $E_1 = p_1 + p_2$. At each value of N , E_1 should be optimized with respect to x to give the optimal value $x = x_0$ and the corresponding optimal E_1 . Since p_2 varies quickly with x , the optimal value x_0 varies slowly with N . If we suppose that x_0 is independent of N , then E_1 simply falls off with N as $1/N^4$. In reality, due to the weak dependence of x_0 on N , E_1 falls off with N slightly slower than $1/N^4$.

F.3 Bethe Ansatz Solution

In this Section, we present a few details regarding the derivation of Eqs. (4.4) and (4.5).

Throughout this Section, we use the Hamiltonian in Eq. (4.2). Assuming periodic boundary conditions, this Hamiltonian can be diagonalized exactly via Bethe ansatz [128] with eigenfunctions of the form

$$|\Psi\rangle_{k,p} = \frac{1}{\mathcal{N}_{k,p}} \sum_{j < j'} \left(e^{ikj} e^{ipj'} - e^{i\theta(k,p)} e^{ipj} e^{ikj'} \right) |j, j'\rangle, \quad (\text{F.25})$$

with energy $\epsilon(k) + \epsilon(p)$, where $\epsilon(k) = -2J \cos(k)$. Here k and p can be adjusted to satisfy the periodic boundary conditions [128], $\mathcal{N}_{k,p}$ is a normalization constant, and

$$\theta(k, p) = 2 \tan^{-1} \left[\frac{\sin(k) - \sin(p)}{\frac{V}{J} + \cos(k) + \cos(p)} \right] + 2(p - k). \quad (\text{F.26})$$

Taking the limit of large N and assuming our spin waves vanish at the boundaries, we can ignore boundary effects. Then considering the limit $N \rightarrow \infty$ and assuming that we would like to describe two spin waves localized in k -space near $-\pi/2$ and $\pi/2$, we can replace $\theta(k, p)$ with $\theta_0 = \theta(\pi/2, -\pi/2)$, approximate $\mathcal{N}_{k,p} \approx N$, and take k

and p quantized in the simple manner (from $-\pi$ to π in intervals of $2\pi/N$) to obtain Eq. (4.4).

We now show how to obtain Eq. (4.5) from Eq. (4.4). For the purposes of describing our two spin waves, $|\Psi\rangle_{k,p}$ form an orthonormal eigenbasis. Therefore, the evolution is given by

$$|\Psi(\tau)\rangle = \sum_{k < p} \langle \Psi_{k,p} | \Psi(0) \rangle e^{-i\tau(\epsilon(k) + \epsilon(p))} |\Psi\rangle_{k,p}. \quad (\text{F.27})$$

Using $|\Psi(0)\rangle$ given in Eq. (F.19), we find

$$\langle \Psi_{k,p} | \Psi(0) \rangle \approx \tilde{f}(k, 0) \tilde{h}(p, 0) |j, j'\rangle, \quad (\text{F.28})$$

which then yields Eq. (4.5) when plugged into Eq. (F.27). We checked Eq. (4.5) numerically for $N = 100$, $k_0 = \pi/2$, $w = 6$, and V between 0 and $200J$. The resulting deviation [Eq. (F.23)] of the true evolution from ideal propagation [Eq. (4.5)] for all V was less than 0.01.

F.4 Implementation with Fermionic Atoms

One possible extension of the implementation discussed in Chapter 4 is the use of fermionic, rather than bosonic, atoms in a chain. For fermions, Eq. (4.1) also holds except the XY interaction is antiferromagnetic, $J = -2t_g t_s / U_{sg}$, while $V = 2(t_g^2 + t_s^2) / U_{sg}$ [126]. This form of V makes it harder to achieve $V = 0$ (although a Feshbach resonance [138, 139] might do the job). On the other hand, it is easier to prepare the band insulator of fermionic g atoms than the bosonic Mott insulator. Other than that, the gate can be accomplished in the same way as for bosons, except the dispersion will be upside down, so the carrier momenta of the two spin waves will have to be switched.

Appendix G

Appendices to Chapter 7

Here we present supplementary materials for Chapter 7.

G.1 Nuclear-Spin Independence of the Scattering Lengths

Independence of scattering lengths from the nuclear spin is a key assumption of Chapter 7. This feature allows us to obtain SU(N)-symmetric models with N as large as 10 and distinguishes alkaline-earth atoms from alkali atoms, which can exhibit at most an SO(5) symmetry [244, 360, 361, 362], a symmetry that is weaker than SU(4). The assumption of nuclear-spin independence of scattering lengths is consistent with recent experiments, where - within experimental precision - the clock shift does not depend on how the Zeeman levels are populated [202, 196]. In this Section, we present the theoretical justification of this assumption.

Direct magnetic dipole-dipole coupling between the nuclear spins of two atoms sitting on the same site of an optical lattice is negligible: even for two magnetic dipole moments as large as 10 nuclear magnetons at a distance of 10 nm (which is significantly smaller than the confinement typically achieved in optical lattices [204]), the interaction energy still corresponds to a frequency smaller than one Hertz. Therefore, nuclei can affect the collisions only via the electrons. All four scattering lengths (a_{gg} , a_{eg}^{\pm} , and a_{ee}) are, thus, expected to be independent of the nuclear spin because both g and e have total electronic angular momentum J equal to zero, which results in the decoupling between nuclear and electronic degrees of freedom during the course of a collision. The decoupling during a collision is a consequence of the fact that each of the four molecular electronic states that correlate with the $J = 0$ separated atom pair has zero projection Ω of total electronic angular momentum on the molecular axis. The nuclear spins in this case can only couple very weakly to other molecular states, even if there is a molecular curve crossing.

While the short-range potential energy structure for a molecule like Sr₂ is very

complex for the excited states [363, 364], we will now show that scattering length differences among different combinations of nuclear spin projections for the same $\Omega = 0$ potential are expected to be very small. The scattering length a can be computed as $a = \bar{a}[1 - \tan(\Phi - \pi/8)]$, where \bar{a} is the average scattering length governed by the asymptotic behavior of the potential and Φ is the semiclassical phase computed at zero energy from the classical turning point R_0 to infinity: $\Phi = \int_{R_0}^{\infty} dR \sqrt{M[-V(R)]}/\hbar$, where $-V(R)$ is the (positive) depth of the interaction potential at separation R and $M/2$ is the reduced mass [285]. Defining $R(t)$ as the classical trajectory from time $t = -\infty$ to time $t = \infty$ of a particle of mass $M/2$ at zero energy in the potential $V(R)$, we can rewrite the phase as $\Phi = -\int_{-\infty}^{\infty} dt V(R(t))/\hbar$. The order of magnitude of the change $\delta\Phi$ in the phase associated with different nuclear spin projections can, thus, be estimated as $\delta\Phi \sim \Delta t \delta V/\hbar$, where Δt is the total time in the short-range part of the collision and δV is the typical energy difference associated with different nuclear spin projections during this time. Since δV vanishes at $R \rightarrow \infty$, only the short range molecular region contributes to the phase difference. Therefore, assuming $\delta\Phi \ll 1$, $a \sim \bar{a}$, and $|\cos(\Phi - \pi/8)| \sim 1$, the nuclear-spin-dependent variation δa in the scattering length can be estimated as $\delta a/a \sim \delta\Phi \sim \Delta t \delta V/\hbar$.

Turning to the actual numbers, Δt can be estimated from the depth ($\sim 10^3 \text{ cm}^{-1} hc$) and the range (~ 10 Bohr radii) of the appropriate interatomic potential (see e.g. [363, 364]) to be $\Delta t \approx 1$ ps. For g - g collisions, $\delta V/h$ can be estimated by the second-order formula $E_{\text{hf}}^2/(hE_{\text{opt}}) \sim 200$ Hz, where $E_{\text{hf}}/h \sim 300$ MHz is the approximate value for the hyperfine splittings in 3P_1 in ^{87}Sr and $E_{\text{opt}}/h \sim 400$ THz is the optical energy difference between 1S_0 and 3P_1 in ^{87}Sr . This yields the following estimate for the dependence of a_{gg} on the nuclear spin: $\delta a_{gg}/a_{gg} \sim \delta\Phi \sim 10^{-9}$. For e - e and e - g collisions, an analogous second-order formula would use the fine structure splitting between 3P_1 and 3P_0 in ^{87}Sr ($E_f/h \sim 6$ THz) instead of E_{opt} to yield $\delta\Phi \sim 10^{-7}$. However, the latter estimate ($\delta\Phi \sim 10^{-7}$) is too optimistic since molecular states that are split by E_f at large interatomic separations may come orders of magnitude closer at short range [365]. Therefore, a more realistic conservative estimate would use the first-order formula $\delta V \sim E_{\text{hf}}$ to yield $\delta a_{ee}/a_{ee} \sim \delta a_{eg}^{\pm}/a_{eg}^{\pm} \sim \delta\Phi \sim 10^{-3}$. It is important to note, however, that these are all only very rough estimates. For example, hyperfine coupling in a molecule will differ from the hyperfine coupling in separated atoms. In fact, since it is very difficult to predict $\delta a/a$ accurately, these values would need to be measured. To conclude this Section, we would like to emphasize that, as mentioned in the main text, if the small nuclear-spin dependence of a_{ee} and a_{eg}^{\pm} is not negligible for some applications, one can use two different ground state atomic species instead of a ground and an excited state of one species.

G.2 Likelihood of Lossy e - e Collisions and Possible Solutions

Collisions of two e atoms are likely to be accompanied by large loss [250]. This can occur if the molecular 0_g^+ potential that correlates with the e - e atoms undergoes an avoided crossing with a potential curve that correlates with a lower energy pair of separated atoms (see, for example, Ref. [364]). Similar crossings that result in inelastic energy transfer collisions were examined for $^1P_1+^1S_0$ collisions of alkaline earth atoms in Ref. [366]. The likelihood of a relatively high probability of an inelastic event during such a crossing with species such as Sr or Yb means that the imaginary part b_{ee} of the scattering length is expected to be large. However, just like a_{ee} , b_{ee} can not be calculated accurately from the potentials but would need to be measured.

The possible effects of b_{ee} on the four examples we discuss [Eqs. (7.6-7.8) and Eq. (G.3)] are as follows. $H_{(p,0)}$ [Eq. (7.7)] is, of course, not affected because it involves only g atoms. In $H_{(1,1)}$ [Eq. (G.3)] and H_{KLM} [Eq. (7.8)], the e lattice is assumed to be so deep that J_e is negligible compared to $U_{ee} + V_{ex}$ and U_{ee} , respectively, or to the experimental timescale, thus, fully suppressing tunneling of e atoms and occupation of one site by more than one e atom. The presence of an imaginary part b_{ee} of the e - e scattering length will give an effective nonzero width to the state with more than one e atom per site and can, therefore, only further suppress this tunneling by a Zeno-like effect [367, 191, 368].

Therefore, $H_{(1,0)}$ [Eq. (7.6)] is the only example that can be affected by large b_{ee} . In order for $H_{(1,0)}$ to contain a nonnegligible term proportional to J_e^2/U_{ee} , the ratio $|b_{ee}/a_{ee}|$ would need to be very small [369]. Several approaches to avoid the losses associated with b_{ee} in $H_{(1,0)}$ are possible. First, the large variety of stable atoms with two valence electrons (which includes not only alkaline-earths, but also Zn, Cd, Hg, and Yb) may have coincidentally an isotope with small $|b_{ee}/a_{ee}|$, which is more likely for lighter atoms [366]. Second, while obtaining a good optical Feshbach resonance [139, 370, 248, 371, 372] to reduce $|b_{ee}/a_{ee}|$ might not be possible, it should be possible to use optical Feshbach resonances to enhance b_{ee} and, thus, suppress [367, 191, 368] the virtual occupation of one site by two e atoms; $H_{(1,0)}$ would then have the same form as in Eq. (7.6), except with U_{ee} effectively set to infinity. Notice that here we suggest to use optical Feshbach resonances to affect e - e scattering, which is different from the typical application to g - g scattering [139, 370, 248, 371, 372]. Third, one can consider using a different ground state atom to represent state $|e\rangle$, which would set $V_{ex} = 0$ in $H_{(1,0)}$. Finally, one could simply use an e -lattice that is deep enough to make J_e negligible, which would, however, lead to the loss of terms in $H_{(1,0)}$ that exchange the pseudospin between neighboring sites.

G.3 Experimental Tools Available for Alkaline-Earth Atoms

Many experimental tools, such as tuning the interaction strength by adjusting laser intensities [204], are common to both alkali and alkaline-earth atoms. There are, however, some experimental tools specific to alkaline earths; we review them in this Section.

First, a combination of optical pumping [215] and direct coherent manipulation of the $|g\rangle - |e\rangle$ transition in the presence of a magnetic field [195, 215] can be used (see Chapter 6) to prepare any desired single-atom state within the $2(2I + 1)$ -dimensional manifold with basis $|\alpha m\rangle$, where $\alpha = g$ or e and $m = -I, \dots, I$. This coherent manipulation can also be used to exchange quantum information between nuclear spin states and electronic states. Second, by using far-detuned probe light or a large magnetic field to decouple the electronic angular momentum J and the nuclear spin I , the electronic $|g\rangle - |e\rangle$ degree of freedom can be measured by collecting fluorescence without destroying the nuclear spin state (see Chapter 6). Fluorescence measurement of the nuclear spins can be achieved by mapping nuclear spin states onto electronic states (see Chapter 6 and Ref. [191]): for example, for a spin-1/2 nucleus, a π pulse between $|g, m = 1/2\rangle$ and $|e, m = -1/2\rangle$ allows one to accomplish a swap gate between the nuclear $\{1/2, -1/2\}$ qubit and the electronic $\{e, g\}$ qubit. Single-site spatial resolution during the coherent manipulation and fluorescence measurement can be achieved using magnetic field gradients [191] or dark-state-based techniques (see Chapters 5, 6 and Ref. [175]) that rely on an auxiliary laser field whose intensity vanishes at certain locations. Third, an appropriate choice of laser frequencies allows one to obtain independent lattices for states g and e [191]. Finally, optical Feshbach resonances [139] may be used to control scattering lengths site-specifically and nearly instantaneously.

G.4 Enhanced Symmetries

While in the general case, our Hubbard model [Eq. (7.2)] satisfies $U(1) \times SU(N)$ symmetry, for particular choices of parameters, higher symmetry is possible. In particular, if $J_g = J_e$ and the interaction energies for all states within the pseudo-spin triplet are equal ($U_{gg} = U_{ee} = U_{eg}^+$), the full $SU(2)$ symmetry (not just $U(1)$) in the pseudo-spin space is satisfied. Alternatively, if $V_{ex} = 0$, then both $S_n^m(i, g)$ and $S_n^m(i, e)$ generate $SU(N)$ symmetries resulting in the overall $U(1) \times SU(N) \times SU(N)$ symmetry. Finally, if both conditions are satisfied, i.e. all four U_X are equal and $J_g = J_e$, then H satisfies the full $SU(2N)$ symmetry ($2N$ can be as high as 20) generated by

$$S_{\beta n}^{\alpha m} = \sum_j S_{\beta n}^{\alpha m}(j) = \sum_j c_{j\beta n}^\dagger c_{j\alpha m}, \quad (\text{G.1})$$

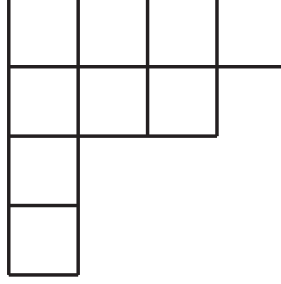


Figure G.1: A general Young diagram.

in which case the interaction reduces to $\frac{U}{2} \sum_j n_j (n_j - 1)$, where $n_j = n_{jg} + n_{je}$.

In the case when $|e\rangle$ and $|g\rangle$ correspond to two ground states of two different atoms (with nuclear spin I_e and I_g , respectively), we will have $a_{eg}^+ = a_{eg}^-$ (i.e $V_{ex} = 0$), which is equivalent to imposing $U(1) \times SU(N_g = 2I_g + 1) \times SU(N_e = 2I_e + 1)$ symmetry, where $SU(2I_\alpha + 1)$ is generated by $S_n^m(i, \alpha)$. While for $I_g \neq I_e$, the m index in $c_{j\alpha m}$ will run over a different set of values depending on α , the Hubbard Hamiltonian will still have the form of Eq. (7.2) (except with $V_{ex} = 0$). If one further assumes that $J_g = J_e$ and $U_{gg} = U_{ee} = U_{eg}$, the interaction satisfies the full $SU(N_g + N_e)$ symmetry. It is worth noting that for the case of two different ground state atoms, this higher symmetry is easier to achieve than for the case of two internal states of the same atom, since $a_{eg}^+ = a_{eg}^-$ automatically. Thus, in particular, it might be possible to obtain $SU(18)$ with ^{87}Sr ($I = 9/2$) and ^{43}Ca ($I = 7/2$) simply by adjusting the intensities of the two lattices (to set $J_g = J_e$ and $U_{gg} = U_{ee}$) and then shifting the two lattices relative to each other (to set $U_{eg} = U_{gg}$).

Enhanced symmetries of the Hubbard model [Eq. (7.2)] are inherited by the spin Hamiltonian [Eq. (7.5)]. In particular, imposing $SU(2) \times SU(N)$ instead of $U(1) \times SU(N)$ forces $\kappa_{ge}^{ij} = \kappa_{ge}^{ji}$, $\tilde{\kappa}_{ge}^{ij} = \tilde{\kappa}_{ge}^{ji}$, $\kappa_g^{ij} = \kappa_e^{ij} = \kappa_{ge}^{ij} + \tilde{\kappa}_{ge}^{ij} \equiv \kappa^{ij}$, $\lambda_{ge}^{ij} = \lambda_{ge}^{ji}$, $\tilde{\lambda}_{ge}^{ij} = \tilde{\lambda}_{ge}^{ji}$, $\lambda_g^{ij} = \lambda_e^{ij} = \lambda_{ge}^{ij} + \tilde{\lambda}_{ge}^{ij} \equiv \lambda^{ij}$. Alternatively, imposing $U(1) \times SU(N) \times SU(N)$ forces $\tilde{\kappa}_{ge}^{ij} = \tilde{\lambda}_{ge}^{ij} = 0$. Finally, imposing the full $SU(2N)$ forces the satisfaction of both sets of conditions, yielding

$$H = \sum_{\langle i,j \rangle} \left[\kappa^{ij} n_i n_j + \lambda^{ij} S_{\alpha m}^{\beta n}(i) S_{\beta n}^{\alpha m}(j) \right], \quad (\text{G.2})$$

which is, of course, equivalent to restricting Eq. (7.5) to g -atoms only and extending labels m and n to run over $2N$ states instead of N .


$$(p, q) = (1, 1)$$


Figure G.2: $(p, q) = (1, 1)$ Young diagram.

G.5 Brief Review of Young Diagrams

Irreducible representations of $SU(2)$ are classified according to the total half-integer angular momentum J and have dimension $2J + 1$. On the other hand, a (semistandard) Young diagram, instead of a single value J , is used to describe an irreducible representation of $SU(N)$ for a general N [373, 374]. As shown in the example in Fig. G.1, a Young diagram has all its rows left-aligned, has the length of rows weakly decreasing from top to bottom, and has at most N rows. The dimension of the representation corresponding to a given diagram is the number of ways to fill the diagram with integers from 1 to N such that the numbers weakly increase across each row and strictly increase down each column. For our purposes, the number of boxes in the diagram is the number of atoms on the site, and the diagram describes the (nuclear) spin symmetry of the particular chosen single-site energy manifold. In particular, columns represent antisymmetrized indices, while rows are related to (but do not directly represent) symmetrized indices. It is the relation between antisymmetrized indices and the columns that limits the number of rows to N . On the other hand, since the full wavefunction (spin and orbital) on each site must satisfy complete fermionic antisymmetry, the relation between rows and symmetrized indices and the fact that we have only two orbital states (g and e) force all our diagrams to have at most two columns.

G.6 The $(p, q) = (1, 1)$ Spin Hamiltonian and the Spin-1 Heisenberg Antiferromagnet

In the main text, we discussed two special cases of the spin Hamiltonian $H_{(p,q)}$, both of which had a single-column $SU(N)$ representation on each site (i.e. $q = 0$). In this Section, we discuss the simplest $SU(N)$ representation with two columns, $(p, q) = (1, 1)$ [see Fig. G.2]. It can be obtained when there is one g and one e atom per site in the electronic singlet $|ge\rangle - |eg\rangle$ configuration. Setting $J_e = 0$ to avoid e - e

collisions, $H_{(p,q)}$ reduces to

$$H_{(1,1)} = \frac{J_g^2}{2(U_{gg} + V_{\text{ex}})} \sum_{\langle i,j \rangle} S_{ij}^2. \quad (\text{G.3})$$

The case of $N = 2$ is the spin-1 antiferromagnetic Heisenberg model. This model has a 1D ground state with hidden topological structure [375]. Recently, applications of related models in one-way quantum computation have been proposed [376, 377]. Models with more complicated two-column representations may have exotic chiral spin liquid ground states that support non-Abelian anyons and that might thus be used for topological quantum computation [243].

G.7 The Kugel-Khomskii Model and the Double-Well Phase Diagram

In the main text, we omitted the values of the parameters in $H_{(p,q)}$ that characterize the Kugel-Khomskii model $H_{(1,0)}$ [Eq. (7.6)]. In this Section, we present these parameters. We also present a detailed discussion of the double-well case phase diagram.

The parameters in $H_{(p,q)}$ that characterize the Kugel-Khomskii model $H_{(1,0)}$ [Eq. (7.6)] are $\lambda_g^{ij} = -\kappa_g^{ij} = \frac{2J_g^2}{U_{gg}} \equiv -\kappa_g$, $\lambda_e^{ij} = -\kappa_e^{ij} = \frac{2J_e^2}{U_{ee}} \equiv -\kappa_e$, $\kappa_{ge}^{ij} = -\frac{J_e^2 + J_g^2}{2U_{eg}^+} - \frac{J_e^2 + J_g^2}{2U_{eg}^-} \equiv \kappa_{ge}$, $\lambda_{ge}^{ij} = \frac{J_e^2 + J_g^2}{2U_{eg}^+} - \frac{J_e^2 + J_g^2}{2U_{eg}^-} \equiv \lambda_{ge}$, $\tilde{\kappa}_{ge}^{ij} = \frac{J_e J_g}{U_{eg}^-} - \frac{J_e J_g}{U_{eg}^+} \equiv \tilde{\kappa}_{ge}$, $\tilde{\lambda}_{ge}^{ij} = \frac{J_e J_g}{U_{eg}^-} + \frac{J_e J_g}{U_{eg}^+} \equiv \tilde{\lambda}_{ge}$. To avoid loss in e - e collisions, we assume for the rest of this Section that $U_{ee} = \infty$ (see Sec. G.2 for a discussion of losses in e - e collisions).

The nontrivial orbital-orbital, spin-spin, and spin-orbital interactions in $H_{(1,0)}$ [Eq. (7.6)] result in competing orders, with the actual ground-state order dependent on the parameters of the Hamiltonian $H_{(1,0)}$. To get a sense of the possible orders, we consider the case $N = 2$ (with the spin states denoted by \uparrow and \downarrow) and discuss the double-well problem, with the wells denoted by L (left) and R (right). Due to the large optical energy separating e and g , which we have ignored after Eq. (7.1), the three manifolds of constant $T^z = T_L^z + T_R^z$ ($T^z = -1, 0, 1$) should each be considered separately.

The four states in the $T^z = 1$ manifold, the subspace of two e atoms, are $|ee\rangle|s\rangle$ and $|ee\rangle|t\rangle$. Here $|ee\rangle = |ee\rangle_{LR}$ is the orbital (or pseudo-spin) state, while $|t\rangle = |\uparrow\uparrow\rangle_{LR}, |\downarrow\downarrow\rangle_{LR}, \frac{1}{\sqrt{2}}(|\uparrow\downarrow\rangle_{LR} + |\downarrow\uparrow\rangle_{LR})$ and $|s\rangle = \frac{1}{\sqrt{2}}(|\uparrow\downarrow\rangle_{LR} - |\downarrow\uparrow\rangle_{LR})$ are the triplet and singlet spin states. Since $U_{ee} = \infty$, all four of these states have zero energy and the ground-state phase diagram is trivial.

The four states in the $T^z = -1$ manifold (two g atoms) are split by $H_{(1,0)}$ into two energy manifolds:

$$|gg\rangle|t\rangle, \quad E = 0, \quad (\text{G.4})$$

$$|gg\rangle|s\rangle, \quad E = -\frac{4J_g^2}{U_{gg}}. \quad (\text{G.5})$$

Only $|gg\rangle|s\rangle$ can take advantage of the virtual tunneling since two g atoms in the triplet spin states cannot sit on the same site. Which of the two manifolds is the ground manifold depends on the sign of U_{gg} , as shown in the ground-state phase diagram in Fig. 7.3a. It is important to emphasize that for $U_{gg} < 0$, the subspace of one g atom per site may be subject to extra loss down to the lower energy states that have both g atoms in the same well. It is also worth noting that the diagram is only valid for $J_g \ll |U_{gg}|$.

Finally, the eight states in the $T^z = 0$ manifold (one g atom and one e atom) are split by $H_{(1,0)}$ into four energy manifolds:

$$|\Sigma\rangle|t\rangle, \quad E = -\frac{(J_g + J_e)^2}{U_{eg}^-}, \quad (\text{G.6})$$

$$|\tau\rangle|s\rangle, \quad E = -\frac{(J_g + J_e)^2}{U_{eg}^+}, \quad (\text{G.7})$$

$$|\tau\rangle|t\rangle, \quad E = -\frac{(J_g - J_e)^2}{U_{eg}^-}, \quad (\text{G.8})$$

$$|\Sigma\rangle|s\rangle, \quad E = -\frac{(J_g - J_e)^2}{U_{eg}^+}, \quad (\text{G.9})$$

where $|\Sigma\rangle = \frac{1}{\sqrt{2}}(|eg\rangle_{LR} - |ge\rangle_{LR})$ and $|\tau\rangle = \frac{1}{\sqrt{2}}(|eg\rangle_{LR} + |ge\rangle_{LR})$ are anti-symmetric and symmetric orbital states, respectively. The denominators U_{eg}^- and U_{eg}^+ in the energies of the $|t\rangle$ and $|s\rangle$ states, respectively, reflect the fact that tunneling preserves the nuclear spin. At the same time, the \pm signs in the numerators can be understood by considering the case $J_g = J_e$, when all states with overall symmetry under particle exchange must have zero energy since for these states tunneling is forbidden due to the Pauli exclusion principle. The corresponding ground-state phase diagram as a function of the signs and relative magnitude of U_{eg}^+ and U_{eg}^- is shown in Fig. 7.3b. As in the case of the $T^z = 1$ phase diagram, negative interaction energies may lead to increased losses.

G.8 Double-Well Kugel-Khomskii and RKKY Experiments

In the main text and in Sec. G.11, we discuss the open questions and previously unexplored regimes associated with the SU(N) Kugel-Khomskii and Kondo lattice models (KLM) that can be studied with ultracold alkaline-earth atoms. As a stepping stone toward these many-body experiments, we propose in this Section two proof-of-principle experiments along the lines of Ref. [204] in an array of isolated double wells with $N = 2$ (with the spin basis $\{\uparrow, \downarrow\}$): one to probe the spin-orbital interactions of

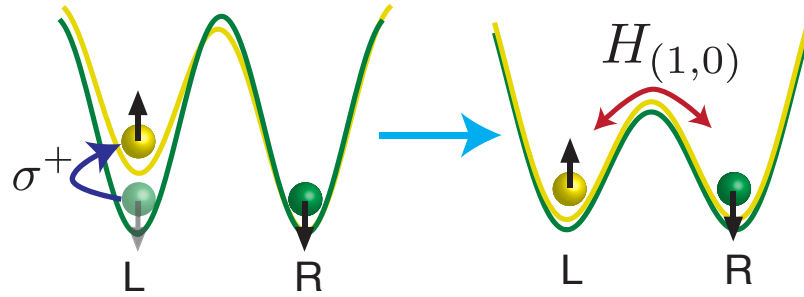


Figure G.3: **A schematic diagram describing the preparation of the double-well state $|e, \uparrow\rangle_L |g, \downarrow\rangle_R$.**

the Kugel-Khomskii model and one to probe the RKKY interactions associated with KLM.

To probe the spin-orbital interactions giving rise to the $T^z = 0$ diagram in Fig. 7.3b, we first have to prepare an array of independent double wells in the state $|e, \uparrow\rangle_L |g, \downarrow\rangle_R$. After loading a band insulator of $|g, \downarrow\rangle$ atoms in a deep optical lattice, an additional lattice for both g (green) and e (yellow) atoms with twice the spacing of the first lattice is turned on in one direction to create an array of independent double wells [204]. Then, as shown in Fig. G.3, in the presence of an e -lattice bias, σ^+ polarized light on resonance with the $|g, \downarrow\rangle_L \rightarrow |e, \uparrow\rangle_L$ transition can be used to prepare the state $|e, \uparrow\rangle_L |g, \downarrow\rangle_R$.

Having shown how to prepare an array of independent double wells in the state $|e, \uparrow\rangle_L |g, \downarrow\rangle_R$, we note that this state is a superposition of the four eigenstates featured in Fig. 7.3b. The energies of these four eigenstates [Eqs. (G.6-G.9)] can be extracted from the Fourier analysis of the population imbalance as a function of time: $\Delta N(t) = n_{eR} + n_{gL} - n_{gR} - n_{eL} = -\cos\left[\frac{4tJ_eJ_g}{\hbar U_{eg}^-}\right] - \cos\left[\frac{4tJ_eJ_g}{\hbar U_{eg}^+}\right]$. ΔN can be measured by combining the dumping technique, band mapping, and Stern-Gerlach filtering of Ref. [204] with the use of two probe laser frequencies to distinguish between $|g\rangle$ and $|e\rangle$. For examples of earlier orbital physics studies with ultracold atoms, where the orbitals are distinguished only by the different motional states of the atoms, we refer the reader to Refs. [378, 379, 380, 381, 382, 383] and references therein.

We now turn to the double-well experiment aimed at probing RKKY interactions. Here we need to prepare the initial state $\frac{1}{\sqrt{2}}(|g, \downarrow\rangle_L + |g, \downarrow\rangle_R)|e, \downarrow\rangle_L |e, \uparrow\rangle_R$ (see Fig. G.4a). The first step to prepare this state is to load a band insulator with three $|g, \downarrow\rangle$ atoms per site on the long lattice and then slowly ramp up the short lattice with a bias so that it is energetically favorable to have two atoms in the left well and one in the right well. Next one can change the state of the right atom from $|g, \downarrow\rangle_R$ to $|e, \uparrow\rangle_R$ by applying a π pulse of σ^+ polarized light resonant with this single-atom transition. The left well will be unaffected because the spectrum is modified by the interactions

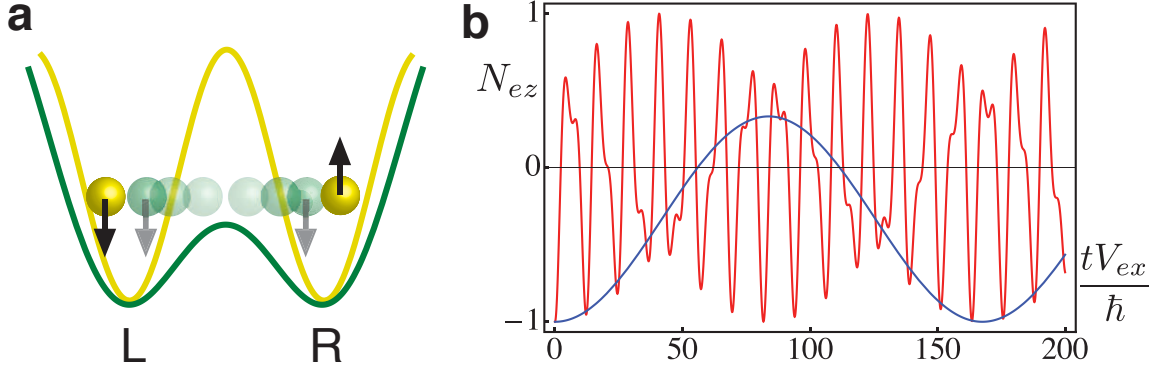


Figure G.4: **Proof-of-principle experiment to probe RKKY interactions in an array of isolated double wells.** **a**, Schematic representation of the initial state $\frac{1}{\sqrt{2}}(|g, \downarrow\rangle_L + |g, \downarrow\rangle_R)|e, \downarrow\rangle_L|e, \uparrow\rangle_R$. **b**, In the limit $|V_{ex}| \ll J_g$, the Neel order parameter for the e atoms $[N_{ez}(t) = \frac{1}{2}[n_{e\uparrow L} - n_{e\downarrow L} - (n_{e\uparrow R} - n_{e\downarrow R})]]$ is $N_{ez}(t) \approx -\frac{1}{3} \cos\left(\frac{V_{ex}t}{\hbar}\right) - \frac{2}{3} \cos\left(\frac{V_{ex}t}{2\hbar} - \frac{3V_{ex}^2t}{8J_g\hbar}\right)$, which is shown in red for $V_{ex} = -J_g/10$. It exhibits fast oscillations with frequency $\sim V_{ex}$, modulated by an envelope of frequency $\sim V_{ex}^2/J_g$ induced by RKKY interactions $\left(-\frac{1}{3} - \frac{2}{3} \cos\left(\frac{3V_{ex}^2t}{8J_g\hbar}\right)\right)$ shown in blue).

(if interactions alone do not provide the desired selectivity, one could, for example, change the bias of the e -lattice). The next step is to change the state of the left well from two $|g, \downarrow\rangle_L$ atoms populating the lowest two vibrational states to $|e, \downarrow\rangle_L|g, \downarrow\rangle_L$ both populating the lowest vibrational state. This can be accomplished by using π -polarized traveling wave laser light to apply a π pulse resonant with the transition between these two many-body states [382]. This results in $|e, \downarrow\rangle_L|g, \downarrow\rangle_L|e, \uparrow\rangle_R$. One can then temporarily shift the g and e lattices relative to each other to set U_{eg}^\pm interactions to zero, then make J_g nonzero, and wait until the g atom evolves into the desired superposition $\frac{1}{\sqrt{2}}(|g, \downarrow\rangle_L + |g, \downarrow\rangle_R)$ via tunneling. This yields the desired state $\frac{1}{\sqrt{2}}(|g, \downarrow\rangle_L + |g, \downarrow\rangle_R)|e, \downarrow\rangle_L|e, \uparrow\rangle_R$.

After preparing the state $\frac{1}{\sqrt{2}}(|g, \downarrow\rangle_L + |g, \downarrow\rangle_R)|e, \downarrow\rangle_L|e, \uparrow\rangle_R$, we propose to monitor the Neel order parameter for the e atoms, $N_{ez} = \frac{1}{2}[n_{e\uparrow L} - n_{e\downarrow L} - (n_{e\uparrow R} - n_{e\downarrow R})]$. In the limit $|V_{ex}| \ll J_g$, $N_{ez}(t) = -\frac{1}{3} \cos\left(\frac{V_{ex}t}{\hbar}\right) - \frac{2}{3} \cos\left(\frac{V_{ex}t}{2\hbar} - \frac{3V_{ex}^2t}{8J_g\hbar}\right)$. In Fig. G.4, we present the plot of $N_{ez}(t)$ for $V_{ex} = -J_g/10$. It exhibits fast oscillations with frequency $\sim V_{ex}$, modulated by an envelope of frequency $\sim V_{ex}^2/J_g$ induced by RKKY interactions. In order to probe RKKY interactions only, it is important to suppress super-exchange $\sim J_e^2/U_{ee}$ and thus to choose J_e/U_{ee} small. To study the full spatial dependence of RKKY interactions, one must of course go beyond the double-well setup. We also note that recent experiments using alkali atoms populating the lowest two vibrational levels of a deep optical lattice have measured the local singlet-triplet splitting induced

by V_{ex} [383].

G.9 Effects of Three-Body Recombination

Three-body recombination [384, 385, 386, 387, 368] is a process during which three atoms come together to form a diatomic bound state and a single atom, and both final products have enough kinetic energy to leave the trap. While in certain cases, three-body recombination can be an asset [368], usually it results in the loss of atoms and, thus, limits the duration of the experiment. For our purposes, we can describe three-body recombination by a decay rate γ_3 [368] resulting in a loss of three particles from one site. This rate will likely depend on what atomic states are involved and, to the best of our knowledge, has not yet been measured or calculated for fermionic alkaline-earth atoms.

Out of the four examples [Eqs. (7.6-7.8) and Eq. (G.3)] that we discuss, only $H_{(1,1)}$ [Eq. (G.3)] and $H_{(p,0)}$ [Eq. (7.7)] may be affected by three-body recombination (H_{KLM} [Eq. (7.8)] assumes negligible g - g interactions, such as in a very shallow g lattice or with a low density of g atoms). In the case of $H_{(1,1)}$, two g atoms and one e atom occupy the same site virtually in the intermediate state that gives rise to the second order spin Hamiltonian with interaction strength $\propto J_g^2/(U_{gg} + V_{ex})$. Thinking of γ_3 as an effective linewidth for the intermediate state, $H_{(1,1)}$ will be valid and losses small provided that γ_3 is smaller than the effective "detuning" $U_{gg} + V_{ex}$. Since scattering lengths for alkaline-earth atoms [248, 249, 215] are comparable to those for alkali atoms, $U_{gg} + V_{ex}$ can be on the order of several kHz [204]. At the same time, $1/\gamma_3$ for bosonic alkali atoms in deep traps can be on the order of 1 s [388]. If γ_3 were the same in our case, $\gamma_3 \ll U_{gg} + V_{ex}$ would be satisfied. Ways of controlling the interactions via optical Feshbach resonances [139, 370, 248, 371, 372] may also be envisioned.

In the case of $H_{(p,0)}$ [Eq. (7.7)], $(n_A, n_B) = (1, 1)$ does not suffer from three-body recombination. $(n_A, n_B) = (1, 2)$ and $(2, 2)$ may have three atoms per site virtually. As in the discussion of $H_{(1,1)}$, provided γ_3 associated with three g atoms per site is smaller than U_{gg} , these configurations should be accessible. For the case $(n_A, n_B) = (1, 2)$, $\gamma_3 \gg U_{gg}$ is also acceptable, since it will effectively prohibit the tunneling of the atoms to the state with 3 atoms on a site [368], but the interaction can still take place through the intermediate state, in which an atom from a B site tunnels to an A site and back. One can also envision ways to use optical Feshbach resonance techniques [139, 370, 248] to induce large γ_3 . To be able to resolve the superexchange coupling $\sim J_g^2/U_{gg}$ in cases where n_A or n_B is equal to 3, one must have $\gamma_3 < J_g^2/U_{gg}$. Given that superexchange coupling can be as high as 1 kHz [204], this condition should also be achievable. Although n_A or n_B greater than 3 will result in even shorter lifetimes [386], there is a good chance that relatively large n_A and n_B can be achieved: at least, for bosonic alkali atoms in an $n = 5$ Mott insulator state, the lifetime can still be as long as 0.2 s [388].

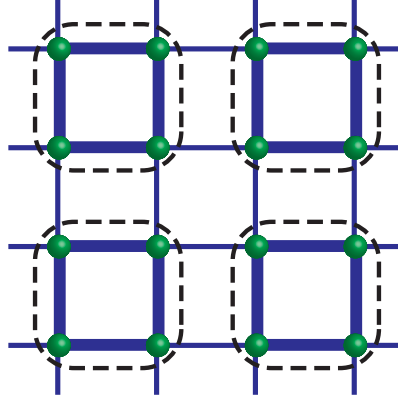


Figure G.5: **Square lattice valence plaquette solid for $N = 4$.** When $N = 4$ and $n_A = n_B = 1$, four sites are required to form an $SU(4)$ singlet; these singlets can in turn form the schematically shown plaquette-ordered state or a disordered phase made of resonant plaquette states [389]. Thick bonds connect spins that are more strongly correlated than spins connected by thin bonds, while dashed lines encircle (approximate) $SU(4)$ singlets.

G.10 The $(p, 0)$ Spin Hamiltonian with $n_A = n_B \neq N/2$

In the main text, we focused on one special case of the antiferromagnetic $(p, 0)$ spin Hamiltonian on a square lattice, that with $n_A + n_B = N$ (where n_A and n_B denote the number of atoms per site on the two sublattices). In this Section, we describe another interesting and experimentally relevant case, $n_A = n_B \neq N/2$ [390, 242, 391, 389, 241, 392, 393, 243]. Potential ground states include states built from valence *plaquettes* (Fig. G.5) [390, 242], resonant *plaquette* states [389], and topological spin liquids [391, 243]. Valence plaquette states and resonant plaquette states are the natural generalization of VBS states and resonant valence bond states (RVB) [394], respectively; for example, when $n_A = n_B = 1$, N lattice sites are needed to form a $SU(N)$ singlet. Fig. G.5 depicts a square lattice valence plaquette solid for $n_A = n_B = 1$ and $N = 4$. Techniques for detecting some of these phases are discussed in Ref. [243]. The experiment described in the main text for the case $n_A + n_B = N$ can also be generalized to probe the $n_A = n_B \neq N/2$ phase diagram including exotic phases such as valence plaquette solids [Fig. G.5], as well as competing magnetically ordered states. The main difference is that after preparing a band insulator of $N g$ atoms per site, each site should be split not necessarily into two sites but into the number of sites that is appropriate for the case being considered (e.g. 4 for the case shown in Fig. G.5).

G.11 Physics Accessible with the Alkaline-Earth Kondo Lattice Model

The alkaline-earth atom realization of the AF KLM is well-suited to access a number of parameter regimes that are out of reach in solid state materials. One example is the one dimensional (1D) limit, since, to our knowledge, real solid state materials exhibiting KLM physics are restricted to 2D or 3D. Another example is the regime of large Kondo exchange ($|V_{ex}| \gg J_g$), which is interesting even for $N = 2$. In this limit the system is well described by the $U \rightarrow \infty$ Hubbard model [227] by identifying the Kondo singlets with empty sites (holes) and the unpaired localized spins with hard core electrons. From this mapping, possible ferromagnetic ordering is expected at small hole concentration (small n_g), however the stability of this phase for increasing hole concentration and finite $|V_{ex}|$ values remains unknown. For general N , in the extreme limit $J_g = 0$, the ground state is highly degenerate: for any distribution of the g atom density $n_{jg} < N$, there is a ground state (with further spin degeneracy), where on each site the spins combine antisymmetrically to minimize the exchange interaction. Lifting of such extensive degeneracies often leads to novel ground states; this will be addressed in future studies using degenerate perturbation theory in J_g/V_{ex} . For $N > 2$, AF SU(N) spin models have a different kind of extensive degeneracy, which was argued to destroy antiferromagnetism and to lead to non-magnetic spin liquid and VBS-like ground states [243]. Similar expectations are likely to apply to the KLM at small $|V_{ex}|/J_g$, where the $N = 2$ antiferromagnetism may give way to situations where the localized spins form a non-magnetic state that is effectively decoupled from the mobile fermions [231].

Even though we have set U_{gg} to zero in Eq. (7.8), it can be tuned, for example, by adjusting the g -lattice depth and can give rise to interesting physics. For example, the $n_g = 1$ case, which is known to be for $N = 2$ either an antiferromagnetic insulator or a Kondo insulator depending on the ratio $|V_{ex}|/J_g$ [228], will become for large enough U_{gg} and $N > 2$ a Mott insulator, because the two atoms on each site cannot combine to form an SU(N) singlet. If n_g is reduced from unity, the doping of this Mott insulator can be studied, and it will be interesting to understand how this physics, usually associated with cuprate superconductors, is related to the other ground states of the KLM, usually associated with heavy fermion compounds.